Seismic Performance of Reinforced Concrete Filled Steel Tubes in Soil

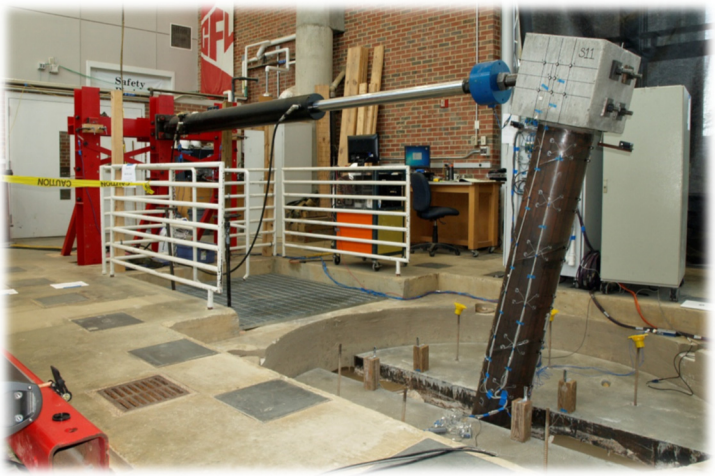

DECEMBER 2016

Prepared By:
Diego A. Aguirre-Realpe, *Research Assistant*
Dr. Mervyn J. Kowalsky, *Principal Investigator*
Dr. James M. Nau, *Co-Principal Investigator*
Dr. Mohammed Gabr, *Co-Principal Investigator*

North Carolina State University Raleigh, NC

Prepared For:
Alaska Department of Transportation & Public Facilities
Research, Development, and Technology Transfer
P.O. Box 112500
3132 Channel Drive
Juneau, Alaska 99811-2500

and

Federal Highway Administration
P.O. Box 21648
709 West 9th Street
Juneau, Alaska 99802-1648

REPORT DOCUMENTATION PAGE

Form approved OMB No.

Public reporting for this collection of information is estimated to average 1 hour per response, including the time for reviewing instructions, searching existing data sources, gathering and maintaining the data needed, and completing and reviewing the collection of information. Send comments regarding this burden estimate or any other aspect of this collection of information, including suggestion for reducing this burden to Washington Headquarters Services, Directorate for Information Operations and Reports, 1215 Jefferson Davis Highway, Suite 1204, Arlington, VA 22202-4302, and to the Office of Management and Budget, Paperwork Reduction Project (0704-1833), Washington, DC 20503

1. AGENCY USE ONLY (LEAVE BLANK)	2. REPORT DATE	3. REPORT TYPE AND DATES COVERED
4000(127)	December 31, 2016	FINAL, August 2013 – December 2016

4. TITLE AND SUBTITLE

Seismic Performance of Reinforced Concrete Filled Steel Tubes in Soil

5. FUNDING NUMBERS

Federal # 4000(127)
IRIS # Z642030000

6. AUTHOR(S)

Mr. Diego A. Aguirre-Realpe, *Graduate Research Assistant*
Dr. Mervyn J. Kowalsky, *Principal Investigator*
Dr. James M. Nau, *Co-Principal Investigator*
Dr. Mohammed Gabr, *Co-Principal Investigator*

7. PERFORMING ORGANIZATION NAME(S) AND ADDRESS(ES)

8. PERFORMING ORGANIZATION REPORT NUMBER

4000(127)

9. SPONSORING/MONITORING AGENCY NAME(S) AND ADDRESS(ES)

Alaska Department of Transportation and Public Facilities
Research, Development &Technology Transfer
3132 Channel Drive
Juneau, Alaska 99811-2500

10. SPONSORING/MONITORING AGENCY REPORT NUMBER

4000(127)

11. SUPPLEMENTARY NOTES

12a. DISTRIBUTION / AVAILABILITY STATEMENT

Copies available online at http://www.dot.alaska.gov/stwddes/research/search_lib.shtml

12b. DISTRIBUTION CODE

13. ABSTRACT (Maximum 200 words)

Reinforced concrete filled steel tube pile-columns are structural elements commonly used in bridge supports in high seismic regions because RCFSTs provide increased levels of strength, ductility, and energy dissipation as compared with traditional systems such as reinforced concrete (RC) or steel substructures. This study includes experimental and analytical studies that considered three main parameters: the diameter-to-thickness (D/t) ratio, the above-ground length (La), and the soil stiffness.

14. KEYWORDS : bridge design, concrete filled, seismic design, soil stiffness

15. NUMBER OF PAGES

517

16. PRICE CODE

N/A

17. SECURITY CLASSIFICATION OF REPORT	18. SECURITY CLASSIFICATION OF THIS PAGE	19. SECURITY CLASSIFICATION OF ABSTRACT	20. LIMITATION OF ABSTRACT
Unclassified	Unclassified	Unclassified	None

Notice

This document is disseminated under the sponsorship of the U.S. Department of Transportation in the interest of information exchange. The U.S. Government assumes no liability for the use of the information contained in this document.

The U.S. Government does not endorse products or manufacturers. Trademarks or manufacturers' names appear in this report only because they are considered essential to the objective of the document.

Quality Assurance Statement

The Federal Highway Administration (FHWA) provides high-quality information to serve Government, industry, and the public in a manner that promotes public understanding. Standards and policies are used to ensure and maximize the quality, objectivity, utility, and integrity of its information. FHWA periodically reviews quality issues and adjusts its programs and processes to ensure continuous quality improvement.

Author's Disclaimer

Opinions and conclusions expressed or implied in the report are those of the author. They are not necessarily those of the Alaska DOT&PF or funding agencies.

SI* (MODERN METRIC) CONVERSION FACTORS

APPROXIMATE CONVERSIONS TO SI UNITS

Symbol	When You Know	Multiply By	To Find	Symbol
		LENGTH		
in	inches	25.4	millimeters	mm
ft	feet	0.305	meters	m
yd	yards	0.914	meters	m
mi	miles	1.61	kilometers	km
		AREA		
in^2	square inches	645.2	square millimeters	mm^2
ft^2	square feet	0.093	square meters	m^2
yd^2	square yard	0.836	square meters	m^2
ac	acres	0.405	hectares	ha
mi^2	square miles	2.59	square kilometers	km^2
		VOLUME		
fl oz	fluid ounces	29.57	milliliters	mL
gal	gallons	3.785	liters	L
ft^3	cubic feet	0.028	cubic meters	m^3
yd^3	cubic yards	0.765	cubic meters	m^3
	NOTE: volumes greater than 1000 L shall be shown in m^3			
		MASS		
oz	ounces	28.35	grams	g
lb	pounds	0.454	kilograms	kg
T	short tons (2000 lb)	0.907	megagrams (or "metric ton")	Mg (or "t")
		TEMPERATURE (exact degrees)		
°F	Fahrenheit	5 (F-32)/9 or (F-32)/1.8	Celsius	°C
		ILLUMINATION		
fc	foot-candles	10.76	lux	lx
fl	foot-Lamberts	3.426	candela/m^2	cd/m^2
		FORCE and PRESSURE or STRESS		
lbf	poundforce	4.45	newtons	N
lbf/in^2	poundforce per square inch	6.89	kilopascals	kPa

APPROXIMATE CONVERSIONS FROM SI UNITS

Symbol	When You Know	Multiply By	To Find	Symbol
		LENGTH		
mm	millimeters	0.039	inches	in
m	meters	3.28	feet	ft
m	meters	1.09	yards	yd
km	kilometers	0.621	miles	mi
		AREA		
mm^2	square millimeters	0.0016	square inches	in^2
m^2	square meters	10.764	square feet	ft^2
m^2	square meters	1.195	square yards	yd^2
ha	hectares	2.47	acres	ac
km^2	square kilometers	0.386	square miles	mi^2
		VOLUME		
mL	milliliters	0.034	fluid ounces	fl oz
L	liters	0.264	gallons	gal
m^3	cubic meters	35.314	cubic feet	ft^3 m^3
	cubic meters	1.307	cubic yards	yd^3
		MASS		
g	grams	0.035	ounces	oz
kg	kilograms	2.202	pounds	lb
Mg (or "t")	megagrams (or "metric ton")	1.103	short tons (2000 lb)	T
		TEMPERATURE (exact degrees)		
°C	Celsius	1.8C+32	Fahrenheit	°F
		ILLUMINATION		
lx	lux	0.0929	foot-candles	fc
cd/m^2	candela/m^2	0.2919	foot-Lamberts	fl
		FORCE and PRESSURE or STRESS		
N	newtons	0.225	poundforce	lbf
kPa	kilopascals	0.145	poundforce per square inch	lbf/in^2

*SI is the symbol for the International System of Units. Appropriate rounding should be made to comply with Section 4 of ASTM E380.
(Revised March 2003)

TABLE OF CONTENTS

LIST OF FIGURES ..... **xiv**
LIST OF TABLES ..... **xxxii**
ACKNOWLEDGEMENTS ..... **xxxiv**
ABSTRACT ..... **xxxiv**
EXECUTIVE SUMMARY ..... **xxxv**

CHAPTER 1 ..... **1**
1. INTRODUCTION **1**
1.1. Background 1
1.2. Motivation 2
1.3. Scope and Layout 2

CHAPTER 2 ..... **3**
2. LITERATURE REVIEW **3**
2.1. Concrete Filled Steel Tubes (CFSTs) 3
2.1.1. Marson and Bruneau (2004) 3
2.1.2. Sakino et al. (2004) 4
2.1.3. Ellobody et al. (2006) 4
2.1.4. Chen et al. (2011) 4
2.1.5. Gajalakshmi and Helena (2012) 5
2.2. Reinforced Concrete Filled Steel Tubes (RCFSTs) 5
2.2.1. Park et al. (1983) 5
2.2.2. Richards et al. (2011) 6
2.2.3. Montejo et al. (2012) 6
2.2.4. Brown et al. (2015) 7
2.3. Relevant Studies on Reinforced Concrete (RC) Pile-Columns 8
2.3.1. Chai and Hutchinson (2002) 8
2.3.2. Suleiman et al. (2006) 9
2.3.3. Chang and Hutchinson (2013) 9
2.4. Soil-Structure Interaction (SSI) 10
2.4.1. Boulanger et al. (1999) 10

2.4.2. El Naggar and Bentley (2000) 11
2.4.3. Sritharan et al. (2007) 11
2.4.4. Allotey and El Naggar (2008a, 2008b) 12
2.4.5. Wotherspoon et al. (2010) 12
2.5. Plastic Hinge Models for Pile-Columns 13
2.5.1. Budek et al. (1995, 2000) 13
2.5.2. Chai (2002) 15
2.5.3. Suarez and Kowalsky (2007) 16
2.5.4. SCDOT Seismic Design Specifications for Highway Bridges (2008) 18
2.5.5. Chiou et al. (2009) 19
2.5.6. Caltrans (2013) 19
2.5.7. Goel (2015) 21

CHAPTER 3 22
3. STUDY PLAN 22
3.1. Research Gap 22
3.2. Objectives 23

CHAPTER 4 24
4. METHODS 24
4.1. Experimental Program 24
4.1.1. Test Specimen Description 24
4.1.2. Soil-Structure Interaction (SSI) Facility 25
4.1.2.1 Geotechnical Laboratory 25
4.1.2.2 Lateral Loading 26
4.1.2.3 Soil-Sandwich Concept 27
4.1.2.4 Soil Surcharge System 28
4.1.2.4.1 Effects of Surcharge Loading on Soil Stresses 30
4.1.2.5 Pile Insertion and Removal 32
4.1.3. Test Setup and Instrumentation 34
4.1.3.1 Determination of Strain and Displacement Profiles from Rotation Data 39
4.1.4. Loading Protocol 42

4.1.5. Test Matrix 43
4.2. Analytical Model 44
4.2.1. Modeling Approach 44
4.2.2. Material Models 47
4.2.3. Non-Linear Soil Springs for Laboratory Conditions 47
4.2.4. Calibration and Validation of FE Analytical Model 51
4.2.5. Non-Linear Soil Springs for Field Conditions 59
4.2.5.1 P-y Curves for Sand 59
4.2.5.2 P-y Curves for Clay 61
4.3. Equivalent Cantilever Plastic Hinge Model for RCFSTs 62
4.3.1. Pinned-Head RCFST Shafts 64
4.3.2. Fixed-Head RCFST Shafts 65
4.3.3. Performance Limit States 67
4.3.3.1 Pinned-Head RCFST Shafts 67
4.3.3.2 Fixed-Head RCFST Shafts 68
4.4. Equivalent Viscous Damping of RCFSTs 69
4.5. Parametric Studies 71
4.5.1. Description 71
4.5.2. Parameter Definition 71
4.5.3. Procedure 72
4.5.3.1 Section Analysis 73
4.5.3.2 Pinned-Head RCFST Shafts 73
4.5.3.3 Fixed-Head RCFST Shafts 74
4.5.3.4 Equivalent Viscous Damping 74

CHAPTER 5 75
5. EXPERIMENTAL RESULTS 75
5.1. Experimental Observations 75
5.1.1. Material Properties 76
5.1.1.1 Steel Tube 76
5.1.1.2 Internal Reinforcement 83
5.1.1.3 Concrete 90
5.1.1.4 Soil 92

5.1.1.5 Summary of Material Properties 92
5.1.2. Test 1 93
5.1.2.1 Test 1 Summary 93
5.1.2.2 Test 1 Observations 93
5.1.2.3 Test 1 Conclusions 95
5.1.3. Test 2 96
5.1.3.1 Test 2 Summary 96
5.1.3.2 Test 2 Observations 96
5.1.3.3 Test 2 Conclusions 98
5.1.4. Test 3 99
5.1.4.1 Test 3 Summary 99
5.1.4.2 Test 3 Observations 99
5.1.4.3 Test 3 Conclusions 101
5.1.5. Test 4 102
5.1.5.1 Test 4 Summary 102
5.1.5.2 Test 4 Observations 102
5.1.5.3 Test 4 Conclusions 104
5.1.6. Test 5 105
5.1.6.1 Test 5 Summary 105
5.1.6.2 Test 5 Observations 105
5.1.6.3 Test 5 Conclusions 107
5.1.7. Test 6 108
5.1.7.1 Test 6 Summary 108
5.1.7.2 Test 6 Observations 108
5.1.7.3 Test 6 Conclusions 110
5.1.8. Test 7 111
5.1.8.1 Test 7 Summary 111
5.1.8.2 Test 7 Observations 111
5.1.8.3 Test 7 Conclusions 113
5.1.9. Test 8 114
5.1.9.1 Test 8 Summary 114
5.1.9.2 Test 8 Observations 114
5.1.9.3 Test 8 Conclusions 116

5.1.10. Test 9 117
5.1.10.1 Test 9 Summary 117
5.1.10.2 Test 9 Observations 117
5.1.10.3 Test 9 Conclusions 119
5.1.11. Test 10 120
5.1.11.1 Test 10 Summary 120
5.1.11.2 Test 10 Observations 120
5.1.11.3 Test 10 Conclusions 122
5.1.12. Test 11 123
5.1.12.1 Test 11 Summary 123
5.1.12.2 Test 11 Observations 123
5.1.12.3 Test 11 Conclusions 125
5.1.13. Test 12 126
5.1.13.1 Test 12 Summary 126
5.1.13.2 Test 12 Observations 126
5.1.13.3 Test 12 Conclusions 128
5.2. Summary of Experimental Observations 129
5.2.1. Failure Mechanism 131
5.2.2. Influence of Tube Spiral Welds 131
5.2.3. Depth to Plastic Hinge 133
5.2.4. Force–Displacement Response 134
5.2.5. Hysteretic Equivalent Viscous Damping 137
5.2.6. Strain Limit States 139

CHAPTER 6 142
6. PARAMETRIC STUDY RESULTS 142
6.1. Section Analysis 142
6.1.1. Yield curvature parameter for RCFSTs 142
6.1.2. Neutral Axis Depth for RCFSTs 143
6.2. Pinned-Head RCFST Shafts 144
6.2.1. Depth to Plastic Hinge 145
6.2.2. Yield Displacement Parameter 149
6.2.3. Plastic Hinge Length 153

6.2.4. Equivalent Viscous Damping 159
6.3. Fixed-Head RCFST Shafts 162
6.3.1. Depth to Plastic Hinge 163
6.3.2. Yield Displacement Parameter 167
6.3.3. Plastic Displacement Parameter 171
6.3.4. Equivalent Viscous Damping 175
6.4. Depth to plastic Hinge Revisited 178
6.5. Evaluation of the Proposed Model 181
6.6. Summary of System Behavior from Simulated Data 183
6.6.1. Pinned-Head RCFST Shafts 183
6.6.1.1 Force-Displacement Response 183
6.6.1.2 Displacement-Moment-Shear Distribution 184
6.6.1.3 Moment-Curvature-Tensile Strain Distribution 186
6.6.1.4 Tensile Strain-Displacement Envelopes 188
6.6.2. Fixed-Head RCFST Shafts 190
6.6.2.1 Force-Displacement Response 190
6.6.2.2 Displacement-Moment-Shear Distribution 191
6.6.2.3 Moment-Curvature-Tensile Strain Distribution 193
6.6.2.4 Tensile Strain-Displacement Envelopes 194

CHAPTER 7 196
7. DESIGN RECOMMENDATIONS 196
7.1. Pinned-Head RCFST Shafts 197
7.1.1. System Behavior and Performance Limit States 197
7.1.2. Proposed Model and Examples 199
7.1.2.1 Equations for Sand 199
7.1.2.2 Equations for Clay 201
7.1.2.3 Example: displacement capacity or design displacement 202
7.1.2.3.1 Sand 203
7.1.2.3.2 Clay 204
7.2. Fixed-Head RCFST Shafts 205
7.2.1. System Behavior 205
7.2.2. Proposed Model and Examples 208

7.2.2.1 Equations for Sand 209
7.2.2.2 Equations for Clay 211
7.2.2.3 Example: displacement capacity or design displacement 212
7.2.2.3.1 Sand 213
7.2.2.3.2 Clay 214
7.3. Final Remarks on Analytical and Experimental Results 216
7.3.1. Summary 216
7.3.2. Laboratory vs. Free-Field Conditions 217
7.3.3. Modeling Approach and Implications 217

CHAPTER 8 219
8. CONCLUSIONS 219
8.1. Summary 219
8.2. Pinned-Head RCFST Shafts 220
8.3. Fixed-Head RCFST Shafts 221
8.4. Future Research 222

CHAPTER 9 224
9. REFERENCES 224

CHAPTER 10 228
10. APPENDICES 228
APPENDIX A: Short reports of experimental tests 228
Test 1 Summary Report 229
Executive Summary 229
Specimen and Test Description 229
Specimen Response 234
Conclusions 246
Test 2 Summary Report 247
Executive Summary 247
Specimen and Test Description 247
Specimen Response 253
Conclusions 260

Test 3 Summary Report 261
Executive Summary 261
Specimen and Test Description 261
Specimen Response 266
Conclusions 275
Test 4 Summary Report 276
Executive Summary 276
Specimen and Test Description 276
Specimen Response 282
Conclusions 290
Test 5 Summary Report 292
Executive Summary 292
Specimen and Test Description 292
Specimen Response 297
Conclusions 310
Test 6 Summary Report 311
Executive Summary 311
Specimen and Test Description 311
Specimen Response 317
Conclusions 330
Test 7 Summary Report 331
Executive Summary 331
Specimen and Test Description 331
Specimen Response 336
Conclusions 350
Test 8 Summary Report 351
Executive Summary 351
Specimen and Test Description 351
Specimen Response 357
Conclusions 369
Test 9 Summary Report 370
Executive Summary 370
Specimen and Test Description 371

Specimen Response 376
Response Comparison 388
Conclusions 391
Test 10 Summary Report 392
Executive Summary 392
Specimen and Test Description 392
Specimen Response 397
Conclusions 410
Test 11 Summary Report 411
Executive Summary 411
Specimen and Test Description 411
Specimen Response 417
Conclusions 427
Test 12 Summary Report 428
Executive Summary 428
Specimen and Test Description 428
Specimen Response 433
Conclusions 446
APPENDIX B: Force, displacement, and tensile strain data 447
APPENDIX C: Steel tube mill certs 470
APPENDIX C: Internal reinforcement mill certs 475

LIST OF FIGURES

Figure 1-1 (a) Gakona River Bridge (courtesy of Elmer Marx), (b) typical RCFST cross section, and (c) pile-column system 1
Figure 2-1 Plastic hinge model for RC drilled shafts (Budek et al. 1995) 14
Figure 2-2 Equivalent cantilever in single bending (Suarez and Kowalsky, 2007) 17
Figure 2-3 Equivalent cantilever in double bending (Suarez and Kowalsky, 2007) 17
Figure 2-4 Plastic hinge model for Type I drilled shafts (Caltrans 2013) 20
Figure 4-1 RCFST pile-column specimen cross section 25
Figure 4-2 CFL geotechnical laboratory floor plan view 25
Figure 4-3 Lateral loading frame 26
Figure 4-4 Soil surcharge system (soil-sandwich concept) 28
Figure 4-5 Soil surcharge system schematic: (a) elevation view and (b) plan view 29
Figure 4-6 Soil surcharge testing 30
Figure 4-7 Vertical pressure increase at: (a) location A and (b) location B 31
Figure 4-8 Confining pressure increase (measured at pit wall) 31
Figure 4-9 New water diffuser: (a) sketch elevation and (b) photograph looking into the pit 33
Figure 4-10 Pinned-head, RCFST pile-column test setup schematic elevation 35
Figure 4-11 Pinned-head, RCFST pile-column test setup with specimen subjected to substantial lateral displacement 36
Figure 4-12 Instrumentation for RCFST pile-column specimen with column length of 5.5D 37
Figure 4-13 Instrumentation for RCFST pile-column specimen with column length of 7.5D 38
Figure 4-14 Strain gauge sensors: (a) SG sensor after installation, (b) hot-glued aluminum angle for friction protection, and (c) butyl tape for moisture protection 39
Figure 4-15 Inclinometer sensors: (a) 2-foot gauge length inclinometer and (b) PVC casing (blue pipe) at centroid of specimen cross section along its length 39
Figure 4-16 Schematic calculation of curvature and displacement profiles 40
Figure 4-17 Example of curvature and displacement profiles calculation 41
Figure 4-18 (a) Typical displacement history and (b) example of a positive deformed shape 43
Figure 4-19 Modeling approach 45
Figure 4-20 Modeling details: (a) soil-pile interface and (b) column-cap beam interface 46
Figure 4-21 Shear modulus of sand (Seed and Idriss, 1970) 49
Figure 4-22 (a) modulus of subgrade reaction and (b) resulting p-y curves 49
Figure 4-23 Soil stiffness parameters: (a) G/G_{max} ratio, and (b) modulus of subgrade reaction 50
Figure 4-24 P-y curves from Test 1: (a) after elastic cycles and (b) after ductility 1 (μ_1) cycles 51
Figure 4-25 Test 1: top lateral force vs. displacement response comparison 53

Figure 4-26 Test 1: top lateral force vs displacement response comparison for (a) elastic and (b) ductility 1 (μ_1) cycles 53
Figure 4-27 Test 1: top lateral force vs displacement response comparison for (a) ductility 1 (μ_1) and (b) ductility 1.5 ($\mu_{1.5}$) cycles 54
Figure 4-28 Test 1 (from left to right): displacement, curvature, and tensile strain (push and pull cycles) profiles during elastic portion of the test 54
Figure 4-29 Test 1 (from left to right): displacement, curvature, and tensile strain (push and pull cycles) profiles at ductilities 1 (μ_1) and 1.5 ($\mu_{1.5}$) cycles 55
Figure 4-30 Test 1 (from left to right): displacement, curvature, and tensile strain (push and pull cycles) profiles at ductilities 2 (μ_2) and 3 (μ_3) cycles 55
Figure 4-31 Test 12: top lateral force vs. displacement response comparison 56
Figure 4-32 Test 12: top lateral force vs displacement response comparison for (a) elastic and (b) ductility 1 (μ_1) cycles 56
Figure 4-33 Test 12: top lateral force vs displacement response comparison for (a) ductility 1 (μ_1) and (b) ductility 1.5 ($\mu_{1.5}$) cycles 57
Figure 4-34 Test 12 (from left to right): displacement, curvature, and tensile strain (push and pull cycles) profiles during elastic portion of the test 57
Figure 4-35 Test 12 (from left to right): displacement, curvature, and tensile strain (push and pull cycles) profiles at ductilities 1 (μ_1) and 1.5 ($\mu_{1.5}$) cycles 58
Figure 4-36 Test 12 (from left to right): displacement, curvature, and tensile strain (push and pull cycles) profiles at ductilities 2 (μ_2) and 3 (μ_3) cycles 58
Figure 4-37 Coefficient of subgrade reaction chart (ATC-32, 1996) 60
Figure 4-38 P-y analysis for sand: (a) variation of soil stiffness and (b) resulting p-y curves 61
Figure 4-39 P-y analysis for clay: (a) variation of soil stiffness and (b) resulting p-y curves 62
Figure 4-40 Equivalent cantilever model for pinned-head RCFST shafts 64
Figure 4-41 Equivalent cantilever model for fixed-head RCFST shafts 66
Figure 4-42 Curvature and associated strains for RCFST sections 68
Figure 4-43 Curvature and associated strains for RC sections 69
Figure 4-44 Area-based damping calculation example 70
Figure 5-1 Example of tests performed on steel tube coupons 76
Figure 5-2 Steel tube material samples: longitudinal (L), transverse (T), and with weld (W) 77
Figure 5-3 Stress-strain curve of samples from tubes with D/t = 48 78
Figure 5-4 Stress-strain curve of samples from tubes with D/t = 68 79
Figure 5-5 Stress-strain curve of samples from tubes with D/t = 95* 80
Figure 5-6 Spiral weld on coupons with D/t = 48 and 95*: (a) outside and (b) inside surfaces 81
Figure 5-7 Tension test results on sample with D/t = 95* across spiral weld 81
Figure 5-8 Spiral weld on coupons with D/t = 95: (a) outside and (b) inside surfaces 81
Figure 5-9 Stress-strain curve of samples from tubes with D/t = 95 82

Figure 5-10 Example of tension test performed on longitudinal and transverse reinforcement 83
Figure 5-11 Stress-strain curve of #5 bars used in pile-columns specimens 1 through 4 84
Figure 5-12 Stress-strain curve of #3 spirals used in pile-columns specimens 1 through 4 85
Figure 5-13 Stress-strain curve of #5 bars used in pile-columns specimens 5 through 8 86
Figure 5-14 Stress-strain curve of #3 spirals used in pile-columns specimens 5 through 8 87
Figure 5-15 Stress-strain curve of #5 bars used in pile-columns specimens 9 through 12 88
Figure 5-16 Stress-strain curve of #3 spirals used in pile-columns specimens 9 through 12 89
Figure 5-17 Example of tests performed on 4”x8” concrete cylinders 90
Figure 5-18 Test 1: lateral force vs. top displacement response 94
Figure 5-19 Test 1: (a) deformed shape, (b) South, and (c) North sides at third cycle of ductility 5; +31.12” of top displacement; 7.78 kips of lateral force 94
Figure 5-20 Test 1: (a) observed damage, (b) tube local buckling on North side, and (c) tube fracture on South side 95
Figure 5-21 Test 2: lateral force vs. top displacement response 97
Figure 5-22 Test 2: (a) deformed shape, (b) South, and (c) North sides at first cycle of ductility 5.5; −31.62” of top displacement; −7.99 kips of lateral force 97
Figure 5-23 Test 2: (a) observed damage, (b) tube fracture on North side, and (c) tube buckling on South side 98
Figure 5-24 Test 3: lateral force vs. top displacement response 100
Figure 5-25 Test 3: (a) deformed shape, (b) South, and (c) North sides at first cycle of ductility 4; –24.99” of top displacement; –13.99 kips of lateral force 100
Figure 5-26 Test 3: (a) observed damage and (b) tube fracture on South side; (c) observed damage and (d) tube buckling on North side 101
Figure 5-27 Test 4: lateral force vs. top displacement response 103
Figure 5-28 Test 4: (a) deformed shape, (b) South, and (c) North sides at second cycle of ductility 2; −11.11” of top displacement; −14.61 kips of lateral force 103
Figure 5-29 Test 4: (a) observed damage and (b) tube buckling on South side 104
Figure 5-30 Test 5: lateral force vs. top displacement response 106
Figure 5-31 Test 5: (a) deformed shape, (b) South, and (c) North sides at third cycle of ductility 4; −22.54” of top displacement; −13.28 kips of lateral force 106
Figure 5-32 Test 5: (a) observed damage, (b) tube fracture and buckling on North side, and (c) tube fracture and buckling on South side 107
Figure 5-33 Test 6: lateral force vs. top displacement response 109
Figure 5-34 Test 6: (a) deformed shape, (b) South, and (c) North sides at third cycle of ductility 4; +21.36” of top displacement; +16.56 kips of lateral force 109

Figure 5-35 Test 6: (a) observed damage observed, (b) tube fracture on South side, and (c) tube buckling on North side 110
Figure 5-36 Test 7: lateral force vs. top displacement response 112
Figure 5-37 Test 7: (a) deformed shape, (b) South, and (c) North sides at second cycle of ductility 4.88; +29.41" of top displacement; +23.25 kips of lateral force 112
Figure 5-38 Test 7: (a) observed damage, (b) tube fracture and buckling on South side, and (c) tube buckling on North side 113
Figure 5-39 Test 8: lateral force vs. top displacement response 115
Figure 5-40 Test 8: (a) deformed shape, (b) South, and (c) North sides at third cycle of ductility 4; +22.95" of top displacement; +23.87 kips of lateral force 115
Figure 5-41 Test 8: (a) observed damage, (b) tube fracture and buckling on South side, and (c) tube fracture and buckling on North side 116
Figure 5-42 Test 9: lateral force vs. top displacement response 118
Figure 5-43 Test 9: (a) deformed shape, (b) South, and (c) North sides at third cycle of ductility 5; +29.50" of top displacement; +6.35 kips of lateral force 118
Figure 5-44 Test 9: (a) observed damage, (b) tube buckling on North side, and (c) tube fracture and buckling on South side 119
Figure 5-45 Test 10: lateral force vs. top displacement response 121
Figure 5-46 Test 10: (a) deformed shape, (b) South, and (c) North sides at fourth cycle of ductility 5; +36.32" of top displacement; +6.95 kips of lateral force 121
Figure 5-47 Test 10: (a) observed damage, (b) tube buckling and fracture on South side, and (c) tube buckling on North side 122
Figure 5-48 Test 11: lateral force vs. top displacement envelopes 124
Figure 5-49 Test 11: (a) deformed shape, (b) South, and (c) North sides at third cycle of ductility 4; −29.07" of top displacement; −17.60 kips of lateral force 124
Figure 5-50 Test 11: (a) observed damage, (b) tube buckling and fracture on North side, and (c) tube buckling on South side 125
Figure 5-51 Test 12: lateral force vs. top displacement response 127
Figure 5-52 Test 12: (a) deformed shape, (b) South, and (c) North sides at second pull cycle of ductility 4; −32.32" of top displacement; −11.53 kips of lateral force 127
Figure 5-53 Test 12: (a) observed damage, (b) tube fracture on North side, and (c) tube buckling on South side 128
Figure 5-54 Typical failure mechanism 131
Figure 5-55 Spiral weld fracture observed on Test 3 and Test 4 due to incomplete weld penetration 132
Figure 5-56 Lateral force vs. top lateral displacement response of Test 3 and Test 4 132
Figure 5-57 Spiral weld coupon tension test (D/t = 95*) 133
Figure 5-58 Spiral weld coupon tension test (D/t = 95) 133
Figure 5-59 Experimental depth to plastic hinge 134
Figure 5-60 Impact of D/t ratio on force vs. displacement response 135

Figure 5-61 Impact of soil stiffness on force vs. displacement response 135
Figure 5-62 Impact of above-ground length on force vs. displacement response 136
Figure 5-63 Experimental elastic stiffness 137
Figure 5-64 Experimental reliable displacement 137
Figure 5-65 Impact of D/t ratio on hysteretic equivalent viscous damping 138
Figure 5-66 Impact of soil stiffness on hysteretic equivalent viscous damping 138
Figure 5-67 Impact of above-ground length on hysteretic equivalent viscous damping 139
Figure 5-68 Impact of D/t ratio on tensile strains 140
Figure 5-69 Impact of soil stiffness on tensile strains 140
Figure 5-70 Impact of above-ground length on tensile strains 141
Figure 5-71 Summary of tensile strain prior tube fracture 141
Figure 6-1 Impact of D/t ratio on $c_{\phi y}$ for: (a) D = 610 mm and (b) D = 1830 mm 142
Figure 6-2 Impact of ALR ratio on $c_{\phi y}$ for: (a) D = 1220 mm and (b) D = 1830 mm 143
Figure 6-3 Impact of D/t ratio on neutral axis depth for: (a) D = 610 mm and (b) D = 1830mm 143
Figure 6-4 Impact of ALR on neutral axis depth for: (a) D = 610 mm and (b) D = 1830mm 144
Figure 6-5 Neutral axis depth data points and Equation 6-2 trends 144
Figure 6-6 Impact of La/D ratio and soil strength on Hig/D ratio for: (a) sand and (b) clay 145
Figure 6-7 Impact of D/t ratio and soil strength on Hig/D ratio for: (a) sand and (b) clay 145
Figure 6-8 Impact of ALR and soil strength on Hig/D ratio for: (a) sand and (b) clay 146
Figure 6-9 Hig/D ratio for sand with ϕ = 30°: (a) simulations and (b) equation trends 147
Figure 6-10 Hig/D ratio for sand with ϕ = 35°: (a) simulations and (b) equation trends 147
Figure 6-11 Hig/D ratio for sand with ϕ = 40°: (a) simulations and (b) equation trends 147
Figure 6-12 Hig/D ratio for clay with Cu = 12kPa: (a) simulations and (b) equation trends 148
Figure 6-13 Hig/D ratio for clay with Cu = 36kPa: (a) simulations and (b) equation trends 148
Figure 6-14 Hig/D ratio for clay with Cu = 72kPa: (a) simulations and (b) equation trends 148
Figure 6-15 Impact of La/D ratio and soil strength on C_1 for: (a) sand and (b) clay 149
Figure 6-16 Impact of D/t ratio and soil strength on C_1 for: (a) sand and (b) clay 149
Figure 6-17 Impact of ALR and soil strength on C_1 for: (a) sand and (b) clay 150
Figure 6-18 C_1 for sand with ϕ = 30°: (a) simulations and (b) equation trends 151

Figure 6-19 C_1 for sand with $\phi = 35°$: (a) simulations and (b) equation trends 151
Figure 6-20 C_1 for sand with $\phi = 40°$: (a) Simulations and (b) equation trends..... 151
Figure 6-21 C_1 for clay with Cu = 12 kPa: (a) simulations and (b) equation trends 152
Figure 6-22 C_1 for clay with Cu = 36 kPa: (a) simulations and (b) equation trends 152
Figure 6-23 C_1 for clay with Cu = 72 kPa: (a) simulations and (b) equation trends 152
Figure 6-24 Back-calculated plastic hinge length for: (a) sand and (b) clay..... 153
Figure 6-25 Ductility at onset of buckling in terms of D/t ratio..... 154
Figure 6-26 Ductility at onset of buckling in terms of L_a/D ratio 154
Figure 6-27 Ductility at onset of buckling in terms of ALR 154
Figure 6-28 Impact of L_a/D ratio on plastic hinge length for: (a) sand and (b) clay 155
Figure 6-29 Impact of D/t ratio on plastic hinge length for: (a) sand and (b) clay..... 155
Figure 6-30 Impact of ALR on plastic hinge length for: (a) sand and (b) clay 156
Figure 6-31 L_p/D for sand with $\phi = 30°$: (a) simulations and (b) equation trends..... 157
Figure 6-32 L_p/D for sand with $\phi = 35°$: (a) simulations and (b) equation trends..... 157
Figure 6-33 L_p/D for sand with $\phi = 40°$: (a) simulations and (b) equation trends..... 157
Figure 6-34 Lp/D for clay with Cu = 12 kPa: (a) simulations and (b) equation trends 158
Figure 6-35 Lp/D for clay with Cu = 36 kPa: (a) simulations and (b) equation trends 158
Figure 6-36 Lp/D for clay with Cu = 72 kPa: (a) simulations and (b) equation trends 158
Figure 6-37 Observed system equivalent viscous damping for sand 159
Figure 6-38 Observed system equivalent viscous damping for clay 159
Figure 6-39 Back-caluclated soil damping for: (a) sand and (b) clay 160
Figure 6-40 Soil damping in terms of L_a/D for: (a) sand and (b) clay 160
Figure 6-41 Soil damping results and equation trends for: (a) sand and (b) clay..... 161
Figure 6-42 System equivalent viscous damping results and equation trends for sand..... 162
Figure 6-43 System equivalent viscous damping results and equation trends for clay..... 162
Figure 6-44 Impact of La/D ratio and soil strength on Hig/D ratio for: (a) sand and (b) clay 163
Figure 6-45 Impact of D/t ratio and soil strength on Hig/D ratio for: (a) sand and (b) clay..... 163
Figure 6-46 Impact of ALR and soil strength on Hig/D ratio for: (a) sand and (b) clay..... 164
Figure 6-47 Hig/D ratio for sand with $\phi = 30°$: (a) Simulations and (b) equation trends 165
Figure 6-48 Hig/D ratio for sand with $\phi = 35°$: (a) Simulations and (b) equation trends 165
Figure 6-49 Hig/D ratio for sand with $\phi = 40°$: (a) Simulations and (b) equation trends 165

Figure 6-50 Hig/D ratio for clay with Cu = 12kPa: (a) Simulations and (b) equation trends 166
Figure 6-51 Hig/D ratio for clay with Cu = 36kPa: (a) Simulations and (b) equation trends 166
Figure 6-52 Hig/D ratio for clay with Cu = 72kPa: (a) Simulations and (b) equation trends 166
Figure 6-53 Impact of La/D ratio and soil strength on C1 for: (a) sand and (b) clay 167
Figure 6-54 Impact of D/t ratio and soil strength on C1 for: (a) sand and (b) clay 167
Figure 6-55 Impact of ALR and soil strength on C1 for: (a) sand and (b) clay 168
Figure 6-56 C_1 for sand with $\phi = 30°$: (a) Simulations and (b) equation trends 169
Figure 6-57 C_1 for sand with $\phi = 35°$: (a) Simulations and (b) equation trends 169
Figure 6-58 C_1 for sand with $\phi = 40°$: (a) Simulations and (b) equation trends 169
Figure 6-59 C_1 for clay with Cu = 12kPa: (a) Simulations and (b) equation trends 170
Figure 6-60 C_1 for clay with Cu = 36kPa: (a) Simulations and (b) equation trends 170
Figure 6-61 C_1 for clay with Cu = 72kPa: (a) Simulations and (b) equation trends 170
Figure 6-62 Plastic displacement parameter (β) for (a) sand and (b) clay 171
Figure 6-63 Impact of L_a/D ratio and soil strength on β for: (a) sand and (b) clay 171
Figure 6-64 Impact of D/t ratio and soil strength on β for: (a) sand and (b) clay 172
Figure 6-65 Impact of ALR and soil strength on β for: (a) sand and (b) clay 172
Figure 6-66 Parameter β for sand with $\phi = 30°$: (a) simulations and (b) equation trends 173
Figure 6-67 Parameter β for sand with $\phi = 35°$: (a) simulations and (b) equation trends 173
Figure 6-68 Parameter β for sand with $\phi = 40°$: (a) simulations and (b) equation trends 173
Figure 6-69 Parameter β for clay with Cu = 12 kPa: (a) simulations and (b) equation trends 174
Figure 6-70 Parameter β for clay with Cu = 36 kPa: (a) simulations and (b) equation trends 174
Figure 6-71 Parameter β for clay with Cu = 72 kPa: (a) simulations and (b) equation trends 174
Figure 6-72 Observed system EVD for: (a) sand and (b) clay 175
Figure 6-73 System EVD for sand with $\phi = 30°$: (a) simulations and (b) equation trends 176
Figure 6-74 System EVD for sand with $\phi = 35°$: (a) simulations and (b) equation trends 176
Figure 6-75 System EVD for sand with $\phi = 40°$: (a) simulations and (b) equation trends 176
Figure 6-76 System EVD for sand with C_u = 12 kPa: (a) simulations and (b) equation trends 177
Figure 6-77 System EVD for sand with C_u = 36 kPa: (a) simulations and (b) equation trends 177

Figure 6-78 System EVD for sand with C_u = 72 kPa: (a) simulations and (b) equation trends 177
Figure 6-79 H_{ig}/D ratio for sand with ϕ = 30°: (a) simulations and (b) equation trends 179
Figure 6-80 H_{ig}/D ratio for sand with ϕ = 35°: (a) simulations and (b) equation trends 179
Figure 6-81 H_{ig}/D ratio for sand with ϕ = 40°: (a) simulations and (b) equation trends 179
Figure 6-82 H_{ig}/D ratio for sand with C_u = 12 kPa: (a) simulations and (b) equation trends 180
Figure 6-83 H_{ig}/D ratio for sand with C_u = 36 kPa: (a) simulations and (b) equation trends 180
Figure 6-84 H_{ig}/D ratio for sand with C_u = 72 kPa: (a) simulations and (b) equation trends 180
Figure 6-85 Predicted to simulated yield displacement for pinned-head shafts 181
Figure 6-86 Predicted to simulated displacement for pinned-head shafts at onset of tube buckling 181
Figure 6-87 Predicted to simulated yield displacement for fixed-head shafts 182
Figure 6-88 Predicted to simulated displacement for fixed-head shafts at onset of bar buckling 182
Figure 6-89 Impact of D/t ratio on force vs. displacement response 183
Figure 6-90 Impact of L_a/D ratio on force vs. displacement response 184
Figure 6-91 Impact of soil stiffness on force vs. displacement response 184
Figure 6-92 Impact of D/t ratio on displacement, moment, and shear profiles 185
Figure 6-93 Impact of L_a/D ratio on displacement, moment, and shear profiles 185
Figure 6-94 Impact of soil stiffness on displacement, moment, and shear profiles 186
Figure 6-95: Impact of D/t ratio on moment, curvature, and tensile strain profiles 187
Figure 6-96: Impact of L_a/D ratio on moment, curvature, and tensile strain profiles 187
Figure 6-97: Impact of soil stiffness on moment, curvature, and tensile strain profiles 188
Figure 6-98 Impact of D/t ratio on tensile strain vs. displacement envelopes 189
Figure 6-99 Impact of L_a/D ratio on tensile strain vs. displacement envelopes 189
Figure 6-100 Impact of soil stiffness on tensile strain vs. displacement envelopes 189
Figure 6-101 Impact of D/t ratio on force vs. displacement response 190
Figure 6-102 Impact of L_a/D ratio on force vs. displacement response 190
Figure 6-103 Impact of soil stiffness on force vs. displacement response 191
Figure 6-104 Impact of D/t ratio on displacement, moment, and shear profiles 191
Figure 6-105 Impact of L_a/D ratio on displacement, moment, and shear profiles 192
Figure 6-106 Impact of soil stiffness on displacement, moment, and shear profiles 192
Figure 6-107 Impact of D/t ratio on moment, curvature, and strain profiles of top plastic hinge 193

Figure 6-108 Impact of L_a/D ratio on moment, curvature, and strain profiles of top plastic hinge 193
Figure 6-109 Impact of soil stiffness on moment, curvature, and strain profiles of top plastic hinge 194
Figure 6-110 Impact of D/t ratio on tensile strain vs. displacement envelopes 195
Figure 6-111 Impact of $L_a/D/t$ ratio on tensile strain vs. displacement envelopes 195
Figure 6-112 Impact of soil stiffness on tensile strain vs. displacement envelopes 195
Figure 7-1 Example: displacement, moment, and curvature profiles of a pinned-head RCFST shaft 197
Figure 7-2 Example: inground plastic hinge curvature and tensile strain profiles of a pinned-head RCFST shaft 198
Figure 7-3 Equivalent cantilever model for pinned-head RCFST shafts 199
Figure 7-4 Curvature and associated strains for RCFST sections 200
Figure 7-5 Curvature and associated strains for RCFST sections 202
Figure 7-6 Example: displacement, moment, and curvature profiles of a fixed-head RCFST shaft 206
Figure 7-7 Example: top hinge curvature and tensile strain profiles at ductility 4 (μ_4) 207
Figure 7-8 Example: inground hinge curvature and tensile strain profiles at ductility 4 (μ_4) 207
Figure 7-9 Equivalent cantilever model for pinned-head RCFST shafts 209
Figure 7-10 Curvature and associated strains for RC sections 210
Figure 7-11 Curvature and associated strains for RC sections 211
Figure 10-1 Test 1: test setup elevation schematic 230
Figure 10-2 Test 1: RCFST specimen cross section 230
Figure 10-3 Test 1: instrumentation 231
Figure 10-4 Test 1: pinned-head, RCFST pile-column test setup 232
Figure 10-5 Test 1: (a) displacement and (b) loading histories 234
Figure 10-6 Test 1: lateral force vs. top displacement response 235
Figure 10-7 Test 1: lateral force vs. top displacement envelopes 235
Figure 10-8 Test specimen #1 after elastic portion was completed: (a) deformed shape, (b) South side and (c) North side 236
Figure 10-9 Test 1: strain profiles from elastic (a) push and (b) pull cycles 237
Figure 10-10 Test 1: curvature, rotation, and displacement profiles (elastic push cycles) 238
Figure 10-11 Test 1: curvature, rotation, and displacement profiles (elastic pull cycles) 239
Figure 10-12 Test specimen #1 at maximum displacement: (a) deformed shape, (b) South side and (c) North side 240
Figure 10-13 Test 1: strain profiles from inelastic (a) push and (b) pull cycles 241
Figure 10-14 Test 1: curvature, rotation, and displacement profiles (inelastic push cycles) 242

Figure 10-15 Test 1: curvature, rotation, and displacement profiles (inelastic pull cycles) 243
Figure 10-16 Test 1: soil surface after testing 244
Figure 10-17 Test 1: half-moon RC plate settlement during testing 244
Figure 10-18 Test 1: (a) Final observed damage, (b) tube local buckling, and (c) tube fracture 245
Figure 10-19 Test 1: primary buckled sections on (a) North side and (b) South side 246
Figure 10-20 Test 1: observed damage in (a) concrete and (b) internal reinforcement on South side 246
Figure 10-21 Test 2: test setup elevation schematic 249
Figure 10-22 Test 2: RCFST specimen cross section 249
Figure 10-23 Test 2: instrumentation 250
Figure 10-24 Test 2: pinned-head, RCFST pile-column test setup 251
Figure 10-25 Test 2: half-moon RC plate settlement prior testing 251
Figure 10-26 Test 2: (a) displacement and (b) loading histories 252
Figure 10-27 Test 2: lateral force vs. top displacement response 253
Figure 10-28 Test 2: lateral force vs. top displacement envelopes 254
Figure 10-29 Test specimen #2 at last pull cycle of elastic portion of the test: (a) deformed shape, (b) South side and (c) North side 254
Figure 10-30 Test 2: strain profiles from elastic (a) push and (b) pull cycles 255
Figure 10-31 Test specimen #2 at maximum displacement: (a) deformed shape, (b) South side and (c) North side 256
Figure 10-32 Test 2: strain profiles from inelastic (a) push and (b) pull cycles 257
Figure 10-33 Test 2: soil surface after testing 258
Figure 10-34 Test 2: half-moon RC plate settlement during testing 258
Figure 10-35 Test 2: (a) Final observed damage, (b) tube fracture, and (c) tube local buckling 259
Figure 10-36 Test 2: primary buckled sections on (a) South side and (b) North side 260
Figure 10-37 Test 2: observed damage in (a) concrete and (b) internal reinforcement on North side 260
Figure 10-38 Test 3: test setup elevation schematic 262
Figure 10-39 Test 3: RCFST specimen cross section 262
Figure 10-40 Test 3: instrumentation 263
Figure 10-41 Test 3: pinned-head, RCFST pile-column test setup 264
Figure 10-42 Test 3: (a) displacement and (b) loading histories 266
Figure 10-43 Test 3: lateral force vs. top displacement response 267
Figure 10-44 Test 3: lateral force vs. top displacement envelopes 267
Figure 10-45 Test specimen #3 after elastic portion was completed: (a) deformed shape, (b) South side and (c) North side 268
Figure 10-46 Test 3: strain profiles from elastic (a) push and (b) pull cycles 269

Figure 10-47 Test specimen #3 at maximum displacement: (a) deformed shape, (b) South side and (c) North side 271
Figure 10-48 Test 3: observed spiral weld fracture 271
Figure 10-49 Test 3: strain profiles from inelastic (a) push and (b) pull cycles 272
Figure 10-50 Test 3: soil surface after testing 273
Figure 10-51 Test 3: half-moon RC plate settlement during testing 273
Figure 10-52 Test 3: (a) Final observed damage, (b) tube fracture, and (c) tube local buckling 274
Figure 10-53 Test 3: primary buckled sections on (a) North side and (b) South side 274
Figure 10-54 Test 3: observed damage in (a) concrete and (b) internal reinforcement on South side 275
Figure 10-55 Test 4: test setup elevation schematic 278
Figure 10-56 Test 4: RCFST specimen cross section 278
Figure 10-57 Test 4: instrumentation 279
Figure 10-58 Test 4: pinned-head, RCFST pile-column test setup 280
Figure 10-59 Test 4: half-moon RC plate settlement prior testing 280
Figure 10-60 Test 4: (a) displacement and (b) loading histories 282
Figure 10-61 Test 4: lateral force vs. top displacement response 283
Figure 10-62 Test 4: lateral force vs. top displacement envelopes 283
Figure 10-63 Test specimen #4 after the elastic portion was completed: (a) deformed shape, (b) South side and (c) North side 284
Figure 10-64 Test 4: strain profiles from elastic (a) push and (b) pull cycles 285
Figure 10-65 Test specimen #4 at maximum displacement: (a) deformed shape, (b) South side and (c) North side 286
Figure 10-66 Test 4: observed spiral weld fracture 286
Figure 10-67 Test 4: strain profiles from inelastic (a) push and (b) pull cycles 287
Figure 10-68 Test 4: soil surface after testing 288
Figure 10-69 Test 4: half-moon RC plate settlement during testing 288
Figure 10-70 Test 4: (a) Final observed damage, (b) tube fracture, and (c) tube local buckling 289
Figure 10-71 Test 4: observed damage in (a) concrete and (b) internal reinforcement on North side 289
Figure 10-72 Steel tube coupon spiral weld on: (a) outside and (b) inside surfaces 290
Figure 10-73 Tension test results of spiral weld coupon with D/t = 95* 291
Figure 10-74 Steel tube coupon with D/t = 95: (a) outside, and (b) inside surface 291
Figure 10-75 Tension test results of coupons with D/t = 95 291
Figure 10-76 Test 5: test setup elevation schematic 293
Figure 10-77 Test 5: RCFST specimen cross section 293
Figure 10-78 Test 5: instrumentation 294
Figure 10-79 Test 5: pinned-head, RCFST pile-column test setup 295
Figure 10-80 Test 5: (a) displacement and (b) loading histories 297
Figure 10-81 Test 5: lateral force vs. top displacement response 298

Figure 10-82 Test 5: lateral force vs. top displacement envelopes 298
Figure 10-83 Test specimen #5 after the elastic portion was completed: (a) deformed shape, (b) South side and (c) North side 299
Figure 10-84 Test 5: strain profiles from elastic (a) push and (b) pull cycles..... 300
Figure 10-85 Test 5: curvature, rotation, and displacement profiles (elastic push cycles)..... 301
Figure 10-86 Test 5: curvature, rotation, and displacement profiles (elastic pull cycles)..... 302
Figure 10-87 Test specimen #5 at maximum displacement: (a) deformed shape, (b) South side and (c) North side..... 303
Figure 10-88 Test 5: strain profiles from inelastic (a) push and (b) pull cycles..... 304
Figure 10-89 Test 5: curvature, rotation, and displacement profiles (inelastic push cycles) 305
Figure 10-90 Test 5: curvature, rotation, and displacement profiles (inelastic pull cycles)..... 306
Figure 10-91 Test 5: soil surface after testing 307
Figure 10-92 Test 5: half-moon RC plate settlement during testing 307
Figure 10-93 Test 5: (a) Final observed damage, (b) tube fracture, and (c) tube local buckling 309
Figure 10-94 Test 5: secondary buckled sections on (a) North side and (b) South side..... 309
Figure 10-95 Test 5: observed damage in (a) concrete and (b) internal reinforcement on North side..... 309
Figure 10-96 Test 5: observed damage in (a) concrete and (b) internal reinforcement on South side..... 309
Figure 10-97 Test 5: observed bar buckling on South side 310
Figure 10-98 Test 6: test setup elevation schematic..... 313
Figure 10-99 Test 6: RCFST specimen cross section..... 313
Figure 10-100 Test 6: instrumentation 314
Figure 10-101 Test 6: pinned-head, RCFST pile-column test setup 315
Figure 10-102 Test 6: half-moon RC plate settlement prior testing..... 315
Figure 10-103 Test 6: (a) displacement and (b) loading histories..... 317
Figure 10-104 Test 6: lateral force vs. top displacement response 318
Figure 10-105 Test 6: lateral force vs. top displacement envelopes 318
Figure 10-106 Test specimen #6 after elastic portion was completed: (a) deformed shape, (b) South side and (c) North side 319
Figure 10-107 Test 6: strain profiles from elastic (a) push and (b) pull cycles..... 320
Figure 10-108 Test 6: curvature, rotation, and displacement profiles (elastic push cycles)..... 321
Figure 10-109 Test 6: curvature, rotation, and displacement profiles (elastic pull cycles)..... 322
Figure 10-110 Test specimen #6 at maximum displacement: (a) deformed shape, (b) South side and (c) North side..... 323

Figure 10-111 Test 6: strain profiles from inelastic (a) push and (b) pull cycles..... 324
Figure 10-112 Test 6: curvature, rotation, and displacement profiles (inelastic push cycles) 325
Figure 10-113 Test 6: curvature, rotation, and displacement profiles (inelastic pull cycles)..... 326
Figure 10-114 Test 6: soil surface after testing 327
Figure 10-115 Test 6: half-moon RC plate settlement during testing 327
Figure 10-116 Test 6: (a) Final observed damage, (b) tube fracture, and (c) tube local buckling 329
Figure 10-117 Test 6: (a) primary and (b) secondary buckled sections on North side..... 329
Figure 10-118 Test 6: observed damage in (a) concrete and (b) internal reinforcement on North side 329
Figure 10-119 Test 6: observed damage in (a) concrete and (b) internal reinforcement on South side 329
Figure 10-120 Test 7: test setup elevation schematic..... 332
Figure 10-121 Test 7: RCFST specimen cross section..... 332
Figure 10-122 Test 7: instrumentation 333
Figure 10-123 Test 7: pinned-head, RCFST pile-column test setup 334
Figure 10-124 Test 7: (a) displacement and (b) loading histories..... 336
Figure 10-125 Test 7: lateral force vs. top displacement response 337
Figure 10-126 Test 7: lateral force vs. top displacement envelopes 337
Figure 10-127 Test specimen #7 after elastic portion of the test was completed: (a) deformed shape, (b) South side and (c) North side..... 339
Figure 10-128 Test 7: strain profiles from elastic (a) push and (b) pull cycles..... 340
Figure 10-129 Test 7: curvature, rotation, and displacement profiles (elastic push cycles)..... 341
Figure 10-130 Test 7: curvature, rotation, and displacement profiles (elastic pull cycles)..... 342
Figure 10-131 Test specimen #7 at maximum displacement: (a) deformed shape, (b) South side and (c) North side..... 343
Figure 10-132 Test 7: strain profiles from inelastic (a) push and (b) pull cycles..... 344
Figure 10-133 Test 7: curvature, rotation, and displacement profiles (inelastic push cycles) 345
Figure 10-134 Test 7: curvature, rotation, and displacement profiles (inelastic pull cycles)..... 346
Figure 10-135 Test 7: soil surface after testing 347
Figure 10-136 Test 7: half-moon RC plate settlement during testing 347
Figure 10-137 Test 7: (a) Final observed damage, (b) tube fracture, and (c) tube local buckling 348
Figure 10-138 Test 7: secondary buckled sections on (a) North side and (b) South side..... 348

Figure 10-139 Test 7: observed damage in (a) concrete and (b) internal reinforcement on North side 349
Figure 10-140 Test 7: observed damage in (a) concrete and (b) internal reinforcement on South side 349
Figure 10-141 Test 7: observed bar buckling on South side 349
Figure 10-142 Test 8: test setup elevation schematic 352
Figure 10-143 Test 8: RCFST specimen cross section 352
Figure 10-144 Test 8: instrumentation 353
Figure 10-145 Test 8: pinned-head, RCFST pile-column test setup 354
Figure 10-146 Test 8: half-moon RC plate settlement prior testing 355
Figure 10-147 Test 8: (a) displacement and (b) loading histories 356
Figure 10-148 Test 8: lateral force vs. top displacement response 358
Figure 10-149 Test 8: lateral force vs. top displacement envelopes 358
Figure 10-150 Test specimen #8 after elastic portion of the test was completed: (a) deformed shape, (b) South side and (c) North side 359
Figure 10-151 Test 8: strain profiles from elastic (a) push and (b) pull cycles 360
Figure 10-152 Test 8: curvature, rotation, and displacement profiles (elastic push cycles) 361
Figure 10-153 Test 8: curvature, rotation, and displacement profiles (elastic pull cycles) 362
Figure 10-154 Test specimen #8 at maximum displacement: (a) deformed shape, (b) South side and (c) North side 363
Figure 10-155 Test 8: strain profiles from inelastic (a) push and (b) pull cycles 364
Figure 10-156 Test 8: curvature, rotation, and displacement profiles (inelastic push cycles) 365
Figure 10-157 Test 8: curvature, rotation, and displacement profiles (inelastic pull cycles) 366
Figure 10-158 Test 8: soil surface after testing 367
Figure 10-159 Test 8: half-moon RC plate settlement during testing 367
Figure 10-160 Test 8: (a) Final observed damage, (b) tube fracture, and (c) tube local buckling 368
Figure 10-161 Test 8: primary buckled sections on (a) North side and (b) South side 369
Figure 10-162 Test 8: observed damage in (a) concrete and (b) internal reinforcement on South side 369
Figure 10-163 Test 9: test setup elevation schematic 372
Figure 10-164 Test 9: RCFST specimen cross section 372
Figure 10-165 Test 9: instrumentation 373
Figure 10-166 Test 9: pinned-head, RCFST pile-column test setup 374
Figure 10-167 Test 9: half-moon RC plate settlement prior testing 374
Figure 10-168 Test 9: (a) displacement and (b) loading histories 376
Figure 10-169 Test 9: lateral force vs. top displacement response 377
Figure 10-170 Test 9: lateral force vs. top displacement envelopes 377

Figure 10-171 Test specimen #9 after elastic portion of the test was completed: (a) deformed shape, (b) South side and (c) North side 378
Figure 10-172 Test 9: strain profiles from elastic (a) push and (b) pull cycles 379
Figure 10-173 Test 9: curvature, rotation, and displacement profiles (elastic push cycles) 380
Figure 10-174 Test 9: curvature, rotation, and displacement profiles (elastic pull cycles) 381
Figure 10-175 Test specimen #9 at maximum displacement: (a) deformed shape, (b) South side and (c) North side 382
Figure 10-176 Test 9: strain profiles from inelastic (a) push and (b) pull cycles 383
Figure 10-177 Test 9: curvature, rotation, and displacement profiles (inelastic push cycles) 384
Figure 10-178 Test 9: curvature, rotation, and displacement profiles (inelastic pull cycles) 385
Figure 10-179 Test 9: soil surface after testing 386
Figure 10-180 Test 9: half-moon RC plate settlement during testing 386
Figure 10-181 Test 9: (a) Final observed damage, (b) tube local buckling, and (c) tube fracture 387
Figure 10-182 Test 9: primary buckled sections on (a) North side and (b) South side 387
Figure 10-183 Test 9: observed damage in (a) concrete and (b) internal reinforcement on North side 388
Figure 10-184 Test 9: observed damage in (a) concrete and (b) internal reinforcement on South side 388
Figure 10-185 Test 9: effect of surcharge level on elastic force vs. displacement response 389
Figure 10-186 Test 9: effect of surcharge level on elastic tensile strains 390
Figure 10-187 Test 9: effect of surcharge level on elastic curvature, rotation, and displacement 390
Figure 10-188 Test 10: test setup elevation schematic 394
Figure 10-189 Test 10: RCFST specimen cross section 394
Figure 10-190 Test 10: instrumentation 395
Figure 10-191 Test 10: pinned-head, RCFST pile-column test setup 396
Figure 10-192 Test 10: (a) displacement and (b) loading histories 397
Figure 10-193 Test 10: lateral force vs. top displacement response 398
Figure 10-194 Test 10: lateral force vs. top displacement envelopes 399
Figure 10-195 Test specimen #10 after elastic portion of the test was completed: (a) deformed shape, (b) South side and (c) North side 399
Figure 10-196 Test 10: strain profiles from elastic (a) push and (b) pull cycles 400
Figure 10-197 Test 10: curvature, rotation, and displacement profiles (elastic push cycles) 401
Figure 10-198 Test 10: curvature, rotation, and displacement profiles (elastic pull cycles) 402

Figure 10-199 Test specimen #10 at maximum displacement: (a) deformed shape, (b) South side and (c) North side 403
Figure 10-200 Test 10: strain profiles from inelastic (a) push and (b) pull cycles 404
Figure 10-201 Test 10: curvature, rotation, and displacement profiles (inelastic push cycles) 405
Figure 10-202 Test 10: curvature, rotation, and displacement profiles (inelastic pull cycles) 406
Figure 10-203 Test 10: soil surface after testing 407
Figure 10-204 Test 10: half-moon RC plate settlement during testing 407
Figure 10-205 Test 10: (a) Final observed damage, (b) tube fracture, and (c) tube local buckling 408
Figure 10-206 Test 10: primary buckled sections on (a) North side and (b) South side 408
Figure 10-207 Test 10: observed damage in (a) concrete and (b) internal reinforcement on North side 409
Figure 10-208 Test 10: observed damage in (a) concrete and (b) internal reinforcement on South side 409
Figure 10-209 Test 11: test setup elevation schematic 413
Figure 10-210 Test 11: RCFST specimen cross section 413
Figure 10-211 Test 11: instrumentation 414
Figure 10-212 Test 11: pinned-head, RCFST pile-column test setup 415
Figure 10-213 Test 11: (a) displacement and (b) loading histories 416
Figure 10-214 Test 11: lateral force vs. top displacement envelopes 417
Figure 10-215 Test specimen #11 after elastic portion of the test was completed: (a) deformed shape, (b) South side and (c) North side 418
Figure 10-216 Test 11: curvature, rotation, and displacement profiles (elastic push cycles) 419
Figure 10-217 Test 11: curvature, rotation, and displacement profiles (elastic pull cycles) 420
Figure 10-218 Test specimen #11 at maximum displacement: (a) deformed shape, (b) South side and (c) North side 421
Figure 10-219 Test 11: curvature, rotation, and displacement profiles (inelastic push cycles) 422
Figure 10-220 Test 11: curvature, rotation, and displacement profiles (inelastic pull cycles) 423
Figure 10-221 Test 11: soil surface after testing 424
Figure 10-222 Test 11: half-moon RC plate settlement during testing 424
Figure 10-223 Test 11: (a) Final observed damage, (b) tube fracture, and (c) tube local buckling 425
Figure 10-224 Test 11: primary buckled sections on (a) North side and (b) South side 426
Figure 10-225 Test 11: observed damage in (a) concrete and (b) internal reinforcement on North side 426

Figure 10-226 Test 11: observed damage in (a) concrete and (b) internal reinforcement on South side 426
Figure 10-227 Test 12: test setup elevation schematic 430
Figure 10-228 Test 12: RCFST specimen cross section 430
Figure 10-229 Test 12: instrumentation 431
Figure 10-230 Test 12: pinned-head, RCFST pile-column test setup 432
Figure 10-231 Test 12: (a) displacement and (b) loading histories 433
Figure 10-232 Test 12: lateral force vs. top displacement response 434
Figure 10-233 Test 12: lateral force vs. top displacement envelopes 434
Figure 10-234 Test specimen #12 after elastic portion of the test was completed: (a) deformed shape, (b) South side and (c) North side 435
Figure 10-235 Test 12: strain profiles from elastic (a) push and (b) pull cycles 436
Figure 10-236 Test 12: curvature, rotation, and displacement profiles (elastic push cycles) 437
Figure 10-237 Test 12: curvature, rotation, and displacement profiles (elastic pull cycles) 438
Figure 10-238 Test specimen #12 at maximum displacement: (a) deformed shape, (b) South side and (c) North side 439
Figure 10-239 Test 12: strain profiles from inelastic (a) push and (b) pull cycles 440
Figure 10-240 Test 12: curvature, rotation, and displacement profiles (inelastic push cycles) 441
Figure 10-241 Test 12: curvature, rotation, and displacement profiles (inelastic pull cycles) 442
Figure 10-242 Test 12: soil surface after testing 443
Figure 10-243 Test 12: half-moon RC plate settlement during testing 443
Figure 10-244 Test 12: (a) Final observed damage, (b) tube fracture, and (c) tube local buckling 444
Figure 10-245 Test 12: primary buckled sections on (a) North side and (b) South side 444
Figure 10-246 Test 12: observed damage in (a) concrete and (b) internal reinforcement on North side 445
Figure 10-247 Test 12: observed damage in (a) concrete and (b) internal reinforcement on South side 445
Figure 10-248 Mill certifications for steel tubes with D/t = 48 470
Figure 10-249 Mill certifications for steel tubes with D/t = 68 471
Figure 10-250 Mill certifications for steel tubes with D/t = 95* 472
Figure 10-251 Mill certifications for steel tubes with D/t = 95 473
Figure 10-252 Mill certifications for steel tubes labeled as ASTM A-139 Gr. B Steel 474
Figure 10-253 Mill certifications for #5 (longitudinal) bars (Tests 1, 2, 3, 4) 475
Figure 10-254 Mill certifications for #3 spirals utilized for tests specimens 1, 2, 3, 4 476

Figure 10-255 Mill certifications for #5 (longitudinal) bars utilized in test specimens 5, 6, 7, and 8 477
Figure 10-256 Mill certifications for #3 spirals utilized for tests specimens 5, 6, 7, and 8 478
Figure 10-257 Mill certifications for #5 (longitudinal) bars utilized in test specimens 9, 10, 11, and 12 479
Figure 10-258 Mill certifications for #3 spirals utilized for tests specimens 9, 10, 11, and 12 480

LIST OF TABLES

Table 4-1 Experimental test matrix 43
Table 4-2 Values of n_h for sand (AASHTO, 2011) 60
Table 4-3 Values of ε_{50} for soft clay (Reese and Van Impe, 2011) 62
Table 4-4 Structural parameters considered in the parametric study 71
Table 4-5 Soil parameters considered in the parametric study 72
Table 4-6 Parameters considered in the section analyses 73
Table 5-1 Experimental test matrix 75
Table 5-2 Tension test results of steel tubes with D/t = 48 78
Table 5-3 Tension test results of steel tubes with D/t = 68 79
Table 5-4 Tension test results of steel tubes with D/t = 95* 80
Table 5-5 Tension test results of steel tubes with D/t = 95 82
Table 5-6 Tension test results of #5 bars used in pile-columns specimens 1 through 4 84
Table 5-7 Tension test results of #3 spirals used in pile-columns specimens 1 through 4 85
Table 5-8 Tension test results of #5 bars used in pile-columns specimens 5 through 8 86
Table 5-9 Tension test results of #3 spirals used in pile-columns specimens 5 through 8 87
Table 5-10 Tension test results of #5 bars used in pile-columns specimens 9 through 12 88
Table 5-11 Tension test results of #3 spirals used in pile-columns specimens 9 through 12 89
Table 5-12 Concrete compressive test results: pile-columns specimens 1 through 4 (phase 1) 90
Table 5-13 Concrete compressive test results: pile-columns specimens 5 through 8 (phase 2) 91
Table 5-14 Concrete compressive test results: pile-columns specimens 9 through 12 (phase 3) 91
Table 5-15 Material Properties 92
Table 5-16 Summary of experimental observations 130
Table 7-1 Inground plastic hinge performance levels and associated strain limits 198
Table 7-2 Top plastic hinge performance levels and associated tensile strain limits POLA (2010) 208
Table 10-1 Test 1: predictions for elastic portion 233
Table 10-2 Test 2: predictions for elastic portion 252
Table 10-3 Test 3: predictions for elastic portion 265
Table 10-4 Test 4: predictions for elastic portion 281
Table 10-5 Test 5: predictions for elastic portion 296
Table 10-6 Test 6: predictions for elastic portion 316
Table 10-7 Test 7: predictions for elastic portion 335
Table 10-8 Test 8: predictions for elastic portion 356

Table 10-9 Test 9: predictions for elastic portion..... 375
Table 10-10 Test 10: predictions for elastic portion..... 396
Table 10-11 Test 11: predictions for elastic portion..... 416
Table 10-12 Test 12: predictions for elastic portion..... 432
Table 10-13 Test 1: peak cycle data (D/t = 48; La = 5.42D; No surcharge) 448
Table 10-14 Test 2: peak cycle data (D/t = 48; La = 5.83D; Surcharge = 960 psf) 450
Table 10-15 Test 3: peak cycle data (D/t = 95*; La = 5.18D; No surcharge) 452
Table 10-16 Test 4: peak cycle data (D/t = 95*; La = 5.18D; Surcharge = 960 psf) 453
Table 10-17 Test 5: peak cycle data (D/t = 95; La = 5.36D; No surcharge) 454
Table 10-18 Test 6: peak cycle data (D/t = 95; La = 5.53D; Surcharge = 960 psf) 456
Table 10-19 Test 7: peak cycle data (D/t = 68; La = 5.43D; No surcharge) 458
Table 10-20 Test 8: peak cycle data (D/t = 68; La = 5.43D; Surcharge = 960 psf) 460
Table 10-21 Test 9: peak cycle data (D/t = 48; La = 5.77D; Surcharge = 960 psf) 462
Table 10-22 Test 10: peak cycle data (D/t = 48; La = 7.77D; No surcharge) 464
Table 10-23 Test 11: peak cycle data (D/t = 95; La = 7.24D; No surcharge) 466
Table 10-24 Test 12: peak cycle data (D/t = 68; La = 7.24D; No surcharge) 468

ACKNOWLEDGEMENTS

This research project was funded by the Alaska Department of Transportation and Public Facilities (AKDOT & PF), and the Alaska University Transportation Center (AUTC); their support is gratefully acknowledged. The authors thank Mr. Elmer Marx from AKDOT & PF for his continuous engagement in the entire research program. The support from students and technical staff at the Constructed Facilities Laboratory (CFL) at North Carolina State University is also very much appreciated.

ABSTRACT

Reinforced concrete filled steel tube (RCFST) pile-columns, also known as RCFST drilled shafts, are structural elements used in bridge support systems in regions of high seismic activity. This system consists of a steel tube that is filled with concrete and internal longitudinal and transverse reinforcement. This system has several advantages over traditional systems. Beyond increased strength and deformation capacities, this type of elements serve as a foundation element (pile) inground and as a column aboveground. Moreover, the steel tube serves as permanent formwork, which in turn contributes toward accelerated and cleaner construction processes.

The main goal of the research described in this document aimed to study the effects of soil stiffness on the performance of RCFST pile-column specimens. For that purpose, twelve half-scale, pinned-head, RCFST specimens were tested under cyclic lateral loading and variable soil stiffness levels at the soil-structure interaction facility at North Carolina State University. The main studied variables included: (1) diameter-to-thickness (D/t) ratio, (2) aboveground length-to-diameter ratio (L_a/D), and (3) soil stiffness. The specimens consisted of steel tubes with outer diameter (D) of either 12 in. or 12.75 in. with D/t ratios of 48, 68, and 95. Aspect ratios (L_a/D) of 5.5 or 7.5 along with two soil stiffness conditions were considered. The soil utilized in the experimental tests consisted of poorly graded sand (SP) with average unit weight γ = 90 pcf (14.2 kN/m^3), friction angle ϕ = 35°, and relative density $D_r \approx 25$ %.

In addition to the experimental component described above, analytical studies were also conducted on both pinned-head and fixed-head RCFST shafts. Variables of such studies included: (1) D/t ratios of 48, 64, and 95; (2) L_a/D ratios of 4, 8, and 12; (3) three levels of axial load ratio (ALR), namely, 5%, 10%, and 15%; (4) two soil types, namely, sand and clay; and (5) three levels of soil stiffness, namely, flexible, medium, and stiff soil profiles.

Results showed that the D/t ratio has a direct impact on the system strength, with a moderate effect on the effective system stiffness, which ultimately affects the displacement capacity. Regarding the soil stiffness, it certainly affects the effective system stiffness but not as much its strength. Moreover, both D/t ratio and soil stiffness have a small effect on the depth to maximum moment and spread of plasticity. Regarding the L_a/D ratio, it was found that is the parameter that impacts the most the performance of the system, affecting the displacement capacity, system strength, shear demand, depth to maximum moment, and spread of plasticity.

EXECUTIVE SUMMARY

This document presents the results of a research program that aimed to study the behavior of reinforced concrete filled steel tube (RCFST) pile-columns, also known as RCFST drilled shafts, and the effects of soil stiffness on their structural response. For that purpose, this report shows results of experimental and analytical studies conducted to evaluate the performance of such elements.

The experimental program consisted of laboratory experiments on twelve half-scale RCFST specimens embedded in sand, tested under cyclic lateral loading by means of a hydraulic actuator pin-connected to the head of the specimens. The RCFST specimens consisted of steel tubes with outer diameter (D) of 12 in. (305 mm) or 12.75 in. (324 mm) and diameter-to-thickness (D/t) ratios of 48, 68, and 95. Such specimens were embedded into clean sand an average depth of 13.5D, and had aboveground length-to-diameter (L_a/D) ratios of either 5.5 or 7.5. The soil stiffness was modified by using a "soil-sandwich" approach that aimed to increase the confining stress in the soil to increase the effective soil stiffness. As such, two soil conditions were considered, namely, a soil profile with pristine sand properties, and a soil profile with a soil surcharge of 960 psf (46 kPa) to induce a stiffer soil stiffness.

The typical behavior of the pinned-head RCFST pile-columns consisted of a plastic hinge developing inground. In this mechanism, ripples develop in the extreme tension and compression fibers, followed by onset of outward tube local buckling as deformations increase. Buckled sections grow due to repeated compression cycles up until the section is significantly weak upon a reversal cycle, resulting in tube fracture. The main buckles as well as tube fracture did not occur over the tube spiral weld for tubes with a complete penetration joint (CPJ) weld detail. For two of the specimens, tube fracture did occur along the spiral weld at low displacement demands, namely, ductility 2 (μ_2). Upon further examination of those two specimens, it was found that the steel tubes contained a partial joint penetration (PJP) weld detail. Therefore, fracture of the spiral weld occurred right after the system yield displacement was imposed at the specimen head of those two specimens.

Based on experimental observations, it was found that the D/t ratio affects the system strength with a moderate effect on the displacement capacity. The latter tends to decrease for increasing D/t ratios. It was concluded that the system has a displacement capacity up to ductility 3 (μ_3), recognizing that thick-wall tubes (D/t = 48) can reach displacement ductility 4 (μ_4) without a significant loss of strength. As such, average displacement capacities of 2.2D, 1.7D, and 1.4D were found for D/t ratios of 48, 68, and 95, respectively. Regarding the soil stiffness, this parameter affects the system stiffness, with a moderate impact on the depth to plastic hinge and moment gradient. As the soil stiffness increases, so does the lateral strength of the system, which in combination with a shorter lever arm induces a higher moment grading with a corresponding shorter spread of plasticity. With respect to the aspect ratio (L_a/D), it was found this parameter significantly impacts the performance of the system, affecting the system strength and displacement capacity, depth to plastic hinge,

moment gradient. The elastic stiffness decreased in average 31% for specimens with L_a/D = 7.5 when compared to those with L_a/D = 5.5. Lastly, it was observed that the tensile strain prior fracture was consistent with the limit 2.5% reported in a previous research project (Brown et al., 2015).

The analytical studies, on the other hand, aimed to evaluate the performance of both pinned-head and fixed-head RCFST drilled shafts embedded into a uniform layer of sand or clay, considering three soil stiffness levels in each case. For that purpose, 648 simulations were conducted using a fiber-based finite element model that was developed using the OpenSees framework software, where the soil was characterized with non-linear spring elements. Beyond the different soil profiles, these simulations also considered: (1) two diameters, namely, 24 in. (610 mm) and 48 in. (1220 mm); (2) diameter-to-thickness (D/t) ratios of 48, 64, and 95; (3) aboveground length-to-diameter (L_a/D) ratios of 4, 8, and 12; and (4) axial load ratios (ALR) of 5%, 10%, and 15%. Moreover, regarding the soil stiffness levels, friction angles (ϕ) of 30°, 35°, and 40° were considered for sand, while undrained shear strengths of 250 psf (12 kPa), 750 psf (36 kPa), and 1,500 psf (72 kPa) were considered for clay.

Regarding pinned-head shafts, simulation results further validated experimental results. The D/t ratio impacts the system strength and it has a moderate influence on the system stiffness, affecting the displacement capacity. Similar observations were made regarding soil stiffness. With respect to the L_a/D ratio, this parameter significantly influences the performance of the system. Considering the range of aspect ratios studied, it was found that for the upper bound (L_a/D = 12) compared to the lower bound (L_a/D = 4) limit, the system strength decreases roughly 50%, the displacement capacity increases roughly three times, the moment gradient decreases, thus increasing the spread of plasticity, and the shear demand decreases because of a longer lever arm. Moreover, the depth to plastic hinge shifts upward closer to the soil surface, while in terms of the system equivalent viscous damping, it was found that the soil contribution is rather low with values within 1% and 4% for low and high ductility levels, respectively.

For fixed-head shafts, on the other hand, simulation results indicated a similar behavior to pinned-head shafts in terms of the impact of D/t ratio, L_a/D ratio, and soil stiffness. The main difference is on the failure mechanism and energy dissipation characteristics of the system. Regarding the former, due to the distribution of flexural stiffness, the system is controlled by the top plastic hinge, which corresponds effectively to a reinforced concrete section confined by a steel tube, namely, the tube does not contribute to the flexural strength. As such, the top hinge reaches its ultimate limit state when onset of the inground hinge occurs. Thus, while the system has reserved capacity provided by the inground hinge, the top hinge is at imminent failure, which means that structural stability issues should be considered. With respect to energy dissipation, the system exhibited a rather linear variation with increasing levels of displacement ductility. Moreover, for high ductility levels the system equivalent viscous damping is smaller than that of a reinforced concrete bridge column. Although damage develops at the top plastic hinge, the flexural behavior of the

system is influenced by the steel tube which provides confinement to the top hinge and increased flexural strength for the shaft below the top hinge.

Using results of the analytical and experimental studies, an equivalent cantilever plastic hinge model was developed for pinned-head and fixed-head RCFST shafts. The main feature of the proposed model is that it relates strain with displacements. The model is intended to be used for calculation of the displacement capacity of the system at a prescribed limit state, or for determination of the design displacement if a displacement-based design approach is implemented. The model accounts for soil flexibility and includes consistent definitions of equivalent plastic hinge lengths for each soil type. Moreover, system equivalent viscous damping models are also provided.

CHAPTER 1

1. INTRODUCTION

1.1. Background

Reinforced concrete filled steel tube (RCFST) pile-columns are structural elements commonly used in bridge supports in high seismic regions because RCFSTs provide increased levels of strength, ductility, and energy dissipation as compared with traditional systems such as reinforced concrete (RC) or steel substructures. RCFST pile-columns offer several benefits, the most important of which are: (1) the pile-column serves as a foundation element below ground, and as a column above soil surface; (2) the steel tube serves as formwork, which simplifies construction; and (3) the steel tube provides high levels of confinement, increasing the strength and ductility capacities of the system. Figure 1-1(a) shows an example of the pile-column system under consideration, in which RCFSTs are utilized. RCFSTs consist of a steel tube filled with concrete reinforced with longitudinal and transverse internal steel, as shown in Figure 1-1(b). Under lateral loading, pile-columns could experience two different moment demands depending on the transverse and longitudinal configuration of the bridge. Under transverse loading, plastic hinges would likely form at the column-cap interface, as the cap beam constrains rotation at the top of the pile-columns (i.e., a fixed-head condition). For longitudinal loading and an assumed simply supported connection between the bridge girders and the cap beam (i.e., pinned-head condition), plastic hinges would likely form below ground, as depicted in Figure 1-1(c), which constitutes the focus of the study presented in this report.

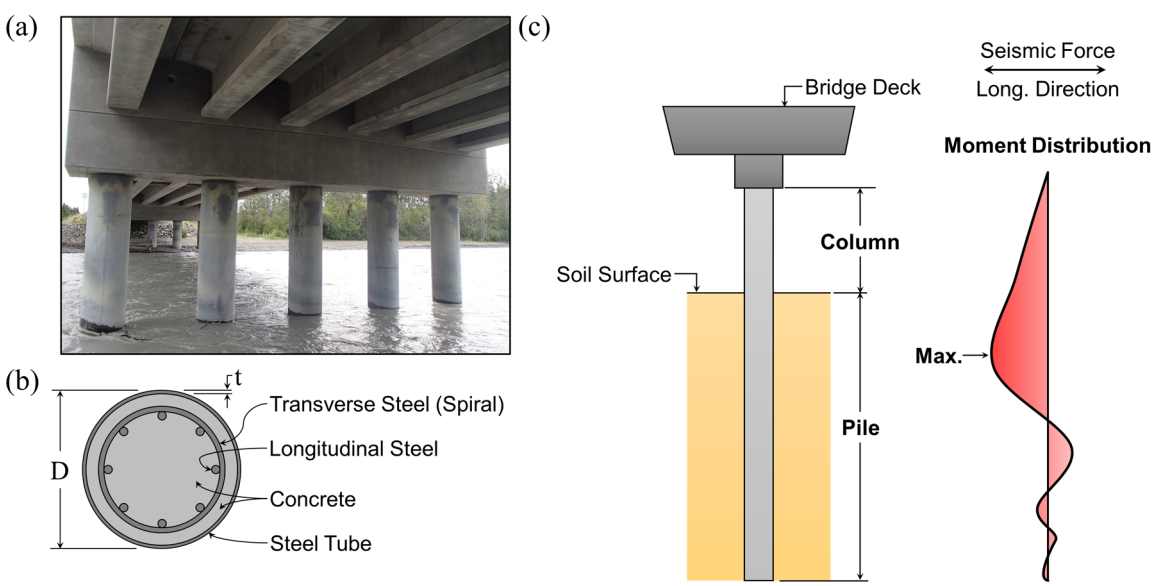

Figure 1-1 (a) Gakona River Bridge (courtesy of Elmer Marx), (b) typical RCFST cross section, and (c) pile-column system

1.2. Motivation

Past research efforts have shown that RCFSTs can sustain large inelastic deformations while maintaining strength. The diameter-to-thickness (D/t) ratio influences the local buckling of the steel tube and energy dissipation of the system. Moreover, the internal reinforcing steel influences the flexural strength but does not affect the overall behavior of RCFST systems (Brown et al., 2015). The failure mechanism is characterized by outward buckling of the steel tube resulting ultimately in tube fracture. This characteristic behavior has been established from experimental tests conducted in air, that is, either cantilever column or four-point bending tests where structural elements are subjected to reversed cyclic loading, most of which are performed on concrete-filled steel tube (CFST) and some on RCFST specimens (e.g., Park et al., 1983; Marson and Bruneau, 2004; González-Román et al., 2008; Montejo et al, 2012; Brown et al., 2015).

While early research efforts on RCFSTs date back to the 1980s, their structural performance is relatively unstudied when compared to conventional RC or steel elements. Moreover, to the knowledge of the authors, there is no research available on the structural performance of RCFSTs that considers soil-structure interaction (SSI) under different levels of soil stiffness. The seismic performance of RCFSTs could be substantially influenced by their interaction with soil and by the effective stiffness that the surrounding soil provides to the system. Therefore, understanding and quantifying such effects will provide analysis and design tools that can significantly improve current design practice of RCFST pile-columns, which in turn will lead to more reliable and safer civil infrastructure.

The work presented in this report builds upon a previous study conducted at NC State University (Brown et al., 2013; Brown et al., 2015). Such study provided insights on the structural performance of RCFSTs in terms of their failure mechanism and strain limit states as characterized by onset of tube local buckling followed by tube fracture. Moreover, an equivalent viscous damping model was proposed, while confinement and strain compatibility were also verified.

1.3. Scope and Layout

Chapter 2 of this document presents an overview of past research performed on reinforced concrete filled steel tube (RCFST) elements; relevant studies on reinforced concrete (RC) piles are also included. The main objective and specific goals of the project are described in Chapter 3. Explained in Chapter 4 are the experimental and analytical components of this study, while results of such studies are presented in Chapter 5. Then, Chapter 7 presents a discussion based upon analytical and experimental results along with evaluation of the proposed model. Finally, Chapter 8 presents a summary of the findings, provides conclusions and recommendations for design, and elaborates on potential topics for future research.

CHAPTER 2

2. LITERATURE REVIEW

Limited literature has been found to date related to the behavior of reinforced concrete filled steel tube (RCFST) elements in soil. While several references are available on concrete filled tubes (CFST), dating back to the 1950s as noted by Park et al. (1983), only few authors have studied the behavior of RCFST elements and even fewer authors have considered the effects of soil stiffness. Literature available shows results of experimental tests conducted in the air, that is, either cantilever column or four-point bending tests where structural elements are subjected to reversed cyclic loading, most of which are performed on CFST and some on RCFST specimens.

To the knowledge of the authors, there is no experimental research available regarding RCFSTs where the inelastic soil-pile interaction is evaluated along with its effects on the performance of the system under consideration. However, while there is not a single study on the response of RCFST embedded in soil, there has been substantial research conducted on conventional reinforced concrete (RC) piles, which is relevant for this project and thus will be included.

The focus of past research can be divided into five areas: (1) concrete filled steel tubes; (2) reinforced concrete filled steel tubes; (3) reinforced concrete pile-columns; (4) soil-structure interaction; and (5) plastic hinge models for pile-columns. Therefore, this report presents a review on each of these areas.

2.1. Concrete Filled Steel Tubes (CFSTs)

2.1.1. Marson and Bruneau (2004)

They evaluated the strength and ductility capacity of four CFST circular columns with a foundation detail that allows for developing the full composite strength at the column base. They utilized column diameters of 324 mm. and 406 mm., along with wall tube thickness values of 6.35 mm. and 9.53 mm., providing nominal diameter-to-thickness (D/t) ratios ranging from 34 to 64. They used steel tubes in accordance with ASTM A500 Grade C specifications for all four specimens (Fy = 350 MPa). The foundation connection detail consisted of 30-mm-thick and 10-mm-thick steel plates, welded to the bottom and top flanges of two C channels, respectively, that were left embedded into the concrete foundation element. They did not add reinforcing bars to the foundation element as the embedded steel members were designed to transfer the column demands to the foundation.

They conducted the experiments at the University of Ottawa Structures Laboratory. Three hydraulic actuators were utilized in their test setup, two of them in vertical position were used to apply axial load, and another actuator was used to induce lateral loading. Regarding instrumentation, they used thirty-six strain gauges to monitor the demands on the foundation connection, and also to assess the flexural and axial deformations along the length of the column including the portion embedded into the foundation element.

They concluded that all tested columns were capable of reaching drifts of 7% prior a significant loss of strength, which occurred as a result of fracture initiation of the steel tube in the section with tube local buckling; the maximum flexural strength was developed at approximately 4% drift. The foundation detail that they proposed was proven to work satisfactorily as the full moment capacity of the CFST column was developed. Finally, the main conclusion of their study was that the experimental results suggested that CFSTs could provide an effective mechanism to dissipate energy when used for bridge piers in seismic regions.

2.1.2. Sakino et al. (2004)

They conducted experiments on CFSTs subjected to monotonic axial loading. The goal of their study was to develop a load-deformation relationship that accounts for the shape of the steel tube (circular or square), width to thickness ratio, tensile strength of the steel tube, and compressive strength of the concrete. For that purpose, they tested a total of 114 specimens that also included hollow steel tubes.

Based upon experimental results, they developed a stress-strain model for confined concrete of concrete filled square steel tube columns. This model allows for calculating the ultimate axial compressive load of such columns. In addition, they also proposed a strength reduction factor that accounts for tube local buckling.

2.1.3. Ellobody et al. (2006)

They conducted a parametric study on reinforced concrete filled steel tube short columns, covering concrete strengths from 30 to 110 MPa and D/t ratios varying from 15 to 80. For that purpose, they conducted finite element (FE) analyses using the ABAQUS framework software. They proposed a material model to represent the stress-strain behavior of confined concrete as a combination of different recommendations made in the past by other researchers. Using such a material model, they developed, validated, and calibrated an FE model using experimental data reported elsewhere. They compared the predicted column strength (axial load) with the design strength of three standard specifications (i.e., American, Australian, and European). Based on the ratio between the modeled and calculated design strength along with a reliability analysis, they concluded that the design strengths of the American and Australian specifications are more conservative than that of the European code.

2.1.4. Chen et al. (2011)

They focused on the behavior of rock-socketed piles. Field tests were conducted under lateral loads, albeit to very low levels of load. Strain in the steel tube reached 300 microstrain at most, which is well below the yield point. The primary outcome of their work was the development of field data for calibration of an elastic finite element model which was then used to conduct parametric studies that showed stress concentrations that developed at the bottom of the pile between the rock and tube. The authors also developed displaced shape information and corresponding P-y curves. Due to the very low level of

loading, these tests are of limited value, although the authors imply that there was some separation between the tube and core concrete. It is not clear how this was measured, and such a result seems surprising given the extensive studies done by others in the past which have shown composite action.

2.1.5. Gajalakshmi and Helena (2012)

They conducted eight tests on CFSTs and eight tests on steel fiber reinforced concrete filled steel tubes (SCFSTs). They focused their study on the impact of the D/t ratio and the type of infill, namely, plain concrete and steel fiber reinforced concrete. They utilized steel tubes with diameter D = 114 mm. and thickness values such that D/t ratios of 38 and 57 were considered; such tubes were seam welded along their longitudinal direction. They used a cantilever column test setup up along with a connection detail to the foundation that allows for contribution of the steel tube to the flexural strength of the system. The loading protocol included cyclic lateral loading, at constant or increasing drift ratios, with constant axial loading.

They found that the SCFST columns had about 2 times more energy dissipation and higher ductility capacity than the columns filled with plain concrete. They claimed that the failure mechanism of all columns was governed only by the D/t ratio and not by the type of infill nor the type of loading pattern. In addition, they proposed a simplified cumulative damage model that allows to estimate a damage index parameter for CFSTs and SCFSTs.

2.2. Reinforced Concrete Filled Steel Tubes (RCFSTs)

2.2.1. Park et al. (1983)

They conducted experimental tests on two CFST and four RCFST piles with a D/t ratio of 72. They performed moment-curvature analyses and then compared such results with experimental observations. Their test setup consisted of a loading frame to conduct experiments on a three-point bending fashion, including axial loading. The test setup was representative of the top portion of a pile-column system with fixed-head condition, where the critical section develops between the cap element and the column, up to the point of contra-flexure. The six specimens were arranged in three pairs, in which axial load ratios of 10% and 30% were induced in each pair of units. Test units 1 to 4 contained a continuous casing detail, while in units 5 and 6 the steel tubes were embedded only 50 mm. into the loading stub. Moreover, units 1 and 2 did not contained any internal reinforcement.

They found that the units with continuous casing detail developed a strength of about twice that of the units where the casing was partially embedded in the loading stub. However, the displacement ductility capacity of the latter units was significantly higher (μ=18) than that of the units with continuous casing (μ=6). They concluded that the steel tube, partially embedded in units 5 and 6, provided high levels of confinement for the concrete without contributing to the flexural strength, which in turn resulted on the lower strength exhibited by those test units. In addition, the lower ductility capacity of units 1 to 4 was attributed to

the failure mechanism which consisted on tube local buckling, and to the high stresses and strains obtained due to the higher strength developed in the section.

2.2.2. Richards et al. (2011)

They studied the behavior of CFST and RCFST pile-to-concrete-cap connections. They conducted field studies to investigate the impact of parameters such as the tube embedment length into the cap on the development of flexural strength. Since their studies focused on elastic pile behavior, and non-linearity of the cap, the outcomes are of limited importance to the subject of this research project.

2.2.3. Montejo et al. (2012)

They examined the performance of RCFST pile-column bridge bents based upon results of large-scale experimental tests, incremental dynamic analyses, and parametric moment curvature analysis. They separately investigated the behavior of the plastic hinges that develop below ground and above the soil surface in RCSFT pile-column bridge bents, that is, plastic hinges that develop in the top of the column and below ground in the foundation element (pile) depending upon the bent configuration and the direction of the seismic loading.

With regard to the below-ground plastic hinge behavior, they performed analytical studies based upon experimental test results reported by González-Román et al. (2008). Such experiments involved full-scale reversed cyclic experimentation on eighteen RCFST piles using a four-point bending test setup, in which cyclic loading was applied using two hydraulic actuators such that a constant moment region between them was generated. The distance between the actuators was varied in order to consider the potential effects of soft and stiff soil conditions. The RCFST specimens had outer diameters of 610 mm. with tube thickness of 12.7 mm., providing a nominal D/t ratio of 48, while the longitudinal reinforcement ratio of the internal bars was ~2%. The steel tubes were manufactured in accordance with API-5L x52 steel specifications, while the internal reinforcement consisted of A706 Grade 60 longitudinal bars and spirals. A concrete compressive strength of 27.6 MPa was specified for all test units.

On the other hand, for the top plastic hinge behavior, they conducted analytical studies based upon experimental test results reported in detail by Montejo et al. (2009). Such experiments involved half-scale reversed cyclic loading on four RCFST columns. An important feature of these tests is that they tested the specimens under reversed cyclic loading while subjected to temperatures that ranged from -36°C (−33°F) to 22°C (72°F). For that purpose, their specimens were tested inside an environmental chamber. The tests were conducted using a cantilever column test setup in which cyclic loading was applied by means of a hydraulic actuator. They applied axial load to the test units using hydraulic jacks and posttensioning bars along with cross beams. The RCFST specimens had outer diameters of 457 mm. with tube thickness of 9.5 mm., providing a nominal D/t ratio of 48. They considered longitudinal reinforcement ratios of 2.1% and 3.1% and a transverse steel ratio of 1.2%. They studied axial load ratios between 3.3% and 5.9%. The steel tubes were

manufactured in accordance with API-5L x52 steel specifications, while the internal reinforcement consisted of A706 Grade 60 longitudinal bars and spirals. They specified a concrete compressive strength of 27.6 MPa for all test units. As a result of this study, they proposed expressions to calculate the equivalent viscous damping and section curvature limit states for members in which the plastic hinge develops below ground. In addition, a plastic hinge length model and section curvature limit states were developed for members where the plastic hinge develops above ground in the top of the column.

Regarding the below-ground plastic hinge, their conclusion was that the moment capacity is larger than that of the top plastic hinge due to the contribution of the steel tube in the flexural strength. In fact, for the top plastic hinge they concluded that strain limit states are controlled by the tensile strain in the longitudinal bars provided the steel tube confines the concrete but does not contribute to the flexural strength. In addition, they suggested that special detailing of the transverse reinforcement is required in the top hinge in order to avoid early rebar buckling or rupture. Furthermore, they concluded that moment curvature analyses based on strain compatibility and equilibrium can be used to accurately predict the flexural response of RCFST members as experimental results (González-Román et al., 2008; Montejo et al., 2009) suggested that the effects of the tube hoop strains on the confinement of the core and its interaction with the tube longitudinal strains do not play an important role on the lateral response of RCFST pile-columns with thick steel tubes (D/t = 48) and low axial load (ALR = 5%).

2.2.4. Brown et al. (2015)

They conducted experimental tests on thirteen RCFST piles with outer diameters of 20 to 24 in. and thickness values such that D/t ratios between 33 and 192 were considered. The purpose of their study aimed to assess the impact of the D/t ratio on the strain limit states of tube local buckling and fracture. In addition, they also addressed the equivalent viscous damping and provided insight on issues of confinement and analysis methods for RCFST members.

Seven of their specimens focused on varying the D/t ratio while the longitudinal and transverse internal reinforcement was varied in the remaining six test units. They used multiple material sources to cover a broad range of D/t ratios. API 5L seam welded tube, and spirally welded tubes manufactured from ASTM A139 and ASTM A709 Grade 50 T3 steel were utilized. The internal reinforcement consisted of ASTM A706 Grade 60 steel using multiple longitudinal and transverse reinforcement ratios. A concrete compressive strength of 5 ksi was specified for all specimens. With regards to the instrumentation, they used strain gauges, string potentiometers, and a non-contact 3D position measurement system. The loading history they used for each test consisted of two parts. First, before yield, single-cycle sets on increments of a quarter of the yield force were applied in a force-controlled fashion. Then after first yield, displacement-controlled three-cycle sets were applied at different ductility levels.

Regarding the variation on the D/t ratio, they concluded that energy dissipation is greater for thicker tubes (i.e., smaller D/t). Also, early onset of tube local buckling does not affect the

strain limit of tube fracture for pipes with larger D/t ratios, which means that thinner tubes develop tube local buckling earlier than thicker tubes, yet they can reach the same ductility level as the thicker tubes. On the other hand, for the variation on the longitudinal and transverse internal reinforcement, they concluded that only the flexural strength is affected by the amount of reinforcement, which means that strain limit states are governed by the tensile strains in the steel tube.

In addition to the observations on the variation of D/t ratio and internal reinforcement, they also developed expressions for the tensile strain prior onset of tube local buckling and suggested a value of 2.5% for the tensile strain at tube fracture. Furthermore, they provided an expression to calculate the equivalent viscous damping of an RCFST member as a function of the displacement ductility level and D/t ratio. They also showed that the Mander et al. model (1988) could be used to characterize the stress-strain behavior of the confined concrete in RCFST members. Moreover, they suggested that strain compatibility applies up to the onset of local buckling. Thus, the use of a linear strain profile results in accurate estimates of flexural response by means of a moment curvature analysis, even beyond local buckling they observed results in good agreement with the experimental data.

Outcomes of this study are of significant importance for this research project as the aforementioned results set a base point for the behavior of RCFST elements, which can be directly used to analyze the effects of soil stiffness on the seismic performance of such elements.

2.3. Relevant Studies on Reinforced Concrete (RC) Pile-Columns

2.3.1. Chai and Hutchinson (2002)

They conducted four full-scale tests on bridge pile-columns embedded in soil, which were subjected to axial and cyclic lateral loading, at the University of California, Davis, CA. Their specimens consisted of RC columns with diameter D = 406 mm., longitudinal steel ratio ρ = 2.1 %, and two different confining steel ratios ρ_s = 0.57 % and ρ_s = 1.06 %. The longitudinal reinforcement was provided using A706 Grade 60 bars, while the transverse reinforcement consisted of MW25 and MW45 smooth wire with spacing s = 50mm. Based on the particle size distribution, the soil was classified as clean, poorly graded sand (SP). Two different soil conditions were considered, that is, loose and dense sand, for which a different compaction procedure was used on each case, resulting on different soil properties and thus different soil stiffness values. The RC pile-column specimens were tested on a 6.71-m. diameter, 5.49-m. deep, soil container which was filled with sand. The first two specimens had a cantilever length of 812 mm., whereas the remaining two units had and aboveground height of 1,624 mm., corresponding to two and six times the pile diameter, that is, 2D and 6D, respectively.

Their study focused on 3 key parameters: (1) the force-displacement response of the soil-pile-column system; (2) the location of the maximum moment below ground; and (3) the plastic hinge length. They found that the force-displacement response was dominated by the flexural strength of the pile and thus the stiffness of the pile-soil system was not sensitive to

the change in density of the soil under consideration. They calculated the spread of plastic action using measures of curvature along the length of the specimens. They concluded that the plastic hinge length below ground is mostly influenced by the above ground height of the column; the extent of plastic action is longer for taller columns as the moment gradient decreases for such cases. In regards to the location of maximum moment, its depth varied between 2 and 3 times the pile diameter, and it was closer to the ground surface for the longer columns; their conclusion was that the depth to maximum moment is not sensitive to the different soil densities that they analyzed.

2.3.2. Suleiman et al. (2006)

They performed three large-scale tests on reinforced concrete bridge column-foundation-soil systems at the Spangler Geotechnical Experimental Site at Iowa State University, Ames, Iowa. The focus of their research was to study the effects of seasonal freezing on the seismic response of the system. The specimens consisted of RC pile-column units. Two of them had a uniform diameter of 0.61 m., whereas the third specimen had an oversized shaft (pile) diameter of 0.91 m., and they were tested at ambient temperatures of 23 °C, –10 °C and –6 °C, respectively. The specimens were subjected to cyclic lateral loading with no axial load. The loading protocol that they utilized consisted of force-controlled single sets and displacement-controlled three-cycle sets for the elastic and inelastic portions of the test, respectively.

By analyzing the experimental results of the first two units, they found that the force-displacement response of this type of systems is significantly influenced by the presence of frozen soil. The main differences the seasonal freezing conditions induced to the system were: (1) the effective elastic stiffness increased by 170%; (2) the location of the maximum moment shifted one pile diameter upward, inducing a higher lateral load, thus increasing the shear demand in the column; (3) the length of the plastic region in the foundation shaft reduced 64%; and (4) the width of the gap in the soil reduced by 60%. They attributed these changes to the plastic hinge shift and the reduction of the plastic region, which was caused by a frozen soil layer of 0.76 m. below the ground surface. On the other hand, the use of an oversized foundation shaft in the third specimen reduced the effects of seasonal freezing in the force-displacement response of the column, as the difference between the experimental and theoretical (i.e., column with fixed-based) was only 10%, indicating that the changes observed in the second specimen were mostly due to the presence of frozen soil rather than the temperature effects on concrete or reinforcing bars.

2.3.3. Chang and Hutchinson (2013)

They conducted an experimental test of a conventional RC pile embedded in a multilayer soil system. The specimen had a diameter D = 250 mm. and it was embedded in a two-degree-sloped laminar soil box, which in turn was mounted on a shake table at the University of California, San Diego. The pile specimen had an above-ground length of 1,000 mm. and it was embedded 1,750 mm. into a three-layer soil profile, which consisted of a stiff uppermost crust (625-mm. thick) overlying a saturated loose sand layer (625-mm. thick), which in turn was on top of a dense sand layer (500-mm. thick); The middle soil

layer corresponds to a loose liquefiable sand layer. The entire soil-pile system was subjected to five ground motions of increasing intensity to induce liquefaction of the middle saturated layer; no axial load was applied to the specimen. They also included white noise signals between ground motions for system identification purposes. In terms of instrumentation, they utilized different sensors that included, among others, pore pressure gauges and soil pressure gauges.

The goal of their study was to analyze plastic demands on the RC pile considering the effects of liquefiable soil conditions. For that purpose, they utilized measured curvature profiles to calculate the plastic hinge length. They found that the plastic hinge length was larger (1.5D) than that used in conventional column design. Such an increase in the plastic hinge length was attributed to liquefaction of the middle soil layer, which in turn induced settlement of the crust layer.

2.4. Soil-Structure Interaction (SSI)

2.4.1. Boulanger et al. (1999)

They conducted experimental tests on pile-column specimens embedded in a soft clay layer overlying dense sand. The tests were conducted on the large shake table on the 9-m-radius centrifuge at the University of California at Davis, CA. The specimens consisted of aluminum piles, equivalent to steel tube piles with a diameter of 670 mm. and a 19-mm. wall thickness. They subjected the specimens to nine ground motions corresponding to scaled versions of the 1989 Loma Prieta and 1995 Kobe earthquakes. No attempts to repair the piles were performed as they remained elastic during all ground motions. However, after the fourth ground motion, they restored the soil profile to its pristine conditions by pulling the pile out of the centrifuge and re-driving it on different locations while the centrifuge was working.

They developed a dynamic p-y analysis method (i.e., beam on a non-linear Winkler foundation), capable of capturing gapping effects, for which they conducted sensitivity and parametric studies to assess the ability of the proposed method of reliably capturing the observed soil-pile-column interaction. They performed one-dimensional equivalent linear site response analysis and then conducted dynamic p-y analyses to determine the structural response of the piles (e.g., displacements, accelerations).

They found that using site response analysis, the structural response can be underestimated by 20%, whereas when recorded free-field ground motions were utilized as inputs to the dynamic p-y model, the structural response was overestimated by 10%. These and other results from their sensitivity analyses suggest that the proposed p-y dynamic method works reasonably well on predicting the soil-foundation-structure interaction, and also that a big source of uncertainty is the site response calculations. As previously mentioned, their specimens remained elastic during the application of all ground motions. Perhaps different results would be obtained when both the soil and pile-column exhibit non-linear behavior.

2.4.2. El Naggar and Bentley (2000)

They developed an analysis approach to account for dynamic loading on piles considering the soil-pile interaction, for which they utilized the beam on non-linear Winkler foundation (BNWF) approach. Their model also accounts for damping from the soil by considering the velocity of the soil particles at a given depth and the frequency of loading. They validated their model based upon lateral loading test data. They also proposed a spring and a dashpot model to perform equivalent linear analyses for the transient response of soil-pile systems. They found that as the frequency of loading increases, the soil response as represented by lateral strength also increases.

2.4.3. Sritharan et al. (2007)

They conducted numerical analyses of a soil-foundation-column system consisting of an RC bridge column supported by a cast-in-drilled-hole (CIDH) foundation shaft with the same diameter, embedded into stiff, low plasticity clay. The system consisted of a 0.61-m-diameter, 2.69-m-tall bridge column, supported by a CIDH foundation shaft with the same diameter and an embedded length of 10.36 m. They validated their numerical models using experimental data recorded from two experimental tests performed in warm (23 °C) and cold (–10 °C) conditions, conducted at an outdoor facility at Iowa State University (Suleiman et al., 2006).

The analysis approach they employed consisted of a two-dimensional representation of the soil-foundation-column system using LPILE. This approach used 100 equal-length beam-column elements in which their hysteretic behavior was determined based upon moment-curvature analysis of the column-foundation shaft section. Beyond the confinement provided by the transverse reinforcement, they included an additional confinement for the cover concrete provided by the pressure of the surrounding soil on the foundation shaft. Although it is not clear how they included this effect on the moment-curvature analyses, they concluded that this additional confinement prevented concrete spalling in the foundation shaft, which was observed during the experimental tests. The soil stiffness was represented with compression-only, non-linear springs located on both sides of the foundation shaft at the mid-height of each element. Properties of such springs were determined by performing p-y curve analyses. Temperatures effects were considered to determine the stress-strain curves of the concrete, reinforcing steel, and soil. Their analyses included ambient temperatures of 23 °C, –1 °C, –7 °C, –10 °C, and –20 °C. They also investigated the effects of axial load and depth of the frozen soil layer.

They found that cold temperatures significantly influence the shear strength and modulus of low plasticity clay, namely, for temperatures of –1 °C and –20 °C those parameters increased by 10 to 35 and 8 to 45 times, respectively. Therefore, the soil stiffness increases such that the location of maximum moment shifts upward (closer to the soil surface) increasing the effective elastic stiffness, the column and foundation shaft shear demand, and reducing the lateral displacement capacity and plastic hinge length. They also concluded that the depth of the frozen soil layer and a 5% axial load ratio have minimal effects on the

response of the soil-foundation-column system, when compared to the overall impact of cold temperatures on the soil and material properties.

2.4.4. Allotey and El Naggar (2008a, 2008b)

These studies build upon previous work conducted by one of the authors (Naggar and Bentley, 2000). They developed a model that allows to conduct dynamic soil-structure interaction analysis. Such model is based on the beam on non-linear Winkler foundation (BNWF) and it incorporates features that include: loading and unloading rules, slack zone development, cyclic degradation, and radiation damping. They validated their model using results from two full-scale tests of RC piles performed in sand and clay, respectively. They found that the maximum moment decreases due to soil cave-in and recompression, which in turn moves the depth-to-maximum moment closer to the ground surface and increases the energy dissipation of the system. However, it is not clear why the moment would decrease with a shorter lever arm as one would expect higher shear and moment demands. They also claimed that their model is computationally more efficient.

2.4.5. Wotherspoon et al. (2010)

They implemented the beam on non-linear Winkler foundation (BNWF) approach in order to model the monotonic and cyclic soil-foundation-column response of two identical RC bridge pile-columns tested at Iowa State University (Suleiman et al., 2006). The difference between the tested units was only the ambient temperature; the first specimen was tested during the summer (i.e., warm conditions, 23°C) and the second one was tested during the winter season (i.e., cold conditions, -10°C). The BNWF approach they implemented consisted of column and pile elements with a plastic rotational spring at each end (concentrated plasticity) and an elastic section in between. Properties of these rotational springs were determined based upon moment-curvature analyses with appropriate material properties to account for the effects of temperature. The soil was modeled using two non-linear spring elements (one on each side of the pile), attached to each node between pile-column elements. The compression only, bi-linear force-displacement relationship of each spring was calculated using p-y curve analysis. For the model with frozen soil conditions, a method was proposed in order to include the effects of a tension crack that developed on the sides of the pile, perpendicular to the direction of loading. This approach reduced the post-yield soil stiffness, in which properties of the modified force-displacement relationships of the soil are calculated based upon the gap opening and tension crack width. They validated their numerical models using horizontal displacements recorded at three points in the column, including the gap between the foundation and the soil at the ground level. In addition, they correlated data from strain gauges, attached to the extreme reinforcing bars along the length of the pile-column, in order to determine the location of maximum moment and the spread of plastic action.

They found that the proposed modeling approach resulted on an accurate representation of the experimental results from the specimens in both warm and cold soil conditions. They concluded that the ambient temperature conditions significantly influence the effective stiffness, maximum moment (and its location), shear demand, and the spread of plastic

action. Furthermore, the moment and shear demand in the pile increased by 20% and 33%, reducing the depth of their location with cold temperatures by 77% and 53%, respectively. They claimed that these differences indicate that if material properties for only non-frozen conditions are considered, it could result in a deficient design.

2.5. Plastic Hinge Models for Pile-Columns

2.5.1. Budek et al. (1995, 2000)

They conducted analytical studies on reinforced concrete (RC) pile-columns considering two fixity conditions, namely, pinned-head and fixed-head. The focus of their study was to determine the ductility capacity, equivalent plastic hinge lengths, depth to fixity, and depth to maximum moment. For that purpose, they developed a non-linear finite element model that utilized the Winkler beam approach, in which the soil behavior was represented by means of springs whose properties were calculated based upon the modulus of subgrade reaction. Their study considered various levels of soil stiffness using cohesionless soils, for which the modulus of subgrade reaction (k) ranged from 3,200 kN/m^3 to 48,000 kN/m^3. They studied three soil models: (1) a linear-elastic relationship; (2) a bilinear model, in which the stiffness changed to a quarter of its initial value after a prescribed lateral displacement; and (3) a hyperbolic p-y curve model. Moreover, they assumed a linear increase of the soil stiffness with depth. Non-linear behavior of the pile-columns was considered using results from moment-curvature analyses such that the effective flexural stiffness at a given deformation was calculated based upon the moment-curvature slope at that level of deformation.

Regarding the soil models, they argued that a linear-elastic soil model might be suitable for large values of the aboveground height of the pile-column and modulus of subgrade reaction of the soil, while a bi-linear soil model could be considered for low values of both parameters. The reason for this is that the lower the soil stiffness and the shorter the column length, the larger is the volume of soil that needs to be mobilized; hence making important to consider the soil non-linearity and its interaction with the pile-column. They claimed that although an elastic approach for the soil may be adequate for some cases, it might over-predict the plastic hinge length and depth to maximum moment.

They found that the plastic hinge length was significantly larger (Equation 2-1) than the value commonly adopted in practice at that time, namely, one pile diameter (1D); this expression provides a conservative estimate of the plastic hinge length based on the pile diameter (D) and the aboveground length (L_a). They found that, due to moment redistribution, the soil-pile-column system stiffness reduces and the point of maximum moment moves closer to the soil surface, which in turn shortens the cantilever length, thereby increasing shear demands when inelastic behavior of the soil is considered. Stated otherwise, the depth to the plastic hinge shifts upwards, closer to the soil surface, when pile-columns develop inelastic action, because after onset of the plastic hinge less soil is mobilized. As such, they concluded that after yielding, the depth to maximum moment reduces to 0.7 times the value found from analysis of the elastic range. They provided charts to determine the depth to plastic hinge, plastic hinge length, and displacement ductility

capacity as a function of a non-dimensional system stiffness parameter and aboveground length (L_a), as shown in Equation 2-2. In this equation, D* = 1.83 m, while EI_{eff} is the effective section stiffness, and k is the modulus of subgrade reaction.

$$L_p = D + 0.06\frac{L_a}{D} \qquad \text{Equation 2-1}$$

$$\frac{k \cdot D^6}{D^* \cdot EI_{eff}} \qquad \text{Equation 2-2}$$

Their recommendations were based on the premise that if the displacement ductility capacity of a pile-column is to be calculated, it can be done using a plastic hinge approach in combination with an equivalent fixed-base column, as shown in Figure 2-1. Using this approach, elastic displacements (Δ_y) can then be calculated assuming the equivalent column has its base at a depth of fixity (D_f), while plastic displacements (Δ_p) are calculated assuming the base of the column is centered at the depth to plastic hinge (D_{ph}), as represented with the elastic and inelastic curvature distributions, respectively. In Figure 2-1, L_a is the aboveground length, D_f is the depth to fixity, D_{ph} is the depth to plastic hinge (maximum moment), and D represents the shaft diameter. Moreover, $Ø_y$ and $Ø_u$ are the equivalent yield and ultimate curvatures, respectively, L_p is the equivalent plastic hinge length (Equation 2-1), while L_{eq1} and L_{eq2} are the equivalent cantilever lengths used to calculate the elastic and plastic components of the ultimate displacement, respectively.

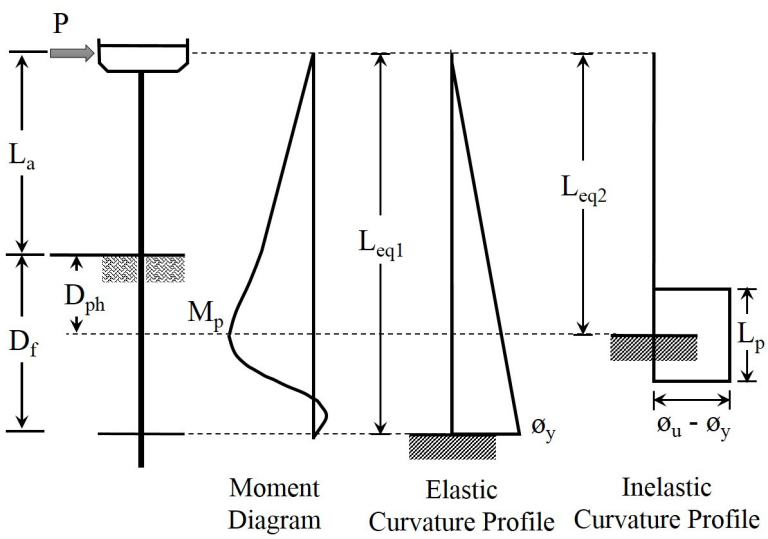

Figure 2-1 Plastic hinge model for RC drilled shafts (Budek et al. 1995)

Using the above model, a bilinear force-displacement response along with the displacement ductility capacity (μ_Δ) can be determined. First, the equivalent yield displacement (Δ_y) is calculated using the equivalent yield curvature ($Ø_y$) by integrating over the length of the pile-column to the depth to fixity (L_{eq1}), as shown in Equation 2-3. The plastic displacement (Δ_p), on the other hand, is determined using the plastic rotation (Equation 2-4), and the equivalent length measured to the depth to plastic hinge (D_{ph}), as shown in Equation 2-5. The ultimate displacement (Δ_u) can then be determined by adding both elastic and plastic

components, as shown in Equation 2-6. Finally, the displacement ductility is calculated using Equation 2-7.

$$\Delta_y = \frac{\phi_y \left(L_{eq1}\right)^2}{3} \qquad \text{Equation 2-3}$$

$$\theta_p = L_p \left(\phi_u - \phi_y\right) \qquad \text{Equation 2-4}$$

$$\Delta_p = \theta_p \left(L_{eq2}\right) = L_p \left(\phi_u - \phi_y\right) L_{eq2} \qquad \text{Equation 2-5}$$

$$\Delta_u = \Delta_y + \Delta_p = \frac{\phi_y L_{eq1}^{\ 2}}{3} + L_p \left(\phi_u - \phi_y\right) L_{eq2} \qquad \text{Equation 2-6}$$

$$\mu_\Delta = \frac{\Delta_u}{\Delta_y} = 1 + \frac{\Delta_p}{\Delta_y} = 1 + \frac{3 L_p L_{eq2} \left(\phi_u - \phi_y\right)}{\phi_y L_{eq1}^{\ 2}} \qquad \text{Equation 2-7}$$

Since the above model was developed considering RC drilled shafts, its applicability to reinforced concrete filled steel tube (RCFST) pile-columns is arguable. The charts that they developed to calculate the depth to plastic hinge, plastic hinge length, and depth to fixity, as a function of a non-dimensional system stiffness parameter, were based upon the effective stiffness of RC shafts, which is in fact smaller than that of RCFST shafts. As such, the latter would potentially have a smaller spread of plasticity, affecting the equivalent plastic hinge length, depth to plastic hinge, and depth to fixity. Moreover, while this model considers part of the soil flexibility in the calculation of the yield displacement (Δ_y), the assumption of a linear curvature distribution to the depth of fixity is arguable.

2.5.2. Chai (2002)

He developed a kinematic model to calculate an idealized, bi-linear, force-displacement response of reinforced concrete (RC) drilled shafts. His approach was based on the equivalent cantilever concept, assuming that the stiffness of an equivalent cantilever column has to equal the stiffness of the soil-pile system.

For that purpose, he used solutions for displacement and ultimate soil pressure distributions (Poulos and Davis, 1980) for both cohesive and cohesionless soils. By considering both force and displacement response of the soil-pile system, the idealized force-displacement response of the equivalent cantilever can be calculated using a plastic hinge model similar to that proposed by Budek et al. (1995), as previously shown in Figure 2-1. The main differences of the plastic hinge model proposed by Chai (2002) are the equivalent lengths used for calculation of elastic and plastic displacement components, and the plastic hinge length. First, the equivalent lengths L_{eq1} and L_{eq2} are measured to the depth to fixity and depth to maximum moment for the elastic and plastic displacements, respectively; however, for both equivalent lengths he provided different recommendations to those by Budek et al. (1995). In regard to the plastic hinge length, based on experimental observations (Chai and Hutchinson, 2002), he argued that the plastic hinge length is insensitive to the soil stiffness and that it is significantly impacted by the aboveground length (L_a), as shown in Equation 2-8.

$$L_p = D + 0.1L_a \leq 1.6$$ Equation 2-8

The total displacement capacity can be calculated by adding both elastic and inelastic contributions with the formulation proposed by Budek et al. (1995), namely, Equation 2-3 through Equation 2-7, recognizing that appropriate values of equivalent lengths and plastic hinge length must be utilized.

2.5.3. Suarez and Kowalsky (2007)

They conducted parametric studies on reinforced concrete (RC) drilled shafts considering soil-structure interaction. For that purpose, they developed a finite element (FE) structural model that considered the non-linear behavior of the materials by using results of bilinear moment-curvature analyses. They characterized the soil as a single uniform layer of either clay or sand, represented in the modeling approach by non-linear springs, whose properties were determined from p-y curve analyses. In addition, they considered two fixity conditions, namely, pinned-head and fixed-head.

Using results from their parametric study, they proposed parameters to be used in combination with an equivalent cantilever plastic hinge approach, which allows for prediction of the displacement capacity and equivalent viscous damping of the system. Their equivalent plastic hinge model approach is similar to those proposed by Budek et al. (1995, 2000) and Chai (2002). The main differences are: (1) they proposed to use only one equivalent length (L_{eq}) for the calculation of both elastic and plastic displacements; and (2) they proposed to use parameters to account for foundation flexibility on the yield displacement calculation, and to account for corrections on plastic deformations when the pile-column system is in double bending (fixed-head condition).

Regarding the equivalent plastic hinge length, they proposed to use the model developed by Chai (2002), as previously described in Equation 2-8, which applies for single bending. However, for double bending, they proposed to use the plastic hinge length model proposed by Priestley et al. (1996), which can be written as:

$$L_p = 0.08L_i + 0.022 f_y d_{lb}$$ Equation 2-9

In the equation above the first term considers the distance from the plastic hinge length to the point of contraflexure (L_i), whereas the second term represents an increase in the plastic hinge length due to strain penetration in the cap beam in terms of the yield strength (f_y) and diameter (d_{lb}) of the longitudinal reinforcement. A schematic representation of the equivalent cantilever approach proposed by Suarez and Kowalsky (2007) for both single and double bending are shown in Figure 2-2 and Figure 2-3.

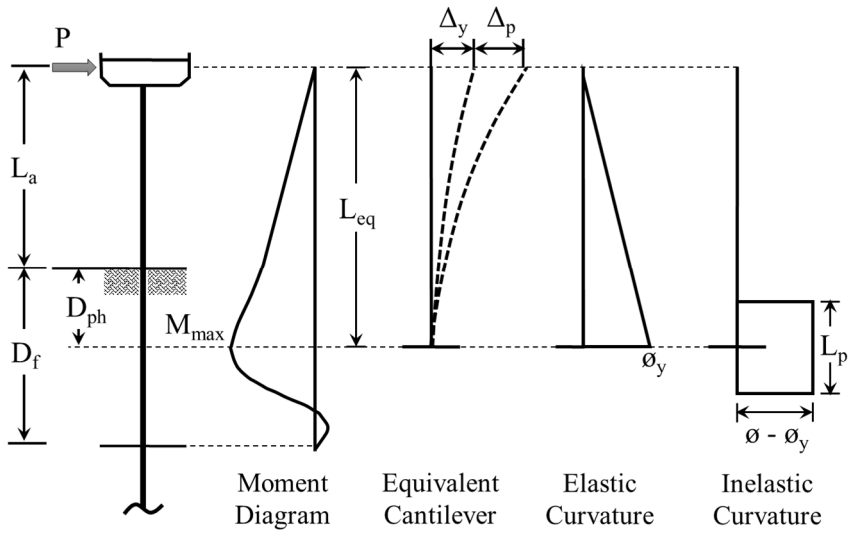

Figure 2-2 Equivalent cantilever in single bending (Suarez and Kowalsky, 2007)

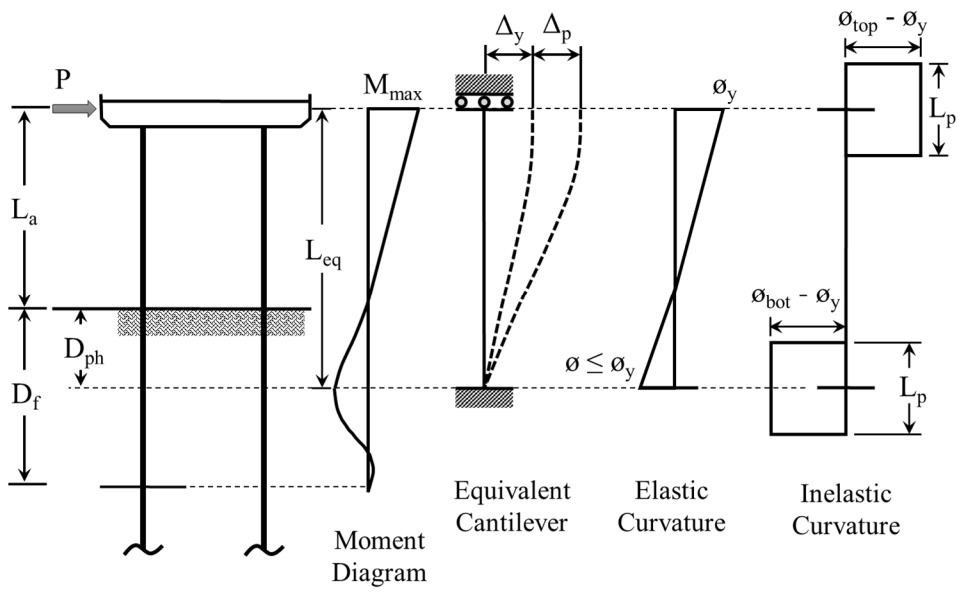

Figure 2-3 Equivalent cantilever in double bending (Suarez and Kowalsky, 2007)

For pile-column systems in single bending, the displacement capacity can then be determined using Equation 2-10 through Equation 2-14, which are a function of the yield curvature ($Ø_y$), ultimate curvature ($Ø_u$), equivalent length (L_{eq}), plastic hinge length(L_p), and a coefficient (α) that accounts for the foundation flexibility.

$$\Delta_y = \alpha \frac{\phi_y L_{eq}^{\ 2}}{3} \qquad \text{Equation 2-10}$$

$$\theta_p = L_p\left(\phi - \phi_y\right) \qquad \text{Equation 2-11}$$

$$\Delta_p = \theta_p L_{eq} = L_p\left(\phi - \phi_y\right) L_{eq} \qquad \text{Equation 2-12}$$

$$\Delta_u = \Delta_y + \Delta_p = \alpha \frac{\phi_y L_{eq}^{\ 2}}{3} + L_p \left(\phi - \phi_y\right) L_{eq} \qquad \text{Equation 2-13}$$

$$\mu_\Delta = \frac{\Delta_u}{\Delta_y} = 1 + \frac{\Delta_p}{\Delta_y} = 1 + \alpha \frac{3 L_p L_{eq} \left(\phi - \phi_y\right)}{\phi_y L_{eq}^{\ 2}} \qquad \text{Equation 2-14}$$

For pile-column systems in double bending, on the other hand, the displacement capacity of the system is determined using Equation 2-15 through Equation 2-19, recognizing that the equivalent length (L_{eq}), plastic hinge length (L_p), and the coefficient α, are those corresponding to the appropriate fixity condition. In addition, Suarez and Kowalsky (2007) recognized that, after onset of the aboveground hinge, displacements continue to increase until the hinge below ground forms. As such, in order to account for this behavior, the plastic displacement (Equation 2-17) is calculated based on the aboveground hinge only, including a correction factor (β) that accounts for the aforementioned behavior.

$$\Delta_y = \alpha \frac{\phi_y L_{eq}^{\ 2}}{6} \qquad \text{Equation 2-15}$$

$$\theta_p = L_p \left(\phi_{top} - \phi_y\right) \qquad \text{Equation 2-16}$$

$$\Delta_p = \theta_p \beta L_{eq} = L_p \left(\phi_{top} - \phi_y\right) \beta L_{eq} \qquad \text{Equation 2-17}$$

$$\Delta_u = \Delta_y + \Delta_p = \alpha \frac{\phi_y L_{eq}^{\ 2}}{6} + L_p \left(\phi_{top} - \phi_y\right) \beta L_{eq} \qquad \text{Equation 2-18}$$

$$\mu_\Delta = \frac{\Delta_u}{\Delta_y} = 1 + \frac{\Delta_p}{\Delta_y} = 1 + \alpha \frac{6 L_p \beta L_{eq} \left(\phi_{top} - \phi_y\right)}{\phi_y L_{eq}^{\ 2}} \qquad \text{Equation 2-19}$$

Suarez and Kowalsky (2007) validated their model upon comparison with experimental data reported by Chai and Hutchinson (2002); results showed close agreement. This model is useful to determined displacement capacity of RC drilled shafts. However, it may not be applicable to RCFST pile-column as their flexural stiffness is larger when compared to RC elements.

2.5.4. SCDOT Seismic Design Specifications for Highway Bridges (2008)

The South Carolina Department of Transportation (SCDOT), seismic design specifications for highway bridges, classifies pile-column elements as drilled shafts. The SCDOT seismic design criteria utilizes an equivalent cantilever approach to determine the displacement capacity of such systems; however, the document explicitly states that the procedure is applicable to reinforced concrete (RC) drilled shafts only, and that if steel casing is used (i.e., RCFSTs) a refined analysis is required to determine the capacity of the system.

Depending upon the direction of loading and connection details, one or two plastic deformations are determined. For single bending, the plastic hinge forms below ground and the displacement capacity of the system is determined using an equivalent cantilever with its base fixed at a depth of fixity (D_f). As such, the equivalent length is measured to the depth of fixity, considering the aboveground length (L_a). The plastic hinge length model is shown in Equation 2-20. For double bending, on the other hand, they consider plastic deformations

from the below ground hinge in combination with those from the top hinge that forms at the top of the column in the column-bent cap interface. The equivalent length is also measured to the depth to fixity (D_f) and the plastic hinge model for the top hinge is shown in Equation 2-21, where L' represents the distance from the point of contraflexure to the column cap.

$$L_p = D + 0.08\left(L_a + D_f\right) \qquad \text{Equation 2-20}$$

$$L_p = 0.08L' + 0.15 f_{ye} d_{bl} \geq 0.3 f_{ye} d_{bl} \qquad \text{Equation 2-21}$$

For the double bending case, consideration of both plastic hinges in the displacement capacity is arguable, because the below ground hinge will only develop after substantial damage has occurred in the top hinge. As such, it could result in over prediction of the drilled shaft capacity. Furthermore, the specifications state that the depth to fixity needs to be determined using a detailed soil-structure interaction (SSI) modeling approach, which means that in order to determine the displacement capacity a detailed finite element structural model must be developed.

2.5.5. Chiou et al. (2009)

They proposed a plastic hinge length model that allows for calculating the force-displacement response capacity of drilled shafts. This model depends only on the yield (M_y) and ultimate (M_u) moments of the drilled shaft cross section, and the lateral soil pressure (p), as shown in Equation 2-22.

$$L_p = \frac{1}{10}\sqrt{\frac{2\left(M_u - M_y\right)}{p}} \qquad \text{Equation 2-22}$$

They developed a finite element (FE) structural model considering distributed plasticity, although it is not clear the implementation of such a model as details regarding the modeling approach are not provided. Their FE model considered the soil behavior by means of non-linear spring whose properties were assigned based upon p-y curve analyses. They showed that using the proposed plastic hinge approach, results are accurate in terms of force and displacement response, when compared to experimental field data. However, they recognized that moments and thus curvatures were not in agreement.

This approach has two main drawbacks. First, the plastic hinge model was developed based on the assumption that the soil pressure is uniform along the pile length, which is not possible because of the effective stresses in the soil and the level of deformations at different depths. Second, the proposed plastic hinge length can only be utilized in combination with a detailed FE structural model that includes non-linear behavior.

2.5.6. Caltrans (2013)

According to the seismic design criteria provided by Caltrans (2013), pile-column elements are classified as "Type I shafts". These type of elements develop a plastic hinge below ground and the designation assumes that the area of transverse and longitudinal reinforcement may vary, but the confined core cross section and cover must be the same for both column and pile portions. The criteria require that the column displacement must

include elastic and plastic components, as well as deformations due to foundation flexibility; however, no guidance is provided with respect to the inclusion of foundation flexibility on the elastic component of the displacement capacity.

For single bending, the drilled shaft displacement capacity, using Caltrans (2013) criteria, is determined using an equivalent fixed-base column, similar to the approach by Suarez and Kowalsky (2007), as shown in Figure 2-4, with the exception that correction factors are not utilized, and for the calculation of the elastic displacements the equivalent cantilever has its base centered at the depth to plastic hinge (D_{ph}). Moreover, the definition of the equivalent plastic hinge length (L_p) is shown in Equation 2-23, and the base of the inelastic curvature distribution coincides with the base of the equivalent cantilever. Using this model the ultimate displacement (Δ_u) can be determined by adding elastic (Δ_y) and plastic components (Δ_p) using Equation 2-24 through Equation 2-28.

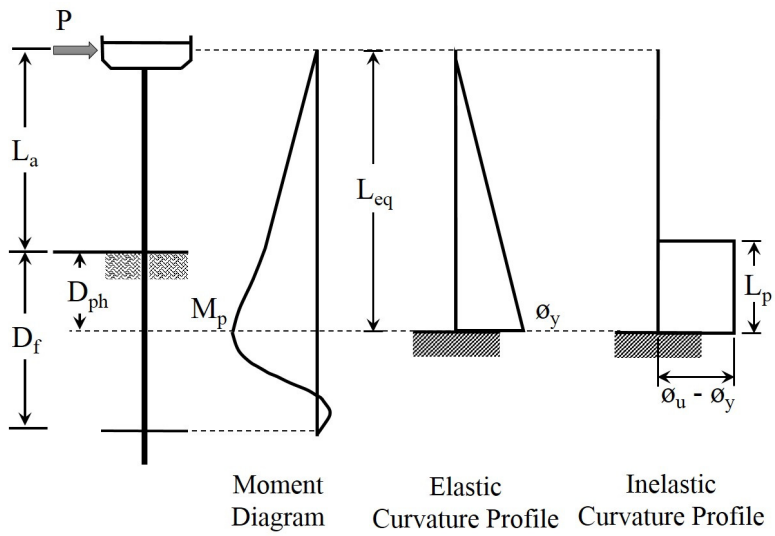

Figure 2-4 Plastic hinge model for Type I drilled shafts (Caltrans 2013)

$$L_p = D + 0.08L_{eq} \qquad \text{Equation 2-23}$$

$$\Delta_u = \Delta_y + \Delta_p \qquad \text{Equation 2-24}$$

$$\Delta_y = \frac{\phi_y L_{eq}^{\ 2}}{3} \qquad \text{Equation 2-25}$$

$$\Delta_p = \phi_p \left(L_{eq} - \frac{L_p}{2} \right) \qquad \text{Equation 2-26}$$

$$\theta_p = L_p \left(\phi_u - \phi_y \right) \qquad \text{Equation 2-27}$$

$$\Delta_u = \Delta_y + \Delta_p = \frac{\phi_y L_{eq}^{\ 2}}{3} + L_p \left(\phi_u - \phi_y \right) \left(L_{eq} - \frac{L_p}{2} \right) \qquad \text{Equation 2-28}$$

Although Caltrans (2013) does not explicitly specify whether the above formulation is applicable for RC or RCFST shafts, the designation of "Type I shafts" assumes a steel core with longitudinal and transverse reinforcement, and cover concrete. As such, it is reasonable to assume that it only refers to RC elements. Furthermore, the plastic hinge model assumes a

linear distribution to the depth to plastic hinge, which neglects the soil contribution on the foundation flexibility. In addition, Caltrans (2013) does not provide provisions or recommendations related to the depth to plastic hinge; similar to the SCDOT (2008) approach, the depth to plastic hinge should be determined based upon SSI analyses.

For double bending of drilled shafts, Caltrans (2013) does not explicitly provides guidance as to how to determine the displacement capacity. However, it provides a plastic hinge length model for plastic hinges forming at the interface with the bent cap for either RC or RCFST, as shown in Equation 2-29. Note that this expression is valid as long as a gap is provided between the steel tube and the bent cap beam.

$$L_p = 0.08L + 0.15 f_{ye} d_{bl} \geq 0.3 f_{ye} d_{bl} \qquad \text{Equation 2-29}$$

2.5.7. Goel (2015)

He conducted analytical studies on prestressed concrete and hollow-steel tube piles to assess the effectiveness of current recommendations for depth to plastic hinge and equivalent plastic hinge lengths. For that purpose, he developed a finite element (FE) structural model to conduct static pushover analyses that considered non-linear behavior using a distributed plasticity, fiber-based approach. The soil was modeled using non-linear springs, whose properties where determine based upon bi-linear p-y curve analyses. Such analyses considered soil variability represented by upper and lower bounds of the p-y curves by using multipliers of 0.67 and 1.5. Six soil types where considered, namely, three soil stiffness levels for both sand and clay.

Goel (2015) found that the plastic hinge length depends on the demand level, while the depth to plastic hinge is not affected. The former is an interesting finding because current plastic hinge length models depend only on the pile dimeter (D) and the aboveground length-to-column diameter (L_a/D) ratio. The latter is expected because after onset of the plastic hinge, the soil-pile interaction reduces as the pile flexural stiffness decreases due to increased damage. In terms of the soil type, he found that current plastic hinge recommendations produce smaller plastic hinge lengths for clays. He also concluded that results showed larger depths to plastic hinge when compared with current approaches.

One of the most significant findings is that both the depth to plastic hinge and the plastic hinge length can significantly change depending upon the soil type and its variability. This suggests that the plastic hinge length and its corresponding depth should be a function of the soil type. In terms of the soil variability, his results suggest that the plastic hinge and its depth can increase within one and three pile diameters (1D and 3D), respectively, for lower-bound when compared to upper-bound p-y curves.

CHAPTER 3

3. STUDY PLAN

3.1. Research Gap

Past experimental and analytical studies (González-Román et al., 2008; Montejo et al., 2012; Brown et al., 2015) have analyzed the performance of reinforced concrete filled steel tube (RCFST) elements at a section and member levels, that is, moment-curvature and force-displacement response, respectively. Thus, the failure mechanism for such elements has been established. The failure mode starts with onset of tube local buckling which continuously grows until tube fracture occurs. Furthermore, strain limits have been proposed for both the tensile strain prior onset of tube buckling and tube fracture. In addition, an equivalent viscous damping expression has been developed and strain compatibility has been verified through experimental tests (Brown et al., 2015).

While past research outcomes, described above, are useful for design of RCFST column elements, there is still a need to understand the behavior of RCFSTs embedded in soil, which is precisely the case of pile-columns (also known as drilled shafts) and the focus of the research described in this report. More specifically, there is a need to understand how the soil stiffness affects the plastic hinge when, due to structural configuration and direction of seismic loading, it develops below ground.

The moment distribution profile and the moment gradient could significantly change depending on the relative soil-pile-column stiffness. This means that for a stiffer soil profile the plastic hinge could move closer to the soil surface and the spread of inelastic action could be smaller due to a higher moment gradient, similar to that of a fixed-base condition, which in turn increases the lateral strength and shear demands of the system (Suleiman et al., 2006). On the other hand, for a soft soil condition, the location of the plastic hinge depends on the effective soil-pile-column stiffness, potentially moving the plastic hinge downward into the ground, modifying the moment distribution and thus the moment gradient, resulting on a greater spread of inelastic due to a smaller moment gradient, which in contrast to a stiffer soil profile decreases the lateral strength and shear demands of the system (Suleiman et al., 2006). Moreover, the hysteretic behavior and energy dissipation of RCFST pile-columns could also be influenced by the soil stiffness as this parameter has a direct effect on the soil-pile-column interaction. Furthermore, the difference in the hysteretic behavior, energy dissipation, moment gradient, and the spread of inelastic action, induced by the effect of the soil stiffness, could have a significant influence on the plastic hinge length, equivalent viscous damping, and performance limit states of the system under consideration. As such, understanding the effects of the soil stiffness on the aforementioned parameters could play an important role for seismic design and assessment of RCFST pile-columns, particularly when displacement-based approaches are implemented (e.g., Priestley et al., 2007), as accurate estimates of the limit states and equivalent viscous damping are essential.

3.2. Objectives

The main goal of the study described in this report is to analyze the effects that soil stiffness could induce on the structural performance of RCFST pile-columns when the plastic hinge develops below ground. More specifically, this study aims to evaluate the effects of soil stiffness on the:

1) Force displacement response. This will provide an insight not only into the shape of the hysteretic behavior but the force and displacement levels the system can undergo when different soil stiffness levels are considered.

2) Energy dissipation characteristics. A revision of the equivalent viscous damping model proposed by Brown et al. (2015) is expected. Besides the D/t ratio parameter, the new model will account for the effective soil-pile-column stiffness, which is directly impacted by the length of the column above ground and the soil stiffness.

3) Plastic hinge length. A plastic hinge model that includes the effects of the diameter-to-thickness (D/t) ratio, aboveground length-to-diameter (L_a/D) ratio, and soil stiffness will be developed. Such a model will allow for determination of the system displacement at different limit states.

4) Performance limits states. Previous research efforts provided strain limits for the design of RCFST elements (Brown et al., 2015). At a global level in a RCFST pile-column system, performance limits states (i.e., system displacement or drift) depend upon the confinement provided by the surrounding soil. As such, performance limit states will be developed considering the effects of the moment gradient induced by such confinement effect, the length of the column above ground (L_a), and ultimately the effective soil-pile-column stiffness.

CHAPTER 4

4. METHODS

In order to accomplish the objectives described in the previous section, this study had two main components. First, an experimental program was conducted on Reinforced Concrete Filled Steel Tube (RCFST) specimens embedded in sand. Then, the second component consisted of conducting parametric studies. For that purpose, a finite element (FE) structural model was developed using the OpenSees framework software (McKenna et al., 2000). The modeling approach consisted of non-linear, fiber-based RCFST elements along with non-linear springs for soil characterization. The developed model was validated and calibrated based upon data collected from the experimental program. This section describes both experimental and analytical components of this study.

4.1. Experimental Program

Twelve half-scale experimental tests were conducted on RCFST pile-column specimens embedded in sand at the soil-structure interaction (SSI) facility at the Constructed Facilities Laboratory (CFL) at North Carolina State University (NCSU). The system was constructed around a 20-foot-deep testing pit, and was designed to apply cyclic lateral loading and to induce different soil stiffness levels by pre-stressing of a soil profile, as explained in subsequent sections. The test specimens, test setup, instrumentation, and main parameters considered in the experimental program are described herein.

4.1.1. Test Specimen Description

The RCFST specimens consisted of steel tubes filled with concrete and internal reinforcing steel. Spirally welded steel tubes without skelp or splice welds were used; performance of such steel tubes for seismic applications has been reported elsewhere (Fulmer and Kowalsky, 2011). The steel tubes were manufactured according to ASTM A-139 Grade B steel, with the exception that they were not pressure tested. Consequently, they were labeled as ASTM A-252 Grade 3 steel, yet met all material specification requirements for ASTM A-139 Grade B steel. The steel tubes had outer diameters (D) of either 12 in. or 12-3/4 in. and three different thicknesses (t), providing nominal diameter-to-thickness (D/t) ratios of 48, 68, and 95. The internal longitudinal reinforcement consisted of eight (8) #5 bars uniformly distributed along the circumference of the section, using a cover (c_{lb}) of 1 in. between the outside of the longitudinal bars and the inside of the steel tube. The internal reinforcement (longitudinal and transverse) was kept constant as past research has shown that it only increases the flexural strength without modifying the ultimate limit state (Brown et al., 2015). The transverse reinforcement consisted of #3 spirals at 6 in. spacing, providing an average internal volumetric steel ratio $\rho_s \approx 0.75\%$. All internal reinforcement consisted of ASTM A-706 Grade 60 steel, while the specified concrete compressive strength was 5 ksi. Each specimen had a reinforced concrete loading stub located at the specimen head, with dimensions 24x18x18 in., which allowed for application of lateral loading. As explained in subsequent sections, inclinometer sensors were installed along the length of the specimens.

For that purpose, a 2-3/4-inch-diameter PVC tube was placed at the centroid of the specimen cross-section along its entire length. The specimen cross-section details are presented in Figure 4-1.

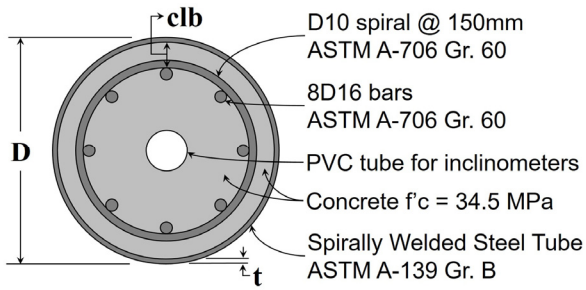

Figure 4-1 RCFST pile-column specimen cross section

4.1.2. Soil-Structure Interaction (SSI) Facility

4.1.2.1 Geotechnical Laboratory

The NCSU-CFL houses multiple environments for large-scale testing of both structural and geotechnical applications. The geotechnical portion of the laboratory includes a 20-foot-deep, 10-foot-diameter pit that can be filled with different types of soil, in which foundation systems can be embedded, allowing for physical testing of soil-structure systems under a variety of loading conditions. The geotechnical laboratory at the CFL is also equipped with an 11-kip capacity overhead crane. The laboratory floor has anchors spaced at 3 ft. on each direction across almost the entire floor. Each anchor location consists of four 3/4-inch threaded rods embedded into a recessed portion of the concrete floor. Figure 4-2 shows a floor plan view of the geotechnical laboratory at CFL.

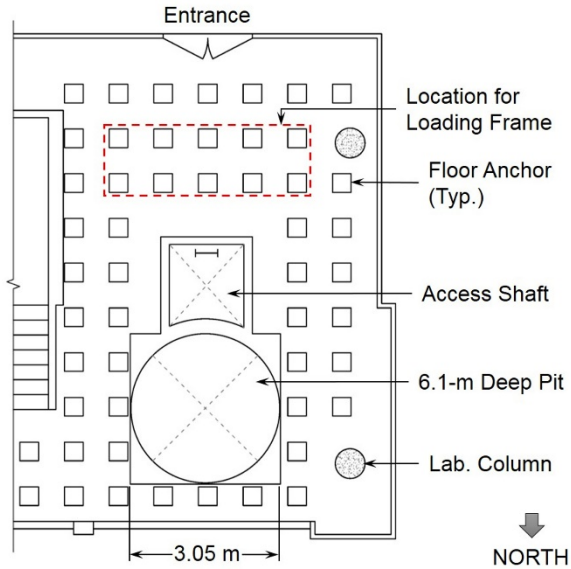

Figure 4-2 CFL geotechnical laboratory floor plan view

Note from Figure 4-2 that there is a rectangular shaft next to the testing pit. This shaft provides access to a water system consisting of an inlet pipe into the pit, a water diffuser (i.e., a set of pipes with holes at different locations utilized to distribute the water evenly at

the bottom of the pit), and a water outlet pipe from the pit. The main water inlet pipe is regulated to deliver a continuous pressure of 100 psi, which in combination with the water diffuser at the bottom of the pit allows for inducing quick conditions (liquefaction) on sandy soils.

4.1.2.2 Lateral Loading

A lateral loading frame was designed, anchored to the laboratory strong floor, to elastically resist the maximum expected lateral load. Predictions using numerical simulations, which included non-linear behavior of materials, suggested that in order to develop a tensile strain of 2.5% in the steel tube, the top of the RCFST pile-column specimens would need to reach a lateral displacement of about 30 in. while sustaining a maximum force of about 30 kips. For design purposes, a lateral load of 100 kips was considered, assuming a factor of safety larger than 3. Multiple steel-braced frame configurations were considered for the lateral loading frame to enable variations in specimen geometry and lateral load location (height off the floor). The final design of the loading frame consisted of three W10x33 vertical columns, three HSS 3-1/2x3-1/2x5/16 5/16 inclined braces, and a single horizontal W 8x67 beam. All structural elements were manufactured using grade 50 steel. Each column includes additional stiffeners to reinforce against localized failure modes at the locations where the beam and diagonal braces frame in. The lateral loading frame was designed and fabricated to allow for two heights (vertical position) of a hydraulic actuator, providing for the ability to include the aboveground height of the RCFST pile-columns as a variable in the experimental program. The horizontal beam allows for distribution of the lateral force from a hydraulic actuator into three floor anchor groups. Figure 4-3 shows the loading frame after construction at the intended location. A custom hydraulic actuator with a stroke capacity of ±35 in. was designed and fabricated. The same maximum lateral load used for the design of the loading frame was considered, namely, 100 kips.

Figure 4-3 Lateral loading frame

4.1.2.3 Soil-Sandwich Concept

The soil-sandwich approach proposed in this study is based upon the premise that the sand modulus varies as a function of the mean effective stress. Past studies have explored the use of confinement in combination with prestress loading to improve both vertical and horizontal stiffness of a given soil profile. Shinoda et al. (2003), for example, developed a construction procedure for mechanically reinforced backfill structures that involved the application of a large pre-load followed by pre-stressing of the soil structure to a constant level during service conditions (i.e., active load in service). They suggested that transient deformations due to traffic load can be minimal and will remain elastic when the pre-stress level is half that of the pre-load level, which in turn results in small residual deformations. In addition, they recommended that the difference between the pre-load and pre-stress levels must be larger than the amplitude of the subsequently applied cyclic load. They validated their approach with results of laboratory experiments and the performance of a prototype railway bridge pier constructed using the proposed pre-loading and pre-stressing construction procedure which they termed "PLPS". Uchimura et al. (2005), on the other hand, conducted vertical and horizontal loading tests on a full-scale PLPS geogrid-reinforced soil pier of a railway bridge. They argued that the high performance, in terms of the transient and residual deformations due to traffic loads, can be attributed to the PLPS procedure. They also concluded that the PLPS procedure is effective for achieving high seismic stability as results from lateral loading tests suggested a larger capacity against over-turning moment and horizontal shear. In both previously mentioned examples, enhanced performance was attributed to confinement, which leads to an increase in the mean effective stress as the soil is restrained from expanding laterally under the applied loading.

Motivated by the concept and literature described above, the soil-sandwich concept was born on the basis of pre-stressing a soil profile while providing confinement to achieve a higher soil stiffness. The term "soil-sandwich" evolved from the idea of applying a surcharge load to the soil through top and bottom RC reaction plates inside the pit, as depicted in Figure 4-4. Note that the round RC wall of the pit confines the soil within the reaction plates. Such reaction plates consist of two half-moon and a circular RC plates located at the top and bottom of the pit, respectively. The two half-moon reaction plates leave a gap of 14 in. between them, allowing lateral movement of pile-column specimens under cyclic lateral loading. The bottom reaction plate has a large diameter hole in its centroid. The purpose of this 14-inch hole is to allow for drainage after liquefaction, which was used for the regeneration of the soil sample, as well as for insertion and removal of the pile-column specimens. The final design of the reaction plates consisted of 8-inch-thick slab elements with a diameter of 9.75 ft., leaving a gap between the pit wall and the reaction plates of 1-1/2 in. The reinforcement consisted of upper and lower two-way mats, each using #5 reinforcing bars at 4-inch-center-to-center spacing with 1-1/2-inch cover. The specified concrete compressive strength was f'c = 8 ksi. The selected reinforcing bars were made from Micro-composite Multi-structural Formable Steel (MMFX) (Yotakhong, 2003), a high strength, corrosion-resistant steel, in an effort to provide additional service life to the concrete elements that may be subjected to severe environmental conditions. The relatively

close spacing of the reinforcing bars and the high strength concrete are intended to reduce strains and mitigate crack widths in the RC reaction plates.

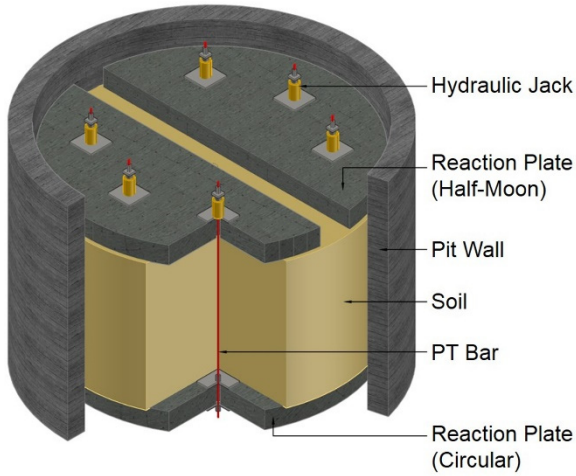

Figure 4-4 Soil surcharge system (soil-sandwich concept)

The surcharge load is applied by pre-stressing the soil vertically by means of 5/8-inch, ASTM A-722 Grade 160, DYWIDAG post-tensioning (PT) bars, which are run through the soil-sandwich profile (Figure 4-4). These are post-tensioned using 44-kip, 2-inch-stroke, center-hole hydraulic jacks reacting on the top reaction plates and the PT bars in order to induce a surcharge load within the sand sample. The sand utilized in this research was classified as poorly graded sand (SP) with an average unit weight γ = 90 pcf and friction angle ϕ = 35°. A total of six PT bars are utilized so that the resultant pre-stressing force coincides with the centroid of the top half-moon RC plates. The PT bars are connected and fixed to the bottom reaction plate utilizing 10x10-inch bearing plates along with hexagonal nuts. At the top, the PT bars run through the half-moon reaction plates and a set of bearing plates and nuts are installed with a center-hole jack at each PT bar location. Then, using a manual hydraulic pump and a set of hoses connected through a seven-port manifold, the PT bars are stressed simultaneously. A load cell is utilized to monitor the applied load to achieve the desired surcharge level. By using this soil-sandwich system and compressing the sand, internal stresses in the soil increase, thus increasing the confining stress within the soil profile, and thereby increasing the effective soil stiffness. Such a system enables the possibility not only to evaluate how the soil impacts the pile-column response, but how the pile response varies depending upon the stiffness level of the surrounding soil.

4.1.2.4 Soil Surcharge System

Preliminary experiments were conducted to evaluate the effectiveness of soil prestressing as a technique of altering soil stresses. This section describes the test setup and experimental results of the soil surcharge system. Further details about these tests can be found elsewhere (Talley, 2014).

As previously mentioned, the soil-sandwich system consists of top and bottom RC reaction plates in combination with PT bars and poorly graded sand (SP) between the reaction plates, all of which is embedded into a round RC pit (Figure 4-4). For this purpose, the bottom

reaction plate was first lowered into the pit on top of a 6-inch layer of sand, which in turn rested on top of a 12-inch layer of gravel. This bottom layer of gravel serves as a filter system to prevent sand from escaping during drainage after liquefaction is conducted for pile insertion or removal, as it will be explained in next section. This gravel layer also overlays the water diffuser and helps to distribute water evenly within the cross section of the pit. After the bottom reaction plate was in position, instrumentation for measurement of soil pressures was installed. A single pressure cell sensor was mounted on top of the bottom reaction plate to measure the vertical pressure at the bottom of the soil profile. Three pressure cell sensors were installed on the pit wall at different depths to measure confinement stresses. The pit was then filled with poorly graded sand and eight additional pressure cell sensors were installed at two locations (i.e., A and B) and four depths, as shown in Figure 4-5. These pressure cells were laid horizontally in the middle section of the pit, allowing for measurement of the vertical pressure. Finally, the half-moon reaction plates were set on top of the filled pit and center-hole hydraulic jacks were placed on each PT bar and were capped with a bearing plate and a nut. Figure 4-6 presents a photograph of the soil surcharge test setup.

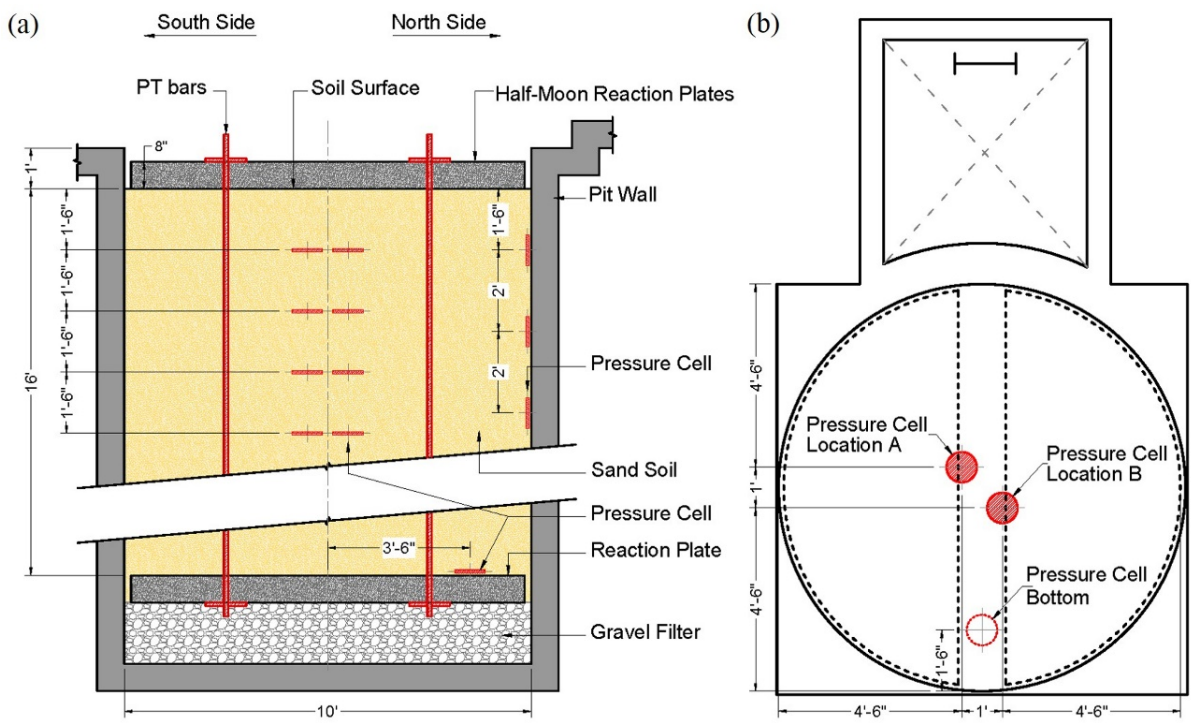

Figure 4-5 Soil surcharge system schematic: (a) elevation view and (b) plan view

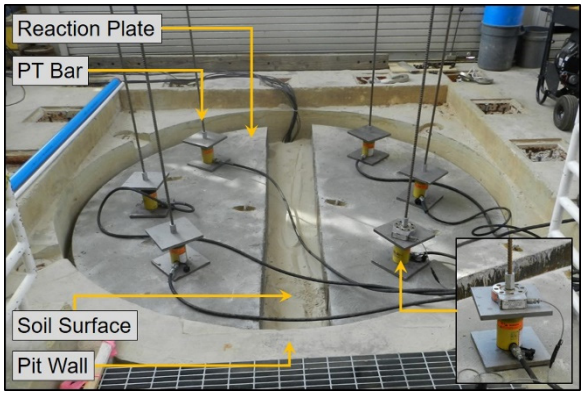

Figure 4-6 Soil surcharge testing

A loading protocol was developed for these tests, where the applied load was increased in pressure increments of 100 psf up to a maximum of 1,200 psf, followed by pressure decrements of 100 psf. In order to control the pressure to be applied, axial load in one of the PT bars was monitored using a load cell that was placed between the top bearing plate and nut (Figure 4-6). The hydraulic pressure was applied equally to each PT bar through a seven-port manifold that connected all hydraulic lines to a manual pump. Readings from the pressure cell sensors were taken at each load increment for both loading and unloading phases.

4.1.2.4.1 Effects of Surcharge Loading on Soil Stresses

Figure 4-7 presents the average increase in vertical pressure distribution in both locations A and B, while Figure 4-8 presents the average increase in lateral confining pressure measured on the test pit wall. These results correspond to the average of three surcharge loading cycles for pressure increments of 200 psf. In Figure 4-7 and Figure 4-8, a depth of zero corresponds to the soil surface. As evidenced from the pressure results, locations A and B showed different pressure gradients. One of the main reasons for this is that the sand was initially more compacted on the north side of the pit as it was initially dumped into the pit over that side and then pulled back to the south side during the initial pit filling process. This result was also observed from the top reaction plates as their southern end experienced more settlement than their northern end. Despite the slightly different stress increase profiles, note that the vertical and confining pressures increased within the soil profile as a result of an increase in the surcharge load on the top. Moreover, while the pressure gradients are different, note that there is a distinct kink in the curves at a depth of about 4 ft. This local maximum represents the point at which the contact stresses become negligible and the impact of the surcharge load starts to decrease with depth. As will be evident in subsequent sections, an active surcharge load of q = 960 psf allows for altering the state of stress within the soil profile so that a stiffer soil profile is simulated.

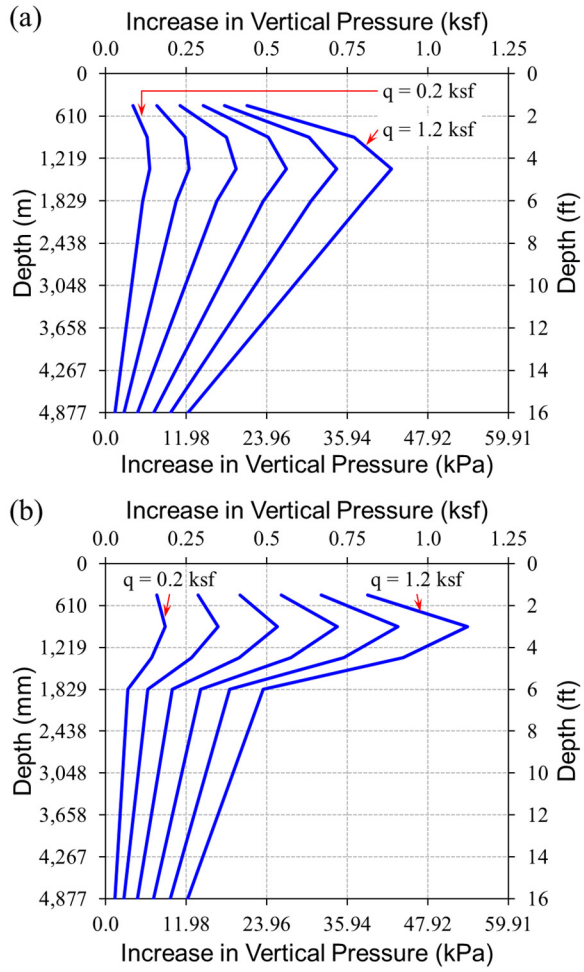

Figure 4-7 Vertical pressure increase at: (a) location A and (b) location B

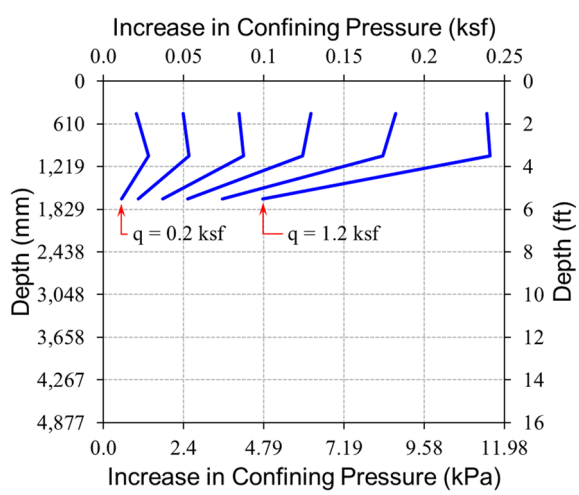

Figure 4-8 Confining pressure increase (measured at pit wall)

4.1.2.5 Pile Insertion and Removal

One of the most important features of this SSI facility is the ability to insert and remove the pile-column specimens quickly and easily by employing liquefaction. The liquefaction process also allows for the regeneration of the uniform sand sample after the pile-column testing is completed and a specimen is set in place for testing.

Initially, the plan was to use the existing water system in the pit, as described in the previous section. Therefore, after the trial tests of the soil surcharge system were conducted, the top reaction plates were removed to perform soil liquefaction trial tests, so as to verify the feasibility of easy insertion and removal of the pile-column specimens. Several attempts were conducted without success, namely, the liquefaction occurred in an abrupt manner inducing only partial liquefaction at some spots within the cross-section of the sand deposit. In addition, during the liquefaction attempts it was observed that the reaction plate at the bottom was moving upward prior soil liquefaction, and suddenly moving downward (dropping) right after liquefaction took place. This was deducted from the movement of the PT bars, connected to the bottom reaction plate as described earlier. It was concluded that this phenomenon occurred due to the position of the water diffuser. As previously mentioned, the water diffuser was located below the bottom RC reaction plate. This means that during the liquefaction process, the water could only go through the reaction plate in the 1-1/2-inch gap between the pit wall and reaction plate, and the 14-inch-drainage hole left at the centroid of the bottom reaction plate. As a consequence, the water did not permeate evenly within the cross section of the soil deposit. This allowed part of the water to remain below the bottom reaction plate, building pressure up until the pressure due to the self-weight of the whole reaction plate-soil system was overpassed, moving the system upward without liquefaction, until eventually partial liquefaction occurred.

The evident solution to this problem was to change the position of the water diffuser so as to avoid the permeability issue due to the presence of the bottom reaction plate. This means that the only feasible option was to put the water diffuser above the bottom reaction plate as depicted in Figure 4-9. In order to accomplish this, the sand was removed from the pit along with the bottom reaction plate and the existing water diffuser, which was disconnected from the water inlet pipe. One of the concerns with the new position of the water diffuser was the additional pressure to which it would be subjected, as the surcharge loading would induce additional stresses in the pipe set, though such pressure is of small magnitude as it can be inferred from Figure 4-7 and Figure 4-8. It was decided then to construct a new water diffuser with the same characteristics and details as the existing one, but using schedule 80 PVC pipes. Construction of the new diffuser also involved and additional pipe line running from the water inlet pipe in the pit wall toward the center of the pit, to then go upward toward the new water diffuser, as this was the only location for a 3-inch-pipe to go through the bottom reaction plate. Figure 4-9(b) shows the new water diffuser installed above the bottom reaction plate.

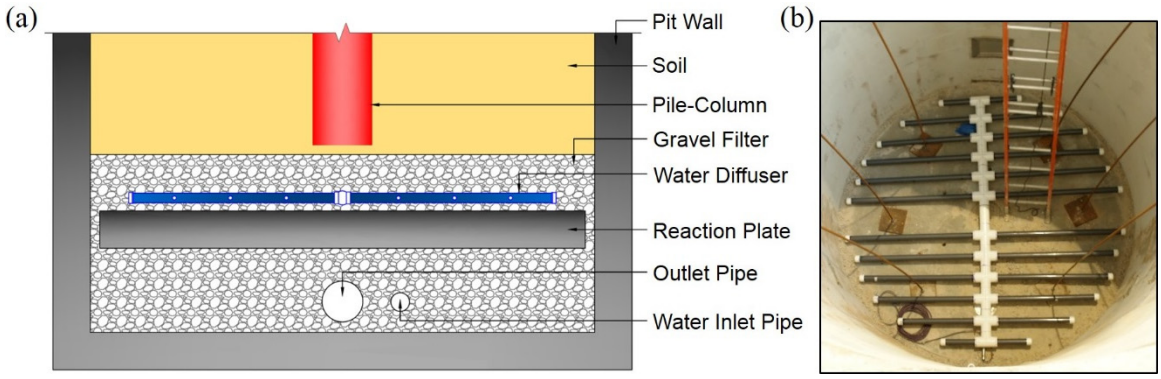

Figure 4-9 New water diffuser: (a) sketch elevation and (b) photograph looking into the pit

Once the new water diffuser was installed, a 14-inch layer of gravel (acting as a filter) was deposited into the pit to embed the new pipe set. Then, the pit was filled with the sand material again and trial tests of liquefaction were conducted. As expected the bottom reaction plate did not move and the liquefaction was evenly distributed within the cross section of the pit. However, it was observed that instead of just opening the water inlet valve, a sequence must be followed in order to achieve an appropriate liquefaction that will allow a pile-column specimen to be installed in the soil profile. Due to the inherent permeability of sand and due to the large volume of water that can be introduced in the pit using the full pressure capacity of the main inlet pipe, namely 100 psi, opening the water valve to full capacity would result in the entire mass of soil moving upward, inducing abrupt and partial liquefaction. The final procedure to effectively liquefy the soil was developed based upon several liquefaction attempts conducted using different sequences when opening the water valve.

The first step toward an adequate liquefaction is to slowly and fully saturate the entire soil mass. For this purpose, the water valve must be opened to 20% of the full capacity. Once the water level overpasses the soil surface, the water valve must be shut-off; this process usually takes about 6 hours. The soil deposit is left overtopped with water for at least one day such that the water fully saturates the pores within the soil profile. The second step consists of draining the pit for 15 minutes at full capacity, after which the drain must be shut-off and then 20 minutes must be left to pass before the next step. The third step consists of the liquefaction itself. The process for this step is listed below, where opening and closing of the water valve is indicated with reference to full capacity and the time frame shown is an approximation with a tolerance of ± 15 seconds.

a. Open water valve to 25% for 1 minute
b. Open water valve to 50% for 2 minutes
c. Open water valve to 75% for 2 minutes
d. Open water valve to 100% for 30 seconds
e. Close water valve to 75% for 30 seconds
f. Open water valve to 100% for 3 minutes

From part a through part c of the process above, saturation of the water system and the soil progresses slowly. At full capacity of the water inlet (d), the entire soil mass slightly moves

upward while cracks appear in the soil surface. At this point the water valve must be closed to 75% of full capacity (e). This slight closure allows liquefaction to slowly start at the bottom of the soil profile and prevents and abrupt and partial liquefaction from occurring. After 30 seconds pass at the end of this step (e), visible signs of liquefaction can be observed on the soil surface and the water starts overpassing the surface. At this point, the water valve must be opened to full capacity (f). Full liquefaction of the soil takes place for about 3 minutes while the water is left to run at 100% of full capacity, until the water level is about 2 in. below the top of the pit wall. The water valve must be shut-off at this level to prevent overflow of the pit. During a pile-column insertion, once the soil particles have settled for about 1 hour after the water valve is shut-off post-liquefaction, the drain valve is slightly opened such the soil drains slowly and evenly. Full drainage of the pit in this manner takes about one day until water barely drips from the drain pipe.

The liquefaction process described above has been shown to work effectively for pile-column insertion and removal purposes. Insertion and removal processes are conducted using the overhead crane to maneuver the pile-column specimens within the laboratory. The main advantage of using liquefaction is that it allows pile-columns to be tested in a much faster and more economical way, as opposed to manually removing the soil and filling the pit back for each test. In addition, soil liquefaction also restores the initial mechanical properties of the sand at the start of each test, meaning that the soil is reset to the same initial conditions after liquefaction.

4.1.3. Test Setup and Instrumentation

As previously mentioned, the NCSU-CFL soil-structure interaction (SSI) facility consists of a 20-foot-deep, 10-foot-diameter pit in which a surcharge system (soil-sandwich) was embedded in order to conduct experimentation on RCFST pile-column specimens under reversed cyclic loading, considering two soil stiffness profiles. For that purpose, the specimens were embedded 14 ft. into loose sand (SP). Two aboveground heights (i.e., column length) were considered, resulting in pile-column lengths of 19.5 ft. and 21.5 ft., measured from the point where the lateral load was applied to the pile-column tip. Reversed cyclic lateral loading was applied to the pile-column head by means of a 100-kip, 70-inch stroke hydraulic actuator. The actuator was supported on a braced steel frame and was connected to the specimen using a pinned connection (i.e., pinned-head condition). The effective soil stiffness was expected to be modified for some of the experimental tests by using the proposed soil-sandwich approach described before. In short, such system consists of two half-moons and a circular reinforced concrete (RC) plates, located at the top and bottom of the pit, respectively, that are used in combination with six 5/8-inch, ASTM A-722 Grade 160, DYWIDAG post-tensioning (PT) bars and 40-kip, 2-inch stroke hydraulic jacks reacting on the half-moon RC plates in order to induce a surcharge on the soil surface, thus modifying the effective soil stiffness. This approach is referred as to the soil-sandwich concept (Talley, 2014). By using this system and compressing the soil, internal stresses in the soil increase, thus increasing the soil stiffness. A schematic elevation and a photograph of the test setup are presented in Figure 4-10 and Figure 4-11, respectively.

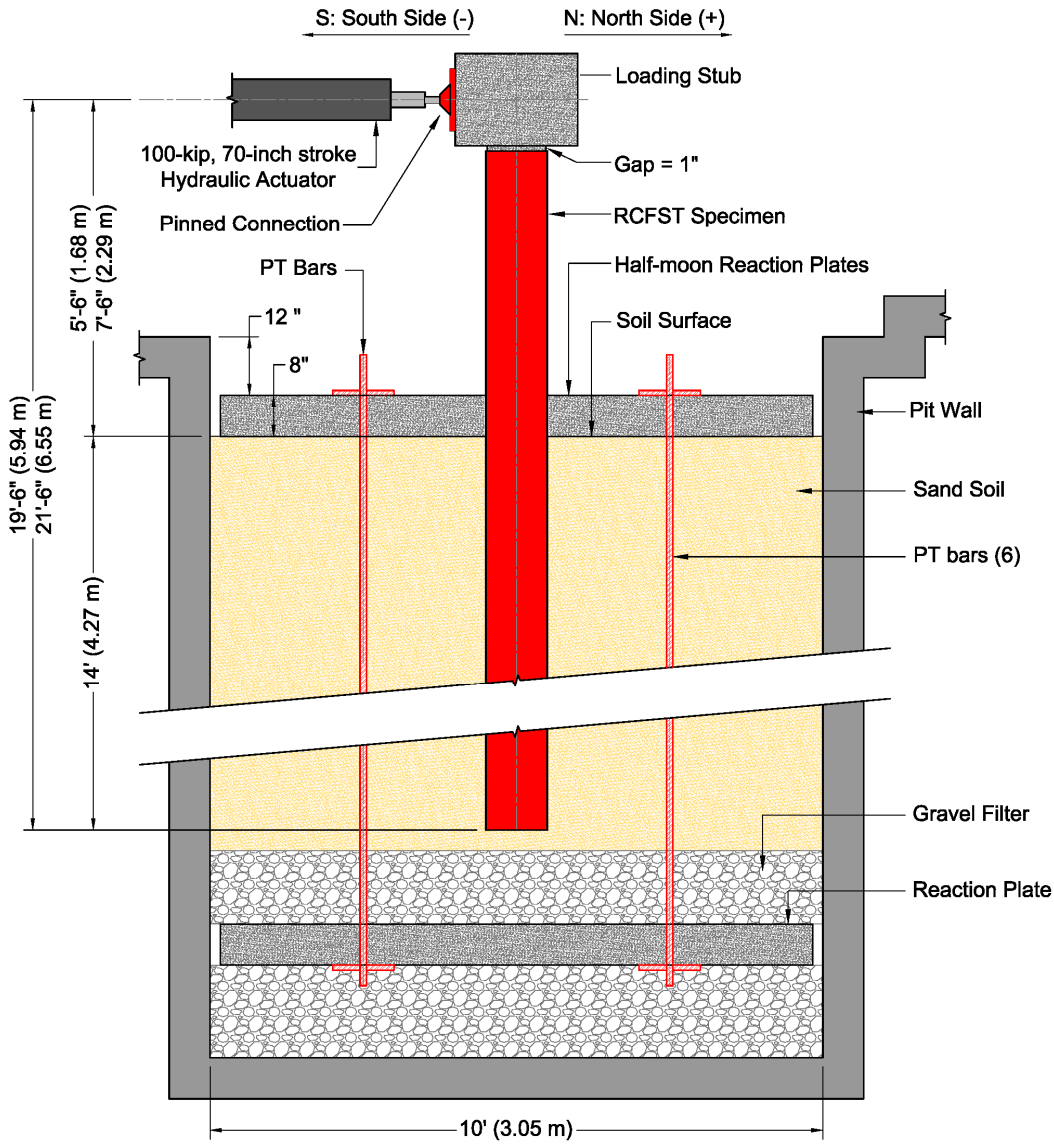

Figure 4-10 Pinned-head, RCFST pile-column test setup schematic elevation

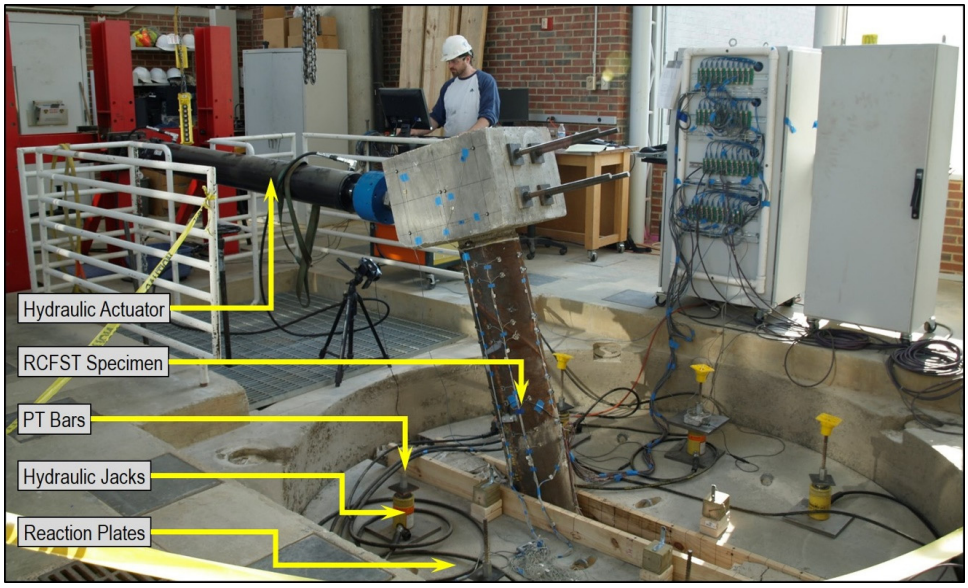

Figure 4-11 Pinned-head, RCFST pile-column test setup with specimen subjected to substantial lateral displacement

Specimen instrumentation included: (1) longitudinal strain gauges, (2) inclinometer (slope indicator) sensors, (3) a non-contact three dimensional position measurement system (herein after referred to as the Optotrak system), (4) load cells, (5) pressure cells, and (6) a linear displacement transducer. Figure 4-12 and Figure 4-13 show schematics of the instrumentation.

In regard to strain gauge (SG) sensors, a total of 22 were placed longitudinally on the extreme tension and compression fibers covering the pile embedded length using 1-foot and 2-foot interval depths inside and outside the plastic hinge zone, respectively, as shown in Figure 4-12 and Figure 4-13. Since some SG sensors were installed in the embedded portion of the specimens, it was necessary to protect them against moisture and friction with the sand. For that purpose, once each SG sensor was installed, it was covered with at least four layers of polyurethane coating. Then, each SG sensor was covered with a 5-inch-long, 5/8-inch aluminum angle which was attached to the steel tube surface using hot glue. Lastly, the aluminum angle was covered with butyl tape for moisture protection. The SG protection process is depicted in Figure 4-14.

Regarding the inclinometer sensors (slope indicators), 2-foot gauge length inclinometers were placed at the centroid of the section along the entire length of the specimen, providing rotation data at different depths. Figure 4-15 shows the inclinometers sensors utilized along with their casing (blue PVC tube), which runs along the length of the specimen at its centroid.

The Optotrak Certus HD, a non-contact, three-dimensional position measurement system, was utilized to verify displacement, rotation, and strain data by monitoring the position of LED markers placed in the specimen above the soil surface. The use of this system for earthquake engineering research is described elsewhere (Goodnight et al., 2014).

As previously mentioned, the surcharge pressure in the soil was controlled by a load cell that monitored the load applied in one of the six PT bars used to compress the soil. The pressure in the hydraulic jacks acting on each PT bar was the same, thereby ensuring the same load in all the PT bars and thus a uniform surcharge. On the other hand, a tempo-sonic transducer and a load cell were used to control the hydraulic actuator. Finally, as described earlier, confining stresses were measured in the round pit wall by using pressure cell sensors.

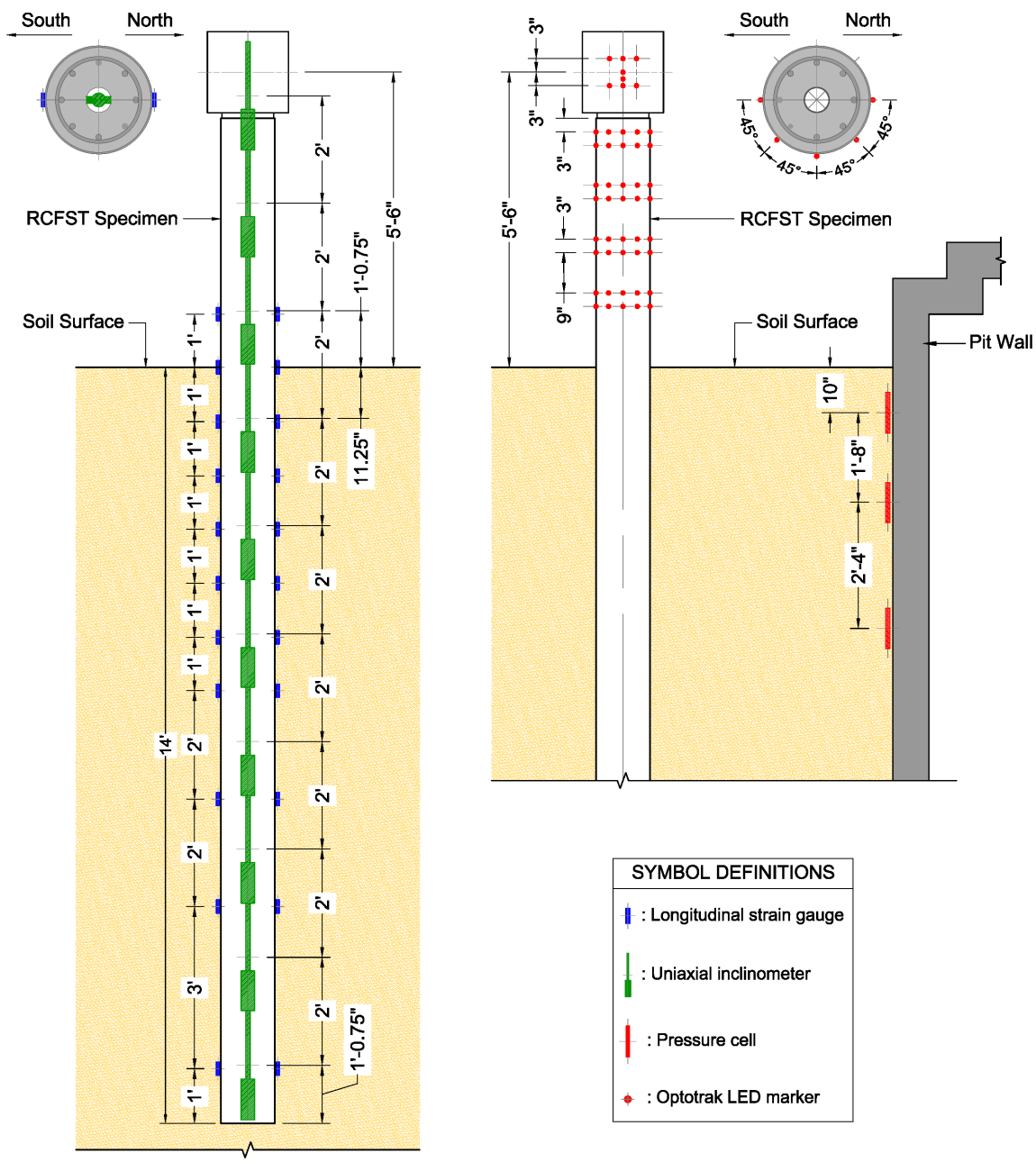

Figure 4-12 Instrumentation for RCFST pile-column specimen with column length of 5.5D

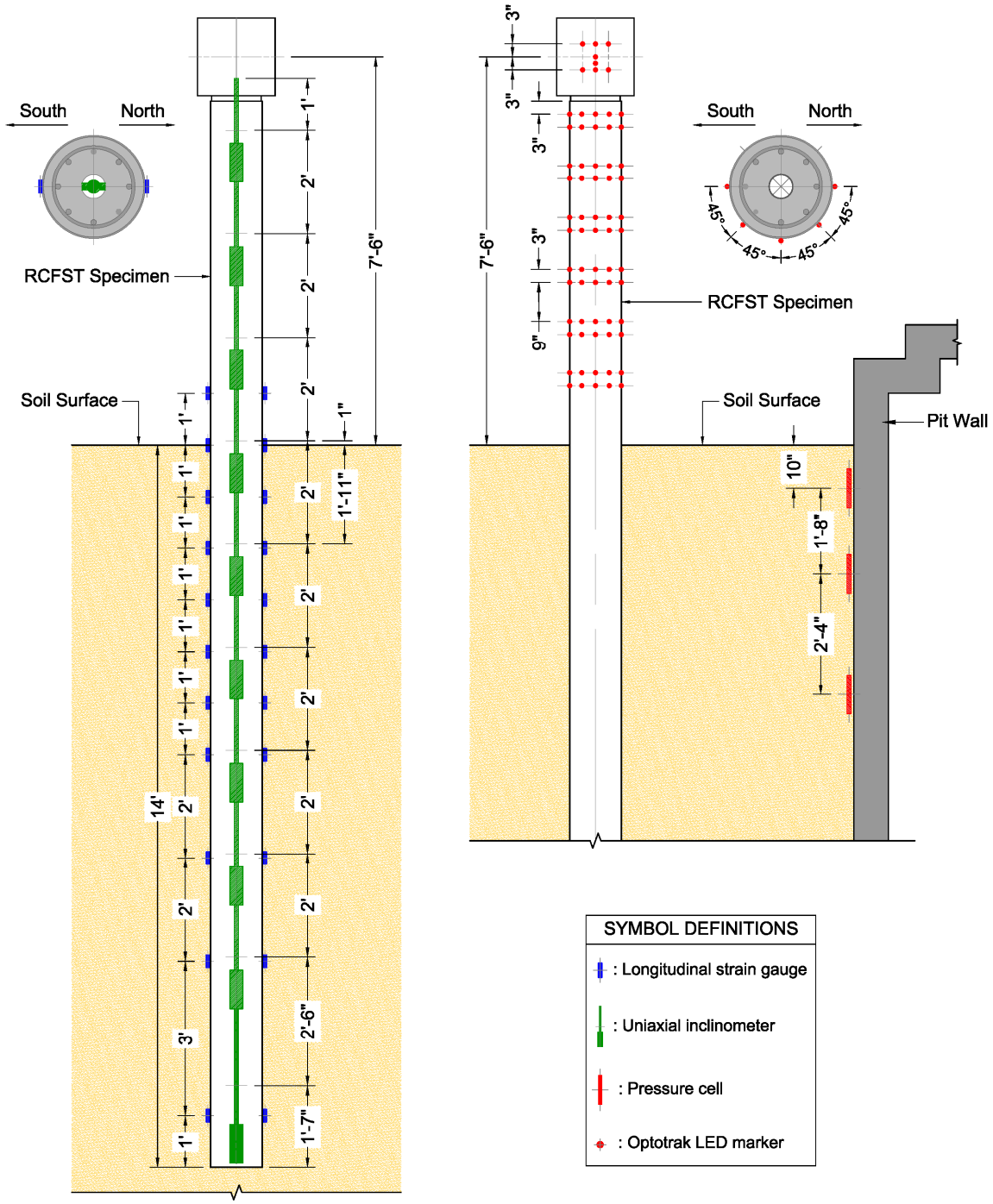

Figure 4-13 Instrumentation for RCFST pile-column specimen with column length of 7.5D

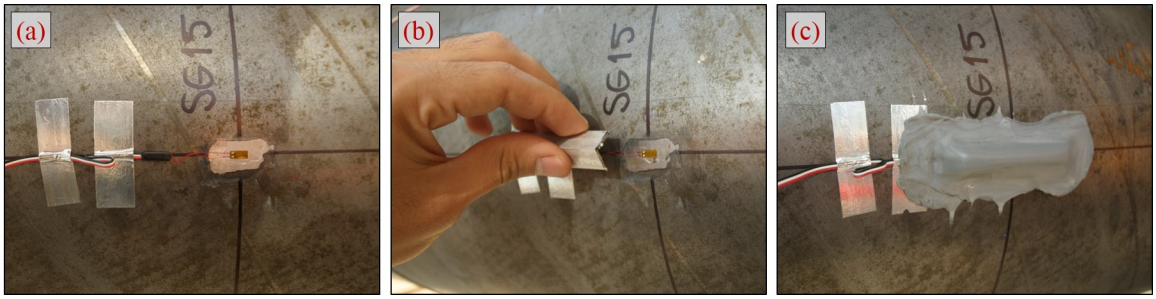

Figure 4-14 Strain gauge sensors: (a) SG sensor after installation, (b) hot-glued aluminum angle for friction protection, and (c) butyl tape for moisture protection

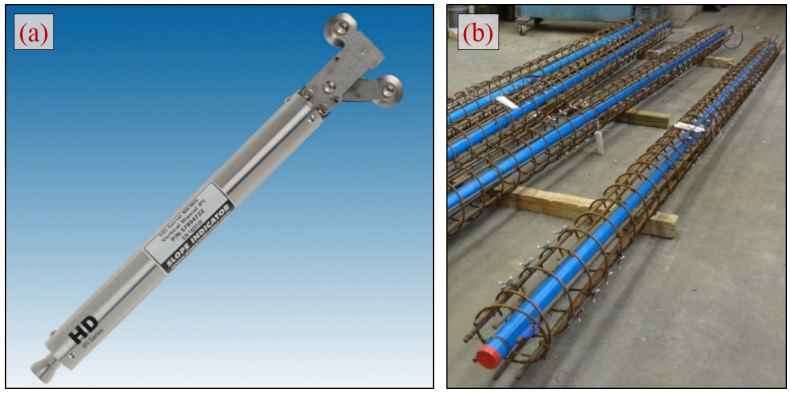

Figure 4-15 Inclinometer sensors: (a) 2-foot gauge length inclinometer and (b) PVC casing (blue pipe) at centroid of specimen cross section along its length

4.1.3.1 Determination of Strain and Displacement Profiles from Rotation Data

Using rotation data from a specimen at different points along its length, curvature and displacements at different depths can be computed by numerical derivation or integration, respectively, considering the appropriate gauge length. It is worth nothing that rotation values at the specimen head and tip are calculated by linear extrapolation using data from the adjacent two inclinometer sensors. For example, with reference to Figure 4-16, where "c", "r", and "d" represent curvature, rotation, and displacement values, respectively, the rotation at the specimen head, $r_{(1)}$, is calculated using linear extrapolation based upon the data of rotations $r_{(2)}$ and $r_{(3)}$. Similarly, the rotation at the specimen tip, $r_{(n+2)}$, is calculated using linear extrapolation based upon the data of rotations $r_{(n)}$ and $r_{(n+1)}$. In Figure 4-16, "n" refers to the total number of inclinometer sensors, which means that there are n+2 rotation values, and n+3 curvature and displacement values, which include the specimen head and tip. Since the gauge length (gl) of each inclinometer sensor is known, the location of each inclinometer along the length of the specimen is also known. Such information is used in combination with the known geometry of the specimen in order to determine the location at which curvature and displacement values are calculated, that is, at midpoints between each rotation value (inclinometer ends), as shown in Figure 4-16.

Curvature values, on the other hand, are calculated based upon the relative rotation between consecutive inclinometer sensors, taking into consideration that rotation values are in units of degrees, as shown in Equation 4-1. Note that at the specimen head and tip curvature

values, namely, $c_{(1)}$ and $c_{(n+3)}$, are zero because no deformation occur at such sections. As such, curvature values are not calculated at those locations.

With regard to displacement values, they are calculated based upon the displacement at the specimen head, $d_{(1)}$, in combination with the deflection recorded by each inclinometer sensor, as shown in Equation 4-2. The displacement at the specimen head, $d_{(1)}$, is measured using the information from the Optotrak system or from the displacements of the actuator. Note that displacements are calculated along the length of the specimen including the specimen tip, $d_{(n+3)}$.

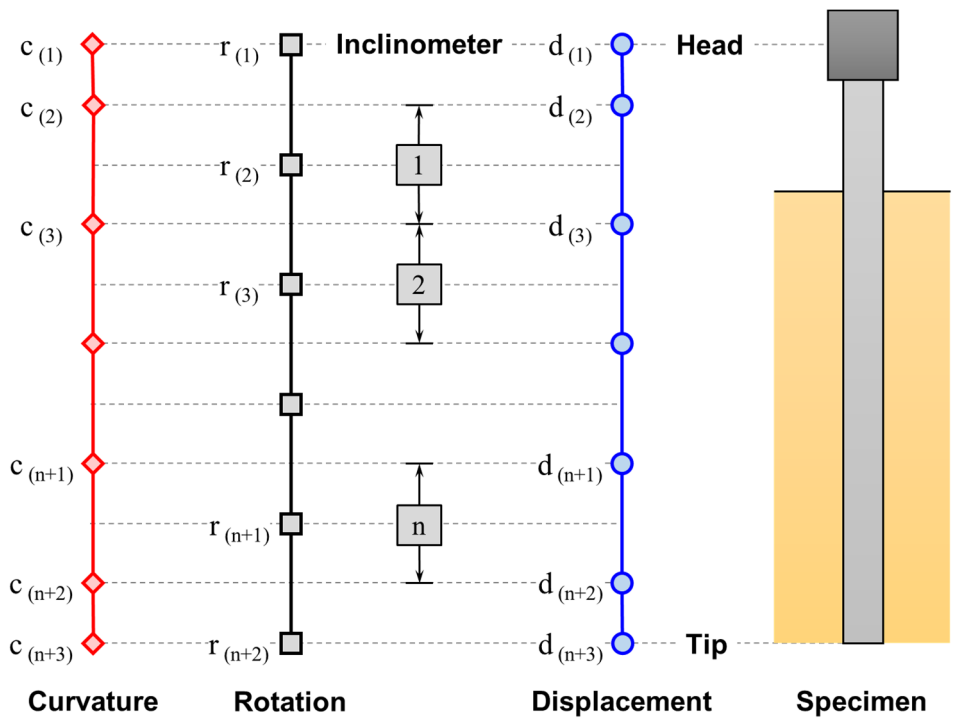

Figure 4-16 Schematic calculation of curvature and displacement profiles

$$c_{(j)} = \frac{\left(r_{(j-1)} - r_{(j)}\right)}{gl} \cdot \frac{\pi}{180°} \quad \rightarrow \quad j = 2, \ldots, \mathrm{n}+2 \qquad \text{Equation 4-1}$$

$$d_{(j)} = d_{(1)} - \sum\left(\frac{r_{(j-1)} \cdot gl \cdot \pi}{180°}\right) \quad \rightarrow \quad j = 2, \ldots, \mathrm{n}+3 \qquad \text{Equation 4-2}$$

In order to verify the use of rotation data for calculation of curvature and strain profiles, a test using inclinometer devices was conducted. For that purpose, five 2-foot gauge length inclinometer sensors where encased in the same PVC tube to be used for the actual RCFST specimen, as was shown earlier in Figure 4-15(b). The test setup consisted of putting the resultant 10-foot-long PVC tube in a cantilever fashion. The tube was attached to a steel column by fixing the first 2 feet at its base. Then, lateral displacements were induced at the top of the tube while displacements and rotations were recorded using the Optotrak system and inclinometer sensors, respectively. The Optotrak system was used to monitor deflections of the PVC tube at 1-foot intervals. Using such data, rotation and curvature data were calculated from numerical derivation considering the appropriate gauge length. On the other

hand, using the inclinometer data (rotation), curvature and displacements were calculated from numerical derivation and integration, respectively, using the 2-foot gauge length of the inclinometer sensors. Results of this test are presented in Figure 4-17, where D_i represents a different displacement reached at the top of the PVC tube.

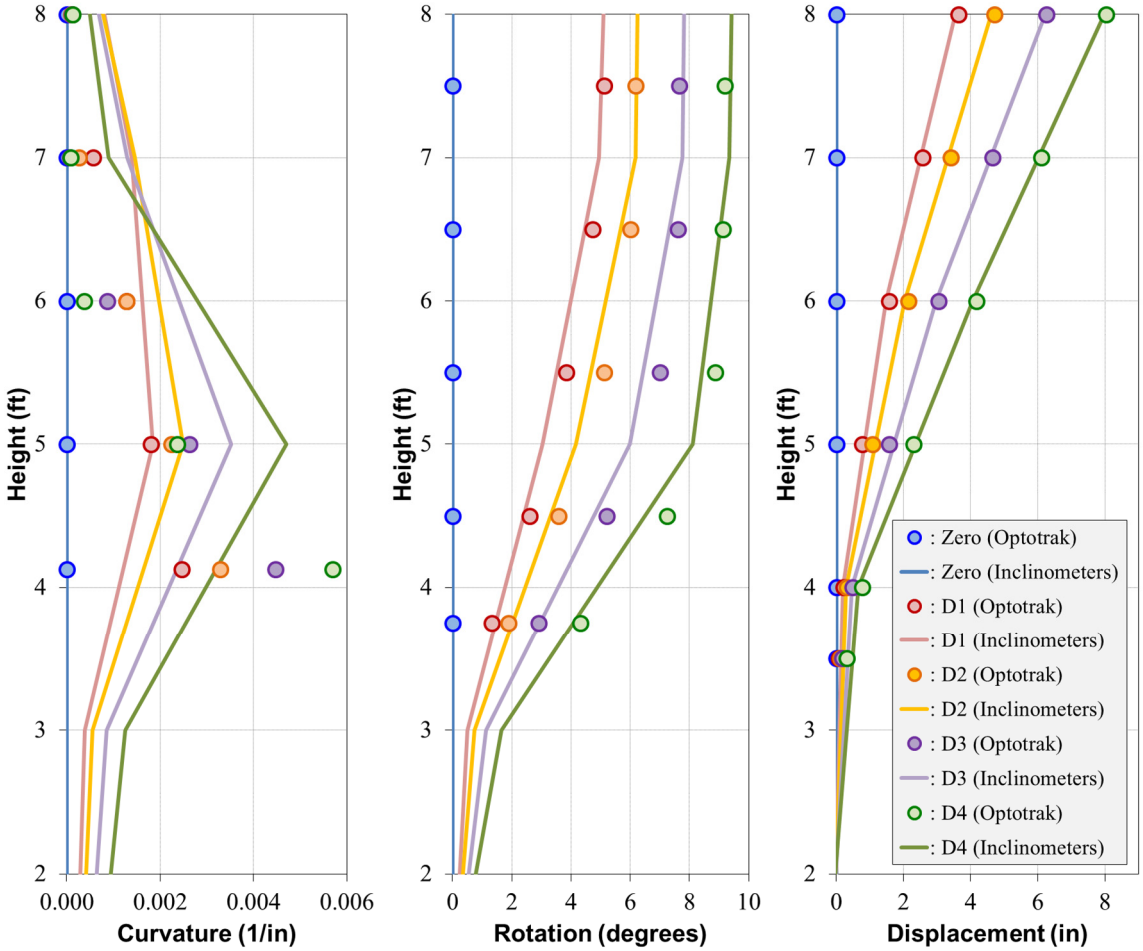

Figure 4-17 Example of curvature and displacement profiles calculation

Note that in terms of displacement and rotation, results are in close agreement using either inclinometer or Optotrak data. In terms of curvatures, on the other hand, while the maximum values are in close agreement, the shape of the profiles calculated using inclinometer data are quite different from those calculated using the Optotrak data. This difference has two sources. First, curvature values from the inclinometers are calculated with a 2-foot gauge length, which means that values correspond to an average curvature in a 2-foot length, whereas values from Optotrak correspond to average values in a 1-foot length. Second, position measurements from Optotrak have precision of 0.1 mm. (Goodnight et al., 2014), which means that for small values of curvatures the error is high. Nonetheless, as previously mentioned, curvatures corresponding to maximum values are in agreement within the corresponding gauge length.

Finally, for the RCFST pile-column tests, strain profiles were calculated using data of curvature profiles in combination with moment-curvature analyses performed using CUMBIA (Montejo and Kowalsky, 2007), with an slight modification to include the steel

tube surrounding the reinforced concrete section. Since values of curvature (ϕ) are known at different points along the length of the RCFST pile-column specimens, compressive and tensile strains in the extreme fibers of the steel tube, ε_c and ε_t, respectively, can be calculated using the neutral-axis depth (c) and the diameter of the cross section (D), as shown in

$$\varepsilon_c = c \cdot \phi \qquad \text{Equation 4-3}$$

$$\varepsilon_t = (D - c) \cdot \phi \qquad \text{Equation 4-4}$$

4.1.4. Loading Protocol

The load history applied to each RCFST pile-column specimens consisted of standard single and three-cycle sets intended to evaluate both elastic and inelastic response. The first portion of the test (i.e., pile-column elastic response up to first yield) consisted of single reversed, displacement-controlled cycles, ramping up to the first yield displacement in ¼ increments of the predicted first yield lateral displacement (Δ_y'). Given the non-linear response from the beginning of the test due to the characteristic soil behavior, target displacements in this portion of the test were determined based upon results of a monotonic and cyclic pushover analyses performed using a detailed fiber-based, finite element model developed using OpenSees (McKenna et al., 2000), which incorporated the non-linear behavior of materials. In such a model, soil-structure interaction was accomplished by means of non-linear springs at 1-foot interval depths, with spring properties assigned based on p-y curves. After the first portion of the test was completed, the measured average displacement at the first yield displacement (Δ_y') was modified by the nominal-to-first yield force (F_n/F_y) ratio as shown in Equation 4-5. The remainder of the test was completed using reversed three-cycle sets in displacement-controlled increments at different levels of displacement ductility (μ) until failure, as shown in Equation 4-6.

$$\mu_1 = \Delta_y = \Delta'_y \frac{F_n}{F_y} \qquad \text{Equation 4-5}$$

$$\mu_i = i \cdot \mu_1 \rightarrow i = 1.0,\ 1.5,\ 2.0,\ 3.0,\ 4.0,\ 5.0, \ldots \qquad \text{Equation 4-6}$$

The first yield force (F_y) and nominal force (F_n), which is defined as the force at a concrete compressive strain of 0.004 or at a steel tube/bar tensile strain of 0.015 (whichever occurs first), were determined based upon tensile and compressive strains monitored during the numerical simulation (i.e., monotonic and cyclic pushover analyses). Presented in Figure 4-18 is the typical displacement history utilized to conduct the experiments. Positive loads and displacements correspond to rightward motion (North) of the specimen in the test setup, as shown in Figure 4-18(b). Further details regarding the analysis approach are presented in subsequent sections.

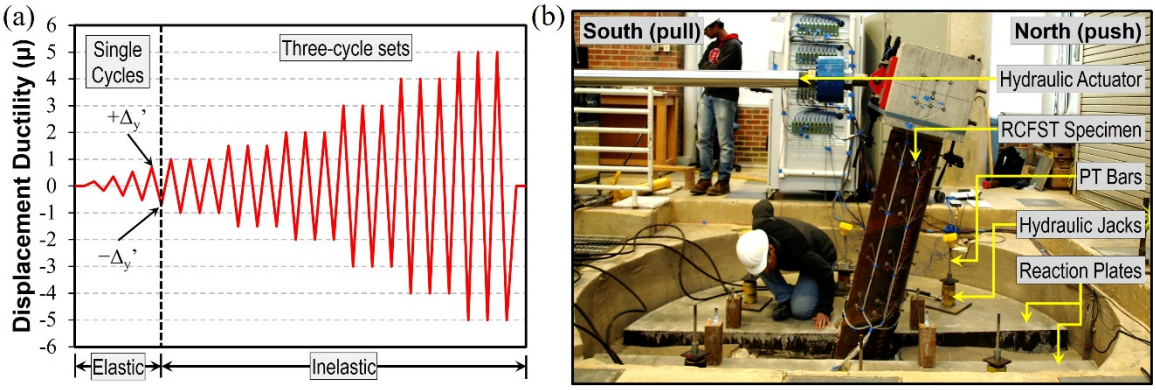

Figure 4-18 (a) Typical displacement history and (b) example of a positive deformed shape

4.1.5. Test Matrix

The main variables to study included the diameter-to-thickness (D/t) ratio, soil stiffness (i.e., soil surcharge), and aboveground height (i.e., column length). The main parameters of the experimental program are summarized in Table 4-1. It is worth noting that the symbol "*" in Table 4-1 (next to the values corresponding to a D/t ratio of 95) represents a particular feature observed on tests 3 and 4. As a consequence, those tests were repeated and they correspond to tests 5 and 6. Therefore, while tests 5 and 6 look similar to tests 3 and 4, respectively, there is a difference related to the failure mechanism of the specimens, which will be discussed in subsequent sections. In addition, due to issues related to instrumentation and to an effective alteration of the soil stiffness, test 9 corresponds to a repetition of test 2.

Table 4-1 Experimental test matrix

Test No.	Diameter		Nominal Thickness		D/t Ratio	Soil Surcharge		Column Length	
	mm	(in)	mm	(in)		kPa	(psf)	m	(ft)
1	305	(12.00)	6.35	(0.250)	48	None	None	1.68	(5.50)
2	305	(12.00)	6.35	(0.250)	48	46	(960)	1.78	(5.83)
3	324	(12.75)	3.42	(0.135)	95*	None	None	1.68	(5.50)
4	324	(12.75)	3.42	(0.135)	95*	46	(960)	1.68	(5.50)
5	324	(12.75)	3.42	(0.135)	95	None	None	1.73	(5.69)
6	324	(12.75)	3.42	(0.135)	95	46	(960)	1.79	(5.88)
7	324	(12.75)	4.76	(0.188)	68	None	None	1.76	(5.77)
8	324	(12.75)	4.76	(0.188)	68	46	(960)	1.76	(5.77)
9	305	(12.00)	6.35	(0.250)	48	46	(960)	1.76	(5.77)
10	305	(12.00)	6.35	(0.250)	48	None	None	2.37	(7.77)
11	324	(12.75)	3.42	(0.135)	95	None	None	2.34	(7.69)
12	324	(12.75)	4.76	(0.188)	68	None	None	2.34	(7.69)

4.2. Analytical Model

As described before, a finite element (FE) structural model was developed for prediction purposes and for conducting parametric studies. Initially, the plan was to develop, validate, and calibrate a single FE model using results from the collected experimental data on twelve half-scale RCFST pile-column specimens. However, after initial efforts to replicate experimental results, it was concluded that this was not possible due to a couple of reasons. First, in order to provide design recommendations that represent actual field conditions, it is necessary to consider different soil types, along with different stiffness and strength properties. Therefore, while the experimental results represent valuable information, they only cover one soil type (sand) with two levels of soil stiffness. Second, the experiments were conducted under controlled laboratory conditions in a geotechnical testing pit, as opposed to free-field conditions. This means that, while inelastic action was developed on the specimens, the restriction imposed by the rigid pit wall, induced an effect on the results as the effective stiffness and resistance of the soil were impacted by the soil-pit wall interaction.

Based on the discussion above and considering that this study is focused on the performance of RCFSTs, it was concluded that if the experimental results are successfully replicated, then the mechanical behavior of RCFST specimens is properly modeled. Therefore, to consider a broad range of soil types and their properties, the only change in the analytical model is the soil characterization. As such, it was decided to develop two analytical models, that is, one that represents laboratory conditions, and another that represents field conditions.

In the remaining of this section, the modeling approach is presented along with the soil characterization for both laboratory and field conditions. A comparison of analytical and experimental results is also presented in support of the analytical model validation and calibration.

4.2.1. Modeling Approach

A two-dimensional model was developed using OpenSees (McKenna et al., 2000). In this approach, distributed plasticity of the RCFST pile-column specimens was represented using force-based elements along with five (5) Gauss-Lobatto integration points and element lengths of 0.25D, where D represents the outer diameter of the steel tube. The pile-columns were modeled considering both aboveground (L_a) and inground (L_b) lengths, as depicted in Figure 4-19. The OpenSees *PDelta* coordinate transformation command was implemented to account for second order effects. Soil-structure interaction, on the other hand, was accomplished by means of non-linear springs at 0.25D interval depths, that is, at each joint of the pile elements. These springs were implemented using zero-length elements to which cyclic force-displacement relationships were assigned based upon p-y curve analyses. At the soil-pile interface, springs were connected using slave nodes at nodes that link two pile elements, as shown in Figure 4-20(a); properties of compatibility for such nodes were assigned using the OpenSees *equalDOF* command. The other end of the springs was fixed to complete the boundary conditions of the zero-length elements.

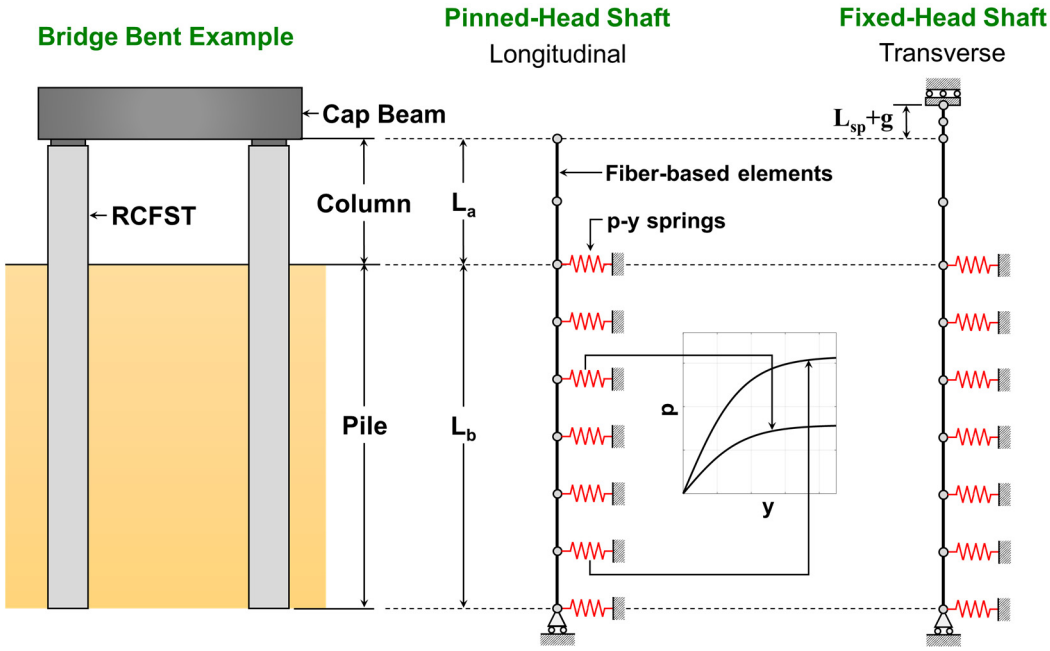

Figure 4-19 Modeling approach

As evidenced from Figure 4-19, the previously described modeling approach was used for both pinned-head and fixed-head conditions. The only difference is on the boundary conditions that were properly assigned in each case, that is, in the latter specimens were additionally restricted to rotate at their head to represent the stiffness provided by a cap beam.

On the other hand, considering standard construction practice, fixed-head specimens had an additional modeling consideration at the column-cap beam interface. In practice, RCFST drilled shafts are constructed such that a 2-inch gap is left at the steel tube-cap beam interface. By doing so, the steel tube only provides additional shear strength and confinement, but not flexural strength of a potential plastic hinge forming at this interface; such a behavior has been observed in the past (e.g., Park et al., 1983; Montejo et al., 2012). Accordingly, to account for this behavior in the FE analytical model, and to include the effects of strain penetration into the cap beam, the modeling detail depicted in Figure 4-20(b) was implemented. Regarding the former, this approach consists of modeling a portion of the RCFST shaft as an RC shaft, whose concrete properties are assigned based on the confinement provided by the steel tube. This approach emulates the actual behavior of the top plastic hinge of a fixed-head RCFST drilled shaft, where the steel tube does not contribute to the flexural strength. While not shown here for the sake of brevity, it was found that, the steel tube should be terminated at a distance of 2.5 times the shaft diameter (2.5D) from where it actually ends. This distance was determined considering that, under lateral loading, strains and stresses are approximately zero at ~2D to ~3D from the column-cap beam interface. By using this approach, a 2.5D portion is modeled effectively as an RC shaft, and below that the shaft is modeled as an RCFST. Moreover, this also helps in terms of the numerical stability of the analytical model due to the smooth force transfer between RC and RCFST elements.

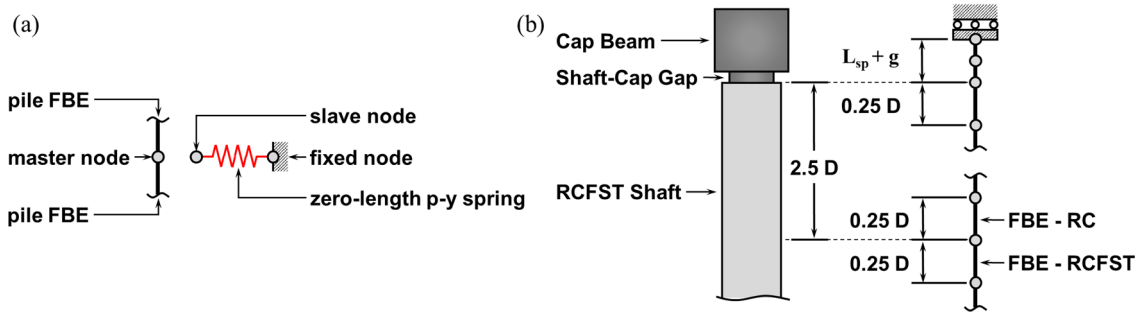

Figure 4-20 Modeling details: (a) soil-pile interface and (b) column-cap beam interface

Regarding the effects of strain penetration, on the other hand, additional fiber-based elements were included over and additional length (L_{sp}) above the column-cap beam interface. These elements account for additional flexibility due to strain penetration of the column longitudinal reinforcement into the cap beam. The strain penetration length (L_{sp}) can be calculated as shown in Equation 4-7 (Priestley et al., 2007), where f_{ye} and d_{bl} represent the expected yield strength and diameter of the longitudinal bars.

$$L_{sp} = 0.022\, f_{ye}\, d_{bl} \qquad \text{Equation 4-7}$$

With respect to the loading history, target displacements were determined in the same manner that it was done for the experimental tests. In short, a monotonic pushover analysis was conducted to identify target displacements at different performance limit states. Then, based on the results, a cyclic pushover analysis was conducted using standard single and three-cycle sets in a displacement-controlled fashion.

On the other hand, it was previously mentioned that two analytical models were developed to represent laboratory and field conditions, where the only difference is on the soil characterization. This means that the p-y curve analysis, utilized to determine properties of the non-linear springs, was different on each analytical model. More specifically, the model developed to replicate laboratory conditions utilized the Poulos and Davis (1980) approach to calculate the stiffness of p-y curves for sand using the effective mean stress of the soil, whereas the field-condition model utilized the API (1993) approach. Moreover, for p-y curve analysis in clay, the Matlock (1970) model was implemented. It is worth nothing that the API (1993) and Matlock (1970) models have been used in the analysis of past laboratory and field experiments (e.g., Boulanger et al., 1999; Chai and Hutchinson, 2002), showing results in close agreement. As such, these two models are widely accepted by the engineering community, and are typically used in professional practice for soil-structure interaction analysis.

Described next are the OpenSees material models utilized in the modeling approach. Subsequently, the definition of the p-y curve analysis is described for both analytical models, that is, laboratory and field conditions.

4.2.2. Material Models

Non-linear behavior of the materials was considered using a fiber-based approach, in which the cross-section is represented by unidirectional fibers corresponding to each material type. Properties of these fibers were assigned based on constitutive material relationships (i.e., stress-strain curves). In this study, different types of fibers were used to represent the materials within the RCFST pile-column specimen cross-section, that is, core concrete (confined concrete), reinforcing steel, and steel tube. Confined concrete fibers were modeled using the *Concrete01* material model, with parameters based upon the concrete compressive strength (f_c') and the Mander et al. (1988) model, considering an effective confinement from the steel tube of 50%. The steel tube and longitudinal steel bar fibers were modeled using the *ReinforcingSteel* material model (Kunnath et al., 2009).

4.2.3. Non-Linear Soil Springs for Laboratory Conditions

As previously mentioned, non-linear behavior of the soil was considered using non-linear springs whose properties were assigned based upon results from p-y curve analyses. In this study, the dynamic p-y method proposed by Boulanger et al. (2003) was utilized. In this method, the non-linear p-y behavior is characterized by using elastic, plastic, and gap components connected in series. The backbone curve was based on the American Petroleum Institute (API) recommendations for sand (API, 1993), as shown in Equation 4-8.

$$p = A \cdot P_u \cdot \tanh\left(\frac{k_h}{A \cdot P_u} y\right) \qquad \text{Equation 4-8}$$

In the equation above, A is a parameter that accounts for cyclic or static loading, P_u is the ultimate resistance of the soil, k_h is the effective lateral soil modulus at a given depth x, and y corresponds to the lateral deformation of the soil at a given depth. The ultimate resistance for sand was calculated based upon two failure mechanisms (Reese and Van Impe, 2011), that is, either assuming a wedge-shaped mechanism that extends to the ground surface (Equation 4-9) or a horizontal plane strain failure (Equation 4-10). In these equations γ' is the effective unit weight and D refers to the pile diameter. Parameters c_1 through c_6 can be calculated as shown in Equation 4-11 through Equation 4-16Equation 4-13, respectively.

$$P_{u1} = \gamma' x\left[\left(c_1 + c_2 + c_3\right)x + c_4 D\right] \qquad \text{Equation 4-9}$$

$$P_{u2} = \gamma' x D\left(c_5 + c_6\right) \qquad \text{Equation 4-10}$$

$$c_1 = \frac{k_0 \tan\phi \sin\beta}{\tan\left(\beta - \phi\right)\cos\alpha} \qquad \text{Equation 4-11}$$

$$c_2 = \frac{\tan^2\beta \tan\alpha}{\tan\left(\beta - \phi\right)} \qquad \text{Equation 4-12}$$

$$c_3 = \frac{k_0 \tan\beta}{\tan\phi \sin\beta - \tan\alpha} \qquad \text{Equation 4-13}$$

$$c_4 = \frac{\tan\beta}{\tan(\beta-\phi)} - k_a \qquad \text{Equation 4-14}$$

$$c_5 = k_a\left(\tan^8\beta - 1\right) \qquad \text{Equation 4-15}$$

$$c_6 = k_0 \tan\phi \tan^4\beta \qquad \text{Equation 4-16}$$

In the equations above, ϕ is the friction angle, k_a is the coefficient of active lateral earth pressure, k_0 is the coefficient of lateral earth pressure at rest, and α and β are angles based upon the friction angle (ϕ). These parameters are calculated as follows:

$$k_a = \tan^2\left(45 - \frac{\phi}{2}\right) \qquad \text{Equation 4-17}$$

$$k_0 = 1 - \sin\phi \qquad \text{Equation 4-18}$$

$$\alpha = \frac{\phi}{2} \qquad \text{Equation 4-19}$$

$$\beta = 45 + \alpha \qquad \text{Equation 4-20}$$

Since in the experimental component of this study the soil stiffness was modified considering an increase in the confinement stress in the soil, the effective modulus of subgrade reaction (k_h) was calculated using the Poulos and Davis (1980) approach, as shown in Equation 4-21. In this equation, D refers to the pile diameter, E_s is the elastic soil modulus (Equation 4-22), EI_p is the flexural stiffness of the pile, and v_s is the Poisson's ratio of the soil (Equation 4-23). In Equation 4-22, G refers to the shear soil modulus and it can be calculated based upon its relationship to the low strain shear modulus (G_{max}), which in turn can be determined from Equation 4-24 based on the recommendations by Seed and Idriss (1970). In this equation, P_{atm} is the atmospheric pressure, σ_m' is the effective mean soil stress which depends upon the effective vertical stress, as shown in Equation 4-25, and K_2 is a parameter that depends on the relative density (D_r), as depicted in Figure 4-21. Regarding the shear modulus-to-low strain shear modulus ratio (G/G_{max}), Boulanger et al. (1999) concluded that a G/G_{max} ratio of 25% can be reasonably assumed for working load levels. However, as it will be explained later, this ratio cannot be implemented for the analysis of the experimental data collected in this study due to the boundary conditions of the test setup and the soil-pit wall interaction.

$$k_h = 0.65\sqrt[12]{\frac{E_s D^4}{EI_p}}\left(\frac{E_s}{1-\upsilon_s}\right) \qquad \text{Equation 4-21}$$

$$E_s = 2(1+\upsilon_s)G \qquad \text{Equation 4-22}$$

$$\upsilon_s = \frac{k_0}{1+k_0} \qquad \text{Equation 4-23}$$

$$\frac{G_{\max}}{P_{atm}} = 21.8K_2\sqrt{\frac{\sigma_m'}{P_{atm}}} \qquad \text{Equation 4-24}$$

$$\sigma_m' = \frac{\sigma_v'(1+2k_0)}{3} \qquad \text{Equation 4-25}$$

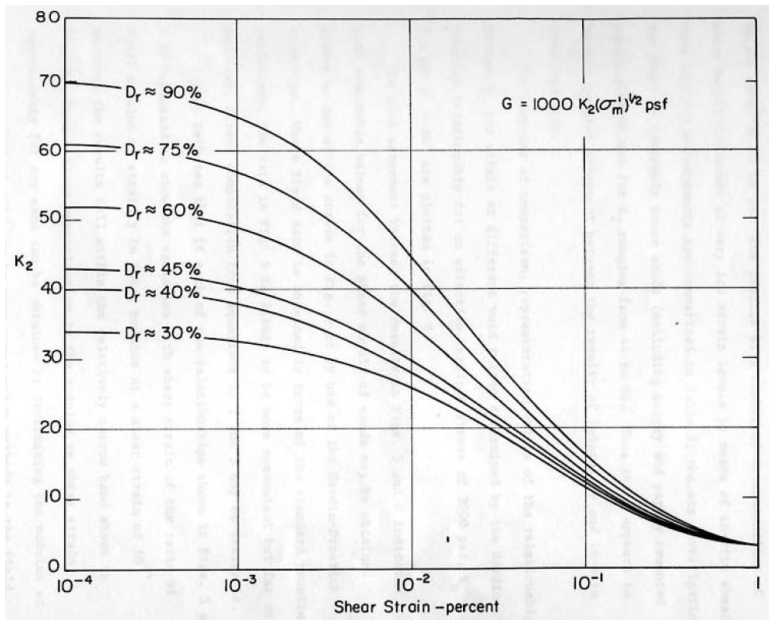

Figure 4-21 Shear modulus of sand (Seed and Idriss, 1970)

Using Equation 4-8 through Equation 4-25, p-y curves can be determined for a given set of parameters. Note that the effect of a soil surcharge is directly considered in the effective vertical stress of the soil. As an example, Figure 4-22 presents p-y curves at different depths along with the effective modulus of subgrade reaction for a soil profile that consist of a uniform sand layer with unit weight γ = 90 pcf, friction angle ϕ = 35°, K_2 = 35, and a shear modulus ratio G/G_{max} = 0.25. Moreover, considering and RCFST shaft with diameter-to-thickness ratio D/t = 48, the flexural stiffness was taken as EI_p = 44,800 kip-ft^2.

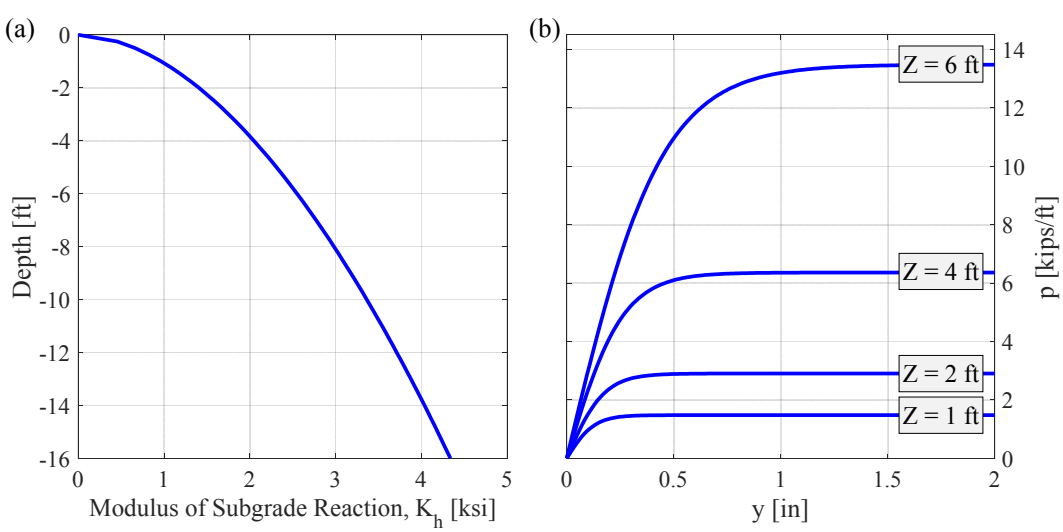

Figure 4-22 (a) modulus of subgrade reaction and (b) resulting p-y curves

The formulation described above was implemented to develop p-y curves that account for laboratory conditions. However, variations on the G/G_{max} ratio and an update process of the p-y curves at different stages during the test were applied. First, based upon validation and calibration of the FE analytical model, which is shown later in this section, it was found that the G/G_{max} ratio varies along the depth of the soil profile, depending upon the level of deformation in the soil. For regions of large soil deformations (i.e., depths within 2D to 3D), a G/G_{max} ratio of 1.0 was considered since the interaction with the pit wall is higher, thus resulting in a higher soil stiffness. On the other hand, for regions of small soil deformations (i.e., depths within 5D to 6D) a G/G_{max} ratio of 0.10 was assumed. For the transition zone, the G/G_{max} ratio varies linearly from 1.0 to 0.1. As an example, the variation of the G/G_{max} ratio along with the resulting horizontal modulus of subgrade reaction are presented in Figure 4-23 for one of the experimental tests.

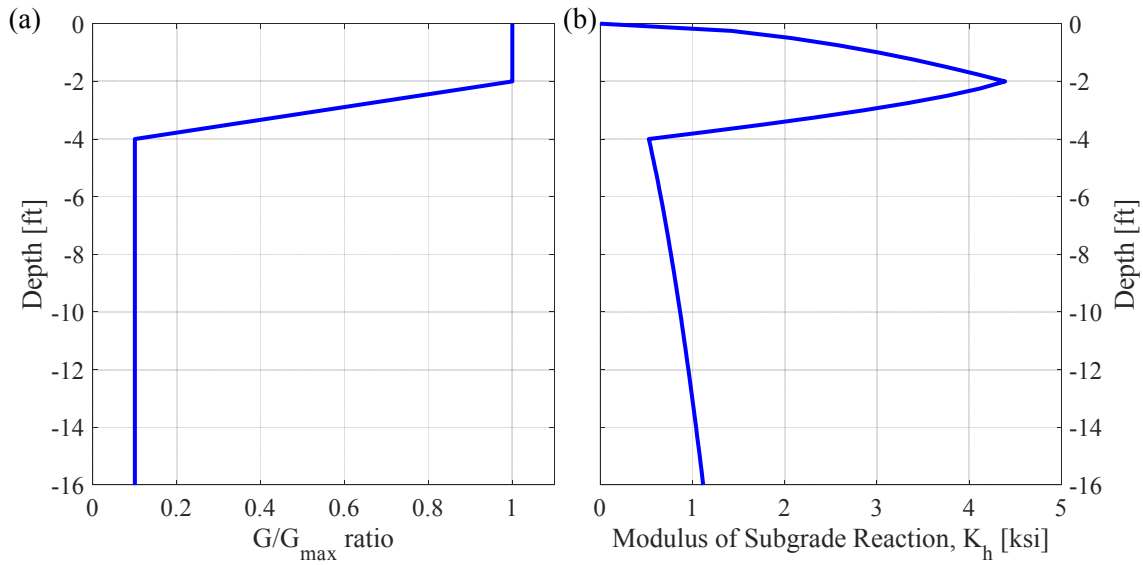

Figure 4-23 Soil stiffness parameters: (a) G/G_{max} ratio, and (b) modulus of subgrade reaction

In addition to the variation of the G/Gmax ratio, the friction angle was modified to consider the stiffening effect of the soil, induced by the large soil deformations and the soil-pit wall interaction. It is worth recognizing that the physical properties of the soil do not change, but rather the effective stresses in the soil increase due to the confinement effect provided by the boundary conditions, and the level of deformation in the soil. As such, the larger the soil deformations, the higher the soil-pit wall interaction, thus resulting in higher soil stiffness and strength. Furthermore, the variation on the friction angle in turn creates a variation in the stiffness and strength properties of the non-linear soil springs utilized in the FE analytical model. As such, this was implemented by updating the properties of such springs using the OpenSees *remove element* command along with the *initialStressMaterial* model, that is, soil springs were replaced after a significant deformation was imposed in the soil profile. More specifically, a new set of non-linear p-y curves with initial conditions was defined at the following stages of the displacement history: (1) after half the elastic portion was completed, (2) after the remaining elastic portion was completed, and (3) after each ductility level was completed.

As an example, Figure 4-24 shows two sets of backbone p-y curves from one of the tests; they correspond to soil conditions after the elastic and ductility 1 (μ_1) cycles were completed. Note that there is a clear difference in the shape of the p-y curves. It is worth nothing that the p-y curves depicted in Figure 4-24, are the result of calibrating and validating the FE analytical model to match experimental results. As such, the previously described p-y curve adjustment would not be expected under free-field conditions, as the soil would not have any restriction to deform as it does in the laboratory environment described before. Further details regarding validation and calibration of the FE analytical model are presented next.

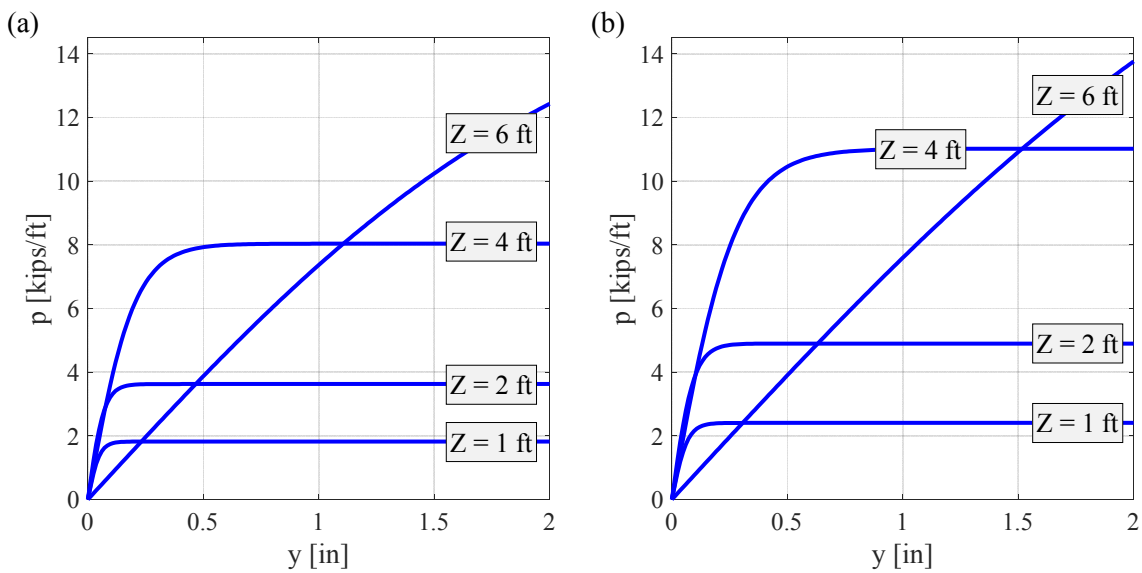

Figure 4-24 P-y curves from Test 1: (a) after elastic cycles and (b) after ductility 1 (μ_1) cycles

4.2.4. Calibration and Validation of FE Analytical Model

The FE analytical model was calibrated and validated based upon the collected experimental data. More specifically, the main goal was to match the recorded structural response in terms of the: (1) top lateral force vs. displacement response, (2) displacement profiles, (3) curvature profiles, and (4) tensile strain profiles.

The calibration and validation process was based on the premise that if experimental results were replicated, the mechanical behavior of the system was properly modeled. Then, the same model could be used to study a broad range of soil and structural parameters. However, the boundary conditions of the test setup and the interaction between soil and pit wall, created a unique scenario that resulted in the need to develop two analytical models, namely, one characterizing the laboratory environment, and another representative of free-field conditions, where the main difference is on the definition of the p-y curve analysis used to determine the soil spring properties.

The previous section described the p-y curve formulation used for the model representative of laboratory conditions. It was shown that p-y curves were updated in terms of their stiffness and strength characteristics at different stages of the loading protocol. It is important to note that while such a process was performed for calibration and validation

purposes, it was not performed for the analytical model representative of free-field conditions, since in that case the soil would not experience the stiffening and strengthening effect observed in the laboratory.

While not shown here for the sake of brevity, it is worth briefly describing the validation and calibration in terms of the structural elements. As previously described, pile-column elements were modeled using force-based elements in combination with five (5) Gauss-Lobatto integration points and element lengths of 0.25D, where D represents the outer diameter of the steel tube. This was implemented based on the results of sensitivity studies. It was found that by using element lengths of 0.25D, results for both displacement and force-based elements were in close agreement using either 3 or 5 integration points. Moreover, the implemented modeling approach allows to properly capture both the spread of inelastic action and soil-structure interaction. Likewise, it helps in terms of convergence of the non-linear solution as force-based elements allow for calculating exact internal forces and deformations based on the stress-strain relationship of the materials, whereas displacement-based elements utilize approximated displacement field solutions to determine internal forces, hence leading to slower convergence.

The remaining of this section shows a comparison of analytical and experimental results for two of the experiments conducted. It is important to note that similar observations were made in other tests; experimental results and observations are discussed in detail later in this report. For brevity, only results of Test 1 and Test 12 are presented next. These tests correspond to RCFST specimens with D/t ratios of 48 and 68, and L_a/D ratios of 5.5 and 7.3, respectively.

Figure 4-25 presents the top lateral force vs displacement response for both analytical and experimental models. The comparison of results is presented up to ductility 3 (μ_3), which corresponds to a level of displacement where onset of tube local buckling takes place. Note that both the analytical and experimental response are in close agreement. This means that at a global level, the experimental response is replicated by the analytical model. Also, note that as displacements increase from cycle to cycle, the lateral force developed also increases for the same level of displacement. It is believed that this occurred until the plastic hinge was fully developed, which occurred between the ductility 1.5 ($\mu_{1.5}$) and ductility 2 (μ_2) cycles. To further validate the results, Figure 4-26 and Figure 4-27 show the force vs. displacement response during the elastic portion and part of the inelastic portion for each ductility level individually. Note that results of the analytical model are in close agreement at each stage of the experimental test.

Figure 4-28 through Figure 4-30 present results of the comparison at a local level, namely, they present displacement, curvature, and tensile strain profiles at different stages of the loading protocol. Each of these figures present results for more than one stage of the loading protocol, where higher values imply a higher performance level. Note that in both elastic and inelastic portions of the loading protocol, the experimental results are replicated by the analytical model in close agreement. However, note that minor differences are observed between the dots, which represent experimental data, and the dotted red lines that represent the results of the analytical model. Such a difference was induced by the resolution of the

rotation data. As previously explained, displacement, curvature, and strain profiles were calculated based on rotation data collected using inclinometer sensors that had a 2-foot gauge length. As such, experimental results related to displacement, curvature and tensile strains are valid for a range of 2 ft. though they are plotted at the centroid of the gauge length.

Despite the minor differences described above, especially in terms of the curvature and strain profiles, it was concluded that the modeling approach was adequate considering that the experimental response was replicated in close agreement at both global and local levels. Similar observations were made from results of Test 12, as shown in Figure 4-31 through Figure 4-36.

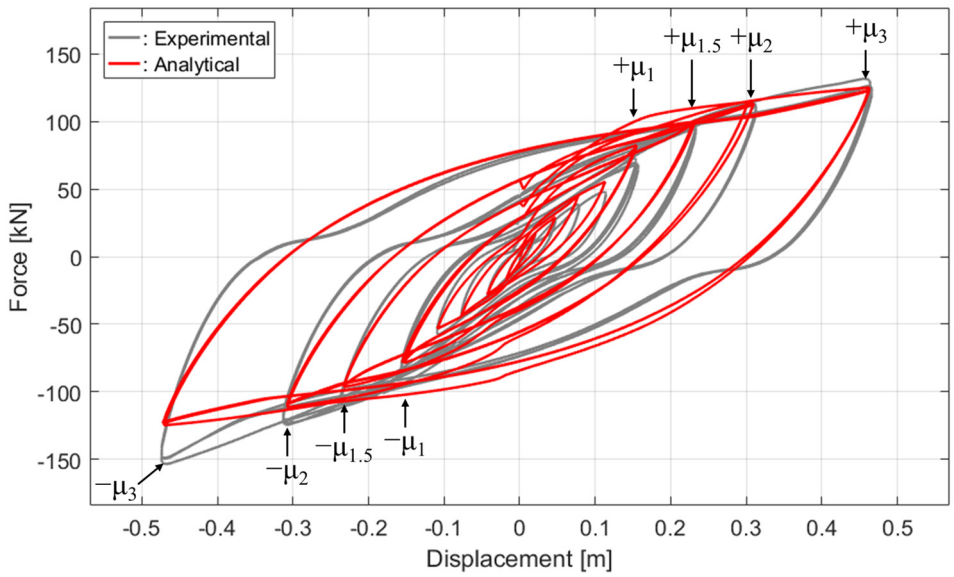

Figure 4-25 Test 1: top lateral force vs. displacement response comparison

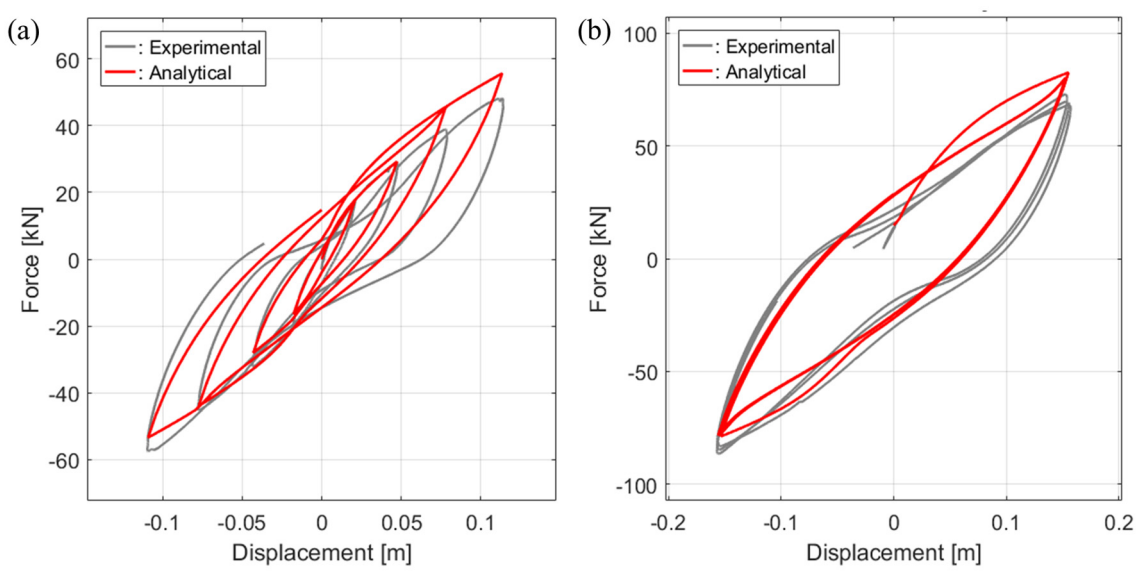

Figure 4-26 Test 1: top lateral force vs displacement response comparison for (a) elastic and (b) ductility 1 (μ_1) cycles

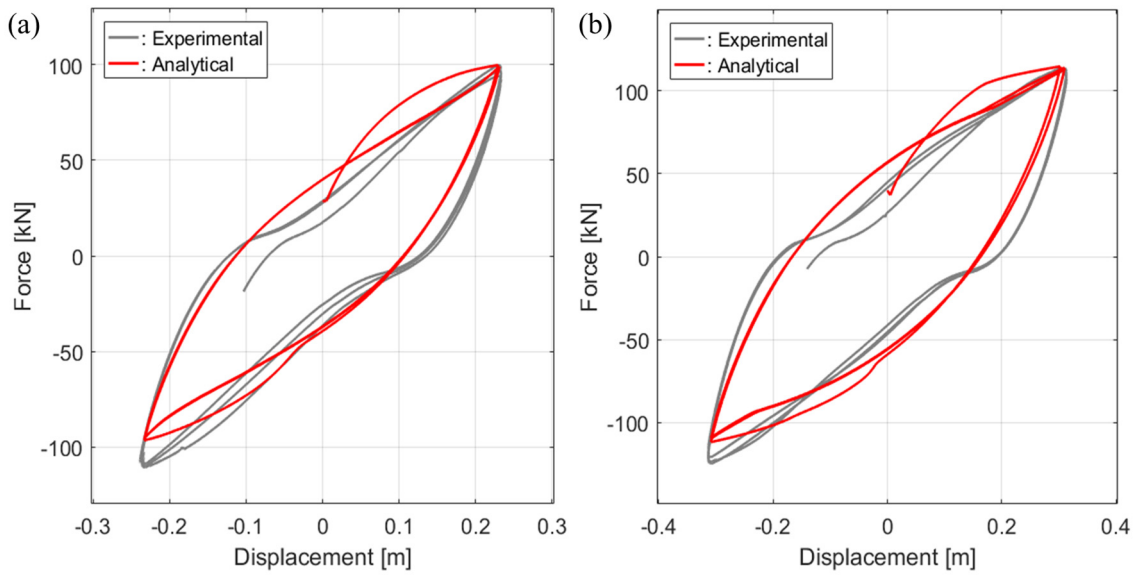

Figure 4-27 Test 1: top lateral force vs displacement response comparison for (a) ductility 1 (μ_1) and (b) ductility 1.5 ($\mu_{1.5}$) cycles

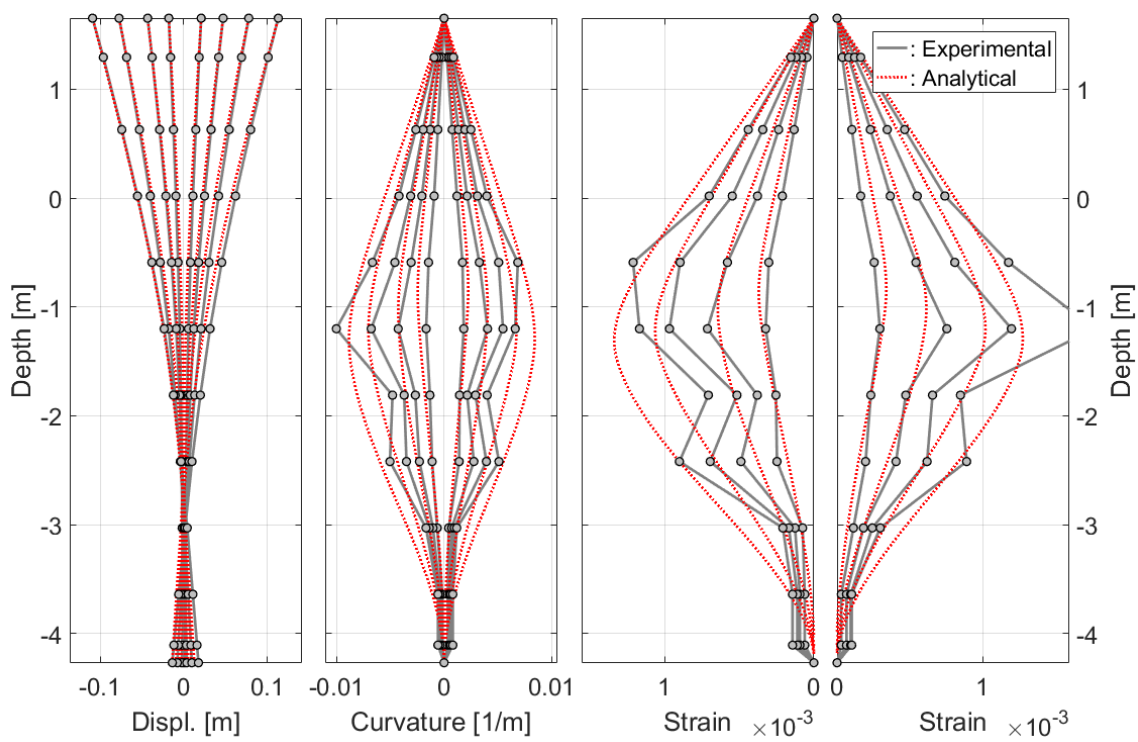

Figure 4-28 Test 1 (from left to right): displacement, curvature, and tensile strain (push and pull cycles) profiles during elastic portion of the test

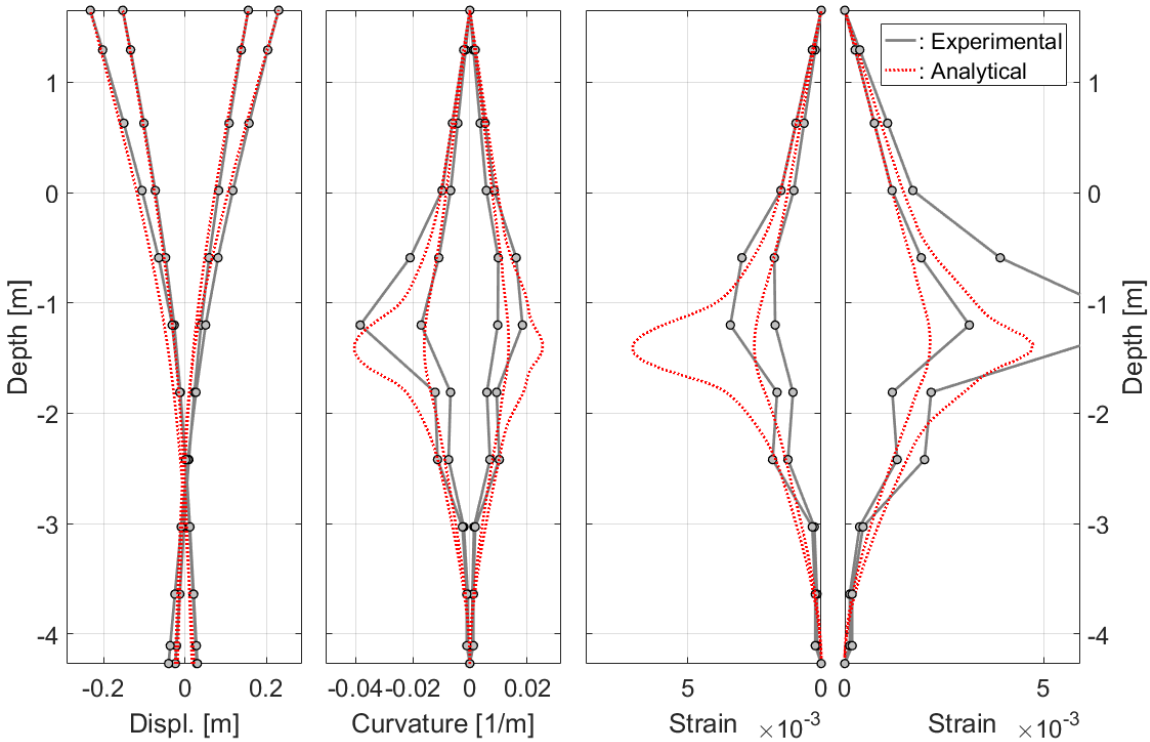

Figure 4-29 Test 1 (from left to right): displacement, curvature, and tensile strain (push and pull cycles) profiles at ductilities 1 (μ_1) and 1.5 ($\mu_{1.5}$) cycles

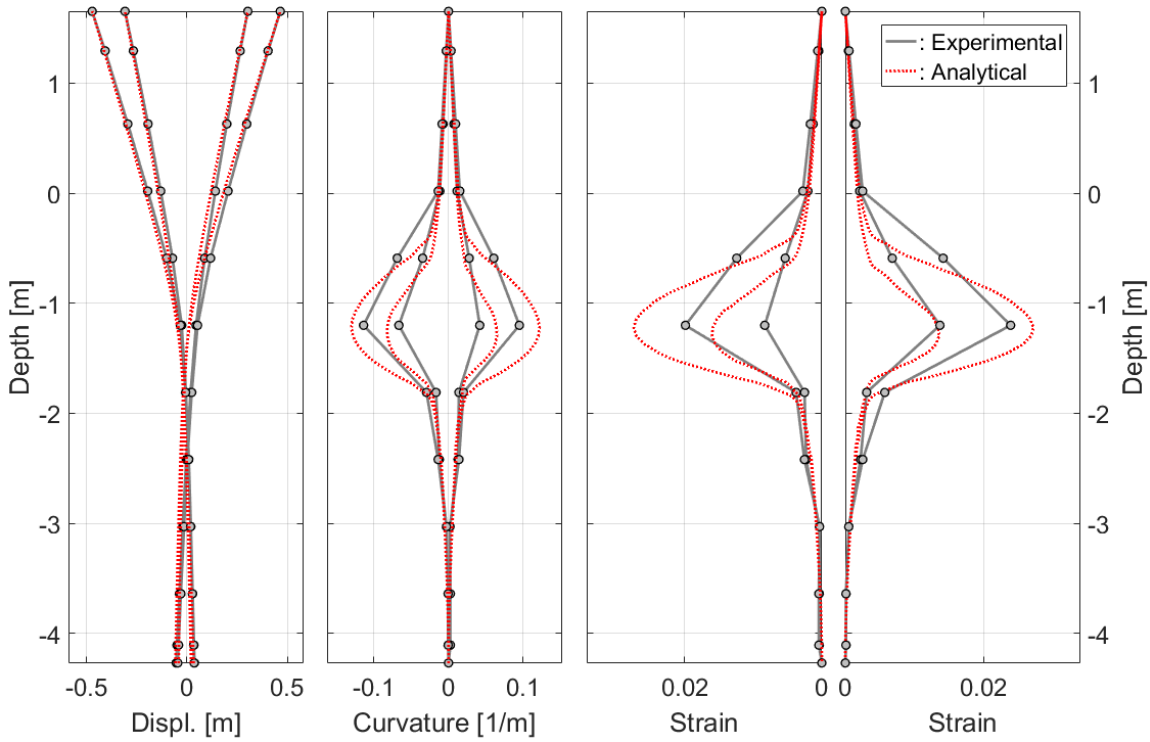

Figure 4-30 Test 1 (from left to right): displacement, curvature, and tensile strain (push and pull cycles) profiles at ductilities 2 (μ_2) and 3 (μ_3) cycles

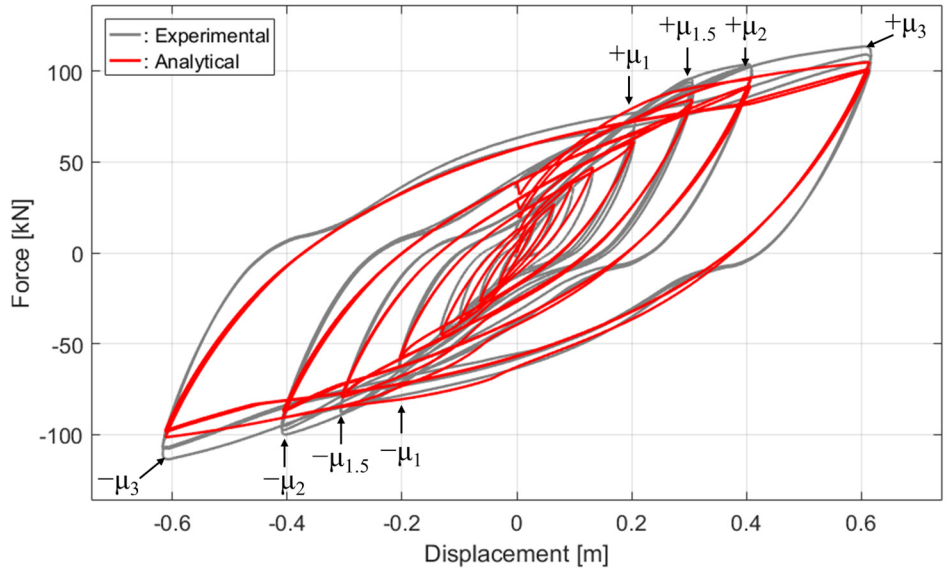

Figure 4-31 Test 12: top lateral force vs. displacement response comparison

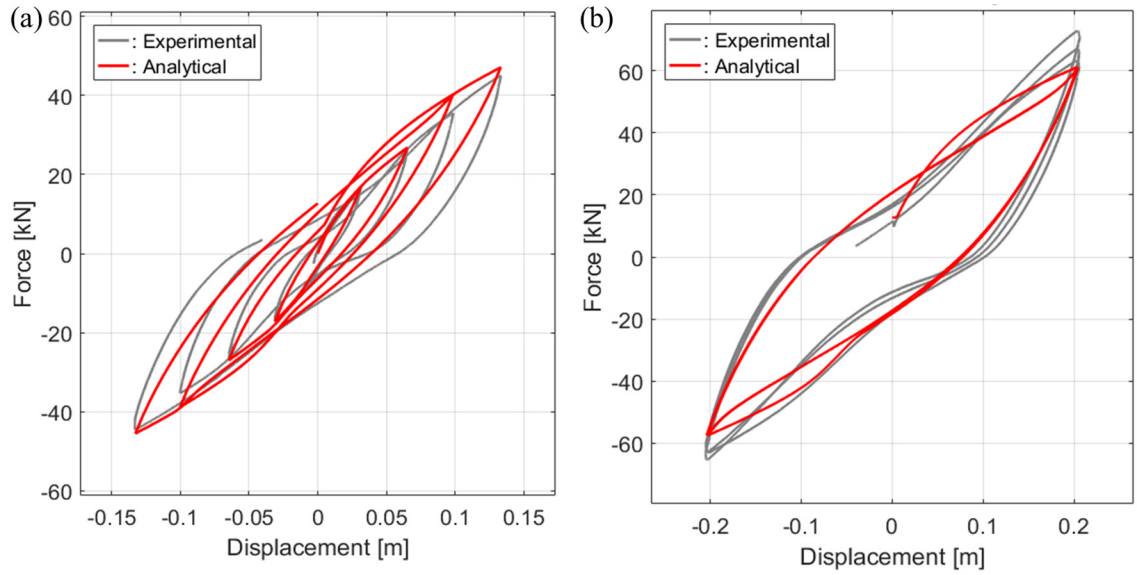

Figure 4-32 Test 12: top lateral force vs displacement response comparison for (a) elastic and (b) ductility 1 (μ_1) cycles

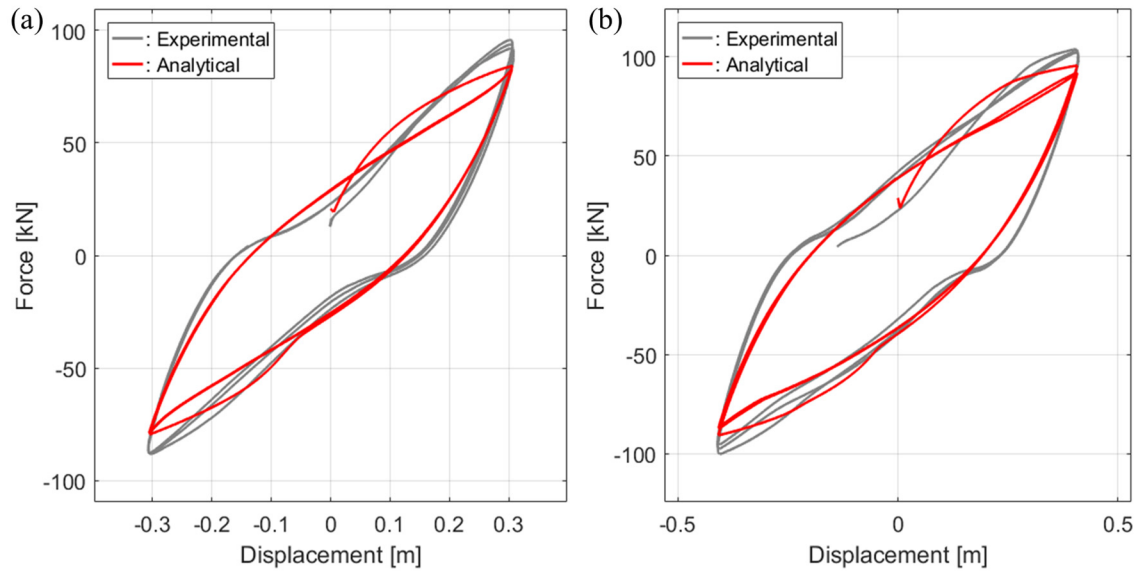

Figure 4-33 Test 12: top lateral force vs displacement response comparison for (a) ductility 1 (μ_1) and (b) ductility 1.5 ($\mu_{1.5}$) cycles

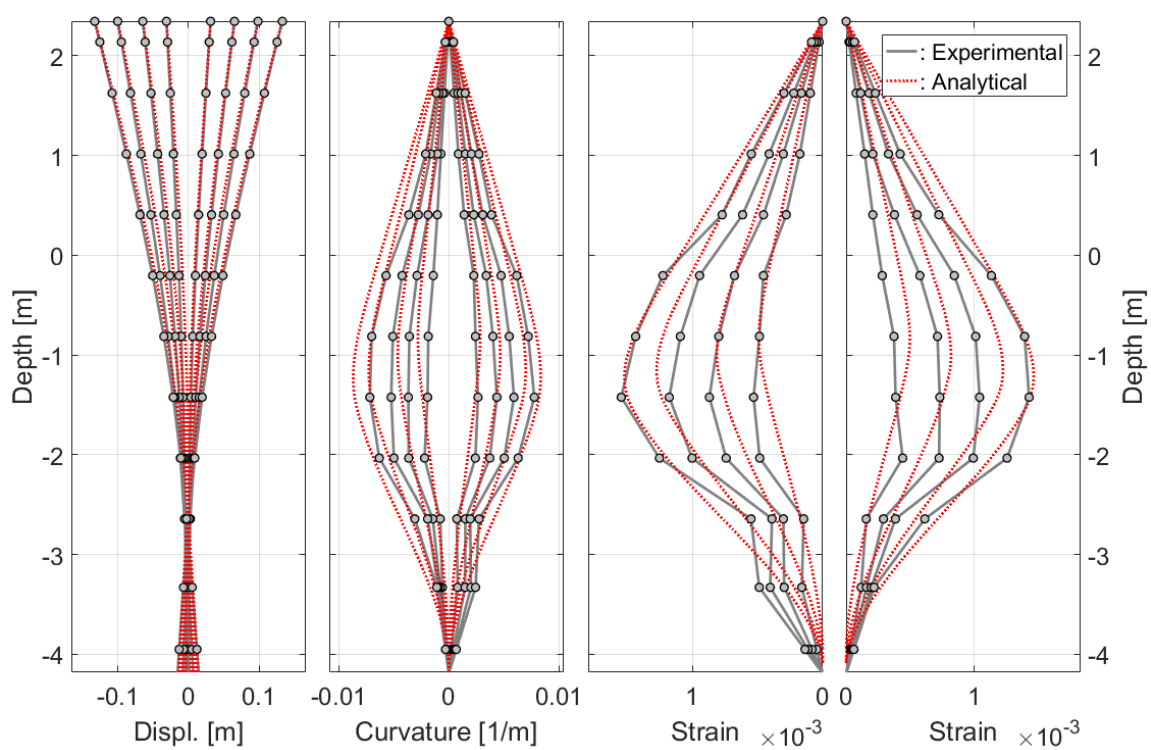

Figure 4-34 Test 12 (from left to right): displacement, curvature, and tensile strain (push and pull cycles) profiles during elastic portion of the test

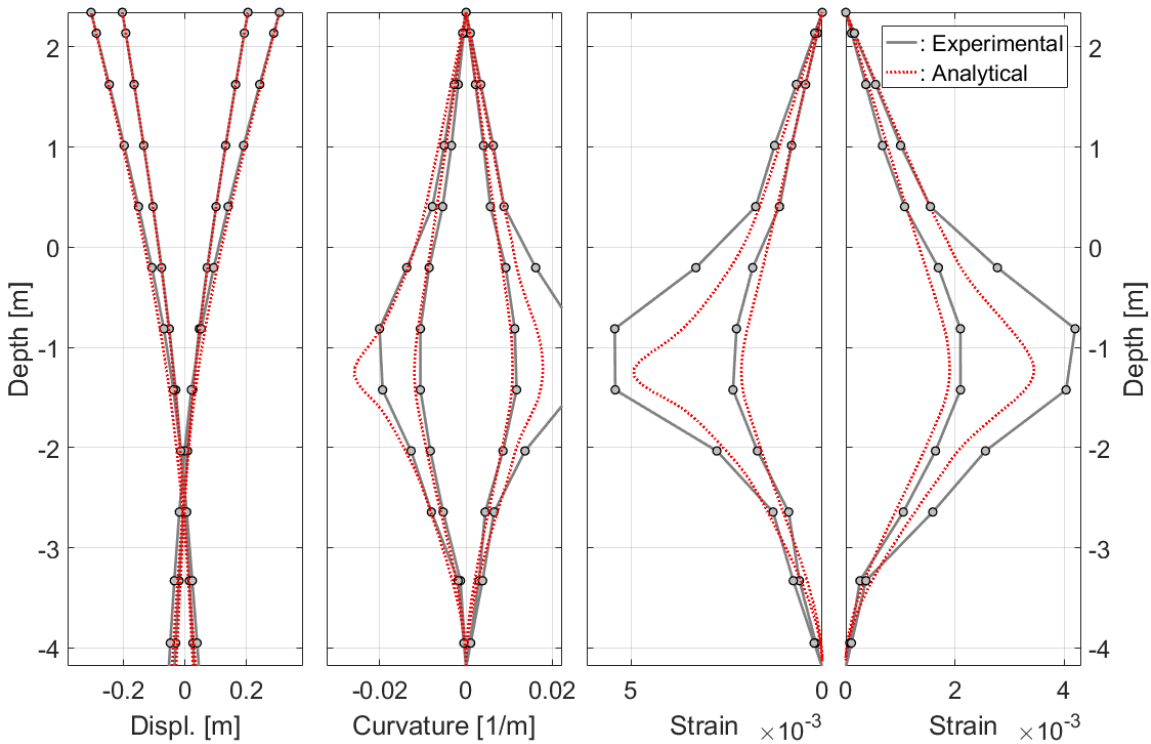

Figure 4-35 Test 12 (from left to right): displacement, curvature, and tensile strain (push and pull cycles) profiles at ductilities 1 (μ_1) and 1.5 ($\mu_{1.5}$) cycles

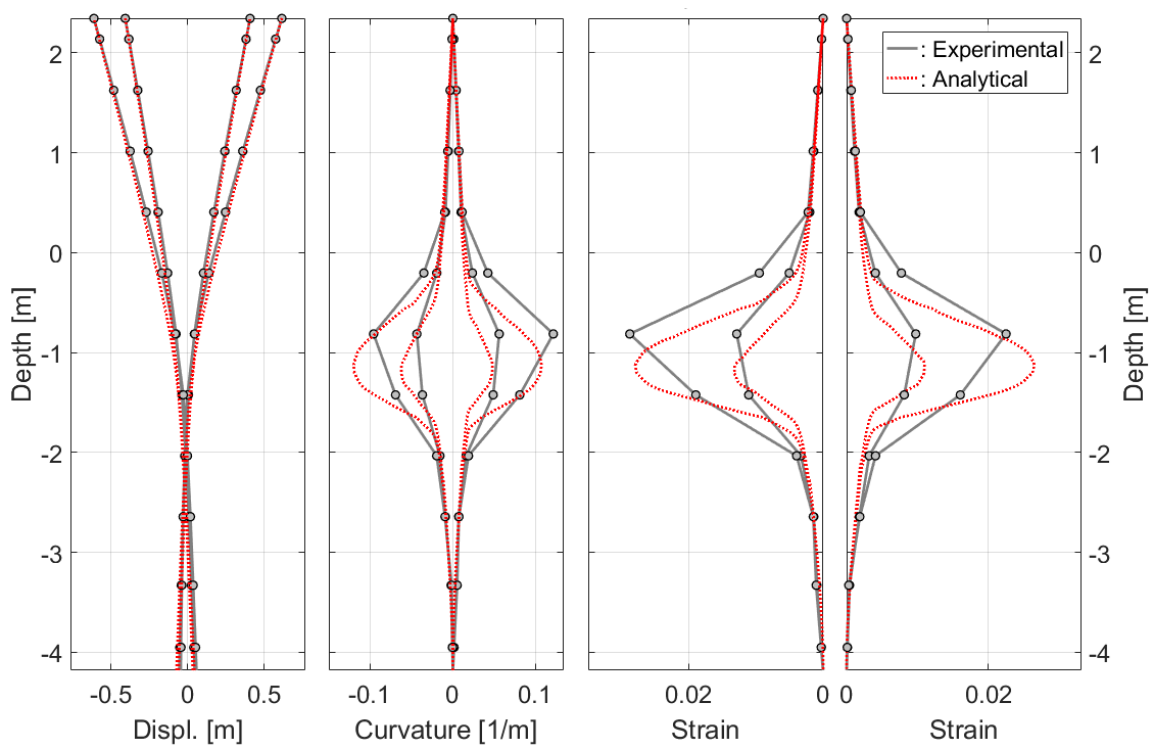

Figure 4-36 Test 12 (from left to right): displacement, curvature, and tensile strain (push and pull cycles) profiles at ductilities 2 (μ_2) and 3 (μ_3) cycles

4.2.5. Non-Linear Soil Springs for Field Conditions

The parametric study of this project was conducted using p-y curve formulations that are frequently used in practice, namely, the API (1993) approach in combination with the Reese and Van Impe (2011) model were selected for sand, while the Matlock (1970) model was selected for clay. This section describes the formulation of each model and presents the main parameters that were utilized.

4.2.5.1 P-y Curves for Sand

As previously shown, the API (1993) approach utilizes a hyperbolic tangent function to describe the force deformation response of sand. The equation was presented before but has been repeated as Equation 4-26 for completion. In this expression, A is a parameter that accounts for the loading type (static or cyclic), P_u is the ultimate resistance of the soil, k_h is the effective lateral soil stiffness at a given depth, and y corresponds to the lateral deformation of the soil at a given depth. Parameters P_u and A can be determined based on the Reese and Van Impe (2011) model, previously presented in Equation 4-9 through Equation 4-20.

$$p = A \cdot P_u \cdot \tanh\left(\frac{k_h}{A \cdot P_u} y\right) \qquad \text{Equation 4-26}$$

The main difference with the p-y curve formulation for laboratory conditions is on the soil stiffness, and more specifically, on the modulus of subgrade reaction (k_h). The API (1993) approach provides a chart that allows for calculating the coefficient of subgrade reaction (n_h) as a function of the friction angle (ϕ) or relative density (D_r). Figure 4-37 presents an updated version of such a chart (ATC-32, 1996). This coefficient is used to determine the modulus of subgrade reaction (k_h), as shown in Equation 4-27. However, it has been recognized in the literature (e.g., Boulanger et al., 1999; Chai and Song, 2012) that values from these type of tables produce rather stiff soil profiles as they were developed from tests that were conducted at shallow depths. The solution to this issue is to correct n_h values considering the reference stress (σ_{ref}' = 50 kPa) at which they were calibrated, as shown in Equation 4-28. Thus, Equation 4-26 can be written as Equation 4-29.

For the analytical portion of this study, the n_h values adopted are within the range of those recommended in the 2011 AASHTO Guide Specification for LRFD Seismic Bridge Design (AASHTO, 2011), and they are presented in Table 4-2. As an example of the formulation above, Figure 4-38 presents p-y curves for sand at different depths along with the effective modulus of subgrade reaction for a soil profile that consist of a uniform sand layer with unit weight γ = 90 pcf, friction angle ϕ = 35°, modulus of subgrade reaction n_h = 100 pci, and a pile diameter D = 1 ft. Note that a depth of about 12 ft the corrected soil stiffness starts to increase at a lower rate. Also, note that the resulting p-y curves increase in both strength and stiffness with an increase in depth.

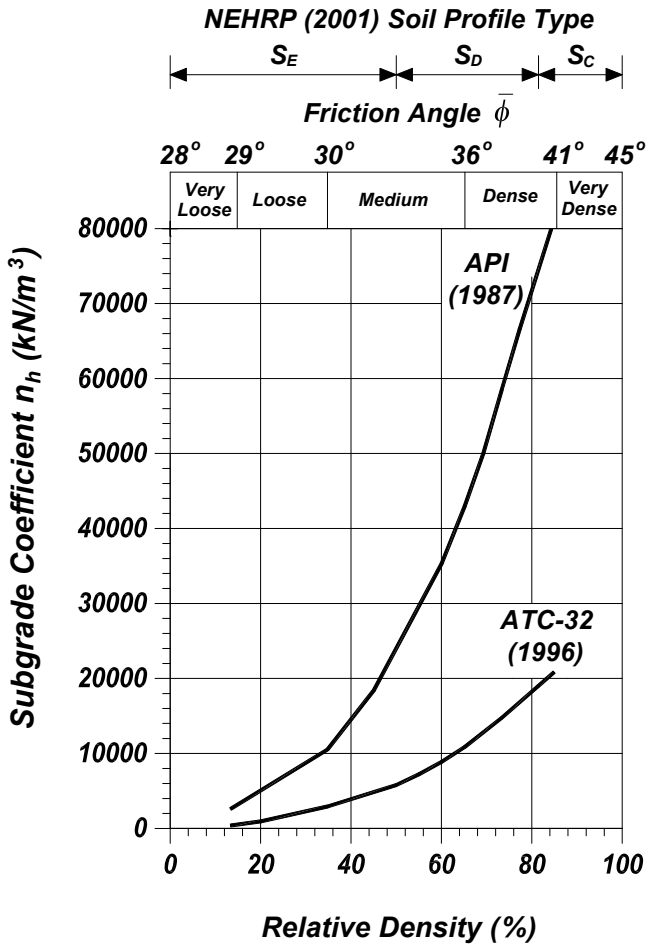

Figure 4-37 Coefficient of subgrade reaction chart (ATC-32, 1996)

$$k_h = n_h\, x \qquad \text{Equation 4-27}$$

$$n_h^* = n_h \sqrt{\frac{\sigma_{ref}'}{\sigma_v'}} \text{ Equation 4-28} \qquad \text{Equation 4-28}$$

$$p = A \cdot P_u \cdot \tanh\left(\frac{n_h^* \cdot x}{A \cdot P_u}\, y\right) \qquad \text{Equation 4-29}$$

Table 4-2 Values of n_h for sand (AASHTO, 2011)

Consistency	nh (pci)
Loose	34.8
Medium	92.5
Dense	231.7

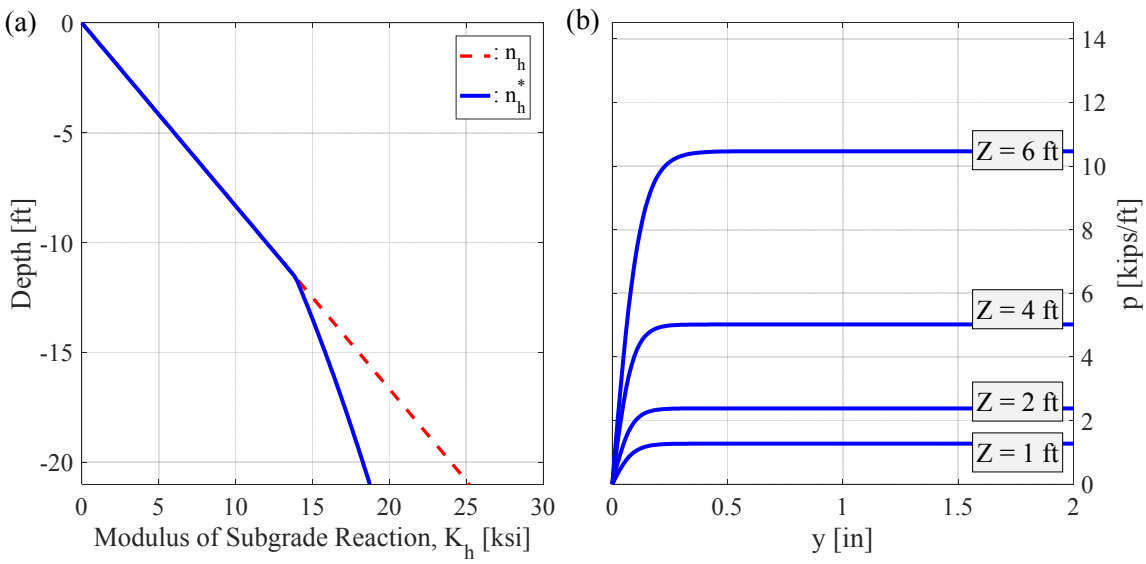

Figure 4-38 P-y analysis for sand: (a) variation of soil stiffness and (b) resulting p-y curves

4.2.5.2 P-y Curves for Clay

The Matlock (1970) model for soft clay is characterized by a parabolic function that depends on the ultimate resistance of the soil (P_u), and the soil deformation when the force is 50% of P_u (y_{50}), as shown in Equation 4-30. The ultimate soil resistance (Equation 4-31) is calculated based on the undrained shear strength (C_u), the pile diameter (D), and a lateral bearing capacity factor (N_p). The latter is calculated as shown in Equation 4-32. In this expression, σ_v' is the effective vertical stress, J is an empirical parameter taken as 0.5 based on Matlock's recommendations for soft clay, and x is the depth at which the p-y curve is calculated. On the other hand, the soil deformation when the force is 50% of P_u (y_{50}), depends on the pile diameter and the strain corresponding to a strength of 50% of the ultimate strength (ε_{50}), as shown in Equation 4-33. In this study, values of ε_{50} recommended by Reese and Van Impe (2011) were adopted, and they are presented in Table 4-3.

Note that the formulation of the Matlock (1970) model results in a constant distribution of stiffness when the lateral bearing capacity factor (N_p) exceeds 9. This means that unlike sand, clay p-y curves do not change after some depth, depending upon soil properties and the diameter of the pile. In fact, Chai and Song (2012) showed that the soil stiffness can be calculated as depicted in Equation 4-34. To illustrate the formulation of p-y curves for clay, Figure 4-39 presents an example that considers a pile diameter D = 1 ft, clay with effective unit weight γ' = 90 pcf, undrained shear strength Cu = 750 psf, and strain corresponding to a strength of 50% of the ultimate strength ε_{50} = 0.01. Note that the effective soil stiffness becomes constant at a depth of about 10 ft, which in turn makes that the shape of p-y curves below this point to be the same. Also, note from Figure 4-39(b) that p-y curves were plotted with a normalized soil deformation (y/y_{50}) and that at y/y_{50} = 8 the curves become flat, reaching the ultimate soil strength, namely, the limiting value in Equation 4-30.

$$\frac{p}{P_u} = 0.5\left(\frac{y}{y_{50}}\right)^{1/3} \leq 1 \qquad \text{Equation 4-30}$$

$$P_u = C_u D N_p \qquad \text{Equation 4-31}$$

$$N_p = \left(3 + \frac{\sigma_v'}{C_u} + J\frac{x}{D}\right) \leq 9 \qquad \text{Equation 4-32}$$

$$y_{50} = 2.5 D \varepsilon_{50} \qquad \text{Equation 4-33}$$

$$k_h = \frac{P_u}{y_{50}} \qquad \text{Equation 4-34}$$

Table 4-3 Values of ε_{50} for soft clay (Reese and Van Impe, 2011)

	Consistency		
	Soft	Medium	Stiff
ε_{50}	0.020	0.010	0.005

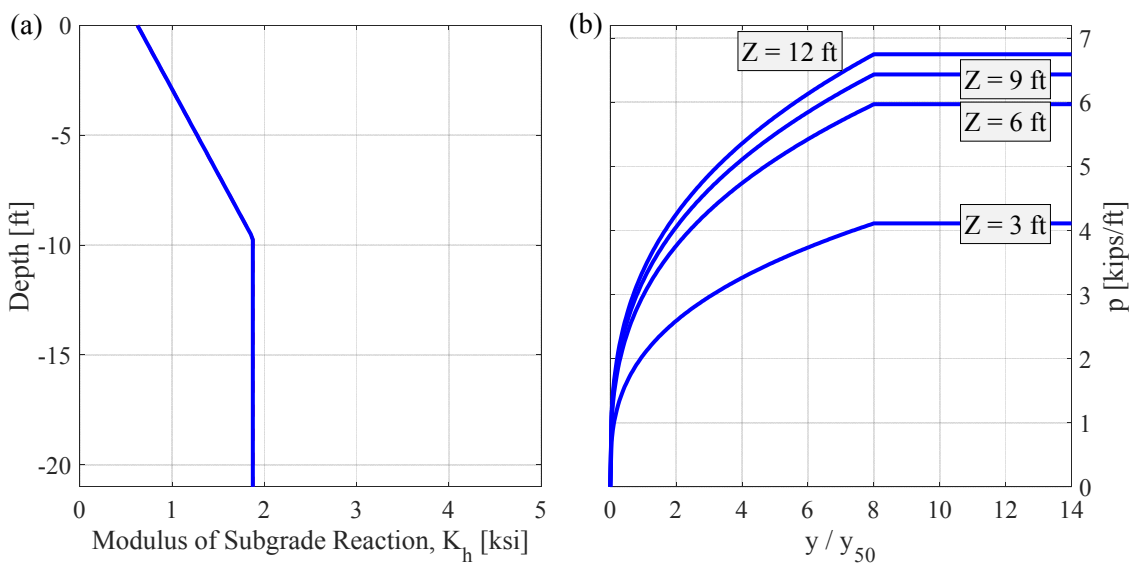

Figure 4-39 P-y analysis for clay: (a) variation of soil stiffness and (b) resulting p-y curves

4.3. Equivalent Cantilever Plastic Hinge Model for RCFSTs

The main goals of the study presented in this report are to understand the behavior of RCFSTs embedded in soil and to provide design recommendations for such a system. As such, one of the objectives was to investigate the inground plastic hinge. However, based upon literature review, it was recognized that a plastic hinge length model alone would not work in terms of providing accurate predictions for seismic design of RCFST drilled shafts. As previously explained, the plastic hinge length is used in combination with an equivalent cantilever approach to calculate the displacement capacity of this type of system. An example of this is the method developed by Suarez and Kowalsky (2007) for RC drilled

shafts. Their method consisted of coefficients that allow for including the flexibility of the soil in the calculation of the yield and plastic displacements, and they also provided consistent equations to calculate the depth to the plastic hinge. Regarding the latter, they adopted the model proposed by Chai (2002), which produces plastic hinge lengths that do not depend on the soil stiffness, as show in Equation 4-35; further details of their method can be found in the literature review section of this report.

$$L_p = D + 0.1L_a \leq 1.6 \qquad \text{Equation 4-35}$$

The main reason that makes the Suarez and Kowalsky (2007) model to produce inaccurate results for RCFST shafts, is that their method was developed for RC drilled shafts. As such, all the parameters utilized in the calculation of the system displacement are tied to the flexural strength of the material, namely, reinforced concrete, which is smaller to that of RCFSTs as the steel tube provides enhanced deformation and strength capacities, thus increasing the effective flexural stiffness. This will be apparent later in this report in the results of the parametric studies.

Regarding the plastic hinge, on the other hand, the literature review revealed that most of the available approaches for RC shafts depend only on the aboveground length (e.g., Budek et al., 1995 and 2000; Chai, 2002; SCDOT, 2008; Caltrans, 2013). However, a recent study (Goel, 2015) suggested that the plastic hinge length can actually by impacted by the effective soil stiffness. This study concluded that for RC drilled shafts in sand, current approaches produce accurate predictions of the plastic hinge length; however, in his study, Goel (2015) considered p-y curves for lower, nominal, and upper bound estimates without actually considering soil profiles with different characteristics.

From the discussion above, it is evident that besides an appropriate plastic hinge model, it is necessary to have an equivalent cantilever method that captures the behavior of RCFST shafts. As such, it was decided to develop an equivalent cantilever plastic hinge model for RCFST drilled shafts that allows to consider both pinned and fixed-head conditions. For that purpose, a parametric study was conducted using the FE analytical model previously described. The advantage of using a fiber-based modeling approach is that the spread of inelastic action and the effects of the moment gradient can be captured in the response of the RCFST drilled shafts, which in turn allows for relating strains and displacements accurately. Details of the parametric study are presented at the end of this chapter.

Described next is the proposed formulation for both pinned and fixed-head conditions. It is worth noting that this approach is similar to that developed by Suarez and Kowalsky (2007) for RC shafts, with appropriate considerations for the system studied.

4.3.1. Pinned-Head RCFST Shafts

Presented in Figure 4-40 is a schematic of the proposed equivalent cantilever model for pinned-head RCFST shafts. In this approach, a single RCFST shaft that can be characterized with a detailed FE analytical model, is in fact simplified to an equivalent fixed-based cantilever with effective length L_e. This equivalent length is measured from the top of the RCFST shaft to the point of maximum moment below ground, namely, to the inground plastic hinge (H_{ig}), as shown in Equation 4-36. In this equivalent system, the lateral displacement at a given limit state (Δ_{LS}) can be calculated based on elastic and plastic displacement components, as shown in Equation 4-37.

The yield displacement (Δ_y) is calculated by integrating the elastic curvature distribution over the effective length and considering a coefficient (c_1) that accounts for end fixity and soil flexibility, as shown in Equation 4-38. In this expression, the yield curvature (ϕ_y) can be determined from a moment-curvature analysis, or from an approximate expression (Equation 4-39) that depends on the yield strain of the steel tube ($\varepsilon_{y\,(tube)}$), its diameter (D), and a yield curvature parameter ($c_{\phi y}$). The latter is a parameter that is usually taken as 2.25 for RC shafts (Priestley et al., 2007), but for RCFSTs it needs to be developed based upon moment-curvature analyses.

The plastic displacement (Equation 4-40), on the other hand, depends on the plastic curvature (ϕ_p) and the equivalent plastic hinge length (L_p). The former is determined from Equation 4-41 depending upon the limit state curvature (ϕ_{LS}), which in turn depends on the target strain limit state; calculation of curvature limit states is explained later. Note from Figure 4-40 that that the inelastic curvature is assumed to be centered at the base of the cantilever. Finally, Equation 4-37 can be written in terms of the previously described parameters, as shown in Equation 4-42.

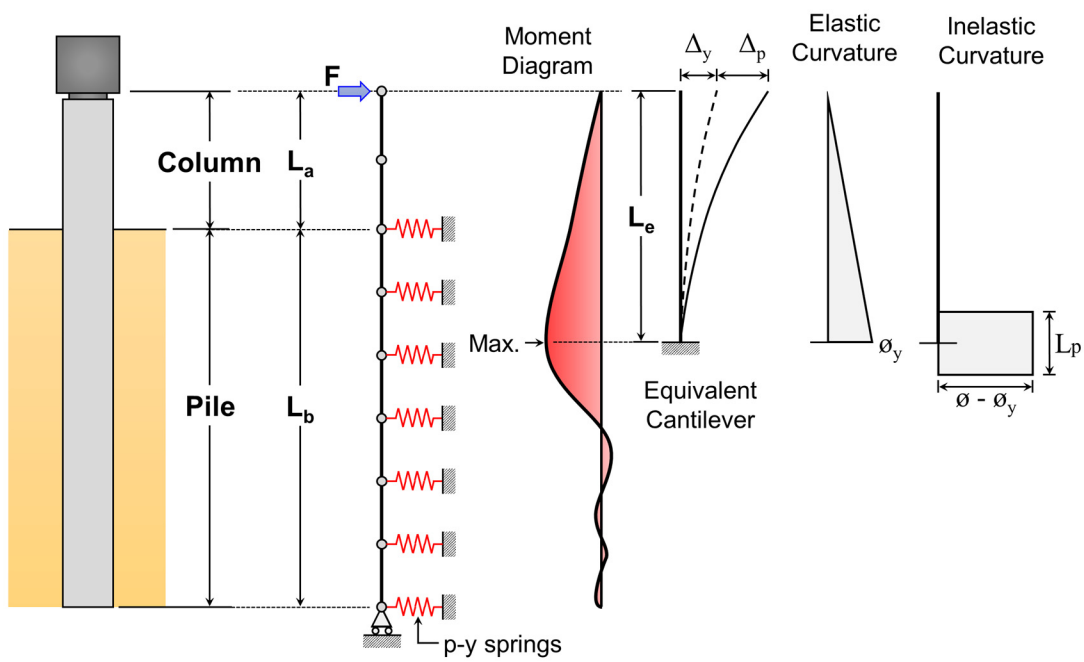

Figure 4-40 Equivalent cantilever model for pinned-head RCFST shafts

$$L_e = H_{ig}$$ Equation 4-36

$$\Delta_{LS} = \Delta_y + \Delta_p$$ Equation 4-37

$$\Delta_y = c_1 \phi_y L_e^2$$ Equation 4-38

$$\phi_y = c_{\phi y} \frac{\varepsilon_{y(tube)}}{D}$$ Equation 4-39

$$\Delta_p = \phi_p L_p L_e$$ Equation 4-40

$$\phi_p = \phi_{LS} - \phi_y$$ Equation 4-41

$$\Delta_{LS} = c_1 \phi_y L_e^2 + \left(\phi_{LS} - \phi_y\right) L_p L_e$$ Equation 4-42

Note that the formulation above requires knowledge on the following parameters: the depth to the inground hinge (H_{ig}), the yield displacement parameter (c_1), the yield curvature parameter ($c_{\phi y}$), and the equivalent plastic hinge length (L_p). These parameters were determined from the parametric study and the details are presented at the end of this chapter.

4.3.2. Fixed-Head RCFST Shafts

The proposed model for fixed-head RCFST shafts is depicted in Figure 4-41. In this type of structural configuration, the system can potentially exhibit two plastic hinges, namely, one at the top at the column-cap beam interface and another one inground. However, RCFST shafts have a unique behavior in that the system is controlled mainly by the top plastic hinge. Since the steel tube is cut short before the cap beam, it does not provide flexural strength to the top plastic hinge, thus the flexural stiffness corresponds effectively to that of an RC section confined by a steel tube. Therefore, after onset of the top plastic hinge, there is a redistribution of moments and the inground moment starts to increase far beyond the level of the top hinge, as the inground plastic hinge corresponds effectively to that of an RCFST section. Based upon this behavior, the equivalent cantilever model for fixed-head shafts was devised. The model assumes that only the top plastic hinge is developed. This assumption was made considering that, while onset of the inground hinge is possible, it would only occur at large levels of damage of the top plastic hinge, at which structural stability issues may be of concern. The model assumes an equivalent length (L_e) measured from the top of the RCFST shaft to the inground plastic hinge (H_{ig}), in addition to the strain penetration length (L_{sp}) into the cap beam, as shown in Equation 4-43; the strain penetration length can be determined from Equation 4-44 (Priestley et al., 2007), where f_{ye} and d_{bl} are the expected yield strength and diameter of the longitudinal bars. The displacement at a given limit state (Δ_{LS}) is determined from Equation 4-45, and it is calculated considering the end fixity and soil flexibility parameter (c_1) along with the yield curvature of the top plastic hinge ($\phi_{y(top)}$), as shown in Equation 4-46. The latter can be determined from Equation 4-47 as a function of the yield curvature parameter ($c_{\phi y(top)}$), taken as 2.25 for RC sections (Priestley et al., 2007), and the yield strain of the longitudinal reinforcement ($\varepsilon_{y\,(rebar)}$).

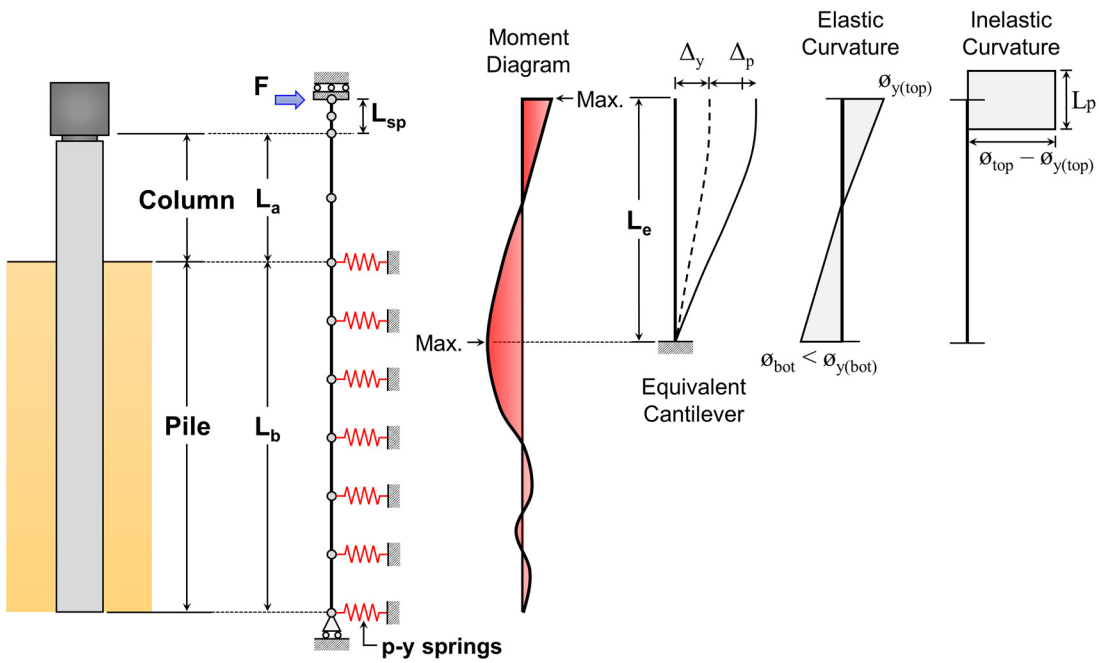

Figure 4-41 Equivalent cantilever model for fixed-head RCFST shafts

The plastic displacement is calculated as shown in Equation 4-48. In this expression, the parameter β has been introduced to adjust the plastic displacement by modifying the effective length (L_e). This adjustment takes into account the moment redistribution. The plastic curvature is determined from the difference between the limit state curvature of the top plastic hinge ($\phi_{LS(top)}$) and the yield curvature. Furthermore, the proposed model adopts the plastic hinge model proposed by Chai et al., (1991). This plastic hinge model was developed for RC columns retrofitted by a steel jacket and it only depends on the strain penetration length (L_{sp}) and the gap (g) between the steel tube and the cap beam, as shown in Equation 4-50. Note that although this model was adopted for the top plastic hinge, the plastic displacement is adjusted by the parameter β, which is of course to be determined from the parametric study. Finally, Equation 4-45 can be written in terms of the above parameters, as shown in Equation 4-60.

$$L_e = H_{ig} + L_{sp} \qquad \text{Equation 4-43}$$

$$L_{sp} = 0.022\, f_{ye}\, d_{bl} \quad , \quad (MPa) \qquad \text{Equation 4-44}$$

$$\Delta_{LS} = \Delta_y + \Delta_p \qquad \text{Equation 4-45}$$

$$\Delta_y = c_1\, \phi_{y(top)}\, L_e^{\,2} \qquad \text{Equation 4-46}$$

$$\phi_{y(top)} = c_{\phi y(top)} \frac{\varepsilon_{y(rebar)}}{D} \qquad \text{Equation 4-47}$$

$$\Delta_p = \phi_{p(top)}\, L_{p(top)}\, \beta\, L_e \qquad \text{Equation 4-48}$$

$$\phi_p = \phi_{LS(top)} - \phi_{y(top)} \qquad \text{Equation 4-49}$$

$$L_{p(top)} = 2\,L_{sp} + g \qquad \text{Equation 4-50}$$

$$\Delta_{LS} = c_1\,\phi_{y(top)}\,L_e^{\,2} + \left(\phi_{LS(top)} - \phi_{y(top)}\right) L_{p(top)}\,\beta\,L_e \qquad \text{Equation 4-51}$$

4.3.3. Performance Limit States

4.3.3.1 Pinned-Head RCFST Shafts

Pinned-head RCFST shafts are controlled by a plastic hinge that develops inground. As such, the flexural stiffness corresponds effectively to that of an RCFST section. Past research has shown that RCFST sections have three limit states: (1) first yield of the tube, (2) onset of tube local buckling, and (3) tube fracture. This behavior has been observed in different experimental studies (e.g., Marson and Bruneau, 2004; González-Román et al., 2008; Brown et al., 2015). Brown et al. (2015) recommended a limit prior to onset of tube local buckling based on the tensile strain of the tube as follows:

$$\varepsilon_{t,\,buckling} = 0.021 - \frac{D}{9100\,t} \geq \varepsilon_{y(tube)} \qquad \text{Equation 4-52}$$

If the limit above is reached or exceeded, the steel tube would experience onset of buckling in a subsequent loading cycle in compression. Furthermore, they suggested that the strain limit at tube fracture can be taken as 0.025. These two limits, namely, tensile strain prior tube local buckling and tube fracture, can be thought of as damage control and ultimate limits, while a serviceability limit state can be determined when the tensile strain in the tube is 0.015 or when the concrete compression strain is 0.004, whichever is smaller. These limits are useful within a displacement-based design approach, where the main goal is to relate strains with system displacements. To do so, it is necessary to relate first strains to curvature and then curvature to displacements.

The relationship between curvature and displacement was established in the equivalent cantilever plastic hinge approach described in the previous section. On the other hand, assuming equilibrium and strain compatibility, the relationship between strain and curvature can be established, as shown in Figure 4-42 and Equation 4-62. Note that the curvature limit state (ϕ_{LS}) is a function of either the extreme tension (ε_t) or compression (ε_c) strains and the neutral axis depth (c), where the distance between extreme tension and compression fibers is calculated at the centerline of the steel tube, as shown in Equation 4-54. Note that Equation 4-62 requires knowledge of the neutral axis depth (c), which can be determined from a moment-curvature analysis. Alternatively, instead of using Equation 4-53, curvature limit states could be determined from a moment-curvature analysis using the appropriate limits described before.

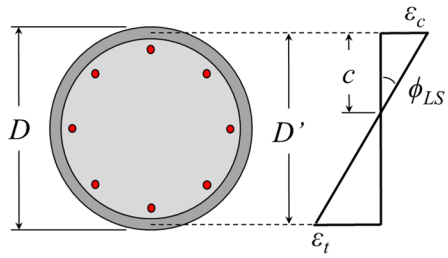

Figure 4-42 Curvature and associated strains for RCFST sections

$$\phi_{LS,c} = \frac{\varepsilon_c}{c} \quad \text{and} \quad \phi_{LS,t} = \frac{\varepsilon_t}{D' - c} \qquad \text{Equation 4-53}$$

$$D' = D - t \qquad \text{Equation 4-54}$$

Although in the literature some authors argue that the hypothesis of equilibrium and strain compatibility is not adequate, it has been shown from experimental and analytical studies that this assumption holds up until to onset of tube buckling and even beyond that level (Brown et al., 2015). As it will be seen later in this report, the experimental data collected in this study further validates the assumption of equilibrium and strain compatibility.

4.3.3.2 Fixed-Head RCFST Shafts

Fixed-head shafts are controlled by the plastic hinge that develops aboveground at the column-cap beam interface. Since the steel tube is cut short before the cap beam, it only provides confinement to the concrete in the column. As such, the flexural behavior of the top plastic hinge is characterized by the effective RC section confined by the steel tube, namely, the steel tube does not contribute to the flexural strength. At a section level, RC shafts confined by a steel tube can be characterized with three limit states: (1) first yield of the longitudinal reinforcement, (2) onset of bar buckling, and (3) bar fracture or concrete compression failure. Strain values that relate to the aforementioned limit states can be taken, for example, as those proposed in the POLA Seismic Code (2010). They provide strain limits for operating, contingency, and design level earthquakes, which can be thought of as serviceability, damage control, and ultimate limits at a structural level. This limits are characterized by bar tensile strains of 0.015, 0.06 or $0.06\varepsilon_{sm}$ (whichever is smaller), and 0.08 or $0.08\varepsilon_{sm}$ (whichever is smaller), respectively; where the parameter ε_{sm} corresponds to the strain at maximum stress of the longitudinal reinforcement. Experimental results on this type of elements (Montejo et al., 2012) suggest that these values are appropriate for RC sections confined by steel tubes with D/t = 48. Regarding the relationship between strains and curvature for RC elements, it is well known that the equilibrium and strain compatibility assumption is appropriate. The strain-curvature relationship is depicted in Figure 4-43 and Equation 4-55.

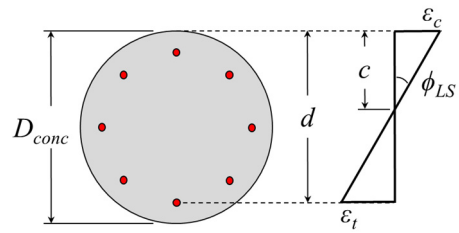

Figure 4-43 Curvature and associated strains for RC sections

$$\phi_{LS,\,c} = \frac{\varepsilon_c}{c} \quad \text{and} \quad \phi_{LS,\,t} = \frac{\varepsilon_t}{d-c} \qquad \text{Equation 4-55}$$

Note that the curvature limit state (ϕ_{LS}) is a function of either the extreme tension (ε_t) or compression (ε_c) strain and the neutral axis depth (c). The distance from the compression extreme fiber to the centroid of the extreme tension bar (d), and the neutral axis depth (c) can be calculated from Equation 4-56 and Equation 4-57 (Priestley et al., 2007), respectively, where D_{conc} is the dimeter of the RC section, C_{bl} is the cover to the longitudinal bars, and d_{bl} is the diameter of the longitudinal bars. It is important to recognize that Equation 4-57 latter would produce an approximate value of the neutral axis depth; thus, some iteration may be required. Alternatively, instead of using Equation 4-55, curvature limit states could be determined from a moment-curvature analysis using the appropriate limits described before.

$$d = D_{conc} - c_{bl} - \frac{d_{bl}}{2} \qquad \text{Equation 4-56}$$

$$\frac{c}{D} = 0.2 + 0.65\frac{P}{f_{ce}'A_g} \qquad \text{Equation 4-57}$$

4.4. Equivalent Viscous Damping of RCFSTs

The equivalent viscous damping (ξ_{eq}) is a parameter that is used within the direct-displacement based seismic design method (Priestley et al., 2007) and it is used to quantify the energy dissipation mechanism in a structural element as it experiences inelastic action. As shown in Equation 4-58, this parameter includes the contribution from the elastic viscous damping (ξ_{el}), often taken as 0.05, and the hysteretic damping (ξ_{hyst}) which corresponds to the energy dissipation of structural elements in the inelastic range.

$$\xi_{eq} = \kappa\,\xi_{el} + \xi_{hyst} \qquad \text{Equation 4-58}$$

Note that the elastic damping is corrected with a parameter κ (Equation 4-59) that depends on the hysteresis rule, represented in the parameter λ, and the assumption on how the elastic viscous damping is calculated. Past research has shown that good results are obtained with tangent stiffness proportional damping (Priestley and Grant, 2005), while λ can be taken as −0.318 based on experimental results suggesting that the "Takeda Thin" hysteresis rule is appropriate for RCFSTs (Brown et al., 2015).

The hysteretic component (Equation 4-60), on the other hand, can be determined using the area-based damping (ξ_{AB}) approach proposed by Jacobsen (1930), as shown in Equation 4-61, in combination with a correction factor (c_f), as shown in Equation 4-62. This factor was determined based on the results of non-linear time history analyses (Priestley et al., 2007), which showed that the area-based approach may largely overestimate the equivalent viscous damping.

$$\kappa = \mu^{\lambda} \qquad \text{Equation 4-59}$$

$$\xi_{hyst} = c_f \, \xi_{AB} \qquad \text{Equation 4-60}$$

$$\xi_{AB} = \frac{2}{\pi}\frac{A_1}{A_2} \qquad \text{Equation 4-61}$$

$$c_f = (0.53\mu + 0.8)\, \xi_{AB}^{-\left(\frac{\mu}{40}+0.40\right)} \qquad \text{Equation 4-62}$$

As previously mentioned, the hysteretic component can be determined from experimental data. This means that in Equation 4-61, A_1 is the area inside of the force displacement response of a structural member at a given ductility level (μ), and A_2 is the area of a rigid, perfectly plastic member with the same peak strength and displacement as the actual structural element. An example of this calculation is presented in Figure 4-44, and it corresponds to the force vs. displacement response from Test 1 at ductility 4 (μ). In this case A_1 is the area enclosed by the blue line, while A_2 is the area enclosed by the rectangle represented with the dashed, red line.

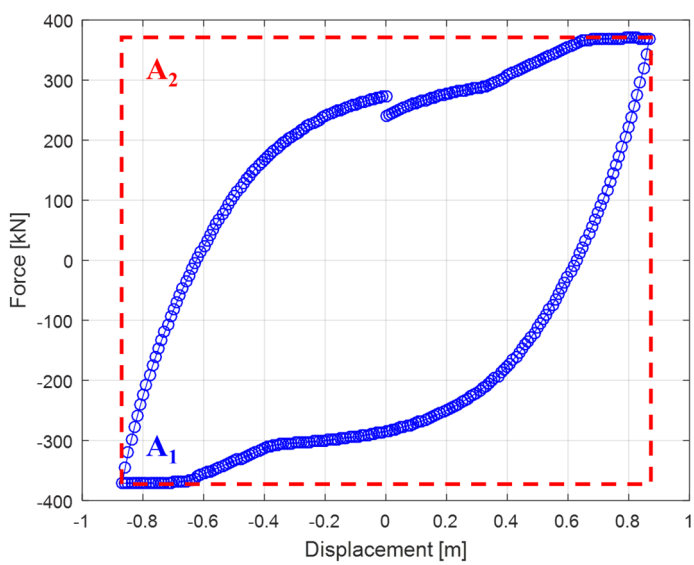

Figure 4-44 Area-based damping calculation example

Using the formulation above, the equivalent viscous damping can be written as:

$$\xi_{eq} = (0.05)\,\mu^{-0.378} + \left(\frac{2}{\pi}\frac{A_1}{A_2}\right)\left[(0.53\,\mu + 0.8)\left(\frac{2}{\pi}\frac{A_1}{A_2}\right)^{-\left(\frac{\mu}{40}+0.40\right)}\right] \qquad \text{Equation 4-63}$$

This expression can be used to determine the equivalent viscous damping of any structural element, if the force vs. displacement response is available. In fact, with regards to RCFST elements, Brown et al., (2015) utilized Equation 4-63 in combination with experimental data to developed an expression that allows for calculating the equivalent viscous damping as a function only on the D/t ratio and the ductility, as shown in Equation 4-64.

$$\xi_{eq} = 0.07 + \left(0.85 - \frac{D}{1000t}\right)\left(\frac{\mu - 1}{10.5 + \mu\pi}\right) \qquad \text{Equation 4-64}$$

It is important to note that the expression above was developed based upon experimental data on twelve large-scale RCFST specimens tested in the air. This means that for RCFST shafts the expression above is lacking the damping contribution from the soil. As such, as it will be apparent later, Equation 4-63 was used for analysis of the experimental and analytical data of this study.

4.5. Parametric Studies

4.5.1. Description

The goal of the parametric studies is to provide parameters that supplement the equivalent cantilever plastic hinge model for RCFSTs described in previous sections. For that purpose, numerical simulations were conducted using the analytical model described before. This section describes the parameters considered in the analyses as well as the procedure utilized to determine the target parameters.

4.5.2. Parameter Definition

In terms of the structural configuration, the following variables were considered: (1) the head fixity condition, (2) the shaft diameter (D), (3) the axial load ratio (ALR), (4) the diameter-to-thickness (D/t) ratio, and (5) the aboveground length-to-diameter (L_a/D) ratio. Regarding the fixity condition, both pinned and fixed-head condition were included, considering two diameters, that is 610 mm. (2 ft.) and 1220 mm. (4 ft.), and axial load ratios of 5%, 10%, and 15%. These values were selected as they are typical expected values in bridge design practice. Moreover, for consistency with the experimental data, D/t ratios of 48, 64, and 95 were considered. Regarding the L_a/D ratio, values of 4, 8, and 12 were considered upon review of the bridge inventory of the Alaska Department of Transportation and Public Facilities; typical values of existing bridges constructed with RCFSTs ranged from L_a/D = 4 through L_a/D = 12. These parameters are summarized in Table 4-4.

Table 4-4 Structural parameters considered in the parametric study

Head Fixity	Diameter (mm)	ALR (%)	D/t Ratio	La/D Ratio
Pinned	610	5	48	4
Fixed	1,220	10	64	8
		15	95	12

Regarding the materials properties, expected values were assumed. As such, the concrete compressive strength was taken as f_{ce}' = 36.4 MPa (5.2 ksi). Moreover, considering steel

tubes manufactured in accordance to API 5L x 52, the expected yield and tensile strengths were taken as f_{ye} = 396 MPa (57.2 ksi) and f_{ue} = 500.5 MPa (72.6 ksi), respectively. As for the internal reinforcement (longitudinal and transverse), A706 Gr. 60 steel was considered with expected yield and tensile strengths f_{ye} = 462 MPa (66 ksi) and f_{ue} = 605 MPa (88 ksi), respectively. The longitudinal and transverse steel ratios were kept constant for all simulations, with values of 2% and 1%, respectively. These values constitute typical values utilized in current design practice.

On the other hand, regarding the soil parameters, the simulations were conducted using a uniform soil layer of either sand or clay, considering three levels of soil stiffness, namely, flexible, medium, and stiff, with corresponding effective unit weights (γ) of 15.7 kN/m^3 (100 pcf), 17.3 kN/m^3 (110 pcf), and 18.9 kN/m^3 (120 pcf), respectively. For sand, assuming properties above the water table, friction angles (ϕ) of 30°, 35°, and 40° with corresponding coefficients of subgrade reaction (n_h) of 9500 kN/m^3 (35 pci), 27200 kN/m^3 (100 pci), and 61100 kN/m^3 (225 pci) were selected. The selected friction angles represent average values of loose, medium, and dense sand. The coefficients of subgrade reaction relate to each type of sand, respectively, and they were selected based on the values recommended by the AASHTO Guide Specification for LRFD Seismic Bridge Design (AASHTO, 2011). For clay, on the other hand, undrained shear strengths (C_u) of 12 kPa (250 psf), 36 kPa (750 psf), and 72 kPa (1500 psf) were considered with corresponding strains at 50% of the ultimate strength (ε_{50}) of 0.02, 0.01, and 0.005, respectively. These parameters were selected based on typical values used in commercial software for soft clay, medium clay, and stiff clay. The soil parameters used in the parametric study are summarized in Table 4-5.

Table 4-5 Soil parameters considered in the parametric study

			Soil Strength and Stiffness			
			Sand		Clay	
Soil Type	Soil Profile	γ (kN/m^3)	Ø (°)	n_h (kN/m^3)	C_u (kPa)	ε_{50}
Sand	Flexible	15.7	30	9500	12	0.020
Clay	Medium	17.3	35	27200	36	0.010
	Stiff	18.9	40	61100	72	0.005

4.5.3. Procedure

The first step consisted of conducting the numerical simulations. Based on the parameters studied, 648 simulations resulted from their combination. As previously mentioned, the analytical model was developed using the OpenSees framework software (McKenna et al., 2000). The simulations were conducted up until ductility 4 (μ_4), as early modeling efforts indicated that a damage control limit state would be reached at that level of displacement. The loading protocol consisted of the same protocol utilized for the experimental program, that is, it had elastic and inelastic portions using single-cycle and three-cycles, respectively, in displacement controlled increments. The sequence of operations conducted for each simulation consisted of: (1) p-y curve analyses to determine the properties of soil springs; (2) a moment-curvature analysis to determine the first yield curvature; (3) a monotonic pushover analysis to determine displacement at different performance levels of the loading

protocol; and (4) a cyclic pushover analysis. Furthermore, in addition to the analytical model, moment-curvature analyses were conducted to determine some of the required parameters. The remaining of this section describes each of the parameters studied.

4.5.3.1 Section Analysis

Moment-curvature analyses were conducted to determine the yield curvature parameter ($c_{\phi y}$) and the corresponding neutral axis depth (c). The former can be determined by normalizing the equivalent yield curvature, as shown in Equation 4-65, while the latter was obtained from interpolation of the moment-curvature results.

The analyses were conducted for: diameters (D) of 610 mm. (2 ft.), 1220 mm. (4 ft.), and 1830 mm. (6 ft.); diameter-to-thickness (D/t) ratios of 48, 64, and 95; and axial load ratios (ALR) of 0%, 5%, 10%, and 15%. These parameters are summarized in Table 4-6. All the moment-curvature analyses were conducted using longitudinal steel ratio (ρ) of 2%.

$$c_{\phi y} = \frac{\phi_y D}{\varepsilon_{y(tube)}} \qquad \text{Equation 4-65}$$

Table 4-6 Parameters considered in the section analyses

Diameter (mm)	D/t	ALR (%)
610	48	0
1219	64	5
1829	95	10
		15

4.5.3.2 Pinned-Head RCFST Shafts

Based on the formulation of the proposed equivalent cantilever plastic hinge model for RCFSTs, the parameters required for pinned-head shafts include the depth to plastic hinge (H_{ig}), the yield displacement parameter (c_1), and the equivalent length (L_p). The parameter H_{ig} was determined from each simulation by averaging the depth to maximum moment at each ductility level. For pinned-head shafts, the depth to plastic hinge corresponds to the effective length (L_e), as shown in Equation 4-66. Regarding c_1, it was back-calculated from the yield displacement (Equation 4-67), while the plastic hinge length (L_p) was determined from the plastic displacement at each ductility level, as shown in Equation 4-68. Note that all the parameters to the right in Equation 4-66 through Equation 4-68 were determined either from the simulations results or the moment-curvature analysis. Details regarding the definition of each of those parameters can be found in the description of the proposed model in section 4.3.

$$L_e = H_{ig} \qquad \text{Equation 4-66}$$

$$c_1 = \frac{\Delta_y}{\phi_y L_e^2} \qquad \text{Equation 4-67}$$

$$L_p = \frac{\Delta_{LS} - \Delta_y}{\left(\phi_{LS} - \phi_y\right) L_e} \qquad \text{Equation 4-68}$$

4.5.3.3 Fixed-Head RCFST Shafts

The procedure to determine the parameters for fixed-head shafts was similar to that for pinned-head shafts with a couple of minor differences. The yield displacement parameter (c_1) was calculated in the same manner, but recognizing that the yield curvature corresponds to the top plastic hinge, as shown in Equation 4-69. The effective length (L_e), on the other hand, includes the effects of strain penetration (L_{sp}), as presented in Equation 4-70. The other difference in fixed-head shafts is that the length of the top plastic hinge was fixed. This resulted on the need to determine the parameter β (Equation 4-71), which is a correction factor that modifies the effective length to adjust the plastic displacement and match results from the simulations. Note that all the parameters to the right in Equation 4-69 through Equation 4-71 were determined either from simulations results or moment-curvature analyses. Details regarding the definition of each of those parameters can be found in the description of the proposed model in section 4.3.

$$c_1 = \frac{\Delta_y}{\phi_{y(top)} L_e^{\,2}} \qquad \text{Equation 4-69}$$

$$L_e = H_{ig} + L_{sp} \qquad \text{Equation 4-70}$$

$$\beta = \frac{\Delta_{LS} - \Delta_y}{\left(\phi_{LS(top)} - \phi_{y(top)}\right) L_{p(top)}\, L_e} \qquad \text{Equation 4-71}$$

4.5.3.4 Equivalent Viscous Damping

Using the force vs. displacement response of each simulation, the equivalent viscous damping was calculated at each ductility level (μ) using the method described in the previous section. For completion, the equation is repeated here as Equation 4-72. Note that the equation below can be applied to both pinned and fixed-head specimens. The parameters A_1 and A_2 were calculated from the force vs. displacement loops at each cycle of the three conducted at each ductility (μ). Then, results were averaged to obtain a single value for each ductility (μ) level.

$$\xi_{eq} = (0.05)\,\mu^{-0.378} + \left(\frac{2}{\pi}\frac{A_1}{A_2}\right)\left[(0.53\,\mu + 0.8)\left(\frac{2}{\pi}\frac{A_1}{A_2}\right)^{-\left(\frac{\mu}{40}+0.40\right)}\right] \qquad \text{Equation 4-72}$$

CHAPTER 5

5. EXPERIMENTAL RESULTS

5.1. Experimental Observations

This section presents a summary regarding the experimental observations made during and after testing of twelve RCFST pile-column specimens. Measured material properties, specimen details, and measured response are provided along with a short discussion of the results and observations. Brief conclusions regarding specimen capacity and failure modes are also provided.

For completion, the experimental test matrix is presented again in Table 5-1. The experimental program was divided into three phases; each consisted of experimental testing of four RCFST pile-column specimens. It is worth noting that the symbol "*" in Table 5-1 (next to the values corresponding to a D/t ratio of 95) represents a particular feature observed on tests 3 and 4. As a consequence, those tests were repeated and they correspond to tests 5 and 6. Therefore, while tests 5 and 6 look similar to tests 3 and 4, respectively, there is a difference related to the failure mechanism of the specimens, which will be discussed in subsequent sections. In addition, due to issues related to instrumentation and also to effective alteration of the soil stiffness, test 9 corresponds to a repetition of test 2.

Table 5-1 Experimental test matrix

Phase	Test No.	Nominal Diameter (in)	Nominal Thickness (in)	Nominal D/t	Soil Sucharge (psf)	Aboveground Height (ft)
1	1	12.00	0.250	48	None	5.50
	2	12.00	0.250	48	960	5.83
	3	12.75	0.135	95*	None	5.50
	4	12.75	0.135	95*	960	5.50
2	5	12.75	0.135	95	None	5.69
	6	12.75	0.135	95	960	5.88
	7	12.75	0.188	68	None	5.77
	8	12.75	0.188	68	960	5.77
3	9	12.00	0.250	48	960	5.77
	10	12.00	0.250	48	None	7.77
	11	12.75	0.135	95	None	7.69
	12	12.75	0.188	68	None	7.69

5.1.1. Material Properties

5.1.1.1 Steel Tube

Steel tube tension tests were performed on coupons that were machined from a ring of material cut off the end of one steel tube of each tube wall thickness utilized. All tension tests were conducted in accordance with ASTM A370-14 (2014) using a MTS high-force test system in combination with the Optotrak system, which was used to determine strains using a 2-inch gauge length. Rates of 0.25 in/min and 1.0 in/min were used up to and after the yield point, respectively. Figure 5-1 shows an example of the tension tests performed on steel tube samples. Three coupons were tested in the longitudinal direction of the tube, another one was tested in the transverse direction, and another one was tested with the spiral weld positioned in the middle of the gauge length, as shown in Figure 5-2; stress-strain curves of the test conducted on steel coupons are presented in Figure 5-3 through Figure 5-5. Tension test results are summarized in Table 5-2 through Table 5-4. In these tables, values of yield strength were calculated using two approaches, namely, the offset method (0.2% offset) and the extension under load method (0.5% EUL).

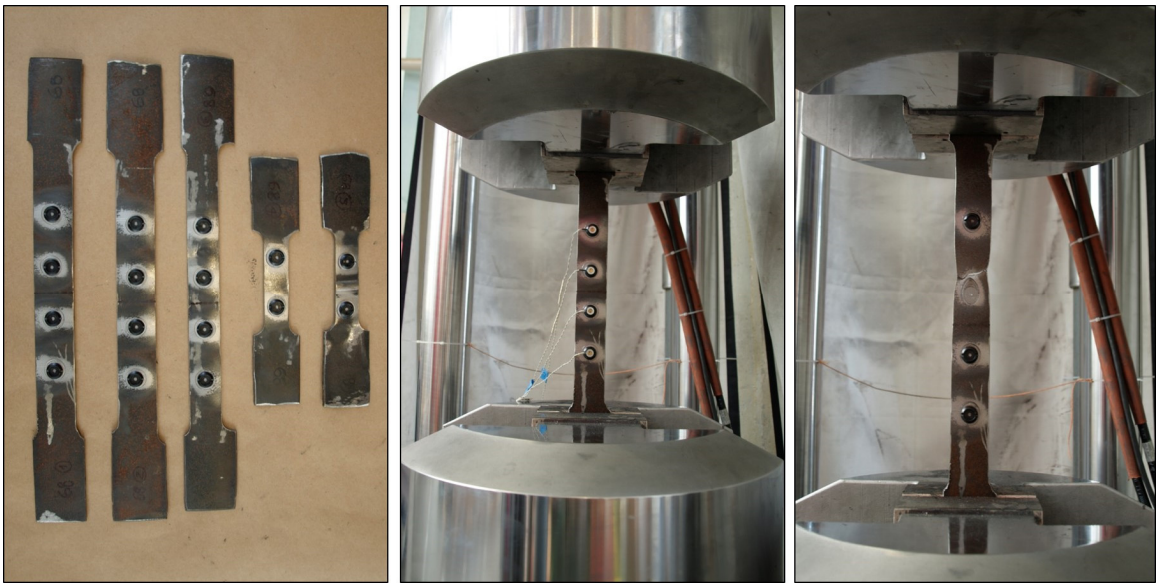

Figure 5-1 Example of tests performed on steel tube coupons

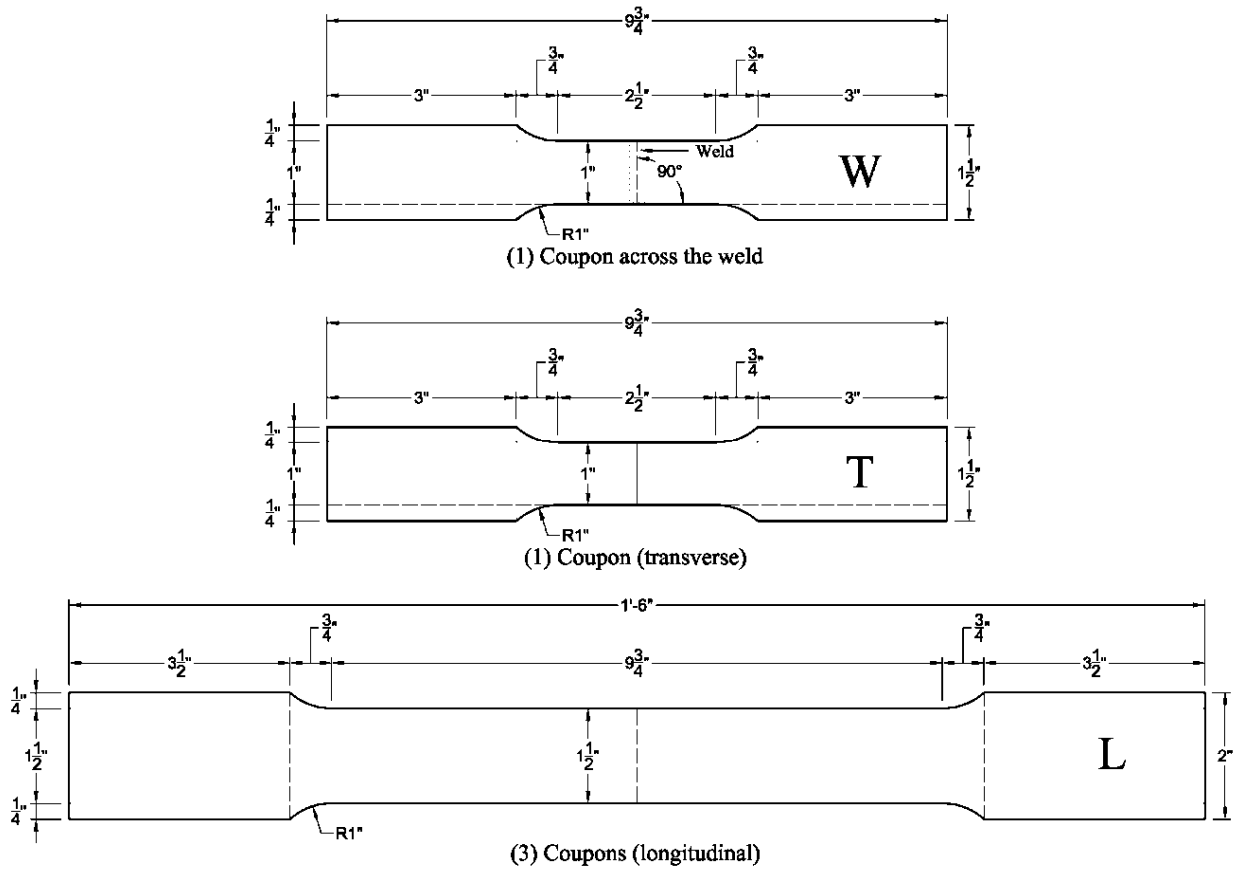

Figure 5-2 Steel tube material samples: longitudinal (L), transverse (T), and with weld (W)

In Figure 5-5 through Figure 5-7, the symbol "*" for the steel tubes with D/t = 95* represents a special feature observed during testing of specimens 3 and 4. Upon further examination of the inside of the spiral welded tubes, it was determined that the thin wall tubes (D/t = 95*) which make up tests 3 and 4 were not welded along the inside surface, but rather only upon the outside surface, as shown in Figure 5-6. For comparison purposes, this figure also shows the steel coupon across the spiral weld of tubes with D/t = 48. Furthermore, the tension test performed on the coupon across the spiral weld with D/t = 95* indicated fracture of the weld at a low strain level, barely developing the yield strength of the material, as shown in Figure 5-7.

The steel tube manufacturer confirmed that the thin wall tubes sent to NC State University, which were used for tests 3 and 4, were only welded on the outside surface; they sent three replacement tubes that are welded on both inside and outside surfaces (Figure 5-8). Tension tests were performed on coupons cut off such replacement tubes (D/t = 95) and the results are presented in Figure 5-9; tension test results are summarized in Table 5-5. The new set of tubes with D/t = 95 were used to repeat tests 3 and 4, which correspond to tests 5 and 6 (Table 5-1).

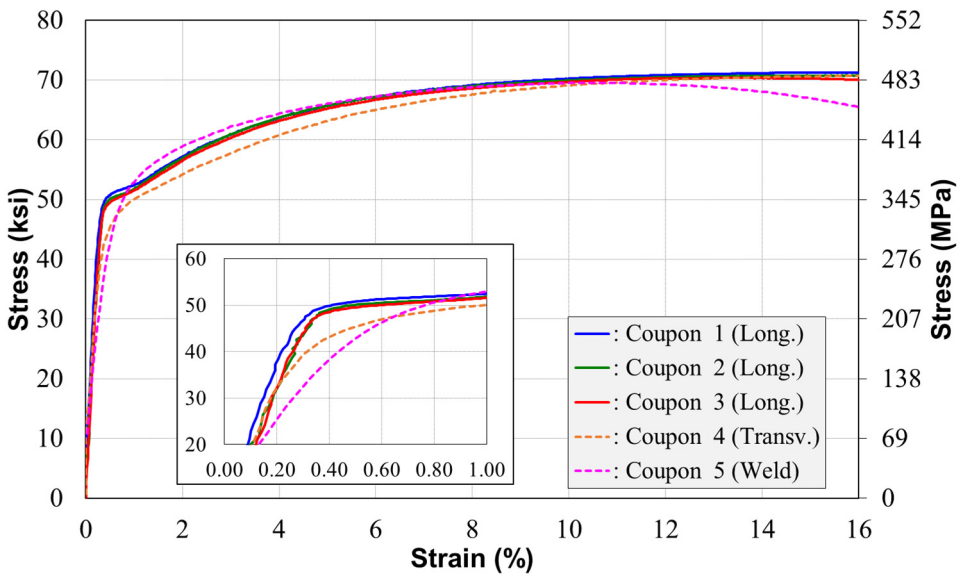

Figure 5-3 Stress-strain curve of samples from tubes with D/t = 48

Table 5-2 Tension test results of steel tubes with D/t = 48

Coupon	Type	Yield Strength (ksi)		Yield Strain	Tensile Strength	Max. Strain
		0.2% offset	0.5% EUL	(in/in)	(ksi)	(in/in)
1	Longitudinal	50.04	50.76	0.00173	71.27	0.152
2	Longitudinal	49.45	50.06	0.00171	71.77	0.172
3	Longitudinal	49.08	49.53	0.00169	70.75	0.134
4	Transverse	43.56	45.37	0.00150	70.76	0.173
5	Across weld	35.86 *	42.76 *	0.00115 *	69.51 *	0.107 *
	Avg. (Longitudinal)	49.52	50.12	0.00171	71.26	0.1527

* Determined from displacement of MTS and the gauge length of the coupon

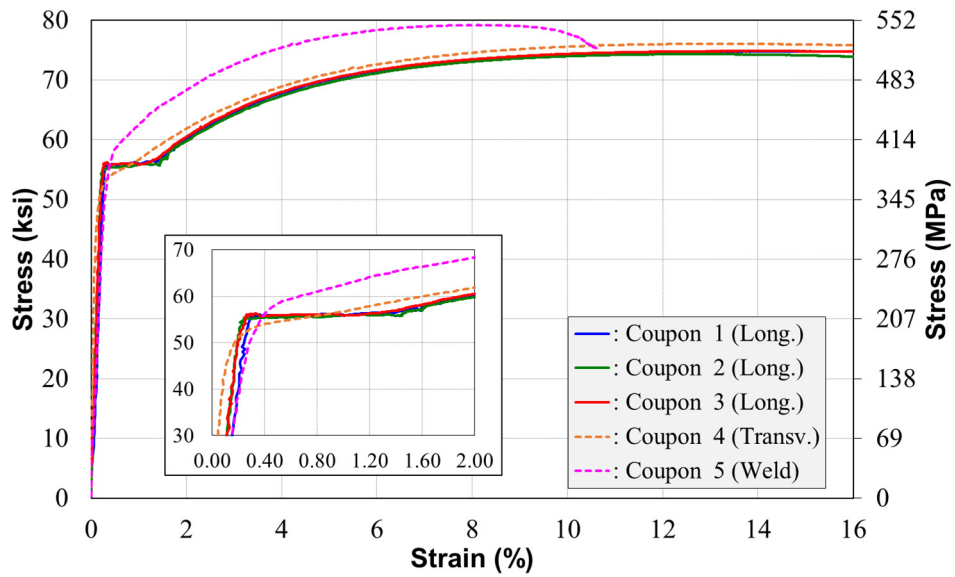

Figure 5-4 Stress-strain curve of samples from tubes with D/t = 68

Table 5-3 Tension test results of steel tubes with D/t = 68

Coupon	Type	Yield Strength (ksi)		Yield Strain	Tensile Strength	Max. Strain
		0.2% offset	0.5% EUL	(in/in)	(ksi)	(in/in)
1	Longitudinal	55.74	55.86	0.00192	74.83	0.147
2	Longitudinal	55.39	55.38	0.00191	74.35	0.126
3	Longitudinal	55.73	55.88	0.00192	74.86	0.138
4	Transverse	53.88	54.48	0.00186	76.09	0.131
5	Across weld	58.37	58.42	0.00201	79.22	0.08
	Avg. (Longitudinal)	55.62	55.71	0.00192	74.68	0.137

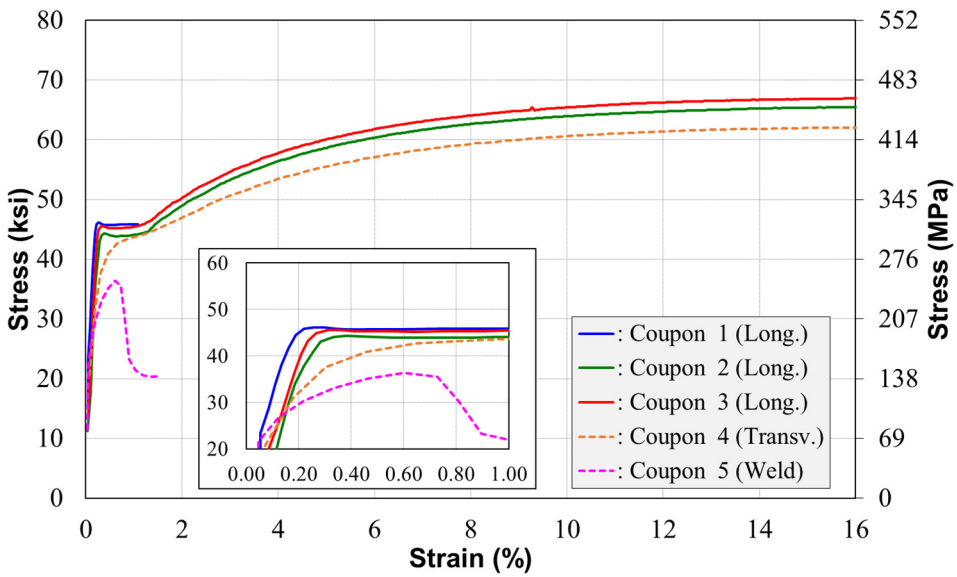

Figure 5-5 Stress-strain curve of samples from tubes with D/t = 95*

Table 5-4 Tension test results of steel tubes with D/t = 95*

Coupon	Type	Yield Strength (ksi)		Yield Strain	Tensile Strength	Max. Strain
		0.2% offset	0.5% EUL	(in/in)	(ksi)	(in/in)
1	Longitudinal	45.91	45.73	0.00158	67.18 *	0.170 *
2	Longitudinal	44.82	44.02	0.00155	65.59	0.190
3	Longitudinal	45.42	45.25	0.00157	66.99	0.181
4	Transverse	38.21	41.33	0.00132	62.11	0.173
5	Across weld	32.61	35.48	0.00112	36.38	0.006
	Avg. (Longitudinal)	45.38	45.00	0.00156	66.59	0.180

* Determined from displacement of MTS and the gauge length of the coupon

Figure 5-6 Spiral weld on coupons with D/t = 48 and 95*: (a) outside and (b) inside surfaces

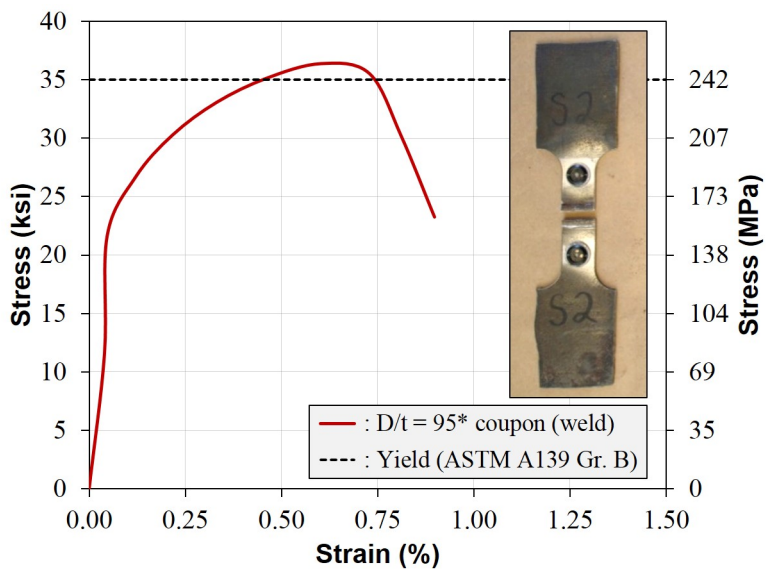

Figure 5-7 Tension test results on sample with D/t = 95* across spiral weld

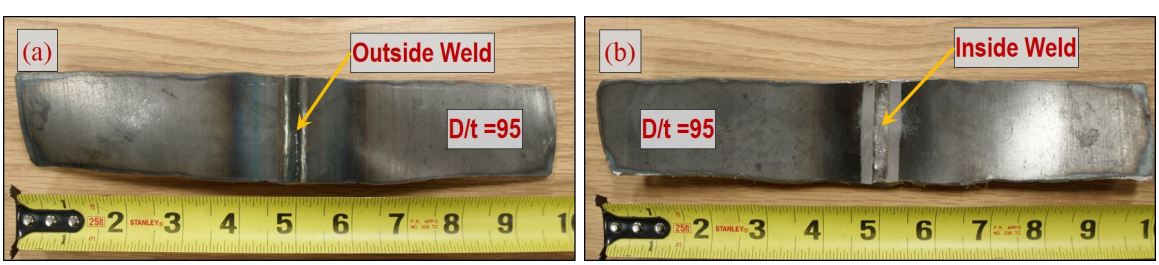

Figure 5-8 Spiral weld on coupons with D/t = 95: (a) outside and (b) inside surfaces

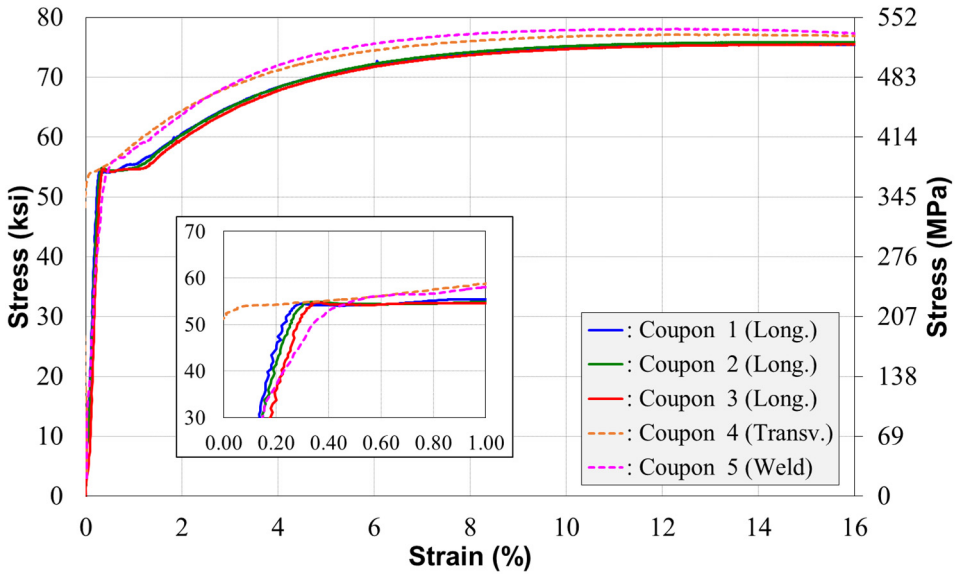

Figure 5-9 Stress-strain curve of samples from tubes with D/t = 95

Table 5-5 Tension test results of steel tubes with D/t = 95

Coupon	Type	Yield Strength (ksi)		Yield Strain	Tensile Strength	Max. Strain
		0.2% offset	0.5% EUL	(in/in)	(ksi)	(in/in)
1	Longitudinal	54.07	54.14	0.00186	75.51	0.142
2	Longitudinal	54.37	54.37	0.00187	75.87	0.146
3	Longitudinal	54.52	54.23	0.00188	75.52	0.156
4	Transverse	55.12	55.6	0.00190	77.15	0.129
5	Across weld	54.01	55.16	0.00186	78.07	0.123
	Avg. (Longitudinal)	54.32	54.25	0.00187	75.63	0.148

5.1.1.2 Internal Reinforcement

Bar tension tests were conducted on bar samples that were taken from the same longitudinal and transverse reinforcement bars used to construct the RCFST pile-column specimens. All bar tension tests were conducted in accordance with ASTM A370-14 (2014) using a MTS high-force system in combination with an extensometer device. Rates of 0.25 in/min and 1.0 in/min were utilized up to and after the yield point, respectively. Figure 5-10 shows an example of the tests conducted on the internal reinforcement; stress-strain curves of the conducted tension tests are presented in Figure 5-11 through Figure 5-16. Tension test results are summarized in Table 5-6 through Table 5-11. In these tables, the elastic modulus was calculated by measuring the average slope of the curves within 10% and 90% of the yield strength; values of yield strength were calculated using two approaches, namely, the offset method (0.2% offset) and the extension under load method (0.5% EUL); onset of strain hardening (SH) and its corresponding slope, E_{sh}, where calculated by intersecting the stress-strain curves with a straight line that connects two points within the curve, namely, 1.02% and 1.05% of the yield strength.

Note from the results corresponding to the #3 spirals (i.e., Figure 5-12, Figure 5-14, and Figure 5-16) that the stress-strain curves do not have a well-defined yield plateau. This was expected as #3 bars were coiled to form the spirals (transverse reinforcement). Moreover, samples were cut off from spirals, utilized for construction of the pile-column specimens, and then they were straightened to conduct the tension tests. In addition, note from Table 5-9 that the calculated moduli for samples 4 and 6 (italic, red values) indicate that there was an issue with the experimental setup or the instrumentation device as the modulus values are not possible.

Figure 5-10 Example of tension test performed on longitudinal and transverse reinforcement

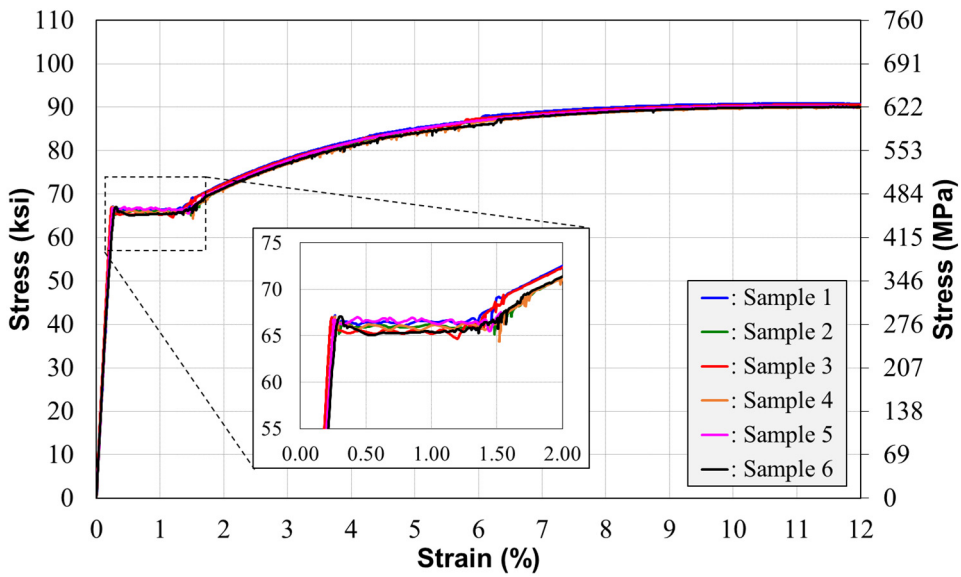

Figure 5-11 Stress-strain curve of #5 bars used in pile-columns specimens 1 through 4

Table 5-6 Tension test results of #5 bars used in pile-columns specimens 1 through 4

Sample	Modulus	Yield Strength (ksi)		Yield Strain	Onset of SH	Esh	Tensile Strength	Max. Strain
	(ksi)	0.2% offset	0.5% EUL	(in/in)	(in/in)	(ksi)	(ksi)	(in/in)
1	27,086	66.15	66.44	0.00244	0.0133	1,068	90.86	0.1096
2	27,663	65.90	65.92	0.00238	0.0145	962	90.09	0.1155
3	30,373	65.45	65.41	0.00215	0.0118	1,093	90.60	0.1172
4	27,530	68.68	66.11	0.00249	0.0127	666	89.99	0.1179
5	27,450	66.95	66.64	0.00244	0.0143	1,073	90.31	0.1097
6	26,912	65.60	65.16	0.00244	0.0136	1,073	90.08	0.1164
Avg.	27,836	66.46	65.95	0.0024	0.013	989	90.32	0.114

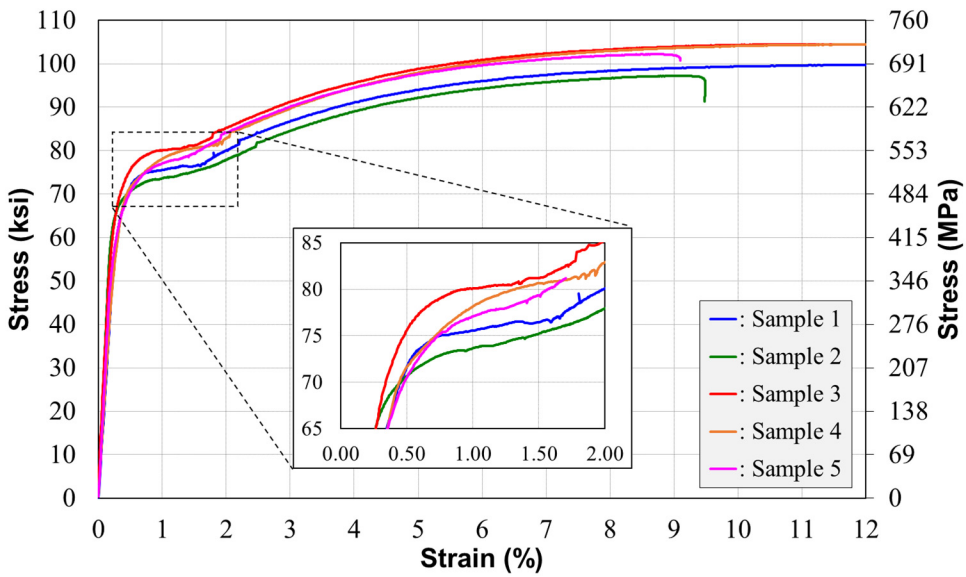

Figure 5-12 Stress-strain curve of #3 spirals used in pile-columns specimens 1 through 4

Table 5-7 Tension test results of #3 spirals used in pile-columns specimens 1 through 4

Sample	Modulus	Yield Strength (ksi)		Yield Strain	Tensile Strength	Max. Strain
	(ksi)	0.2% offset	0.5% EUL	(in/in)	(ksi)	(in/in)
1	20,766	72.18	71.62	0.00348	99.75	0.118
2	27,499	70.24	70.65	0.00255	97.21	0.090
3	26,468	75.03	75.57	0.00283	104.48	0.114
4	20,473	72.42	71.62	0.00354	104.46	0.121
5	23,303	70.55	70.48	0.00303	102.21	0.088
Avg.	23,702	72.08	71.99	0.0031	101.62	0.116

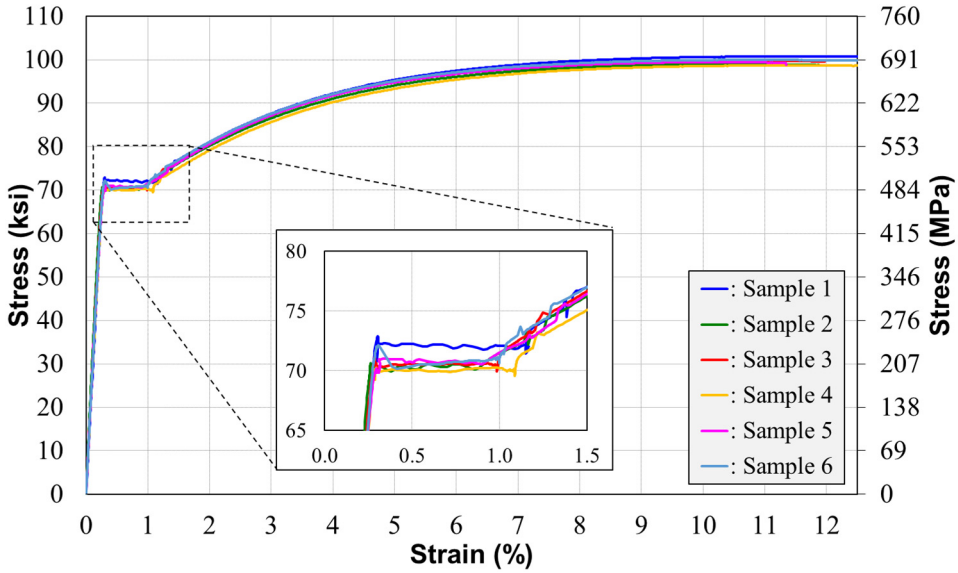

Figure 5-13 Stress-strain curve of #5 bars used in pile-columns specimens 5 through 8

Table 5-8 Tension test results of #5 bars used in pile-columns specimens 5 through 8

Sample	Modulus	Yield Strength (ksi)		Yield Strain	Onset of SH	Esh	Tensile Strength	Max. Strain
	(ksi)	0.2% offset	0.5% EUL	(in/in)	(in/in)	(ksi)	(ksi)	(in/in)
1	26,438	72.23	72.25	0.00249	0.0110	1,213	100.75	0.112
2	30,090	70.44	70.16	0.00243	0.0106	983	98.94	0.107
3	27,870	70.50	70.56	0.00243	0.0094	1,227	99.80	0.106
4	27,231	70.02	70.05	0.00241	0.0102	1,146	98.68	0.111
5	27,805	70.82	70.71	0.00244	0.0112	964	99.47	0.101
6	27,701	70.28	70.4	0.00242	0.0088	916	99.99	0.109
Avg.	27,856	70.72	70.69	0.0024	0.010	1,075	99.61	0.108

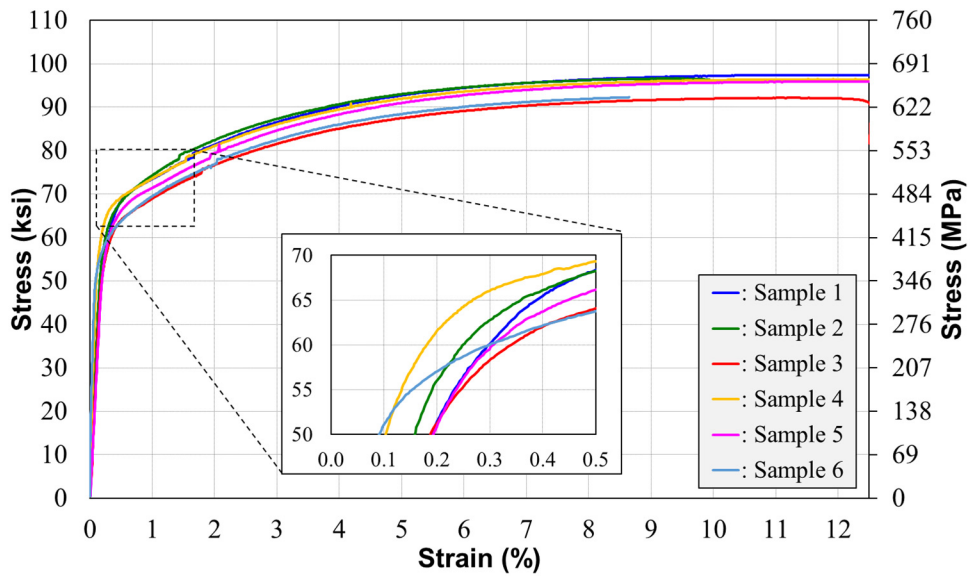

Figure 5-14 Stress-strain curve of #3 spirals used in pile-columns specimens 5 through 8

Table 5-9 Tension test results of #3 spirals used in pile-columns specimens 5 through 8

Coupon	Modulus	Yield Strength (ksi)		Yield Strain	Tensile Strength	Max. Strain
	(ksi)	0.2% offset	0.5% EUL	(in/in)	(ksi)	(in/in)
1	28,582	66.70	68.37	0.00230	97.43	0.1138
2	33,064	66.15	68.28	0.00228	96.61	0.0926
3	28,800	62.51	64.09	0.00216	92.17	0.1111
4	*46,346*	66.98	69.31	0.00231	96.41	0.1167
5	27,268	64.86	66.22	0.00224	95.92	0.1246
6	*57,046*	60.29	63.8	0.00208	92.94	0.1158
Avg.	36,851	64.58	66.68	0.0022	95.25	0.112

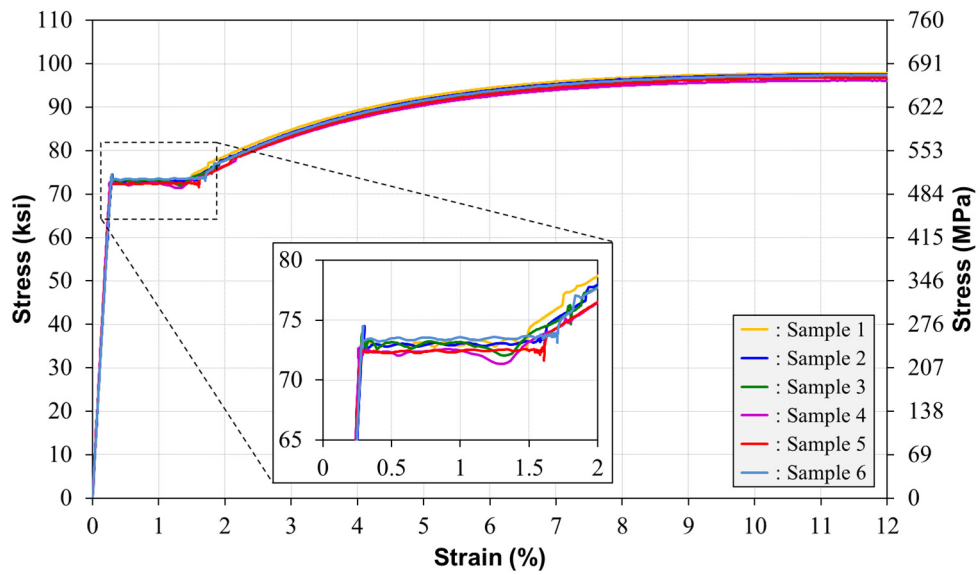

Figure 5-15 Stress-strain curve of #5 bars used in pile-columns specimens 9 through 12

Table 5-10 Tension test results of #5 bars used in pile-columns specimens 9 through 12

Sample	Modulus	Yield Strength (ksi)		Yield Strain	Onset of SH	Esh	Tensile Strength	Max. Strain
	(ksi)	0.2% offset	0.5% EUL	(in/in)	(in/in)	(ksi)	(ksi)	(in/in)
1	27,182	73.13	73.14	0.00252	0.0140	953	97.82	0.113
2	27,399	72.79	72.87	0.00251	0.0150	988	97.55	0.117
3	28,910	73.07	73.18	0.00252	0.0180	765	97.01	0.114
4	29,075	72.37	72.29	0.00250	0.0130	956	96.12	0.114
5	27,434	72.26	72.30	0.00249	0.0150	994	96.85	0.123
6	26,603	73.40	73.49	0.00253	0.0160	885	97.36	0.117
Avg.	27,767	72.84	72.88	0.0025	0.015	924	97.12	0.116

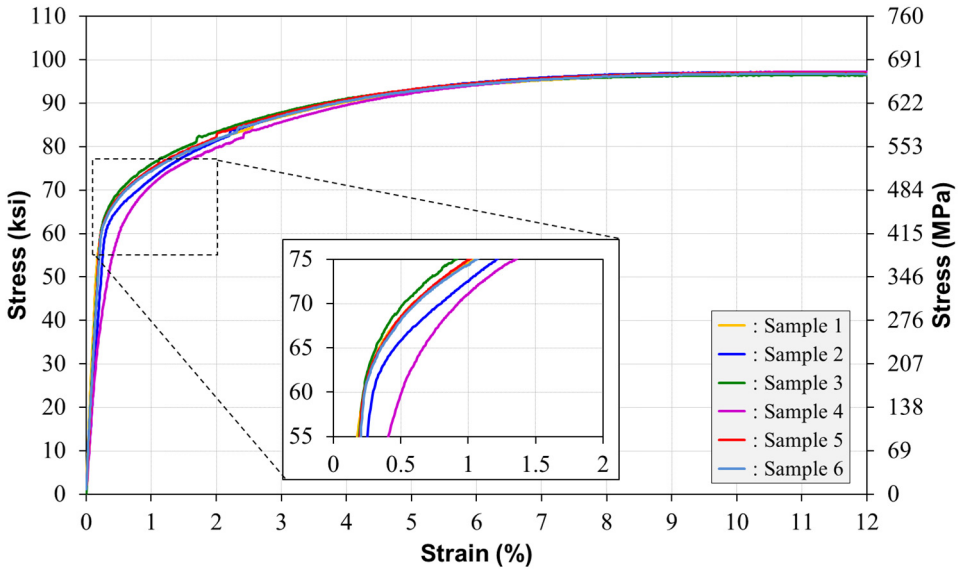

Figure 5-16 Stress-strain curve of #3 spirals used in pile-columns specimens 9 through 12

Table 5-11 Tension test results of #3 spirals used in pile-columns specimens 9 through 12

Sample	Modulus	Yield Strength (ksi)		Yield Strain	Tensile Strength	Max. Strain
	(ksi)	0.2% offset	0.5% EUL	(in/in)	(ksi)	(in/in)
1	35,312	66.24	68.52	0.00228	96.70	0.110
2	22,958	65.56	65.80	0.00226	97.16	0.104
3	29,093	68.40	69.61	0.00236	96.48	0.115
4	23,856	56.66	59.69	0.00195	97.27	0.118
5	31,732	66.55	68.48	0.00229	97.00	0.109
6	31,421	66.23	68.14	0.00228	96.82	0.107
Avg.	29,062	64.94	66.71	0.0022	96.91	0.111

5.1.1.3 Concrete

Compressive tests were conducted on 4”x8” concrete cylinders in accordance with ASTM C39 using confined neoprene caps. Three cylinders were tested at 28 days to verify the target concrete compressive strength (f_c’). Three additional cylinders were tested within 24 hours of each pile-column test. Figure 5-17 shows an example of the conducted compression tests. Concrete compressive test results are tabulated in Table 5-12 through Table 5-14 for phases 1 through 3 of the experimental program (Table 5-1), respectively.

Figure 5-17 Example of tests performed on 4”x8” concrete cylinders

Table 5-12 Concrete compressive test results: pile-columns specimens 1 through 4 (phase 1)

Pile-Column Specimen	Cylinder	Test Date	Peak Load (lbs)	Peak Stress (ksi)	Average (ksi)	Standard Deviation (ksi)	Coef. of Variation (%)
1, 2, 3, 4	1	12/3/2014	70,346	5.60	5.39	0.24	4.43
	2	12/3/2014	68,254	5.43			
	3	12/3/2014	64,437	5.13			
1	1	2/6/2015	81,288	6.47	6.54	0.09	1.41
	2	2/6/2015	83,522	6.65			
	3	2/6/2015	81,882	6.52			
2	1	5/1/2015	87,226	6.94	6.92	0.12	1.68
	2	5/1/2015	88,272	7.02			
	3	5/1/2015	85,388	6.79			
3	1	5/26/2015	84,794	6.75	6.88	0.16	2.39
	2	5/26/2015	85,727	6.82			
	3	5/26/2015	88,753	7.06			
4	1	6/12/2015	87,637	6.97	7.14	0.15	2.14
	2	6/12/2015	89,940	7.16			
	3	6/12/2015	91,439	7.28			

Table 5-13 Concrete compressive test results: pile-columns specimens 5 through 8 (phase 2)

Pile-Column Specimen	Cylinder	Test Date	Peak Load (lbs)	Peak Stress (ksi)	Average (ksi)	Standard Deviation (ksi)	Coef. of Variation (%)
5 (28 days)	1	8/21/2015	50,215	4.00	4.06	0.16	4.01
	2	8/21/2015	53,297	4.24			
	3	8/21/2015	49,423	3.93			
6, 7, 8 (28 days)	1	8/21/2015	66,246	5.27	5.24	0.10	1.94
	2	8/21/2015	64,493	5.13			
	3	8/21/2015	66,981	5.33			
5	1	9/23/2015	58,923	4.69	4.81	0.32	6.64
	2	9/23/2015	57,425	4.57			
	3	9/23/2015	65,000	5.17			
6	1	10/19/2015	86,151	6.86	6.58	0.37	5.59
	2	10/19/2015	77,443	6.16			
	3	10/19/2015	84,483	6.72			
7	1	11/10/2015	79,959	6.36	6.66	0.26	3.86
	2	11/10/2015	85,755	6.82			
	3	11/10/2015	85,331	6.79			
8	1	12/9/2015	91,156	7.25	6.89	0.32	4.58
	2	12/9/2015	83,861	6.67			
	3	12/9/2015	84,794	6.75			

Table 5-14 Concrete compressive test results: pile-columns specimens 9 through 12 (phase 3)

Pile-Column Specimen	Cylinder	Test Date	Peak Load (lbs)	Peak Stress (ksi)	Average (ksi)	Standard Deviation (ksi)	Coef. of Variation (%)
9, 10, 11, 12 (28 days)	1	7/1/2016	85,407	6.80	7.07	0.25	3.48
	2	7/1/2016	91,467	7.28			
	3	7/1/2016	89,501	7.12			
9	1	7/13/2016	90,647	7.21	7.24	0.04	0.58
	2	7/13/2016	90,590	7.21			
	3	7/13/2016	91,523	7.28			
10	1	8/4/2016	106,509	8.48	8.40	0.14	1.63
	2	8/4/2016	103,597	8.24			
	3	8/4/2016	106,650	8.49			
11	1	8/18/2016	109,676	8.73	8.85	0.17	1.91
	2	8/18/2016	112,673	8.97			
	3	8/18/2016	-	-			
12	1	9/22/2016	114,284	9.09	9.33	0.21	2.21
	2	9/22/2016	119,204	9.49			
	3	9/22/2016	118,158	9.40			

5.1.1.4 Soil

Soil properties were determined by in-house material tests. Soil samples were taken directly from the pit to conduct experiments that included: particle size, water content, unit weight, specific gravity, void ratio, and axial compression triaxial tests. The soil was classified as poorly graded sand (SP) with an average unit weight γ = 90 pcf (14.2 kN/m^3), friction angle ϕ = 35°, relative density $D_r \approx 25\%$, and specific gravity G_s = 2.66. The water content did not affect the pile-column testing program as the measured average was w = 2.8%. Complete details regarding the conducted soil tests can be found elsewhere (Vo, 2016).

5.1.1.5 Summary of Material Properties

Material properties are summarized in Table 5-15. These properties were used to perform numerical simulations for predictions of the experimental test and to determine the displacement histories utilized during the experiments.

Table 5-15 Material Properties

Test No.	Concrete	Tube Steel (A-139 Gr. B)			Long. Rebar (A-706 Gr. 60)		
	f'c (ksi) (Mpa)	Yield (ksi) (Mpa)	Tensile (ksi) (Mpa)	Strain at max. stress	Yield (ksi) (Mpa)	Tensile (ksi) (Mpa)	Strain at max. stress
1	6.54	49.5	71.3	15.3%	66.5	90.3	11.4%
	(45)	(342)	(492)		(459)	(623)	
2	6.92	49.5	71.3	15.3%	66.5	90.3	11.4%
	(48)	(342)	(492)		(459)	(623)	
3	6.88	45.4	66.6	18.0%	66.5	90.3	11.4%
	(47)	(313)	(460)		(459)	(623)	
4	7.14	45.4	66.6	18.0%	66.5	90.3	11.4%
	(49)	(313)	(460)		(459)	(623)	
5	4.81	54.3	75.6	14.8%	70.7	99.6	10.8%
	(33)	(375)	(522)		(488)	(687)	
6	6.58	54.3	75.6	14.8%	70.7	99.6	10.8%
	(45)	(375)	(522)		(488)	(687)	
7	6.66	55.6	74.7	13.7%	70.7	99.6	10.8%
	(46)	(384)	(515)		(488)	(687)	
8	6.89	55.6	74.7	13.7%	70.7	99.6	10.8%
	(48)	(384)	(515)		(488)	(687)	
9	7.24	49.5	71.3	15.3%	72.8	97.1	11.6%
	(50)	(342)	(492)		(503)	(670)	
10	8.40	49.5	71.3	15.3%	72.8	97.1	11.6%
	(58)	(342)	(492)		(503)	(670)	
11	8.85	54.3	75.6	14.8%	72.8	97.1	11.6%
	(61)	(375)	(522)		(503)	(670)	
12	9.33	55.6	74.7	13.7%	72.8	97.1	11.6%
	(64)	(384)	(515)		(503)	(670)	

5.1.2. Test 1

5.1.2.1 Test 1 Summary

Test 1 was conducted between February 11th and 25th, 2015 at the North Carolina State University Constructed Facilities Laboratory. The tested pile-column specimen was a reinforced concrete filled steel tube with a diameter-to-thickness (D/t) ratio of 48. No surcharge was applied to the soil, thus the soil stiffness was not modified. The test was successfully conducted to failure, which was caused by a combination of tube local buckling, tube fracture, and rebar rupture, resulting in a large strength degradation (~75%) in the third cycle at ductility level 5.0 (μ_5).

5.1.2.2 Test 1 Observations

Test specimen #1 consisted of a 19-foot 6-inch long, reinforced concrete filled, 12-inch diameter spirally welded steel tube without skelp or splice welds. The specimen was embedded 14 ft. into sand. The nominal wall thickness of the tube was ¼ in., providing a nominal D/t ratio of 48. The test was conducted with a 5-foot-6-inch cantilever length, measured from the soil surface to the point at which the lateral load was applied.

Test specimen #1 performed well through the elastic portion of the test and also during all three cycles of ductility level 4.0 (μ_4). It is believed that onset of buckling occurred during the displacement cycles of that ductility level as minor loss of strength was observed in each cycle. A significant loss of strength, indicating failure, occurred during the initial leg of the third cycle at ductility level 5.0 (μ_5), as shown in Figure 5-18, where the lateral force vs. top displacement response is presented. The test was terminated (Figure 5-19) after the third push cycle load at ductility 5.0 (μ_5) when a significant drop in the force of the actuator was observed (i.e., ~75%). Sounds indicating steel fracture were heard at the same time when the strength loss occurred, indicating probable rebar or tube fracture. Figure 5-20 presents the observed damage after the pile-column specimen was extracted from the soil. As it was thought during the test, tube fracture, tube local buckling, bar fracture and bar buckling did occur. Tube local buckling developed on both sides of the specimen. The sections with the largest local buckling occurred at depths of 3 ft. – 1 ¼ in. and 3 ft. – 4 ¼ in. on the South and North sides of the specimen, respectively, which means that the plastic hinge developed at an average depth of 3 ft. – 2 ¾ in. with respect to the soil surface. Several minor buckled regions were observed equally spaced (~6 in.) on both sides of the specimen, close to the main buckled regions. The main buckled regions protruded ~¾ in. and ~½ in. on the North and South sides of the specimen, respectively. Tube fracture occurred on the South side of the specimen and it extended about half of the cross section perimeter, resulting in a significant drop in strength due to lost tension capacity.

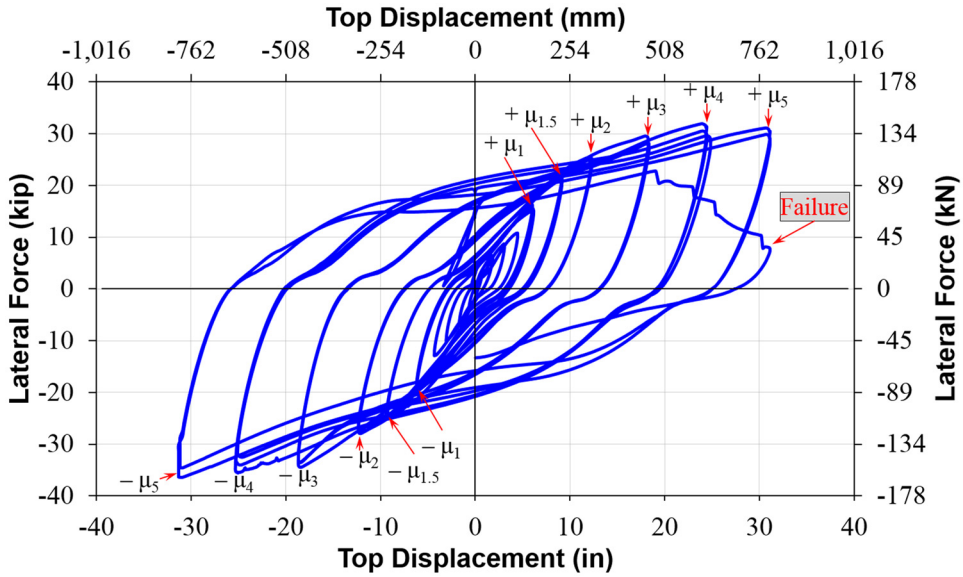

Figure 5-18 Test 1: lateral force vs. top displacement response

Figure 5-19 Test 1: (a) deformed shape, (b) South, and (c) North sides at third cycle of ductility 5; +31.12" of top displacement; 7.78 kips of lateral force

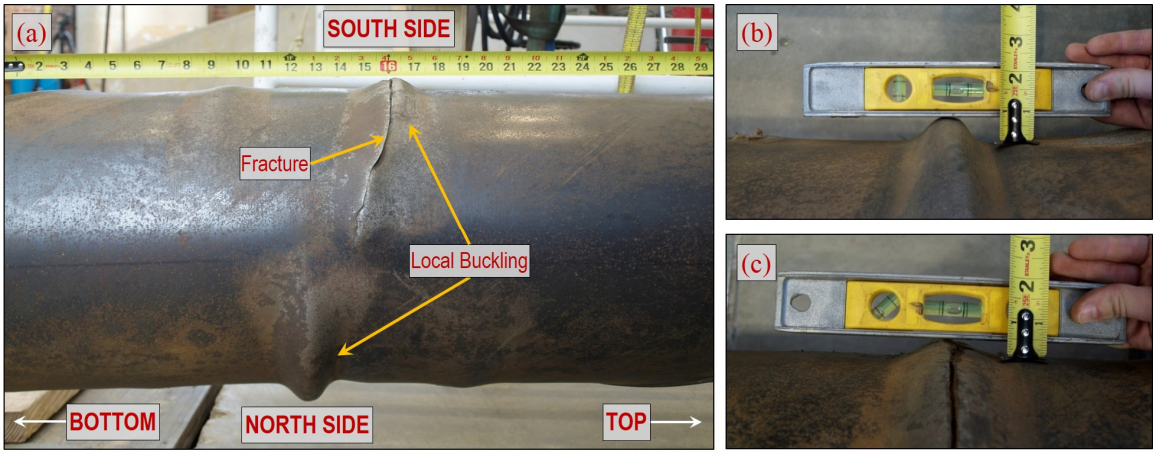

Figure 5-20 Test 1: (a) observed damage, (b) tube local buckling on North side, and (c) tube fracture on South side

5.1.2.3 Test 1 Conclusions

Test specimen #1 showed a reliable response through all ductility 4 (μ_4) cycles. It is believed that onset of local buckling occurred during this ductility level when subtle strength loss was observed. The test specimen completed all cycles of ductility 4 (μ_4) without significant loss of strength. Failure of the specimen occurred at ductility level 5 (μ_5) when a significant drop in the strength was observed. Further investigations revealed that failure occurred due to a combination of tube local buckling, tube fracture, bar fracture, and bar buckling. It is believed that this particular specimen is capable of having a reliable displacement up to ductility 4 (μ_4). The main buckles as well as tube fracture did not occur over the spiral weld, so the tube spiral welds do not appear to negatively influence the behavior.

5.1.3. Test 2

5.1.3.1 Test 2 Summary

Test 2 was conducted May 4th, 2015 at the North Carolina State University Constructed Facilities Laboratory. The tested pile-column specimen was a reinforced concrete filled steel tube with a diameter-to-thickness (D/t) ratio of 48. A surcharge of ~960 psf was applied to the soil prior to and during the test, so the soil stiffness was expected to change. The test was successfully conducted to failure, which was caused by a combination of tube local buckling, tube fracture, and bar rupture, resulting in a large strength degradation (~76.5%) in the first cycle at ductility level 5.5 ($\mu_{5.5}$).

5.1.3.2 Test 2 Observations

Test specimen # 2 consisted of a 19-foot 5-inch long, reinforced concrete filled, 12-inch diameter spirally welded steel tube without skelp or splice welds. The specimen was embedded 13 ft. – 7 in. into sand. The nominal wall thickness of the tube was ¼ in., providing a nominal D/t ratio of 48. The test was conducted with a 5-foot-10-inch cantilever length, measured from the soil surface to the point at which the lateral load was applied.

Test specimen #2 performed well through the elastic portion of the test and during all three cycles of ductility level 5 (μ_5). It is believed that onset of buckling occurred during the displacement cycles at ductility level 4 (μ_4) as minor loss of strength was observed in each cycle at that displacement level. A significant loss of strength, indicating failure, occurred during the first pull cycle at ductility level 5.5 ($\mu_{5.5}$), as shown in Figure 5-21, where the lateral force vs. top displacement response is presented. The test was terminated (Figure 5-22) after the first pull cycle load at ductility 5.5 ($\mu_{5.5}$), when a significant drop in the force of the actuator was observed (i.e., ~75%). Sounds indicating steel fracture were heard at the same time when the strength loss occurred, indicating probable rebar or tube fracture. Figure 5-23 presents the observed damage after the pile-column was extracted from the soil. As it was thought during the test, tube fracture, tube local buckling, bar fracture and bar buckling did occur. Tube local buckling developed on both sides of the specimen. Note that three main local buckling zones developed on both North and South sides. The sections with the largest tube local buckling occurred at depths of 1 ft. – 9 in. and 2 ft. – 5 ¼ in. on the South and North sides of the specimen, respectively. The plastic hinge developed at an average depth of 2 ft. – 6 ¼ in. with respect to the soil surface. Several minor buckled regions were observed on both sides of the specimen, close to the main buckled regions. The main buckled regions protruded ~5/8 in. on both North and South sides of the specimen. Tube fracture occurred on the North side of the specimen and it extended about half of the cross section perimeter, resulting in a significant drop in strength due to lost tension capacity.

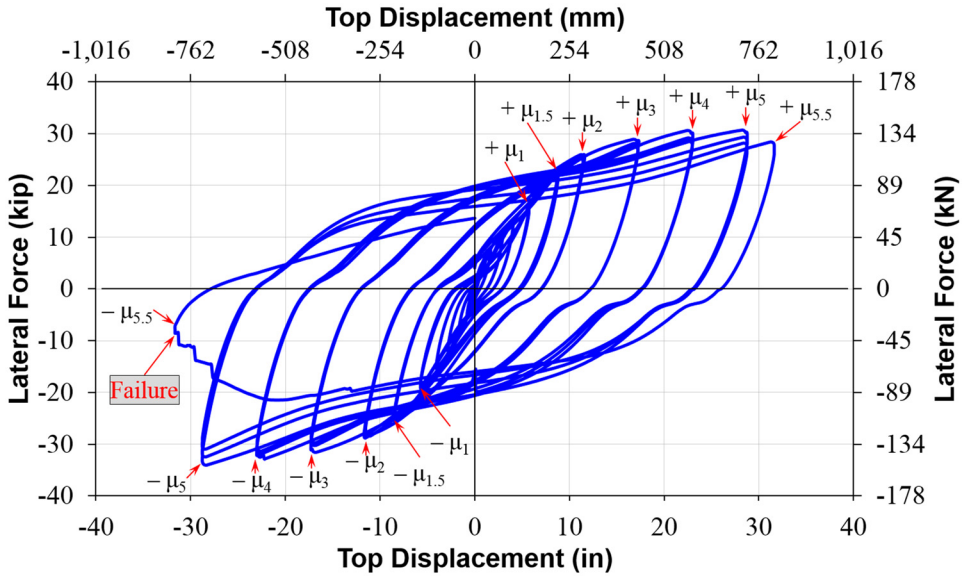

Figure 5-21 Test 2: lateral force vs. top displacement response

Figure 5-22 Test 2: (a) deformed shape, (b) South, and (c) North sides at first cycle of ductility 5.5; −31.62” of top displacement; −7.99 kips of lateral force

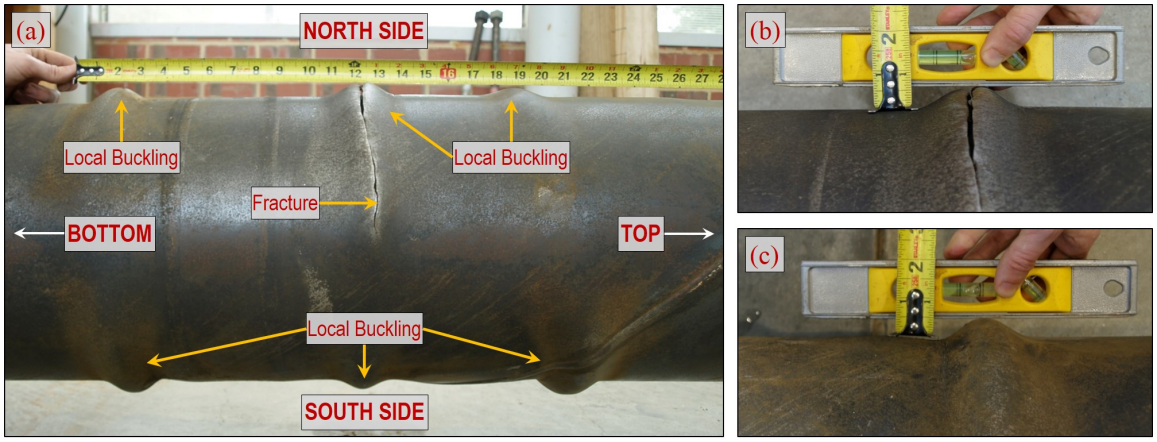

Figure 5-23 Test 2: (a) observed damage, (b) tube fracture on North side, and (c) tube buckling on South side

5.1.3.3 Test 2 Conclusions

Test specimen #2 showed a reliable response through all ductility 5 (μ_5) cycles. It is believed that the onset of tube local buckling occurred during the test at ductility 4 (μ_4), when subtle strength loss was observed. The test specimen completed all cycles of ductility 5 (μ_5) without significant loss of strength. Failure of the specimen occurred at ductility level 5.5 ($\mu_{5.5}$) when a significant drop in the strength was observed. Further investigations revealed that failure occurred due to a combination of tube local buckling, tube fracture, bar buckling, and bar fracture. It is believed that this particular specimen is capable of having a reliable displacement up to ductility 5.0 (μ_5). The main buckles as well as tube fracture did not occur over the spiral weld, so the tube spiral welds do not appear to negatively influence the behavior.

5.1.4. Test 3

5.1.4.1 Test 3 Summary

Test 3 was conducted May 29th, 2015 at the North Carolina State University Constructed Facilities Laboratory. The tested pile-column specimen was a reinforced concrete filled steel tube with a diameter-to-thickness (D/t) ratio of 95. No surcharge was applied to the soil, thus the soil stiffness was not modified. The test was successfully conducted to failure, which was caused by a combination of tube local buckling and fracture of the tube spiral weld, resulting in a large strength degradation (~36.35%) in the first cycle at ductility 4 (μ_4).

5.1.4.2 Test 3 Observations

Test specimen # 3 consisted of a 19-foot 5-inch long, reinforced concrete filled, 12-3/4-inch diameter spirally welded steel tube without skelp or splice welds. The specimen was embedded 13 ft. – 11 in. into sand. The nominal wall thickness of the tube was 0.134", providing a nominal D/t ratio of 95. The test was conducted with a 5-foot-6-inch cantilever length, measured from the soil surface to the point at which the lateral load was applied.

Test specimen #3 performed well through the elastic portion of the test and during all three cycles of ductility level 2 (μ_2). It is believed that onset of buckling occurred during the displacement cycles at ductility level 1.5 ($\mu_{1.5}$), as large tensile strains were recorded on the North side of the specimen at this displacement level. A moderate strength loss (~12.84%), indicating onset of fracture, was recorded during the first pull cycle at ductility level 3 (μ_3). A significant loss of strength, indicating failure, occurred during the first push cycle at ductility level 4 (μ_4), as shown in Figure 5-24, where the lateral force vs. top displacement response is presented. The test was terminated (Figure 5-25) after the first push cycle load at ductility 4 (μ_4), when a significant drop in the force of the actuator was observed (i.e., ~36.4%); tube spiral weld fracture was also observed at this displacement ductility level. Sounds indicating steel fracture were not heard. Figure 5-26 presents the observed damage after the pile-column was extracted from the soil. As it was thought during the test, tube local buckling and tube spiral weld fracture did occur. Tube local buckling developed on both sides of the specimen. Three tube local buckling zones developed on the South side, whereas only one developed on the North Side. The sections with the largest tube local buckling occurred at depths of 4 ft. – 1 3/8 in. and 2 ft. – 5 ½ in. on the South and North sides of the specimen, respectively. The plastic hinge developed at an average depth of 2 ft. – 11 5/8 in. with respect to the soil surface. Several minor buckled regions were observed on both sides of the specimen, close to the main buckled regions. The main buckled regions protruded ~3/8 in. on both North and South sides of the specimen. Tube fracture occurred on both North and South sides of the specimen along a segment of the tube spiral weld, and it extended to the East and West extreme fibers, resulting in the strength loss observed on both push and pull cycle loads due to loss of tension capacity.

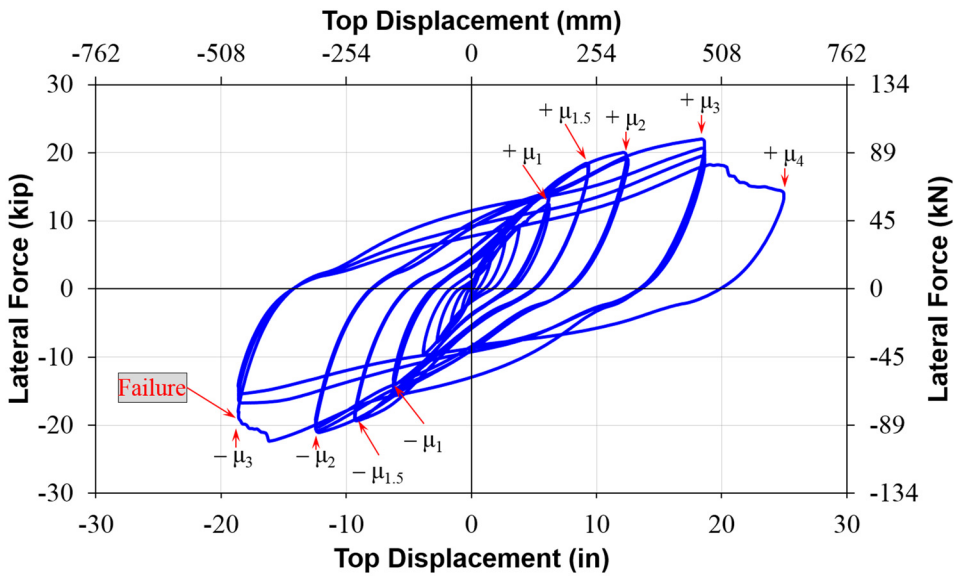

Figure 5-24 Test 3: lateral force vs. top displacement response

Figure 5-25 Test 3: (a) deformed shape, (b) South, and (c) North sides at first cycle of ductility 4; –24.99" of top displacement; –13.99 kips of lateral force

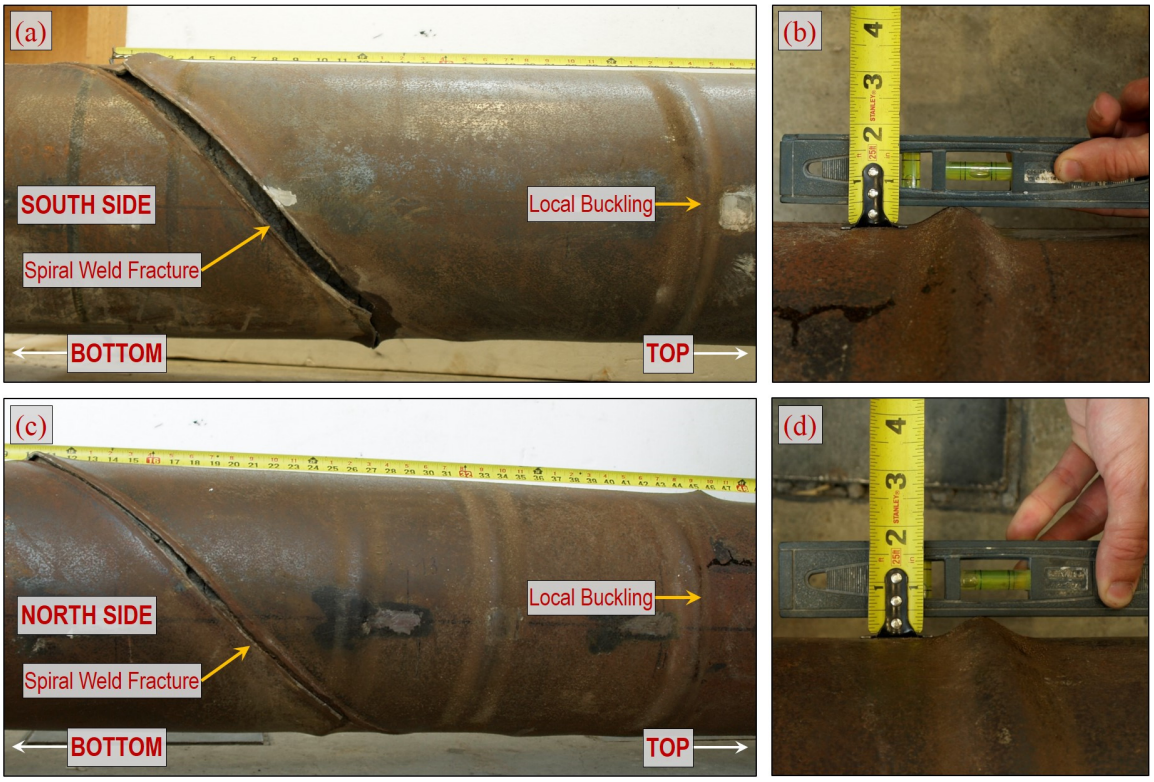

Figure 5-26 Test 3: (a) observed damage and (b) tube fracture on South side; (c) observed damage and (d) tube buckling on North side

5.1.4.3 Test 3 Conclusions

Test specimen #3 showed a reliable response through all ductility 2 (μ_2) cycles. It is believed that the onset of local buckling occurred early during the test at ductility level 1.5 ($\mu_{1.5}$), when large tensile strains were recorded. The test specimen completed all cycles of ductility 3 (μ_3) without significant loss of strength, though indicating onset of tube spiral weld fracture. A significant drop in strength occurred at ductility level 4 (μ_4) when fracture of the spiral weld was observed. Further investigations revealed that failure occurred due to a combination of tube local buckling and tube spiral weld fracture. It is believed that this specimen is capable of having a reliable displacement up to ductility 2 (μ_2). Tube fracture occurred over the spiral weld, so the tube spiral welds appear to negatively influence the behavior, limiting the deformation capacity of this specimen.

5.1.5. Test 4

5.1.5.1 Test 4 Summary

Test 4 was conducted June 16th, 2015 at the North Carolina State University Constructed Facilities Laboratory. The tested pile-column specimen was a reinforced concrete filled steel tube with a diameter-to-thickness (D/t) ratio of 95. A surcharge of ~960 psf was applied to the soil prior to and during the test, so the soil stiffness was expected to change. The test was successfully conducted to failure, which was caused by a combination of tube local buckling and fracture of the tube spiral weld, resulting in a large strength degradation (~37.2%) in the second cycle at ductility level 2 (μ_2).

5.1.5.2 Test 4 Observations

Test specimen # 4 consisted of a 19-foot 5-inch long, reinforced concrete filled, 12-3/4-inch diameter spirally welded steel tube without skelp or splice welds. The specimen was embedded 13 ft. – 11 in. into sand. The nominal wall thickness of the tube was 0.134", providing a nominal D/t ratio of 95. The test was conducted with a 5-foot-6-inch cantilever length, measured from the soil surface to the point at which the lateral load was applied.

Test specimen #4 performed well through the elastic portion of the test and during all three cycles of ductility level 1 (μ_1). It is believed that onset of tube buckling and tube spiral weld fracture occurred early during the displacement cycles at ductility level 1.5 ($\mu_{1.5}$) as strength losses were observed in both push and pull cycle loads at this level. A moderate strength loss (~18%), indicating onset of fracture, was recorded during the second pull cycle at ductility level 1.5 ($\mu_{1.5}$). A significant loss of strength, indicating failure, occurred during the second pull cycle at ductility level 2 (μ_2), as shown in Figure 5-27, where the lateral force vs. top displacement response is presented. The test was terminated (Figure 5-28) after the second pull cycle load at ductility 2 (μ_2) when a significant drop in the force of the actuator was observed (i.e., ~37.2%); tube spiral weld fracture was also observed at this displacement ductility level. Sounds indicating steel fracture were not heard. Figure 5-29 presents the observed damage after the pile-column was extracted from the soil. As it was thought during the test, tube local buckling and tube spiral weld fracture did occur. Tube local buckling developed only on the South side of the specimen at a depth of 3 ft. – 3 in., which protruded ~1/4 in. Tube fracture occurred on the North side of the specimen over a segment of the tube spiral weld, and it extended to the East and West extreme fibers, resulting in the strength loss observed in the pull cycle loads due to loss of tension capacity.

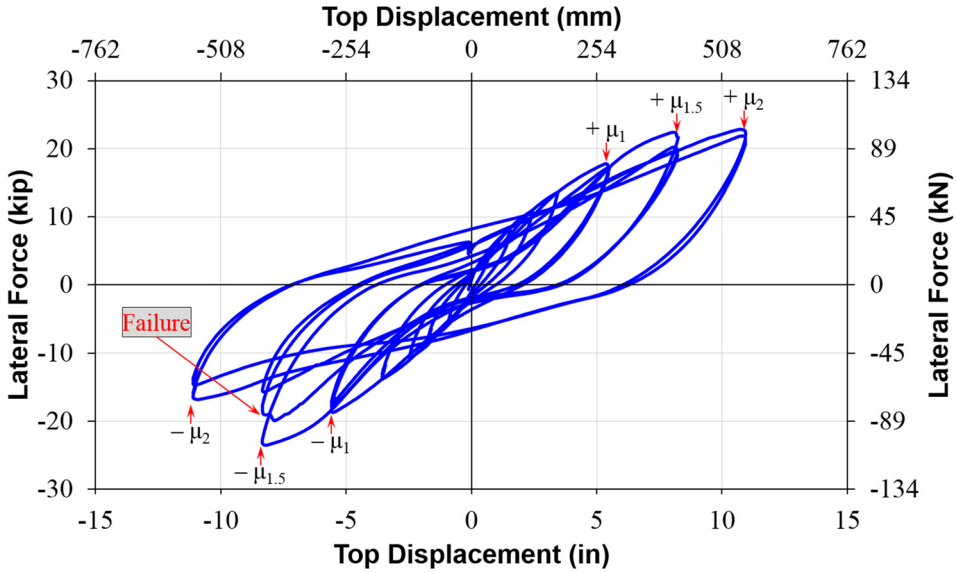

Figure 5-27 Test 4: lateral force vs. top displacement response

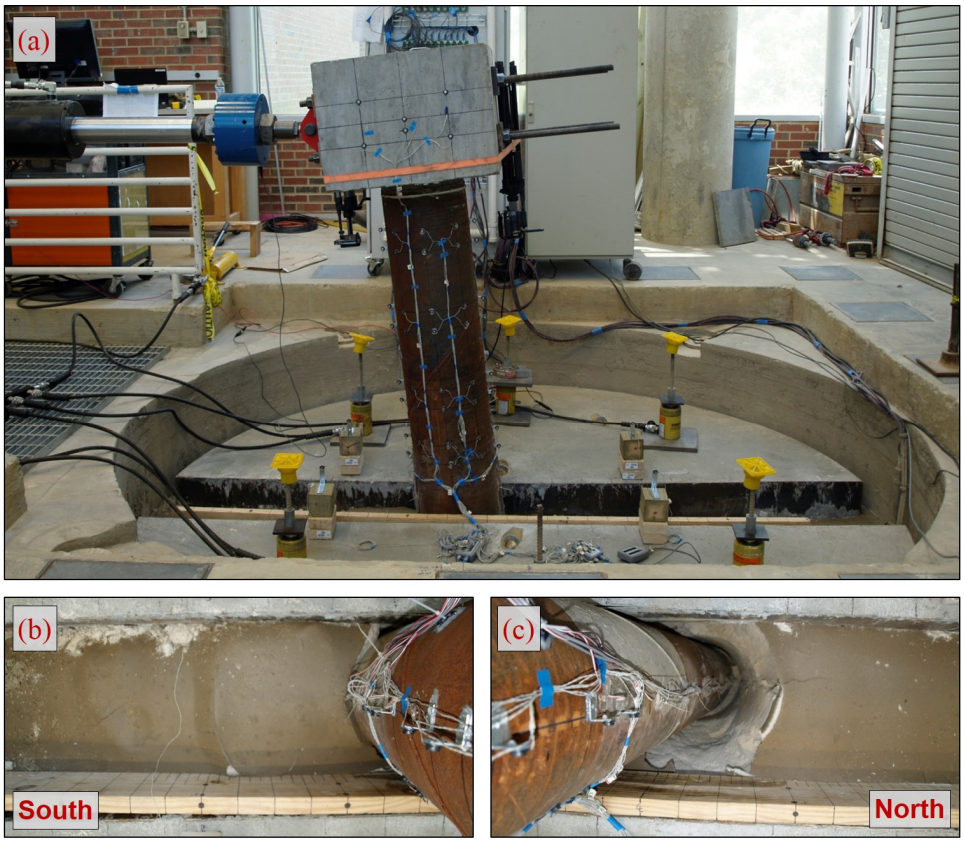

Figure 5-28 Test 4: (a) deformed shape, (b) South, and (c) North sides at second cycle of ductility 2; −11.11" of top displacement; −14.61 kips of lateral force

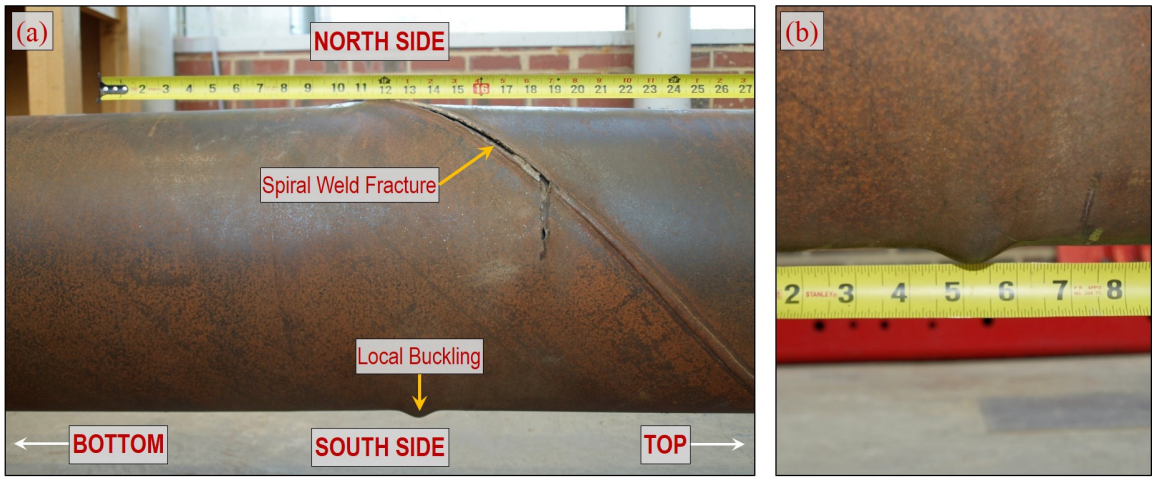

Figure 5-29 Test 4: (a) observed damage and (b) tube buckling on South side

5.1.5.3 Test 4 Conclusions

Test specimen #4 showed a reliable response through all ductility 1 (μ_1) cycles. It is believed that onset of tube fracture and tube local buckling occurred early during the test at a ductility level of 1.5 ($\mu_{1.5}$), when large tensile strains were recorded along with strength losses. The test specimen completed all cycles of ductility 1.5 ($\mu_{1.5}$) with a moderate loss of strength, indicating onset of tube fracture. A significant drop in strength occurred at ductility level 2 (μ_2) when fracture of the tube spiral weld was observed. Further investigations revealed that failure occurred due to a combination of tube local buckling and fracture of the tube spiral weld. It is believed that this particular specimen is capable of having a reliable displacement up to ductility 1 (μ_1). Tube fracture occurred over the spiral weld, so the tube spiral welds appear to negatively influence the behavior limiting the deformation capacity of this particular specimen.

Upon further examination of the inside of the spirally welded tube, it was determined that the thin wall tubes which made up tests 3 and 4 were not welded along the inside surface, but rather only upon the outside surface. Furthermore, tension tests done on coupons across the spiral weld after the tests were completed indicated abrupt rupture at low strain levels. Further details regarding this issue with the tube spiral welds was previously discussed in the Material Properties section.

5.1.6. Test 5

5.1.6.1 Test 5 Summary

Test 5 was conducted September 28th, 2015 at the North Carolina State University Constructed Facilities Laboratory. The tested pile-column specimen was a reinforced concrete filled steel tube with a diameter-to-thickness (D/t) ratio of 95. No surcharge was applied to the soil, thus the soil stiffness was not modified. The test was successfully conducted to failure, which was caused by a combination of tube local buckling and tube fracture, resulting in a large strength degradation (~47.8%) in the third cycle at ductility level 4 (μ_4).

5.1.6.2 Test 5 Observations

Test specimen #5 consisted of a 19-foot-5-inch long, reinforced concrete filled, 12-3/4-inch diameter spirally welded steel tube without skelp or splice welds. The specimen was embedded 13 ft. – 9 in. into sand. The nominal wall thickness of the tube was 0.134", providing a nominal D/t ratio of 95. The test was conducted with a 5-foot-8.25-inch cantilever length, measured from the soil surface to the point at which the lateral load was applied.

Test specimen #5 performed well through the elastic portion of the test and during all three cycles of ductility level 3 (μ_3). It is believed that onset of tube buckling occurred during the displacement cycles of ductility level 2 (μ_2) as large tensile strain in combination with minor loss of strength were observed in each cycle. A significant loss of strength, indicating failure, occurred during the third pull cycle at ductility level 4 (μ_4), as shown in Figure 5-30, where the lateral force vs. top displacement response is presented; the deformed shape at this performance level is presented in Figure 5-31. The test was terminated after the first push cycle load at ductility 5 (μ_5) when a significant drop in the force of the actuator was observed (i.e., ~47.8%). Sounds indicating steel fracture were heard at the same time when the strength loss occurred, indicating probable rebar or tube fracture. Figure 5-32 presents the observed damage after the pile-column was extracted from the soil. As it was thought during the test, tube fracture and tube local buckling did occur; bar buckling also occurred. Tube local buckling developed on both sides of the specimen. The sections with the largest tube local buckling occurred at depths of 3 ft. – ¼ in. and 2 ft. – 10 in. on the North and South sides of the specimen, respectively, which means that the plastic hinge developed at an average depth of 2 ft. – 11 1/8 in. with respect to the soil surface. The main buckled regions protruded ~7/8 in. and ~½ in. on the North and South sides of the specimen, respectively. Tube fracture occurred on both sides of the specimen and it extended about half of the cross section perimeter, resulting in a significant drop in strength due to lost tension capacity.

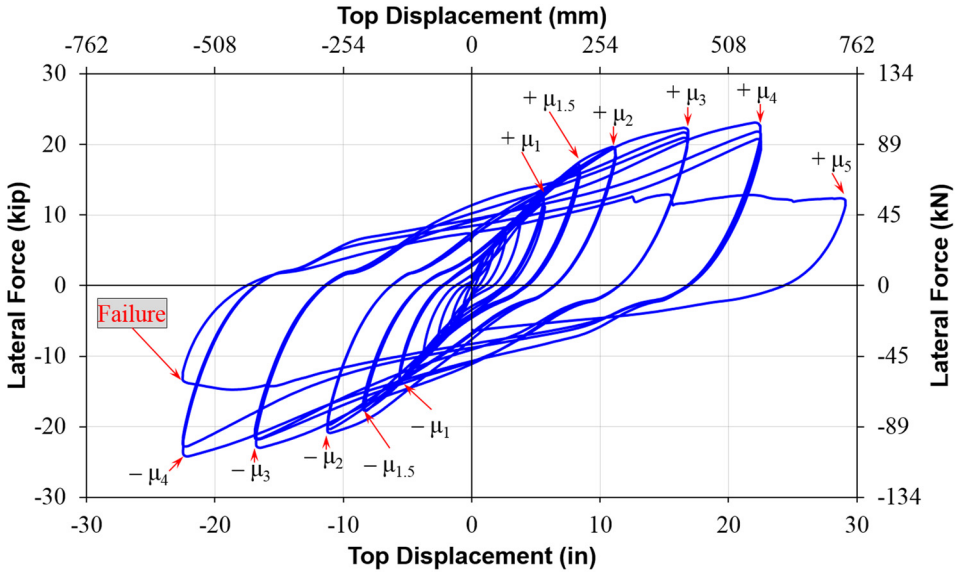

Figure 5-30 Test 5: lateral force vs. top displacement response

Figure 5-31 Test 5: (a) deformed shape, (b) South, and (c) North sides at third cycle of ductility 4; −22.54” of top displacement; −13.28 kips of lateral force

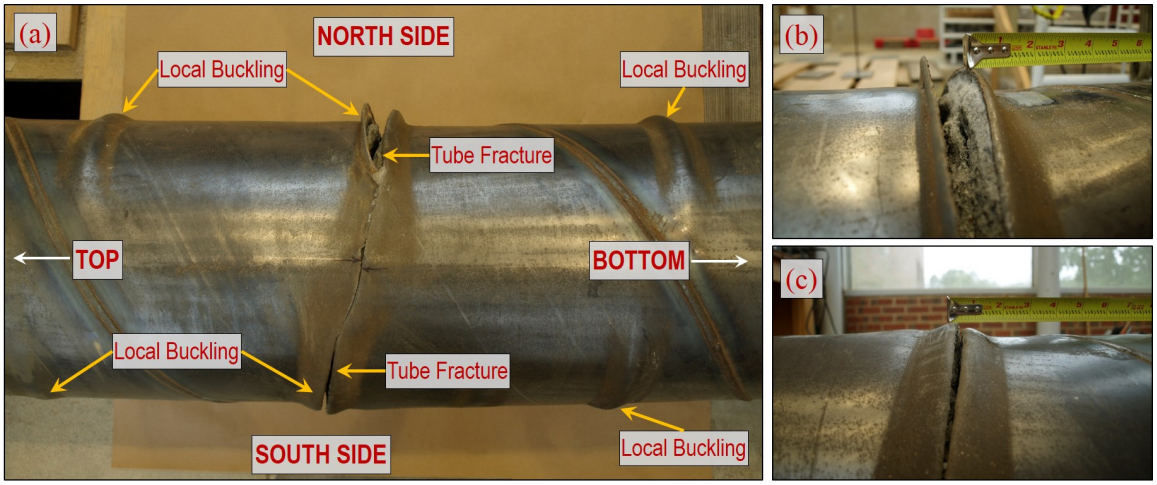

Figure 5-32 Test 5: (a) observed damage, (b) tube fracture and buckling on North side, and (c) tube fracture and buckling on South side

5.1.6.3 Test 5 Conclusions

Test specimen #5 showed a reliable response through all ductility 3 (μ_3) cycles. It is believed that onset of tube local buckling occurred early during the test at a ductility level of 1.5 ($\mu_{1.5}$), when large tensile strains were recorded. The test specimen completed all cycles of ductility 3 (μ_3) with minor loss of strength. A significant drop in strength occurred at displacement ductility level 4 (μ_4) when tube fracture developed on the North side of the specimen during the third pull cycle at this level. Further investigations revealed that failure occurred due to a combination of tube local buckling, tube fracture, and bar buckling. It is believed that this particular specimen is capable of having a reliable displacement up to ductility 3 (μ_3). The main buckles as well as tube fracture did not occur over the spiral weld, so the spiral welds do not appear to negatively influence the behavior.

5.1.7. Test 6

5.1.7.1 Test 6 Summary

Test 6 was conducted October 21st, 2015 at the North Carolina State University Constructed Facilities Laboratory. The tested pile-column specimen was a reinforced concrete filled steel tube with a diameter-to-thickness (D/t) ratio of 95. A surcharge of ~960 psf was applied to the soil prior to and during the test, so the soil stiffness was expected to change. The test was successfully conducted to failure, which was caused by a combination of tube local buckling and tube fracture, resulting in a large strength degradation (~34.7%) in the third cycle at ductility level 4 (μ_4).

5.1.7.2 Test 6 Observations

Test specimen # 6 consisted of a 19-foot 5.25-inch long, reinforced concrete filled, 12-3/4-inch diameter spirally welded steel tube without skelp or splice welds. The specimen was embedded 13 ft. – 6.75 in. into sand. The nominal wall thickness of the tube was 0.134", providing a nominal D/t ratio of 95. The test was conducted with a 5-foot-10.5-inch cantilever length, measured from the soil surface to the point at which the lateral load was applied.

Test specimen #6 performed well through the elastic portion of the test and during all three cycles of ductility level 3 (μ_3). It is believed that onset of buckling occurred during the displacement cycles at ductility level 1.5 ($\mu_{1.5}$) as large tensile strains were recorded in each cycle at that displacement level. A significant loss of strength, indicating failure, occurred during the third push cycle at ductility level 4 (μ_4), as shown in Figure 5-33, where the lateral force vs. top displacement response is presented. The test was terminated (Figure 5-34) after the third push cycle load at ductility 4 (μ_4) when a significant drop in the force of the actuator was observed (i.e., ~34.7%). Sounds indicating steel fracture were heard at the same time when the strength loss occurred, indicating probable rebar or tube fracture. Figure 5-35 presents the observed damage after the pile-column was extracted from the soil. As it was thought during the test, tube fracture and tube local buckling did occur. Neither bar buckling nor bar fracture were observed. Tube local buckling developed on both sides of the specimen. It can be seen that two main local buckling zones developed on the North side, while only one developed on the South side of the specimen. The sections with the largest tube local buckling occurred at depths of 2 ft. – 6 in. and 2 ft. – 8 in. on the South and North sides of the specimen, respectively, which means that the plastic hinge developed at an average depth of 2 ft. – 7 in. with respect to the soil surface. Several minor buckled regions were observed on both sides of the specimen, close to the main buckled regions. The main buckled regions protruded ~1/2 in. and ~7/16 in. on the South and North sides of the specimen, respectively. Tube fracture occurred on the South side of the specimen and it extended about half of the cross section perimeter, resulting in a significant drop in strength due to lost tension capacity.

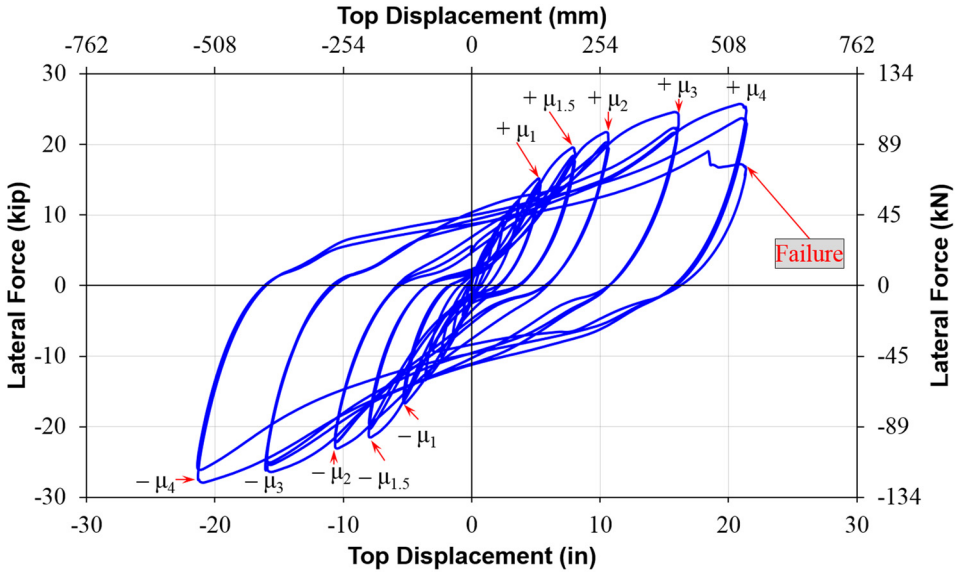

Figure 5-33 Test 6: lateral force vs. top displacement response

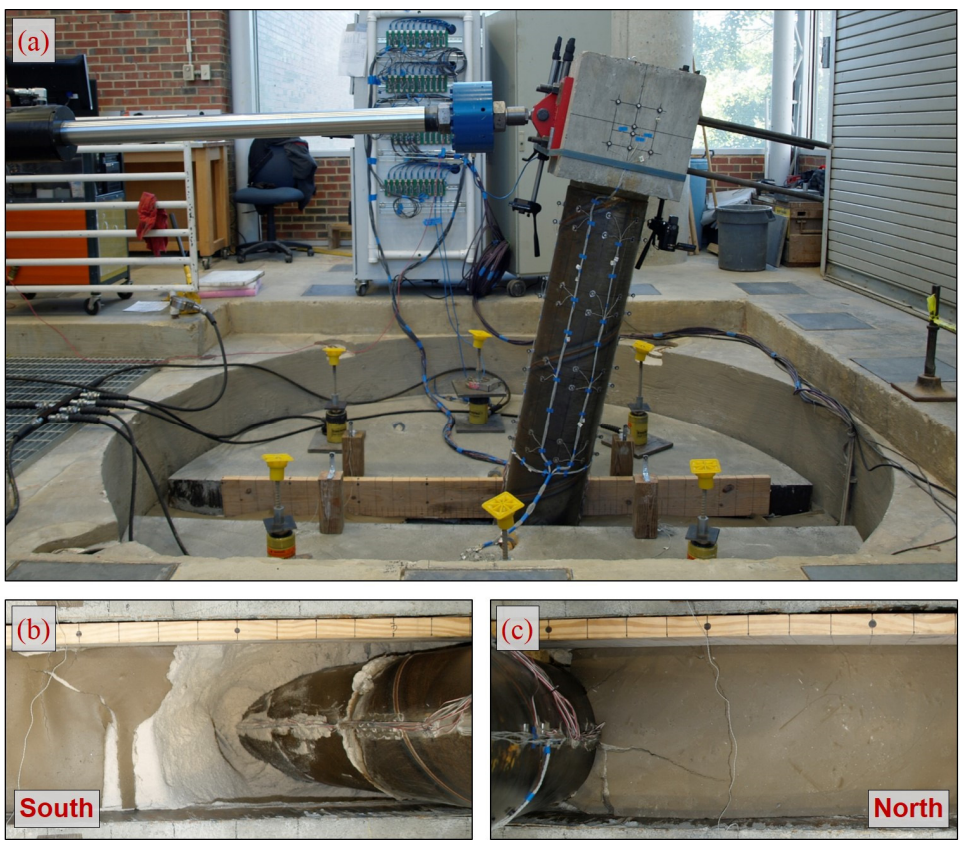

Figure 5-34 Test 6: (a) deformed shape, (b) South, and (c) North sides at third cycle of ductility 4; +21.36" of top displacement; +16.56 kips of lateral force

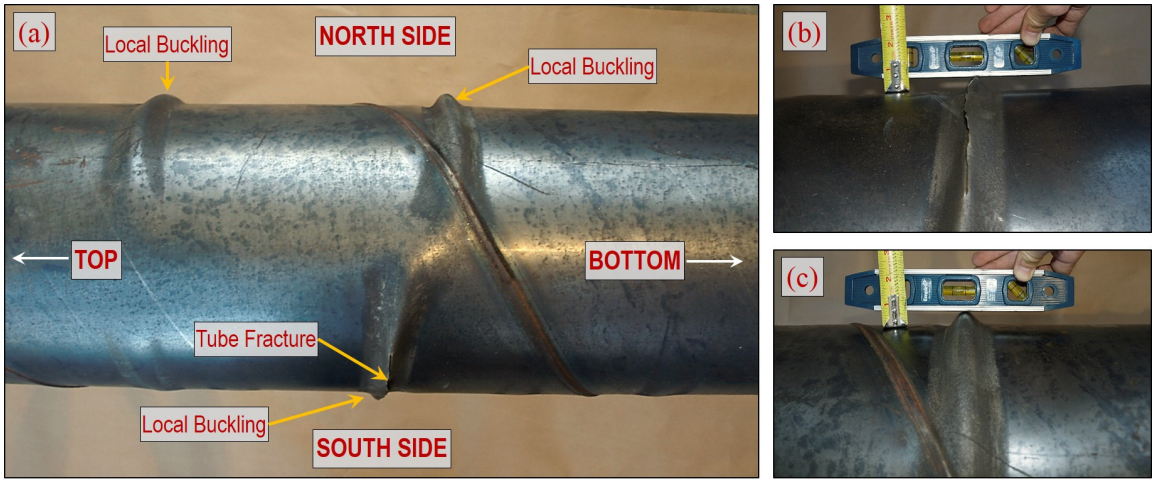

Figure 5-35 Test 6: (a) observed damage observed, (b) tube fracture on South side, and (c) tube buckling on North side

5.1.7.3 Test 6 Conclusions

Test specimen #6 showed a reliable response through all ductility 3 (μ_3) cycles. It is believed that onset of tube local buckling occurred early during the test at a ductility level 1.5 ($\mu_{1.5}$), when large tensile strains were recorded. The test specimen completed all cycles of ductility 3 (μ_3) with minor loss of strength. A significant drop in strength occurred at ductility level 4 (μ_4) when tube fracture developed on the South side of the specimen during the third push cycle at this level. Further investigations revealed that failure occurred due to a combination of tube local buckling and tube fracture. Neither bar fracture nor bar buckling were observed in the internal reinforcement. It is believed that this particular specimen is capable of having a reliable displacement up to ductility 3 (μ_3). The main buckles as well as the tube fracture did not occur over the spiral weld, so the tube spiral welds do not appear to negatively influence the behavior.

5.1.8. Test 7

5.1.8.1 Test 7 Summary

Test 7 was conducted November 11th, 2015 at the North Carolina State University Constructed Facilities Laboratory. The tested pile-column specimen was a reinforced concrete filled steel tube with a diameter-to-thickness (D/t) ratio of 68. No surcharge was applied to the soil, thus the soil stiffness was not modified. The test was successfully conducted to failure, which was caused by a combination of tube local buckling, tube fracture, and bar buckling, resulting in a large strength degradation (~25.4%) in the second cycle at ductility level 5 (μ_5).

5.1.8.2 Test 7 Observations

Test specimen #7 consisted of a 19-foot 5.25-inch long, reinforced concrete filled, 12-3/4-inch diameter spirally welded steel tube without skelp or splice welds. The specimen was embedded 13 ft. – 8 in. into sand. The nominal wall thickness of the tube was 3/16 in., providing a nominal D/t ratio of 68. The test was conducted with a 5-foot-9.25-inch cantilever length, measured from the soil surface to the point at which the lateral load was applied.

Test specimen #7 performed well through the elastic portion of the test and during all three cycles of ductility level 4 (μ_4). It is believed that onset of tube buckling occurred during the displacement cycles of ductility level 2 (μ_2) as large tensile strains were recorded in each cycle at this level. A significant loss of strength, indicating failure, occurred during the second push cycle at ductility level 4.88 ($\mu_{4.88}$), as shown in Figure 5-36, where the lateral force vs. top displacement response is presented. Due to setup constrains, a maximum displacement ductility of 4.88 ($\mu_{4.88}$) was induced in the specimen head for all push cycles corresponding to ductility 5(μ_5). The test was terminated (Figure 5-37) after the first push cycle load at ductility 4.88 ($\mu_{4.88}$) when a significant drop in the force of the actuator was observed (i.e., ~25.4%). Sounds indicating steel fracture were not heard. Figure 5-38 presents the observed damage after the pile-column was extracted from the soil. As it was thought during the test, tube fracture and tube local buckling did occur; bar buckling also occurred. Tube local buckling developed on both sides of the specimen. The sections with the largest tube local buckling occurred at a depth of 2 ft. – 8 ¼ in. on both North and South sides of the specimen, where deformations protruded ~5/8 in. The plastic hinge developed at an average depth of 3 ft. – ¼ in. with respect to the soil surface. Tube fracture occurred on the South side of the specimen and it extended about half of the cross section perimeter, resulting in a significant drop in strength due to lost tension capacity.

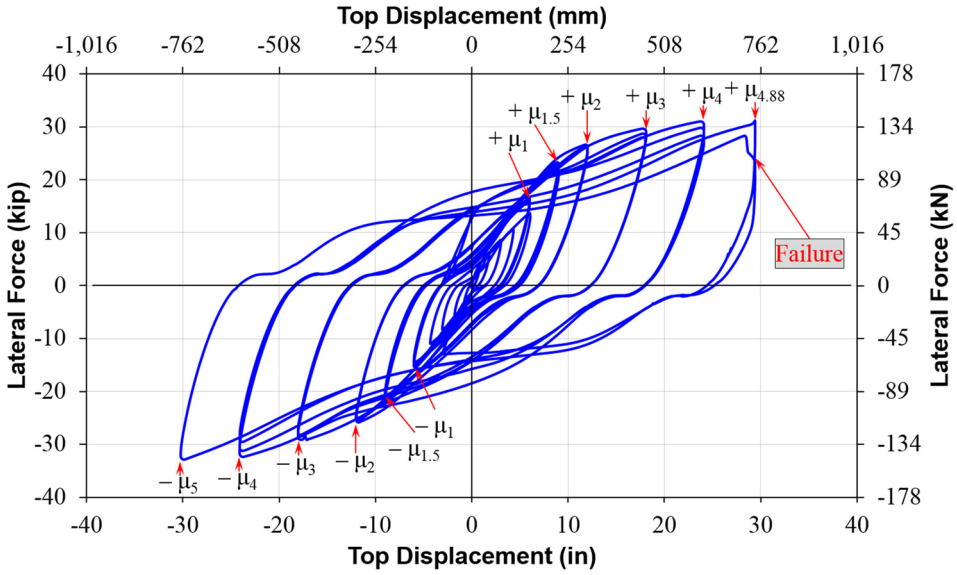

Figure 5-36 Test 7: lateral force vs. top displacement response

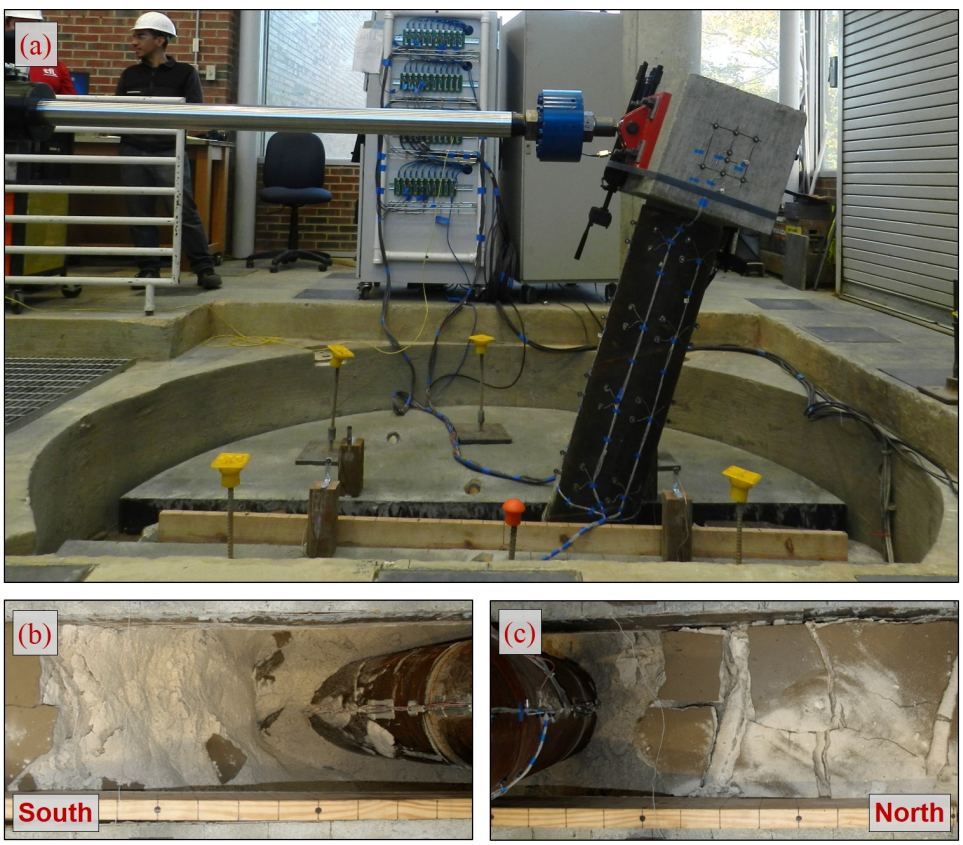

Figure 5-37 Test 7: (a) deformed shape, (b) South, and (c) North sides at second cycle of ductility 4.88; +29.41" of top displacement; +23.25 kips of lateral force

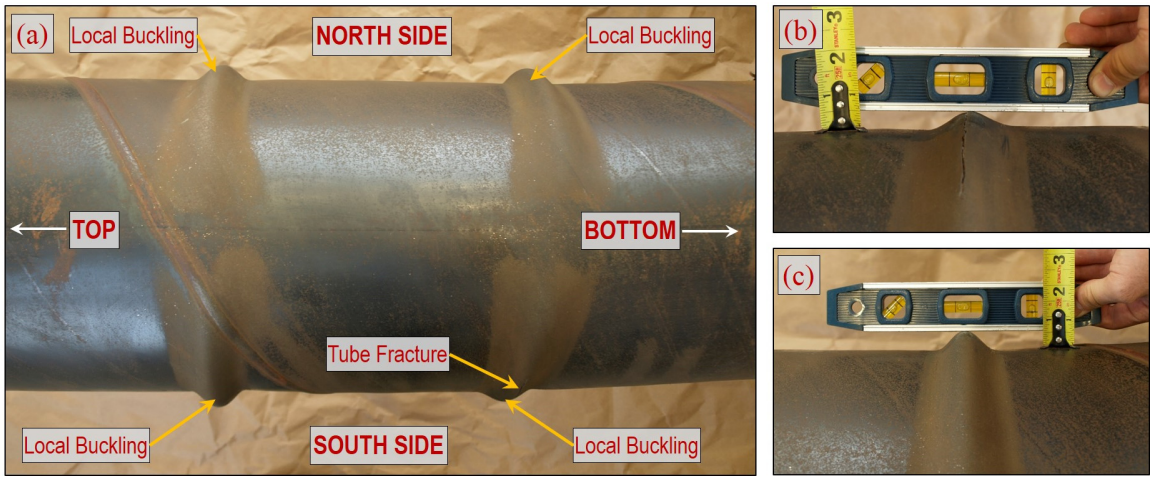

Figure 5-38 Test 7: (a) observed damage, (b) tube fracture and buckling on South side, and (c) tube buckling on North side

5.1.8.3 Test 7 Conclusions

Test specimen #7 showed a reliable response through all ductility 4 (μ_4) cycles. It is believed that onset of tube local buckling occurred during the test at ductility level 2 (μ_2), when large tensile strains were recorded. The test specimen completed all cycles of ductility 4 (μ_4) with minor loss of strength. A significant drop in strength occurred at ductility level 4.88 ($\mu_{4.88}$) when tube fracture developed on the South side of the specimen during the second push cycle at this level. Further investigations revealed that failure occurred due to a combination of tube local buckling, tube fracture, and bar buckling. Although the specimen was subjected to a maximum displacement ductility of 4.88 ($\mu_{4.88}$) in the push cycles, it is believed that this particular specimen is capable of having a reliable displacement up to ductility 4 (μ_4). The main buckles as well as the tube fracture did not occur over the spiral weld, so the tube spiral welds do not appear to negatively influence the behavior.

5.1.9. Test 8

5.1.9.1 Test 8 Summary

Test 8 was conducted December 9th, 2015 at the North Carolina State University Constructed Facilities Laboratory. The tested pile-column specimen was a reinforced concrete filled steel tube with a diameter-to-thickness (D/t) ratio of 68. A surcharge of ~960 psf was applied to the soil prior to and during the test, so the soil stiffness was expected to change. The test was successfully conducted to failure, which was caused by a combination of tube local buckling and tube fracture, resulting in a large strength degradation (~24.8%) in the third cycle at ductility level 4 (μ_4).

5.1.9.2 Test 8 Observations

Test specimen # 8 consisted of a 19-foot 5.25-inch long, reinforced concrete filled, 12-3/4-inch diameter spirally welded steel tube without skelp or splice welds. The specimen was embedded 13 ft. – 8 in. into sand. The nominal wall thickness of the tube was 3/16 in., providing a nominal D/t ratio of 68. The test was conducted with a 5-foot-9.25-inch cantilever length, measured from the soil surface to the point at which the lateral load was applied.

Test specimen #8 performed well through the elastic portion of the test and during all three cycles of ductility level 3 (μ_3). It is believed that onset of tube local buckling occurred during the displacement cycles at ductility level 2 (μ_2) as large tensile strains were recorded in each cycle at that performance level. A significant loss of strength, indicating failure, occurred during the third push cycle at ductility level 4 (μ_4), as shown in Figure 5-39, where the lateral force vs. top displacement response is presented. The test was terminated (Figure 5-40) after the third push cycle load at ductility 4 (μ_4) when a significant drop in the force of the actuator was observed (i.e., ~24.83%). Sounds indicating steel fracture were heard at the same time when the strength loss occurred, indicating probable bar or tube fracture. Figure 5-41 presents the observed damage after the pile-column was extracted from the soil. As it was thought during the test, tube fracture and tube local buckling did occur. Neither bar buckling nor bar fracture were observed. Tube local buckling developed on both sides of the specimen. The sections with the largest local buckling occurred at depths of 2 ft. – 5.5 in. and 2 ft. – 7 in. on the South and North sides of the specimen, respectively, where deformations protruded ~5/8 in. on both sides. The plastic hinge developed at an average depth of 2 ft. – 6.25 in. with respect to the soil surface. Several ripples were observed on the North side of the specimen, close to the main buckled region. Tube fracture occurred on the South side of the specimen and it extended about half of the cross section perimeter, resulting in a significant drop in strength due to lost tension capacity.

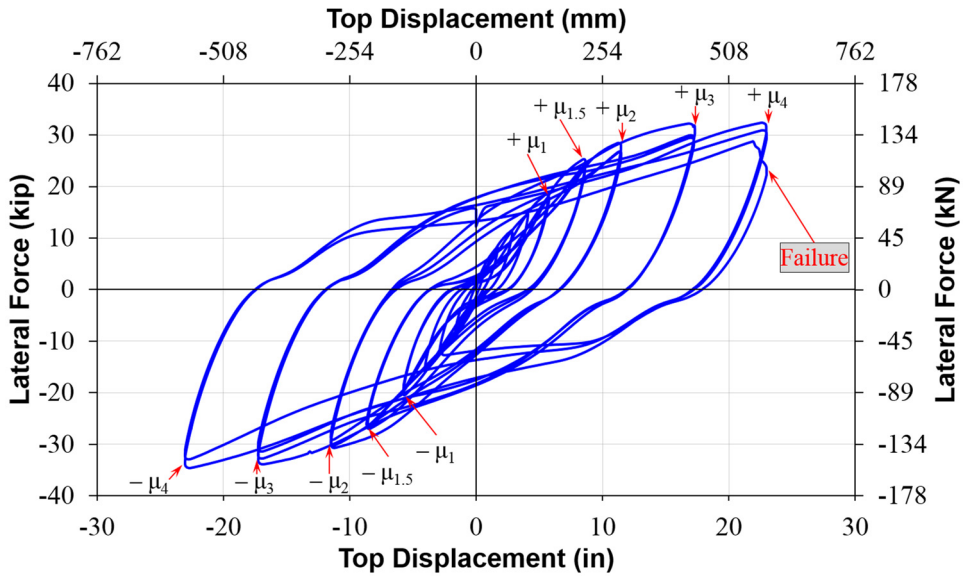

Figure 5-39 Test 8: lateral force vs. top displacement response

Figure 5-40 Test 8: (a) deformed shape, (b) South, and (c) North sides at third cycle of ductility 4; +22.95" of top displacement; +23.87 kips of lateral force

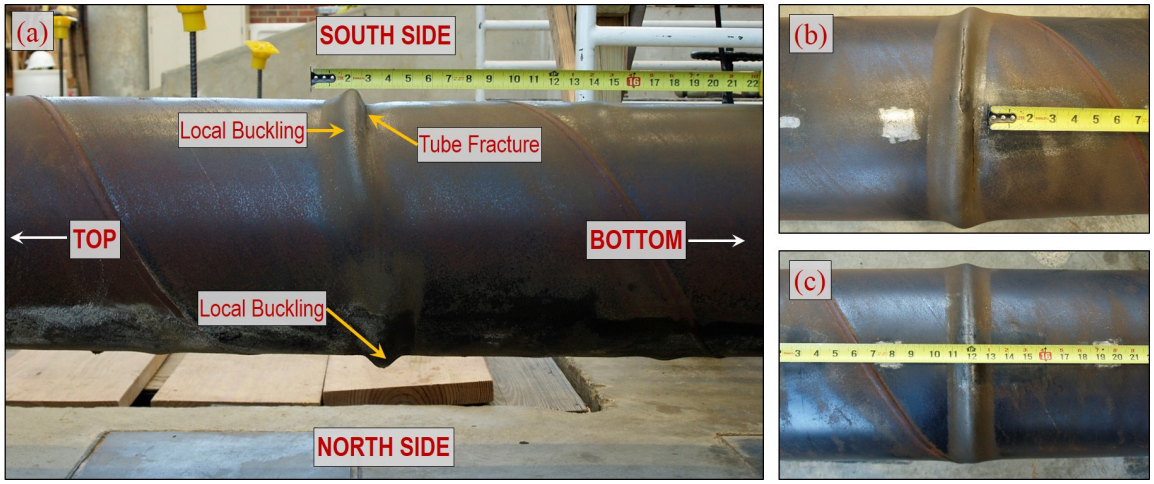

Figure 5-41 Test 8: (a) observed damage, (b) tube fracture and buckling on South side, and (c) tube fracture and buckling on North side

5.1.9.3 Test 8 Conclusions

Test specimen #8 showed a reliable response through all ductility 3 (μ_3) cycles. It is believed that onset of pipe local buckling occurred early during the test at a ductility level of 2 (μ_2), when large curvatures were recorded. The test specimen completed all cycles of ductility 3 (μ_3) with minor loss of strength. A significant drop in strength occurred at ductility 4 (μ_4) when tube fracture developed on the South side of the specimen during the third push cycle at this level. Further investigations revealed that failure occurred due to a combination of tube local buckling and tube fracture. Neither bar fracture nor bar buckling were observed in the internal reinforcement on the South side of the specimen. It is believed that this particular specimen is capable of having a reliable displacement up to ductility 3 (μ_3). The main buckles as well as tube fracture did not occur over the spiral weld, so the tube spiral welds do not appear to negatively influence the behavior.

5.1.10. Test 9

5.1.10.1 Test 9 Summary

Test 9 was conducted July 13th, 2016 at the North Carolina State University Constructed Facilities Laboratory. The tested pile specimen was a reinforced concrete filled steel tube with a diameter-to-thickness (D/t) ratio of 48. Test 9 was conducted in two phases. First, the specimen was tested in its elastic range using a soil surcharge of ~1920 psf prior and during pile testing. Subsequently, the specimen was removed from the pit and the soil was regenerated to its pristine conditions by liquefying the pit. Then, for the second phase of the test, the specimen was inserted in the pit and was tested in both the elastic and inelastic ranges using a soil surcharge of ~960 psf prior and during pile testing. Phase 1 revealed that by increasing the soil surcharge the effective soil stiffness does increase thereby increasing the lateral strength and tensile strains. For Phase 2 the test was successfully conducted to failure, which was caused by a combination of tube local buckling, tube fracture, and bar fracture, resulting in a large strength degradation (~80.3%) in the third push cycle at ductility level 5 (μ_5). Results presented herein are focused on Phase 2 of the experiment.

5.1.10.2 Test 9 Observations

Test specimen #9 consisted of a 19-foot 5.25-inch long, reinforced concrete filled, 12-inch diameter spirally welded steel tube without skelp or splice welds. The specimen was embedded 13 ft. – 8 in. into sand. The nominal wall thickness of the tube was ¼ in., providing a nominal D/t ratio of 48. The test was conducted with a 5-foot-9.25-inch cantilever length, measured from the soil surface to the point at which the lateral load was applied.

Test specimen #9 performed well through the elastic portion of the test and during all three cycles of ductility level 4 (μ_4). It is believed that onset of tube local buckling occurred during the displacement cycles at that displacement ductility as large tensile strains were recorded in each cycle. A significant loss of strength, indicating failure, occurred during the third push cycle at ductility level 5 (μ_5), as shown in Figure 5-42, where the lateral force vs. top displacement response is presented. The test was terminated (Figure 5-43) after the third push cycle load at ductility 5 (μ_5) when a significant drop in the force of the actuator was observed (i.e., ~80.3%). Sounds indicating steel fracture were heard at the same time when the strength loss occurred, indicating probable bar or tube fracture. Figure 5-44 presents the observed damage after the pile-column was extracted from the soil. As it was thought during the test, tube fracture, tube local buckling and bar fracture did occur. Tube local buckling developed on both sides of the specimen. The sections with the largest tube buckling occurred at depths of 2 ft. – 2 in. and 2 ft. – 4 in. on the South and North sides of the specimen, respectively, where deformations protruded ~5/8 in. The plastic hinge developed at an average depth of 2 ft. – 3 in. with respect to the soil surface. Tube fracture occurred on the South side of the specimen and it extended about half of the cross section perimeter, resulting in a significant drop in strength due to lost tension capacity.

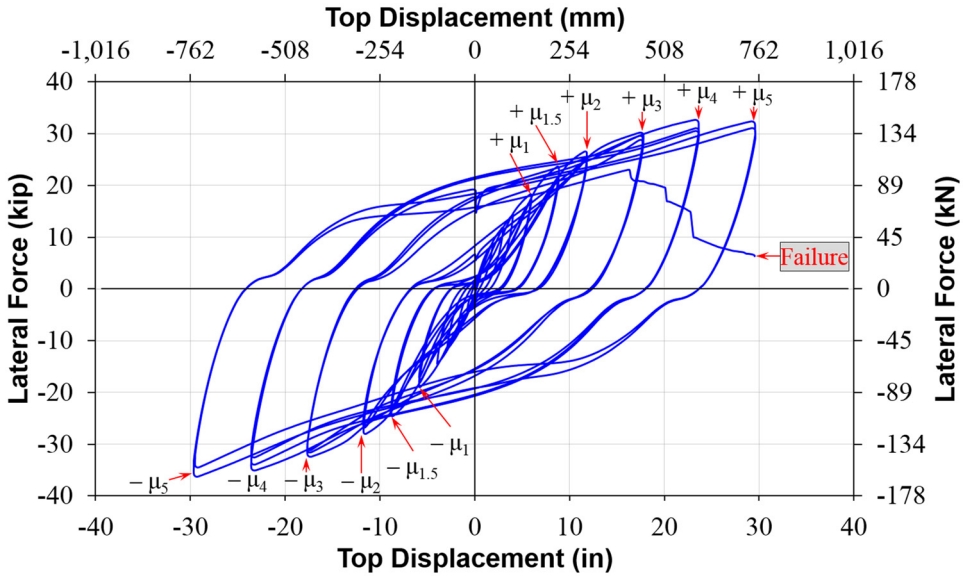

Figure 5-42 Test 9: lateral force vs. top displacement response

Figure 5-43 Test 9: (a) deformed shape, (b) South, and (c) North sides at third cycle of ductility 5; +29.50" of top displacement; +6.35 kips of lateral force

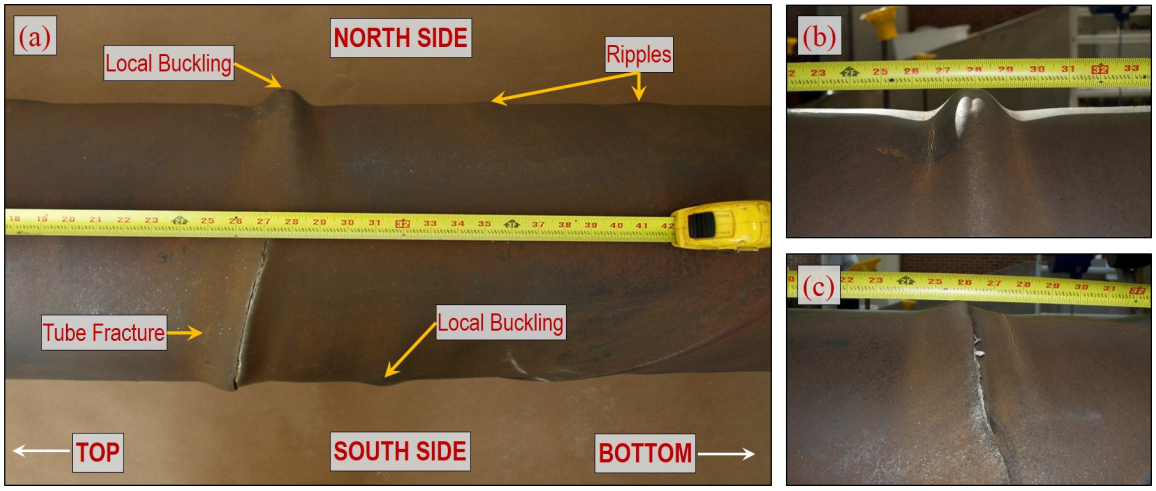

Figure 5-44 Test 9: (a) observed damage, (b) tube buckling on North side, and (c) tube fracture and buckling on South side

5.1.10.3 Test 9 Conclusions

Test specimen #9 showed a reliable response through all ductility 4 (μ4) cycles. It is believed that onset of local buckling occurred at that ductility level as subtle strength loss was observed. The test specimen completed all cycles of ductility 4 (μ_4) with minor loss of strength. Failure of the specimen occurred at ductility level 5 (μ_5) when a significant drop in the strength was observed as the third push cycle was imposed at the specimen head. Further investigations revealed that failure occurred due to a combination of tube local buckling, tube fracture, and bar fracture. It is believed that this particular specimen is capable of having a reliable displacement capacity up to ductility 4 (μ_4). The main buckles as well as the tube fracture did not occur over the spiral weld, so the tube spiral welds do not appear to negatively influence the behavior.

5.1.11. Test 10

5.1.11.1 Test 10 Summary

Test 10 was conducted August 5th, 2016 at the North Carolina State University Constructed Facilities Laboratory. The tested pile-column specimen was a reinforced concrete filled steel tube with a diameter-to-thickness (D/t) ratio of 48. No surcharge was applied to the soil, thus the soil stiffness was not modified. The aboveground height (column length) was increased by 2 ft. with respect to previous tests using the same D/t ratio. The test was successfully conducted to failure, which was caused by a combination of tube local buckling, tube fracture, and bar fracture, resulting in a large strength degradation (~73%) in an additional push cycle at ductility level 5 (μ_5), after three cycle sets at that level were completed. Due to setup constrains, displacements in the pull direction only reached a maximum displacement ductility level 3 (μ_3) for cycles of displacement ductility levels 4 (μ_4) and 5 (μ_5).

5.1.11.2 Test 10 Observations

Test specimen #10 consisted of a 21-foot 5.25-inch long, reinforced concrete filled, 12-inch diameter spirally welded steel tube without skelp or splice welds. The specimen was embedded 13 ft. – 8 in. into sand. The nominal wall thickness of the tube was ¼ in., providing a nominal D/t ratio of 48. The test was conducted with a 7-foot-9.25-inch cantilever length, measured from the soil surface to the point at which the lateral load was applied.

Test specimen #10 performed well through the elastic portion of the test and during all three cycles of ductility level 4 (μ_4). It is believed that onset of tube buckling occurred during the displacement cycles at ductility level 3 (μ_3) as minor loss of strength was observed at the second and third cycle loads at that level. A significant loss of strength, indicating failure, occurred during an additional cycle at ductility level 5 (μ_5), as shown in Figure 5-45, where the lateral force vs. top displacement response is presented. The test was terminated (Figure 5-46) after the fourth cycle load at ductility 5 (μ_5) when a significant drop in the force of the actuator was observed (i.e., ~73%). Sounds indicating steel fracture were heard at the same time when the strength loss occurred, indicating probable bar or tube fracture. Figure 5-47 presents the observed damage after the pile-column was extracted from the soil. As it was thought during the test, tube fracture, tube local buckling and bar fracture did occur; bar buckling was not observed. Tube local buckling developed on both sides of the specimen. The sections with the largest local buckling occurred at depths of 3 ft. – ½ in. on the South side and 2 ft. – 9.5 in. and 3 ft. – 4 in. on the North side of the specimen, respectively, which implies that the plastic hinge developed at an average depth of 3 ft. – 5/8 in. with respect to the soil surface. The largest deformations due to local buckling protruded ~5/8 in. and ~1/2 in. on the South and North sides of the specimen. Tube fracture occurred on the South side of the specimen and it extended about half of the cross section perimeter, resulting in a significant drop in strength due to lost tension capacity.

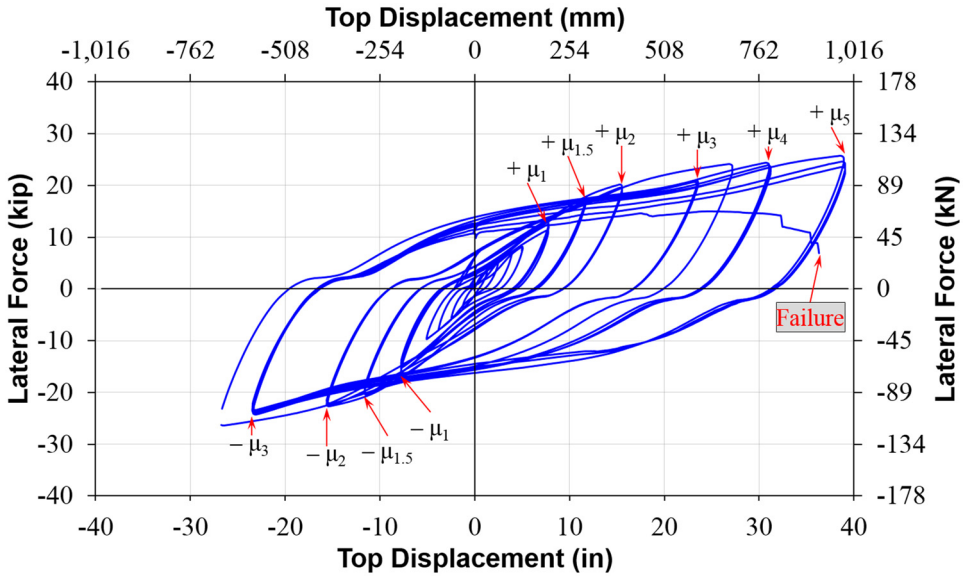

Figure 5-45 Test 10: lateral force vs. top displacement response

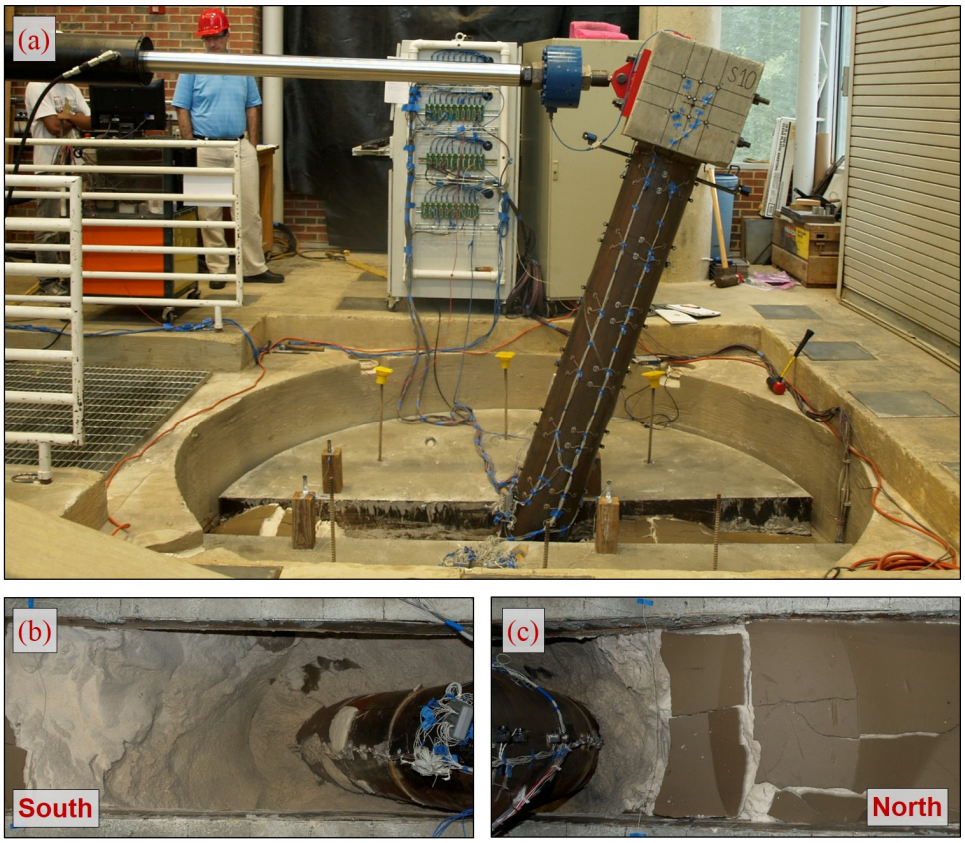

Figure 5-46 Test 10: (a) deformed shape, (b) South, and (c) North sides at fourth cycle of ductility 5; +36.32" of top displacement; +6.95 kips of lateral force

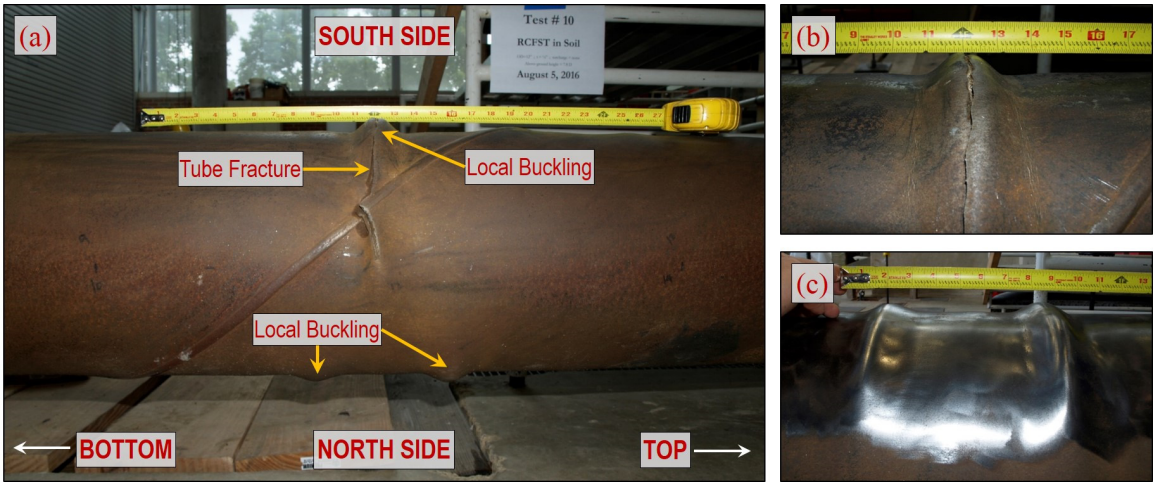

Figure 5-47 Test 10: (a) observed damage, (b) tube buckling and fracture on South side, and (c) tube buckling on North side

5.1.11.3 Test 10 Conclusions

Test specimen #10 showed a reliable response through all ductility 4 (μ_4) cycles. It is believed that onset of tube local buckling occurred at ductility level 3 (μ_3) as subtle strength loss was observed. The test specimen completed all cycles of ductility 4 (μ_4) without significant loss of strength. After all cycles of ductility 5 (μ_5) were completed, an additional push cycle at the same ductility level was induced in the specimen head. Failure of the specimen occurred during that additional push cycle at ductility level 5 (μ_5) when a significant drop in the strength was observed. Further investigations revealed that failure occurred due to a combination of tube local buckling, tube fracture, and bar fracture. Although in the pull direction the specimen was subjected only to a displacement ductility level 3 (μ_3), it is believed that this particular specimen is capable of having a reliable displacement capacity up to ductility 5 (μ_5). The main buckles as well as tube fracture did not occur over the spiral weld, so the tube spiral welds do not appear to negatively influence the behavior.

5.1.12. Test 11

5.1.12.1 Test 11 Summary

Test 11 was conducted August 19th, 2016 at the North Carolina State University Constructed Facilities Laboratory. The tested pile-column specimen was a reinforced concrete filled steel tube with a diameter-to-thickness (D/t) ratio of 95. No surcharge was applied to the soil, thus the soil stiffness was not modified. The aboveground height (column length) was increased by 2 ft. with respect to previous tests using the same D/t ratio. The test was successfully conducted to failure, which was caused by a combination of tube local buckling, tube fracture, and bar buckling, resulting in a large strength degradation (~43%) in the third pull cycle at ductility level 4 (μ_4). Due to issues related to one of the data acquisition systems, part of the data from the experiment was lost. As such, unlike in previous tests observations where the lateral force vs. top displacement response is presented, the envelopes are presented for test 11 in Figure 5-48, as part of the lost information included the lateral force induced by the actuator. These envelopes were plotted using manually recorded data at different performance levels.

5.1.12.2 Test 11 Observations

Test specimen #11 consisted of a 21-foot 5.25-inch long, reinforced concrete filled, 12-3/4-inch diameter spirally welded steel tube without skelp or splice welds. The specimen was embedded 13 ft. – 9 in. into sand. The nominal wall thickness of the tube was 0.134", providing a nominal D/t ratio of 95. The test was conducted with a 7-foot-8.25-inch cantilever length, measured from the soil surface to the point at which the lateral load was applied.

Test specimen #11 performed well through the elastic portion of the test and during all three cycles of ductility level 3 (μ_3). It is believed that onset of tube buckling occurred during the displacement cycles at ductility level 2 (μ_2) as minor loss of strength was observed at the second and third cycles at that level. A significant loss of strength, indicating failure, occurred during the third pull cycle at ductility level 4 (μ_4), as shown in Figure 5-48, where the lateral force vs. top displacement envelopes are presented. The test was terminated (Figure 5-49) after the third pull cycle load at ductility 4 (μ_4) when a significant drop in the force of the actuator was observed (i.e., ~43%). Sounds indicating steel fracture were heard at the same time when the strength loss occurred, indicating probable bar or tube fracture. Figure 5-50 presents the observed damage after the pile-column was extracted from the soil. As it was thought during the test, tube fracture and tube local buckling did occur; bar buckling was also observed. Tube local buckling developed at depths of 2 ft. – 5.5 in. and 3 ft. – 6 in. on the South side, and 2 ft. – 2 in. and 3 ft. – 2 in. on the North side of the specimen, which implies that the plastic hinge developed at an average depth of 2 ft. – 10.12 in. with respect to the soil surface. The largest deformations due to local buckling protruded ~½ in. on both South and North sides of the specimen. Tube fracture occurred on the North side of the specimen and it extended about half of the cross section perimeter, resulting in a significant drop in strength due to lost tension capacity.

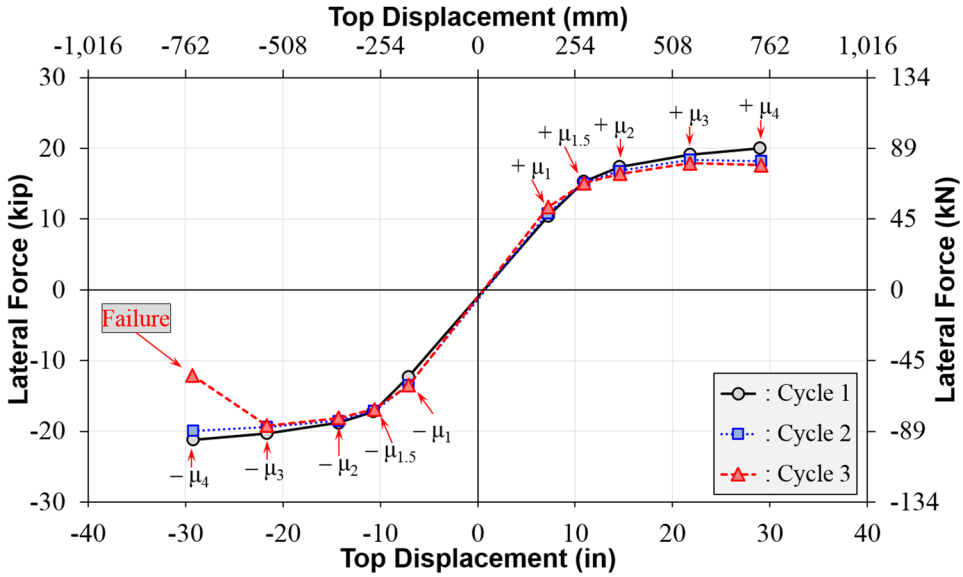

Figure 5-48 Test 11: lateral force vs. top displacement envelopes

Figure 5-49 Test 11: (a) deformed shape, (b) South, and (c) North sides at third cycle of ductility 4; −29.07" of top displacement; −17.60 kips of lateral force

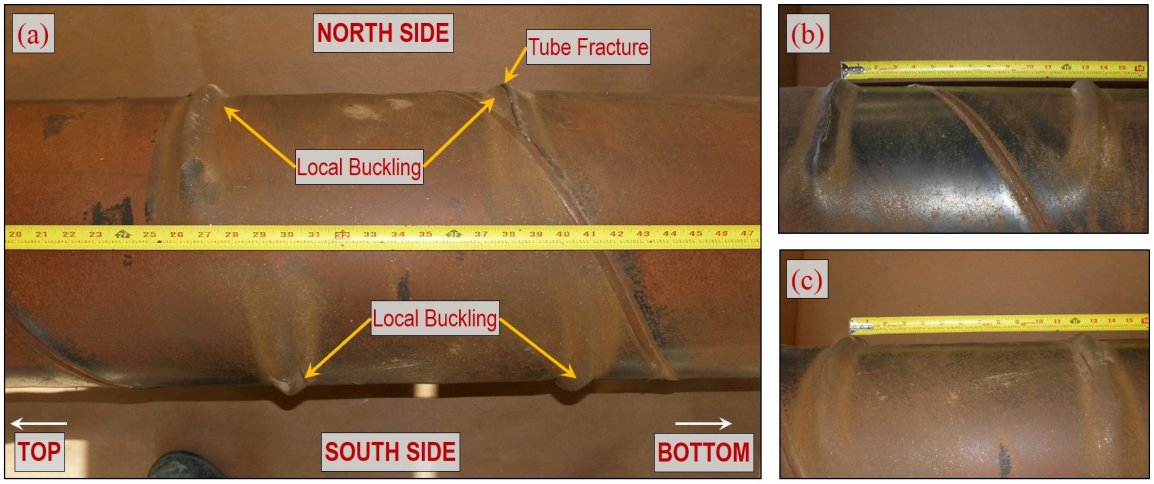

Figure 5-50 Test 11: (a) observed damage, (b) tube buckling and fracture on North side, and (c) tube buckling on South side

5.1.12.3 Test 11 Conclusions

Test specimen #11 showed a reliable response through all ductility 3 (μ_3) cycles. It is believed that onset of tube local buckling occurred at ductility level 2 (μ_2) as subtle strength loss was observed. The test specimen completed all cycles of ductility 3 (μ_3) without significant loss of strength. Failure of the specimen occurred during the third pull cycle at ductility level 4 (μ_4) when a significant drop in the strength was observed. Further investigations revealed that failure occurred due to a combination of tube local buckling, tube fracture, and bar buckling. It is believed that this particular specimen is capable of having a reliable displacement capacity up to ductility 3 (μ_3). The main buckles as well as tube fracture did not occur over the spiral weld, so the tube spiral welds do not appear to negatively influence the behavior.

5.1.13. Test 12

5.1.13.1 Test 12 Summary

Test 12 was conducted September 22nd, 2016 at the North Carolina State University Constructed Facilities Laboratory. The tested pile-column specimen was a reinforced concrete filled steel tube with a diameter-to-thickness (D/t) ratio of 68. No surcharge was applied to the soil, thus the soil stiffness was not modified. The aboveground height (column length) was increased by 2 ft. with respect to previous tests using the same D/t ratio. The test was successfully conducted to failure, which was caused by a combination of tube local buckling, tube fracture, bar buckling, and bar fracture, resulting in a large strength degradation (~57.9%) in the second pull cycle at ductility level 4 (μ_4). Due to setup constrains, displacements in the push direction only reached a maximum displacement ductility level 3.5 ($\mu_{3.5}$) for all push cycles of displacement ductility level 4 (μ_4).

5.1.13.2 Test 12 Observations

Test specimen #12 consisted of a 21-foot 5.25-inch long, reinforced concrete filled, 12-3/4-inch diameter spirally welded steel tube without skelp or splice welds. The specimen was embedded 13 ft. – 9 in. into sand. The nominal wall thickness of the tube was 3/16 in., providing a nominal D/t ratio of 68. The test was conducted with a 7-foot-8.25-inch cantilever length, measured from the soil surface to the point at which the lateral load was applied.

Test specimen #12 performed well through the elastic portion of the test and during all three cycles of ductility level 3 (μ_3). It is believed that onset of tube buckling occurred during the displacement cycles at ductility level 2 (μ_2) as large tensile strains in combination with minor loss of strength were observed at the second and third cycles at that level. A significant loss of strength, indicating failure, occurred during the second pull cycle at ductility level 4 (μ_4), as shown in Figure 5-51, where the lateral force vs. top displacement response is presented. The test was terminated (Figure 5-52) after the second pull cycle load at ductility 4 (μ_4) when a significant drop in the force of the actuator was observed (i.e., ~57.9%). Sounds indicating steel fracture were heard at the same time when the strength loss occurred, indicating probable bar or tube fracture. Figure 5-53 presents the observed damage after the pile-column was extracted from the soil. As it was thought during the test, tube fracture, tube local buckling, and bar fracture did occur; bar buckling was observed on the North side of the specimen. Tube local buckling developed at depths of 2 ft. – 11.25 in. and 2 ft. – 11.50 in. on the South and North sides of the specimen, respectively, which implies that the plastic hinge developed at an average depth of 2 ft. – 11.37 in. with respect to the soil surface. The largest deformations due to local buckling protruded ~½ in. and ~¾ in. on the South and North sides of the specimen. Tube fracture occurred on the North side of the specimen and it extended about half of the cross section perimeter, resulting in a significant drop in strength due to lost tension capacity.

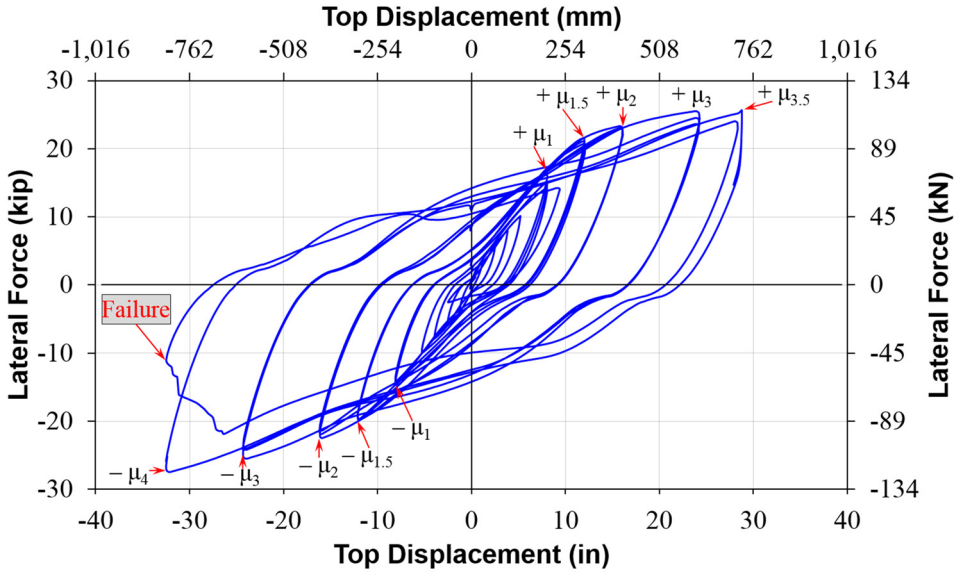

Figure 5-51 Test 12: lateral force vs. top displacement response

Figure 5-52 Test 12: (a) deformed shape, (b) South, and (c) North sides at second pull cycle of ductility 4; −32.32” of top displacement; −11.53 kips of lateral force

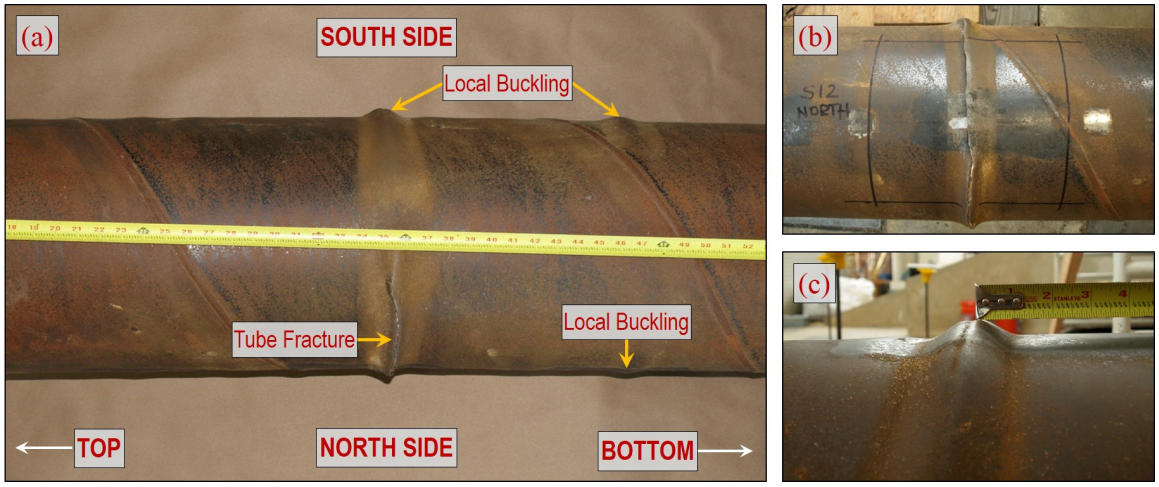

Figure 5-53 Test 12: (a) observed damage, (b) tube fracture on North side, and (c) tube buckling on South side

5.1.13.3 Test 12 Conclusions

Test specimen #12 showed a reliable response through all ductility 3 (μ_3) cycles. It is believed that onset of tube local buckling occurred at ductility level 2 (μ_2) as large tensile strains and subtle strength loss were observed. The test specimen completed all cycles of ductility 3 (μ_3) without significant loss of strength. Failure of the specimen occurred during the second pull cycle at ductility level 4 (μ_4) when a significant drop in the strength was observed. Further investigations revealed that failure occurred due to a combination of tube local buckling, tube fracture, bar buckling, and bar fracture. Although in the push direction the pile was subjected only to a displacement ductility level 3.5 ($\mu_{3.5}$), it is believed that this particular specimen is capable of having a reliable displacement capacity up to ductility 3 (μ_3). The main buckles as well as tube fracture did not occur over the spiral weld, so the tube spiral welds do not appear to negatively influence the behavior.

5.2. Summary of Experimental Observations

Summarized in Table 5-16 are the results of the experimental tests. This table includes the following: (1) the effective elastic stiffness, which was calculated using the average force and displacement from the three cycles at ductility 1 (μ_1); (2) the reliable displacement, which was calculated as the average displacement at the ductility cycle before that at which the pile-column specimens reached failure; (3) the tensile strain, which corresponds to the average maximum tensile strain within the strain profiles recorded at the ductility level corresponding to the reliable displacement; and (4) the depth to the plastic hinge, which is the average depth at which tube local buckling and tube fracture were observed. Further details regarding experimental observations of each pile-column specimen can be found at the end of this document in APPENDIX A: Short reports of experimental tests.

The remaining of this section presents a discussion based upon the experimental observations and analysis of the data. For that purpose, and for the sake of brevity, comparison of results of six of the twelve specimens is presented considering the impacts of: (1) D/t ratio, (2) soil stiffness, and (3) aboveground length. It is important to note that results of Test 2, Test 3, and Test 4 were not considered in the analysis due to issues related to the data acquisition or due to issues related to fracture of the tube spiral welds.

Table 5-16 Summary of experimental observations

Test No.	D/t Ratio	La/D Ratio	Soil Surcharge (psf)	Yield Displ. (in)	Yield Force (kips)	Elastic Stiffness (kip/in)	Reliable Displacement	(in)	Tensile Strain (%)	Depth to Tensile Strain (ft)	Depth to Plastic Hinge (ft)
1	48	5.42	None	6.07	17.41	2.87	μ 4.0	24.92	3.28	3.27	3.23
2	48	5.83	960	5.70	17.41	3.06	μ 5.0	28.75	NA	NA	2.52
3	95*	5.18	None	6.17	14.32	2.32	μ 2.0	12.50	NA	NA	NA
4	95*	5.18	960	5.50	17.56	3.19	μ 1.5	8.30	NA	NA	NA
5	95	5.35	None	5.60	12.70	2.27	μ 3.0	16.92	2.09	3.69	2.93
6	95	5.53	960	5.29	15.47	2.92	μ 3.0	16.02	2.39	1.48	2.58
7	68	5.43	None	5.99	15.10	2.52	μ 4.0	24.08	3.17	3.58	3.02
8	68	5.43	960	5.72	18.91	3.31	μ 3.0	17.25	2.28	2.25	2.52
9	48	5.77	960	5.87	17.73	3.02	μ 4.0	23.56	3.43	1.62	2.25
10	48	7.77	None	7.73	13.75	1.78	μ 4.0	31.20	2.63	2.58	3.05
11	95	7.24	None	7.16	12.03	1.68	μ 3.0	21.96	2.84	2.67	2.84
12	68	7.24	None	8.03	14.74	1.84	μ 3.0	24.30	2.75	2.67	2.95

* Steel tube spiral weld fracture due to partial joint penetration weld detail

5.2.1. Failure Mechanism

The characteristic failure mode of the tested RCFST pile-column specimens was in agreement with that reported from experimental tests of RCFST piles in the air (Brown et al., 2015; González-Román et al., 2008). This failure mode is described as follows. First, as curvature deformations increase below ground, due to a lateral displacement induced at the pile-column head, ripples develop on the extreme compression and tension fibers of the RCFST cross section at region within the location of maximum moment. Eventually, onset of outward tube local buckling takes place in one or more sections on both extreme compression and tension fibers. As lateral displacement demands increase, deformations due to local buckling also increase; deformations due to local buckling protruded in average ~5/8 in. Due to large local deformations at the buckled sections, the effective thickness of the tube is reduced. Therefore, these sections weaken as tube local buckling develops further due to repeated cycles of compression. Finally, steel tube fracture occurs at the section with the largest deformations due to tube local buckling. In most of the specimens tested, fracture developed along half of the cross section perimeter. This failure mechanism is depicted in Figure 5-54.

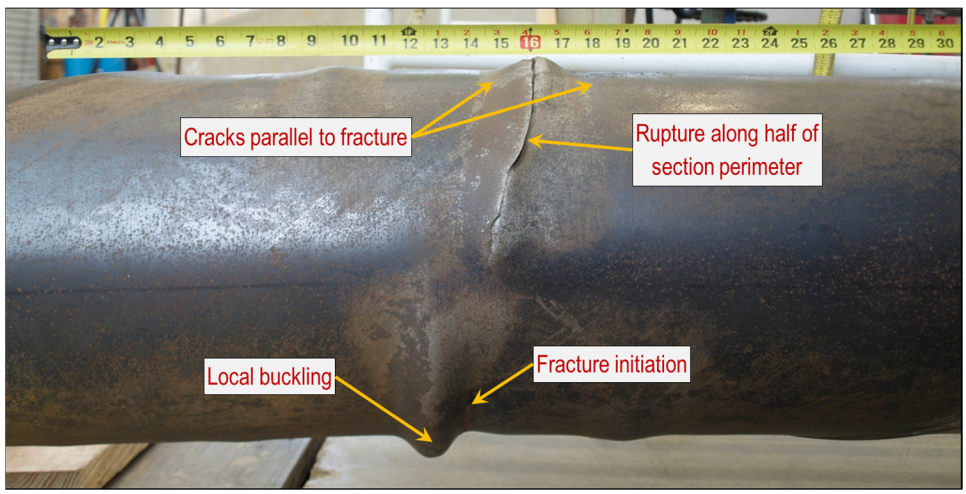

Figure 5-54 Typical failure mechanism

5.2.2. Influence of Tube Spiral Welds

As previously mentioned, two of the twelve RCFST pile-column specimens exhibited a different failure mechanism to that described earlier in this section. Such specimens were those of Test 3 and Test 4, which utilized tubes with D/t = 95*. The symbol "*" indicates the unexpected failure mechanism of those tubes. Such a failure mechanism consisted of tube spiral weld fracture (Figure 5-55) at low displacement demands, namely, ductility 3 (μ_3) and ductility 2 (μ_2), respectively, as shown in Figure 5-56.

After the test were completed, further examination of the inside of the spirally-welded tubes revealed that the thin wall tubes (D/t = 95*) which make up tests 3 and 4 were not welded along the inside surface, but rather only upon the outside surface. This indicates that a partial joint penetration (PJP) weld process was utilized to manufacture such tubes.

Furthermore, the tension test performed on the coupon with D/t =95*, across the spiral weld, indicated fracture of the weld at a low strain levels, and barely developing the yield strength of the material, as shown in Figure 5-57.

As previously noted, the steel tube manufacturer sent three replacement tubes with D/t = 95 that were welded on both inside and outside surfaces, namely, a complete penetration joint (CPJ) weld process was utilized to manufacture this tubes. Tension tests conducted on coupons cut off the new set of tubes revealed that full plastic capacity was developed, including the coupon across the spiral weld, in which failure occurred away from the welded section, as shown in Figure 5-58. The new set of three tubes with D/t = 95 were utilized to conduct Test 5, Test 6, and Test 11.

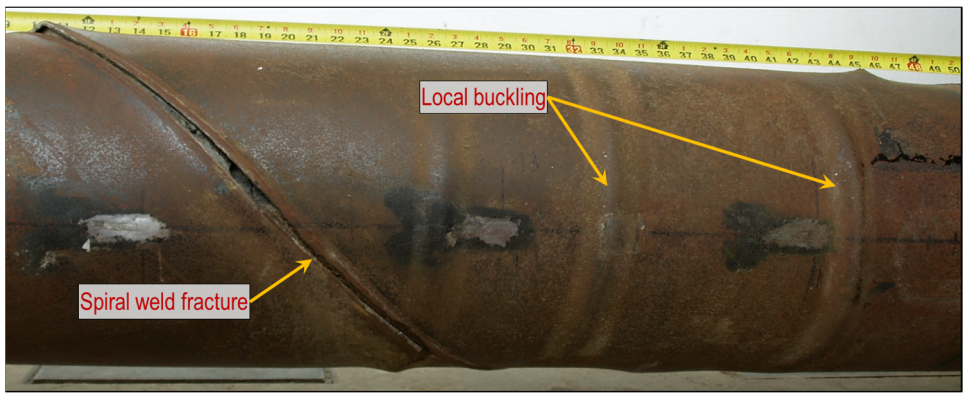

Figure 5-55 Spiral weld fracture observed on Test 3 and Test 4 due to incomplete weld penetration

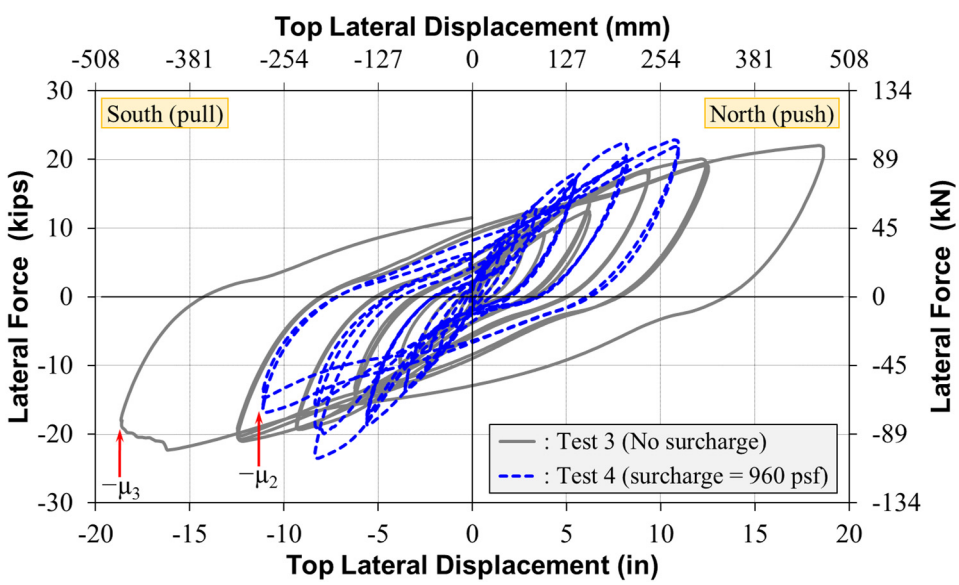

Figure 5-56 Lateral force vs. top lateral displacement response of Test 3 and Test 4

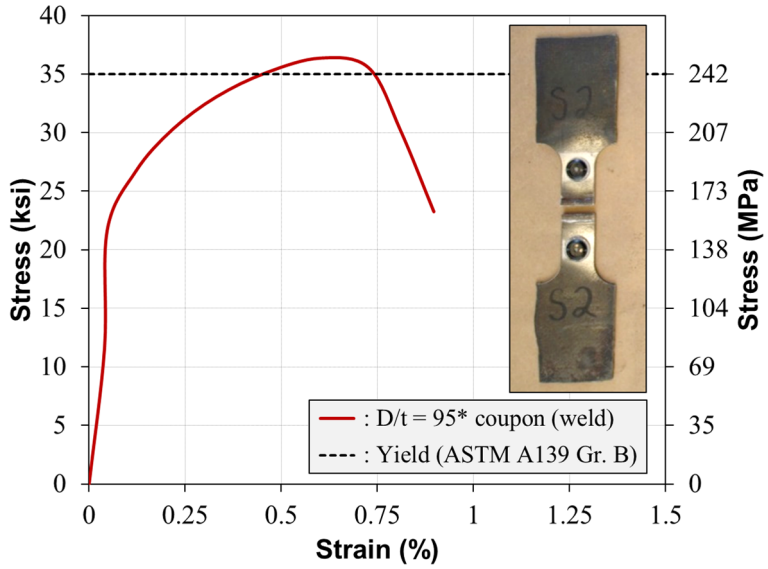

Figure 5-57 Spiral weld coupon tension test (D/t = 95*)

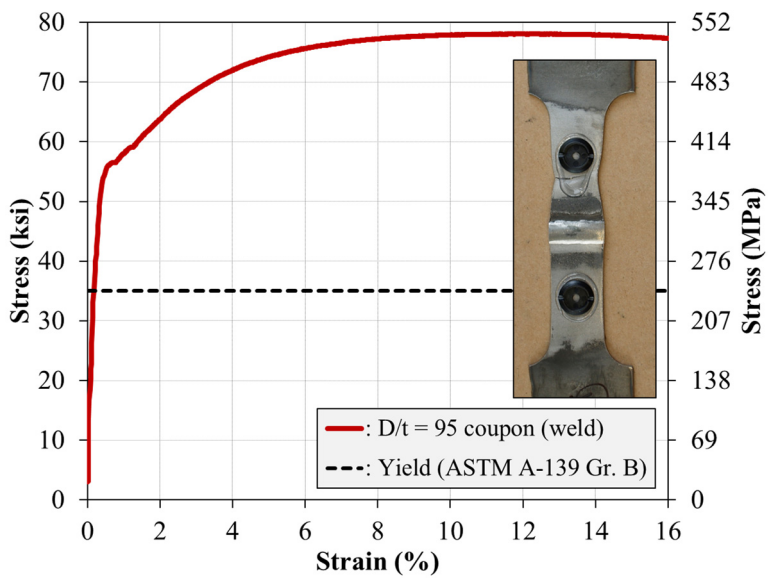

Figure 5-58 Spiral weld coupon tension test (D/t = 95)

5.2.3. Depth to Plastic Hinge

The depth to the plastic hinge was determined from the observed damage in the specimens once each test was completed, namely, measurements of the depth to each section with tube fracture, and to sections with evident signs of tube local buckling, were averaged to determine the depth to the plastic hinge. As previously mentioned, tube fracture occurred in the section with the largest deformations due to tube buckling. It is worth noting that some specimens exhibited more than one buckled section. The location of such sections depends on the depth to the maximum moment, which in turn depends on the lever arm. As such, depending upon the interaction of the sand filling the soil-pile gap, the lever arm will change, thereby moving the point to the maximum moment during the test.

Figure 5-59 shows the measured depth to plastic hinge. Note that he above-ground length does not impact the depth to the plastic hinge. The soil stiffness (i.e., soil surcharge) does have an effect on the depth to the plastic hinge. For example, for the specimen with D/t = 48 and a stiff soil profile (surcharge = 960 psf), the depth to the plastic hinge moved about one pile diameter closer to the surface when compared to test specimens using the same D/t ratio without surcharge on the soil surface.

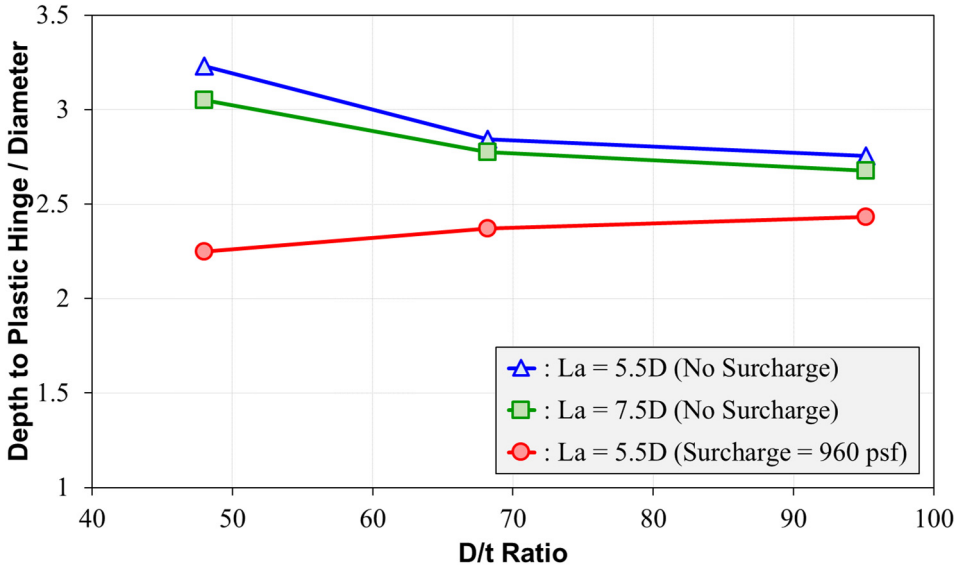

Figure 5-59 Experimental depth to plastic hinge

5.2.4. Force–Displacement Response

As an example of the overall response, Figure 5-60 through Figure 5-62 present a comparison of the top lateral force vs. displacement response for six of the twelve specimens. The percentage values in Figure 5-60 and Figure 5-61 represent the large-to-small ratio between the forces of two tests, recorded at the first cycle of each displacement ductility level. Note from this figures that the displacements at each ductility level are slightly different due to the difference on the equivalent yield displacement of each specimen. In Figure 5-62 the forces developed by the specimens is not compared because there is a significant difference on the displacements at each ductility level.

Regarding the impact of the D/t ratio, as expected, note from Figure 5-60 that this parameter has a direct effect on the behavior. For the thick wall tube (D/t = 48) the developed lateral strength is higher than that of the thin wall tube (D/t = 95). Note that during the pull cycles the developed lateral strength is slightly higher than that of the push cycles.

Regarding the impact of the soil stiffness (soil surcharge), Figure 5-61 compares the response of specimens with D/t = 95 for two different soil conditions, namely, without soil surcharge (Test 5) and with a soil surcharge of 960 pfs (Test 6). Note that for the stiffer soil condition (Test 6) the specimen developed a higher lateral strength overall. However, as the displacement demand increased the difference in the lateral strength dropped from ~30% at ductility 1 (μ_1) to ~10% at ductility 4 (μ_4).

As for the impact of the aboveground length on the force-displacement response, it can be seen from Figure 5-62 that a longer aboveground length (Test 12) will result in a smaller lateral strength when specimens with the same D/t are compared.

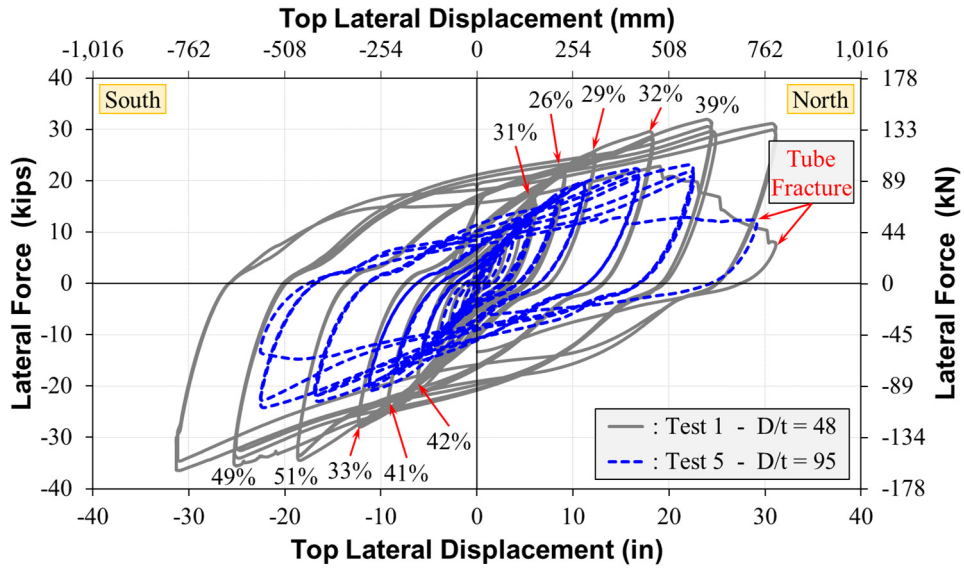

Figure 5-60 Impact of D/t ratio on force vs. displacement response

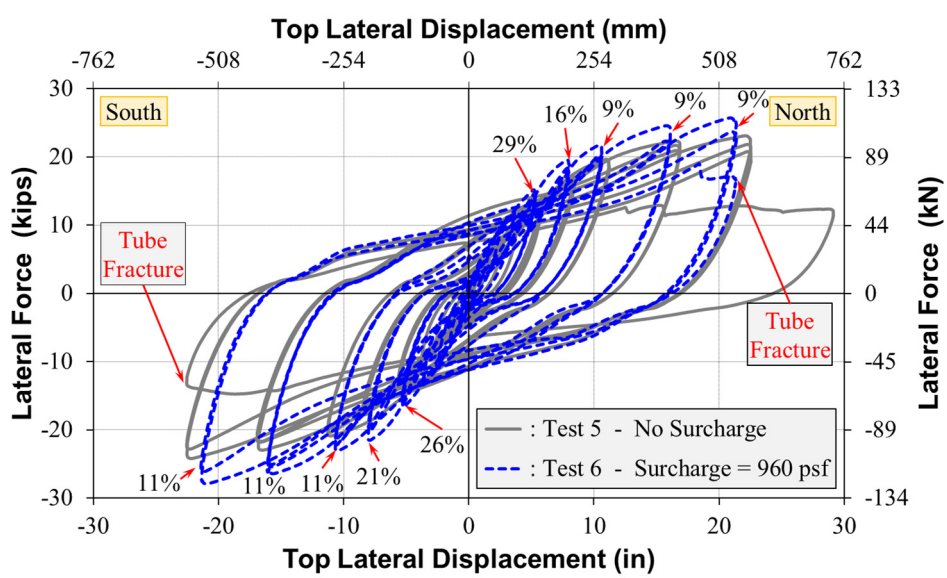

Figure 5-61 Impact of soil stiffness on force vs. displacement response

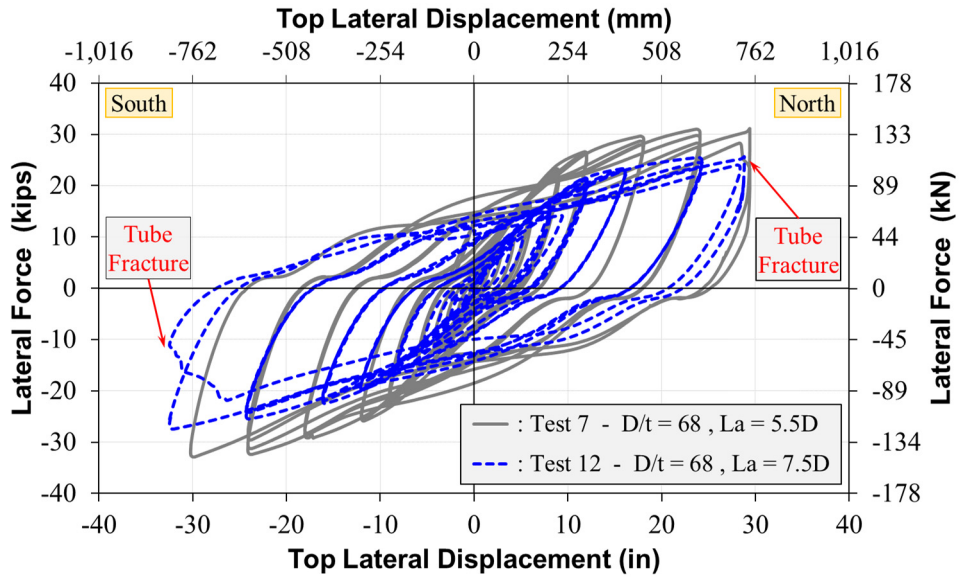

Figure 5-62 Impact of above-ground length on force vs. displacement response

The main differences of the force-displacement response can also be seen by comparing the effective elastic stiffness and the reliable displacement, as shown in Figure 5-63 and Figure 5-64, respectively. The effective elastic stiffness was calculated using the average force and displacement recorded at the peaks of the three loading cycles at ductility 1 (μ_1). The reliable displacement was calculated using the average force and displacement recorded at the peaks of the three loading cycles at the ductility level prior to that when failure of the specimen was observed.

Note from Figure 5-63 that the effective elastic stiffness does not change as much for different D/t ratios. The soil stiffness (soil surcharge) and the aboveground length, on the other, do have an evident impact on the system stiffness. In the case of the elastic stiffness, note that only for the specimen using a tube with D/t = 48, and a soil surcharge of 960 psf (i.e., Test 9), this parameter did not change significantly when compared to results of Test 1, in which a soil surcharge was not applied. In regards to the reliable displacement on the other hand, note from Figure 5-64 that there is a clear trend for such a displacement to decrease with an increase on the D/t ratio. Note that all specimens with D/t = 48 reached a reliable displacement ductility 4 (μ_4), whereas all other specimens reached ductility 3 (μ_3), except for the specimen from Test 7 (D/t = 68, no surcharge), which reached a reliable displacement ductility 4 (μ_4).

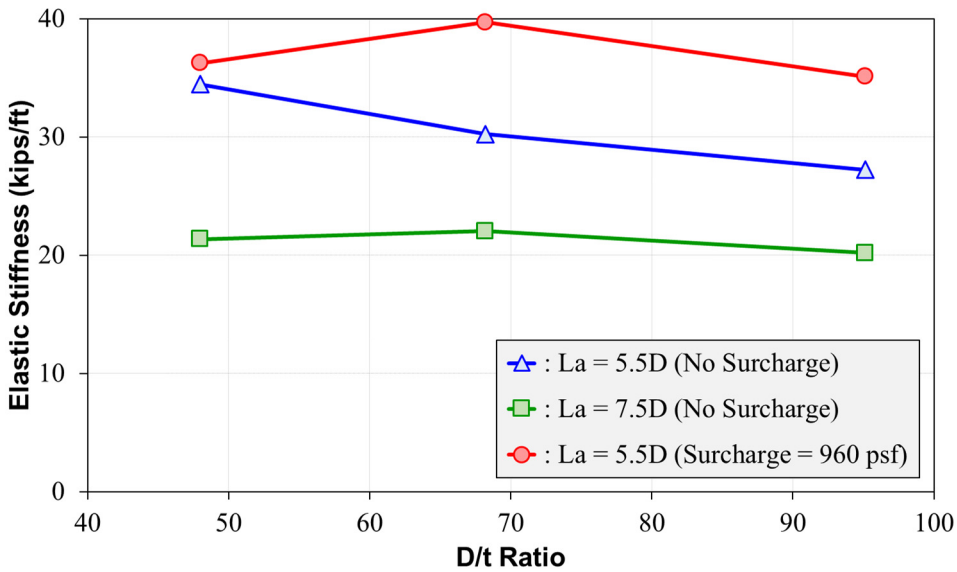

Figure 5-63 Experimental elastic stiffness

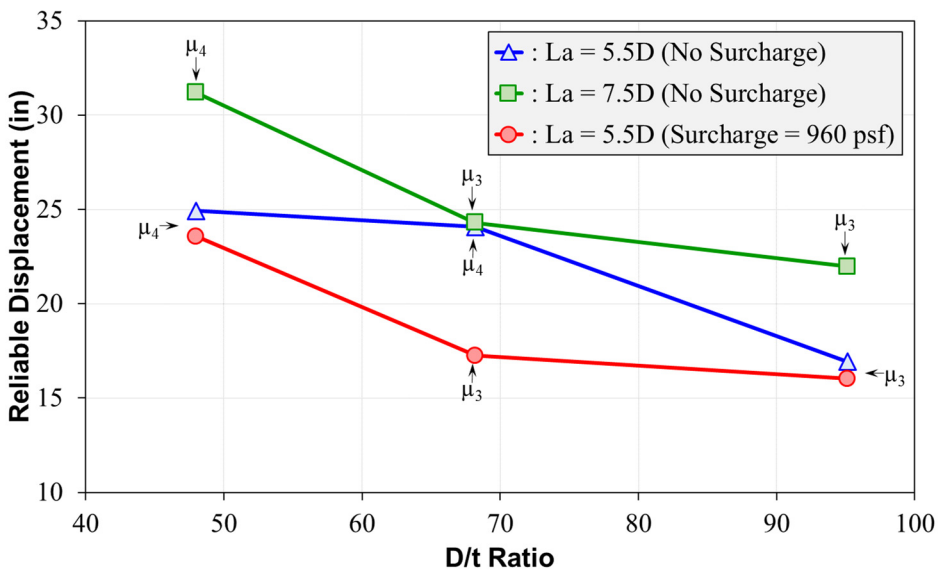

Figure 5-64 Experimental reliable displacement

5.2.5. Hysteretic Equivalent Viscous Damping

The effects of the D/t ratio, soil stiffness (surcharge), and aboveground length on the hysteretic equivalent viscous damping (EVD) are presented in Figure 5-65 through Figure 5-67, respectively. It can be seen from Figure 5-65 that major differences on the hysteretic EVD due to the D/t ratio occurred mostly at small and large ductility levels, namely, ductility 1 (μ_1) and ductility 4 (μ_4). Furthermore, the contribution of the soil and the effect of the soil stiffness on the hysteretic EVD can be seen in Figure 5-66. This figure also includes results (continuous black line) calculated using the equation proposed by Brown et al. (2015), which only accounts for the contribution of the RCFST element to the hysteretic EVD by considering the D/t ratio. Note that there is a clear difference with the experimental results of Test 5 (D/t = 95, no surcharge) and Test 6 (D/t = 95, surcharge = 960 psf), that is,

the hysteretic EVD was ~3.5% and ~2% higher, respectively, than that of the results which do not consider the soil contribution. Also, note that results from Test 6 (surcharge = 960 psf) are consistently smaller than those from Test 5 (no surcharge); this is indeed related to the higher lateral strength observed in Test 6 in combination with the smaller induced displacements that resulted from the smaller equivalent yield displacement of Test 6.

In Figure 5-66, of especial interest are the experimental results at ductility 1 (μ_1); note that EVD values of 6.6% and 5.9% were obtained for Test 5 and Test 6, respectively. This implies that for small displacement demands, in the range of the equivalent yield displacement, there is a large energy dissipation. This could be an important consideration for seismic design because for low-to-moderate seismic activity the soil contribution could potentially result in a significant reduction in the demand of a pile-column system.

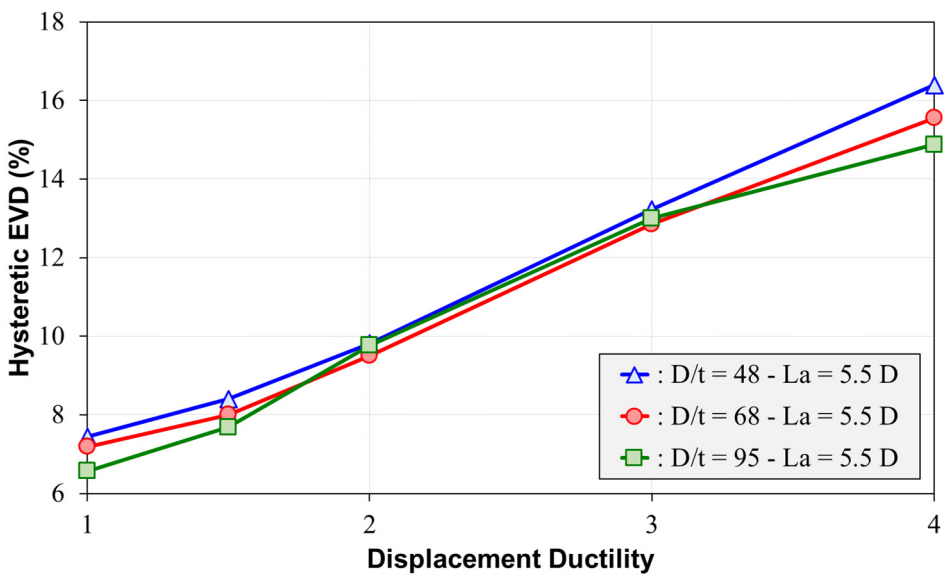

Figure 5-65 Impact of D/t ratio on hysteretic equivalent viscous damping

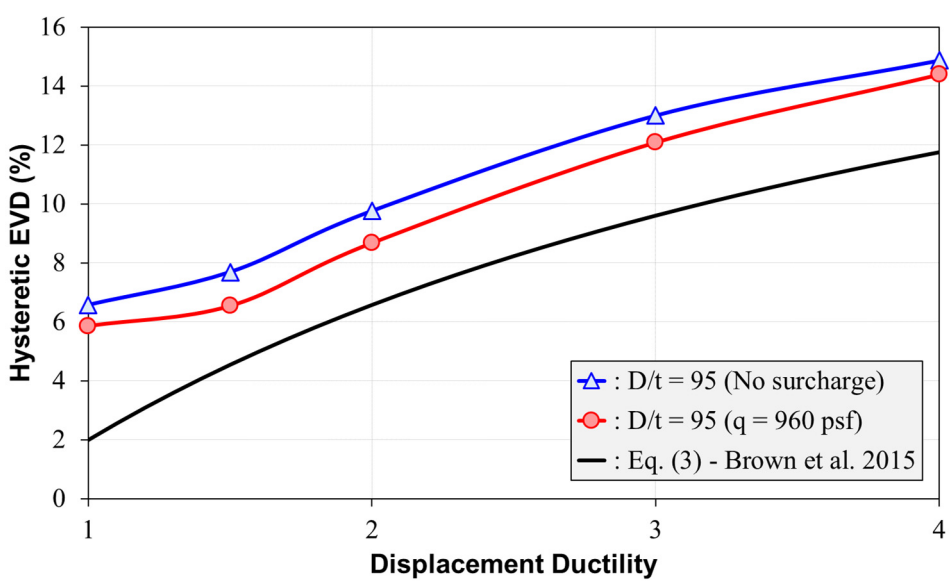

Figure 5-66 Impact of soil stiffness on hysteretic equivalent viscous damping

Figure 5-67 shows the effects of the aboveground length on the hysteretic EVD for specimens with D/t = 68. Note that there is a small difference (~0.5%) on the results due to the different aspect ratio.

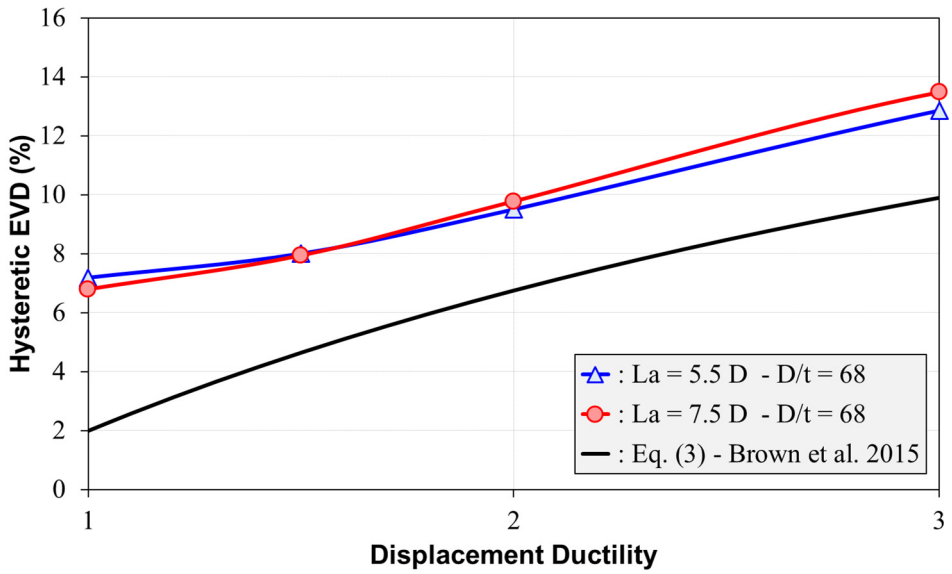

Figure 5-67 Impact of above-ground length on hysteretic equivalent viscous damping

5.2.6. Strain Limit States

Tensile strain profiles for the first push and pull cycles at different ductility levels are presented in Figure 5-68 through Figure 5-69. Note that the D/t ratio has a minor impact on the tensile strains, as shown in Figure 5-68. The soil stiffness (surcharge), on the other hand, does have a significant impact on the strain profiles. Note from Figure 5-69 that not only does the depth to the maximum strain is different, between specimens of Test 5 (no surcharge) and Test 6 (surcharge =960 psf), but also the strain gradient (i.e., moment gradient) changes. This means that, as evidenced from the strain profiles with a stiffer soil profile, the maximum strains occurred closer to the soil surface, which correlates well with an increased lateral strength due to a shorter lever arm. Therefore, the spread of inelastic action is reduced, which causes slightly larger tensile strains.

Moreover, of particular interest are the results presented in Figure 5-70. In this case, the comparison of strain profiles is focused on specimens with D/t = 68 and different aboveground lengths, namely, Test 7 (La = 5.5 D) and Test 12 (La = 7.5 D). Note that for a longer aboveground length, the spread of inelastic action increases and the depth to the maximum strain moves closer to the soil surface. In addition, note that tensile strains are consistently higher (~0.5%) for a longer aboveground length. A summary of the tensile strains, observed at the ductility level prior to that when tube fracture occurred, is presented in Figure 5-71. Note that the experimental results do not have a clear trend but rather they are consistent with the limit of 2.5% reported by Brown et al., 2015.

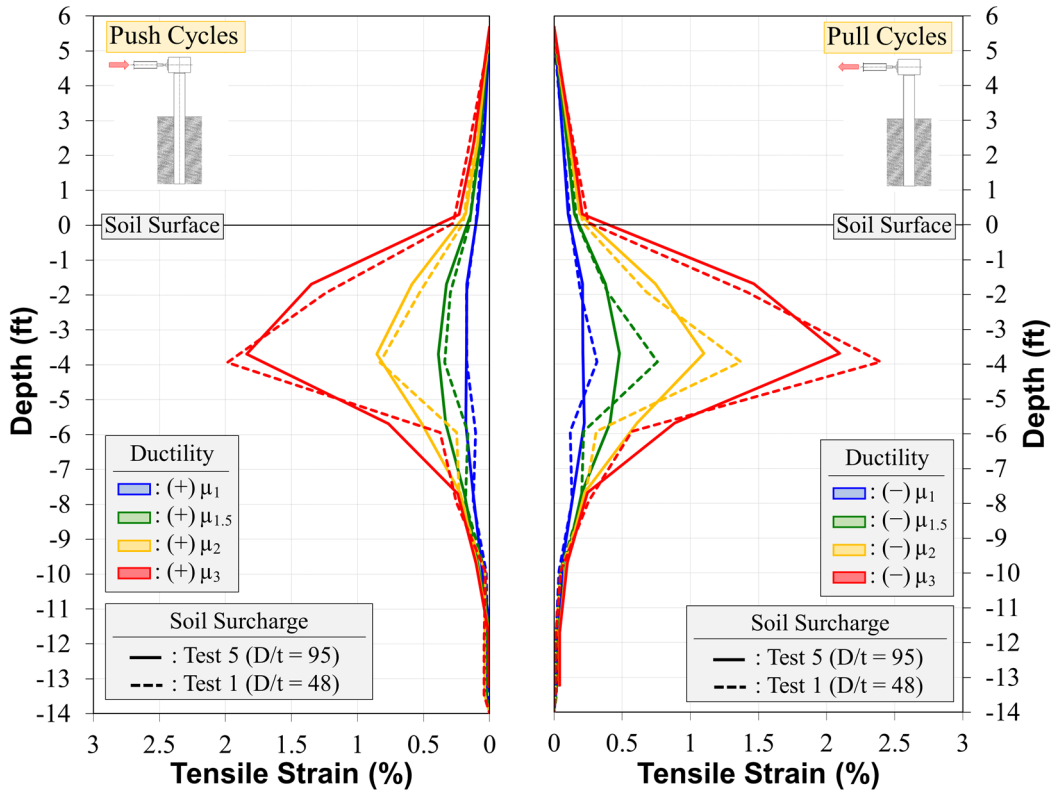

Figure 5-68 Impact of D/t ratio on tensile strains

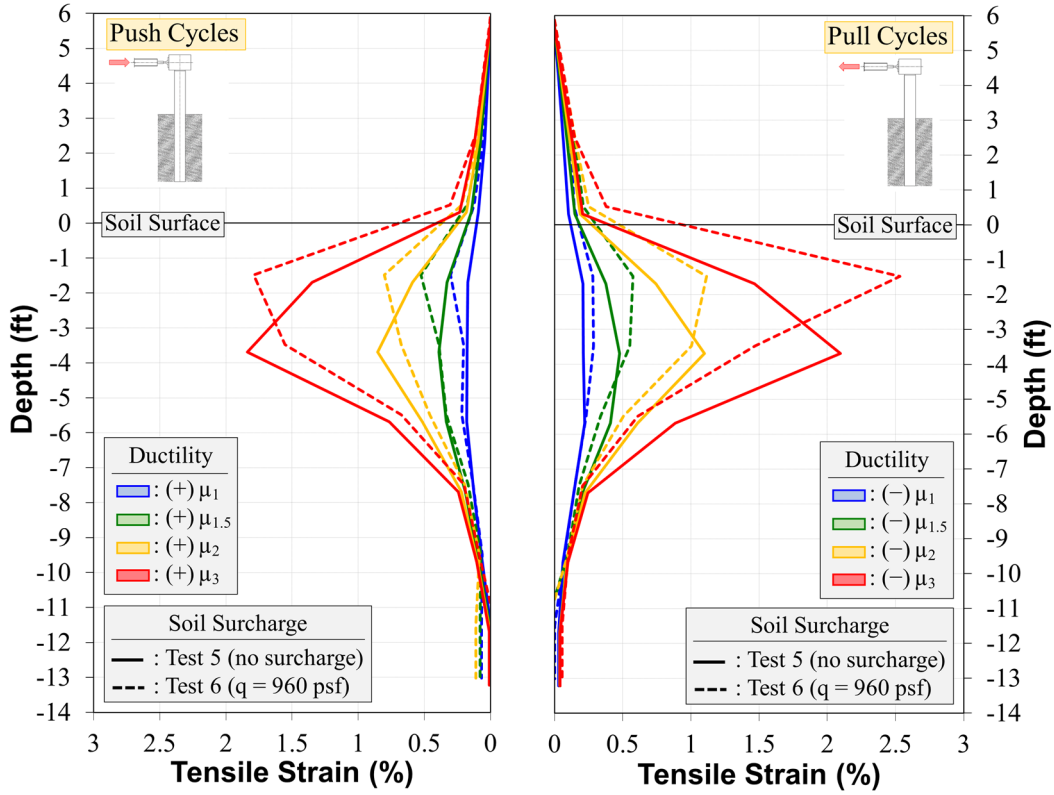

Figure 5-69 Impact of soil stiffness on tensile strains

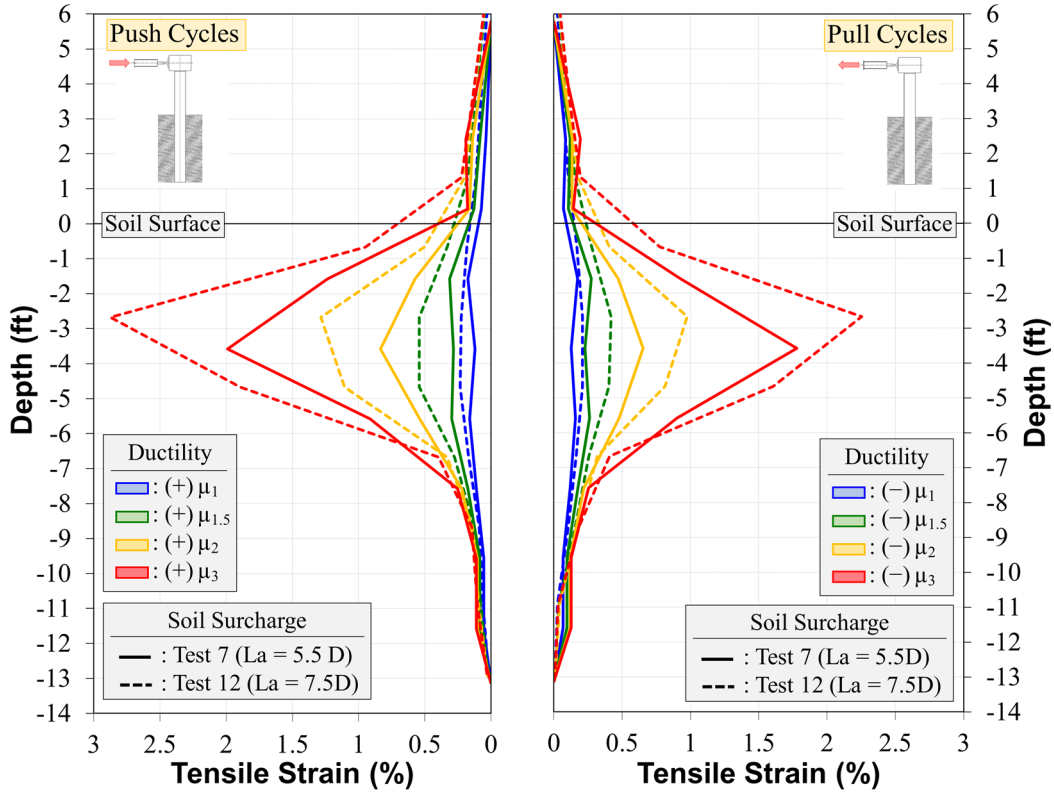

Figure 5-70 Impact of above-ground length on tensile strains

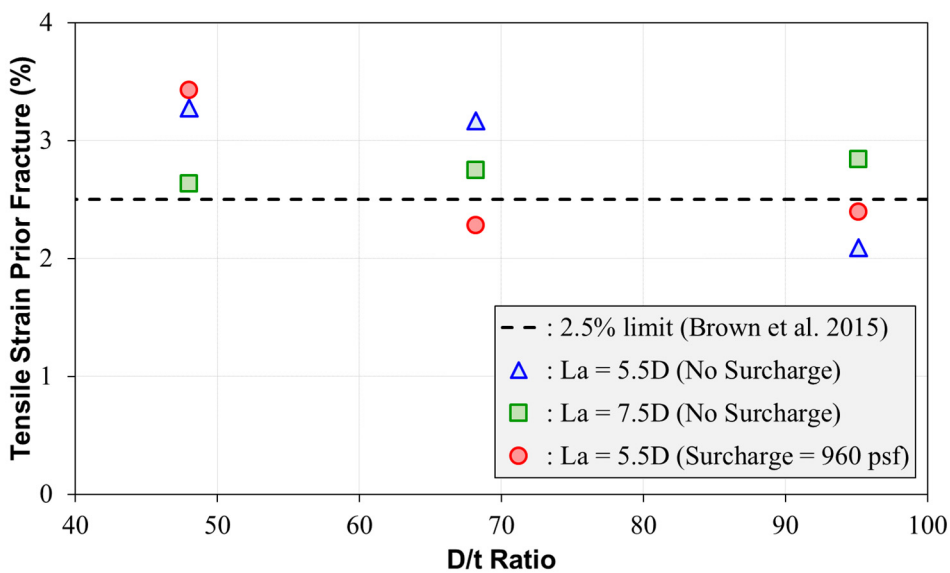

Figure 5-71 Summary of tensile strain prior tube fracture

CHAPTER 6

6. PARAMETRIC STUDY RESULTS

This chapter presents the results of the 36 moment-curvature analyses and the 648 simulations, conducted on RCFST shafts. The results are presented in terms of the variables studied and the resulting equations in four parts. The first part shows the results of the section analyses. Then, the second and third parts show results of the simulations on pinned-head and fixed-head RCFST shafts, respectively. Finally, an evaluation of the proposed model is presented by means of a comparison between simulated results and those predicted using the proposed equations.

6.1. Section Analysis

Moment-curvature analyses were conducted on RCFST sections using three diameters and D/t ratios, along with four levels of axial load. Analysis for RC sections were not conducted as recommendations regarding the yield curvature parameter ($c_{\phi y}$) and the neutral axis depth (c) can be found in the literature (Priestley et al., 2007); for completion, such recommendations are presented here, though they were introduced in previous sections. For circular RC columns, Priestley et al. (2007) suggest $c_{\phi y}$ to be taken as 2.25 and the neutral axis depth to be calculated as show in Equation 6-1.

$$\frac{c}{D} = 0.2 + 0.65\frac{P}{f_{ce}'A_g} \qquad \text{Equation 6-1}$$

6.1.1. Yield curvature parameter for RCFSTs

Figure 6-1 and Figure 6-2 show the impact of D/t ratio and axial load ratio (ALR) on the yield curvature parameter ($c_{\phi y}$). Note that in both cases the impact is negligible. In fact, note from the dotted lines in Figure 6-2 that the results fall within ± 2.5% of the predicted average value $c_{\phi y}$ = 2.67.

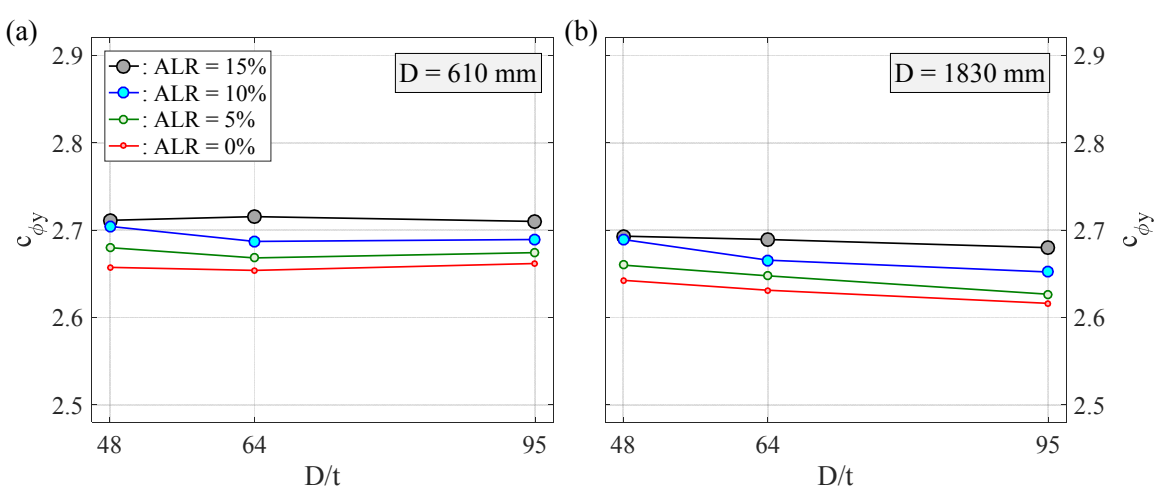

Figure 6-1 Impact of D/t ratio on $c_{\phi y}$ for: (a) D = 610 mm and (b) D = 1830 mm

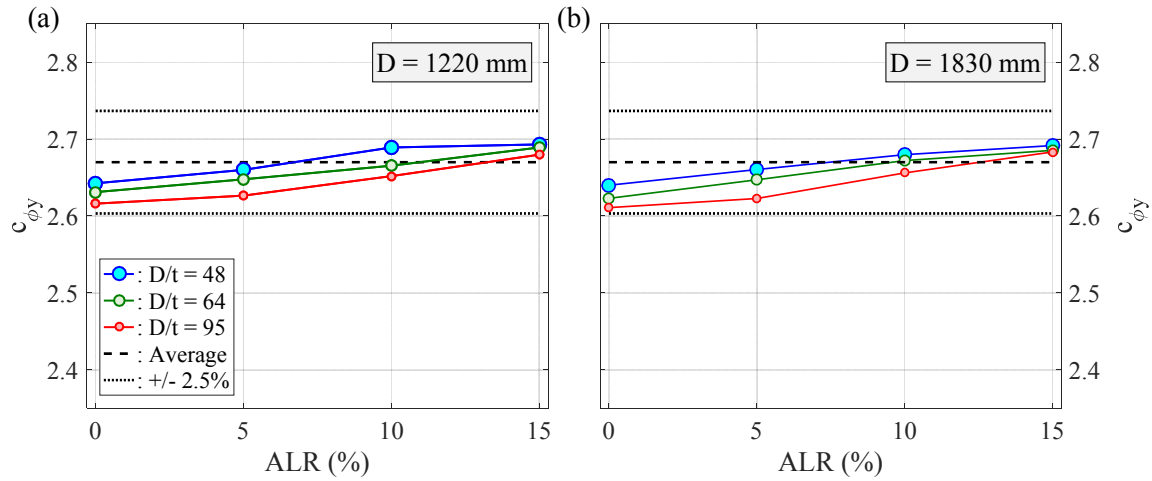

Figure 6-2 Impact of ALR ratio on $c_{\phi y}$ for: (a) D = 1220 mm and (b) D = 1830 mm

6.1.2. Neutral Axis Depth for RCFSTs

Figure 6-3 and Figure 6-4 show the impact of D/t ratio and axial load ratio (ALR) on the normalized neutral axis depth (c/D). In both cases, note that although there is a slight non-linear relationship with the parameter under consideration, a linear assumption would not induce significant errors. As such, Equation 6-2 was developed using linear regression analysis, with a corresponding R-squared value of 0.91, which means that the results are in close agreement with the equation. This is observed in Figure 6-5, where all the collected data points are presented along with the results of Equation 6-2.

It is worth noting that Equation 6-2 produces larger results than Equation 6-1 (RC sections). This is expected since RCFSTs have more area of steel in tension, which in turn requires a larger concrete compression zone. Moreover, note that depending upon the D/t ratio, predicted values can have differences of up to 5%. However, it is important to mention that Equation 6-2 is to be used at the beginning of the analysis or design processes. Some iteration may be required depending on the curvature limit state.

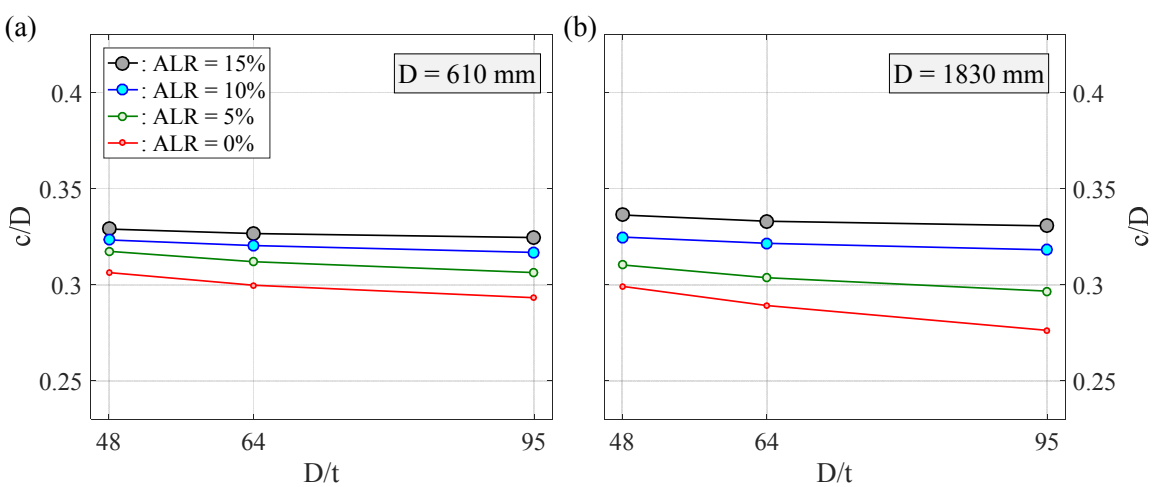

Figure 6-3 Impact of D/t ratio on neutral axis depth for: (a) D = 610 mm and (b) D = 1830mm

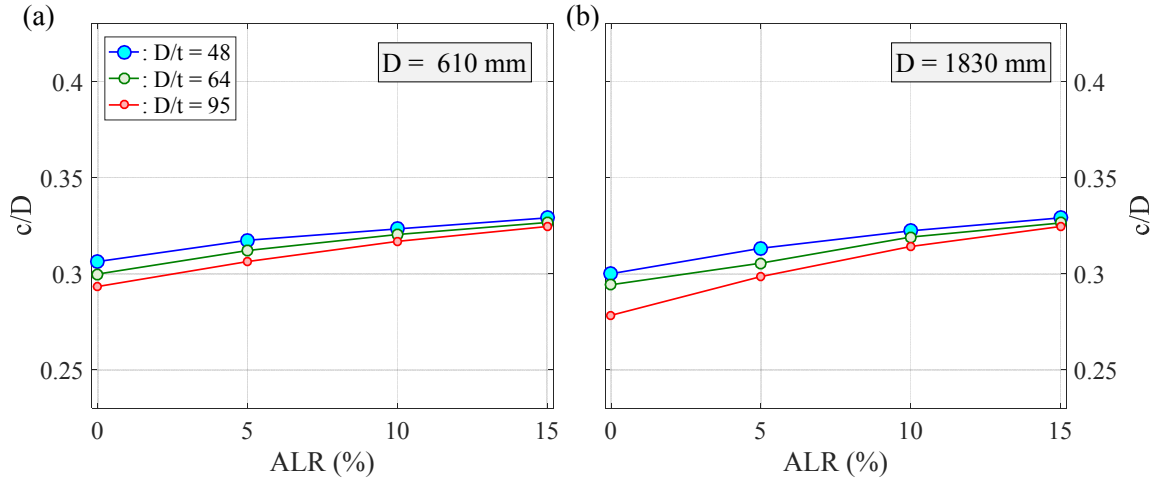

Figure 6-4 Impact of ALR on neutral axis depth for: (a) D = 610 mm and (b) D = 1830mm

$$\frac{c}{D} = 0.31 + 0.242\frac{P}{f_{ce}'A_g} - \frac{D}{4300t} \qquad \text{Equation 6-2}$$

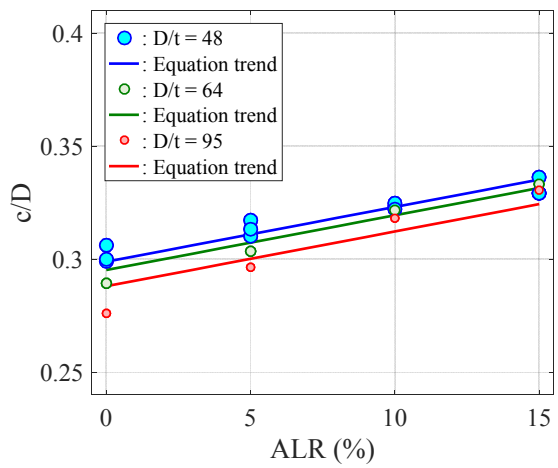

Figure 6-5 Neutral axis depth data points and Equation 6-2 trends

6.2. Pinned-Head RCFST Shafts

The depth to plastic hinge (H_{ig}), yield displacement parameter (Δ_y), plastic hinge length (L_p), and equivalent viscous damping (ξ_{eq}) were analyzed from 324 the simulations on pinned-head RCFST shafts. First, each parameter was plotted in a surface as a function of the La/D ratio, D/t ratio, and axial load ratio (ALR), in combination with the soil strength. In each case, the remaining variables were fixed for a prescribed value. For example, to assess the impact of the L_a/D ratio on the depth to plastic hinge for sand, a surface plot was generated with L_a/D ratios on the X axis, friction angles on the Y axis, and corresponding H_{ig}/D values on the Z axis, as shown in Figure 6-6(a), where results correspond to fixed values of ALR and D/t of 10% and 48, respectively. After the surface plots were generated for each variable and soil type, regression analyses were conducted to determine the best fit equation. Lastly, equation trends along with the corresponding data points are plotted for each soil type to show the accuracy.

6.2.1. Depth to Plastic Hinge

Figure 6-6 through Figure 6-8 present the variation of the depth to plastic hinge (H_{ig}) with L_a/D ratio, D/t ratio, and ALR. Notice that all the variables have a linear relationship for sand, including the friction angle. Moreover, H_{ig}/D values within 6.5 and 16.5 were observed for sand.

For clay, on the other hand, results vary in a non-linear manner in terms of D/t and ALR and for the different undrained shear strengths considered. However, the impact of ALR is not as significant, and the variation with the D/t ratio can be assumed linear. H_{ig}/D values within 7.5 and 19.5 were observed for clay.

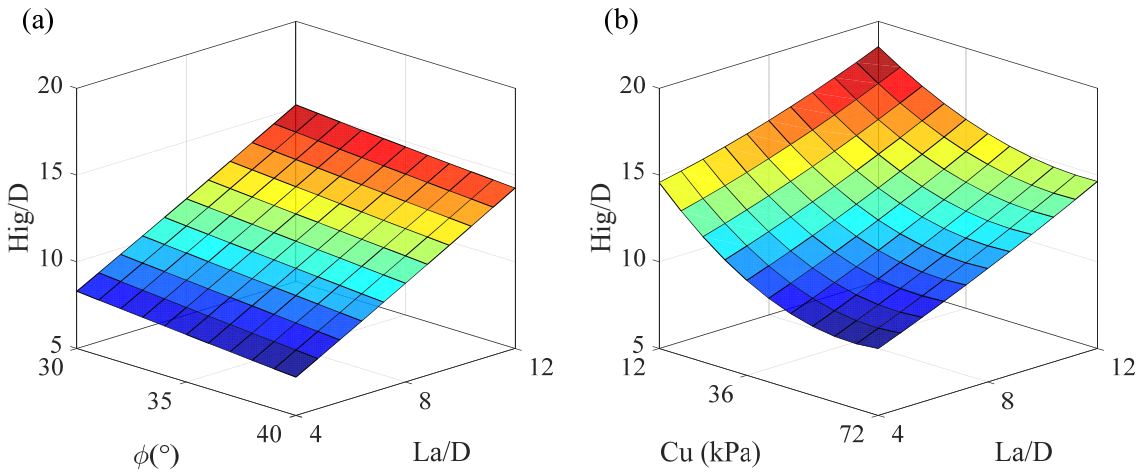

Figure 6-6 Impact of La/D ratio and soil strength on Hig/D ratio for: (a) sand and (b) clay

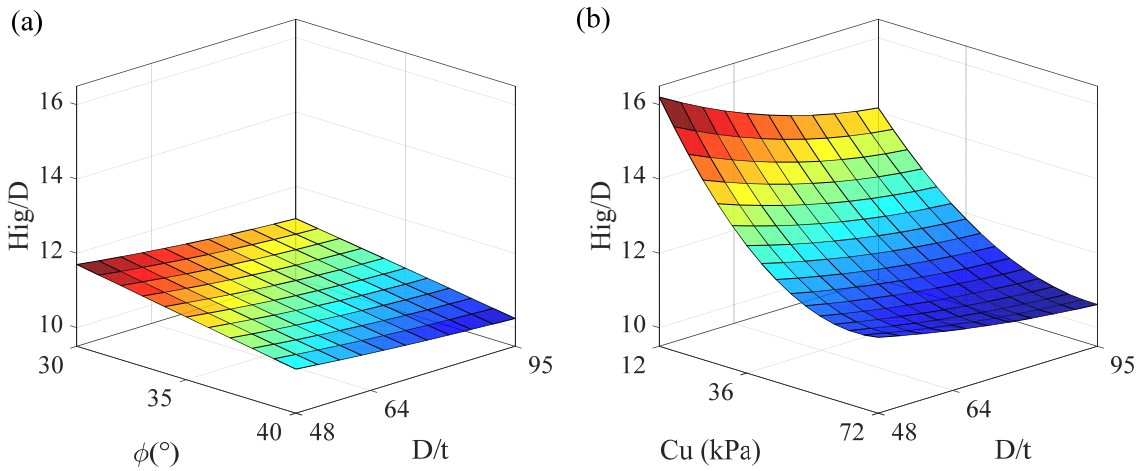

Figure 6-7 Impact of D/t ratio and soil strength on Hig/D ratio for: (a) sand and (b) clay

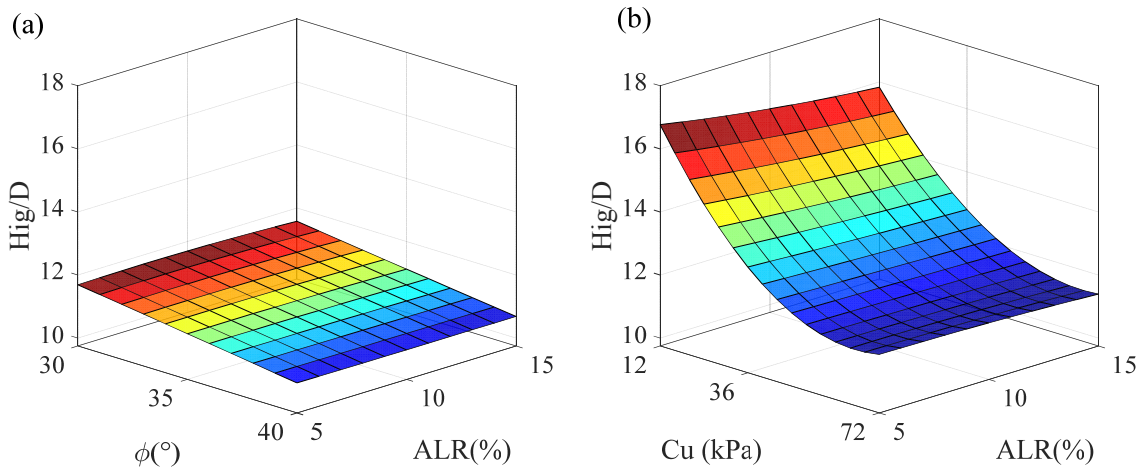

Figure 6-8 Impact of ALR and soil strength on Hig/D ratio for: (a) sand and (b) clay

Results of the regression analyses are presented in Equation 6-3 and Equation 6-4 for sand and clay, with corresponding R-squared values of 0.98 and 0.97, respectively. Regarding clay, the resulting equation depends upon the units of the undrained shear strength (C_u). There were attempts to normalize C_u using the unit weight and diameter to make Equation 6-4 not dependent of units, but the results were not successful. Alternatively, different versions of the equation could have been developed for each value of C_u studied. However, it was decided to keep the format such that the equation can be used for any value of C_u within the range of values studied.

$$\frac{H_{IG}}{D} = 8.61 + 0.86\frac{L_a}{D} - \frac{D}{90t} - \frac{\phi}{10} \quad , \quad \phi(°) \qquad \text{Equation 6-3}$$

$$\frac{H_{IG}}{D} = 18.2 + 0.65\frac{L_a}{D} - \frac{D}{35t} - 2.39Ln(C_u) \quad , \quad C_u\,(kPa) \qquad \text{Equation 6-4}$$

Figure 6-9 through Figure 6-11 present simulation results for sand along with the trends generated using Equation 6-3 for each of the friction angles studied. Similarly, Figure 6-12 through Figure 6-14 show simulation results for clay along with the trends generated using Equation 6-4 for each undrained shear strength studied. Note that in both cases, predicted and simulated results are in close agreement.

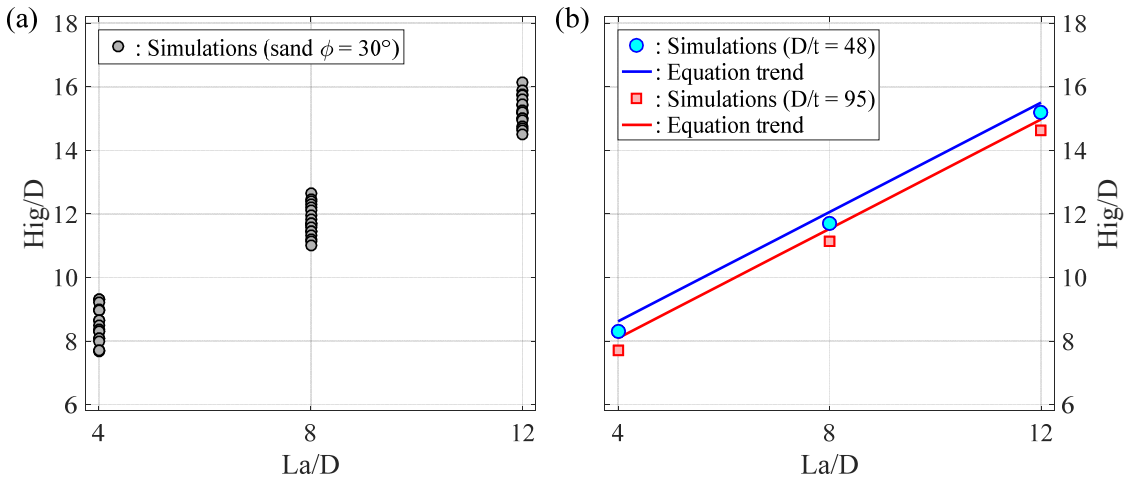

Figure 6-9 Hig/D ratio for sand with ϕ = 30°: (a) simulations and (b) equation trends

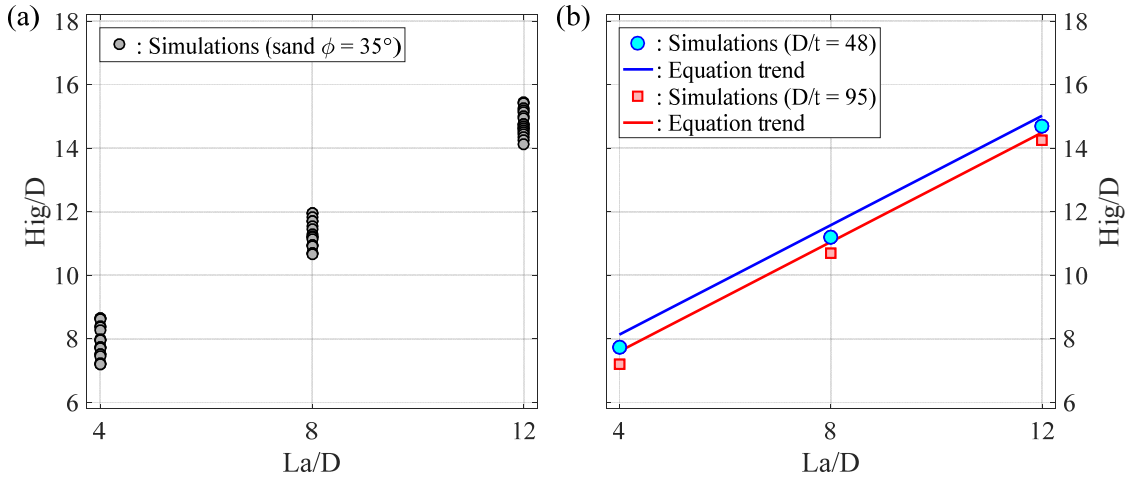

Figure 6-10 Hig/D ratio for sand with ϕ = 35°: (a) simulations and (b) equation trends

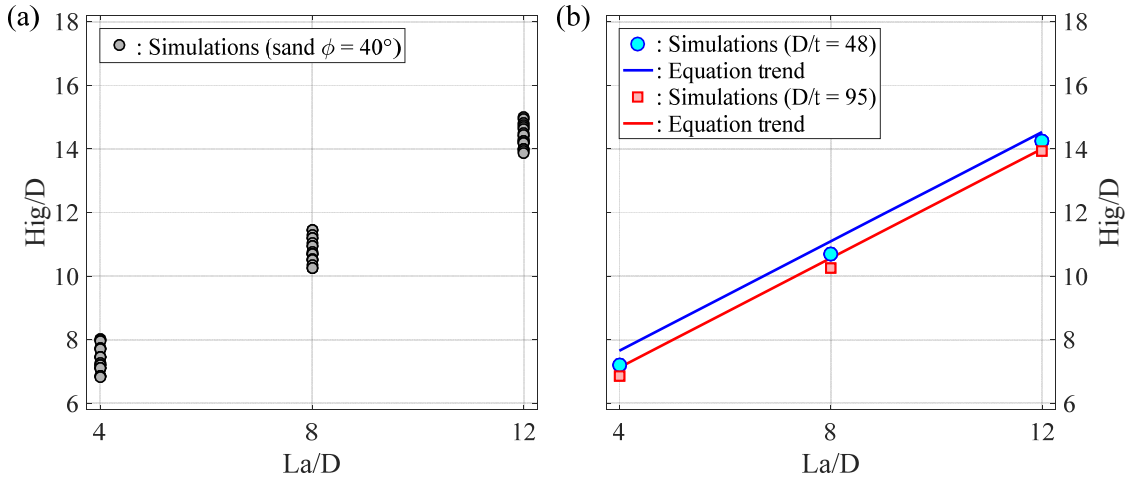

Figure 6-11 Hig/D ratio for sand with ϕ = 40°: (a) simulations and (b) equation trends

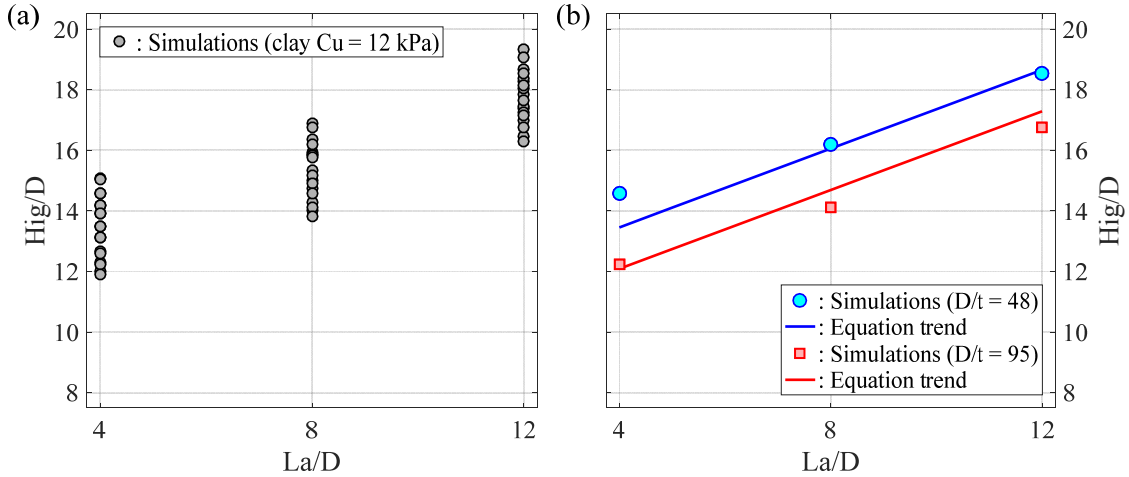

Figure 6-12 Hig/D ratio for clay with Cu = 12kPa: (a) simulations and (b) equation trends

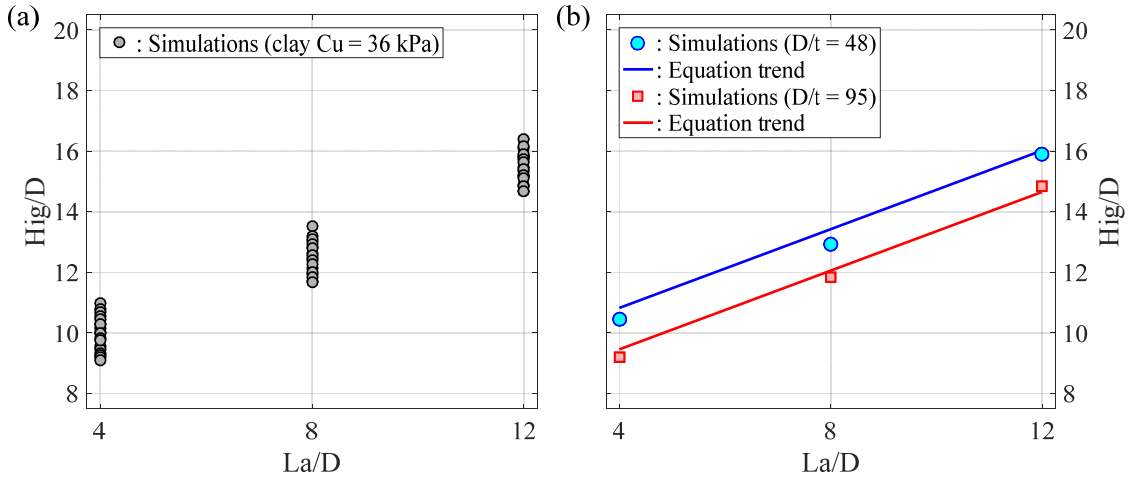

Figure 6-13 Hig/D ratio for clay with Cu = 36kPa: (a) simulations and (b) equation trends

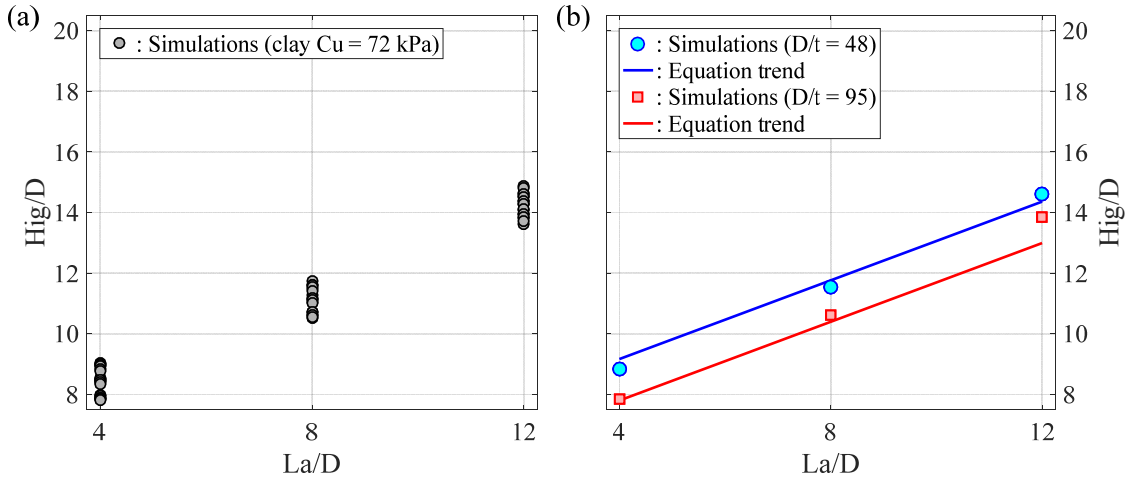

Figure 6-14 Hig/D ratio for clay with Cu = 72kPa: (a) simulations and (b) equation trends

6.2.2. Yield Displacement Parameter

Figure 6-15 through Figure 6-17 show the variation of the yield displacement parameter (c_1) with L_a/D, D/t, and ALR. Regarding sand, note that in terms of L_a/D ratio, the parameter has a non-linear variation, while the other two variables have a clear linear variation; c_1 values within 0.5 and 0.9 were observed. In terms of the friction angle, overall the variation is linear.

Regarding results for clay on the other hand, the scatter in the simulated data is higher. This is reflected in the shape of the shown surfaces. However, it can be concluded that there is a linear variation with L_a/D. Moreover, note from Figure 6-17 that the ALR has no effect at all in the results, neither for clay nor for sand, since values remain constant.

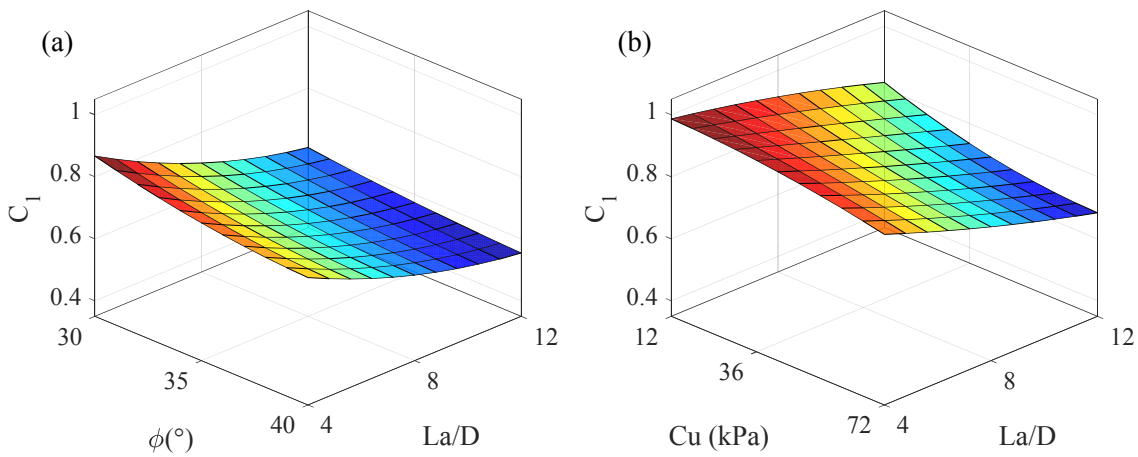

Figure 6-15 Impact of La/D ratio and soil strength on C_1 for: (a) sand and (b) clay

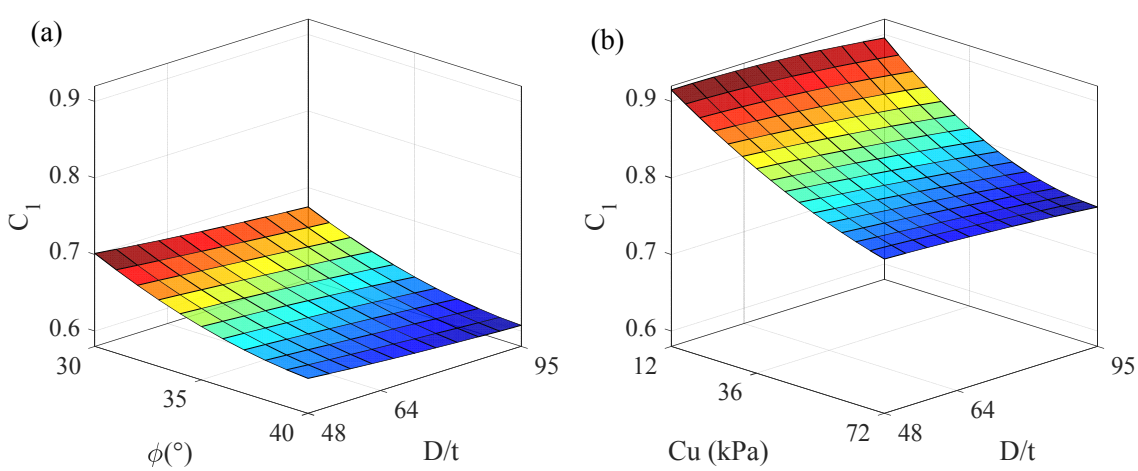

Figure 6-16 Impact of D/t ratio and soil strength on C_1 for: (a) sand and (b) clay

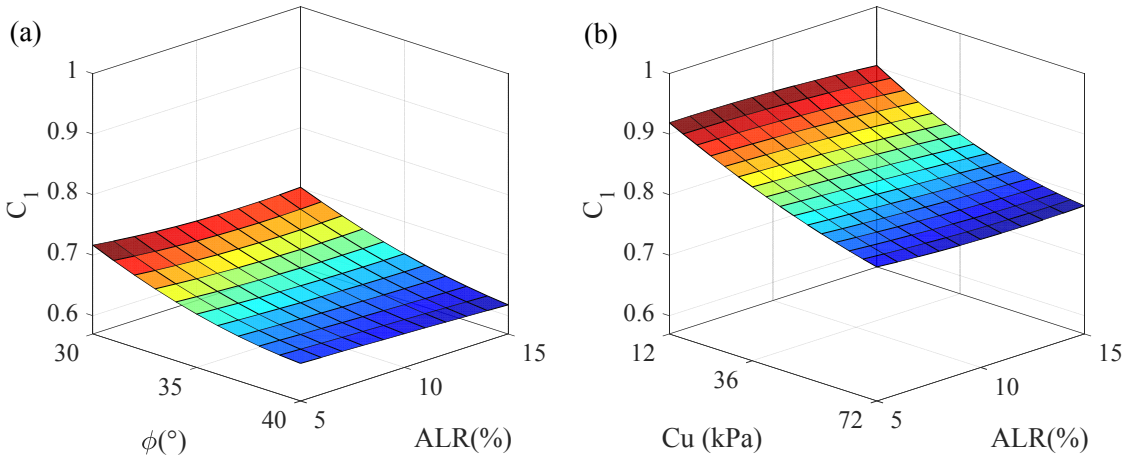

Figure 6-17 Impact of ALR and soil strength on C_1 for: (a) sand and (b) clay

Results of the regression analyses are presented in Equation 6-5 and Equation 6-6 for sand and clay, with an R-squared value of 0.97 in both cases. For clay, note that the same conclusion from the previous section applies regarding the units.

$$C_1 = 1.378 - 0.20\,Ln\left(\frac{L_a}{D}\right) - \frac{D}{2050t} - \frac{\phi}{130} \quad , \quad \phi(°) \qquad \text{Equation 6-5}$$

$$C_1 = 1.279 - \frac{L_a}{40D}\left(1 + \frac{D}{430t}\right) - \frac{Ln(C_u)}{16} \quad , \quad C_u\,(kPa) \qquad \text{Equation 6-6}$$

Figure 6-18 through Figure 6-20 present simulation results for sand along with the trends generated using Equation 6-5 for each of the friction angles studied. Similarly, Figure 6-21 through Figure 6-23 show simulation results for clay along with the trends generated using Equation 6-6 for each undrained shear strength studied. Note that in both cases, predicted and simulated results are in close agreement. However, some of the simulated points are outside the trends, especially for clay, though note that the predicted values are not that far off.

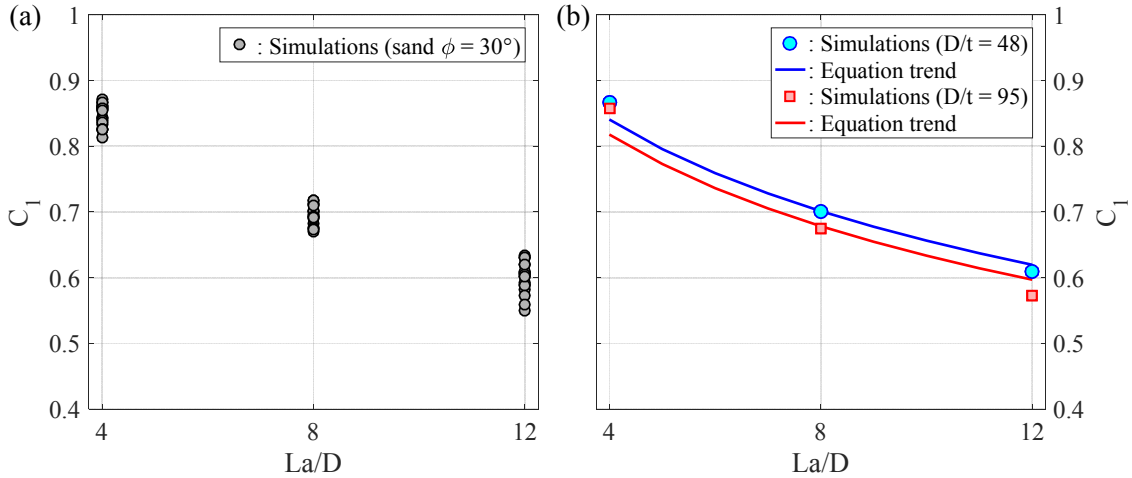

Figure 6-18 C_1 for sand with ϕ = 30°: (a) simulations and (b) equation trends

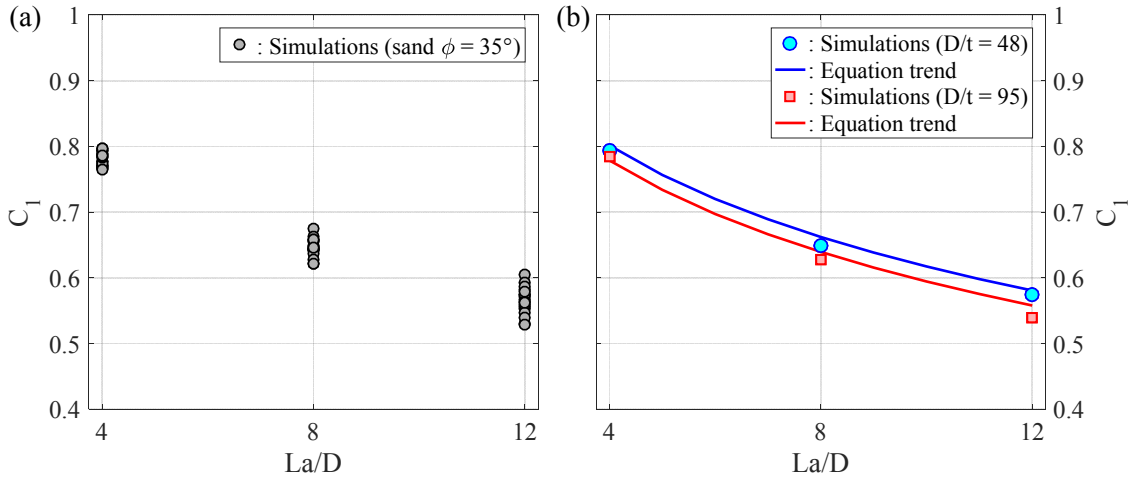

Figure 6-19 C_1 for sand with ϕ = 35°: (a) simulations and (b) equation trends

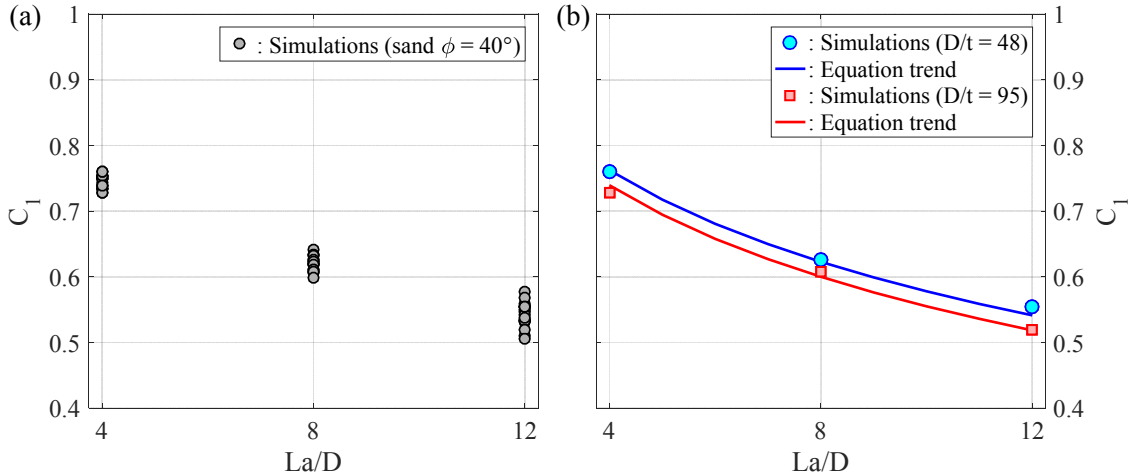

Figure 6-20 C_1 for sand with ϕ = 40°: (a) Simulations and (b) equation trends

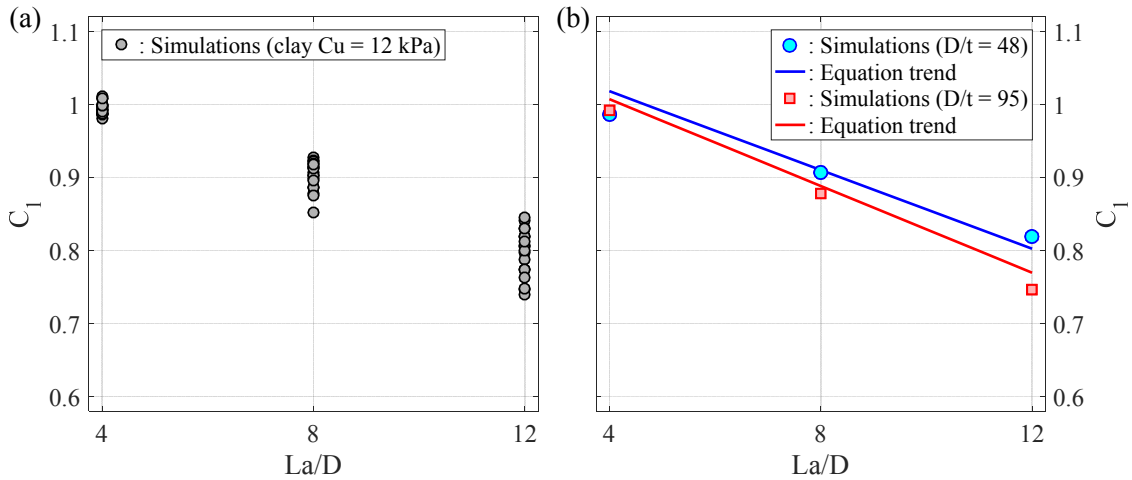

Figure 6-21 C_1 for clay with Cu = 12 kPa: (a) simulations and (b) equation trends

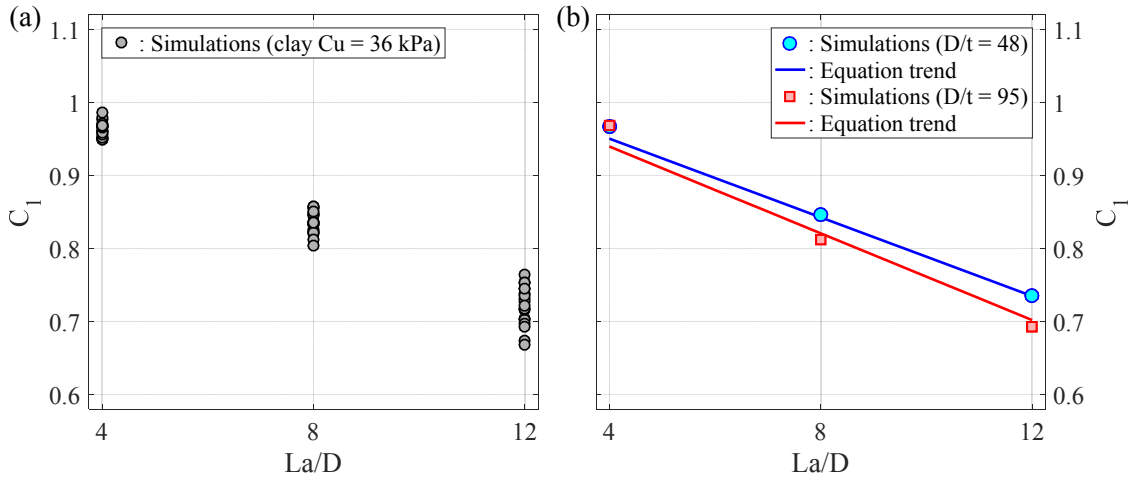

Figure 6-22 C_1 for clay with Cu = 36 kPa: (a) simulations and (b) equation trends

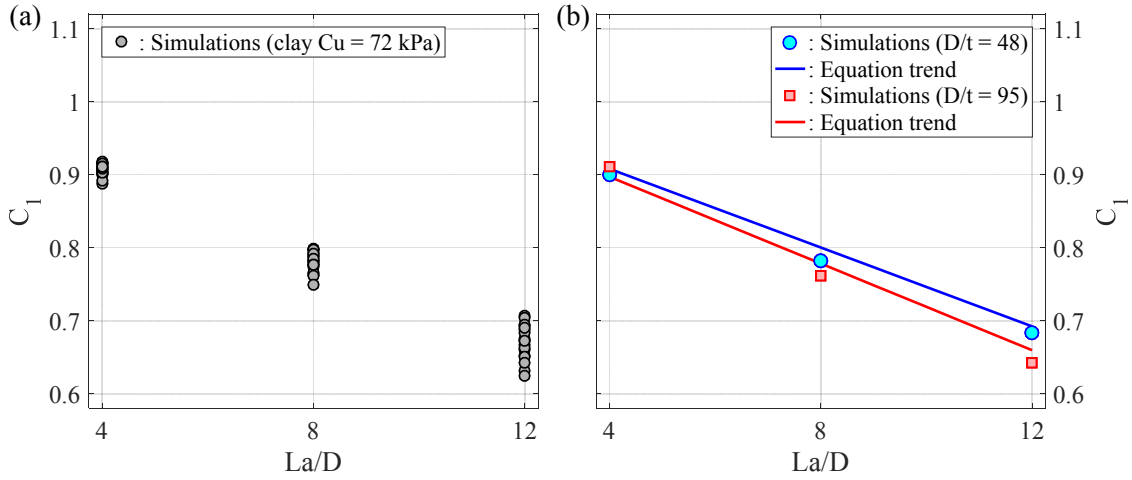

Figure 6-23 C_1 for clay with Cu = 72 kPa: (a) simulations and (b) equation trends

6.2.3. Plastic Hinge Length

Figure 6-24 shows the normalized plastic hinge length (L_p/D) for both sand and clay as a function of the displacement ductility induced at the head of the specimens. Notice that in both cases the plastic hinge length tends to saturate after ductility 2 (μ_2). Observed values range within 3 and 5 for sand and within 4 and 15 for clay. Regarding the latter, it was expected to obtain larger values as clay is more flexible than sand, thus displacements are higher for a prescribed ductility level. However, note from Figure 6-24(b) that some of the simulation results indicate values within 10 and 20. These results correspond to the lowest level in terms of undrained shear. The reason is that under the most flexible soil condition (C_u = 12 kPa), displacements are large as more soil is mobilized.

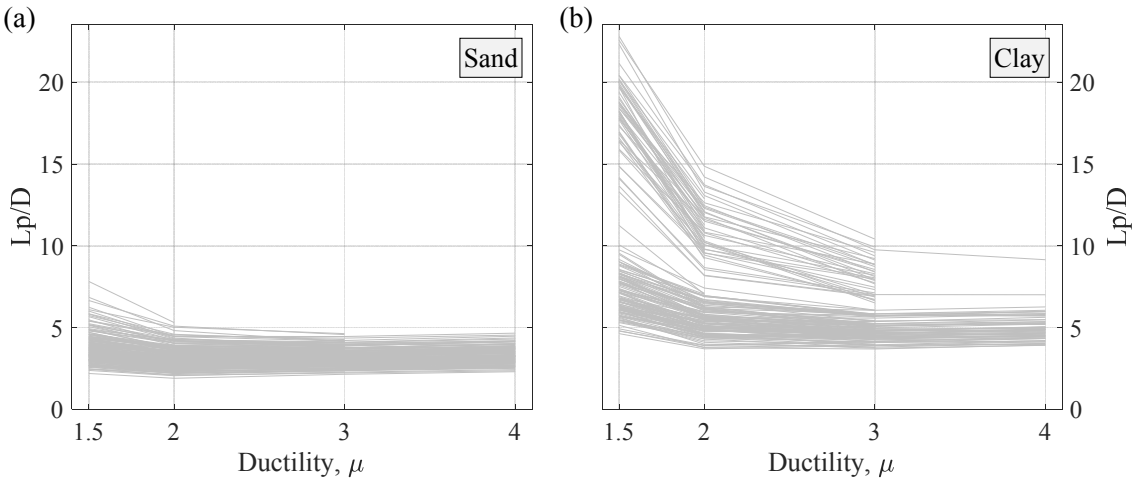

Figure 6-24 Back-calculated plastic hinge length for: (a) sand and (b) clay

Considering the discussion above, it was decided to further study the role of the plastic hinge in terms of ductility (μ). For that purpose, strain limit states at onset of tube local buckling and at tube fracture were analyzed. Regarding the former, the displacement ductility prior tube local buckling was calculated using the Brown et al. (2015) model, as shown in Equation 6-7. As such, for each simulation this strain limit state was calculated to determine the corresponding displacement ductility by interpolating results of the recorded tensile strain data. Figure 6-25 through Figure 6-27 show the displacement ductility at onset of tube buckling. Results are organized in terms of D/t ratio, L_a/D ratio, and ALR, respectively. Note that most of the points fall within ductility 2 (μ_2) and ductility 3 (μ_3).

$$\varepsilon_{t,tb} = 0.021 - \frac{D}{9100\,t} \geq \varepsilon_{y(tube)} \qquad \text{Equation 6-7}$$

Regarding the limit state at tube fracture, based on the experimental results, a maximum displacement ductility capacity of 3 (μ_3) can be assumed for RCFST shafts, though for thicker tubes (D/t = 48) higher values could be expected. Note from Figure 6-25 that onset of tube buckling occurs closer to a ductility level 3 (μ_3). This is tune with the experimental observations presented in the previous chapter, which also suggested a maximum displacement ductility capacity of 4 (μ_4) for tubes with D/t = 48.

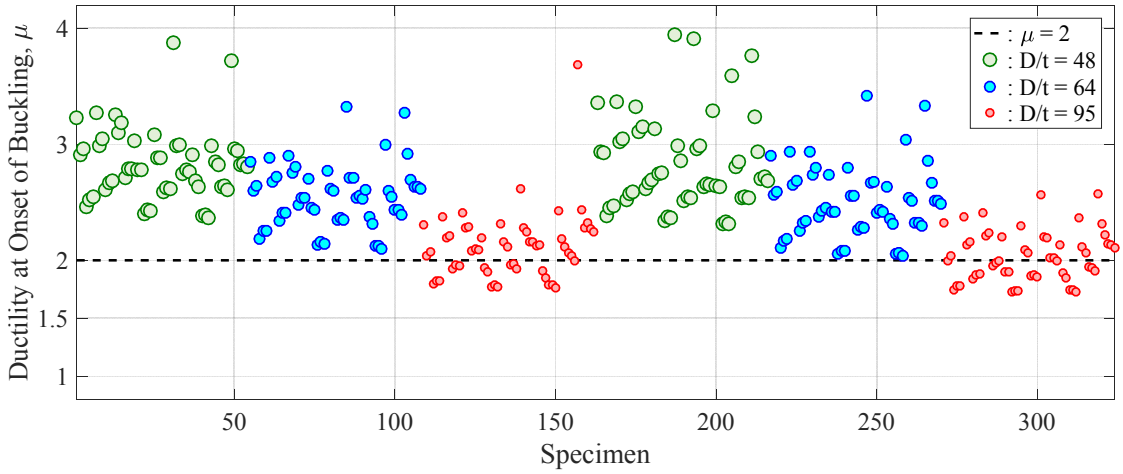

Figure 6-25 Ductility at onset of buckling in terms of D/t ratio

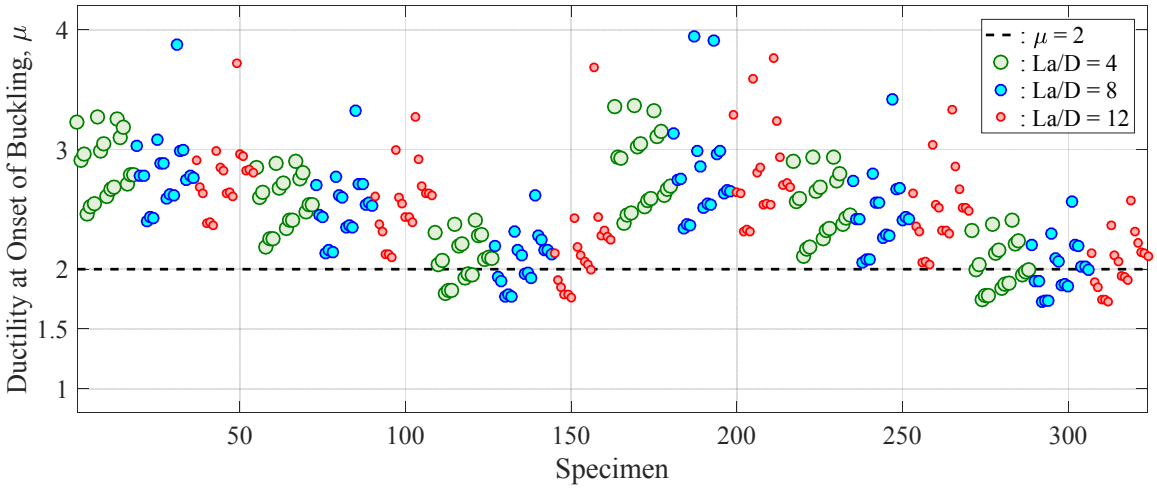

Figure 6-26 Ductility at onset of buckling in terms of L_a/D ratio

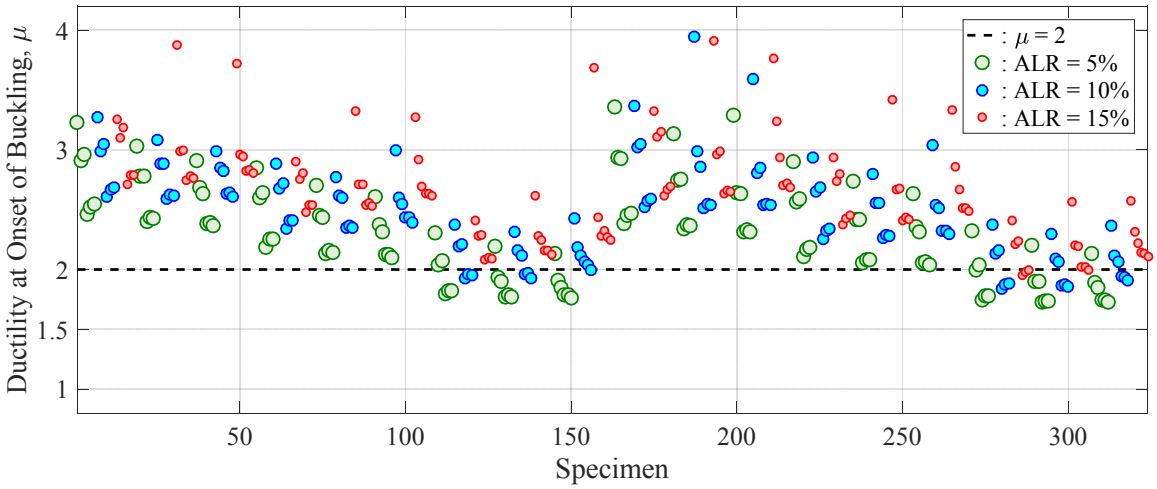

Figure 6-27 Ductility at onset of buckling in terms of ALR

Based upon the discussion above, it was decided to average the normalized plastic hinge length (L_p/D) using the values corresponding to ductility 2 (μ_2) and ductility 3 (μ_3), since some of the data was not available at ductility 4 (μ_4) due to second order effects and convergence issues on some of the simulated specimens. By doing this, the plastic hinge length parameter is not a function of ductility (μ), and thus an analysis like that of the previous section can be conducted.

Figure 6-28 through Figure 6-30 show the variation of the plastic hinge length parameter (L_p/D) with L_a/D, D/t, and ALR. Regarding sand, note that all variables indicate a linear relationship, including the friction angle; values of L_p/D within 2 and 5 were observed.

Regarding results for clay, on the other hand, the parameter has a non-linear and more complex variation with all the variables. This is reflected in the shape of shown surfaces and in the scatter of the data, as shown at the end of this section; values of L_p/D within 3.5 and 13 were observed.

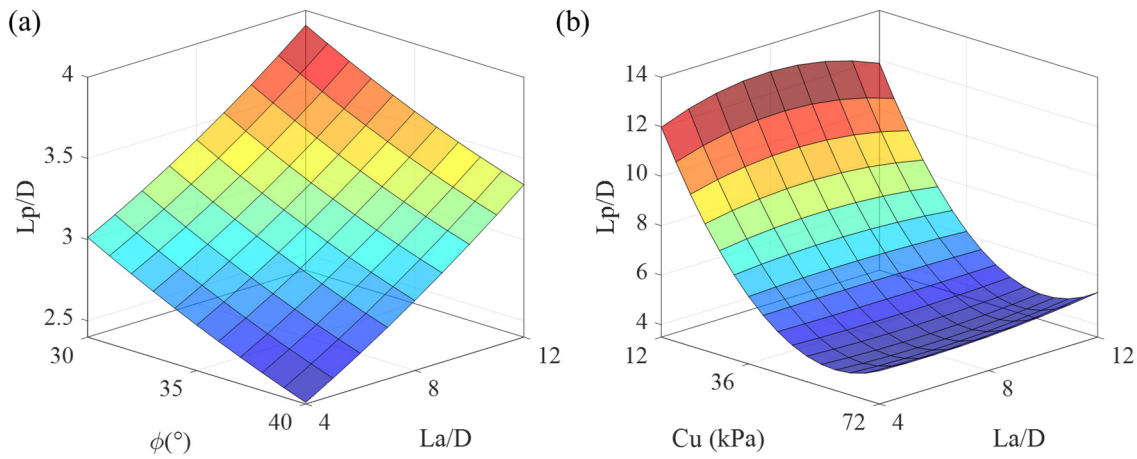

Figure 6-28 Impact of L_a/D ratio on plastic hinge length for: (a) sand and (b) clay

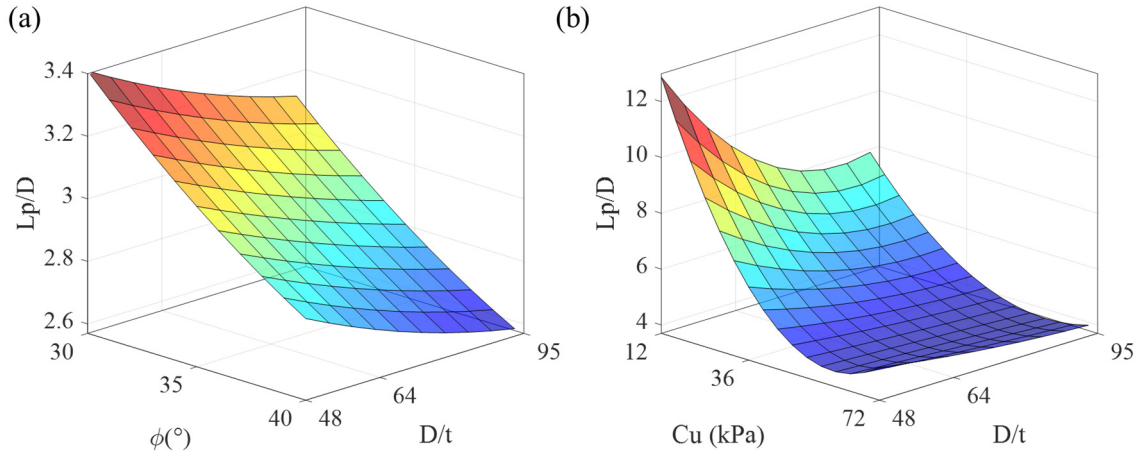

Figure 6-29 Impact of D/t ratio on plastic hinge length for: (a) sand and (b) clay

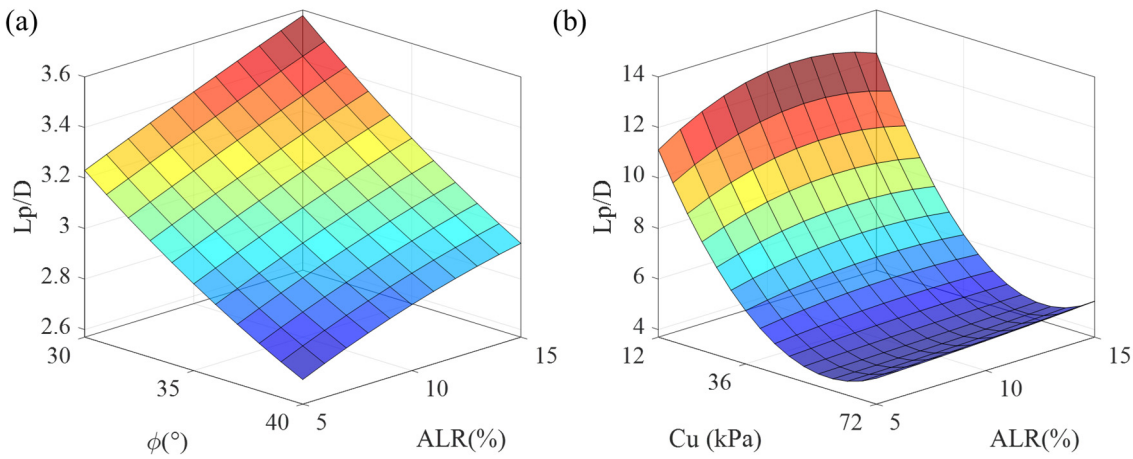

Figure 6-30 Impact of ALR on plastic hinge length for: (a) sand and (b) clay

Results of the regression analyses are presented in Equation 6-8 and Equation 6-9 for sand and clay, respectively, with R-squared values of 0.97 and 0.94, respectively. Note that the equations depend on the units of the diameter and the undrained shear strength.

$$\frac{L_p}{D} = 5.44 - 0.74D + 0.06\frac{L_a}{D}\left(1 + 9.85ALR\right) - \frac{D}{210t} - 0.063\phi \quad , \quad D(m)\,,\,\phi(^\circ) \qquad \text{Equation 6-8}$$

$$\frac{L_p}{D} = 50.91 + 0.06\frac{L_a}{D}\left(0.23ALR\frac{D}{t} - 1\right) - 8.02Ln\left(\frac{D}{t}\right) + 4.54Ln\left(C_u\right)\left(\frac{D}{220t} - 1\right) \quad , \quad C_u\,(kPa) \qquad \text{Equation 6-9}$$

Figure 6-31 through Figure 6-33 present simulation results for sand along with the trends generated using Equation 6-8 for each of the friction angles studied. Similarly, Figure 6-34 through Figure 6-36 show simulation results for clay along with the trends generated using Equation 6-9 for each undrained shear strength studied. The complexity of the equations above is related to the scatter in the data. Note that for sand, for example, simulation data indicated a spread in the result of the plastic hinge length (L_p) within 1D and 2D. For clay, on the other hand, the spread in the results is within 2D and 5D. However, note that in both cases, predicted and simulated results are in close agreement.

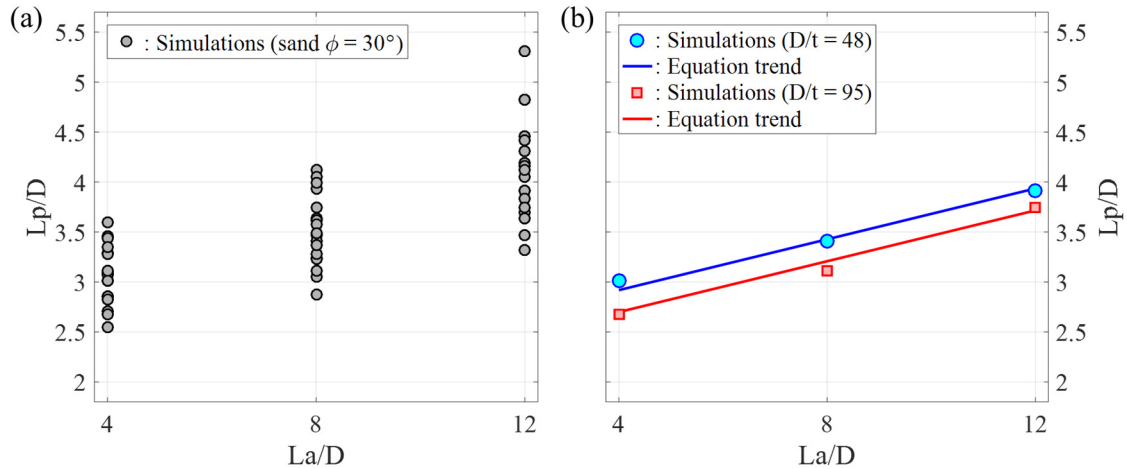

Figure 6-31 L_p/D for sand with ϕ = 30°: (a) simulations and (b) equation trends

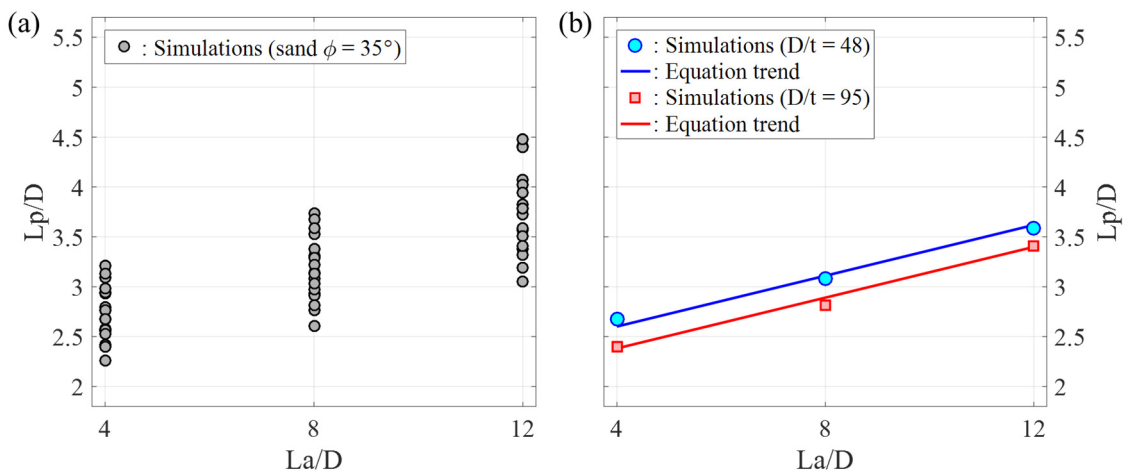

Figure 6-32 L_p/D for sand with ϕ = 35°: (a) simulations and (b) equation trends

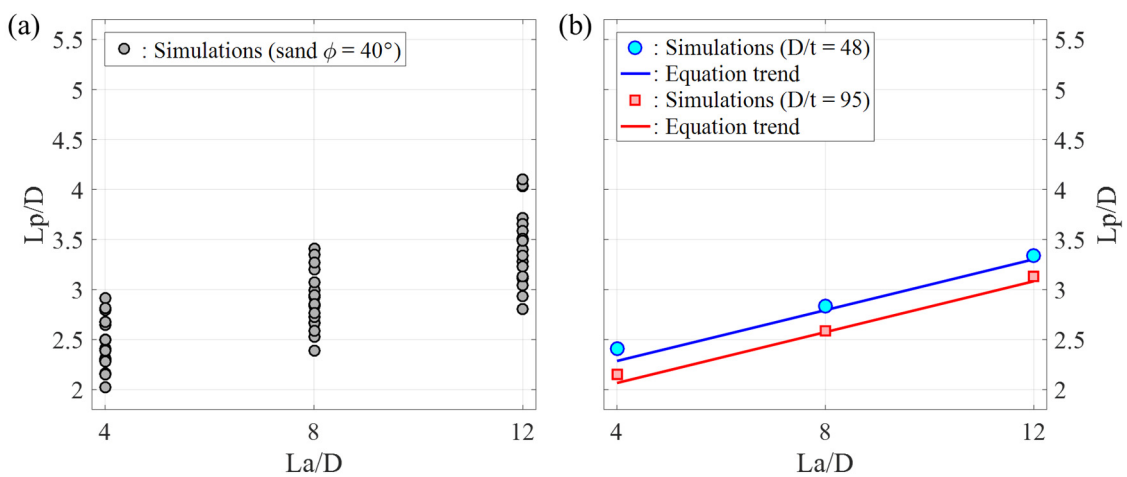

Figure 6-33 L_p/D for sand with ϕ = 40°: (a) simulations and (b) equation trends

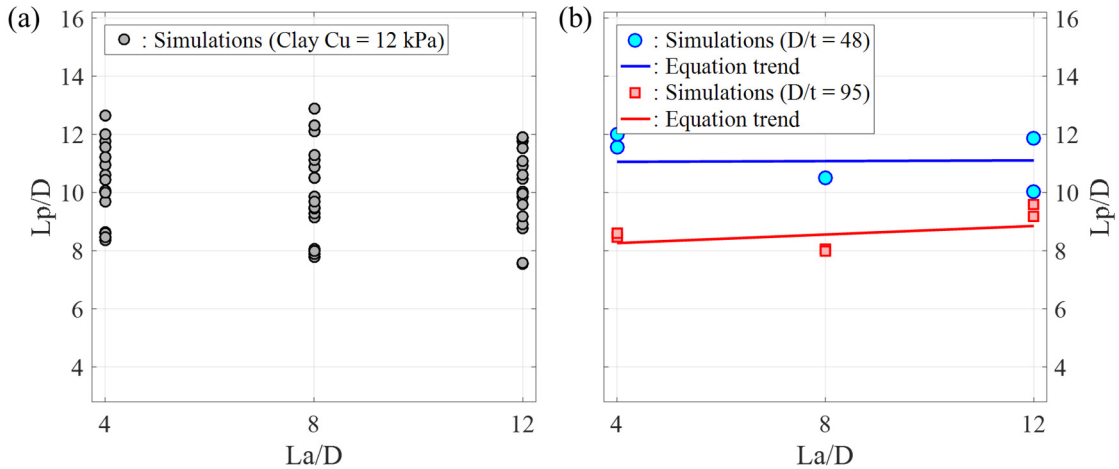

Figure 6-34 Lp/D for clay with Cu = 12 kPa: (a) simulations and (b) equation trends

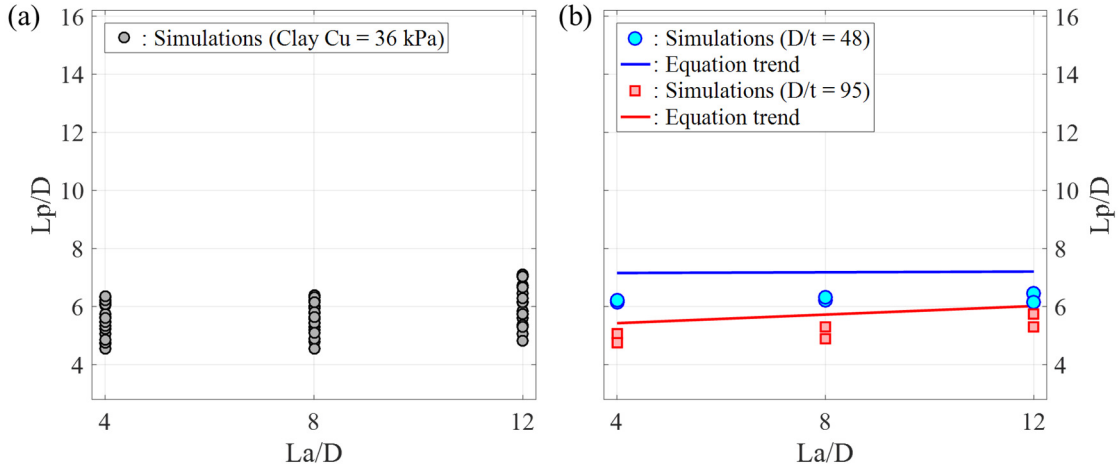

Figure 6-35 Lp/D for clay with Cu = 36 kPa: (a) simulations and (b) equation trends

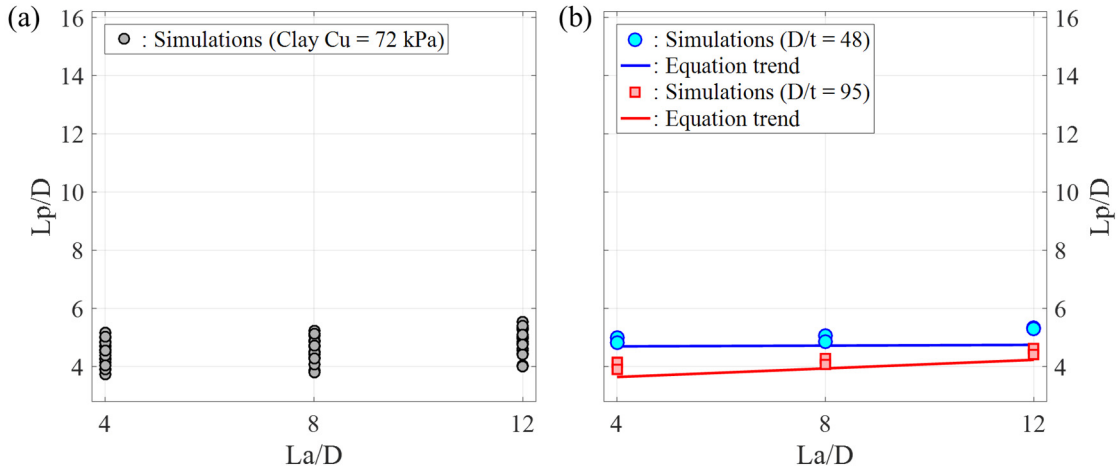

Figure 6-36 Lp/D for clay with Cu = 72 kPa: (a) simulations and (b) equation trends

6.2.4. Equivalent Viscous Damping

Figure 6-37 and Figure 6-38 show the observed system equivalent viscous damping (EVD) for sand and clay, respectively, as a function of the displacement ductility (μ). Along with the simulation results, these figures also present results of Equation 6-10, which was developed for RCFSTs in the air (Brown et al., 2015). Note that for both sand and clay simulation results show consistently higher values, which can be attributed to the soil contribution to the equivalent damping.

$$\xi_{eq} = 0.07 + \left(0.85 - \frac{D}{1000\,t}\right)\left(\frac{\mu - 1}{10.5 + \mu\pi}\right) \qquad \text{Equation 6-10}$$

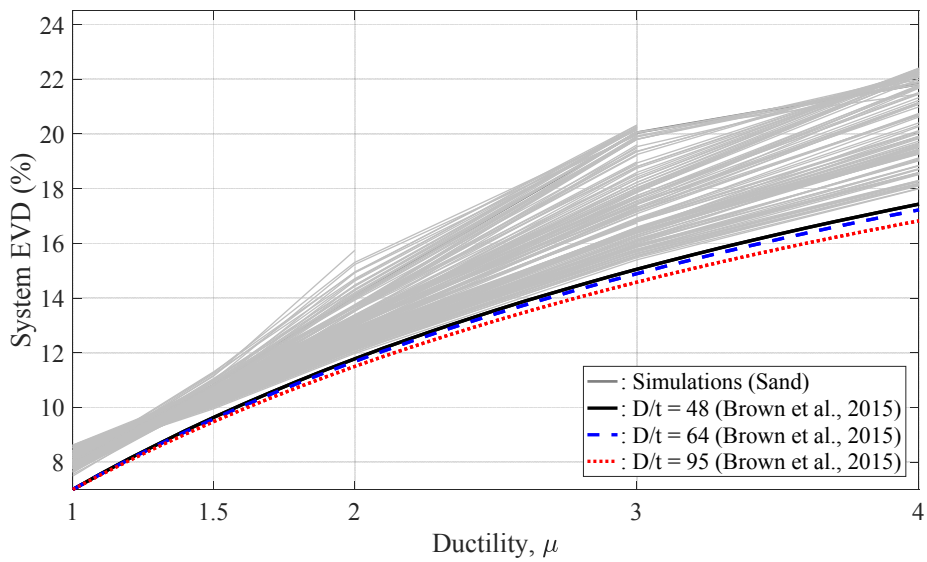

Figure 6-37 Observed system equivalent viscous damping for sand

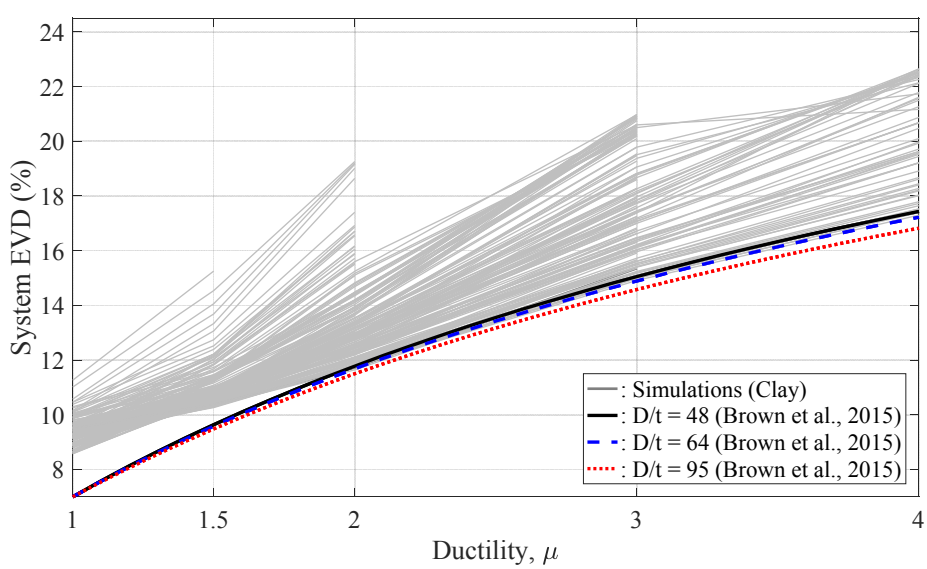

Figure 6-38 Observed system equivalent viscous damping for clay

Considering the results presented in Figure 6-37 and Figure 6-38, there are two alternatives that could be implemented to predict the system EVD. The first option could be to develop a new model to include the energy dissipation of both the RCFST shaft and soil. A second alternative could be to consider the model developed by Brown et al. (2015), and back-calculate the soil damping. The feasibility of implementing the latter was explored first and the results are presented in Figure 6-39 for both sand and clay. Note that there seems to be a wide spread in the results. As such, to better understand the results, Figure 6-39 is repeated in Figure 6-40 but with results plotted in terms of L_a/D ratio. Note that there is a trend in the data to change the slope of the curves as a function of L_a/D. However, note that overall soil damping results vary within 1% and 5%. On the other hand, if the averaged soil damping at each ductility level is utilized for prediction purposes, then the predicted soil damping could be within 0.5% and 2.5% of the actual value. By comparing these values with the total system EVD values shown in Figure 6-37 and Figure 6-38, it can be concluded that predicting the soil damping with average results could induce errors within 5% and 10% of the actual system EVD.

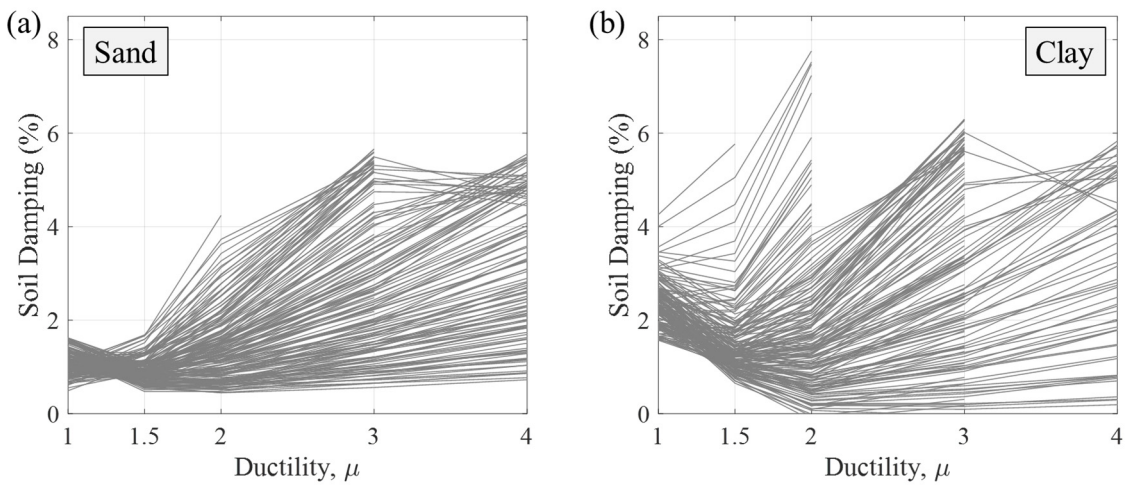

Figure 6-39 Back-caluclated soil damping for: (a) sand and (b) clay

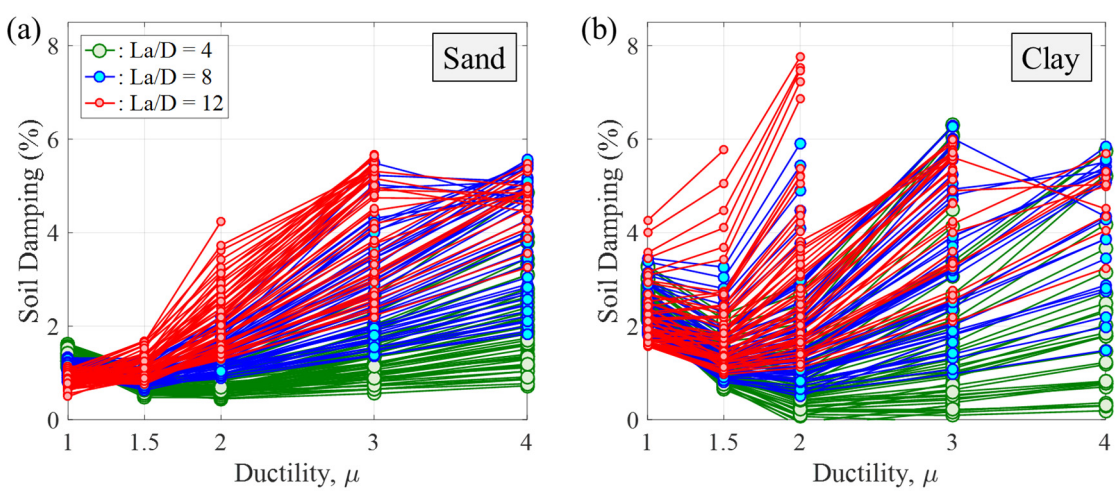

Figure 6-40 Soil damping in terms of L_a/D for: (a) sand and (b) clay

Considering the inherent uncertainty of soils and their properties, and recognizing that the RCFST shaft dissipates most of the energy, it seems reasonable to propose a bilinear model for soil damping. In such a model, a constant value of soil damping can be assumed up to ductility 2 (μ_2), and a linear variation can be considered up until ductility 4 (μ_4). This approach was implemented and the results are shown in Equation 6-11 and Equation 6-12 for sand and clay, respectively. Moreover, results of these equations are presented in Figure 6-41 along with the simulated results.

$$\xi = \begin{cases} 0.012 & 1 \le \mu \le 2 \\ 0.012 + 0.009(\mu - 2) & \mu > 2 \end{cases} \qquad \text{Equation 6-11}$$

$$\xi = \begin{cases} 0.019 & 1 \le \mu \le 2 \\ 0.019 + 0.0055(\mu - 2) & \mu > 2 \end{cases} \qquad \text{Equation 6-12}$$

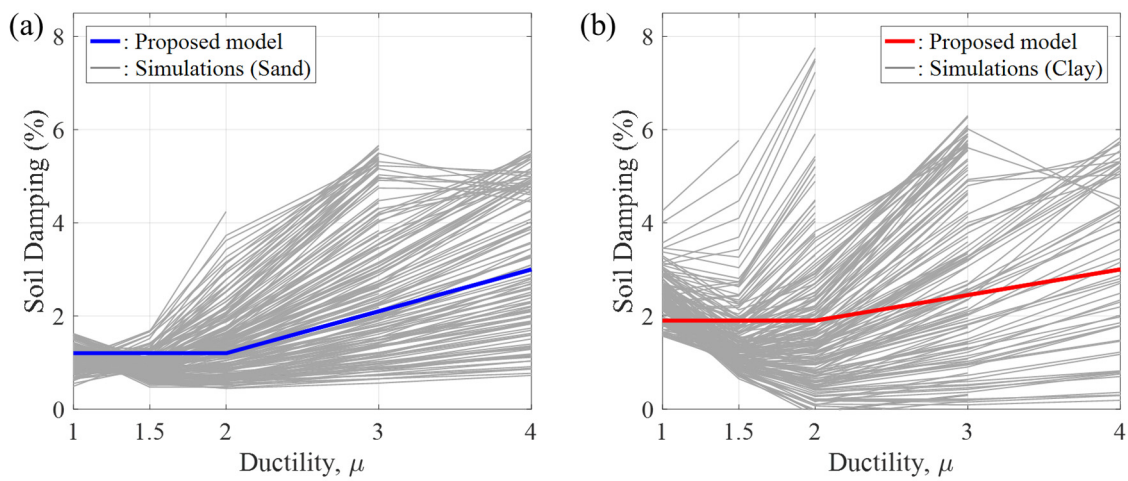

Figure 6-41 Soil damping results and equation trends for: (a) sand and (b) clay

Equation 6-11 and Equation 6-12 represent the soil contribution to the system EVD. As such, by adding the equivalent viscous damping of the RCFST shaft (Brown et al., 2015), the system EVD can be calculated for sand and clay, as shown in Equation 6-13 and Equation 6-14, respectively. Results of these equations have been plotted along with the simulated data in Figure 6-42 and Figure 6-43 for sand and clay, respectively. Note that results are in close agreement, especially at low ductility levels.

$$\xi_{eq,sand} = 0.07 + \left(0.85 - \frac{D}{1000t}\right)\left(\frac{\mu - 1}{10.5 + \pi\mu}\right) + \begin{cases} 0.012 & 1 \le \mu \le 2 \\ 0.012 + 0.009(\mu - 2) & \mu > 2 \end{cases} \qquad \text{Equation 6-13}$$

$$\xi_{eq,clay} = 0.07 + \left(0.85 - \frac{D}{1000t}\right)\left(\frac{\mu - 1}{10.5 + \pi\mu}\right) + \begin{cases} 0.019 & 1 \le \mu \le 2 \\ 0.019 + 0.0055(\mu - 2) & \mu > 2 \end{cases} \qquad \text{Equation 6-14}$$

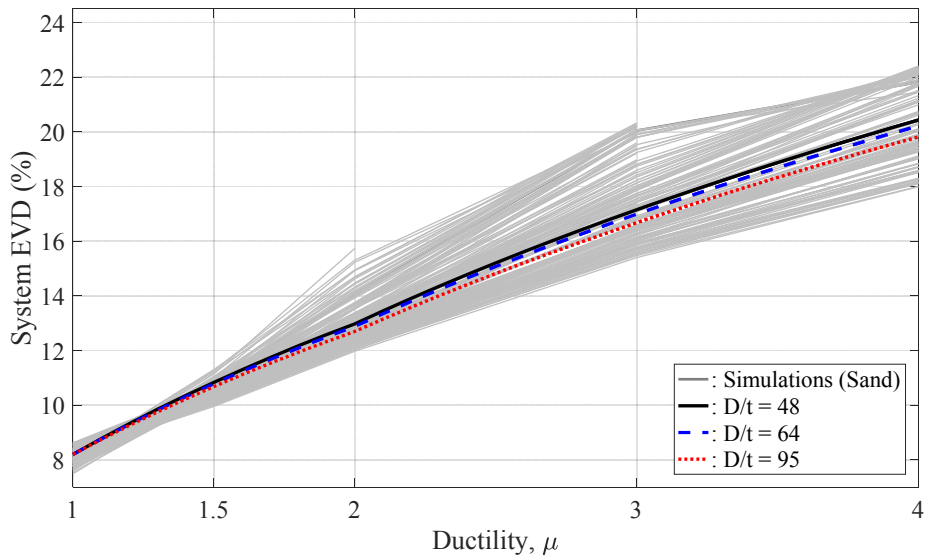

Figure 6-42 System equivalent viscous damping results and equation trends for sand

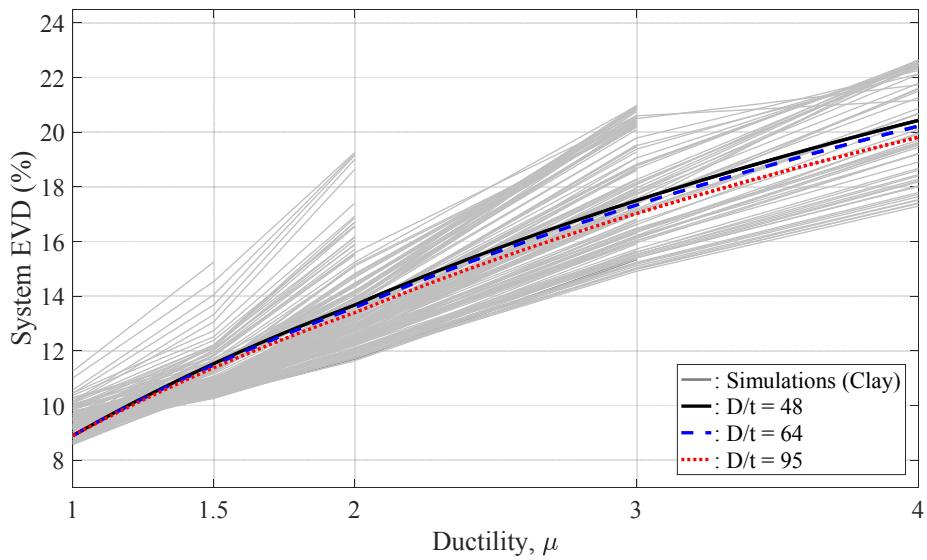

Figure 6-43 System equivalent viscous damping results and equation trends for clay

6.3. Fixed-Head RCFST Shafts

Similar analyses were conducted for fixed-head RCFST shafts. Besides the depth to plastic hinge (H_{ig}), yield displacement (Δ_y), and equivalent viscous damping (ξ_{eq}), the main difference is that instead of the plastic hinge length (L_p) the parameter β was analyzed. The process in general was the same as that implemented for pinned-head shafts, that is, each parameter was plotted in a surface plot as a function of the La/D ratio, D/t ratio, and axial load ratio (ALR), in combination with the soil strength. In each case, the remaining variables were fixed for a prescribed value. For example, to assess the impact of the L_a/D ratio on the depth to plastic hinge for sand, a surface plot was generated with L_a/D ratios on the X axis, friction angles on the Y axis, and corresponding H_{ig}/D values on the Z axis, as shown in Figure 6-44(a). These results correspond to fixed values of ALR and D/t of 10%

and 48, respectively. After the surface plots were generated for each variable and soil type, regression analyses were conducted to determine the best-fit equation. Lastly, equation trends along with the corresponding data points are plotted for each soil type to show the accuracy.

6.3.1. Depth to Plastic Hinge

Figure 6-44 through Figure 6-46 present the variation of the depth to plastic hinge (H_{ig}) with L_a/D ratio, D/t ratio, and ALR. Notice that all the variables have a linear relationship for sand, including the friction angle; values of H_{ig}/D within 7 and 16.5 were observed. For clay, on the other hand, results vary in a linear manner except in terms of the undrained shear strength considered; values of H_{ig}/D within 8 and 19.5 were observed.

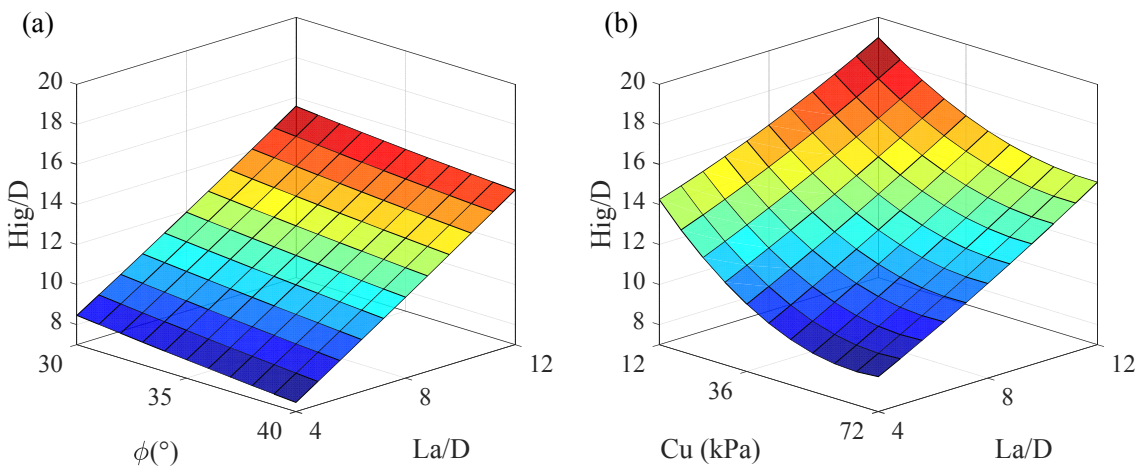

Figure 6-44 Impact of La/D ratio and soil strength on Hig/D ratio for: (a) sand and (b) clay

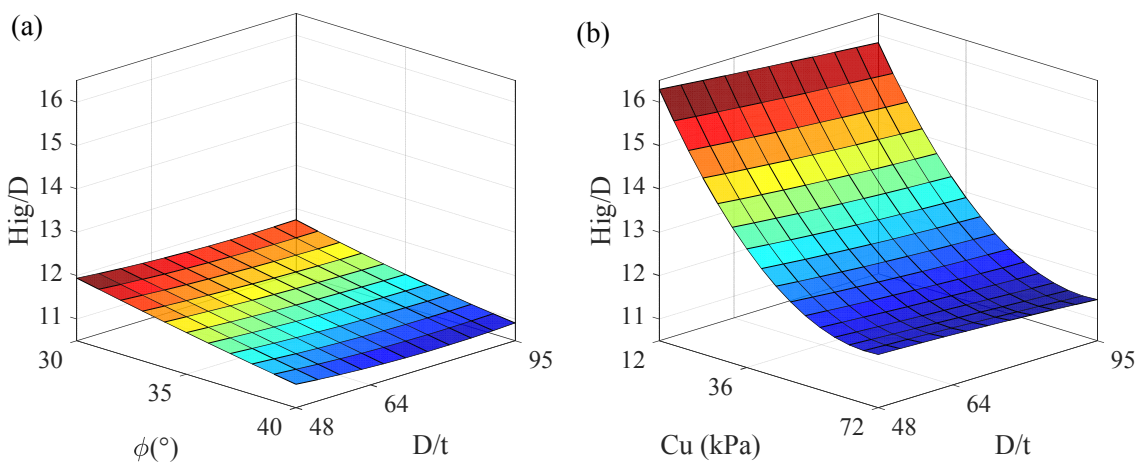

Figure 6-45 Impact of D/t ratio and soil strength on Hig/D ratio for: (a) sand and (b) clay

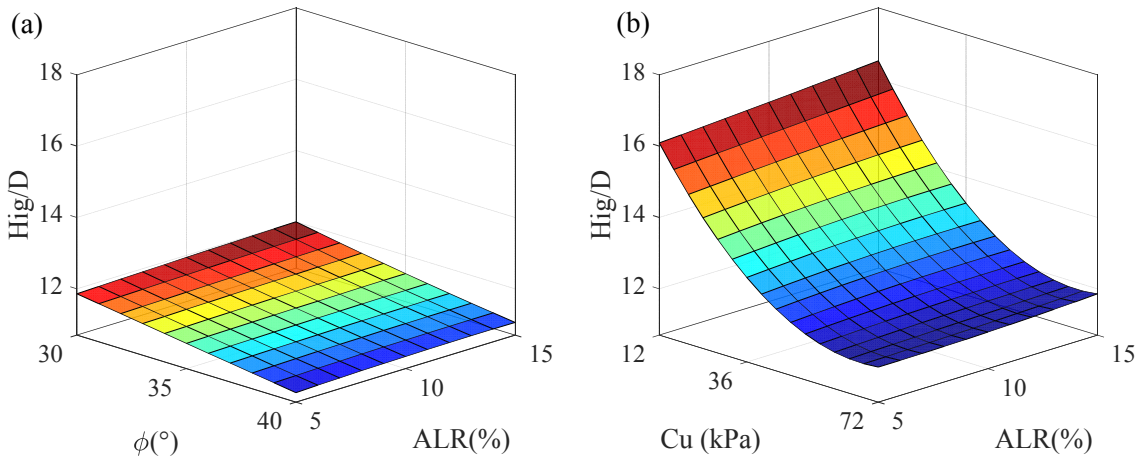

Figure 6-46 Impact of ALR and soil strength on Hig/D ratio for: (a) sand and (b) clay

Results of the regression analyses are presented in Equation 6-15 and Equation 6-16 for sand and clay, with corresponding R-squared values of 0.99 and 0.98, respectively. Regarding clay, the resulting equation depends upon the units of the undrained shear strength (C_u).

$$\frac{H_{IG}}{D} = 8.53 + 0.9\frac{L_a}{D} - \frac{D}{240t} - \frac{\phi}{10} \quad , \quad \phi(°) \qquad \text{Equation 6-15}$$

$$\frac{H_{IG}}{D} = 17.6 + 0.71\frac{L_a}{D} - \frac{D}{120t} - 2.60Ln(C_u) \quad , \quad C_u(kPa) \qquad \text{Equation 6-16}$$

Figure 6-47 through Figure 6-49 present simulation results for sand along with the trends generated using Equation 6-15 for each of the friction angles studied. Similarly, Figure 6-50 through Figure 6-52 show simulation results for clay along with the trends generated using Equation 6-16 for each undrained shear strength studied. Note that in both cases, predicted and simulated results are in close agreement.

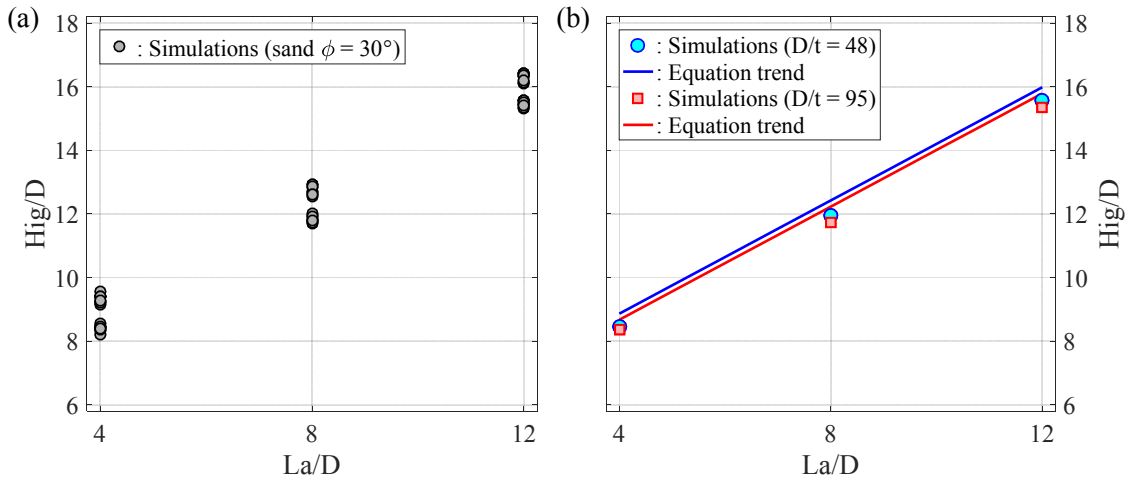

Figure 6-47 Hig/D ratio for sand with ϕ = 30°: (a) Simulations and (b) equation trends

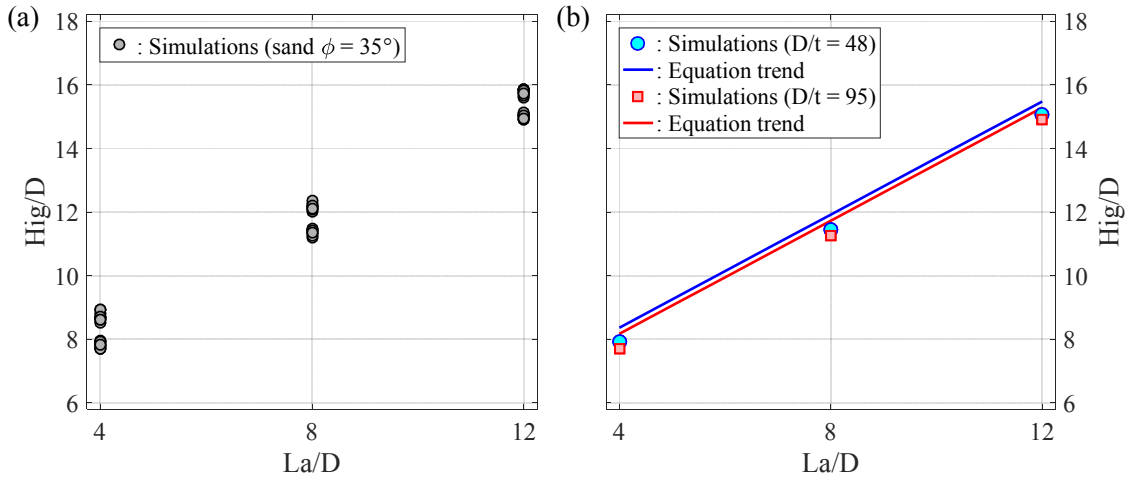

Figure 6-48 Hig/D ratio for sand with ϕ = 35°: (a) Simulations and (b) equation trends

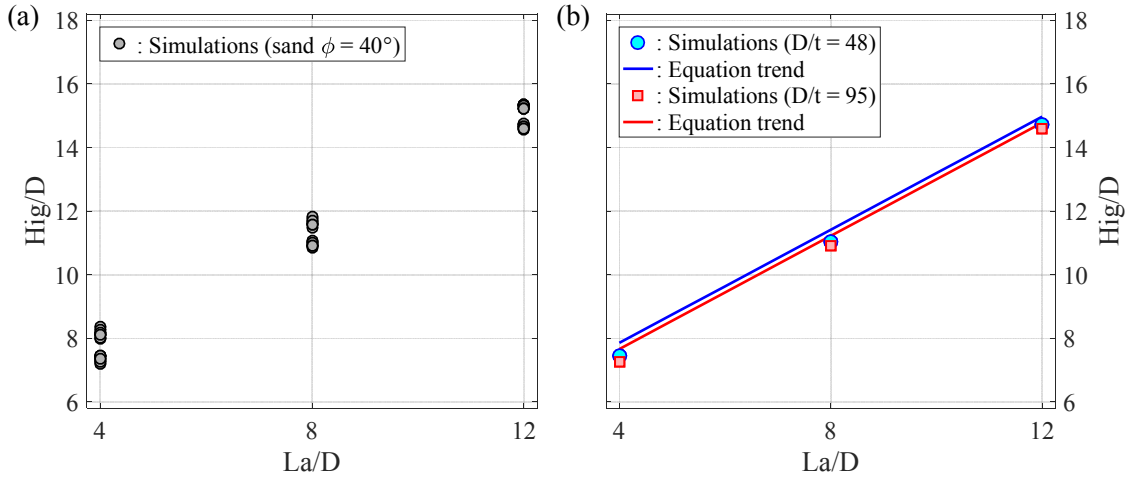

Figure 6-49 Hig/D ratio for sand with ϕ = 40°: (a) Simulations and (b) equation trends

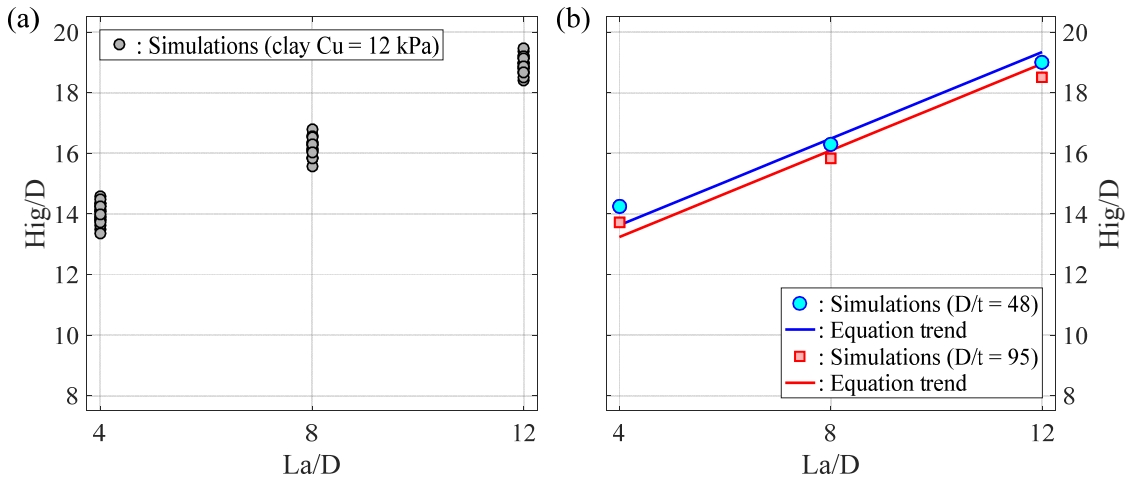

Figure 6-50 Hig/D ratio for clay with Cu = 12kPa: (a) Simulations and (b) equation trends

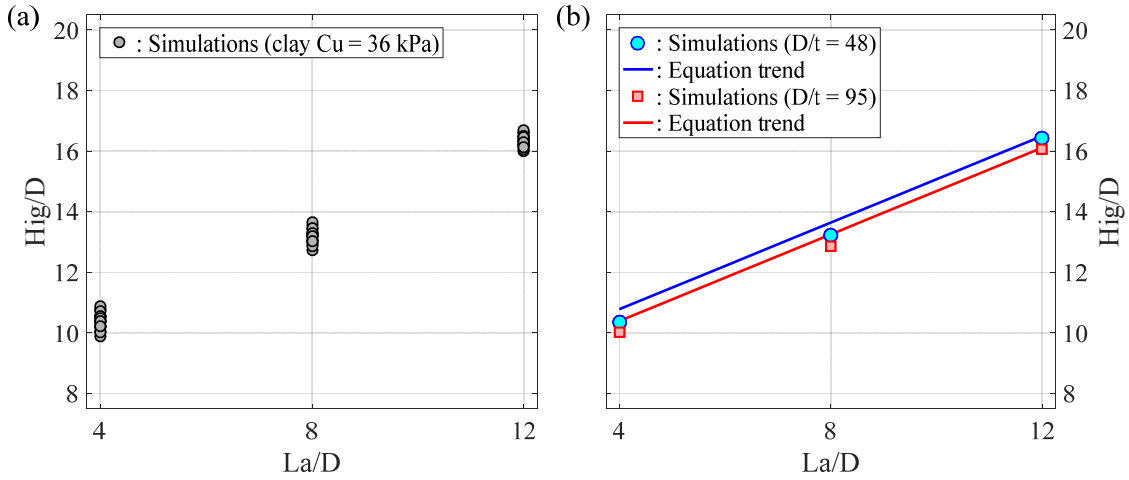

Figure 6-51 Hig/D ratio for clay with Cu = 36kPa: (a) Simulations and (b) equation trends

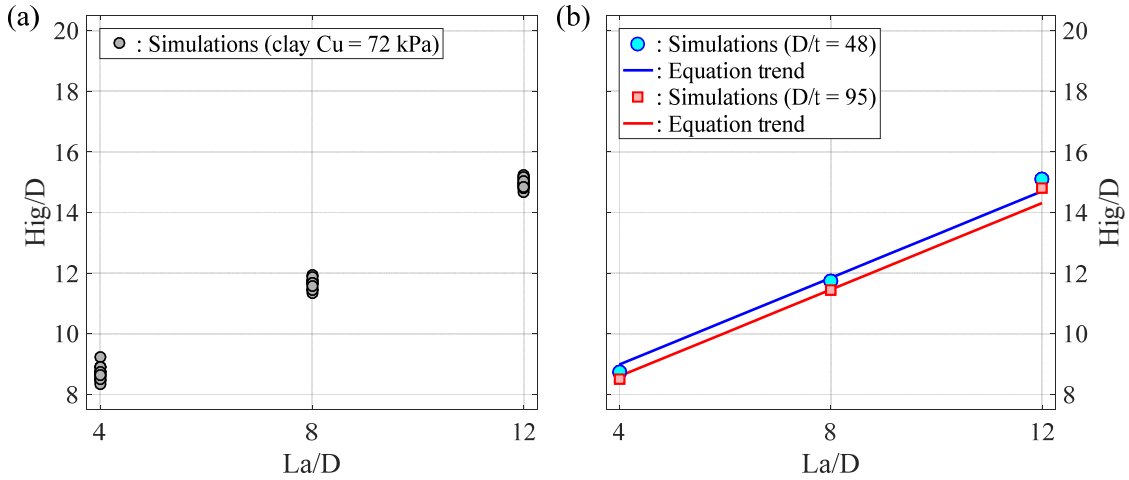

Figure 6-52 Hig/D ratio for clay with Cu = 72kPa: (a) Simulations and (b) equation trends

6.3.2. Yield Displacement Parameter

Figure 6-53 through Figure 6-55 show the variation of the yield displacement parameter (c_1) with L_a/D, D/t, and ALR. Regarding sand, note that the parameter varies linearly only with L_a/D. However, note that in terms of D/t and ALR the values do not change as much, thus a linear approximation could be appropriate; values of c_1 within 0.14 and 0.21 were observed.

Regarding results for clay on the other hand, the variable that has more influence on c_1 is the D/t ratio, while values vary non-linearly in terms of the undrained shear strength.

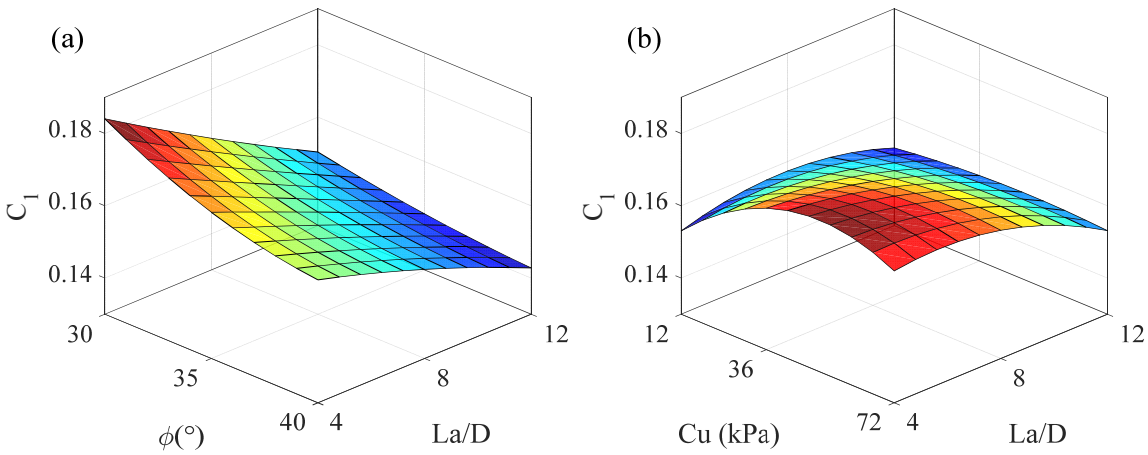

Figure 6-53 Impact of La/D ratio and soil strength on C1 for: (a) sand and (b) clay

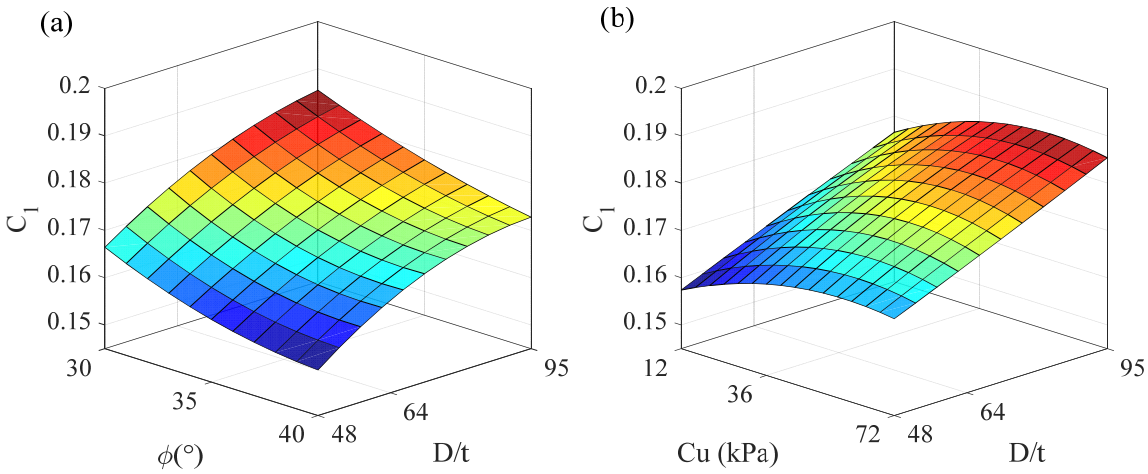

Figure 6-54 Impact of D/t ratio and soil strength on C1 for: (a) sand and (b) clay

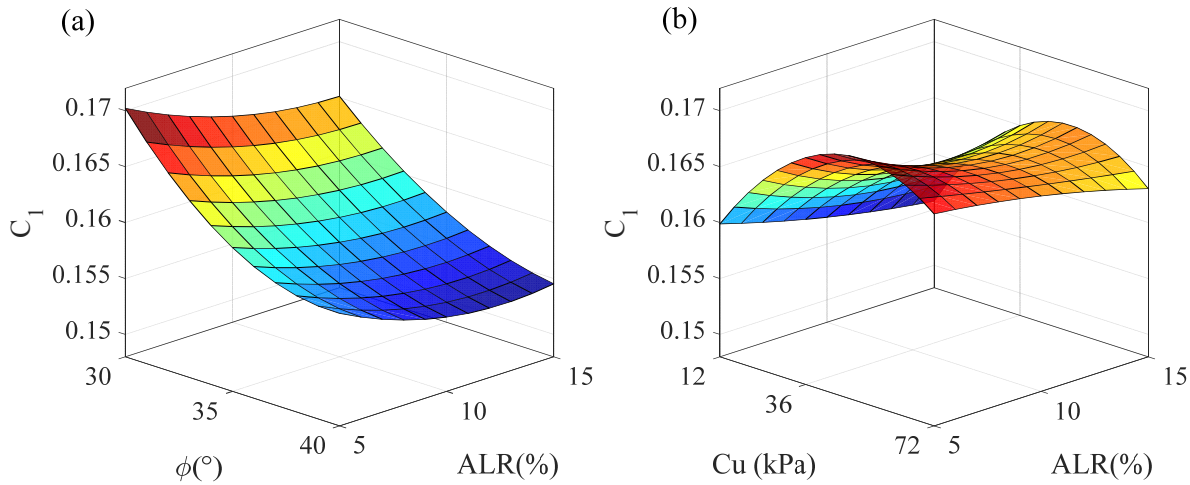

Figure 6-55 Impact of ALR and soil strength on C1 for: (a) sand and (b) clay

Results of the regression analyses are presented in Equation 6-17 and Equation 6-18 for sand and clay, with R-squared values of 0.91 and 0.81, respectively. For clay, note that the equation depends on the units of the undrained shear strength. Moreover, although the R-squared values are not as high as in other of the previous regression analyses, it will be seen that the prediction are rather good.

$$C_1 = 0.207 - \frac{L_a}{300\,D} + \frac{D}{2800\,t} - \frac{\phi}{960} \quad , \quad \phi(^\circ) \qquad \text{Equation 6-17}$$

$$C_1 = 0.135 - \frac{L_a}{900\,D} + \frac{D}{2500\,t} + \frac{Ln(C_u)}{200} \quad , \quad C_u\,(kPa) \qquad \text{Equation 6-18}$$

Figure 6-56 through Figure 6-58 present simulation results for sand along with the trends generated using Equation 6-17for each of the friction angles studied. Similarly, Figure 6-59 through Figure 6-61 show simulation results for clay along with the trends generated using Equation 6-18 for each undrained shear strength studied. Note that in both cases, predicted and simulated results are in close agreement. However, some of the simulated points are outside the trends, especially for clay, though note that the difference of the predicted values is only about 0.01.

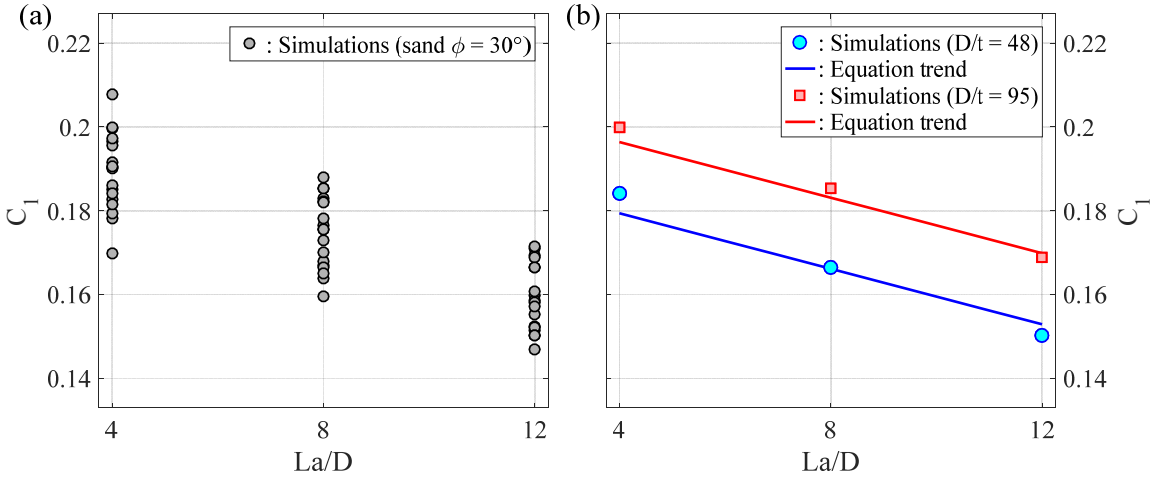

Figure 6-56 C_1 for sand with ϕ = 30°: (a) Simulations and (b) equation trends

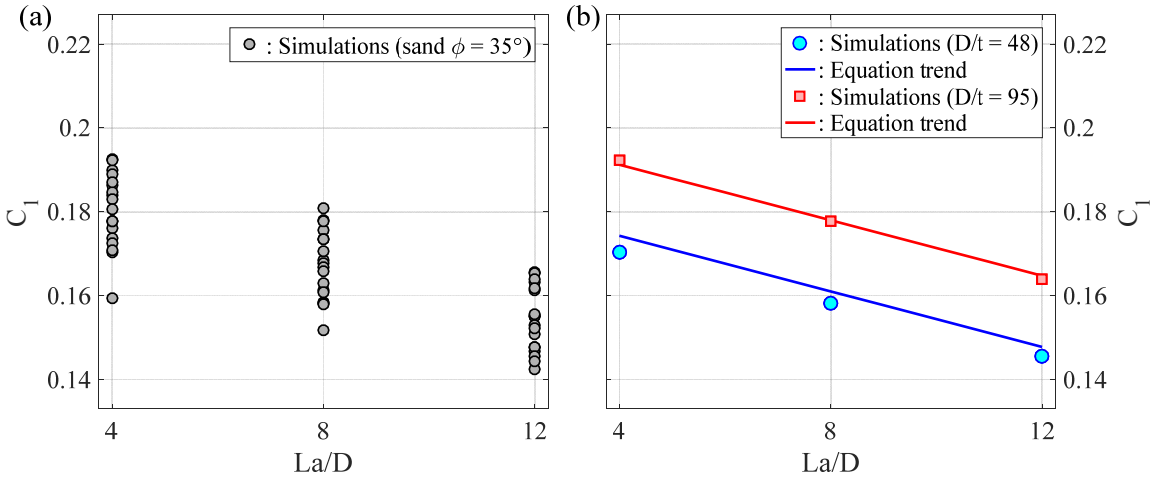

Figure 6-57 C_1 for sand with ϕ = 35°: (a) Simulations and (b) equation trends

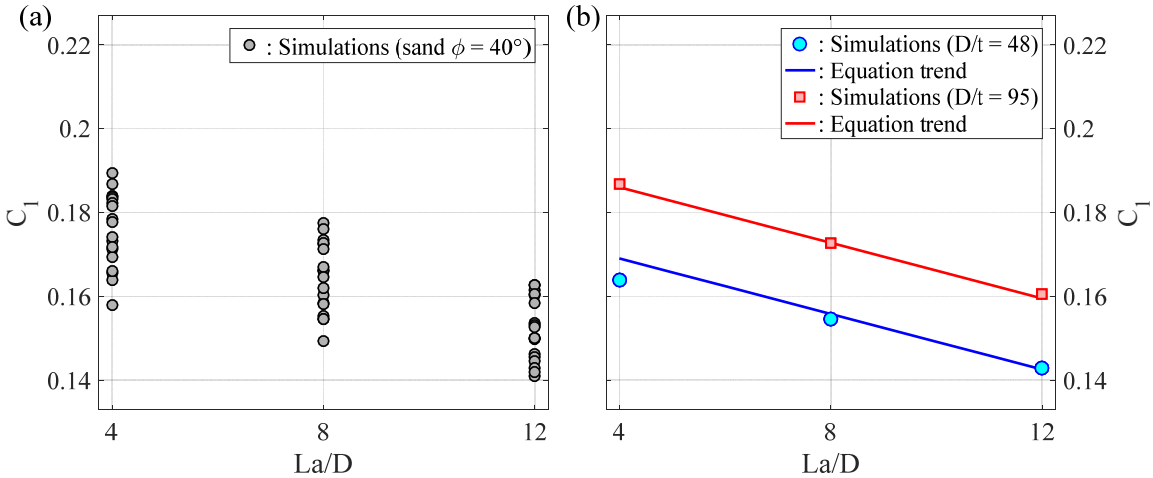

Figure 6-58 C_1 for sand with ϕ = 40°: (a) Simulations and (b) equation trends

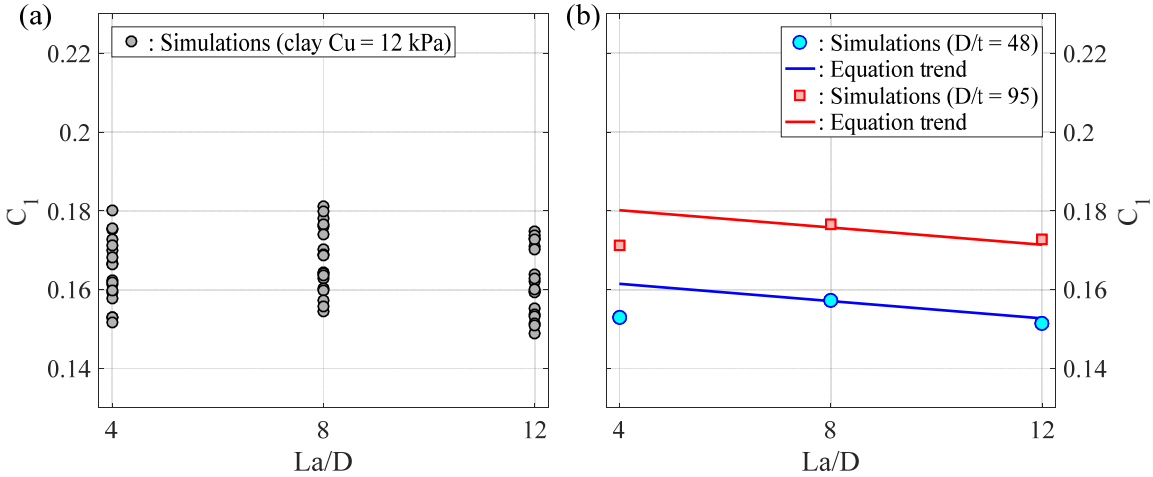

Figure 6-59 C_1 for clay with Cu = 12kPa: (a) Simulations and (b) equation trends

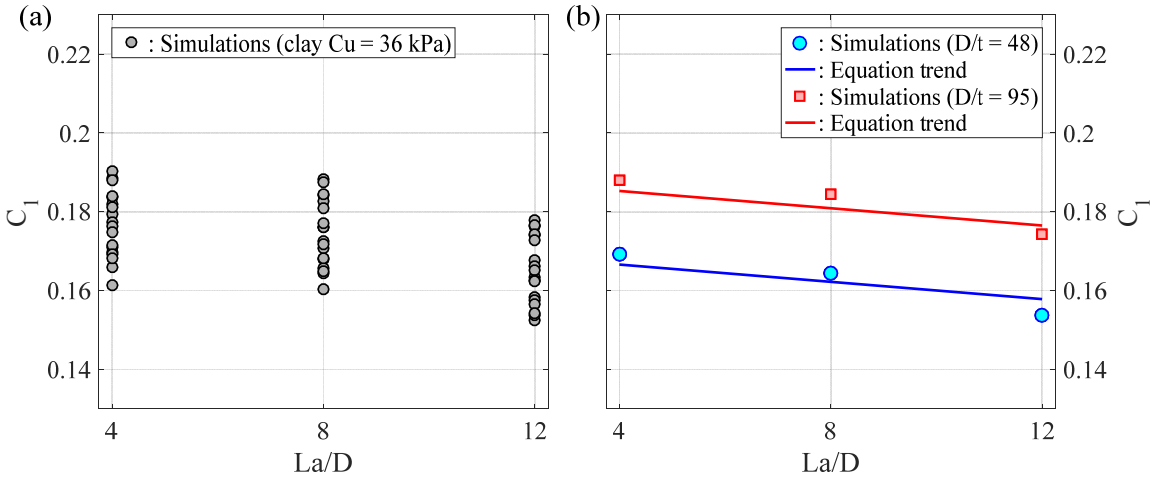

Figure 6-60 C_1 for clay with Cu = 36kPa: (a) Simulations and (b) equation trends

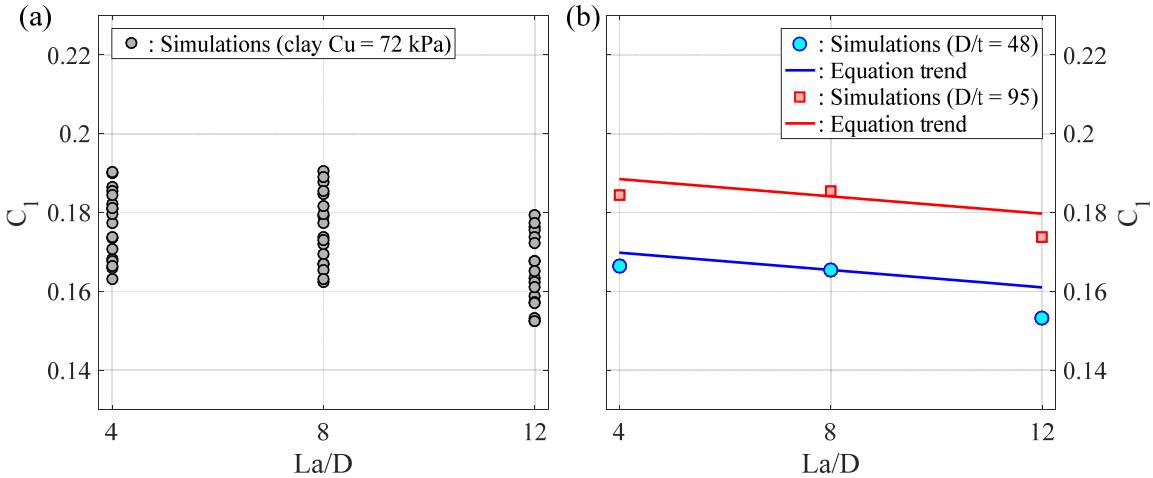

Figure 6-61 C_1 for clay with Cu = 72kPa: (a) Simulations and (b) equation trends

6.3.3. Plastic Displacement Parameter

Figure 6-62 shows the variation of the parameter β in terms of the displacement ductility (μ) for both sand and clay. Note that the parameter tends to saturate after ductility 1.5. As such, it was decided to average the results within ductility 1.5($\mu_{1.5}$) and ductility 4 (μ_4).

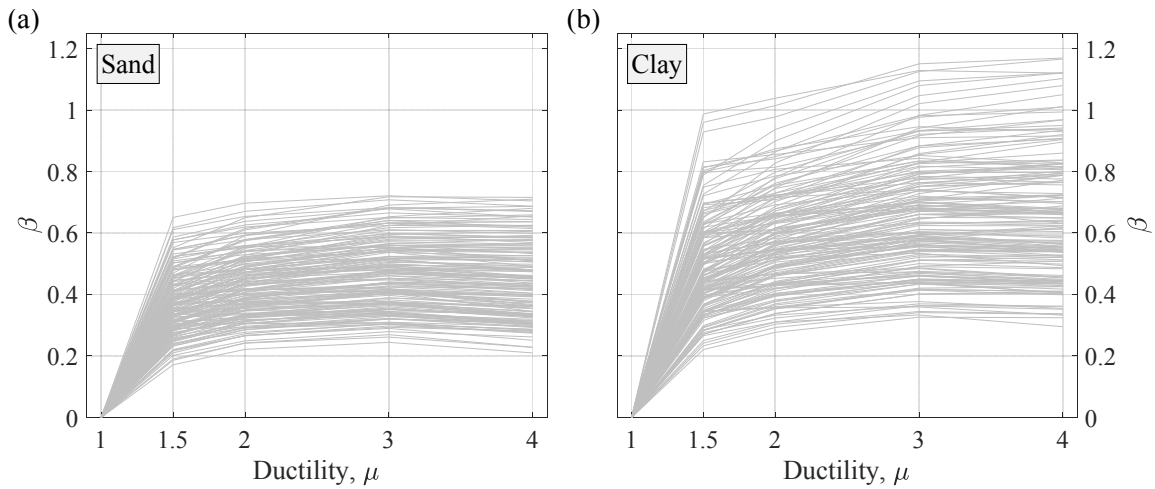

Figure 6-62 Plastic displacement parameter (β) for (a) sand and (b) clay

Using the averaged values of the parameter β, Figure 6-63 through Figure 6-65 show the variation of the parameter with L_a/D, D/t, and ALR. Regarding sand, note that all variables indicate a linear relationship, including the friction angle; values of β within 0.2 and 0.7 were observed.

Regarding results for clay, on the other hand, it can be inferred that results vary linearly with all the parameters except in terms of the undrained shear strength; values of β within 0.3 and 1.1 were observed.

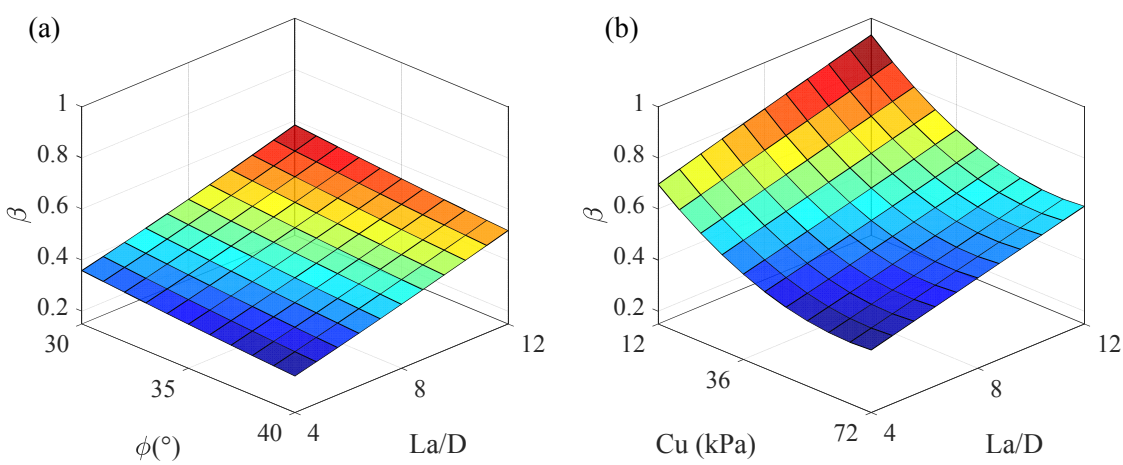

Figure 6-63 Impact of L_a/D ratio and soil strength on β for: (a) sand and (b) clay

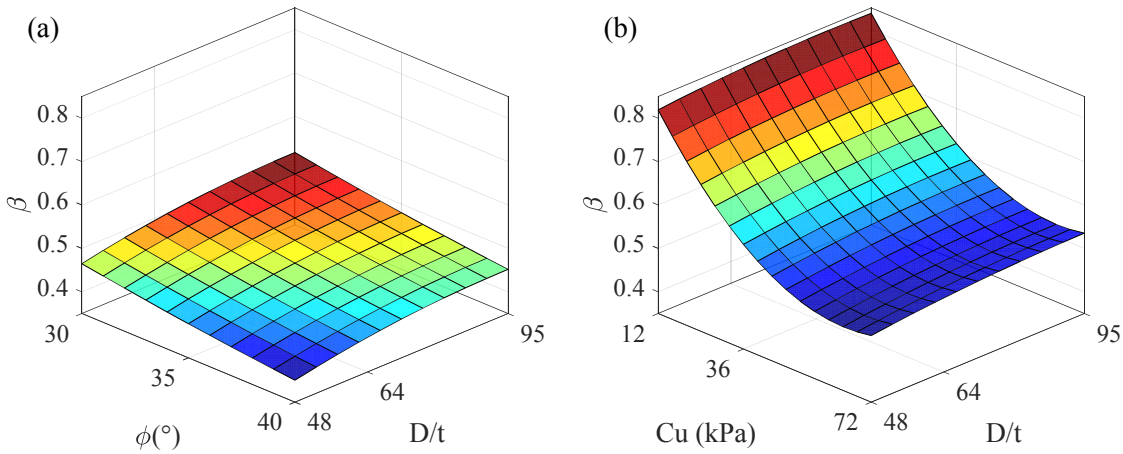

Figure 6-64 Impact of D/t ratio and soil strength on β for: (a) sand and (b) clay

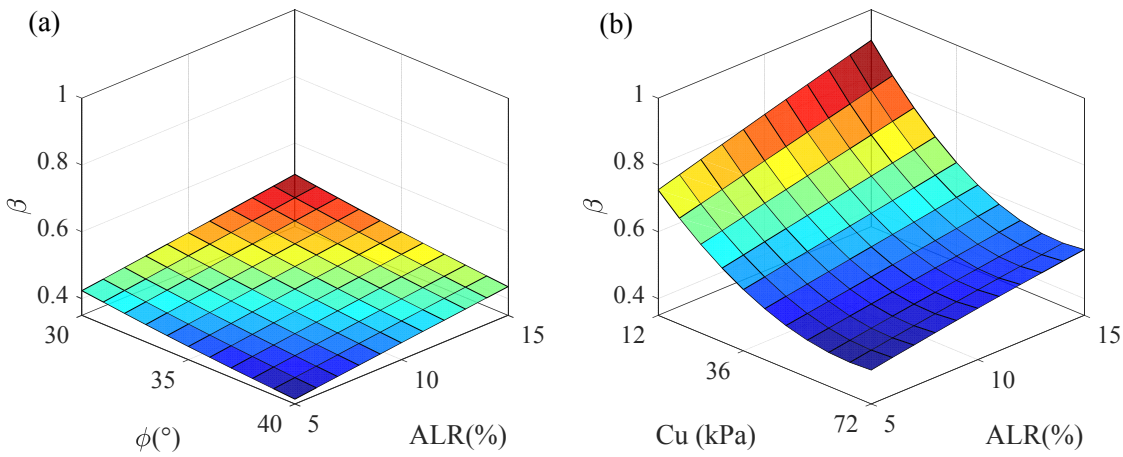

Figure 6-65 Impact of ALR and soil strength on β for: (a) sand and (b) clay

Results of the regression analysis are presented in Equation 6-19 and Equation 6-20 for sand and clay, with corresponding R-squared values of 0.98 and 0.97, respectively. Although the equations seem long and somewhat complex, it is worth recognizing that accurate prediction of the parameter β is important as it is used to modify the effective length (L_e) of the RCFST shaft to calculate the plastic displacement. Therefore, small variations in the prediction of β could lead to large errors in the calculated displacement.

$$\beta = 0.255 + 0.1D + \frac{L_a}{50D}\left(1 + \frac{D}{170t}\right) + 0.7\,ALR - \frac{\phi}{160} \quad , \quad D(m), \phi(°) \qquad \text{Equation 6-19}$$

$$\beta = 0.631 + 0.2D + \frac{L_a}{40D}\left(1 + \frac{D}{380t}\right) + 1.08\,ALR - 0.16\,Ln(C_u) \quad , \quad D(m), C_u(kPa) \qquad \text{Equation 6-20}$$

Figure 6-66 through Figure 6-68 present simulation results for sand along with the trends generated using Equation 6-19 for each of the friction angles studied. Similarly, Figure 6-69 through Figure 6-71 present simulation results for clay along with the trends generated using Equation 6-20. Note that in all cases results are in close agreement.

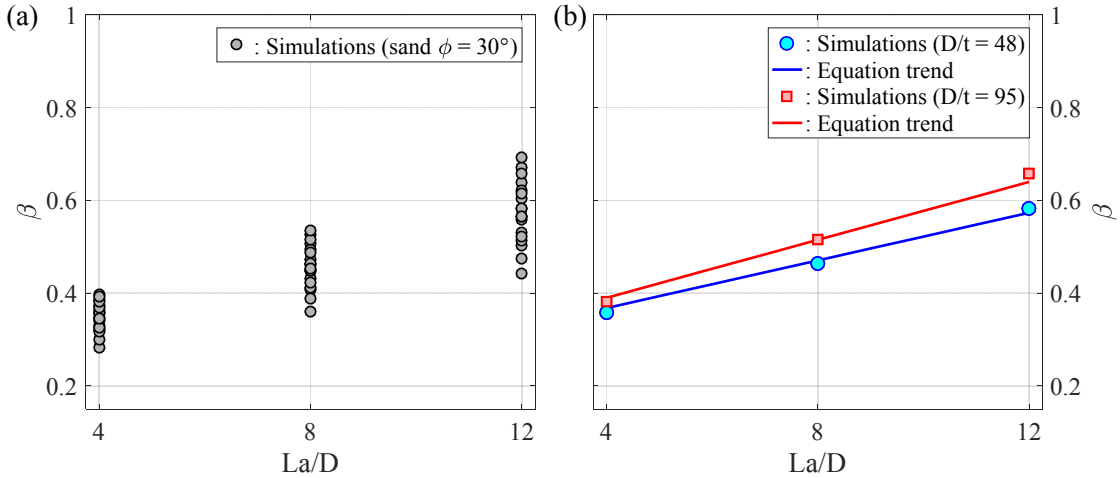

Figure 6-66 Parameter β for sand with ϕ = 30°: (a) simulations and (b) equation trends

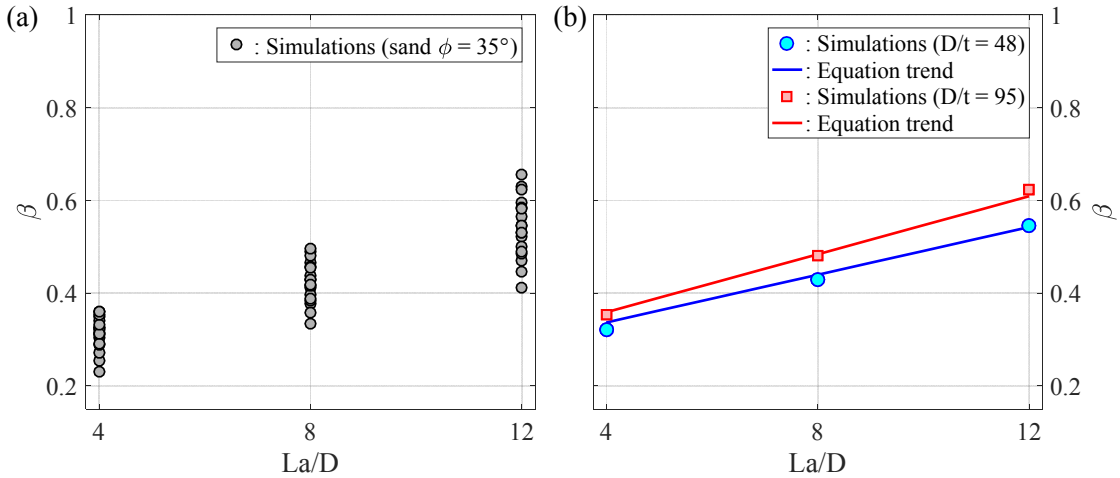

Figure 6-67 Parameter β for sand with ϕ = 35°: (a) simulations and (b) equation trends

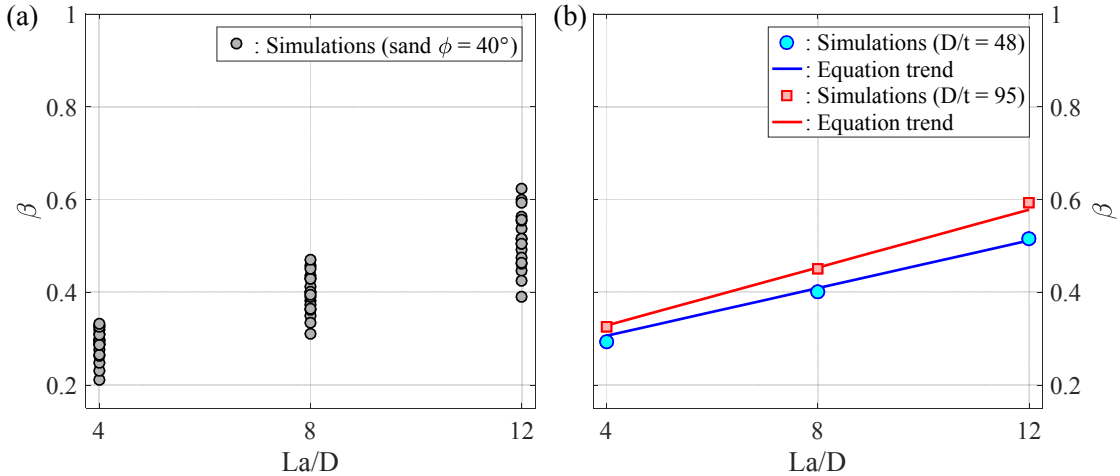

Figure 6-68 Parameter β for sand with ϕ = 40°: (a) simulations and (b) equation trends

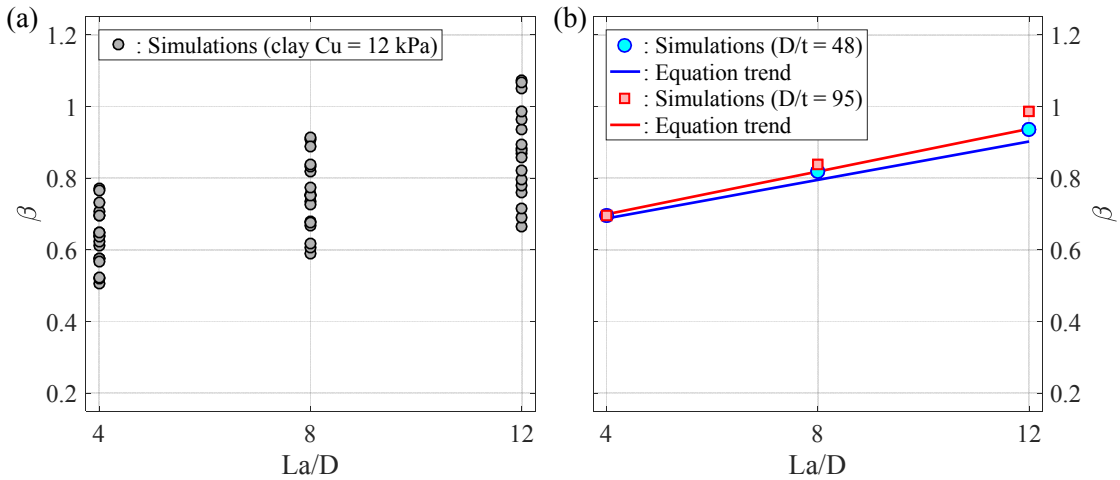

Figure 6-69 Parameter β for clay with Cu = 12 kPa: (a) simulations and (b) equation trends

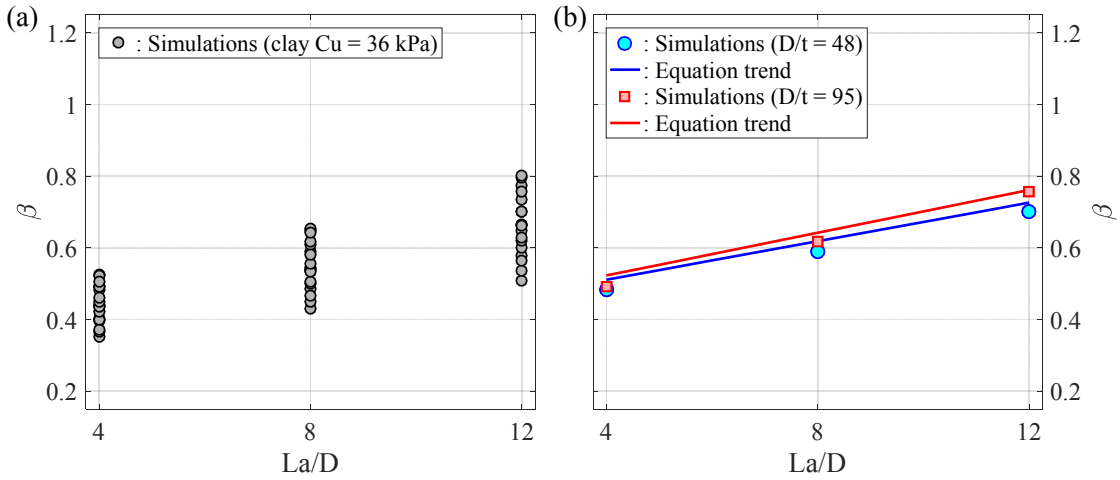

Figure 6-70 Parameter β for clay with Cu = 36 kPa: (a) simulations and (b) equation trends

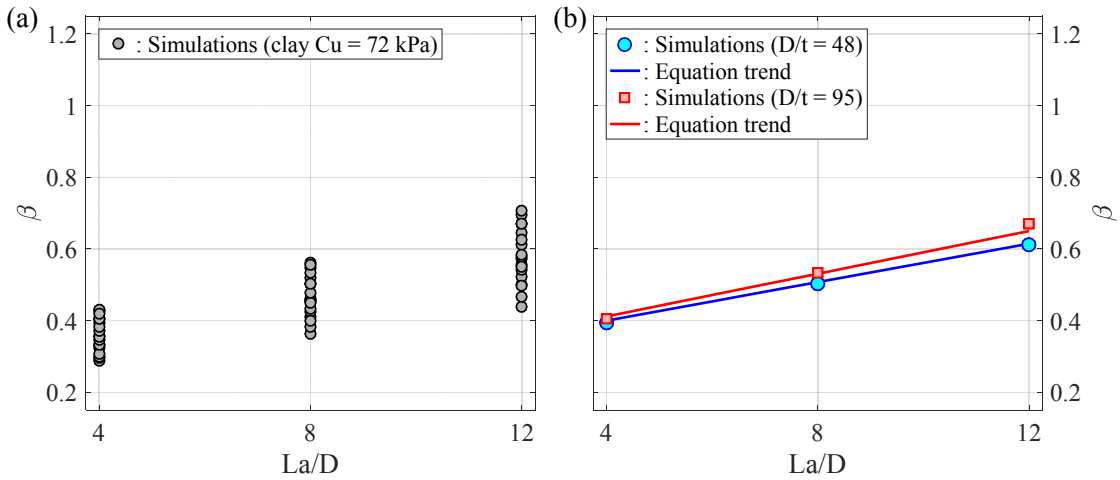

Figure 6-71 Parameter β for clay with Cu = 72 kPa: (a) simulations and (b) equation trends

6.3.4. Equivalent Viscous Damping

Fixed-head RCFST shafts are controlled by the plastic hinge that develops at the column-cap beam interface, where the steel tube only provides confinement and not flexural strength. Simulation results in terms of the system equivalent viscous damping (EVD) are plotted in Figure 6-72 along with results from Equation 6-21, which corresponds to EVD of reinforced concrete bridge columns (Priestley et al., 2007). Note that there is a linear trend in the simulated results. Moreover, notice that at ductility 1 (μ_1) simulated results are consistently higher than those from Equation 6-21, this is due to the contribution of the soil to the system EVD. Furthermore, for high ductility levels the simulated results are consistently lower. This is due to the fact that, although there is energy dissipation at the top plastic hinge, the system has reserved capacity as the flexural stiffness below the top plastic hinge is provided by the RCFST. This means that while the system experiences degradation, the strength continues to develop as the bottom plastic hinge is activated.

$$\xi_{eq} = 0.05 + 0.444\left(\frac{\mu - 1}{\mu\pi}\right) \qquad \text{Equation 6-21}$$

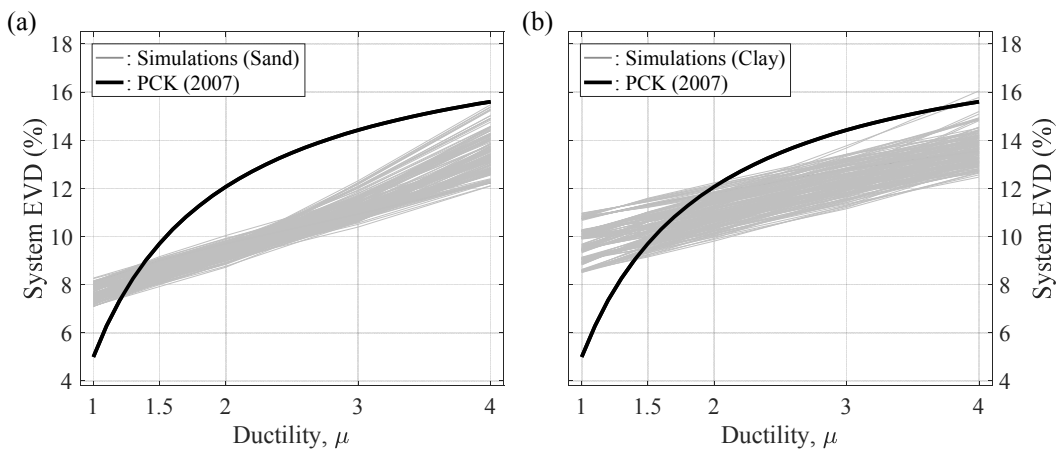

Figure 6-72 Observed system EVD for: (a) sand and (b) clay

Based on the discussion above, simulated data was analyzed first as a function of ductility (μ). As such, a linear relation variation was assumed as results showed linear, concave, and convex trends. Thus, the form of Equation 6-22 was adopted. Then, the coefficients b_0 and b_1 were determined as a function of the L_a/D ratio, D/t ratio, and ALR, for both sand and clay independently.

$$\xi_{eq} = b_0 + b_1(\mu - 1) \qquad \text{Equation 6-22}$$

Results of the regression analyses are presented in Equation 6-23 and Equation 6-24 for sand and clay, with corresponding R-squared values of 0.98 and 0.97. Furthermore, Figure 6-73 through Figure 6-75 show the simulated results for sand along with the trends generated using Equation 6-23. Similarly, Figure 6-76 through Figure 6-78 show the simulated results for clay along with the trends generated using Equation 6-24. Notice tha although a linear variation was assumed with ductility, the results are in close agreement in all cases.

$$\xi_{eq} = 0.094 - \frac{L_a}{1000\,D} - \frac{\phi}{3200} + \left(\frac{1}{160} + \frac{L_a}{1200\,D} + \frac{D}{12000\,t}\right)(\mu - 1) \qquad \text{Equation 6-23}$$

$$\xi_{eq} = 0.13 - \frac{L_a}{600\,D} - \frac{Ln(C_u)}{160} + \left(\frac{1}{300} + \frac{L_a}{1400\,D} + \frac{D}{14000\,t}\right)(\mu - 1) \quad , \quad C_u\,(kPa) \qquad \text{Equation 6-24}$$

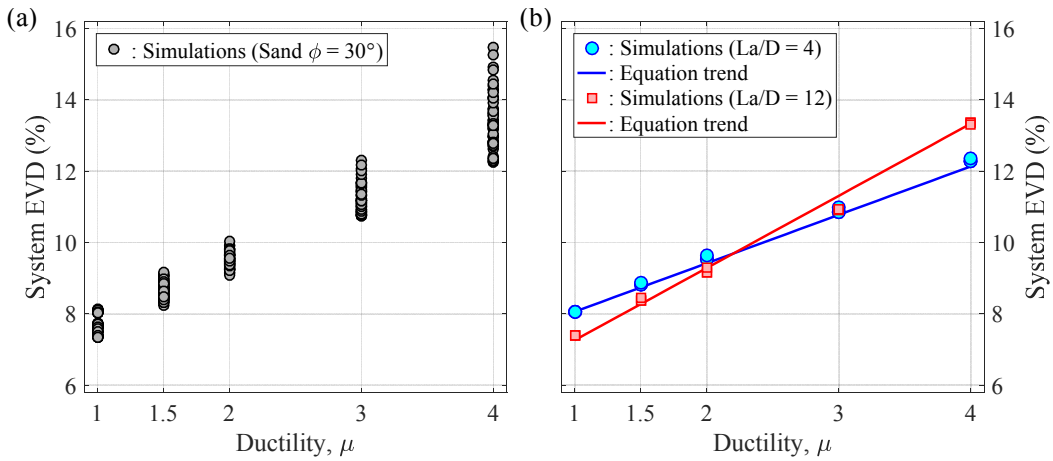

Figure 6-73 System EVD for sand with ϕ = 30°: (a) simulations and (b) equation trends

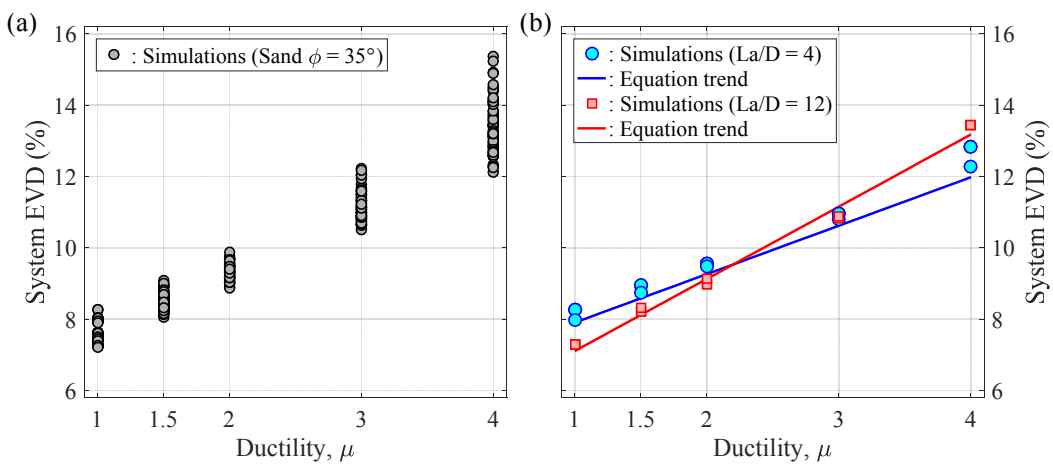

Figure 6-74 System EVD for sand with ϕ = 35°: (a) simulations and (b) equation trends

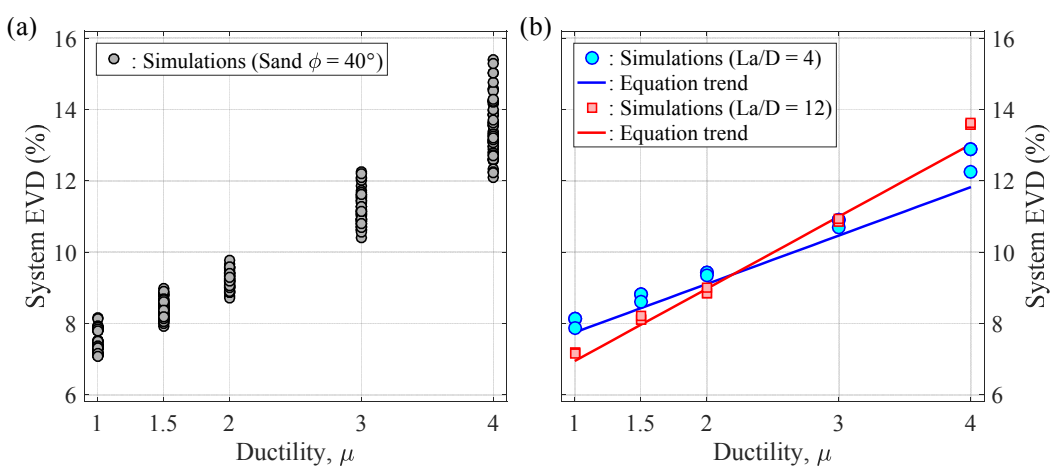

Figure 6-75 System EVD for sand with ϕ = 40°: (a) simulations and (b) equation trends

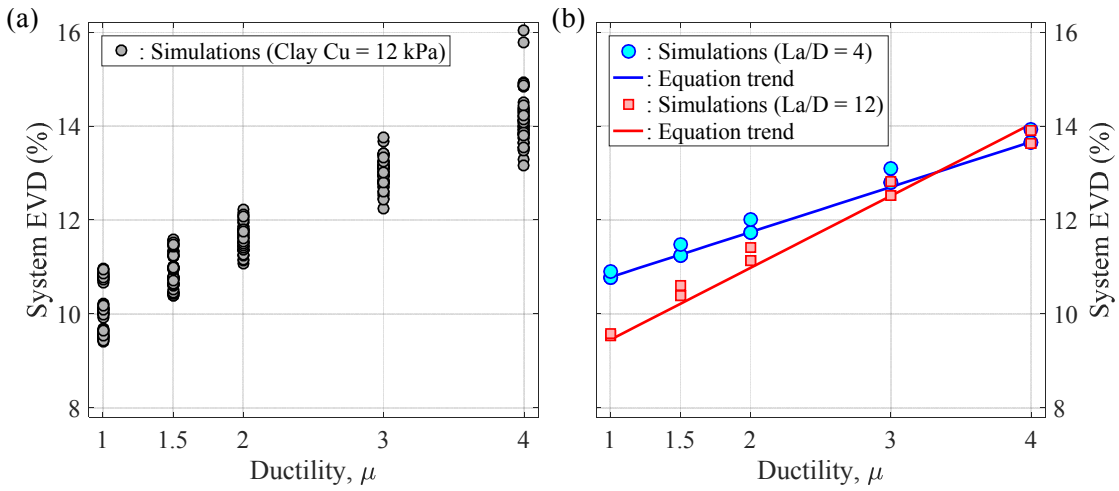

Figure 6-76 System EVD for sand with C_u = 12 kPa: (a) simulations and (b) equation trends

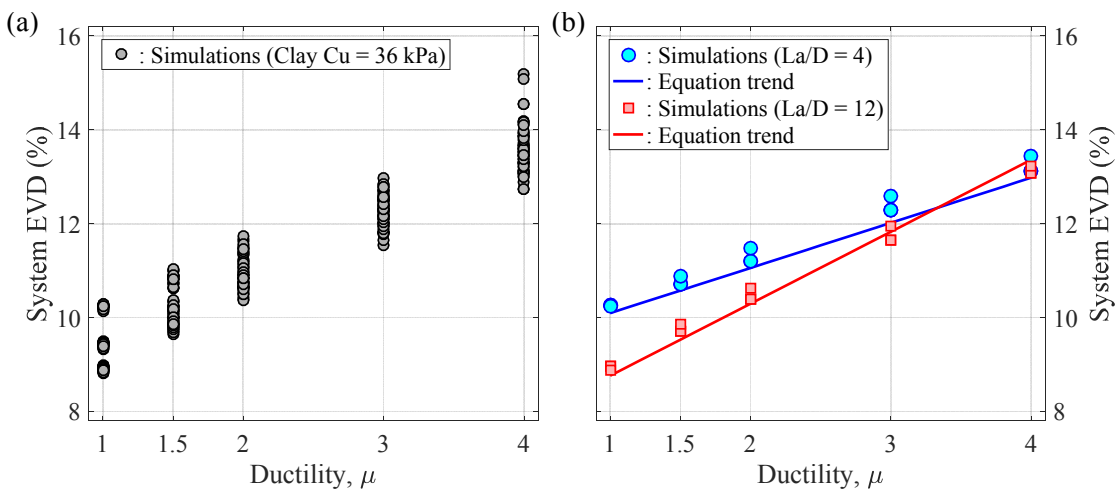

Figure 6-77 System EVD for sand with C_u = 36 kPa: (a) simulations and (b) equation trends

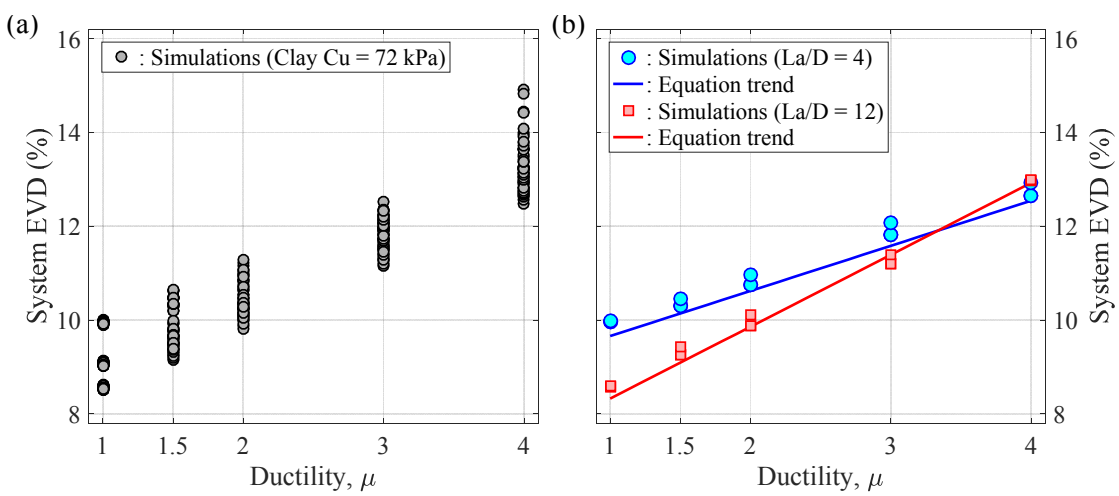

Figure 6-78 System EVD for sand with C_u = 72 kPa: (a) simulations and (b) equation trends

6.4. Depth to plastic Hinge Revisited

Based on the results of the regression analyses for both pinned-head and fixed-head shafts, it was noticed that the resulting equations for the depth top plastic hinge parameter (H_{ig}/D) were similar. Thus, and additional analysis was conducted for this parameter, considering data from both types of specimens. Results are presented in Equation 6-25 and Equation 6-26 for sand and clay, with corresponding R-squared values of 0.97 and 0.96, respectively.

$$\frac{H_{ig}}{D} = 8.57 + 0.88\frac{L_a}{D} - \frac{D}{130t} - \frac{\phi}{10} \qquad \text{Equation 6-25}$$

$$\frac{H_{ig}}{D} = 17.90 + 0.68\frac{L_a}{D} - \frac{D}{55t} - 2.49\,Ln\left(C_u\right) \;\;,\;\; C_u\left(kPa\right) \qquad \text{Equation 6-26}$$

Figure 6-79 through Figure 6-81 present the simulated results for sand along with the trends generated using Equation 6-25. Similarly, Figure 6-82 through Figure 6-84 present the simulated results for clay along with the trends generated using Equation 6-26. Note in all cases that, although there is more variation in the results, due to the consideration of data from both pinned and fixed-head specimens, the results are in close agreement and the differences would not lead to significant errors.

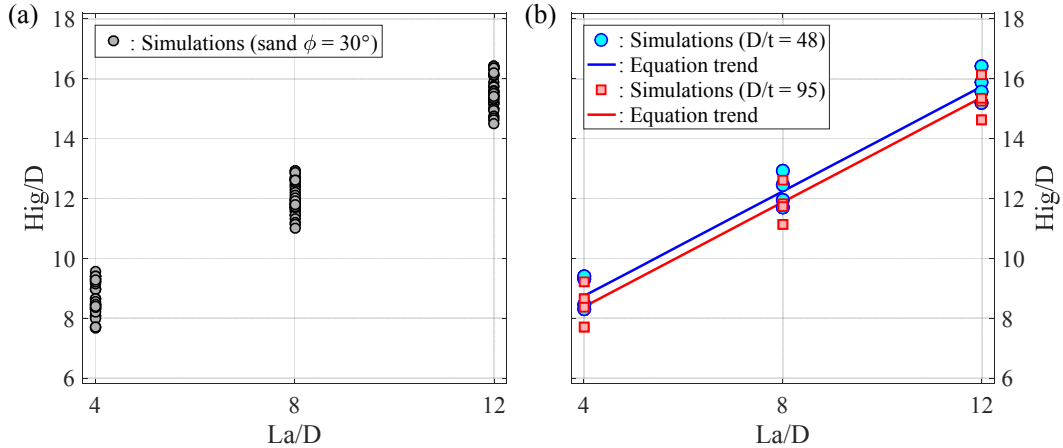

Figure 6-79 H_{ig}/D ratio for sand with ϕ = 30°: (a) simulations and (b) equation trends

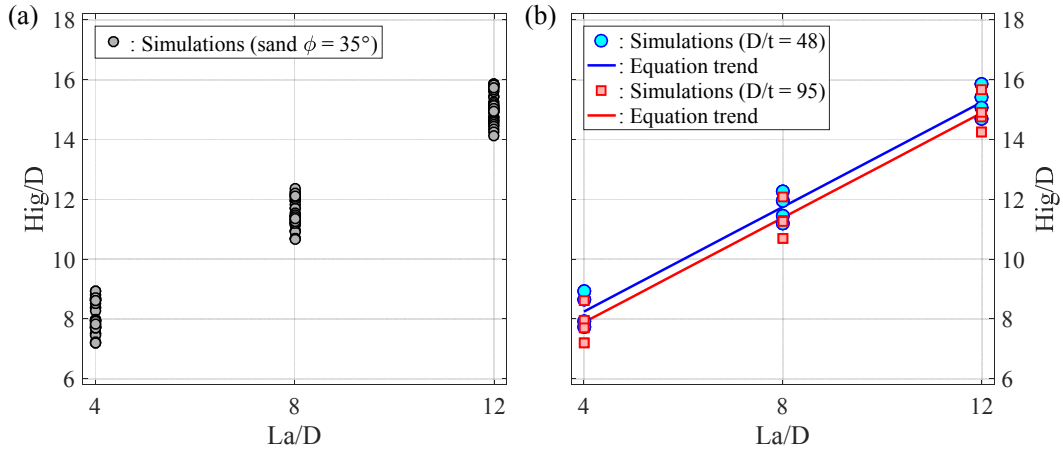

Figure 6-80 H_{ig}/D ratio for sand with ϕ = 35°: (a) simulations and (b) equation trends

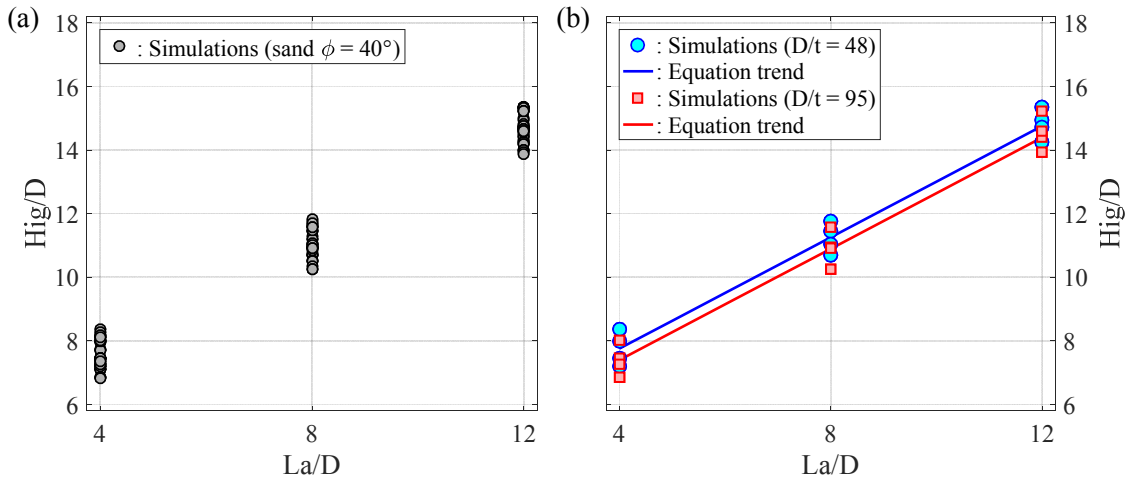

Figure 6-81 H_{ig}/D ratio for sand with ϕ = 40°: (a) simulations and (b) equation trends

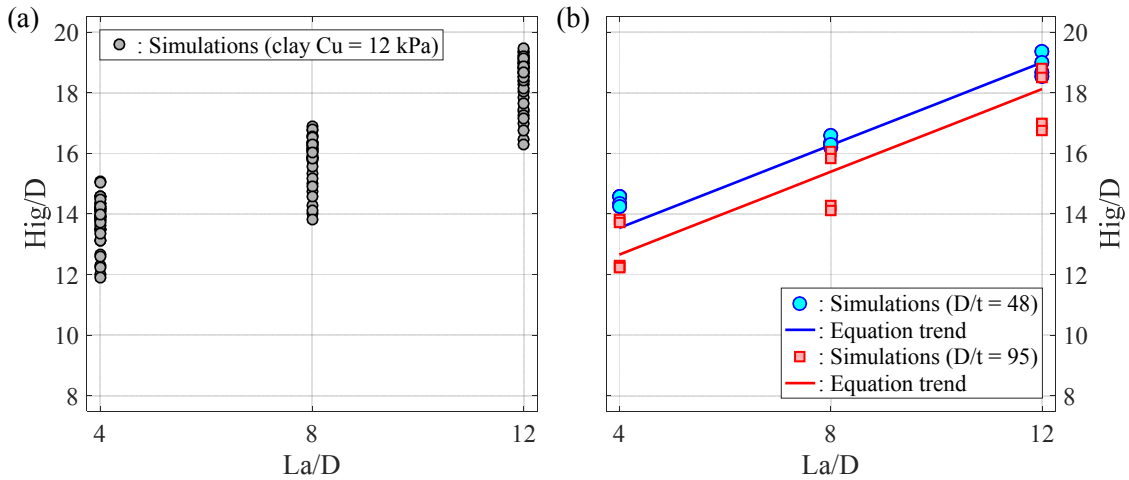

Figure 6-82 H_{ig}/D ratio for sand with C_u = 12 kPa: (a) simulations and (b) equation trends

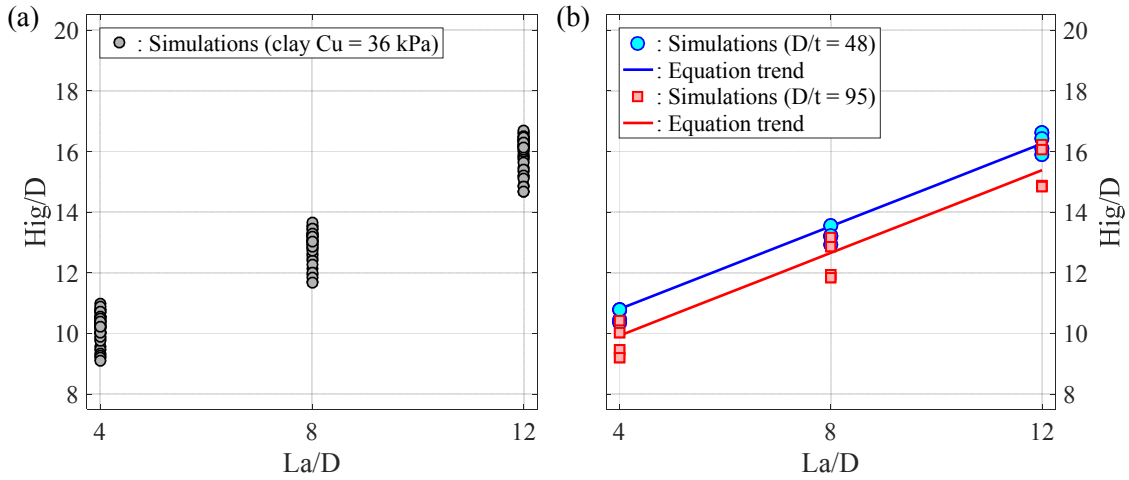

Figure 6-83 H_{ig}/D ratio for sand with C_u = 36 kPa: (a) simulations and (b) equation trends

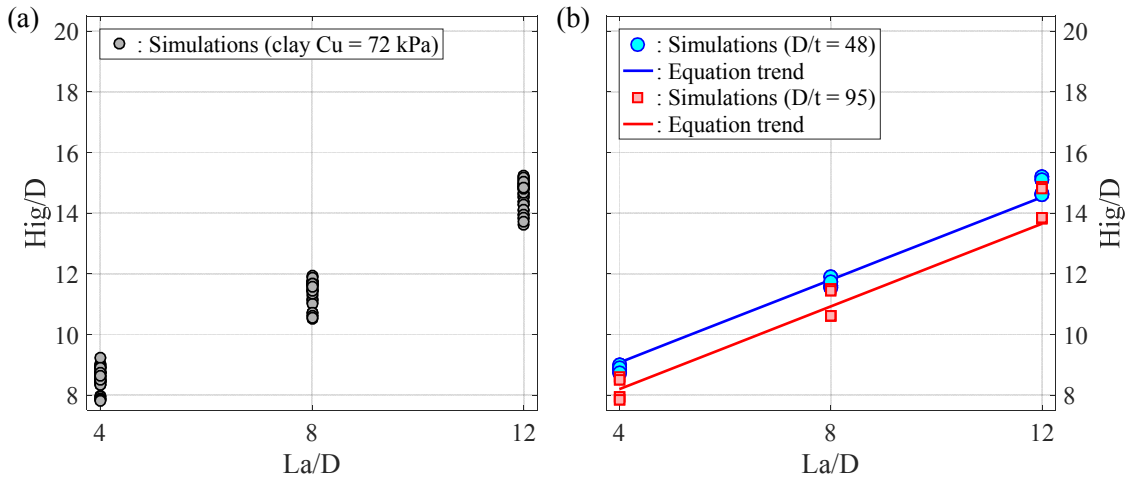

Figure 6-84 H_{ig}/D ratio for sand with C_u = 72 kPa: (a) simulations and (b) equation trends

6.5. Evaluation of the Proposed Model

The proposed equivalent cantilever plastic hinge approach was evaluated by comparison with the simulated data. For that purpose, the proposed method was implemented to predict displacements at two limit states for each of the specimens considered in the parametric study. Figure 6-85 and Figure 6-86 show the predicted to measured displacement ratio for the yield displacement and the displacement at onset of tube local buckling of the pinned-head specimens, respectively. Results are presented along with mean values (continuous line) and 95% confidence upper and lower bounds (dotted line). Note that predicted values fall within 16.4% and 16.0% of the simulated results.

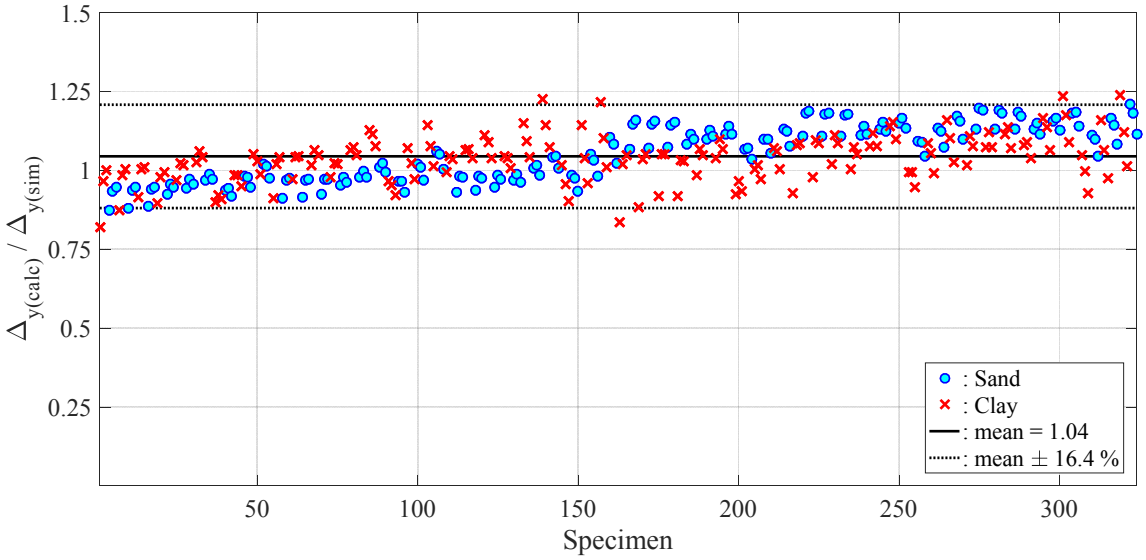

Figure 6-85 Predicted to simulated yield displacement for pinned-head shafts

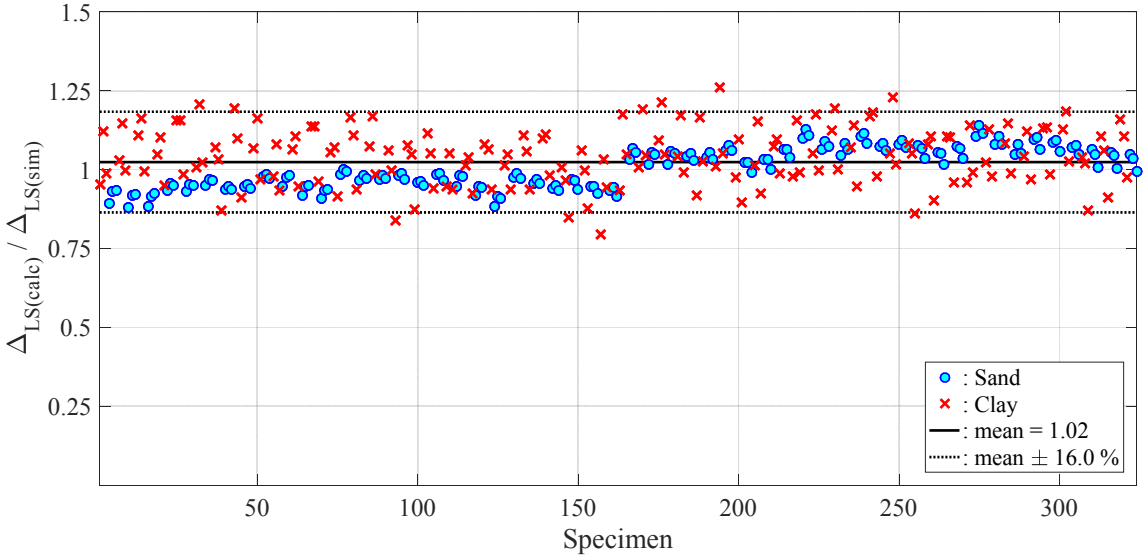

Figure 6-86 Predicted to simulated displacement for pinned-head shafts at onset of tube buckling

Similarly, Figure 6-87 and Figure 6-88 show the predicted to measured displacement ratio for the yield displacement and the displacement at bar buckling of the pinned-head specimens, respectively. Results are presented along with mean values (continuous line) and 95% confidence upper and lower bounds (dotted line). Note that predicted values fall within 15.9% and 17.1% of the simulated results.

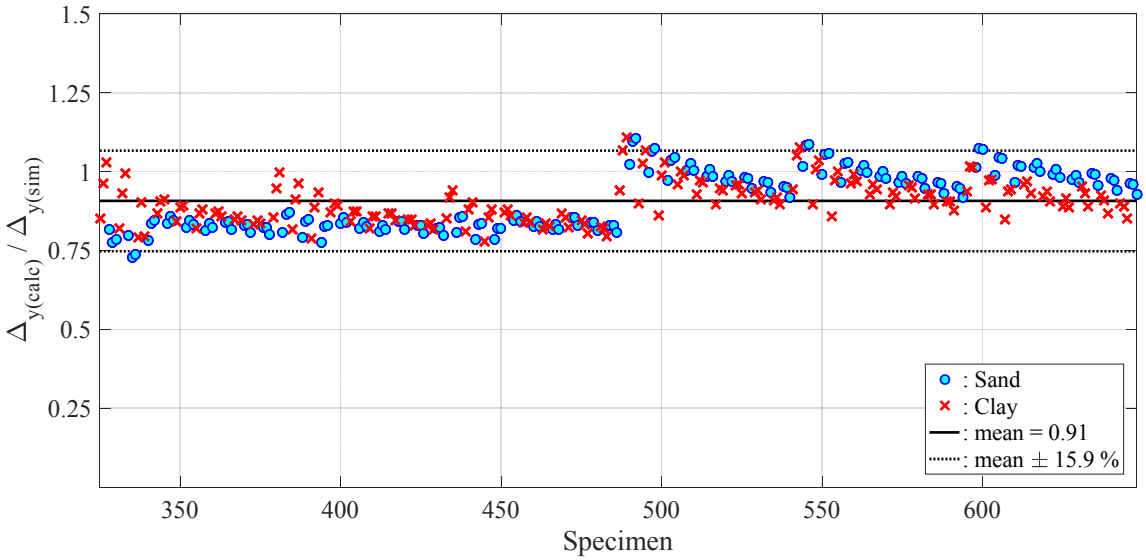

Figure 6-87 Predicted to simulated yield displacement for fixed-head shafts

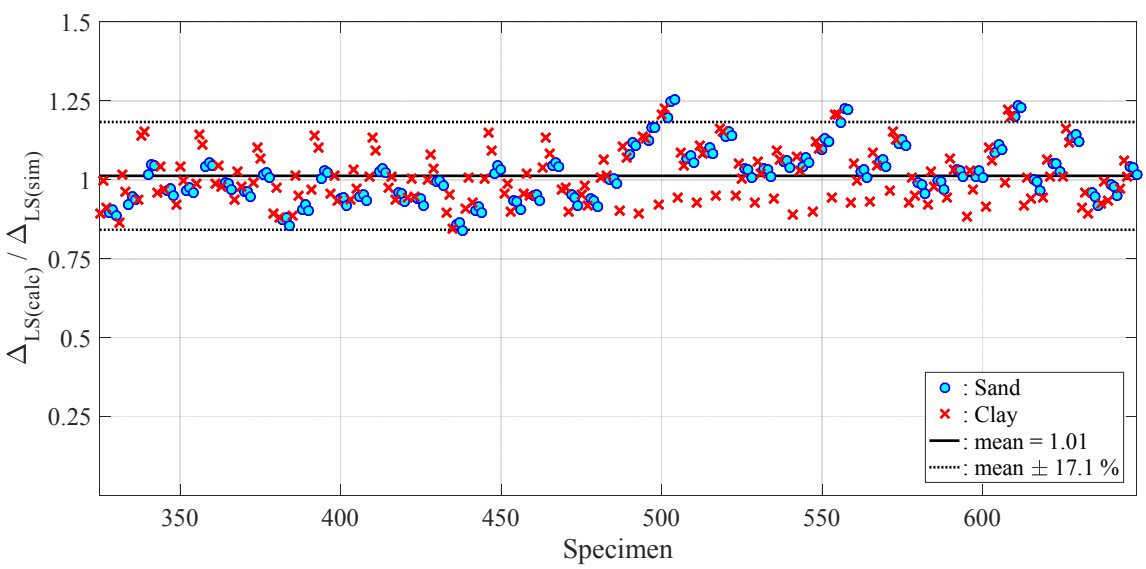

Figure 6-88 Predicted to simulated displacement for fixed-head shafts at onset of bar buckling

6.6. Summary of System Behavior from Simulated Data

This section presents a summary of the behavior of pinned-head and fixed-head RCFST shafts based upon the simulated data. For that purpose, performance was evaluated in terms of: (1) force vs. displacement response; (2) displacement, moment, and shear distribution profiles; (3) moment, curvature, and tensile strain distribution profiles; and (4) tensile strain vs. displacement envelopes. Results are presented in terms of the impact induced by the D/t ratio, L_a/D ratio, and soil stiffness. Moreover, all results correspond to a 1220-mm (4 ft.) diameter RCFST shaft embedded in sand, with all other variables varying, depending upon the parameter under consideration as follows: (1) to examine the impact of D/t ratio, two cases were considered, namely, D/t = 48 and D/t = 95, both with L_a/D = 8, ALR = 10%, and medium sand (ϕ = 35°) ; (2) regarding L_a/D ratio, cases corresponding to La/D = 4 and La/D = 12 were studied, both with D/t = 48, ALR = 10%, and medium sand (ϕ = 35°); and (3) to evaluate the impact of soil stiffness, the cases considered were loose (ϕ = 30°) and dense sand (ϕ = 40°), both with D/t = 48, La/D = 8, and ALR = 10%.

6.6.1. Pinned-Head RCFST Shafts

6.6.1.1 Force-Displacement Response

Regarding the impact of D/t ratio, note from Figure 6-89 that this parameter clearly influences the strength of the system, though the displacement ductility levels are rather similar. In terms of L_a/D ratio, note from Figure 6-90 that for L_a/d = 12 the strength of the system is less than half that for L_a/D = 4; however, notice that the latter has a larger displacement ductility capacity. At ductility 4 (μ_4), the displacement is more than 3.0 m. and although the system has a negative post-yield stiffness, it shows a stable response. Lastly, regarding soil stiffness, the strength of the system is not impacted as much, as shown in Figure 6-91, whereas lower displacements are observed for increasing levels of soil stiffness (i.e., dense sand, ϕ = 40°).

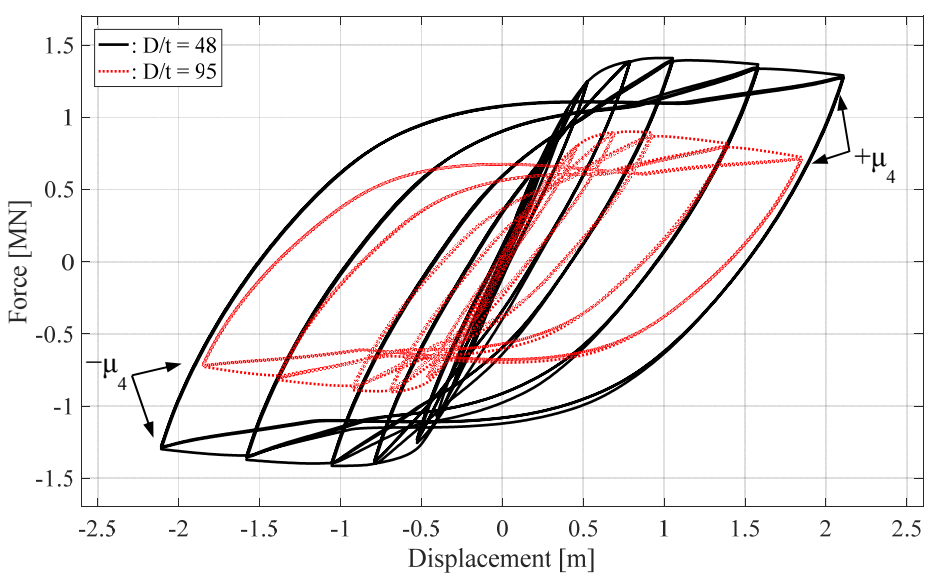

Figure 6-89 Impact of D/t ratio on force vs. displacement response

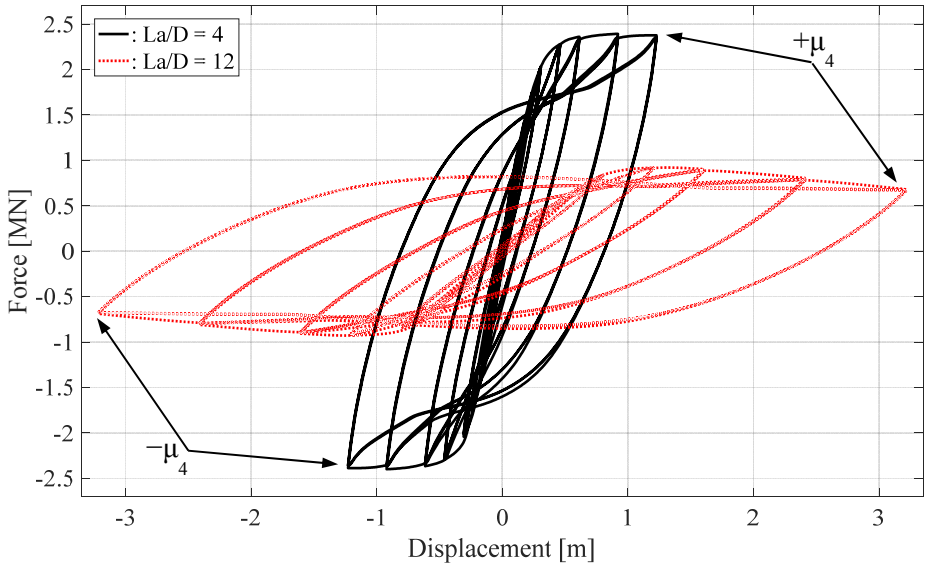

Figure 6-90 Impact of L_a/D ratio on force vs. displacement response

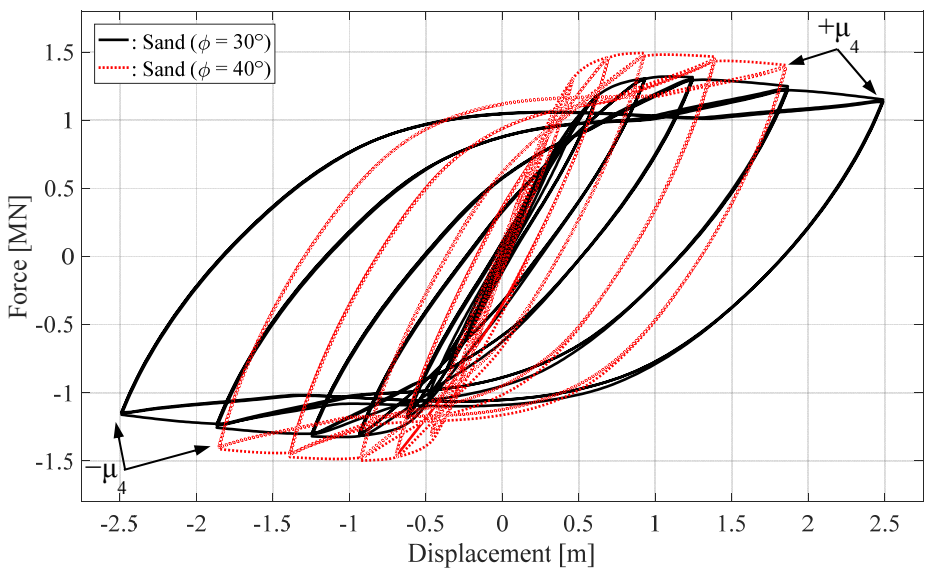

Figure 6-91 Impact of soil stiffness on force vs. displacement response

6.6.1.2 Displacement-Moment-Shear Distribution

Figure 6-92, Figure 6-93, and Figure 6-94 show the impact of D/t ratio, L_a/d ratio, and soil stiffness, respectively, on the displacement, moment and shear profiles at displacement ductility 3 (μ_3) . Note that thicker tubes (D/t = 48) induce higher shear forces, which correlates with the higher strength of the system, also represented in increased moments below ground; this parameter does not seem to affect the depth to maximum moment as much. On the other hand, note that a larger L_a/D ratio decreases the shear demand as the lever arm increases, pushing the plastic hinge slightly upward, closer to the ground surface, as shown in Figure 6-93, due to the increased spread of plasticity. Regarding the soil stiffness, note from Figure 6-94 that it affects the moment grading, which is also reflected with an increased shear demand below ground, though moments values are rather similar.

However, note that the top displacements are different due to the definition of the equivalent yield displacement on each system. This means that for similar displacement moment are expected to be larger for stiffer soil conditions.

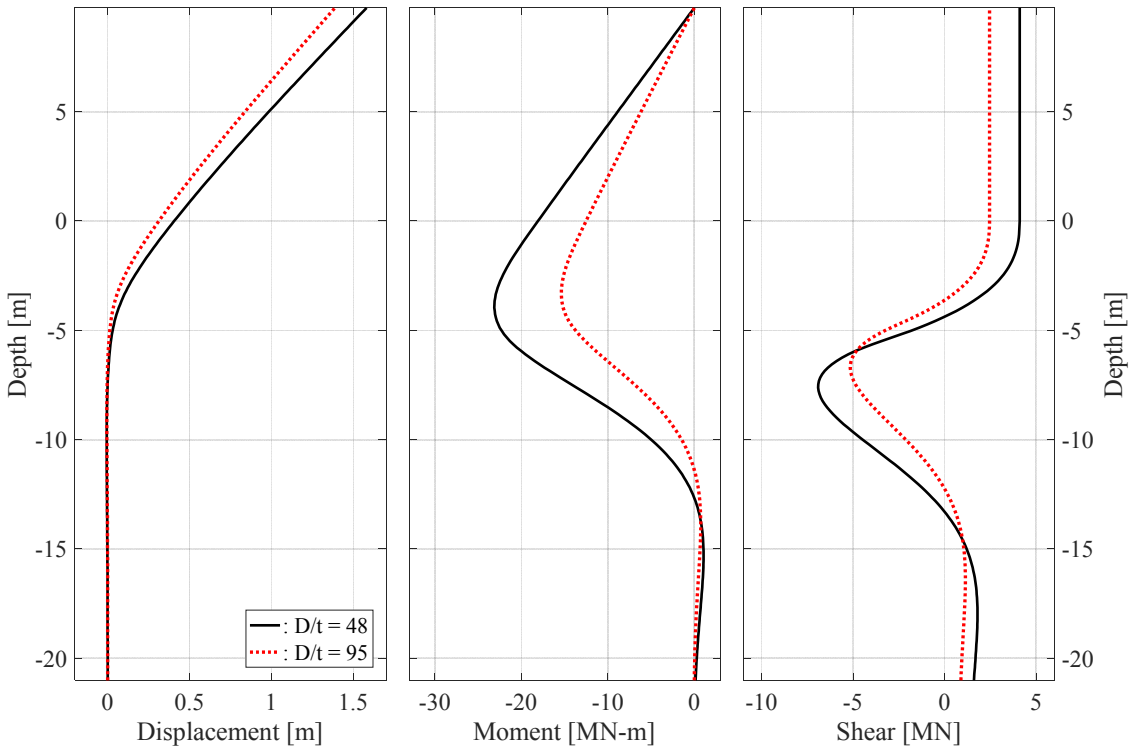

Figure 6-92 Impact of D/t ratio on displacement, moment, and shear profiles

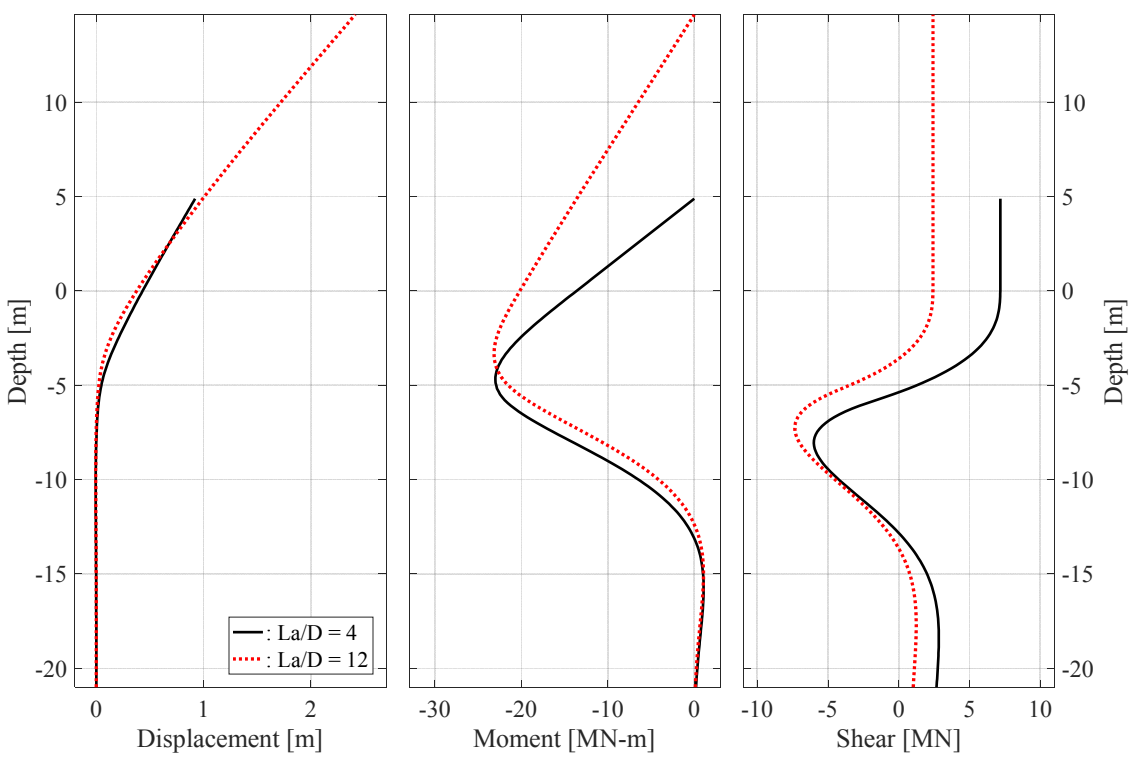

Figure 6-93 Impact of L_a/D ratio on displacement, moment, and shear profiles

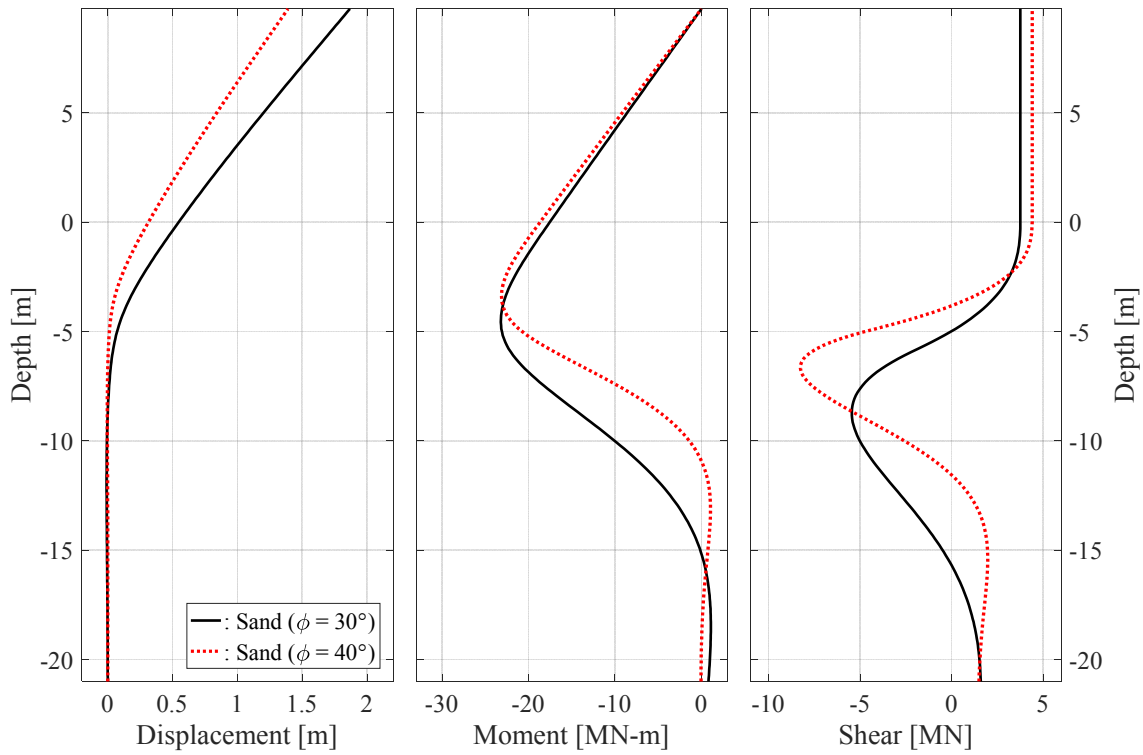

Figure 6-94 Impact of soil stiffness on displacement, moment, and shear profiles

6.6.1.3 Moment-Curvature-Tensile Strain Distribution

The impacts of D/t ratio, L_a/d ratio, and soil stiffness on the displacement, moment and shear profiles at displacement ductility 3 (μ_3) are presented in Figure 6-95, Figure 6-96, and Figure 6-97, respectively. In terms of D/t ratio, note that while moments are larger for ticker tubes (D/t = 48), curvature and thus strains are rather similar, as shown in Figure 6-95. Moreover, note from Figure 6-96 that although for L_a/D = 12 there is a larger spread of plasticity, curvature and strains are similar. This means that a prescribed ductility level induces about the same curvature demand in systems with different aspect ratio. In terms of soil stiffness, a stiffer soil profile induces a higher moment gradient, thus inducing a smaller spread of plasticity, as shown in Figure 6-97. However, curvature and strain levels are similar, though recognizing that higher values should be expected for similar levels of displacement in stiffer soil profiles.

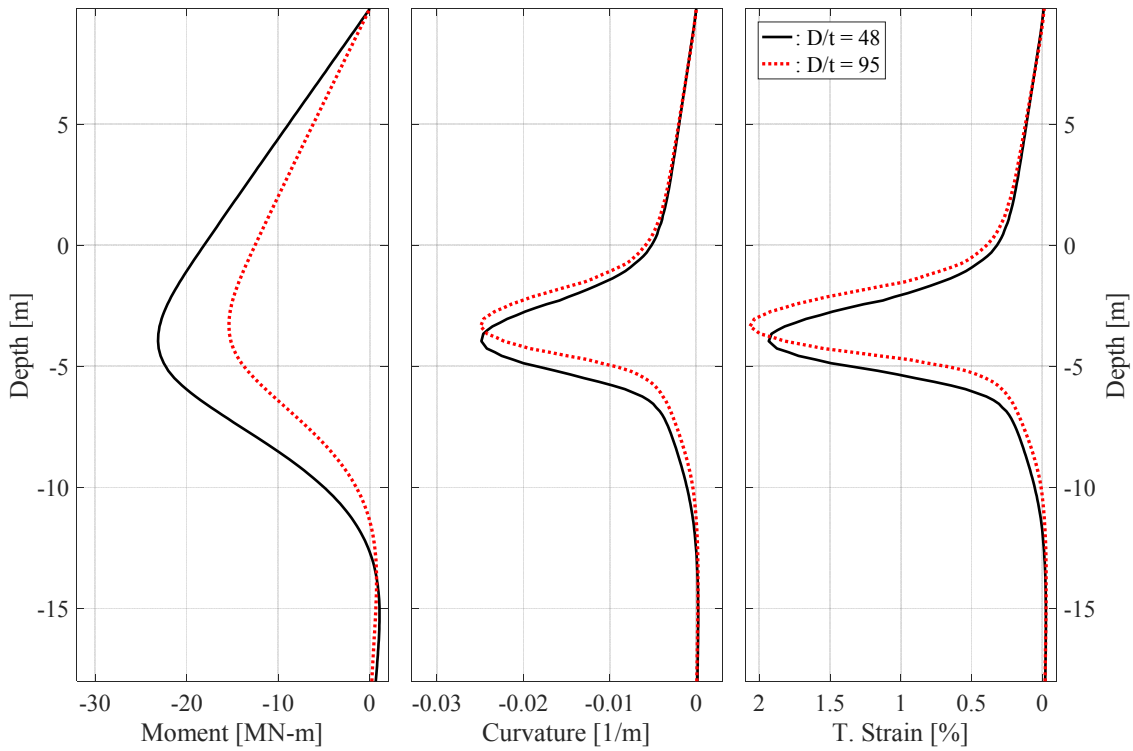

Figure 6-95: Impact of D/t ratio on moment, curvature, and tensile strain profiles

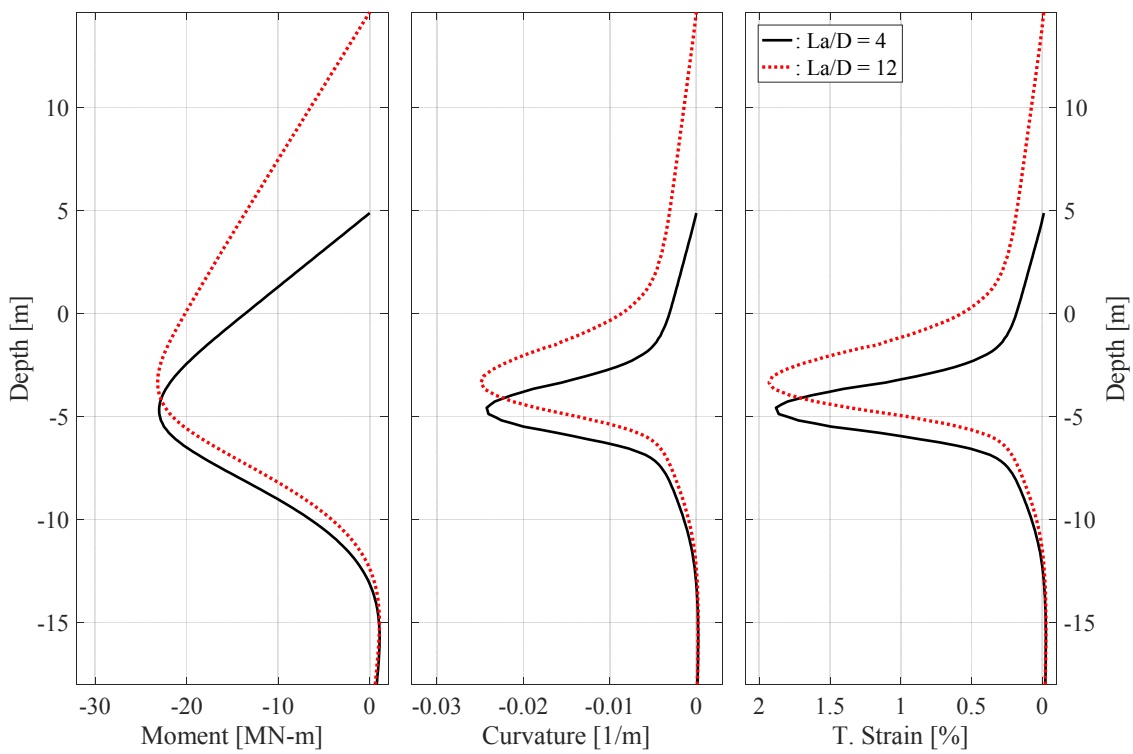

Figure 6-96: Impact of L_a/D ratio on moment, curvature, and tensile strain profiles

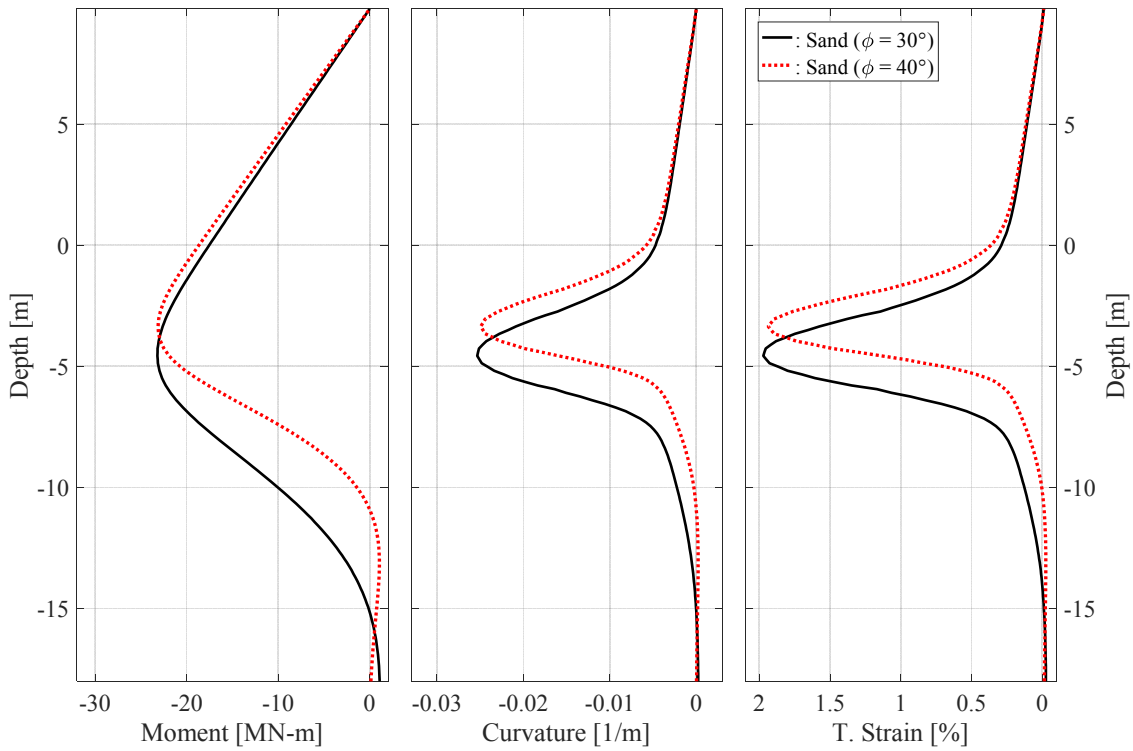

Figure 6-97: Impact of soil stiffness on moment, curvature, and tensile strain profiles

6.6.1.4 Tensile Strain-Displacement Envelopes

The impact of D/t ratio, L_a/D ratio, and soil stiffness, are presented in terms of the tensile strain vs. displacement envelopes on Figure 6-98, Figure 6-99, an Figure 6-100, respectively; note that all the figures have been plotted at the same scale for comparison purposes. In these figures, each dot represents the results from a prescribed ductility level. Notice that strains are consistent at each ductility level within all figures. Moreover, as noted in previous sections, note from Figure 6-98 that results are similar when compared in terms of D/t ratio. Also, note from Figure 6-99 that while the strain levels are similar, the required displacements to achieve such levels are significantly higher for large L_a/D ratios. A similar trend was observed in terms of soil stiffness, though required displacement in that case are not significantly different.

In terms of strain limit states, note that for all cases onset of tube buckling occurs between ductility 2 (μ_2) and 3 (μ_3). Moreover, tube fracture was exceeded before ductility 4 (μ_4). However, it is important to note that these limits would be reach at large displacements demand. Note that except for the case with La/D = 4 (Figure 6-99), for example, all other cases shown require a displacement demand of more than 1200 mm.

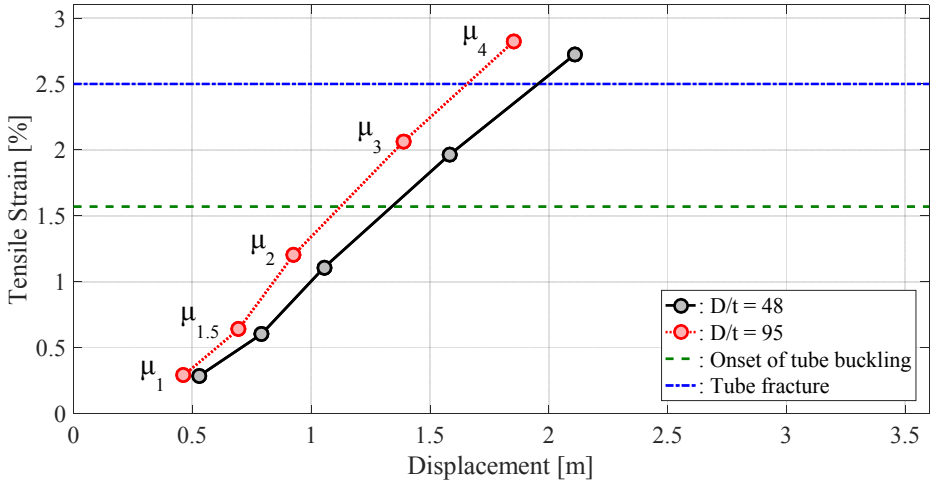

Figure 6-98 Impact of D/t ratio on tensile strain vs. displacement envelopes

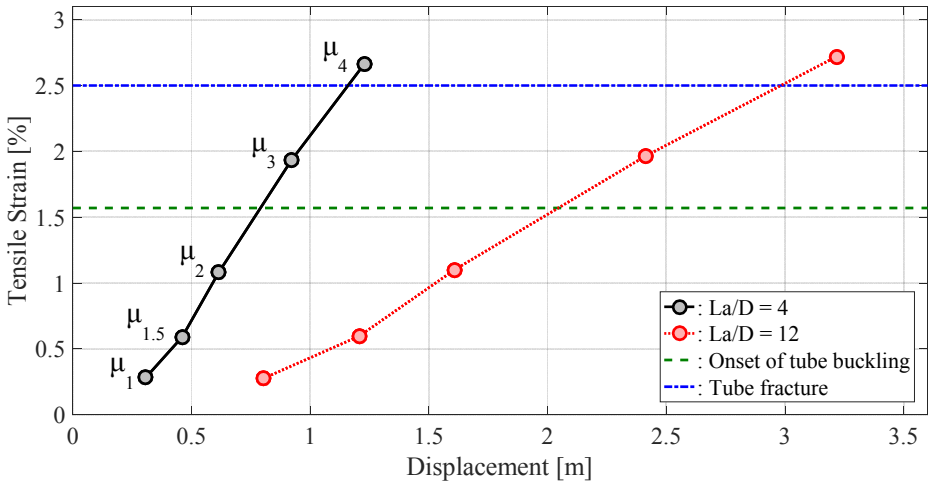

Figure 6-99 Impact of L_a/D ratio on tensile strain vs. displacement envelopes

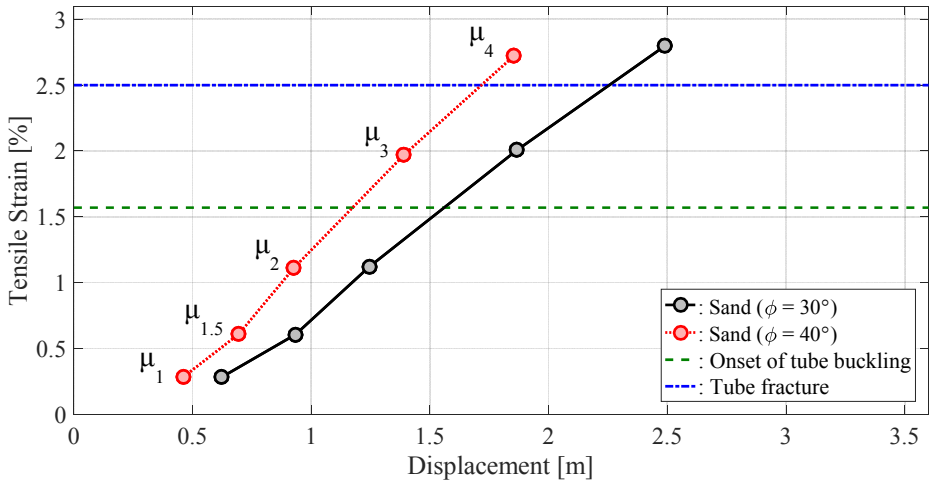

Figure 6-100 Impact of soil stiffness on tensile strain vs. displacement envelopes

6.6.2. Fixed-Head RCFST Shafts

6.6.2.1 Force-Displacement Response

Regarding D/t ratio, note from Figure 6-101 that this parameter impacts the strength of the system, decreasing about 25% for thinner tubes (D/t = 95), though displacement levels are similar. In terms of L_a/D ratio, this parameter induces the most significant impact, as shown in Figure 6-102. Notice that for an aspect ratio $L_a/D = 12$, the system has roughly half of the strength and more than twice the displacement capacity than that for $L_a/D = 4$. Regarding soil stiffness, note from Figure 6-103 that for a stiffer soil profile (dense sand with $\phi = 40°$) the displacements at a prescribed ductility decrease. It is worth nothing that these observations are similar to those corresponding to pinned-head shafts. However, note that in terms of the developed strength, the values are similar, but displacement levels are significantly lower, with values roughly three times larger for pinned-head shafts.

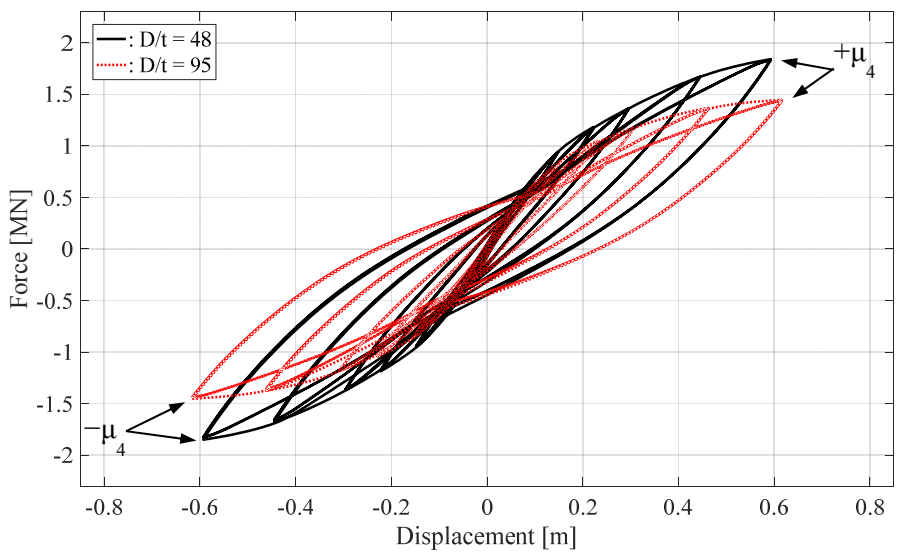

Figure 6-101 Impact of D/t ratio on force vs. displacement response

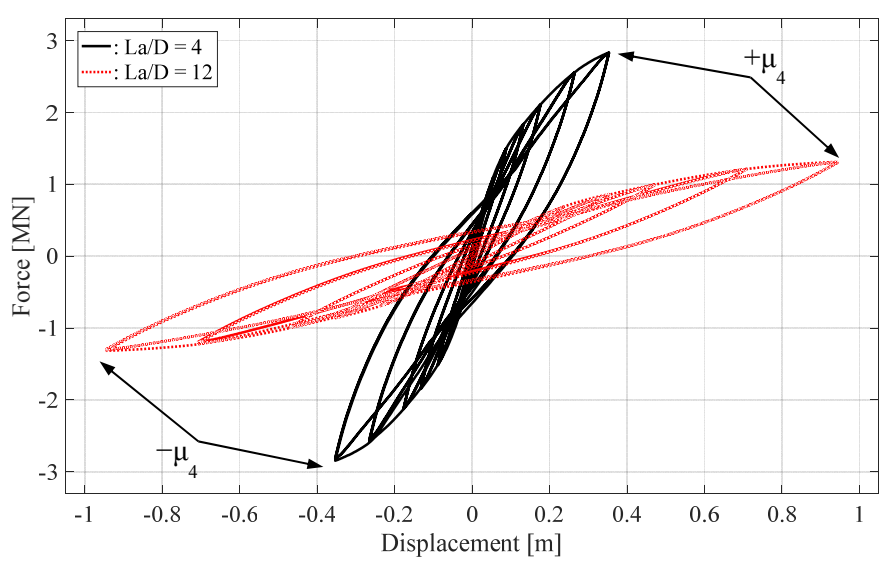

Figure 6-102 Impact of L_a/D ratio on force vs. displacement response

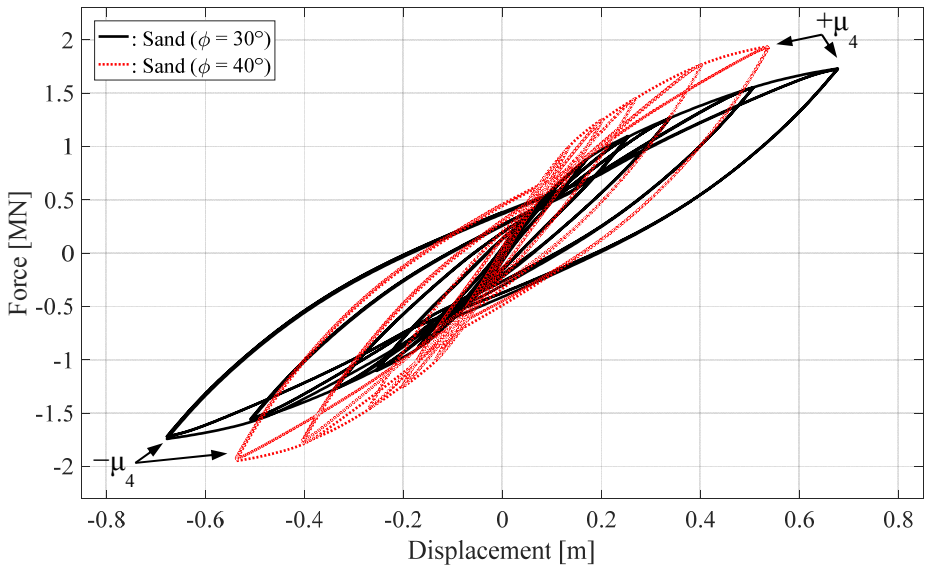

Figure 6-103 Impact of soil stiffness on force vs. displacement response

6.6.2.2 Displacement-Moment-Shear Distribution

Regarding D/t ratio, although displacements are similar, Figure 6-104 shows an increase in the moment and shear demands for ticker tubes (D/t= 48). In terms of L_a/D ratio, note from Figure 6-105 that the spread of plasticity increases with similar peak moments, but with reduced shear demand for $L_a/D = 12$. Regarding soil stiffness, Figure 6-106 shows that for stiffer soil profiles (dense sand with $\phi = 40°$), there is an increase in shear demand due to an increase in the moment gradient.

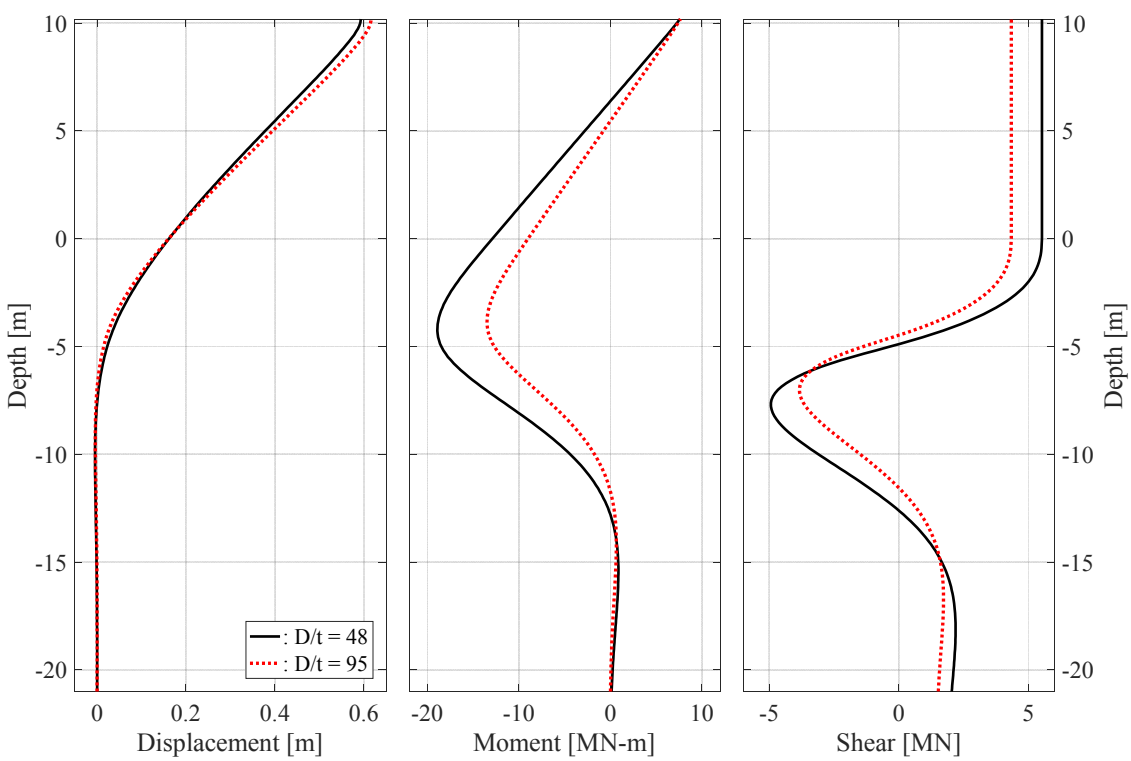

Figure 6-104 Impact of D/t ratio on displacement, moment, and shear profiles

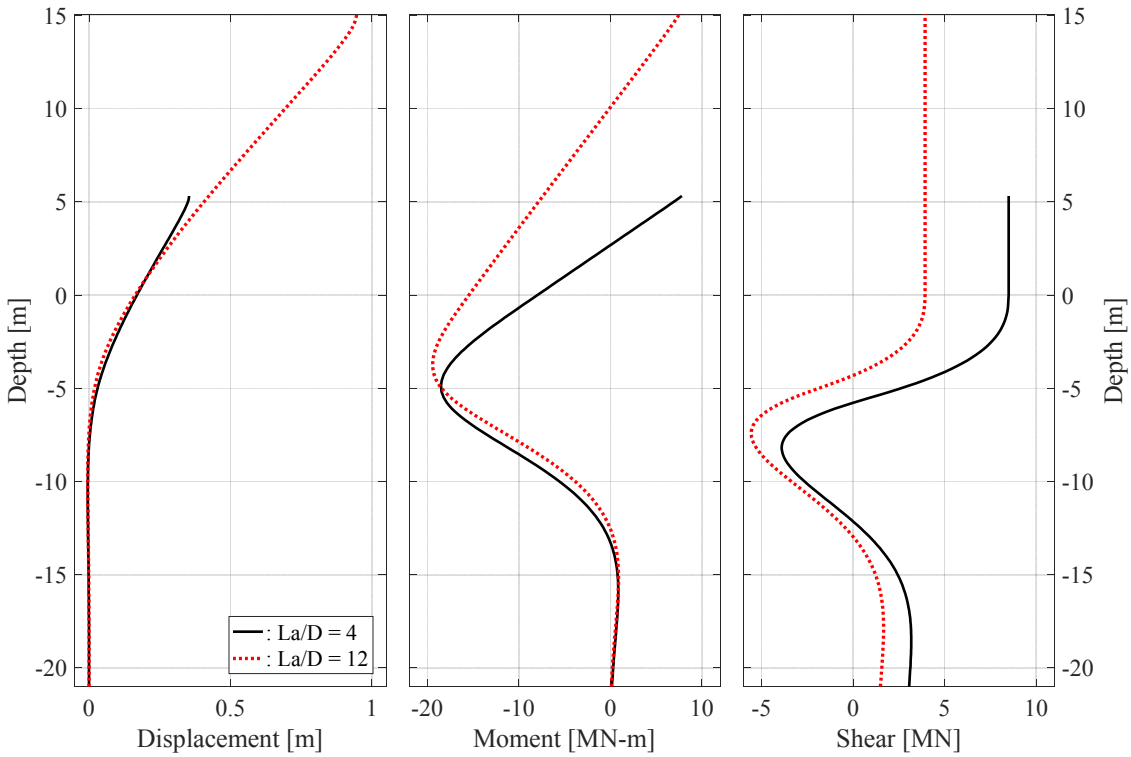

Figure 6-105 Impact of L_a/D ratio on displacement, moment, and shear profiles

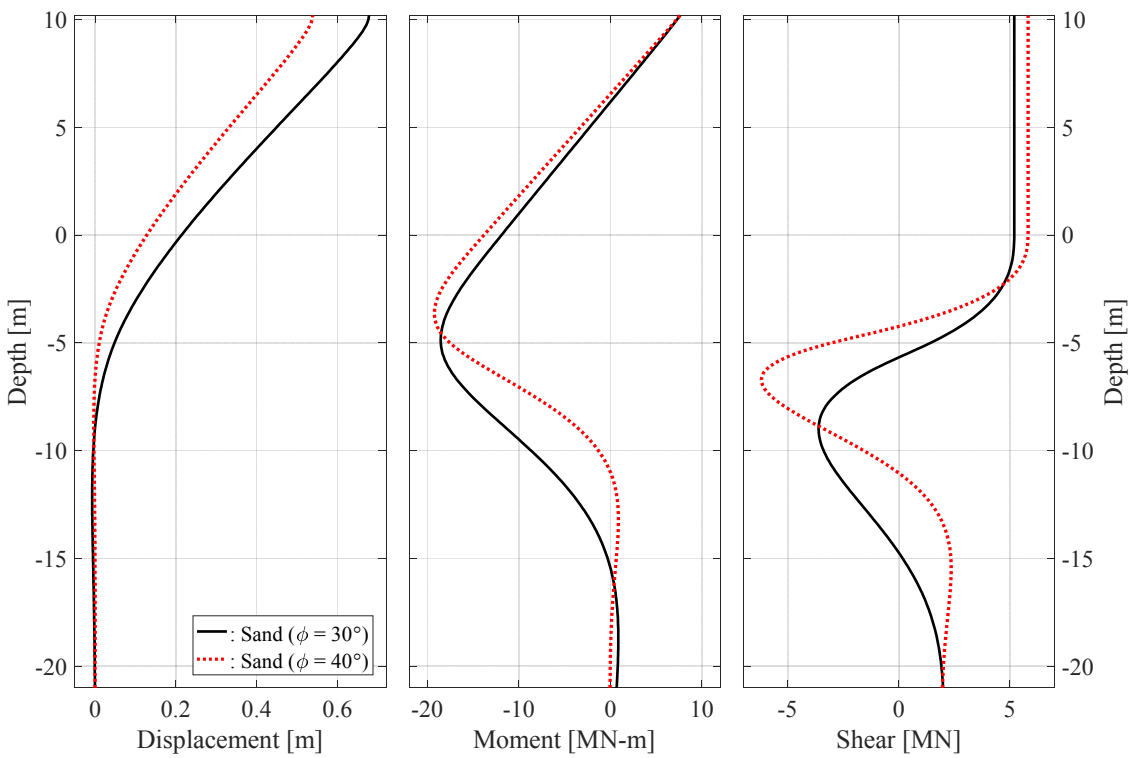

Figure 6-106 Impact of soil stiffness on displacement, moment, and shear profiles

6.6.2.3 Moment-Curvature-Tensile Strain Distribution

In terms of D/t ratio, note from Figure 6-107 that it does not affect the top plastic hinge at all, this is expected because the flexural strength of the top plastic hinge is controlled by the longitudinal reinforcement. Moreover, note from Figure 6-108 that due to an increased spread of plasticity for $L_a/D = 12$, curvature and thus strains result smaller for such a case, which is in turn due to a reduced moment grading. It is worth noting that these results correspond to displacements of about twice those corresponding to $L_a/D = 4$. Lastly, in terms of soil stiffness, note from Figure 6-109 that the soil stiffness has no effect on the top plastic hinge for a prescribed displacement ductility level; however, larger curvature and thus trains would be expected for similar levels of displacement.

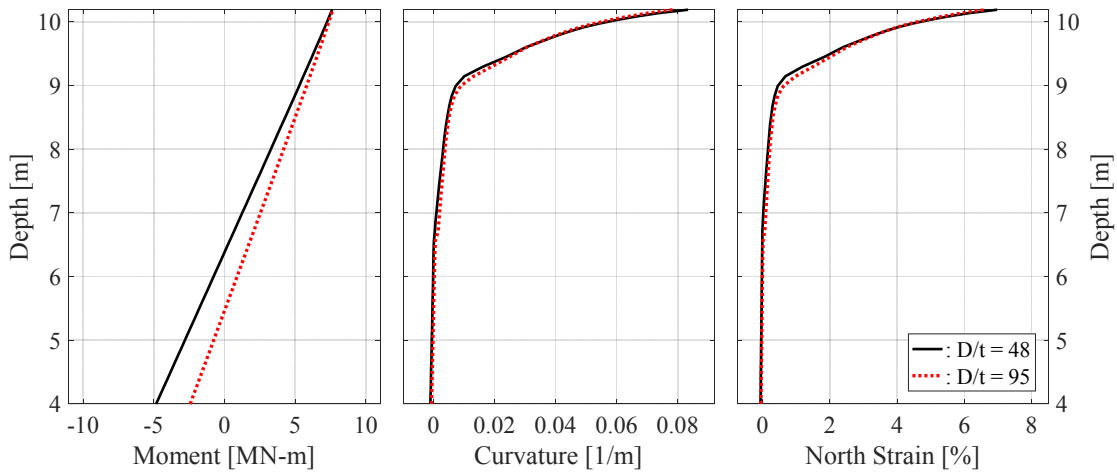

Figure 6-107 Impact of D/t ratio on moment, curvature, and strain profiles of top plastic hinge

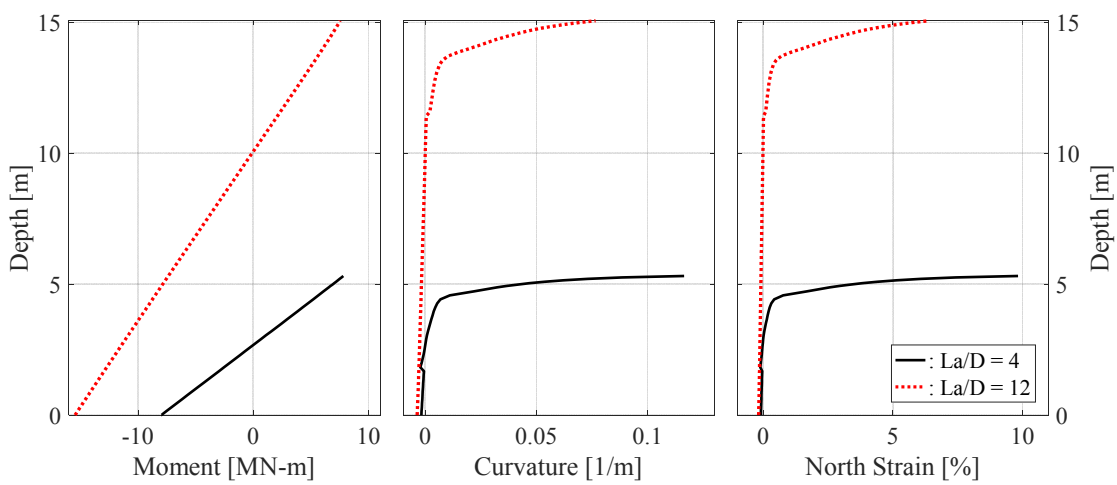

Figure 6-108 Impact of L_a/D ratio on moment, curvature, and strain profiles of top plastic hinge

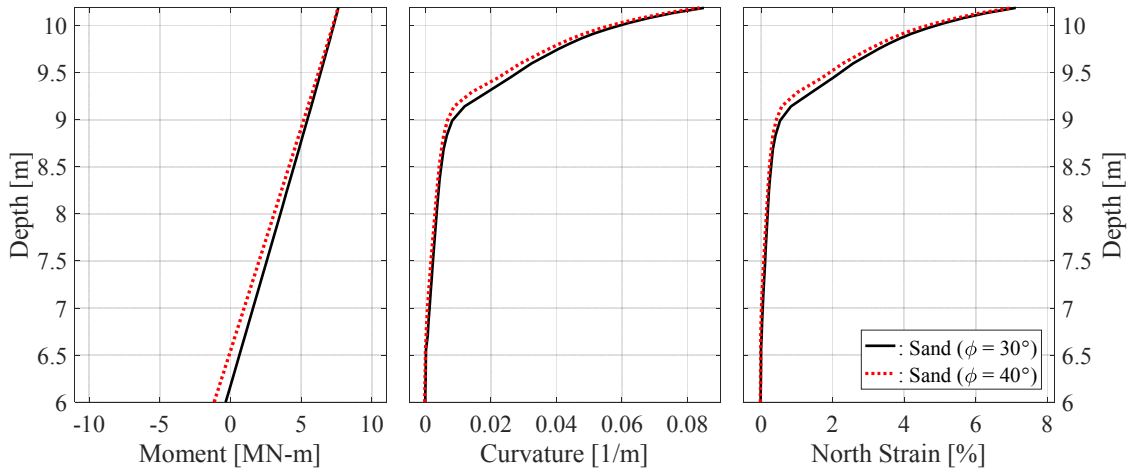

Figure 6-109 Impact of soil stiffness on moment, curvature, and strain profiles of top plastic hinge

6.6.2.4 Tensile Strain-Displacement Envelopes

The impact of D/t ratio, L_a/D ratio, and soil stiffness, are presented in terms of the tensile strain vs. displacement envelopes on Figure 6-110, Figure 6-111, and Figure 6-112, respectively; note that all the figures have been plotted at the same scale for comparison purposes. In these figures, each dot represents the results from a prescribed ductility level. Notice that strains are consistent at each ductility level in terms of D/t ratio and soil stiffness.

As noted in previous sections, note from Figure 6-110 that results are similar when compared in terms of D/t ratio. A significant difference is clearly seen in terms of L_a/D ratio (Figure 6-111). Notice that for L_a/D = 12 the required displacement to develop onset of tube buckling is more than 900 mm., whereas for L_a/D = 4 the required displacement is less than one-third of that value. Also, note from Figure 6-99 that while the strain levels are similar, the required displacements to achieve such levels are significantly higher for large L_a/D ratios. A similar trend was observed in terms of soil stiffness, though required displacement in that case are not significantly different. This effect is attributed to the distribution of lateral stiffness and the spread of plasticity. A longer aspect ratio results in more flexibility in the system thus inducing smaller curvature demands, which in turn results in smaller strains. Lastly, in terms of soil stiffness, note from Figure 6-112 that the impact of a stiffer soil profile slightly alters the displacement at a prescribed ductility level.

In terms of strain limit states, note that for all cases onset of bar buckling occurs between ductility 3 (μ_3) and 4 (μ_4). Moreover, while bar fracture was exceeded at ductility 4 (μ_4) in one of the cases studied, it seems appropriate to establish ductility 4 (μ_4) as an ultimate limit state. Furthermore, note that for all the studied cases, displacement demands are certainly possible to occur during an earthquake event. Note that in all case the required displacements are below 1000 mm.

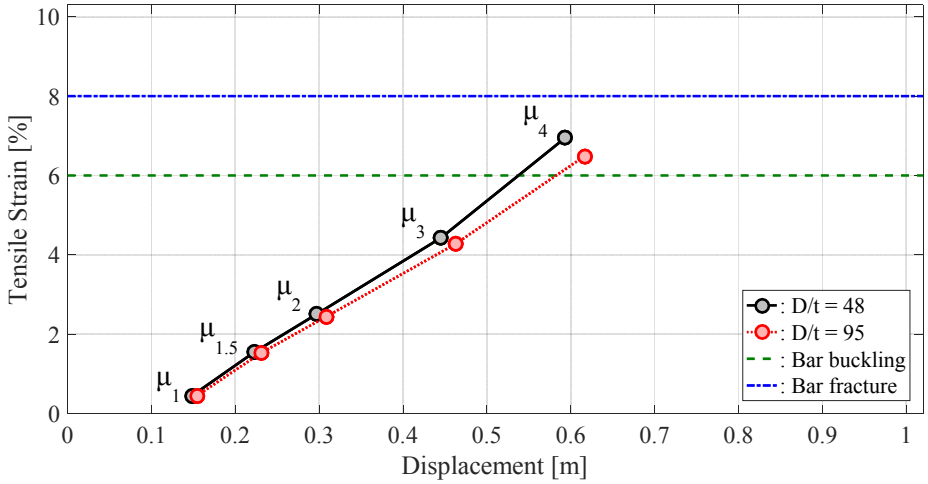

Figure 6-110 Impact of D/t ratio on tensile strain vs. displacement envelopes

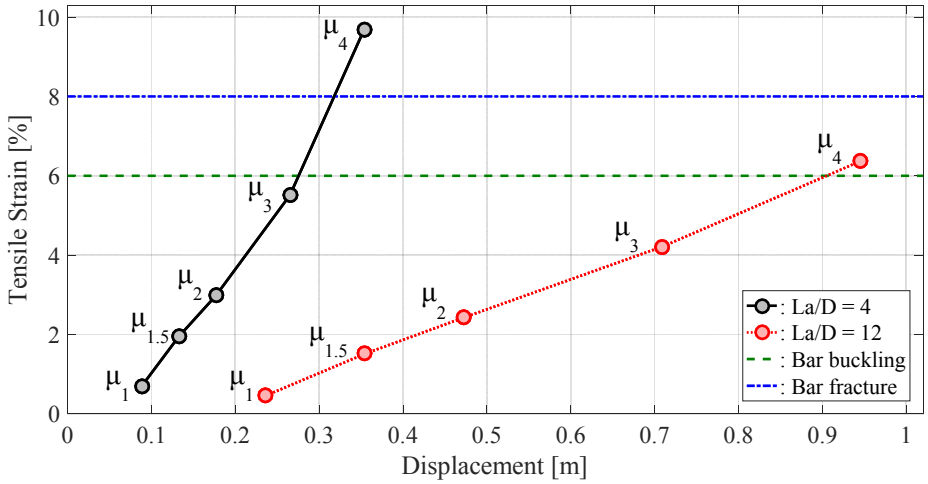

Figure 6-111 Impact of L_a/D/t ratio on tensile strain vs. displacement envelopes

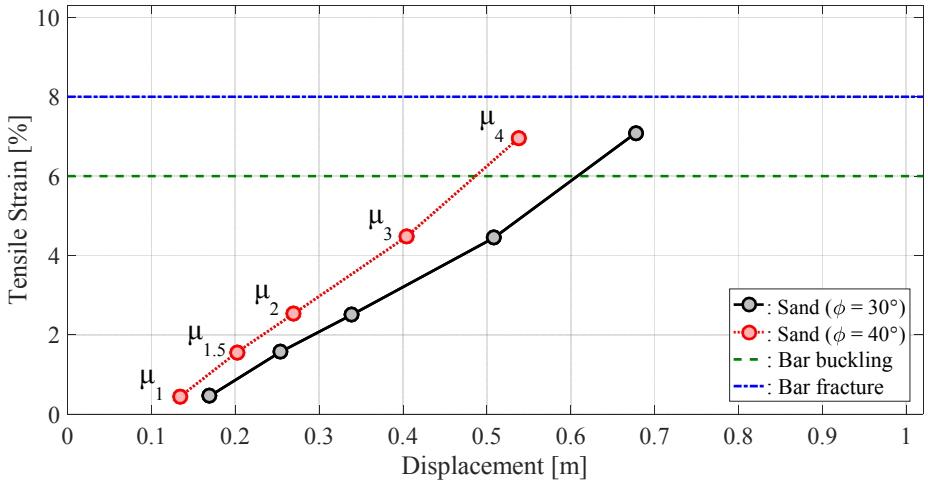

Figure 6-112 Impact of soil stiffness on tensile strain vs. displacement envelopes

CHAPTER 7

7. DESIGN RECOMMENDATIONS

The proposed equivalent cantilever plastic hinge approach can be used in two different ways. Within the current bridge design practice (AASHTO, 2011), designers could use the method for design or assessment to calculate the displacement capacity of RCFST shafts, and then compare the results with the displacement demand. On the other hand, if a displacement based design approach is implemented (e.g., Priestley et al., 2007), the proposed method can be used to determine the design displacement RCFST shafts.

The method was developed considering a uniform layer of sand or clay and it accounts for effects of the diameter-to-thickness (D/t) ratio, aboveground length-to-diameter (L_a/D) ratio, axial load ratio (ALR), and P-Δ effects. Regarding material properties, an expected concrete compressive strength f_c' = 36.4 MPa (5.2 kis) was assumed. Moreover, the model assumes steel tubes manufactured in accordance to API 5L x 52, with expected yield and tensile strengths f_{ye} = 396 MPa (57.2 ksi) and f_{ue} = 500.5 MPa (72.6 ksi), respectively. As for the internal reinforcement (longitudinal and transverse), A706 Gr. 60 steel was considered with expected yield and tensile strengths f_{ye} = 462 MPa (66 ksi) and f_{ue} = 605 MPa (88 ksi), respectively. Regarding the steel content, the longitudinal and transverse steel ratios were assumed to be 2% and 1%, respectively.

While the method was not developed for layered soil profiles or for soil layers with potential for liquefaction, the designer is encouraged to use judgment and experience to use the method with equivalent uniform layer properties. By doing this, the resulting displacements will be approximate, though these could be useful in preliminary stages of design or assessment. For final design and verification purposes, designers should develop a detailed analytical model that accounts for the effects of layered soil profiles and/or soil layers with potential for liquefaction.

The model requires knowledge of the following parameters: tube yield strain ($\varepsilon_{y,tube}$), bar yield strain ($\varepsilon_{y,bar}$), tube diameter (D), tube thickness (t), tube-cap beam gap (g), clear cover to longitudinal reinforcement (c_{bl}), La/D ratio, and axial load ratio (ALR). The latter is defined as shown in Equation 7-1, where P is the axial load acting on the shaft, f_{ce}' is the expected concrete compressive strength, and A_g is the gross area of the RCFST.

$$ALR = \frac{P}{f_{ce}' A_g} \qquad \text{Equation 7-1}$$

Furthermore, the model also requires the soil strength in terms of the friction angle (ϕ) for sand, and in terms of the undrained shear strength (C_u) for clay. The equations that will be presented later in this chapter, are valid for friction angles within 30° and 40° for sand, and undrained shear strengths of 12 kPa (250 psf) and 72 kPa (1500 psf) for clay. The remaining of this chapter presents a description of the system behavior, equations, and examples for each system and soil type. The chapter concludes with final remarks that are aimed to reconcile the results observed during the experimental and analytical portions of this study.

7.1. Pinned-Head RCFST Shafts

7.1.1. System Behavior and Performance Limit States

The inelastic behavior of pinned-head RCFST shafts is controlled by a plastic hinge that develops inground. As lateral displacements are induced at the shaft head under cyclic lateral loading, maximum moments develop below ground at a depth within three to five times the shaft diameter. As tension stresses increase for increased displacement demands, onset of tube buckling takes place at the location of maximum moment. As deformations increase, so does tube buckling, weakening the system up until tube fracture occurs at the same location.

To illustrate this behavior, Figure 7-1 presents an example of the displacement, curvature, and moment profiles of a 1.22 m (4 ft.) diameter, pinned-head RCFST shaft embedded into medium sand (ϕ = 35°), with D/t = 48, L_a/D = 8, and supporting and axial load ratio ALR = 10%. Results are presented for displacement ductility 1 (μ_1) and 4 (μ_4). Note that the maximum moment in both cases occurs at the same depth because after onset of the inground hinge this location does not change. To further explain the behavior of this system, Figure 7-2 presents the curvature distribution and the tensile strain profiles at ductility 4 (μ_4). Note that damage control and ultimate performance limit states are also presented; definitions of such limits are presented later in this section. Notice that both limits have been exceeded at this displacement level. However, note from Figure 7-1 that such a displacement corresponds to more than 2,000 mm, which in terms of a displacement demand is unlikely to occur.

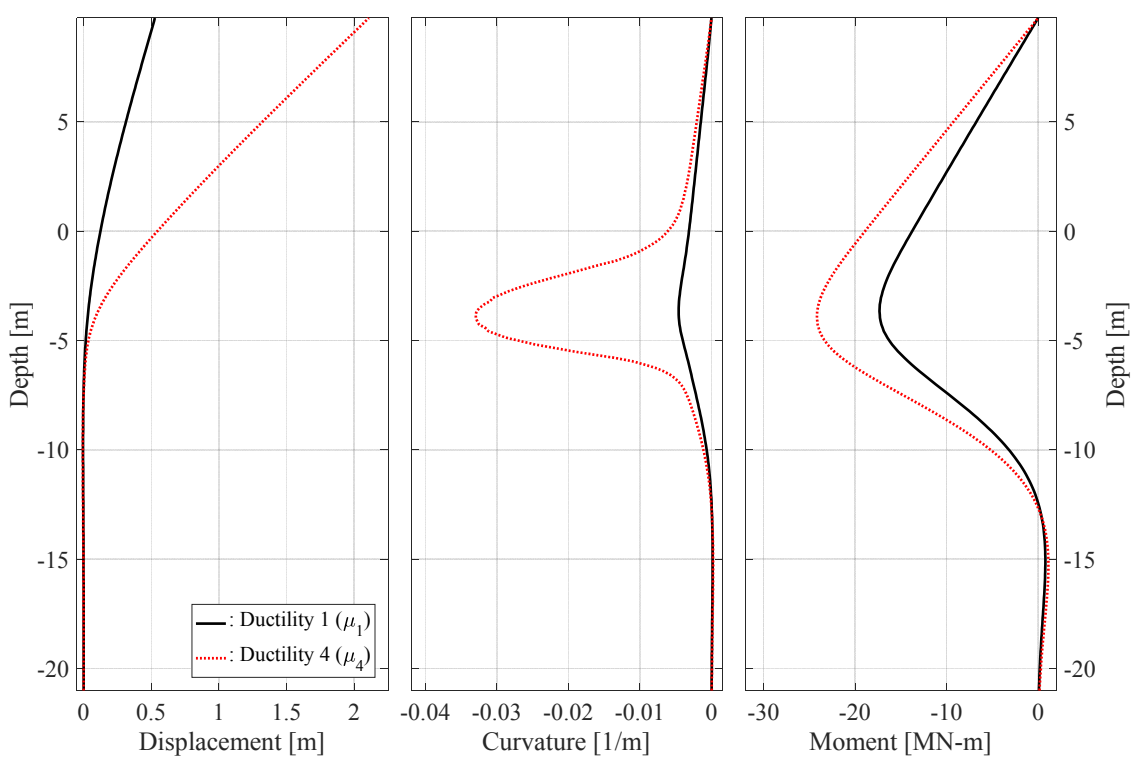

Figure 7-1 Example: displacement, moment, and curvature profiles of a pinned-head RCFST shaft

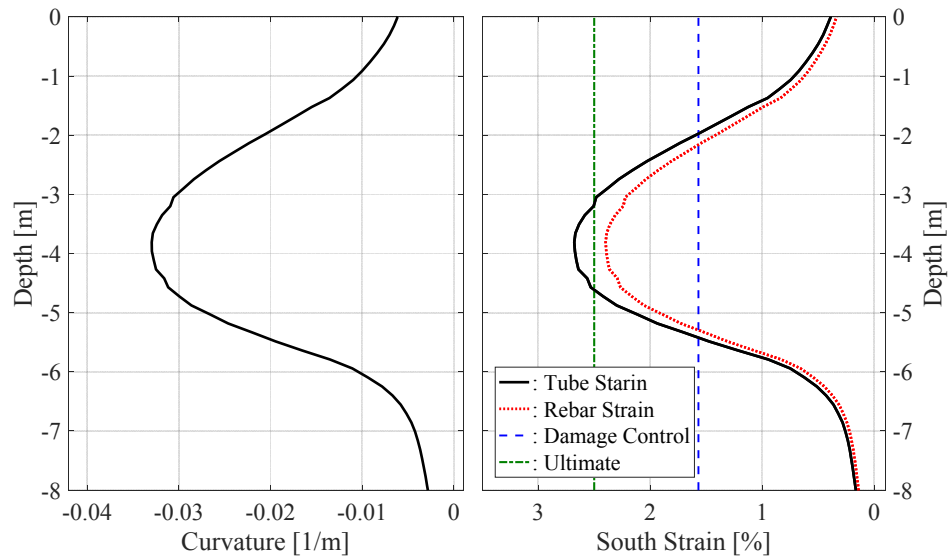

Figure 7-2 Example: inground plastic hinge curvature and tensile strain profiles of a pinned-head RCFST shaft

Based upon analytical and experimental observations, it was found that the system can exhibit a stable and reliable response up to displacement ductility 3 (μ_3), though recognizing that for ticker tubes (D/t = 48) the system can have a displacement capacity of up to ductility 4 (μ_4), as was shown in the previous example. In terms of performance limit states, the system can be characterized with serviceability, damage control, and ultimate limits. The serviceability limit state corresponds to a tube tensile strain of 1.5%. The damage control limit state can be associated with onset of tube local buckling, where the tube tensile strain is limited as shown in Equation 7-2, based on the recommendations by Brown et al. (2015).

$$\varepsilon_{t,\,buckling} = 0.021 - \frac{D}{9100t} \geq \varepsilon_{y(tube)} \qquad \text{Equation 7-2}$$

Analytical and experimental data revealed that this limit state can be expected to develop within a displacement ductility of 2 (μ_2) and 3 (μ_3). Furthermore, the ultimate limit state is associated to onset of tube fracture, with a maximum tube tensile strain of 2.5% (Brown et al. 2015). Based on analytical and experimental data, this limit is expected to develop at a displacement ductility 3 (μ_3), though recognizing that thick tubes (e.g., D/t = 48) can reach displacement ductility 4 (μ_4). Performance limit states for the inground plastic hinge are summarized in Table 7-1. In terms of the analysis method, RCFST sections can be analyzed assuming equilibrium and strain compatibility, as experimental results show that this assumption is adequate up until onset of tube local buckling, and even beyond that level (Brown et al. 2015).

Table 7-1 Inground plastic hinge performance levels and associated strain limits

Strain	Performance Level		
	Serviceability	Damage Control	Ultimate
Tension	0.015	$\varepsilon_t = 0.021 - \frac{D}{9100t} \geq \varepsilon_{y(tube)}$	0.025

Described next is the formulation of the proposed equivalent cantilever plastic hinge model for pinned-head RCFST shafts. Application examples for both sand and clay are also presented in the next section.

7.1.2. Proposed Model and Examples

Figure 7-3 presents a schematic of the proposed equivalent cantilever model for pinned-head RCFST shafts. In this approach, a single RCFST shaft that can be characterized with a detailed FE analytical model, is simplified to an equivalent fixed-base cantilever with effective length L_e. This length is measured from the pile head to the depth-to-maximum moment, which is also known as the depth-to-plastic hinge (H_{ig}). The model is used to determine the displacement at the column head at a prescribed limit state (Δ_{LS}) by calculating elastic (Δ_y) and plastic (Δ_p) displacement components, which depend on the elastic curvature (ϕ_y) and an equivalent plastic hinge length (L_p). The performance limit state is dictated by the inground plastic hinge based upon strain limit states, as previously described. Described next is the step-by-step calculation process for sand and clay along with examples at the end of this section.

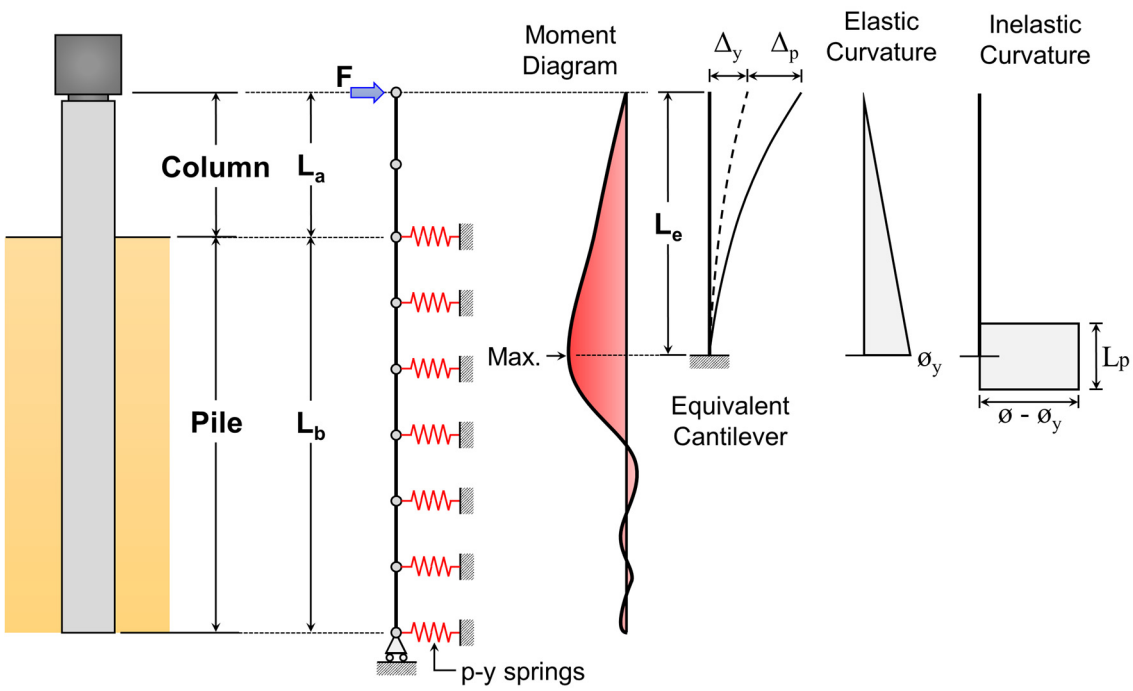

Figure 7-3 Equivalent cantilever model for pinned-head RCFST shafts

7.1.2.1 Equations for Sand

Step 1: calculate the yield curvature. For RCFST columns, $c_{\phi y} = 2.67$

$$\phi_y = c_{\phi y} \frac{\varepsilon_{y(tube)}}{D} \qquad \text{Equation 7-3}$$

Step 2: calculate the yield displacement

a. Calculate the yield displacement parameter:

$$C_1 = 1.378 - 0.20\,Ln\left(\frac{L_a}{D}\right) - \frac{D}{2050t} - \frac{\phi}{130} \quad , \quad \phi(°)$$ Equation 7-4

b. Calculate the depth to plastic hinge:

$$\frac{H_{ig}}{D} = 8.57 + 0.88\frac{L_a}{D} - \frac{D}{130t} - \frac{\phi}{10}$$ Equation 7-5

c. Determine the effective length:

$$L_e = H_{ig}$$ Equation 7-6

d. Lastly, determine the yield displacement as follows:

$$\Delta_y = c_1\,\phi_y\,L_e^{\,2}$$ Equation 7-7

Step 3: calculate the plastic displacement

a. Calculate the equivalent plastic hinge length:

$$\frac{L_p}{D} = 5.44 - 0.74D + 0.06\frac{L_a}{D}(1 + 9.85ALR) - \frac{D}{210t} - 0.063\phi \quad , \quad D(m)\,,\,\phi(°)$$ Equation 7-8

b. Calculate the limit state curvature:

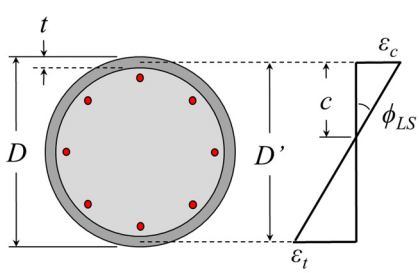

Figure 7-4 Curvature and associated strains for RCFST sections

$$\frac{c}{D} = 0.31 + 0.242ALR - \frac{D}{4300t}$$ Equation 7-9

$$D' = D - t$$ Equation 7-10

$$\phi_{LS,\,t} = \frac{\varepsilon_t}{D' - c}$$ Equation 7-11

c. Determine the plastic curvature:

$$\phi_p = \phi_{LS} - \phi_y$$ Equation 7-12

d. Lastly, calculate the plastic displacement as follows:

$$\Delta_p = \phi_p \, L_p \, L_e \qquad \text{Equation 7-13}$$

Step 4: calculate the limit state displacement

$$\Delta_{LS} = \Delta_y + \Delta_p \qquad \text{Equation 7-14}$$

Step 5: calculate the system equivalent viscous damping (for DDBD design)

$$\xi_{eq} = 0.07 + \left(0.85 - \frac{D}{1000t}\right)\left(\frac{\mu - 1}{10.5 + \pi\mu}\right) + \begin{cases} 0.012 & 1 \le \mu \le 2 \\ 0.012 + 0.009(\mu - 2) & \mu > 2 \end{cases} \qquad \text{Equation 7-15}$$

7.1.2.2 Equations for Clay

Step 1: calculate the yield curvature. For RCFST columns, $c_{\phi y} = 2.67$

$$\phi_y = c_{\phi y} \frac{\varepsilon_{y(tube)}}{D} \qquad \text{Equation 7-16}$$

Step 2: calculate the yield displacement

a. Calculate the yield displacement parameter:

$$C_1 = 1.279 - \frac{L_a}{40D}\left(1 + \frac{D}{430t}\right) - \frac{Ln(C_u)}{16} \quad , \quad C_u\,(kPa) \qquad \text{Equation 7-17}$$

b. Calculate the depth to plastic hinge:

$$\frac{H_{ig}}{D} = 17.90 + 0.68\frac{L_a}{D} - \frac{D}{55t} - 2.49\,Ln(C_u) \quad , \quad C_u\,(kPa) \qquad \text{Equation 7-18}$$

c. Determine the effective length:

$$L_e = H_{ig} \qquad \text{Equation 7-19}$$

d. Lastly, calculate the yield displacement as follows:

$$\Delta_y = c_1 \, \phi_y \, L_e^{\,2} \qquad \text{Equation 7-20}$$

Step 3: calculate the plastic displacement

a. Calculate the equivalent plastic hinge length:

$$\frac{L_p}{D} = 50.91 + 0.06\frac{L_a}{D}\left(0.23ALR\frac{D}{t} - 1\right) - 8.02Ln\left(\frac{D}{t}\right) + 4.54Ln(C_u)\left(\frac{D}{220t} - 1\right) \;,\; C_u\,(kPa) \qquad \text{Equation 7-21}$$

b. Calculate the limit state curvature:

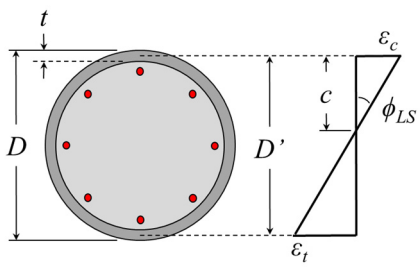

Figure 7-5 Curvature and associated strains for RCFST sections

$$\frac{c}{D} = 0.31 + 0.242\,ALR - \frac{D}{4300t} \qquad \text{Equation 7-22}$$

$$D' = D - t \qquad \text{Equation 7-23}$$

$$\phi_{LS,\,t} = \frac{\varepsilon_t}{D' - c} \qquad \text{Equation 7-24}$$

c. Determine the plastic curvature:

$$\phi_p = \phi_{LS} - \phi_y \qquad \text{Equation 7-25}$$

d. Lastly, calculate the plastic displacement as follows:

$$\Delta_p = \phi_p\, L_p\, L_e \qquad \text{Equation 7-26}$$

Step 4: calculate the limit state displacement

$$\Delta_{LS} = \Delta_y + \Delta_p \qquad \text{Equation 7-27}$$

Step 5: calculate the system equivalent viscous damping (for DDBD design)

$$\xi_{eq} = 0.07 + \left(0.85 - \frac{D}{1000t}\right)\left(\frac{\mu - 1}{10.5 + \pi\mu}\right) + \begin{cases} 0.019 & 1 \le \mu \le 2 \\ 0.019 + 0.55(\mu - 2) & \mu > 2 \end{cases} \qquad \text{Equation 7-28}$$

7.1.2.3 Example: displacement capacity or design displacement

To illustrate the sequence of operations for sand and clay, consider an RCFST pile-column part of a bridge bent, pin-connected to the superstructure under seismic response in the longitudinal direction. The RCFST shaft has a tube outer diameter D = 1.22 m. (4 ft.), a D/t ratio of 48, which means the tube has a wall thickness t = 25.4 mm (1 in.), an aspect ratio $L_a/D = 8$, and supports an axial load, including self weight, of 4,260 kN (960 kips). Material properties are concrete compressive strength $f_c' = 28$ MPa (hence $f_{ce}' = 36.4$ MPa (5.2 ksi)), and tube yield strength $f_{yt} = 360$ MPa (hence $f_{ype} = 396$ MPa (57.2 ksi)).

The goal of this example is to illustrate calculations for both sand and clay to determine the displacement at onset of tube buckling, which is determined based on the tensile strain from Equation 7-2 as $\varepsilon_t = 0.0157$. Furthermore, for sand, consider a uniform profile with friction angle $\phi = 35°$ (medium sand). For clay, consider a uniform profile with undrained shear

strength C_u = 36 kPa (medium clay). It is assumed that the RCFST shaft is embedded deep enough into the ground. The solutions for both soil types are presented next.

7.1.2.3.1 Sand

Step 1: calculate the yield curvature. From Equation 7-3:

$$\phi_y = c_{\phi y}\frac{\varepsilon_{y(tube)}}{D} = 2.67\left(\frac{396/200,000}{1.22}\right) = 0.00433\frac{1}{m}$$

Step 2: calculate the yield displacement.

a. Calculate the yield displacement parameter, from Equation 7-4:

$$C_1 = 1.378 - 0.20\,Ln\left(\frac{L_a}{D}\right) - \frac{D}{2050t} - \frac{\phi}{130} = 1.378 - 0.20Ln(8) - \frac{48}{2050} - \frac{35}{130} = 0.6695$$

b. Calculate the depth to plastic hinge, from Equation 7-5:

$$\frac{H_{ig}}{D} = 8.57 + 0.88\frac{L_a}{D} - \frac{D}{130t} - \frac{\phi}{10} = 8.57 + 0.88(8) - \frac{48}{130} - \frac{35}{10} = 11.741$$

$$H_{ig} = 11.74D = 11.74(1.22m) = 14.324m$$

c. Determine the effective length, from Equation 7-6:

$$L_e = H_{ig} = 14.32m$$

d. Lastly, from Equation 7-7, the yield displacement is:

$$\Delta_y = c_1\,\phi_y\,L_e^2 = 0.669\left(0.00433\frac{1}{m}\right)\left(14.32m^2\right) = 0.595m$$

Step 3: calculate the plastic displacement

a. Calculate the equivalent plastic hinge length, from Equation 7-8:

$$\frac{L_p}{D} = 5.44 - 0.74D + 0.06\frac{L_a}{D}(1 + 9.85ALR) - \frac{D}{210t} - 0.063\phi$$

$$ALR = \frac{P}{f_{ce}'A_g} = \frac{4,260kN}{36.4MPa\left(1.169m^2\right)(1000)} = 0.10$$

$$\frac{L_p}{D} = 5.44 - 0.74(1.22) + 0.06(8)(1 + 9.85(0.10)) - \frac{48}{210} - 0.063(35) = 3.056$$

$$L_p = 3.056D = 3.056(1.22m) = 3.730m$$

b. Calculate the limit state curvature:

From Equation 7-9, the neutral axis depth is:

$$\frac{c}{D} = 0.31 + 0.242(0.10) - \frac{48}{4300} = 0.323$$

$$c = 0.323D = 0.323(1.22) = 0.394m$$

From Equation 7-10:

$$D' = D - t = 1,220mm - 25.4mm = 1,194.6mm$$

From Equation 7-11:

$$\phi_{LS,t} = \frac{\varepsilon_t}{D' - c} = \frac{0.0157}{1.1946 - 0.394} = 0.0196\frac{1}{m}$$

c. Determine the plastic curvature from Equation 7-12:

$$\phi_p = \phi_{LS} - \phi_y = 0.0196 - 0.00433 = 0.0153\frac{1}{m}$$

d. Lastly, calculate the plastic displacement from Equation 7-13:

$$\Delta_p = \phi_p L_p L_e = \left(0.0153\frac{1}{m}\right)(3.73m)(14.32m) = 0.817m$$

Step 4: calculate the limit state displacement from Equation 7-14:

$$\Delta_{LS} = \Delta_y + \Delta_p = 0.595m + 0.817m = 1.412m$$

7.1.2.3.2 Clay

Step 1: calculate the yield curvature. From Equation 7-16:

$$\phi_y = c_{\phi y}\frac{\varepsilon_{y(tube)}}{D} = 2.67\left(\frac{396/200,000}{1.22}\right) = 0.00433\frac{1}{m}$$

Step 2: calculate the yield displacement.

a. Calculate the yield displacement parameter, from Equation 7-20:

$$C_1 = 1.279 - \frac{L_a}{40D}\left(1 + \frac{D}{430t}\right) - \frac{Ln(C_u)}{16}$$

$$C_1 = 1.279 - \frac{8}{40}\left(1 + \frac{48}{430}\right) - \frac{Ln(36)}{16} = 0.833$$

b. Calculate the depth to plastic hinge, from Equation 7-18:

$$\frac{H_{ig}}{D} = 17.90 + 0.68\frac{L_a}{D} - \frac{D}{55t} - 2.49\,Ln(C_u)$$

$$\frac{H_{ig}}{D} = 17.90 + 0.68(8) - \frac{48}{55} - 2.49\,Ln(36) = 13.544$$

$$H_{ig} = 13.544D = 13.544(1.22m) = 16.524m$$

c. Determine the effective length, from Equation 7-19:

$$L_e = H_{ig} = 16.524m$$

d. Lastly, from Equation 7-20, the yield displacement is:

$$\Delta_y = c_1 \phi_y L_e^2 = 0.833\left(0.00433\frac{1}{m}\right)\left(16.524\,m^2\right) = 0.985\,m$$

Step 3: calculate the plastic displacement

a. Calculate the equivalent plastic hinge length, from Equation 7-21:

$$\frac{L_p}{D} = 50.91 + 0.06\frac{L_a}{D}\left(0.23ALR\frac{D}{t} - 1\right) - 8.02Ln\left(\frac{D}{t}\right) + 4.54Ln\left(C_u\right)\left(\frac{D}{220t} - 1\right)$$

$$ALR = \frac{P}{f_{ce}'A_g} = \frac{4,260kN}{36.4MPa\left(1.169m^2\right)\left(1000\right)} = 0.10$$

$$\frac{L_p}{D} = 50.91 + 0.06\left(8\right)\left[0.23\left(0.1\right)\left(48\right) - 1\right] - 8.02Ln\left(48\right) + 4.54Ln\left(36\right)\left(\frac{48}{220} - 1\right) = 7.194$$

$$L_p = 7.194D = 7.194\left(1.22m\right) = 8.776m$$

b. Calculate the limit state curvature:

From Equation 7-22, the neutral axis depth is:

$$\frac{c}{D} = 0.31 + 0.242\left(0.10\right) - \frac{48}{4300} = 0.323$$

$$c = 0.323D = 0.323\left(1.22\right) = 0.394m$$

From Equation 7-23:

$$D' = D - t = 1,220mm - 25.4mm = 1,194.6mm$$

From Equation 7-24:

$$\phi_{LS,t} = \frac{\varepsilon_t}{D' - c} = \frac{0.0157}{1.1946 - 0.394} = 0.0196\frac{1}{m}$$

c. Determine the plastic curvature from Equation 7-25:

$$\phi_p = \phi_{LS} - \phi_y = 0.0196 - 0.00433 = 0.0153\frac{1}{m}$$

d. Lastly, calculate the plastic displacement from Equation 7-26:

$$\Delta_p = \phi_p L_p L_e = \left(0.0153\frac{1}{m}\right)\left(8.776m\right)\left(16.524m\right) = 2.216m$$

Step 4: calculate the limit state displacement from Equation 7-27:

$$\Delta_{LS} = \Delta_y + \Delta_p = 0.985m + 2.216m = 3.20m$$

7.2. Fixed-Head RCFST Shafts

7.2.1. System Behavior

Fixed-head RCFST shafts can potentially develop two plastic hinges, one of the at the top at the column-cap beam interface, and another one at the bottom, below ground. However, due

to the distribution of flexural stiffness, fixed-head RCFST shafts are controlled by the plastic hinge that develops above ground at the column-cap beam interface. Since the steel tube is cut short before the cap-beam, it does not provide flexural strength to the top plastic hinge, thus the flexural stiffness of the top plastic hinge corresponds effectively to that of an RC section confined by a steel tube. After onset of the top plastic hinge, there is a redistribution of moments and the maximum inground moment starts to increase far beyond the level of the top hinge, since the flexural stiffness of the inground hinge corresponds effectively to that of an RCFST section, which is larger than that of the RC section at the top hinge.

To illustrate this behavior, Figure 7-6 presents an example of the displacement, curvature, and moment profiles of a 1.22 m (4 ft.) diameter, fixed-head RCFST shaft embedded into medium sand (ϕ = 35°), with D/t = 48, L_a/D = 8, and supporting and axial load ratio ALR = 10%. Results are presented for displacement ductility 1 (μ_1) and 4 (μ_4). Notice that curvature demands at the top plastic hinge are significantly larger to those of the inground hinge. On the other hand, notice that while at ductility 1 (μ_1) moments are rather similar at top and inground hinges, at ductility 4 (μ_4) the inground moment is more than twice that of the top hinge.

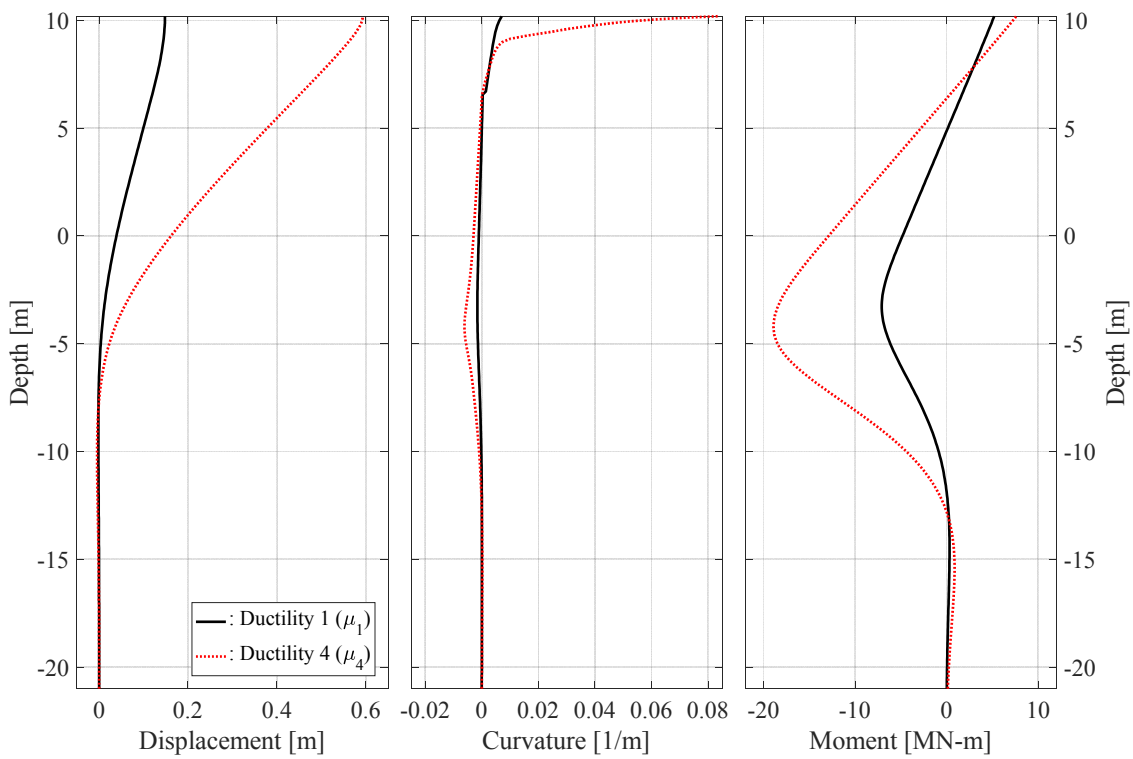

Figure 7-6 Example: displacement, moment, and curvature profiles of a fixed-head RCFST shaft

These two observations are directly associated to the effective flexural stiffness, as the top hinge corresponds to an RC section confined by a steel tube, while the inground hinge corresponds to an RCFST section. This behavior can be thought in terms of capacity design principles, where the enhanced deformation and strength capacity of the RCFST shaft forces inelastic action to occur at the top plastic hinge (weak link). This can be beneficial because

it could be used to ensure that damage will occur only above ground during an earthquake event, where it is easy to inspect and repair.

To further explain the behavior of this system, Figure 7-7 and Figure 7-8 presents the curvature distribution and the tensile strain profiles at ductility 4 (μ_4) for the top and inground plastic hinges, respectively. Note that strain limits at damage control and ultimate have been included for the top plastic hinge, while yield and serviceability are plotter for the inground hinge. Regarding the top plastic hinge, notice that at displacement ductility 4 (μ_4), the damage control limit state has been exceeded and the top hinge is close to reach failure. At the same level of displacement, note that the inground hinge has barely exceeded first yield of the tube. This means that the system has reserved capacity in terms of the inground hinge; however, at this level of deformation the top hinge is close to imminent failure.

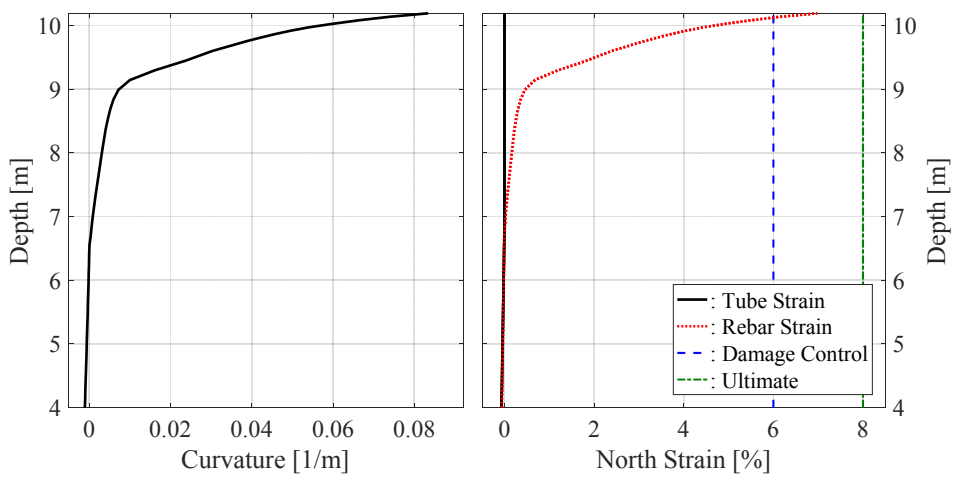

Figure 7-7 Example: top hinge curvature and tensile strain profiles at ductility 4 (μ_4)

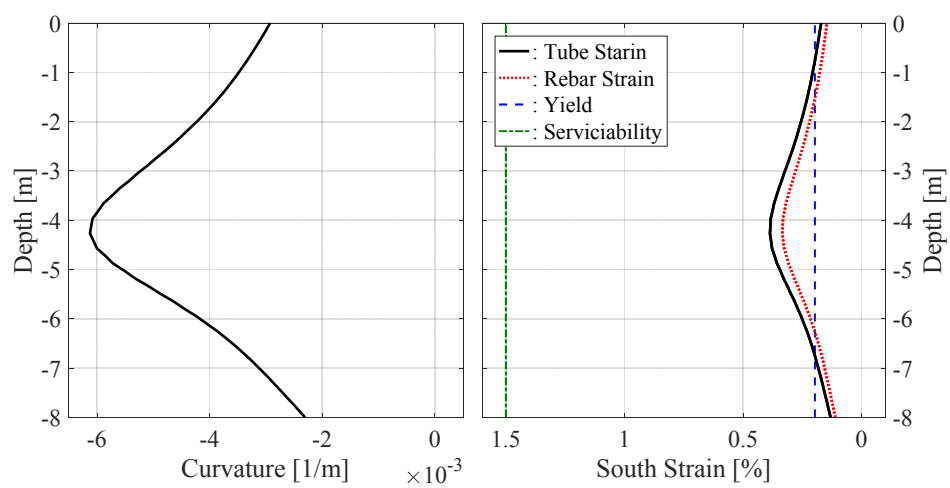

Figure 7-8 Example: inground hinge curvature and tensile strain profiles at ductility 4 (μ_4)

Based upon analytical results, it was found that the system can exhibit a stable and reliable response up to displacement ductility 4 (μ_4). It was observed that at this level of displacement, the top plastic hinge reaches its ultimate limit state while the inground plastic hinge reaches its yield limit state. As such, while the system has reserved displacement

capacity, attributed to the inground plastic hinge, at this level of displacement the top plastic hinge is close to its ultimate limit state. Therefore, displacement demands beyond a displacement ductility 4 (μ_4) would result in issues related to structural stability, since the top plastic hinge is at imminent failure.

In terms of performance limit states, recommendations of the POLA Seismic Code (2010) seem appropriate considering results of experimental tests conducted on fixed-head RCFST columns (Montejo et al., 2012). As such, the system can be characterized with serviceability, damage control and ultimate limit states, that are defined based on tensile strain limits of 1.5%, 6% or $0.6\varepsilon_{sm}$ (whichever is smaller), and 8% or $0.08\varepsilon_{sm}$ (whichever is smaller), respectively. Performance limit states and corresponding strain limits are summarized in Table 7-2. In terms of the analysis method, the assumption of strain compatibility is appropriate as the top plastic hinge corresponds to an RC section.

Table 7-2 Top plastic hinge performance levels and associated tensile strain limits POLA (2010)

Strain	Performance Level		
	Serviceability	Damage Control	Ultimate
Tension	0.015	$0.6\varepsilon_{sm} \leq 0.06$	$0.8\varepsilon_{sm} \leq 0.08$

Described next is the formulation of the proposed equivalent cantilever plastic hinge model for fixed-head RCFST shafts. Application examples for both clay and sand are also presented at the end.

7.2.2. Proposed Model and Examples

Figure 7-9 presents a schematic of the proposed equivalent cantilever model for fixed-head RCFST shafts. In this approach, a single RCFST shaft that can be characterized with a detailed FE analytical model, is simplified to an equivalent fixed-base cantilever with effective length L_e. This length is measured from the pile head to the depth-to-maximum moment, which is also known as the depth-to-plastic hinge (H_{ig}), in addition to the strain penetration length (L_{sp}) into the cap beam. The model assumes that only the top plastic hinge is developed. This assumption was made considering that, while onset of the inground hinge is possible, it would only occur at large levels of damage of the top plastic hinge, at which structural stability issues may be of concern. The model is used to calculate the displacement at the pile head at a prescribed limit state (Δ_{LS}) by calculating elastic (Δ_y) and plastic (Δ_p) displacement components, which depend on the elastic curvature (ϕ_y) and a plastic displacement parameter (β). The performance limit state is dictated by the top plastic hinge based upon strain limit states, as previously described. Described next is the step-by-step calculation process.

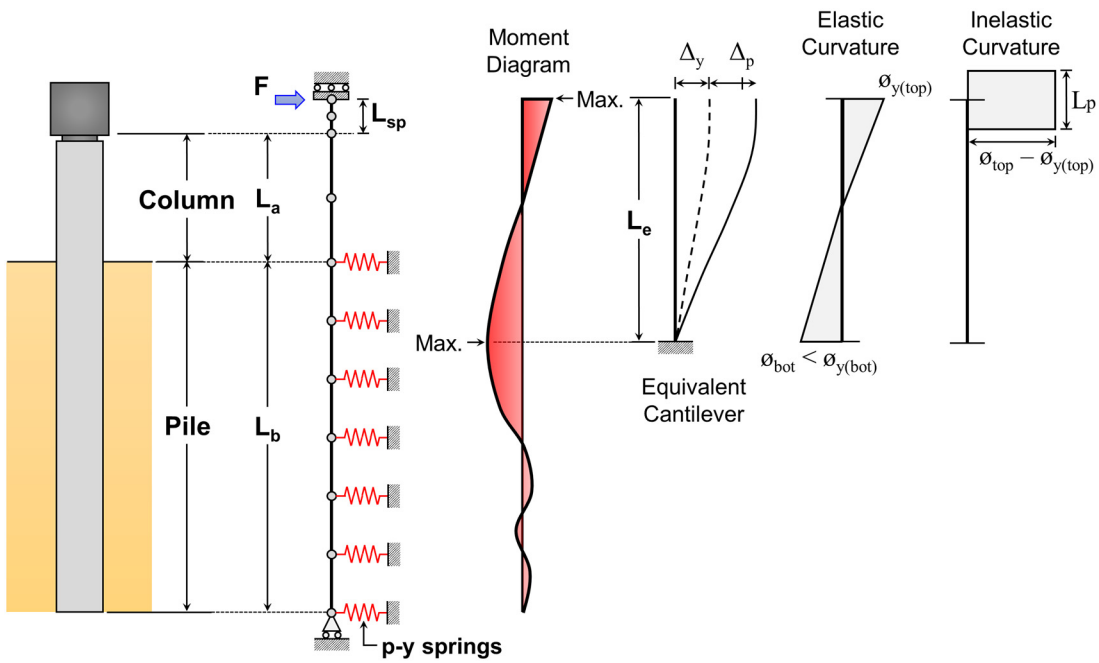

Figure 7-9 Equivalent cantilever model for pinned-head RCFST shafts

7.2.2.1 Equations for Sand

Step 1: calculate the yield curvature. For RC columns, $c_{\phi y} = 2.25$

$$\phi_{y(top)} = c_{\phi y(top)} \frac{\varepsilon_{y(rebar)}}{D}$$ Equation 7-29

Step 2: calculate the yield displacement

a. Calculate the yield displacement parameter:

$$C_1 = 0.207 - \frac{L_a}{300\,D} + \frac{D}{2800\,t} - \frac{\phi}{960} \quad , \quad \phi(^\circ)$$ Equation 7-30

b. Calculate the depth to plastic hinge:

$$\frac{H_{ig}}{D} = 8.57 + 0.88\frac{L_a}{D} - \frac{D}{130\,t} - \frac{\phi}{10}$$ Equation 7-31

c. Calculate the strain penetration length:

$$L_{sp} = 0.022\, f_{ye}\, d_{bl} \quad , \quad (MPa)$$ Equation 7-32

d. Determine the effective length:

$$L_e = H_{ig} + L_{sp}$$ Equation 7-33

e. Lastly, calculate the yield displacement as follows:

$$\Delta_y = c_1 \phi_{y(top)} L_e^2 \qquad \text{Equation 7-34}$$

Step 3: calculate the plastic displacement

a. Calculate the equivalent plastic hinge length (Chai et al., 1991):

$$L_{p(top)} = 2 L_{sp} + g \qquad \text{Equation 7-35}$$

b. Calculate the plastic displacement parameter:

$$\beta = 0.255 + 0.1 D + \frac{L_a}{50 D}\left(1 + \frac{D}{170 t}\right) + 0.7\, ALR - \frac{\phi}{160} \quad , \quad D(m), \phi(°) \qquad \text{Equation 7-36}$$

c. Calculate the limit state curvature:

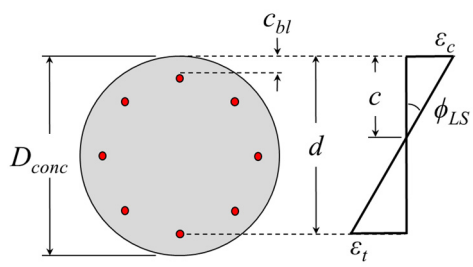

Figure 7-10 Curvature and associated strains for RC sections

$$\frac{c}{D} = 0.2 + 0.65 ALR \qquad \text{Equation 7-37}$$

$$D_{conc} = D - 2t \qquad \text{Equation 7-38}$$

$$d = D_{conc} - c_{bl} - \frac{d_{bl}}{2} \qquad \text{Equation 7-39}$$

$$\phi_{LS,t} = \frac{\varepsilon_t}{d - c} \qquad \text{Equation 7-40}$$

d. Determine the plastic curvature:

$$\phi_{p(top)} = \phi_{LS(top)} - \phi_{y(top)} \qquad \text{Equation 7-41}$$

e. Lastly, calculate the plastic displacement as follows:

$$\Delta_p = \phi_{p(top)} L_{p(top)} \beta L_e \qquad \text{Equation 7-42}$$

Step 4: calculate the limit state displacement

$$\Delta_{LS} = \Delta_y + \Delta_p \qquad \text{Equation 7-43}$$

Step 5: calculate the system equivalent viscous damping (for DDBD design)

$$\xi_{eq} = 0.094 - \frac{L_a}{1000 D} - \frac{\phi}{3200} + \left(\frac{1}{160} + \frac{L_a}{1200 D} + \frac{D}{12000 t}\right)(\mu - 1) \qquad \text{Equation 7-44}$$

7.2.2.2 Equations for Clay

Step 1: calculate the yield curvature. For RC columns, $c_{\phi y} = 2.25$

$$\phi_{y(top)} = c_{\phi y(top)} \frac{\varepsilon_{y(rebar)}}{D}$$ Equation 7-45

Step 2: calculate the yield displacement

a. Calculate the yield displacement parameter:

$$C_1 = 0.135 - \frac{L_a}{900\,D} + \frac{D}{2500\,t} + \frac{Ln(C_u)}{200} \quad , \quad C_u\,(kPa)$$ Equation 7-46

b. Calculate the depth to plastic hinge:

$$\frac{H_{ig}}{D} = 17.90 + 0.68\frac{L_a}{D} - \frac{D}{55\,t} - 2.49\,Ln(C_u) \quad , \quad C_u\,(kPa)$$ Equation 7-47

c. Calculate the strain penetration length:

$$L_{sp} = 0.022\,f_{ye}\,d_{bl} \quad , \quad (MPa)$$ Equation 7-48

d. Determine the effective length:

$$L_e = H_{ig} + L_{sp}$$ Equation 7-49

e. Lastly, calculate the yield displacement as follows:

$$\Delta_y = c_1\,\phi_{y(top)}\,L_e^{\,2}$$ Equation 7-50

Step 3: calculate the plastic displacement

a. Calculate the equivalent plastic hinge length (Chai et al., 1991):

$$L_{p(top)} = 2\,L_{sp} + g$$ Equation 7-51

b. Calculate the plastic displacement parameter:

$$\beta = 0.631 + 0.2\,D + \frac{L_a}{40\,D}\left(1 + \frac{D}{380\,t}\right) + 1.08\,ALR - 0.16\,Ln(C_u) \quad , \quad D\,(m), C_u\,(kPa)$$ Equation 7-52

c. Calculate the limit state curvature:

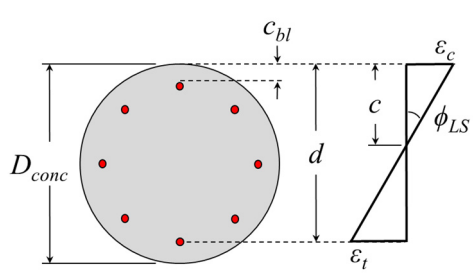

Figure 7-11 Curvature and associated strains for RC sections

$$\frac{c}{D} = 0.2 + 0.65ALR$$ Equation 7-53

$$D_{conc} = D - 2t$$ Equation 7-54

$$d = D_{conc} - c_{bl} - \frac{d_{bl}}{2}$$ Equation 7-55

$$\phi_{LS,t} = \frac{\varepsilon_t}{d - c}$$ Equation 7-56

d. Determine the plastic curvature:

$$\phi_{p(top)} = \phi_{LS(top)} - \phi_{y(top)}$$ Equation 7-57

e. Lastly, calculate the plastic displacement as follows:

$$\Delta_p = \phi_{p(top)} L_{p(top)} \beta L_e$$ Equation 7-58

Step 4: calculate the limit state displacement

$$\Delta_{LS} = \Delta_y + \Delta_p$$ Equation 7-59

Step 5: calculate the system equivalent viscous damping (for DDBD design)

$$\xi_{eq} = 0.13 - \frac{L_a}{600D} - \frac{Ln(C_u)}{160} + \left(\frac{1}{300} + \frac{L_a}{1400D} + \frac{D}{14000t}\right)(\mu - 1) \quad , \quad C_u\,(kPa)$$ Equation 7-60

7.2.2.3 Example: displacement capacity or design displacement

To illustrate the sequence of operations for sand and clay, consider an RCFST pile-column, part of a bridge bent, and connected to other shafts with a cap beam, under seismic response in the transverse direction. The geometry and material properties are the same as for the example for pinned-head shafts; those details are repeated here for convenience. Additional required details are also provided.

The RCFST shaft has a tube outer diameter D = 1.22 m. (4 ft.), a D/t ratio of 48, which means the tube has a wall thickness t = 25.4 mm (1 in.), an aspect ratio L_a/D = 8, and supports an axial load, including self weight, of 4,260 kN (960 kips). Specified material properties are concrete compressive strength f_c' = 28 MPa (hence f_{ce}' = 36.4 MPa (5.2 ksi)); tube yield strength f_{yt} = 360 MPa (hence f_{ype} = 396 MPa (57.2 ksi)); and reinforcing steel (longitudinal and transverse) yield strength f_{yr} = 420 MPa (hence f_{yre} = 462 MPa (66 ksi)). Longitudinal bar diameter is 43 mm (1.693 in.), with 50 mm (1.97 in) cover between the inside of the steel tube and outside of the transverse reinforcement. Spiral bar diameter is 16 mm (0.625 in).

The goal of this example is to illustrate calculations for both sand and clay to determine the displacement at onset of bar buckling, which is determined at a tensile strain ε_t = 0.06. Furthermore, for sand, consider a uniform profile with friction angle ϕ = 35° (medium sand), while for clay, consider a uniform profile with undrained shear strength C_u = 36 kPa (medium clay). It is assumed that the RCFST shaft is embedded deep enough into the ground. The solutions for both soil types are presented next.

7.2.2.3.1 Sand

Step 1: calculate the yield curvature. For RC columns, $c_{\phi y}$ = 2.25. From Equation 7-29:

$$\phi_{y(top)} = c_{\phi y(top)} \frac{\varepsilon_{y(rebar)}}{D} = 2.25\left(\frac{462/200,000}{1.22m}\right) = 0.00426\frac{1}{m}$$

Step 2: calculate the yield displacement

a. Calculate the yield displacement parameter, from Equation 7-30:

$$C_1 = 0.207 - \frac{L_a}{300D} + \frac{D}{2800t} - \frac{\phi}{960} = 0.207 - \frac{8}{300} + \frac{48}{2800} - \frac{35}{960} = 0.161$$

b. Calculate the depth to plastic hinge, from Equation 7-31:

$$\frac{H_{ig}}{D} = 8.57 + 0.88\frac{L_a}{D} - \frac{D}{130t} - \frac{\phi}{10} = 8.57 + 0.88(8) - \frac{48}{130} - \frac{35}{10} = 11.741$$

$$H_{ig} = 11.741D = 11.741(1.22m) = 14.324m$$

c. Calculate the strain penetration length, from Equation 7-32:

$$L_{sp} = 0.022 f_{ye} d_{bl} = 0.022(462)(43) = 437mm = 0.437m$$

d. Determine the effective length, from Equation 7-33:

$$L_e = H_{ig} + L_{sp} = 14.324m + 0.437m = 14.761m$$

e. Lastly, calculate the yield displacement from Equation 7-34:

$$\Delta_y = c_1 \phi_{y(top)} L_e^2 = 0.161\left(0.00426\frac{1}{m}\right)(14.761)^2 = 0.149m$$

Step 3: calculate the plastic displacement

a. Calculate the top plastic hinge length (Chai et al., 1991), from Equation 7-35:

$$L_{p(top)} = 2L_{sp} + g = 2(0.437m) + 0.050m = 0.924m$$

b. Calculate the plastic displacement parameter, from Equation 7-36:

$$\beta = 0.255 + 0.1D + \frac{L_a}{50D}\left(1 + \frac{D}{170t}\right) + 0.7\,ALR - \frac{\phi}{160}$$

$$ALR = \frac{P}{f_{ce}' A_g} = \frac{4,260kN}{36.4MPa\left(1.169m^2\right)\left(1000\right)} = 0.10$$

$$\beta = 0.255 + 0.1\left(1.22\right) + \frac{8}{50}\left(1 + \frac{48}{170}\right) + 0.7\left(0.1\right) - \frac{35}{160} = 0.433$$

c. Calculate the limit state curvature:

From Equation 7-37:

$$\frac{c}{D} = 0.2 + 0.65ALR = 0.2 + 0.65\left(0.1\right) = 0.265$$

$$c = 0.265D = 0.265\left(1.22m\right) = 0.323m$$

From Equation 7-38:

$$D_{conc} = D - 2t = 1,220mm - 2\left(25.4mm\right) = 1,169mm = 1.169m$$

From Equation 7-39:

$$d = D_{conc} - c_{bl} - \frac{d_{bl}}{2} = 1,169mm - 50mm - 16 - \frac{43mm}{2} = 1,081mm = 1.081m$$

From Equation 7-40:

$$\phi_{LS,\,t} = \frac{\varepsilon_t}{d - c} = \frac{0.06}{1.081 - 0.323} = 0.0791\frac{1}{m}$$

d. Determine the plastic curvature, from Equation 7-41:

$$\phi_{p(top)} = \phi_{LS(top)} - \phi_{y(top)} = 0.0791\frac{1}{m} - 0.00426\frac{1}{m} = 0.0749\frac{1}{m}$$

e. Lastly, calculate the plastic displacement from Equation 7-42:

$$\Delta_p = \phi_{p(top)}\, L_{p(top)}\, \beta\, L_e = \left(0.0749\frac{1}{m}\right)\left(0.924m\right)\left(0.433\right)\left(14.761m\right) = 0.443m$$

Step 4: calculate the limit state displacement, from Equation 7-43:

$$\Delta_{LS} = \Delta_y + \Delta_p = 0.149m + 0.443m = 0.592m$$

7.2.2.3.2 Clay

Step 1: calculate the yield curvature. For RC columns, $c_{\phi y}$ = 2.25. From Equation 7-45:

$$\phi_{y(top)} = c_{\phi y(top)}\frac{\varepsilon_{y(rebar)}}{D} = 2.25\left(\frac{462 / 200,000}{1.22m}\right) = 0.00426\frac{1}{m}$$

Step 2: calculate the yield displacement

a. Calculate the yield displacement parameter, from Equation 7-46:

$$C_1 = 0.135 - \frac{L_a}{900\,D} + \frac{D}{2500\,t} + \frac{Ln(C_u)}{200} = 0.135 - \frac{8}{900} + \frac{48}{2500} + \frac{Ln(36)}{200} = 0.163$$

b. Calculate the depth to plastic hinge, from Equation 7-47:

$$\frac{H_{ig}}{D} = 17.90 + 0.68\frac{L_a}{D} - \frac{D}{55\,t} - 2.49\,Ln(C_u) = 17.90 + 0.68(8) - \frac{48}{55} - 2.49\,Ln(36) = 13.544$$

$$H_{ig} = 13.544D = 13.544(1.22m) = 16.524m$$

c. Calculate the strain penetration length, from Equation 7-48:

$$L_{sp} = 0.022\,f_{ye}\,d_{bl} = 0.022(462)(43) = 437mm = 0.437m$$

d. Determine the effective length, from Equation 7-49:

$$L_e = H_{ig} + L_{sp} = 16.524m + 0.437m = 16.961m$$

e. Lastly, calculate the yield displacement from Equation 7-50:

$$\Delta_y = c_1\,\phi_{y(top)}\,L_e^{\,2} = 0.163\left(0.00426\frac{1}{m}\right)(16.961)^2 = 0.200m$$

Step 3: calculate the plastic displacement

a. Calculate the top plastic hinge length (Chai et al., 1991), from Equation 7-51:

$$L_{p(top)} = 2\,L_{sp} + g = 2(0.437m) + 0.050m = 0.924m$$

b. Calculate the plastic displacement parameter, from Equation 7-52:

$$\beta = 0.631 + 0.2\,D + \frac{L_a}{40\,D}\left(1 + \frac{D}{380\,t}\right) + 1.08\,ALR - 0.16\,Ln(C_u)$$

$$\beta = 0.631 + 0.2(1.22) + \frac{8}{40}\left(1 + \frac{48}{380}\right) + 1.08(0.1) - 0.16\,Ln(36) = 0.635$$

c. Calculate the limit state curvature:

From Equation 7-53:

$$\frac{c}{D} = 0.2 + 0.65ALR = 0.2 + 0.65(0.1) = 0.265$$

$$c = 0.265D = 0.265(1.22m) = 0.323m$$

From Equation 7-54:

$$D_{conc} = D - 2\,t = 1{,}220mm - 2(25.4mm) = 1{,}169mm = 1.169m$$

From Equation 7-55:

$$d = D_{conc} - c_{bl} - \frac{d_{bl}}{2} = 1{,}169mm - 50mm - 16 - \frac{43mm}{2} = 1{,}081mm = 1.081m$$

From Equation 7-56:

$$\phi_{LS,\,t} = \frac{\varepsilon_t}{d-c} = \frac{0.06}{1.081-0.323} = 0.0791\frac{1}{m}$$

d. Determine the plastic curvature, from Equation 7-57:

$$\phi_{p(top)} = \phi_{LS(top)} - \phi_{y(top)} = 0.0791\frac{1}{m} - 0.00426\frac{1}{m} = 0.0749\frac{1}{m}$$

e. Lastly, calculate the plastic displacement from Equation 7-58:

$$\Delta_p = \phi_{p(top)}\, L_{p(top)}\, \beta\, L_e = \left(0.0749\frac{1}{m}\right)(0.924m)(0.635)(16.961m) = 0.745m$$

Step 4: calculate the limit state displacement from Equation 7-59:

$$\Delta_{LS} = \Delta_y + \Delta_p = 0.200m + 0.745m = 0.945m$$

7.3. Final Remarks on Analytical and Experimental Results

7.3.1. Summary

Analytical and experimental studies were conducted on pinned-head RCFST shafts. While experimental and analytical results were not directly compared, as it is explained later in this section, agreement in terms of the behavior of the system was observed considering the variables studied. It was found that the D/t ratio affects the strength of the system but it does not impact the displacement capacity as much. Regarding the L_a/D ratio, it was found that it is the most important parameter, having a direct impact on the strength and displacement capacity of the system, shear demand, location of maximum moment, and spread of plasticity. As for the soil stiffness, it was found that this parameter affects mostly the displacement capacity of the system, as it influences the shaft fixity.

On the other hand, regarding fixed-head RCFST shaft, only analytical studies were conducted. It was found that the D/t ratio has a small impact on the system strength and displacement capacity, with similar observations regarding the soil stiffness. The most important variable on the behavior of fixed-head shaft is the L_a/D ratio. This parameter affects the strength and displacement capacity of the system, the shear demand, location of moment, spread of plasticity, and the tensile strains of the top plastic hinge. Regarding the latter, it was found that the strain can be reduced by increasing the L_a/D ratio. By increasing the aspect ratio, the system becomes more flexible and the curvature demand at the top hinge reduces due to a reduced moment grading. This can be beneficial not only to reduce tensile strains but to increase the displacement capacity of the system.

7.3.2. Laboratory vs. Free-Field Conditions

The experimental results were impacted by the boundary conditions of the test setup and the observed rigid body rotation of the tested pile specimens. This means that pile specimens were not fully fixed into the ground, but rather fixity was developed as lateral displacements increased, thereby increasing the interaction of the soil and the rigid reinforced concrete pit wall. This behavior induced a unique soil stiffness profile that changed as lateral displacement demands increased. As such, two analytical models were developed, that is, one representative of laboratory conditions, and another one characteristic of free-field conditions. The only difference between these two analytical models was on the formulation of the p-y curve analysis utilized to determine properties of the non-linear soil springs. This means that characterization of the pile-column elements was not altered between both analytical models.

Since this study is focused on the performance of RCFSTs embedded in soil, the analytical model was developed based upon the observed behavior and response of the tested specimens. This means that the analytical model was calibrated and validated based on the premise that if the laboratory experiments were replicated, then characterization of the pile specimens was adequate, which means that the non-linear behavior of the pile specimens was properly captured. Then, the same analytical model was used to develop the analytical model representative of free-field conditions, with the exception that the new model would use p-y curve formulations that are accepted by the engineering community, and currently used in design practice.

The proposed equivalent cantilever plastic hinge model presented in previous sections of this chapter was developed for a uniform layer of sand or clay. The API (1993) approach in combination with the Reese and Van Impe (2011) model were selected to develop p-y curves for sand, while the Matlock (1970) model was selected to develop p-y curves for clay. These p-y curve models have been validated by other authors based upon results of laboratory and field experiments (e.g., Wilson, 1998; Boulanger et al., 1999; Chai and Hutchinson, 2002; Suleiman et al., 2006), where issues related to boundary conditions or pile rigid body rotation were not observed. Moreover, these p-y curve models are widely used for soil-structure interaction problems (e.g., Curras et al., 2001; Song et al., 2005; Chai and Song, 2012; Chang and Hutchinson, 2013; Sritharan et al., 2007; Suarez and Kowalsky, 2007; Wotherspoon et al., 2010).

7.3.3. Modeling Approach and Implications

The developed FE analytical model utilized a fiber-based section approach in combination with force-based non-linear beam-column elements to capture the non-linear behavior of RCFST shafts. This modeling approach allows for accurate representation of the structural response in terms of displacement, strain, and spread of plasticity. However, complex physical phenomena as represented by tube or bar buckling cannot be capture by such a model. Recommendations presented in this study rely on tensile strains to determine displacements at a prescribed limit state. For pinned-head RCFST shafts, whose performance is controlled by inground plastic hinges, recommended strain limits at onset of

tube buckling or fracture are based upon experimental observations of RCFST specimens tested in the air (e.g., Park et al., 1983; Marson and Bruneau, 2004; Brown et al., 2015). For fixed-head RCFTS shaft, on the other hand, whose performance is controlled by top plastic hinges, recommended strain limits at onset of bar buckling or fracture were adopted from the POLA Seismic Code (2010) as the values seems to be appropriate based on experimental results recently conducted at NC State University (Montejo et al., 2012).

It is important to note that the analytical model does not account for uncertainties in the soil properties. This means that each simulation was conducted for prescribed parameters of soil stiffness and strength. As such, the proposed equivalent cantilever plastic hinge model does not account for soil variability. However, the method can be used for calculations at various levels of soil stiffness and strength, if needed, though a detailed FE analytical model should be developed to account for soil variability. This is usually considered through p-y curve multipliers, whose purpose is to alter the ultimate soil pressure and initial stiffness of p-y curves, respectively. Some studies suggest that p-y curve multipliers can vary within 0.5 and 2.0 when considering soil variability (Curras et al., 2001). This means that both ultimate force and initial stiffness can vary between half and twice the nominal values of p-y curve definitions.

CHAPTER 8

8. CONCLUSIONS

8.1. Summary

The research project described in this document aimed to study the effects of soil stiffness into performance of reinforced concrete filled steel tube (RCFST) pile-columns with a pinned-head condition, that is, a soil-pile-column system that utilizes RCFST elements which due to seismic demands develop a plastic hinge below ground.

As such, this study included experimental and analytical studies that considered three main parameters: (1) the diameter-to-thickness (D/t) ratio, (2) the aboveground length-to-diameter ratio (L_a/D), and the soil stiffness. The experimental program consisted of cyclic experimentation on twelve half-scale RCFST pile-columns embedded into clean sand at the soil-structure interaction (SSI) facility at North Carolina State University. Cyclic lateral loading was applied to the specimens using a hydraulic actuator that was pin-connected to the specimen head, effectively creating a pinned-head condition, thereby ensuring plastic deformations to occur below ground. Steel tubes with outer diameter of either 12 in. or 12.75 in. were utilized in combination with thickness values such that D/t ratios of 48, 68, and 95 were considered, along with aboveground lengths of either 5.5D or 7.5D; where D represents the outer diameter of the steel tube. A "soil-sandwich" approach was devised as a soil surcharge system that was used for altering the effective soil stiffness. Such system allowed to increase the soil stiffness by increasing the confinement in the soil surrounding the specimens.

In addition to the experiments described above, analytical studies were conducted on both pinned-head and fixed-head RCFST shafts. For that purpose, a detailed finite element (FE) analytical model was developed using OpenSees (McKenna et al., 2000). The modeling approach consisted of distributed plasticity non-linear elements, representing the RCFST pile-column elements, embedded into a uniform soil layer of either sand or clay; non-linear soil springs were implemented to characterize the soil behavior. Variables for the analytical study included the same variables of the experimental program, in addition to three levels of axial load ratio (5%, 10%, and 15%) and three levels of soil stiffness (flexible, medium, and stiff). Regarding the latter, friction angles of 30°, 35°, and 40° were considered for sand, while for clay, undrained shear strengths of 12 kPa, 36 kPa, and 72 kPa were utilized.

Using results of the analytical and experimental studies, an equivalent cantilever plastic hinge model was developed for pinned-head and fixed-head RCFST shafts. The main feature of the proposed model is that it relates strain with displacements. The model is intended to be used for calculation of the displacement capacity of the system at a prescribed limit state, or for determination of the design displacement if a displacement-based design approach is implemented. The model accounts for soil flexibility and includes consistent definitions of equivalent plastic hinge lengths for each soil type. Moreover, system equivalent viscous damping models are also provided. The main conclusions of this study are summarized next for pinned-head and fixed head shafts.

8.2. Pinned-Head RCFST Shafts

- The inelastic behavior of pinned-head RCFST shaft is controlled by a plastic hinge that develops inground. The observed failure mechanism was consistent with that reported in past research (e.g., González-Román et al., 2008; Brown et al., 2015). This mechanism consisted of ripples forming at the extreme tension and compression fibers, followed by onset of tube local buckling as the curvature demands increases. Tube local buckling continues to increase with repeated compression cycles, which causes the strength of such sections to weaken up until a reversal cycle (tension) that causes tube fracture at a tensile strain of 2.5%.

- A characteristic feature was observed during Test 3 and Test 4, in the set of specimens with D/t = 95*. It was found that the tubes used in those tests were welded only on the outside surface with a partial joint penetration detail. Thus, the failure mechanism of those specimens was characterized by fracture along the tube spiral weld at low displacement demands, namely, ductility 1.5 ($\mu_{1.5}$). The steel tubes used in the remaining tests were indeed welded on both inside and outside surfaces (provided with complete joint penetration welds) and the main buckles as well as tube fracture did not occur over the spiral weld, so the tube spiral welds do not appear to negatively influence the behavior of those specimens. Therefore, it was concluded that spirally-welded tubes with a partial joint penetration weld process must be avoided as the performance is negatively influenced, resulting in low displacement capacities and modifying the failure mode.

- The tested RCFST specimens showed a stable top lateral force vs. displacement response, including those corresponding to the thin-wall tubes (i.e., large D/t ratios), in which it is believed onset of tube local buckling initiated at low displacement ductility levels, yet the response was stable and reliable up until all cycles of ductility 3 (μ_3). The specimens with low D/t ratios (thick-wall tubes) showed a stable and reliable force-displacement response up until all cycles of ductility 4 (μ_4). Moreover, it was found that the D/t ratio affects the strength of the system with a minor impact on the system stiffness. The aboveground length and soil stiffness, on the other hand, do have a significant impact, inducing 21% higher and 31% lower elastic stiffness values for the for the change in soil stiffness (surcharge = 960 psf) and the change in the aboveground length (L_a/D = 7.5), respectively, when compared to tests using pristine soil conditions and L_a/D = 5.5. These observations were further validated upon comparison with the analytical studies, which confirmed that the most important variable is the L_a/D ratio. I t was found that for L_a/D = 12 the system strength and displacement capacity are half and twice, respectively, that of a system with L_a/D = 4.

- The depth to the plastic hinge is mostly impacted by the L_a/D ratio and effective soil stiffness. The D/t ratio showed to have a minor impact on this parameter. Average depths to the plastic hinge of 2.9 D and 2.4 D were found for the pristine soil conditions and for the stiffer soil condition (i.e., soil surcharge = 960 psf), respectively; D represents the outer diameter of the steel tube. These results were validated upon results of the analytical study, which suggested that depending upon the soil type, stiffness, and

aspect ratio (L_a/D), the system can develop a plastic hinge within 2D and 5D from the soil surface for sand, and within 2D and 10D from the soil surface for clay; D represents the shaft diameter.

- It was found that the D/t ratio and the above-ground length parameters have a minor impact on the hysteretic equivalent viscous damping (EVD); the effective soil stiffness appears to have a larger impact. From experimental observations, the contribution of the soil appears to increase the total EVD of the RCFST specimens within 1% and 3%. This observation was also made from the analytical studies. A revised version of the model proposed by Brown et al., (2015) was suggested. The proposed model assumes a bilinear contribution of the soil into the total EVD. Based on this model and the results observed at ductility 1 (μ_1), it is suggested that a total EVD of 8% and 9% can be reasonably assumed when performing elastic response spectrum analysis (RSA) of RCFST pile-column shafts embedded in sand and clay, respectively.
- Regarding strain limit states, based upon experimental results, it was found that the tensile strain prior tube fracture was consistent with the limit previously reported by Brown et al. (2015), namely, 2.5%. Only three out of the nine considered test results were below this limit, though close to it. For the specimens with a stiffer soil profile and D/t ratios of 68 and 95, tensile strains prior tube fracture of 2.3% and 2.4% were found, respectively. At a D/t ratio of 95, the specimen with pristine soil conditions showed a tensile strain of 2.1%. Moreover, all specimens with D/t =48 showed strains higher than 2.5%.

8.3. Fixed-Head RCFST Shafts

- The inelastic behavior of fixed-head RCFT shafts is controlled by a plastic hinge that develops aboveground at the column-cap beam interface. While an inground plastic hinge can be potentially developed, it would only occur at large levels of deformation of the top plastic hinge, where issues related to structural stability may be of concern. This behavior makes that the displacement capacity of the system is rather in the low-to-moderate range of displacements, depending upon the aboveground length-to-diameter (L_a/D) ratio.
- Based on analytical results, the system showed a reliable and stable top lateral force vs. displacement response up to ductility 4 (μ_4). At this level of deformation, the inground hinge is at onset of yielding, while the top plastic hinge exhibits ultimate conditions. Moreover, the force vs. displacement response is influenced by the top plastic hinge and the flexural stiffness of the pile-column below, making the system behave as a hybrid system since the flexural stiffness depends corresponds to an RC section confined by a steel tube at the top, and to and RCFST below the top hinge, where the flexural stiffness is mostly provided by the steel tube. Furthermore, it was observed that the D/t ratio and the soil stiffness have a minor impact on the system response, whereas the L_a/D ratio has a significant impact on both the system strength and displacement capacity. For large L_a/D ratios, moment and curvature gradients decrease, thus reducing strain and increasing the displacement capacity.

- In terms of the system equivalent viscous damping (EVD), since the system response is influence by the distribution of flexural stiffness along the length of the pile-column, the system exhibited a linear increase in system EVD as a function of ductility. Moreover, it was observed that the energy dissipated was smaller than that of a typical RC bridge column. This is related to the distribution of flexural stiffness. Although the top plastic hinge develops damage, that is not the case of the remaining length of the pile-column, thus the overall energy dissipated is small.
- Regarding performance limit states, this study adopted recommendations provided in the POLA Seismic Code (2010) as they seem appropriate based on the experimental data reported by (i.e., Montejo et al., 2009; Montejo et al., 2012). In short, these limits include serviceability, damage control, and ultimate limit states that are defined based on tensile strain limits of 1.5%, 6% or $0.6\varepsilon_{sm}$ (whichever is smaller), and 8% or $0.08\varepsilon_{sm}$ (whichever is smaller), respectively, where ε_{sm} is the strain corresponding to maximum stress of the longitudinal reinforcement.

8.4. Future Research

The pinned-head and fixed-head RCFST shafts studied in the research described in this document were subjected to standard single-set and three-cycle set intended to evaluate both elastic and inelastic behavior of the specimens. Additional analytical studies must be performed to verify the design recommendations, and to study the effects of loading history. Moreover, while this research considered the impact of the soil stiffness, it did not include the effects of layered soil profiles, nor the effect of soil profiles that include layers with potential for soil liquefaction. The analytical studies presented in this document could be expanded to include such effects.

Recommendations and conclusions related to fixed-head RCFST shafts were developed based on results from analytical studies only. Experimental studies must be performed to verify the behavior of this system and performance limit states described earlier. Of interest is the conclusion that the system would develop yielding of the inground plastic hinge when the top plastic hinge reaches its ultimate limit state. While this is beneficial in the sense that damage will occur only at the top hinge, it was found that it can occur at low-to-moderate levels of displacement. As such, experimental studies should be conducted to determine appropriate strain limits of the top plastic hinge at damage control and ultimate limit states. It is worth noting that these limits are affected by the confinement provided by the steel tube, and that provided by the connection with the cap beam. Furthermore, such experimental studies would also help to validate recommendations regarding the system equivalent viscous damping for fixed-head shafts.

As previously mentioned, the proposed equivalent cantilever plastic hinge model allows for calculating the displacement capacity, or design displacement for DDBD, of pinned-head and fixed-head RCFST shafts. The feasibility of using parameters such as the effective length could be studied to determine if they are appropriate for simplified modeling approaches in bridge design. This means that instead of modeling a bridge bent including soil-structure interaction, it could be examined if an equivalent fixed-base approach is

appropriate in terms of modeling of pile-columns, where the properties of such equivalent elements could be determined from the proposed method.

CHAPTER 9

9. REFERENCES

AASHTO. (2011). *AASHTO Guide Specifications for LRFD Bridge Design*.

Allotey, N., & El Naggar, M. H. (2008a). A numerical study into lateral cyclic nonlinear soil–pile response. *Canadian Geotechnical Journal*, *45*(August 2008), 1268–1281.

Allotey, N., & El Naggar, M. H. (2008b). Generalized dynamic Winkler model for nonlinear soil–structure interaction analysis. *Canadian Geotechnical Journal*, *45*(4), 560–573.

API. (1993). *Recommended Practice for Planning, Design, and Constructing Fixed Offshore Platforms - Working Stress Design 20th Edition*. American Petroleum Institute.

Applied Technology Council, (ATC). (1996). *Improved Seismic Design Criteria for California Bridges: Provisional Recommendations*. Redwood City, CA.

ASTM A370-14. (2014). Standard Test Methods and Definitions for Mechanical Testing of Steel Products. *ASTM International*. West Conshohocken, PA.

Boulanger, R., Curras, C., Kutter, B., Wilson, D., & Abghari, A. (1999). Seismic Soil-Pile-Structure Interaction Experiments and Analyses. *ASCE Journal of Geotechnical and Geoenvironmental Engineering*, *125*(9), 750–759.

Boulanger, R., Kutter, B., Brandenberg, S., Singh, P., & Chang, D. (2003). *Pile foundations in liquefied and laterally spreading ground during earthquakes: centrifuge experiments & analyses*. *Report No. UCD/CGM-03/01*. University of California at Davis, CA.

Brown, N. K., Kowalsky, M. J., & Nau, J. (2013). *Strain Limits for Concrete Filled Steel Tubes in AASHTO Seismic Provisions*.

Brown, N. K., Kowalsky, M. J., & Nau, J. M. (2015). Impact of D/t on Seismic Behavior of Reinforced Concrete Filled Steel Tubes. *Journal of Constructional Steel Research*, *107*, 111–123.

Budek, A. M., Benzoni, G., & Priestley, M. J. N. (1995). *An Analytical Study of the Inelastic Seismic Response of Reinforced Concrete Pile-Columns in Cohesionless Soil*.

Budek, A. M., Priestley, M. J. N., & Benzoni, G. (2000). Inelastic Seismic Response of Bridge Drilled-Shaft RC Pile/Columns. *ASCE Journal of Structural Engineering*, *126*(4), 510–517.

Caltrans. (2013). *Seismic Design Criteria Version 1.7. California Department of Transportation: Sacramento, CA, U.S.*

Chai, Y. H. (2002). Flexural Strength and Ductility of Extended Pile-Shafts. I: Analytical Model. *Journal of Structural Engineering*, *128*(5), 595–602.

Chai, Y. H., & Hutchinson, T. C. (2002). Flexural Strength and Ductility of Extended Pile-Shafts II: Experimental Study. *ASCE Journal of Structural Engineering*, *128*(5), 595–602.

Chai, Y. H., Priestley, M. J. N., & Seible, F. (1991). Seismic Retrofit of Circular Bridge Columns for Enhanced Flexural Performance. *ACI Structural Journal*, *88*(5), 572–584.

Chai, Y. H., & Song, S.-T. (2012). Inelastic Deformation of Extended Pile-Shafts. *Journal of Engineering Mechanics*, *138*(July), 842–852.

Chang, B. J., & Hutchinson, T. C. (2013). Experimental Investigation of Plastic Demands in Piles Embedded in Multi-Layered Liquefiable Soils. *Soil Dynamics and Earthquake Engineering*, *49*, 146–156.

Chen, J., Wang, J., & Ke, X. (2011). Behavior of Large-Diameter Rock-Socketed Piles Under Lateral Loads, *21*(4), 5381.

Chiou, J.-S., Yang, H.-H., & Chen, C.-H. (2009). Use of Plastic Hinge Model in Nonlinear Pushover Analysis of a Pile. *ASCE Journal of Geotechnical and Geoenvironmental Engineering*, *135*(September), 1341–1346.

Curras, C. J., Hutchinson, T. C., Boulanger, R. W., Chai, Y., & Idriss, I. M. (2001). Lateral Loading and Seismic Response of CIDH Pile Supported Bridge Structures. In *Procedings, Geo-Odyssey - ASCE*.

El Naggar, M. H., & Bentley, K. J. (2000). Dynamic analysis for laterally loaded piles and dynamic p-y curves. *Canadian Geotechnical Journal*, *37*(6), 1166–1183.

Ellobody, E., Young, B., & Lam, D. (2006). Behaviour of Normal and High Strength Concrete-Filled Compact Steel Tube Circular Stub Columns. *Journal of Constructional Steel Research*, *62*(7), 706–715.

Fulmer, S. J., & Kowalsky, M. J. (2011). Reversed Cyclic Flexural Behavior of Spiral DSAW and Single Seam ERW Steel Pipe Piles. *ASCE Journal of Structural Engineering*, *138*(9), 1099–1109.

Gajalakshmi, P., & Helena, H. J. (2012). Behaviour of concrete-filled steel columns subjected to lateral cyclic loading. *Journal of Constructional Steel Research*, *75*, 55–63.

Goel, R. K. (2015). Evaluation of in-ground plastic-hinge length and depth for piles in marine oil terminals. *Earthquake Spectra*, *31*(4), 2397–2417.

González-Román, L. A., Kowalsky, M. J., Nau, J. M., & Hassan, T. (2008). *Reversal Cyclic Testing of Full Scale Pipe Piles*.

Goodnight, J. C., Fulmer, S. J., Brown, N. K., Kowalsky, M. J., & Nau, J. M. (2014). Experimental Applications of 3D Position Monitoring Systems for Earthquake Engineering Research. In *Tenth U.S. National Conference on Earthquake Engineering*. Anchorage, AK.

Jacobsen, L. S. (1930). Steady Force Vibrations as Influenced by Damping. *Trans. ASME*, *52*(1), 169–181.

Kunnath, S. K., Heo, Y., & Mohle, J. F. (2009). Nonlinear Uniaxial Material Model for Reinforcing Steel Bars, *135*(April), 335–343.

Mander, J. B., Priestley, M. J. N., & Park, R. (1988). Theoretical Stress-Strain Model for Confined Concrete. *ASCE Journal of Structural Engineering*, *114*(8), 1804–1826.

Marson, J., & Bruneau, M. (2004). Cyclic Testing of Concrete-Filled Circular Steel Bridge Piers Having Encased Fixed-Based Detail. *ASCE Journal of Bridge Engineering*, *9*(February), 14–23.

Matlock, H. (1970). Correlations for Design of Laterally Loaded Piles in Soft Clay. In *2nd Annual Offshore Technology Conference*. Houston, TX.

McKenna, F., Fenves, G. L., Scott, M. H., & Jeremic, B. (2000). Open System for Earthquake Engineering Simulation – OpenSees.

Montejo, L. A., González-Román, L. A., & Kowalsky, M. J. (2012). Seismic Performance Evaluation of Reinforced Concrete-Filled Steel Tube Pile/Column Bridge Bents. *Journal of Earthquake Engineering*, *16*(3), 401–424.

Montejo, L. A., & Kowalsky, M. J. (2007). *CUMBIA - Set of Codes for the Analysis of Reinforced Concrete Members*. Raleigh, NC.

Montejo, L. A., Kowalsky, M. J., & Hassan, T. (2009). Seismic Behavior of Flexural Dominated Reinforced Concrete Bridge Columns at Low Temperatures. *ASCE Journal of Cold Regions Engineering*, *23*(1), 18–42.

Park, R. J. T., Priestley, M. J. N., & Walpole, W. R. (1983). The Seismic Performance of Steel Encased Reinforced Concrete Bridge Piles. *Bulletin of the New Zealand National Society for Earthquake Engineering*, *16*(2), 123–140.

POLA. (2010). *Port of Los Angeles Code for Seismic Design , Upgrade and Repair of Container Wharves*. Los Angeles, CA.

Poulos, H. G., & Davis, E. H. (1980). Pile Foundation Analysis and Design.

Priestley, M. J. N., Calvi, G. M., & Kowalsky, M. J. (2007). *Displacement-Based Seismic Design of Structures*. IUSS Press.

Priestley, M. J. N., & Grant, D. N. (2005). Viscous Damping in Seismic Design and Analysis. *Journal of Earthquake Engineering*, *9*(2), 229–255.

Priestley, M. J. N., Seible, F., & Calvi, G. M. (1996). *Seismic Design and Retrofit of Bridges*. New York: John Wiley & Sons, Inc.

Reese, L., & Van Impe, W. (2011). *Single Piles and Pile Groups Under Lateral Loading* (2nd ed.). Taylor & Francis.

Richards, P. W., Rollins, K. M., & Stenlund, T. E. (2011). Experimental Testing of Pile-to-Cap Connections for Embedded Pipe Piles. *Journal of Bridge Engineering*, *16*(April), 286–294.

Sakino, K., Nakahara, H., Morino, S., & Nishiyama, I. (2004). Behavior of Centrally Loaded Concrete-Filled Steel-Tube Short Columns. *Journal of Structural Engineering*, *130*(2), 180–188.

SCDOT. (2008). *Seismic Design Specifications for Highway Bridges Version 2.0*.

Seed, H. B., & Idriss, I. M. (1970). Soil Moduli and Damping Factors for Dynamic Response Analyses. Berkeley, CA: Earthquake Engineering Research Center, University of California.

Shinoda, M., Uchimura, T., & Tatsuoka, F. (2003). Increasing the Stiffness of Mechanically Reinforced Backfill by Preloading and Prestressing. *Soils and Foundations*, *43*(1), 75–92.

Song, S. T., Chai, Y. H., & Hale, T. H. (2005). Analytical Model for Ductility Assessment of Fixed-Head Concrete Piles. *ASCE Journal of Structural Engineering*, *131*(7), 1051–1059.

Sritharan, S., Suleiman, M. T., & White, D. J. (2007). Effects of seasonal freezing on bridge column-foundation-soil interaction and their implications. *Earthquake Spectra*, *23*(1), 199–222.

Suarez, V., & Kowalsky, M. J. (2007). Displacement-Based Seismic Design of Drilled Shaft Bents with Soil-Structure Interaction. *Journal of Earthquake Engineering*, *11*(6), 1010–1030.

Suleiman, M. T., Sritharan, S., & White, D. J. (2006). Cyclic Lateral Load Response of Bridge Column-Foundation-Soil Systems in Freezing Conditions. *ASCE Journal of Structural Engineering*, *132*(11), 1745–1754.

Talley, L. K. (2014). *Design and Implementation of a Testing Facility for Jacketed Piles in Soils with Variable Stiffness*. North Carolina State University.

Uchimura, T., Tamura, Y., Tateyama, M., Tanaka, I., & Tatsuoka, F. (2005). Vertical and Horizontal Loading Tests on Full-Scale Preloaded and Prestressed Geogrid-Reinforced Soil Structures. *Soils and Foundations*, *45*(1), 75–88.

Vo, L. H. (2016). *Determination of P-y Curves for Sand by Laboratory Experiments and Three-Dimensional Numerical Analyses of Laterally Loaded Piles*. North Carolina State University.

Wilson, D. W. (1998). *Soil-Pile-Superstructure Interaction in Liquefying Sand*. Davis, CA.

Wotherspoon, L. M., Sritharan, S., & Pender, M. J. (2010). Modelling the response of cyclically loaded bridge columns embedded in warm and seasonally frozen soils. *Engineering Structures*, *32*(4), 933–943.

Yotakhong, P. (2003). *Flexural Performance of MMFX Reinforcing Rebars in Concrete Structures*. *Statewide Agricultural Land Use Baseline 2015*. North Carolina State University.

CHAPTER 10

10. APPENDICES

APPENDIX A: Short reports of experimental tests

This appendix presents a short report for each of the conducted experimental tests. These reports expand over the summaries presented in Chapter 5 and include details of the specimen response and the experimental observations.

Test 1 Summary Report

March 3, 2015

Prepared for

Alaska Department of Transportation

Alaska University Transportation Center

Project Team

RA: Diego Aguirre

PIs: Mervyn Kowalsky, James Nau, Mo Gabr

Other Senior Personnel: Greg Lucier, Ben Smith

North Carolina State University

Executive Summary

Test 1 was conducted between February 11th and 25th, 2015 at the North Carolina State University Constructed Facilities Laboratory. The tested pile-column specimen was a reinforced concrete filled steel tube with a diameter-to-thickness (D/t) ratio of 48. No surcharge was applied to the soil, thus the soil stiffness was not modified. The test was successfully conducted to failure, which was caused by a combination of tube local buckling, tube fracture, and rebar rupture, resulting in a large strength degradation (~75%) in the third cycle at ductility level 5.0 (μ_5).

Specimen and Test Description

Test 1 consisted of a 19-foot-6-inch long, reinforced concrete filled, 12-inch diameter spirally welded steel tube without skelp or splice welds. The pile-column specimen was embedded 14 ft. into sand in the soil-structure interaction facility at the NCSU-CFL. Lateral load was applied in the top of the pile specimen by means of a 100-kip hydraulic actuator, with accompanying braced steel frames, and a pinned connection at the top. The nominal wall thickness of the pipe was 0.25 in., providing a nominal diameter-to-thickness ratio (D/t) of 48. The test was conducted with a 5-foot-6-inch cantilever length, measured from the soil surface to the point at which the lateral load was applied. Figure 10-1 and Figure 10-2 present a schematic of the test setup (elevation) and the specimen #1 cross-section,

respectively, while Figure 10-3 shows the instrumentation used for testing. A photograph of the test setup is included in Figure 10-4.

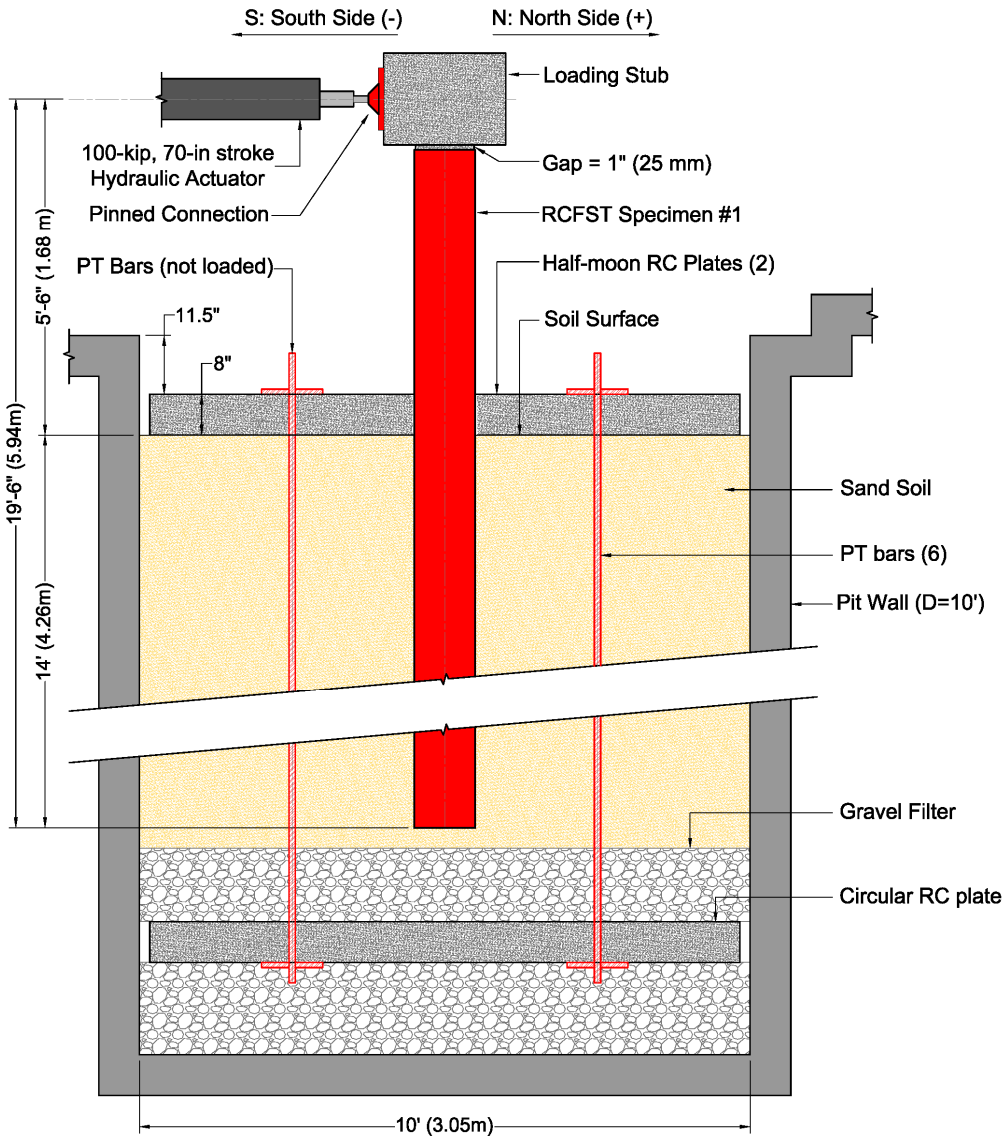

Figure 10-1 Test 1: test setup elevation schematic

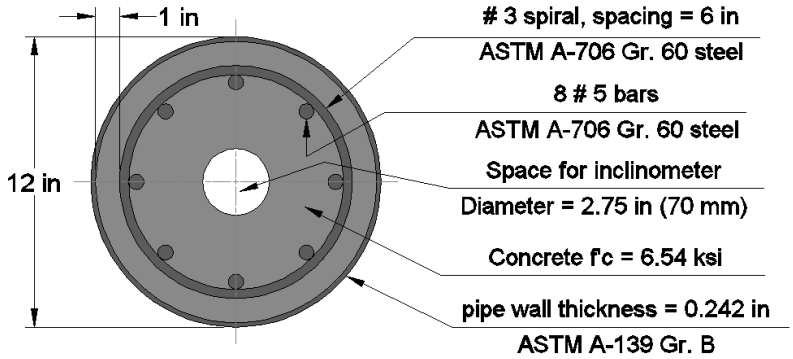

Figure 10-2 Test 1: RCFST specimen cross section

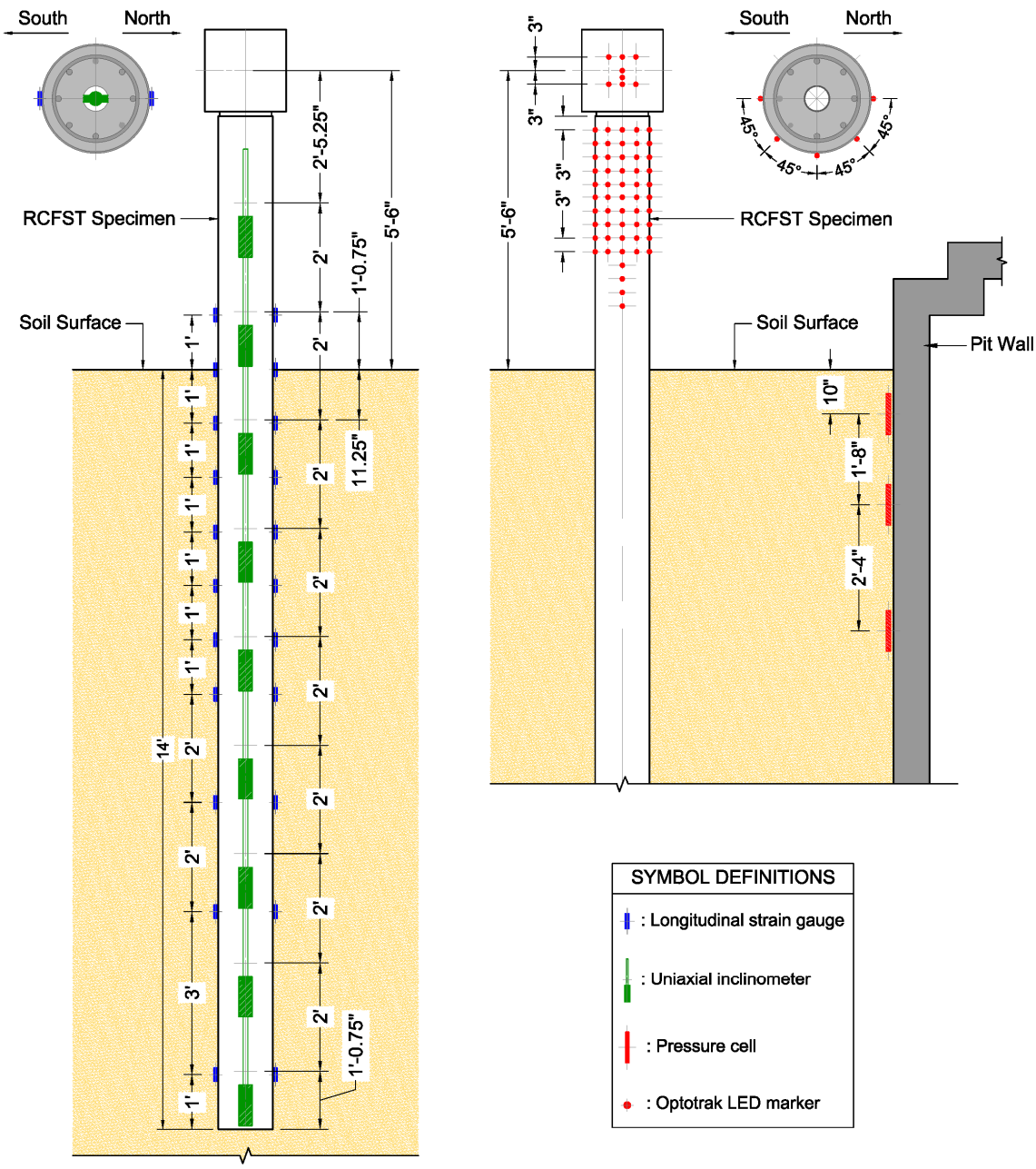

Figure 10-3 Test 1: instrumentation

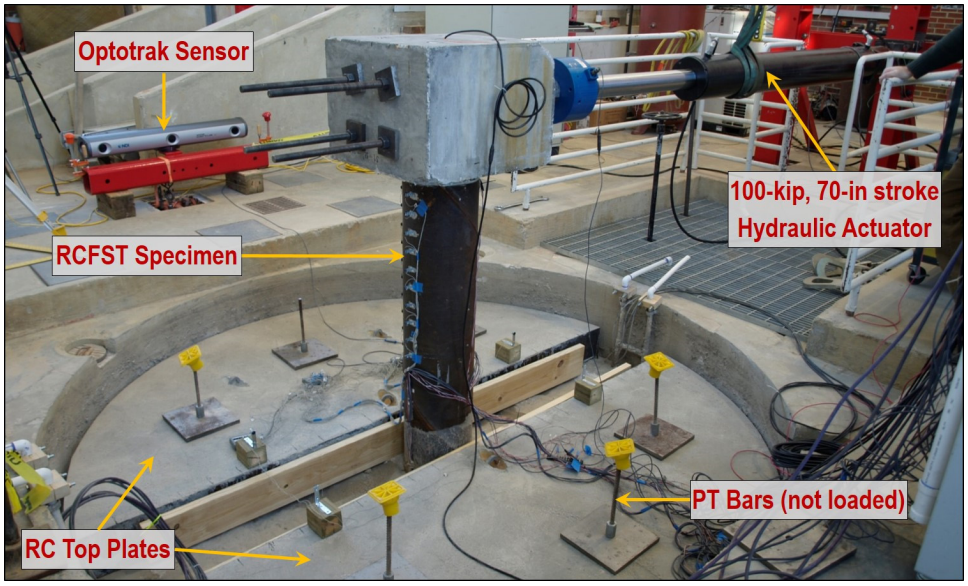

Figure 10-4 Test 1: pinned-head, RCFST pile-column test setup

Material properties were determined by in-house material tests. The yield and ultimate stresses of the steel tube were 49.5 ksi and 71.3 ksi, respectively, based on tests conducted on three (3) steel coupons cut from the end of the test pile specimen. The yield and ultimate stresses of the ASTM A706 Grade 60 longitudinal reinforcement were 66.5 ksi and 90.3 ksi, respectively, based on tests conducted on six (6) bar specimens from the same heat of the longitudinal reinforcement. The yield and ultimate stresses of the spiral reinforcement were 72.1 ksi and 101.6 ksi, respectively, based on tests conducted on six (6) bar specimens from the same heat of the transverse reinforcement. An average concrete compressive strength of 6.54 ksi (standard deviation of ± 0.09 ksi) was determined from three (3) compression tests of 4”x8” concrete cylinders.

Soil properties were also determined by in-house material tests. Based on a tube sample taken at a 20-inch depth, average values of specific gravity and unit weight were 2.67 and 86.8 pcf, respectively. Based on a measured particle size distribution, the soil was classified as poorly-graded sand (SP). Since the test was conducted over a period of fourteen days, the moisture content was measured twice. The first measure (w_1 = 2.93%) was taken on February 4th, 2015 and the second one (w_2 = 2.20%) was taken on February 20th, 2015. Notice that the moisture content does not change as much, thus it is believed it does not have a significant impact in the test results. Using the specific gravity, unit weight and moisture content a void ratio of e = 0.957 was obtained. Based on the soil properties and its classification, an internal friction angle ϕ = 35° was reasonably assumed. Active surcharge was not applied in the soil surface, only the self-weight of the half-moon RC plates was acting in the soil surface (i.e., ~100 psf).

The load history applied to the pile specimen consisted of standard three-cycle sets intended to evaluate both the elastic and inelastic response of the specimen. The first portion (i.e., pile elastic response up to first yield) of the test consisted of single reversed, displacement-controlled cycles, ramping up to the first yield displacement in ¼ increments. Given the non-linear response from the beginning of the test due to the characteristic soil behavior,

target displacements in this portion of the test were determined based on the results of a monotonic pushover analysis performed using a detailed non-linear, fiber-based, finite element model developed using the OpenSees framework software, in which soil-structure interaction was included by means of non-linear springs at 1-foot interval depths, with spring properties assigned based on p-y curves analyses.

The first yield force (F_y) and nominal force (F_n), which is defined as the force at a concrete compression strain of 0.004 or at a pipe/rebar tensile strain of 0.015 (whichever occurs first), were determined based upon tensile and compressive strains, monitored during the numerical simulation (i.e., pushover analysis), as 16.97 kips and 23.77 kips, respectively. Table 10-1 summarizes the target displacements for the first portion of the test. After the first portion of the test was completed, the measured average displacement at the first yield displacement (Δ'_y = 4.45 in.) was modified by the nominal-to-first yield force ratio as shown in Equation 10-1. This value is defined as ductility level 1.0 (μ_1 = 6.23 in). The remainder of the test was completed using reversed three-cycle sets in displacement-controlled increments at different levels of displacement ductility until failure, as shown in Equation 10-2. The entire displacement and load histories can be seen in Figure 10-5. Positive loads and displacements correspond to rightward (North) motion of the pile in the test setup. The positive legs of all cycles were completed before the negative legs.

Table 10-1 Test 1: predictions for elastic portion

Performance Level	Displacement (in)	Force (kip)
1/4 Δy'	0.74	5.35
1/2 Δy'	1.81	9.65
3/4 Δy'	3.10	13.62
Δy'	4.45	16.97

$$\Delta_y = \mu_1 = \Delta'_y \cdot \frac{F_n}{F_y} = 4.45\,in \cdot \frac{23.77\,kip}{16.97\,kip} = 6.23\,in \qquad \text{Equation 10-1}$$

$$\mu_i = i \cdot \mu_1 \rightarrow i = 1.0,\ 1.5,\ 2.0,\ 3.0,\ 4.0,\ 5.0 \qquad \text{Equation 10-2}$$

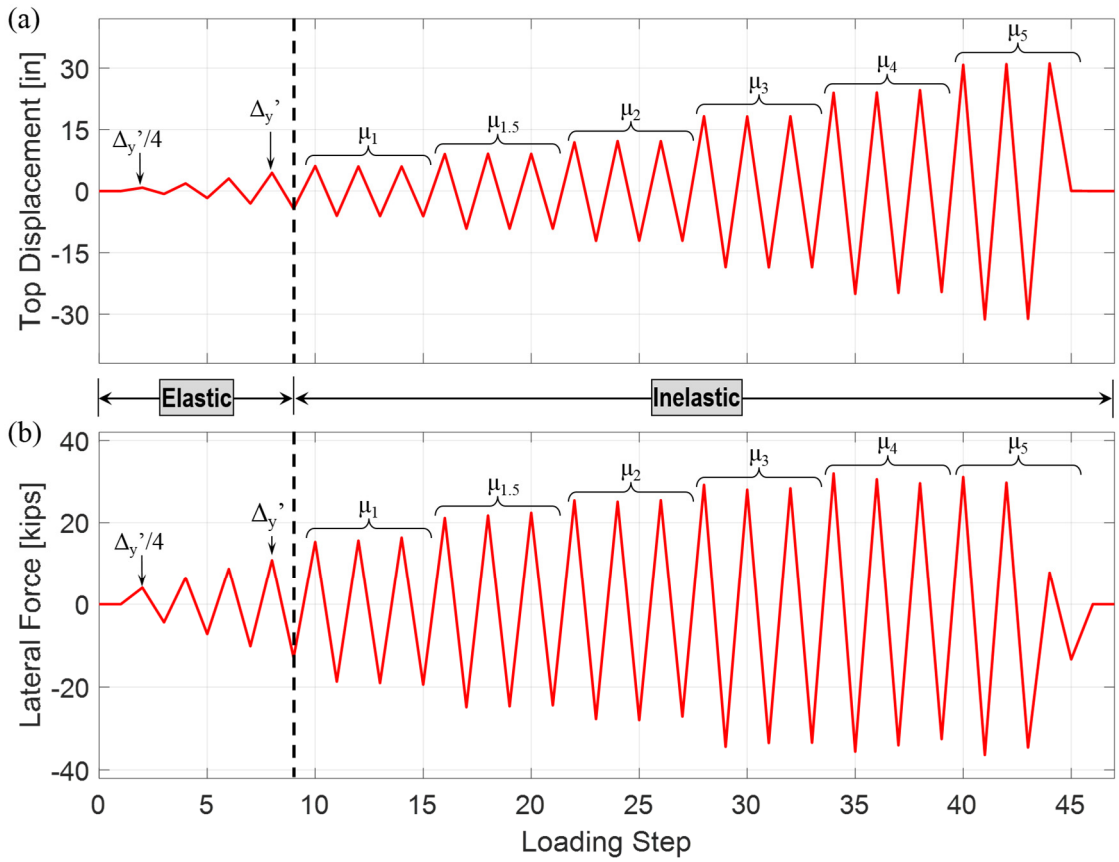

Figure 10-5 Test 1: (a) displacement and (b) loading histories

Specimen Response

Specimen #1 performed very well through the elastic portion of the test and during all three cycles of ductility level 4.0 (μ_4). It is believed that onset of buckling occurred during the displacement cycles of that ductility level as minor loss of strength was observed in each cycle at that displacement level. A significant loss of strength, indicating failure, occurred during the initial leg of the third cycle at ductility level 5.0 (μ_5). Figure 10-6 and Figure 10-7 present the lateral force vs. top displacement response and envelopes, respectively. It can be seen that, the system has a characteristic large energy dissipation capacity due to both damping sources, that is, the pile itself and the surrounding soil. In addition, it can be clearly seen from both figures that a significant loss of strength (~75%) occurred during the third cycle of ductility level 5.0 (μ_5).

Figure 10-8 presents specimen # 1 and the gaps in the soil, respectively, at zero displacement after the first portion of the test was conducted. Notice that during this portion of the test the gap on the sides of the pile developed in agreement with the displacement history. At this point of the test strain profiles on the sides of the pile were verified in order to further conduct the test at the aforementioned ductility levels. Figure 10-9 presents the strain profiles recorded during the first portion of the test. Notice that a tensile strain larger than the yield strain (ε_y = 1700 $\mu\varepsilon$) was recorded in the tube during the pull cycle when the predicted first yield displacement was imposed to the system. Furthermore, Figure 10-10

and Figure 10-11 show the curvature, rotation and displacement profiles calculated using the rotation data from the inclinometers. Note that the curvature profiles agree with the measured strains, namely, the cross section reaches its first yield curvature at the last pull cycle when the first yield displacement was induced in the specimen head. The circles in the top portion of the displacement profiles in Figure 10-10 and Figure 10-11 represent the Optotrak LED markers; note that they are in agreement with the calculated displacement profiles. In Figure 10-9 through Figure 10-11, the symbols N and S in the legend refer to the North and South sides, $Ø_y'$ stands for the first yield curvature, Δ_y' stands for first yield displacement, and a depth equal to 0 ft. represents the soil surface.

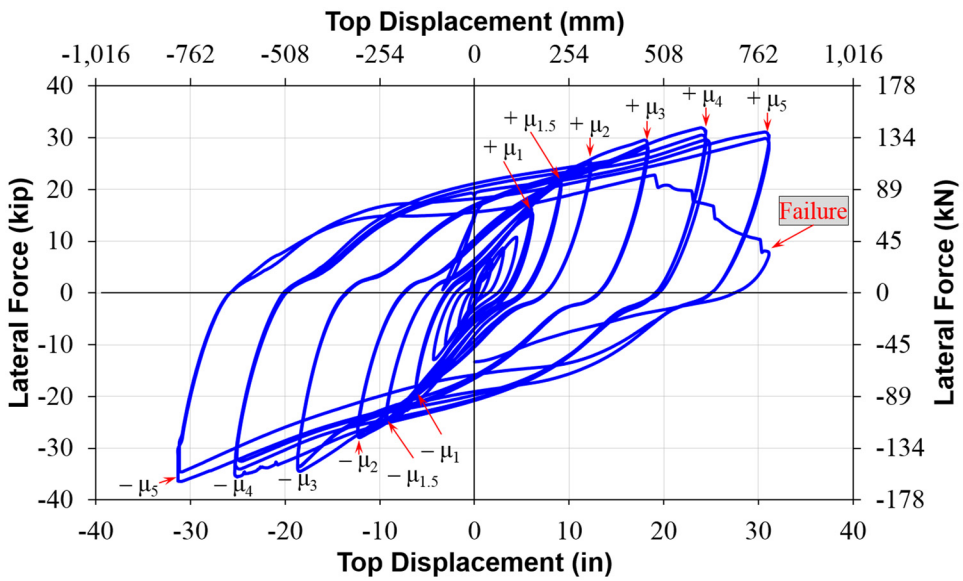

Figure 10-6 Test 1: lateral force vs. top displacement response

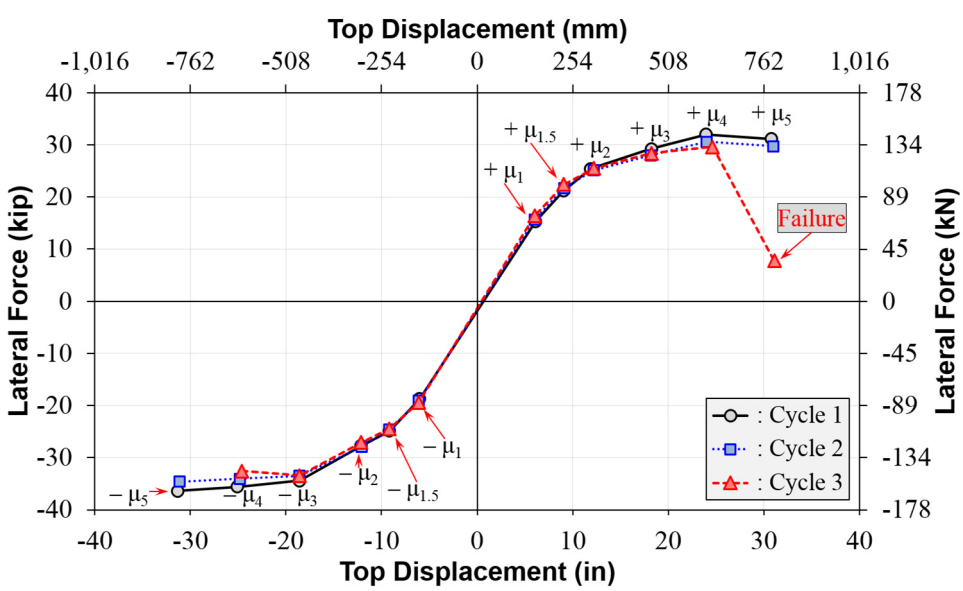

Figure 10-7 Test 1: lateral force vs. top displacement envelopes

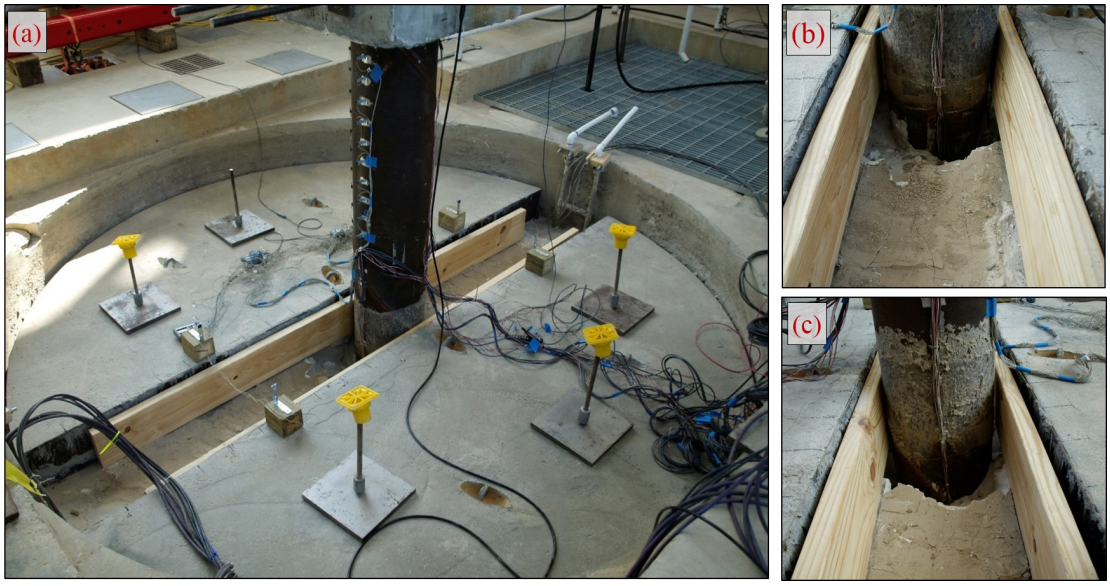

Figure 10-8 Test specimen #1 after elastic portion was completed: (a) deformed shape, (b) South side and (c) North side

As the test continued, the gap on the sides of the pile increased in size as the displacement ductility level increased. Minor loss of strength was observed up until all ductility level 4.0 (μ_4) cycles. The test was terminated (Figure 10-12) after the third push cycle load at ductility 5.0 (μ_5) when a significant drop in the force on the actuator was observed (i.e., ~75%). Sounds indicating steel fracture were heard at the same time when the strength loss occurred, indicating probable rebar or pipe fracture. Moreover, a twist rotation of the pile occurred for all push cycles at ductility level 5.0 (μ_5), similar to that observed in the last cycle (Figure 10-12). Finally, the specimen was taken to zero displacement in order to facilitate its extraction from the soil.

Figure 10-13 presents the strain profiles for the first push and pull cycles at different displacement ductility levels. Similarly, Figure 10-14 and Figure 10-15 present the curvature, rotation, and displacement profiles for the first push and pull cycles. Note from Figure 10-13 that the largest tensile and compressive strains in the steel tube were recorded at a depth between 1 ft. and 6ft, which is in close agreement with the curvature profiles presented in Figure 10-14 and Figure 10-15. It is believed that the displacement profile corresponding to the first pull cycle at ductility 5.0 (μ_5) is not an accurate reading but rather indicated that something occurred to the slope indicator device at that level of displacement, probably induced by the observed twist rotation.

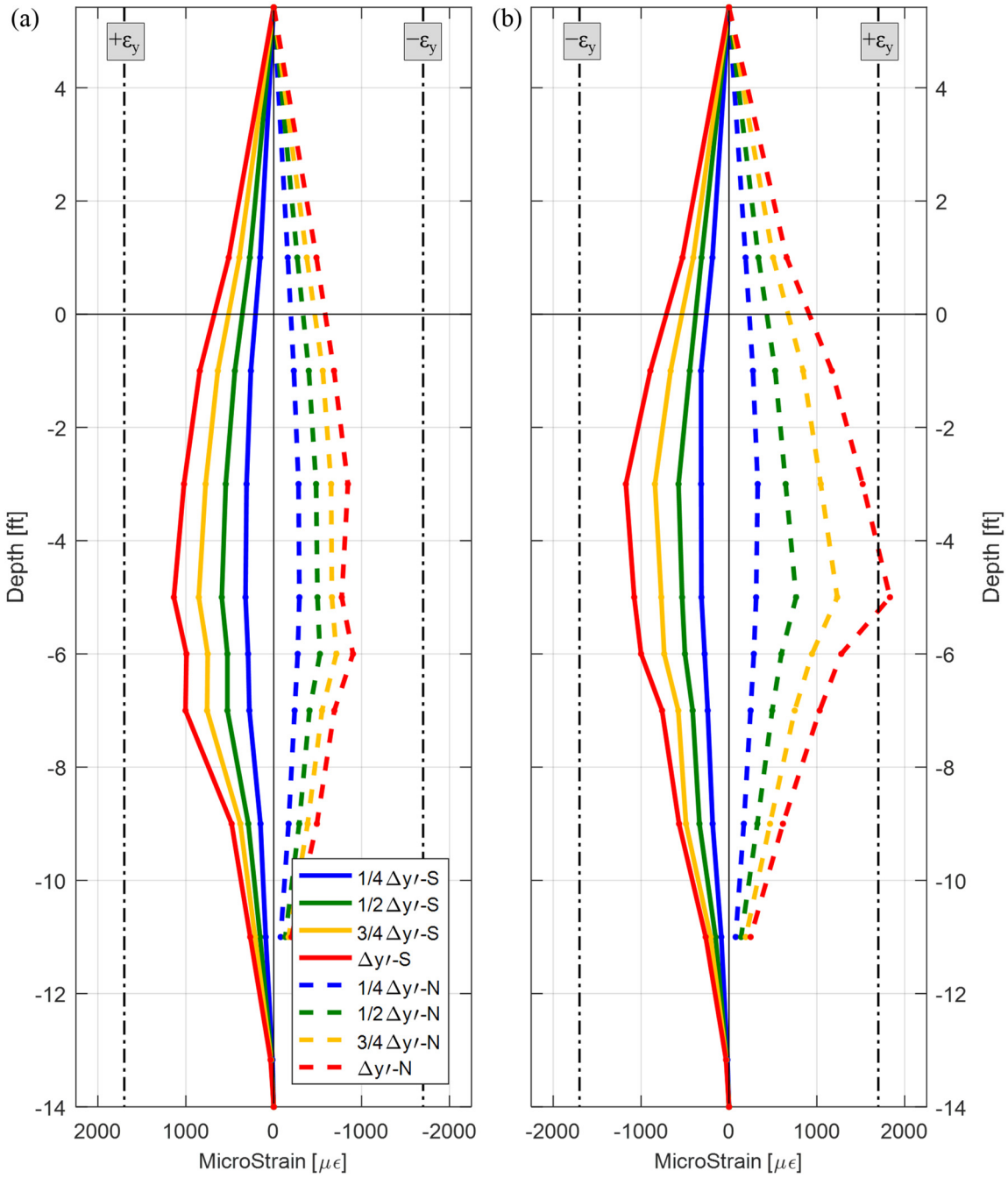

Figure 10-9 Test 1: strain profiles from elastic (a) push and (b) pull cycles

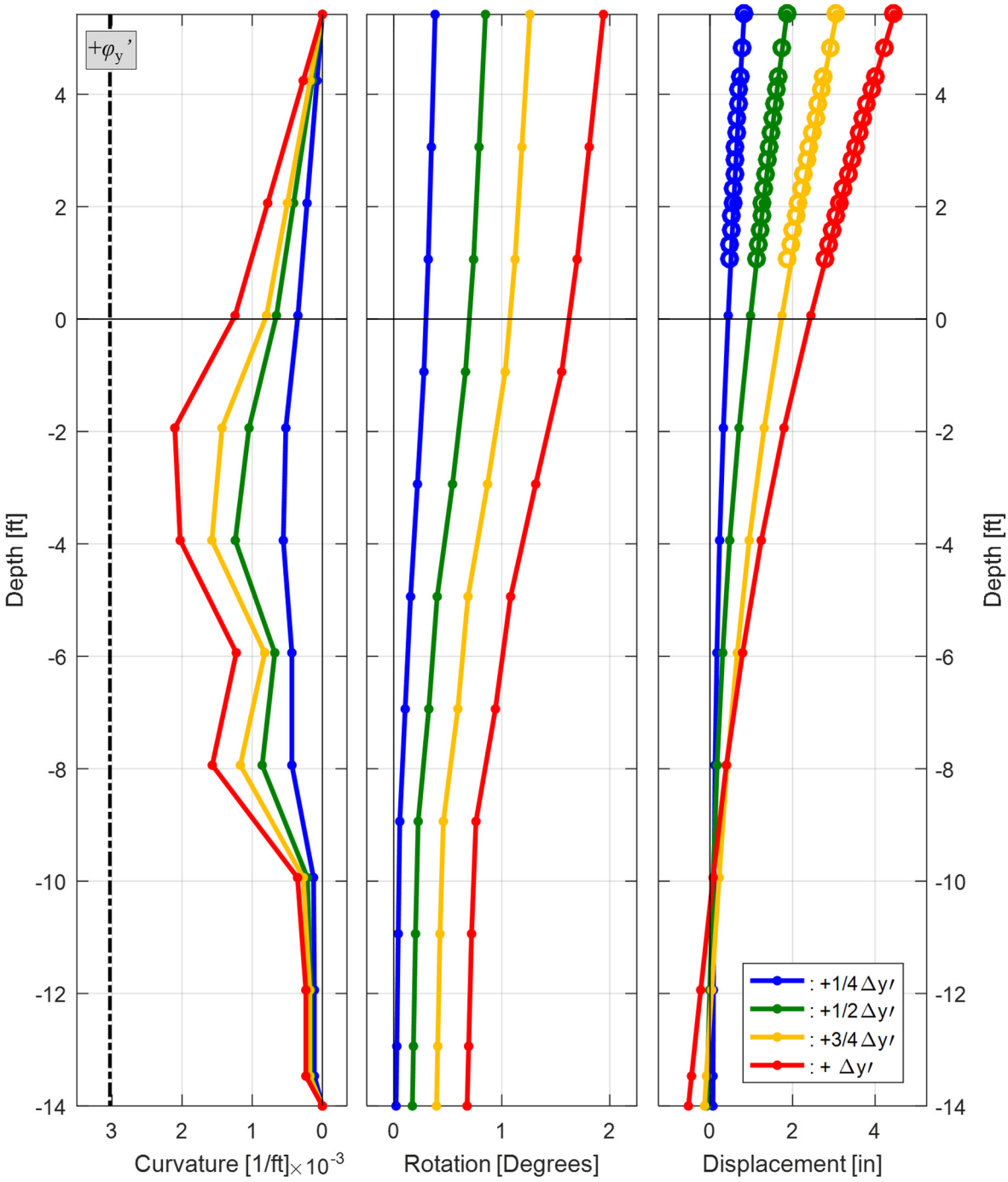

Figure 10-10 Test 1: curvature, rotation, and displacement profiles (elastic push cycles)

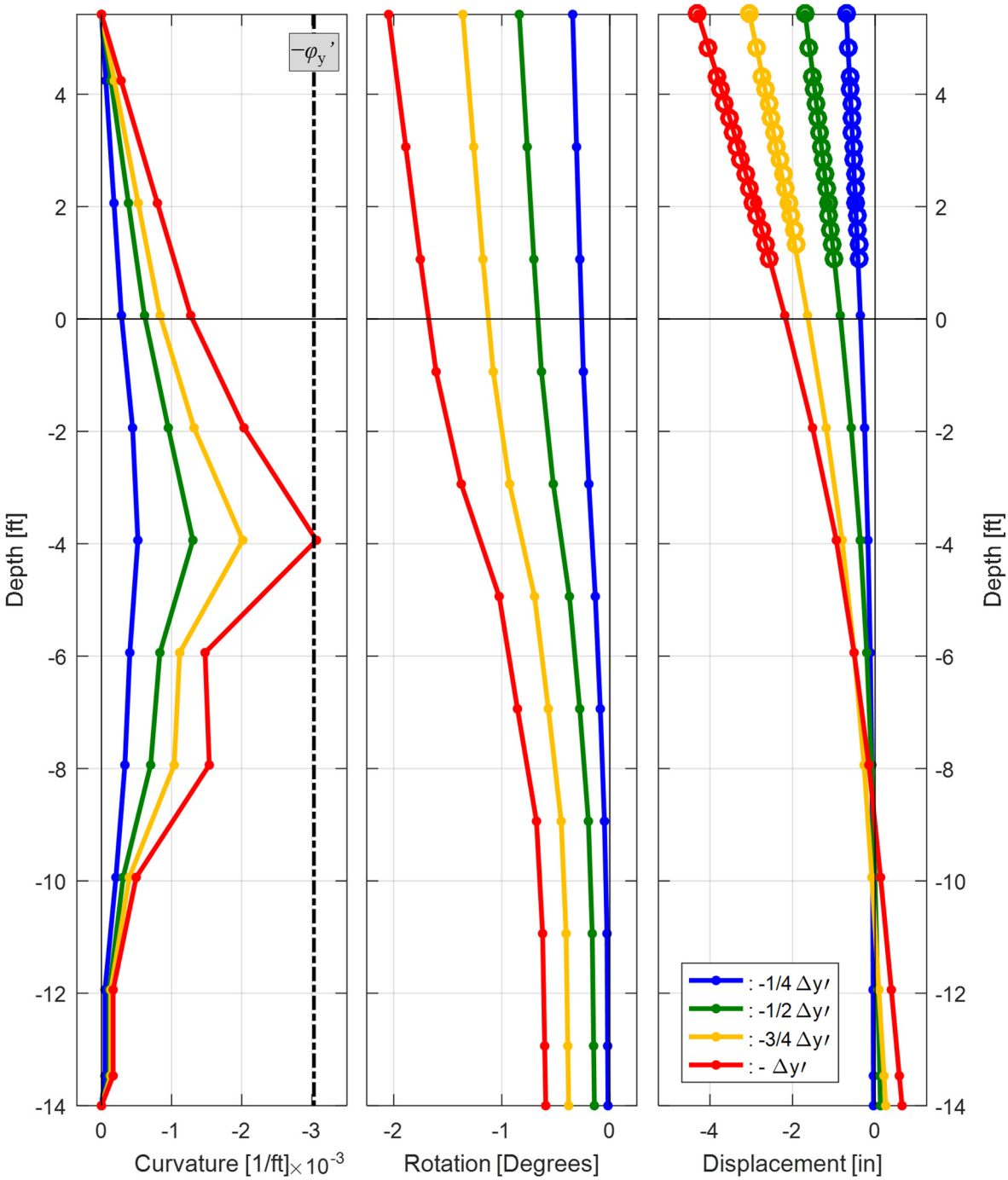

Figure 10-11 Test 1: curvature, rotation, and displacement profiles (elastic pull cycles)

Figure 10-12 Test specimen #1 at maximum displacement: (a) deformed shape, (b) South side and (c) North side

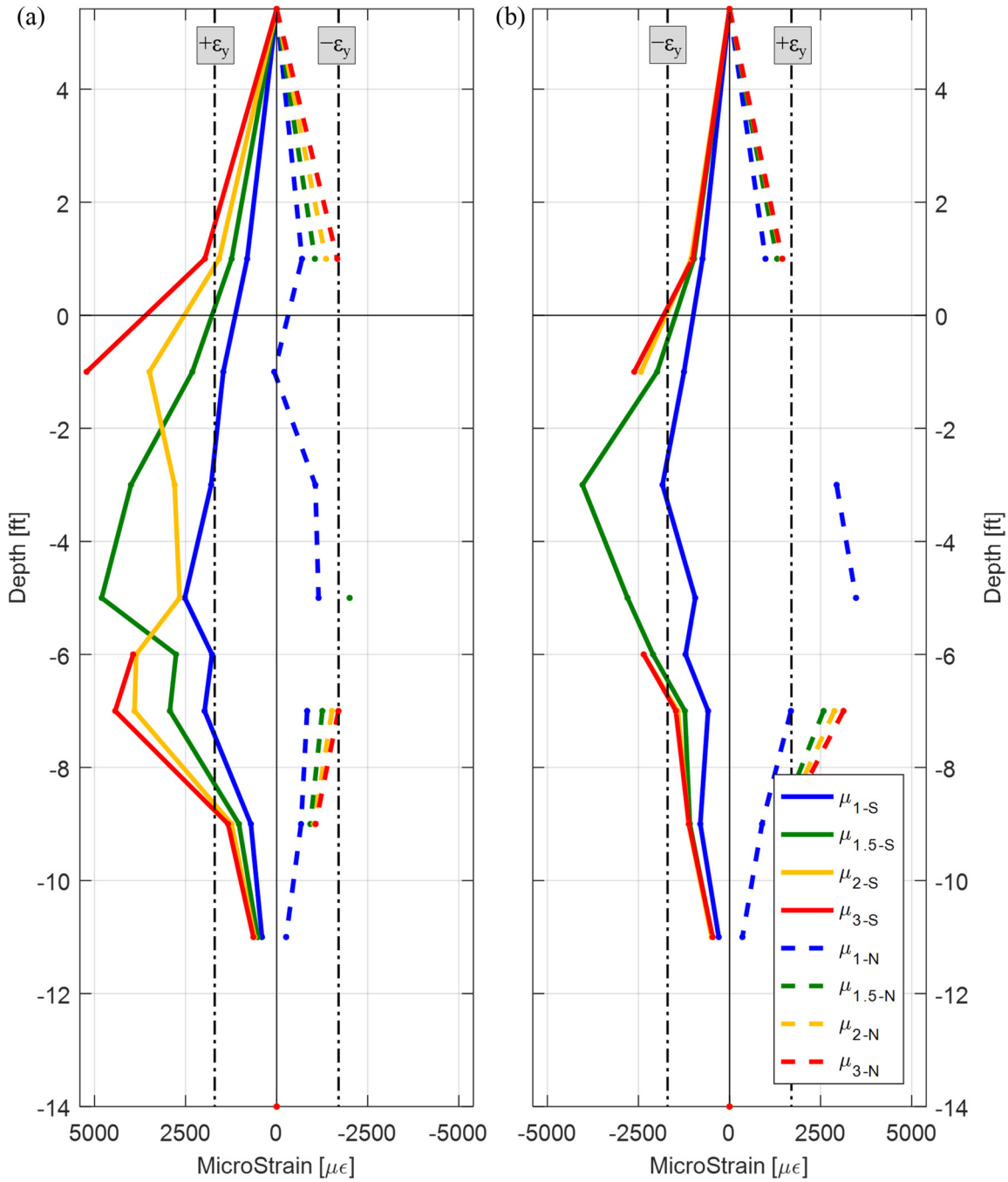

Figure 10-13 Test 1: strain profiles from inelastic (a) push and (b) pull cycles

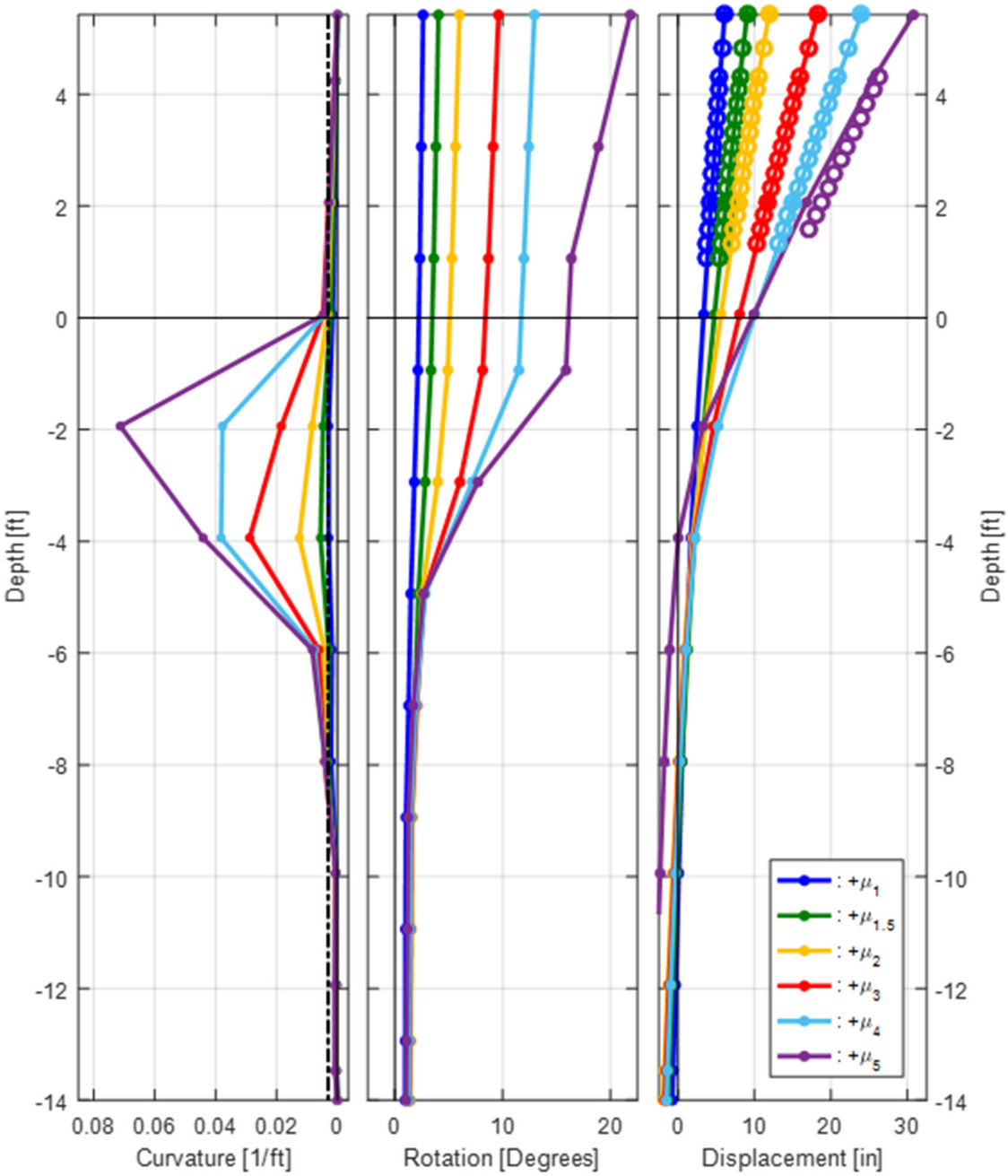

Figure 10-14 Test 1: curvature, rotation, and displacement profiles (inelastic push cycles)

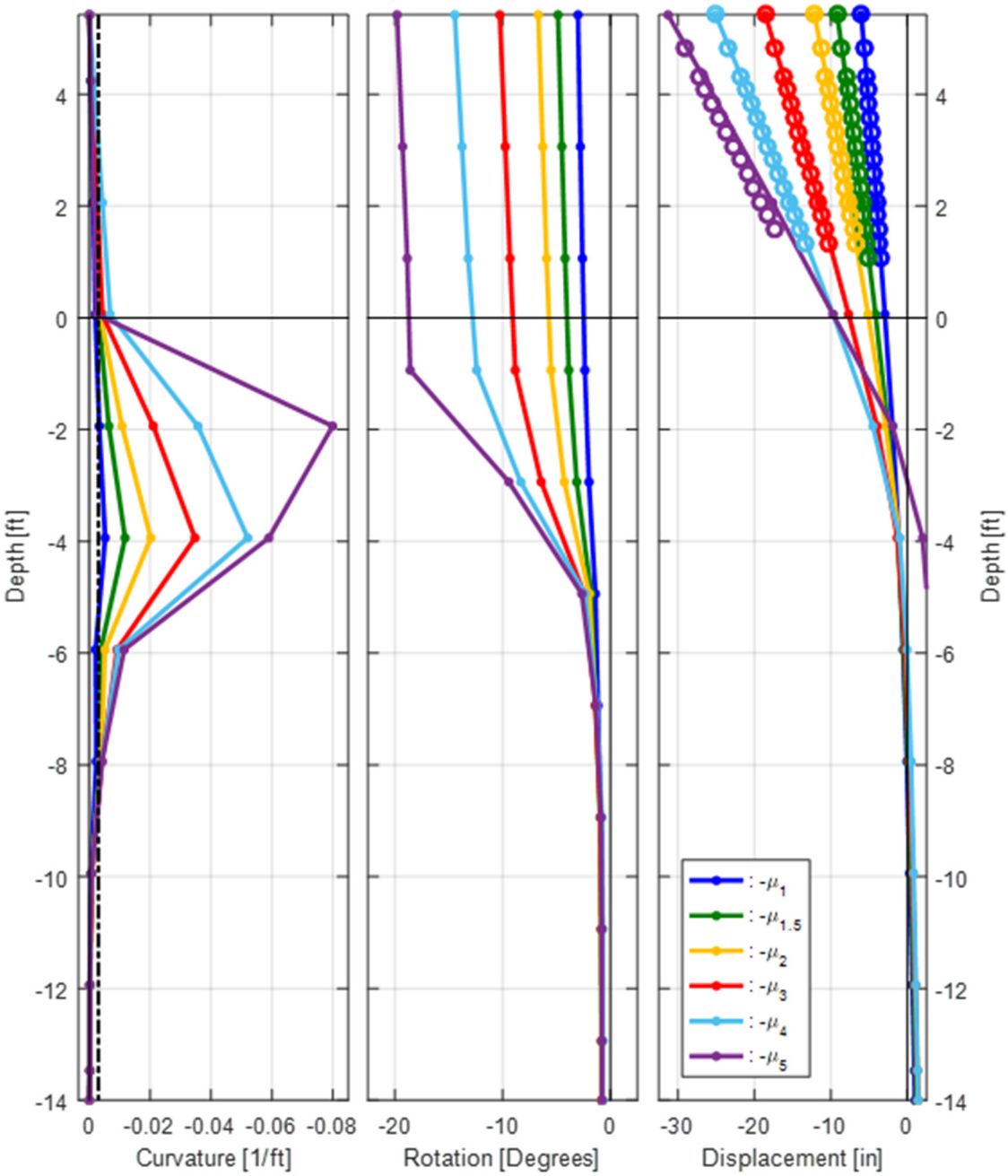

Figure 10-15 Test 1: curvature, rotation, and displacement profiles (inelastic pull cycles)

Figure 10-16 shows the state of the soil surface after the test was completed. Notice that despite the presence of the half-moon RC plates in the surface, deformations in the soil followed an expected oval-shaped surface failure in which active and passive pressures developed around the pile. This surface extended ~12 in. on both sides of the direction of loading and ~10 in. on the perpendicular direction. The total average settlement of the RC plates was 2.15 in. This value was averaged based on the vertical displacement of 4 points on the RC plates. In Figure 10-16, the holes in the soil next to the specimen are points in which soil samples were taken in order to perform soil tests. Figure 10-17 shows the average settlement of the half-moon RC plates during the test as a function of the imposed displacements in the top of the pile. Note that, as the displacement history is applied, the settlement increases, though its magnitude is larger at the beginning of the test

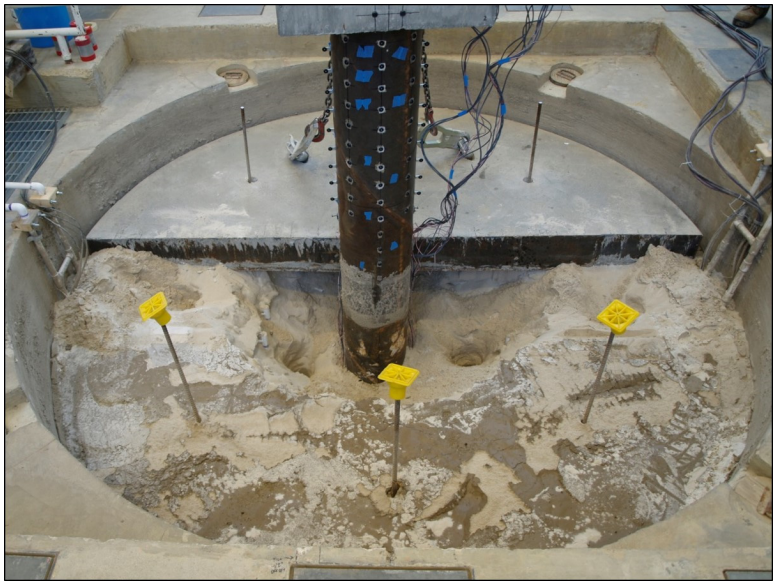

Figure 10-16 Test 1: soil surface after testing

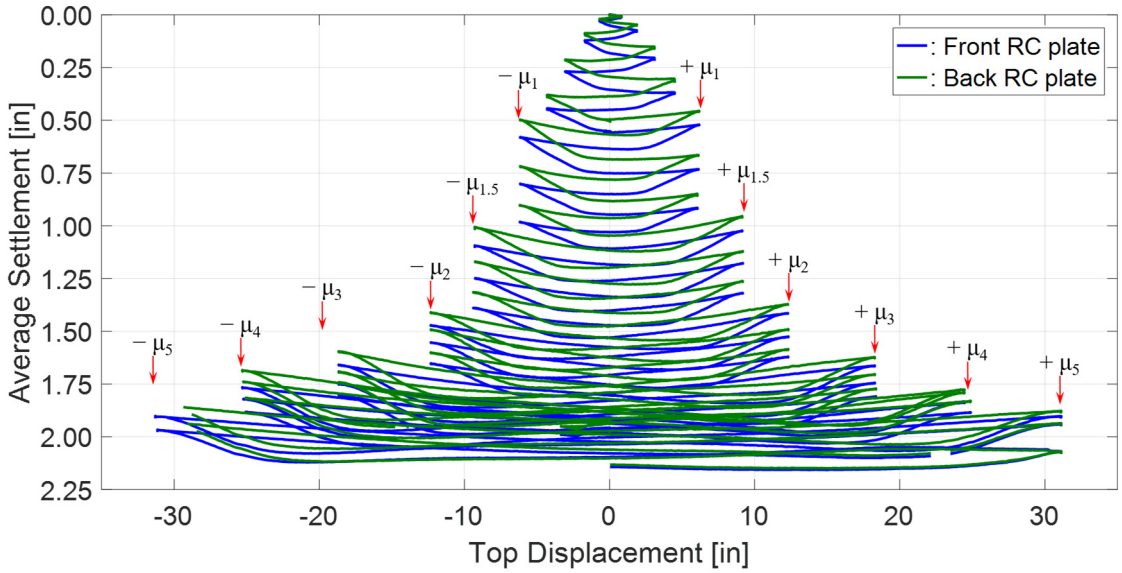

Figure 10-17 Test 1: half-moon RC plate settlement during testing

Figure 10-18 through Figure 10-20 present the damage observed after the specimen was extracted from the soil. As it was thought during the test, tube fracture, tube local buckling, and bar fracture and buckling did occur. Note that local buckling developed on both sides of the specimen. The sections with the largest local buckling occurred at a depth of 3 ft. – 1 ¼ in. and 3 ft. – 4 ¼ in. on the South and North sides of the specimen, respectively, which means that the plastic hinge developed at an average depth of 3 ft. – 2 ¾ in. with respect to the soil surface. Several minor buckled regions were observed equally spaced (~6 in.) on both sides of the specimen, next to the main buckled regions. Figure 10-19 presents measurements of the main buckled regions. Deformations due to buckling protruded ~¾ in. and ~½ in. on the North and South sides of the specimen, respectively.

Pipe fracture (Figure 10-18) occurred on the South side of the specimen and it extended about half of the cross-section perimeter, resulting in a significant drop in strength due to lost tension capacity. Therefore, after rupture, tension capacity is provided by the longitudinal reinforcement, which has a smaller area in comparison with that provided by the steel tube, inducing high stresses and deformations resulting in bar rupture (Figure 10-20).

In order to further investigate the significant strength loss and to verify that rebar fracture occurred, a portion of the tube (i.e., 6 in. x10 in.) was removed at the ruptured section on the South side, extreme fiber (Figure 10-20). Notice that the core concrete was crushed close to the ruptured area; it was relatively easy to remove. However, digging further to the center of the section the concrete was not crushed thus stronger and more difficult to remove. In addition, several cracks can be seen perpendicular to the longitudinal direction of the specimen. It can be seen from Figure 10-20 that a total of two (2) bars ruptured and one (1) bar buckled. One of the bars that fractured was located in the South side, extreme fiber of the specimen and the other adjacent to that one.

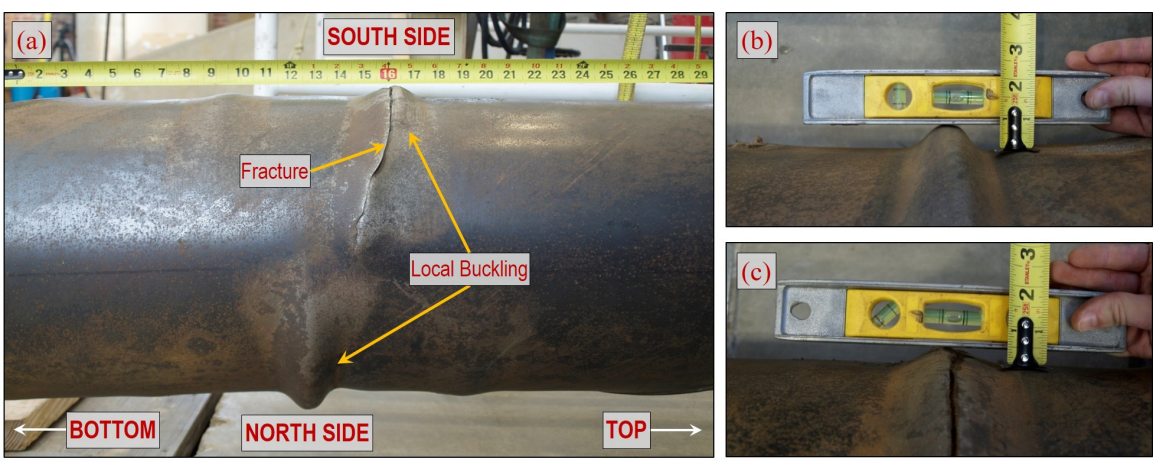

Figure 10-18 Test 1: (a) Final observed damage, (b) tube local buckling, and (c) tube fracture

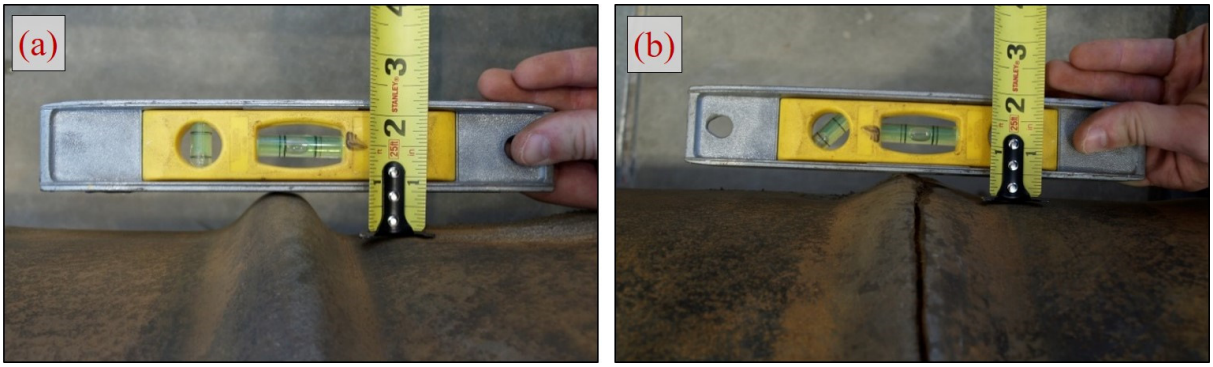

Figure 10-19 Test 1: primary buckled sections on (a) North side and (b) South side

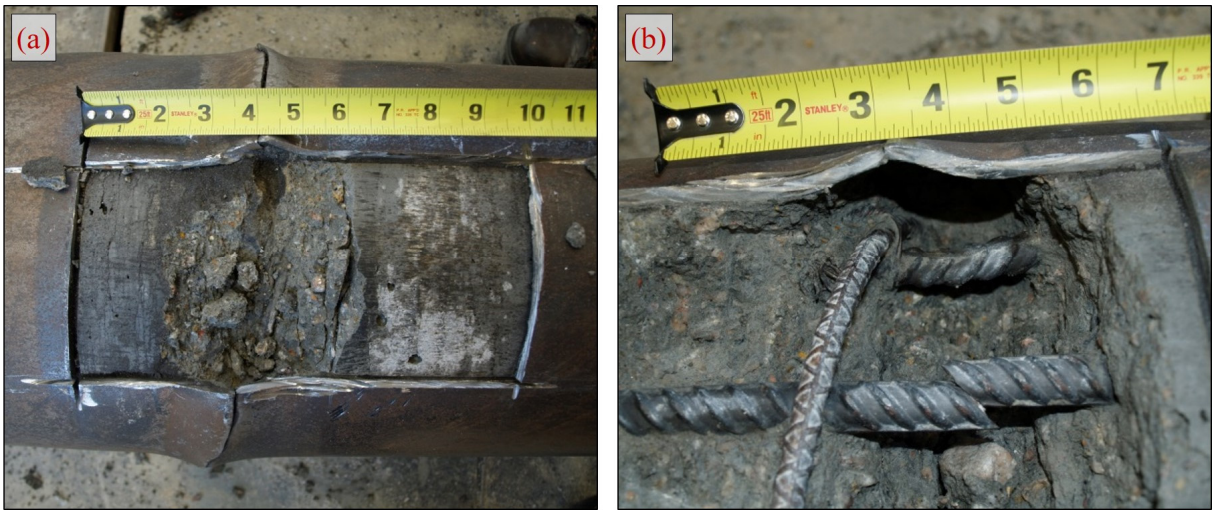

Figure 10-20 Test 1: observed damage in (a) concrete and (b) internal reinforcement on South side

Conclusions

Test specimen #1 showed a reliable response through all ductility 4.0 (μ_4) cycles. It is believed that onset of local buckling occurred during this ductility level when subtle strength loss was observed. The test specimen completed all cycles of ductility 4.0 (μ_4) without significant loss of strength. Failure of the specimen occurred at ductility level 5.0 (μ_5) when a significant drop in the strength was observed. Further investigations revealed that failure occurred due to a combination of tube local buckling, tube fracture, bar fracture, and bar buckling. It is believed that this particular specimen is capable of having a reliable displacement up to ductility 4.0 (μ_4). The main buckles as well as tube fracture did not occur over the spiral weld, so the tube spiral welds do not appear to negatively influence the behavior.

Test 2 Summary Report

May 12, 2015

Prepared for

Alaska Department of Transportation

Alaska University Transportation Center

Project Team

RA: Diego Aguirre

PIs: Mervyn Kowalsky, James Nau, Mo Gabr

Other Senior Personnel: Greg Lucier, Ben Smith

North Carolina State University

Executive Summary

Test 2 was conducted May 4th, 2015 at the North Carolina State University Constructed Facilities Laboratory. The tested pile-column specimen was a reinforced concrete filled steel tube with a diameter-to-thickness (D/t) ratio of 48. A surcharge of ~960 psf was applied to the soil prior to and during the test, so the soil stiffness was expected to change. The test was successfully conducted to failure, which was caused by a combination of tube local buckling, tube fracture, and bar rupture, resulting in a large strength degradation (~76.5%) in the first cycle at ductility level 5.5 ($\mu_{5.5}$).

Specimen and Test Description

Test 2 consisted of a 19-foot-5-inch long, reinforced concrete filled, 12-inch diameter spirally welded steel tube without skelp or splice welds. The pile-column specimen was embedded 13 ft. - 7 in. into clean sand in the soil-structure interaction facility at the NCSU-CFL. Lateral load was applied at the pinned connection at the top of the pile specimen by means of a 100-kip, 70-inch stroke hydraulic actuator. The nominal wall thickness of the tube was 0.25 in., providing a nominal diameter-to-thickness ratio (D/t) of 48. The test was conducted with a 5-foot-10-inch cantilever length, measured from the soil surface to the point at which the lateral load was applied. Figure 10-21 and Figure 10-22 present a schematic of the test setup (elevation) and the specimen #2 cross-section, respectively, while

Figure 10-23 shows the instrumentation used for testing. Due to an issue related to the casing of the slope indicators, such devices were not utilized in Test 2. As a consequence, curvature, rotation, and displacement profiles are not available for this specimen. A photograph of the test setup is included in Figure 10-24.

Material properties were determined by in-house material tests. The yield and ultimate stresses of the steel tube were 49.5 ksi and 71.3 ksi, respectively, based on tests conducted on three (3) coupons cut from the end of the test pile specimen. The yield and ultimate stresses of the ASTM A706 Grade 60 longitudinal reinforcement were 66.5 ksi and 90.3 ksi, respectively, based on tests conducted on six (6) bar specimens from the same heat of the longitudinal reinforcement. The yield and ultimate stresses of the spiral reinforcement were 72.1 ksi and 101.6 ksi, respectively, based on tests conducted on six (6) bar specimens from the same heat of the transverse reinforcement. An average concrete compressive strength of 6.92 ksi (standard deviation of ± 0.12 ksi) was determined from three (3) compression tests of 4”x8” concrete cylinders.

Soil properties were also determined by in-house material tests. Based on a measured particle size distribution, the soil was classified as poorly-graded sand (SP). The unit weight and moisture content (γ = 84.3 pcf and w = 2.6%, respectively) were measured on April 30th, 2015. However, based on soil tests conducted after testing of pile specimen #1, an average unit weight γ = 90 pcf was assumed. An active surcharge was applied to the soil surface by means of 20-kip, 2-inch stroke hydraulic jacks reacting on the half-moon RC plates. An axial load of 10.1 kips was applied to each of the six (6) PT bars, resulting on a surcharge pressure of 960 psf. In addition to the active pressure, the self-weight of the half-moon RC plates was acting on the soil surface as well (i.e., ~100 psf). Based on the soil properties and due of the applied active pressure, an internal friction angle ϕ = 35° was reasonably assumed

In an attempt to modify the soil properties, prior to pile testing three (3) surcharge cycles were performed using the same surcharge level to be applied during the test, i.e. q = 960 psf. The first surcharge cycle was applied on April 23rd; the pressure was released on April 24th allowing the pressure to act on the soil for 24 hours. The second surcharge cycle was applied on April 24th; the pressure was released on April 27th allowing the pressure to act on the soil for 72 hours. The third surcharge cycle was applied on April 27th. The pressure was not sustained but rather it was a load-unload cycle which took approximately 30 minutes. The average settlement of the RC plates prior pile testing was ~0.5 in. This value was averaged based on the vertical displacement of 4 points on the RC plates. Results of the surcharge cycles are presented in Figure 10-25.

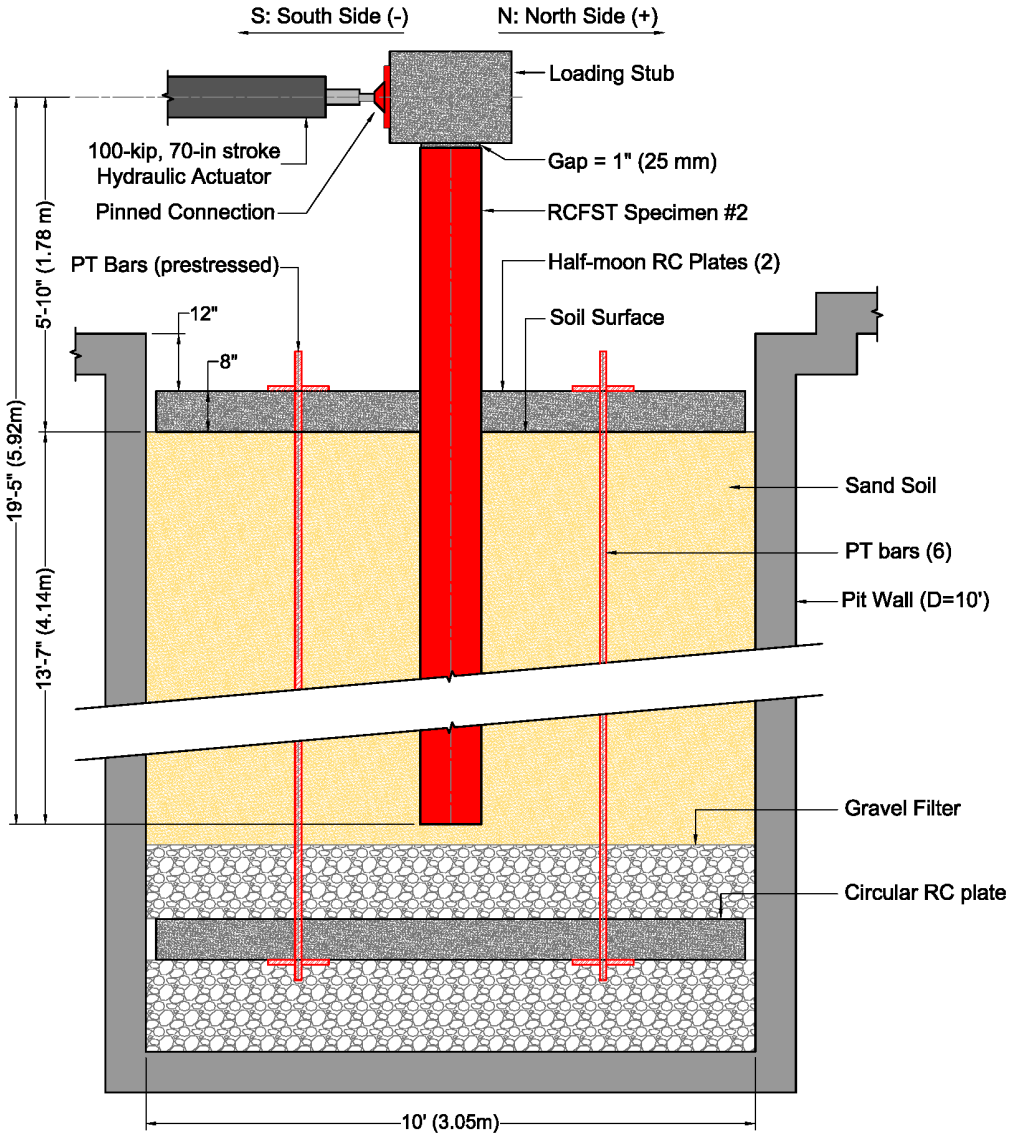

Figure 10-21 Test 2: test setup elevation schematic

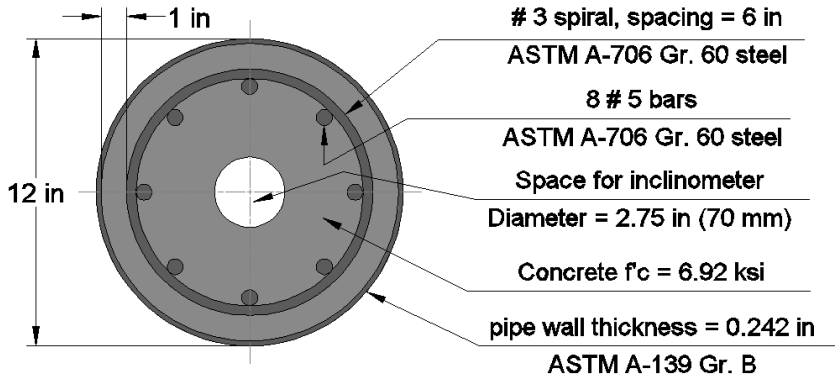

Figure 10-22 Test 2: RCFST specimen cross section

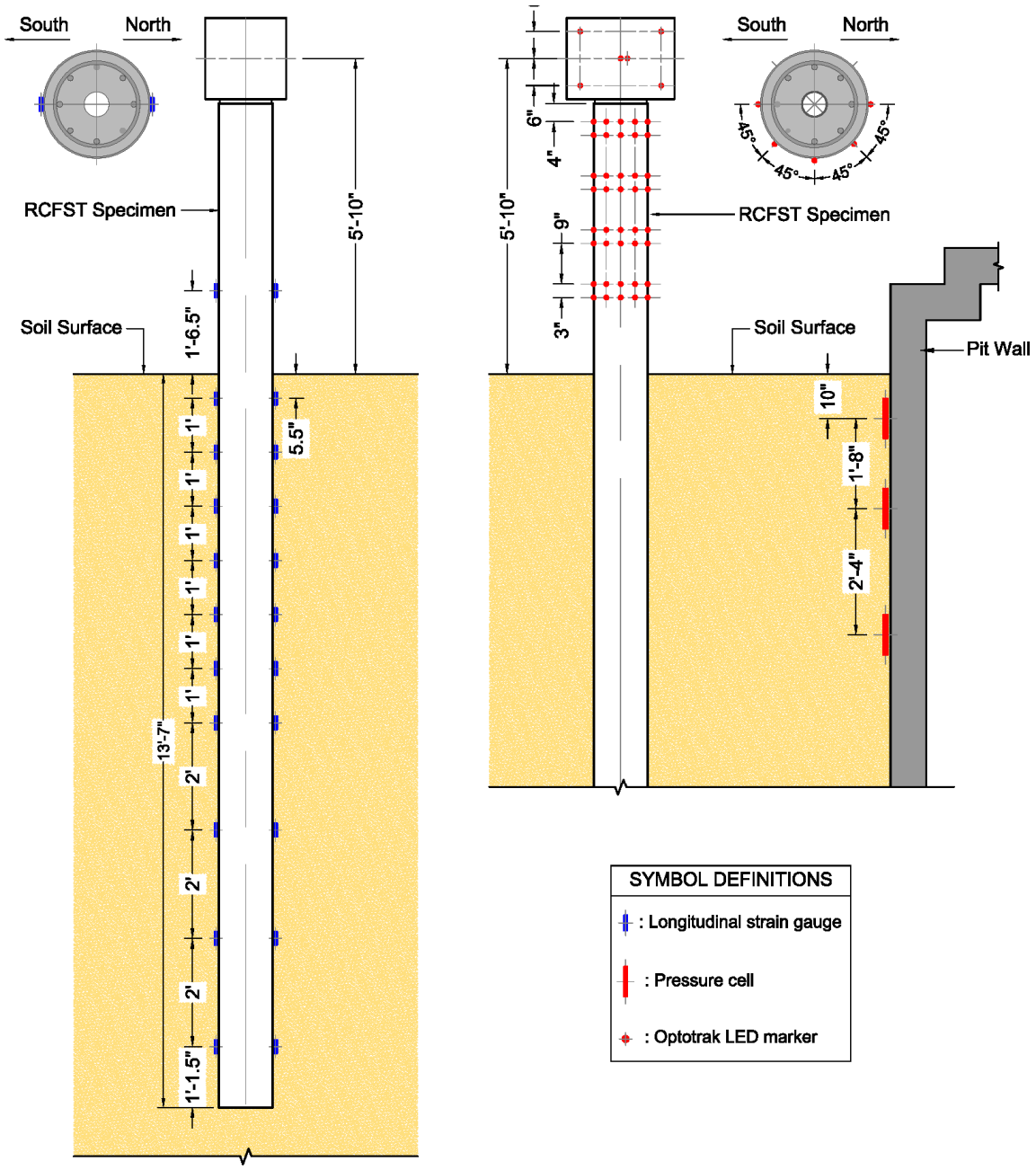

Figure 10-23 Test 2: instrumentation

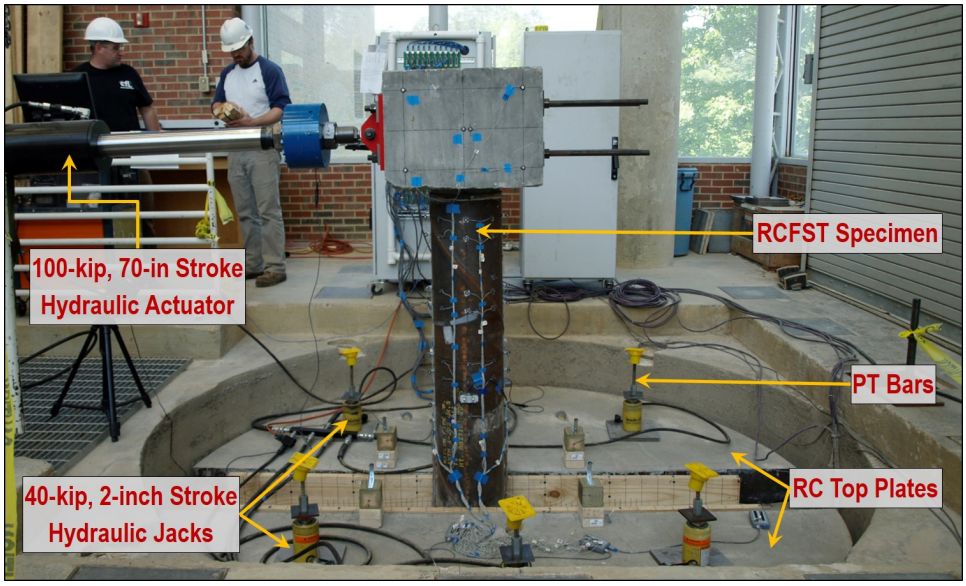

Figure 10-24 Test 2: pinned-head, RCFST pile-column test setup

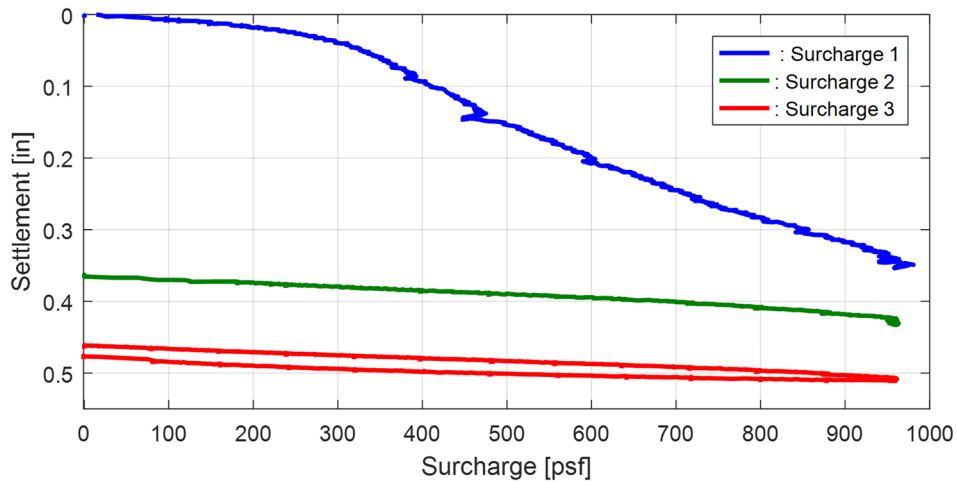

Figure 10-25 Test 2: half-moon RC plate settlement prior testing

The load history applied to the pile specimen consisted of standard three-cycle sets intended to evaluate both the elastic and inelastic response of the specimen. The first portion (i.e., pile elastic response up to first yield) of the test consisted of single reversed, displacement-controlled cycles, ramping up to the first yield displacement in ¼ increments. Given the non-linear response from the beginning of the test due to the characteristic soil behavior, target displacements in this portion of the test were determined based on the results of a monotonic pushover analysis performed using a detailed non-linear, fiber-based, finite element model developed using the OpenSees framework software. Soil-structure interaction was included by means of non-linear springs at 1-foot interval depths, with spring properties assigned based on p-y curves.

The first yield force (F_y) and nominal force (F_n), which is defined as the force at a concrete compression strain of 0.004 or at a tube/rebar tensile strain of 0.015 (whichever occurs first), were determined based upon tensile and compressive strains, monitored during the numerical simulation (i.e., pushover analysis), as 18.07 kips and 25.52 kips, respectively.

Table 10-2 summarizes the target displacements for the first portion of the test. After the first portion of the test was completed, the measured average displacement at the first yield displacement (Δ'_y = 4.07 in) was modified by the nominal-to-first yield force ratio as shown in Equation 10-3. This value is defined as ductility level 1.0 (μ_1 = 5.75 in). The remainder of the test was completed using reversed three-cycle sets in displacement-controlled increments at different levels of displacement ductility until failure, as shown in Equation 10-4. The entire displacement and load histories can be seen in Figure 10-26. Positive loads and displacements correspond to rightward (North) motion of the pile in the test setup. The positive legs of all cycles were completed before the negative legs.

Table 10-2 Test 2: predictions for elastic portion

Performance Level	Displacement (in)	Force (kip)
1/4 Δy'	0.78	5.42
1/2 Δy'	1.72	10.10
3/4 Δy'	2.85	14.37
1 Δy'	4.07	18.07

$$\Delta_y = \mu_1 = \Delta'_y \cdot \frac{F_n}{F_y} = 4.07\,in \cdot \frac{25.52\,kip}{18.07\,kip} = 5.75\,in \qquad \text{Equation 10-3}$$

$$\mu_i = i \cdot \mu_1 \rightarrow i = 1.0,\ 1.5,\ 2.0,\ 3.0,\ 4.0,\ 5.0,\ 5.5 \qquad \text{Equation 10-4}$$

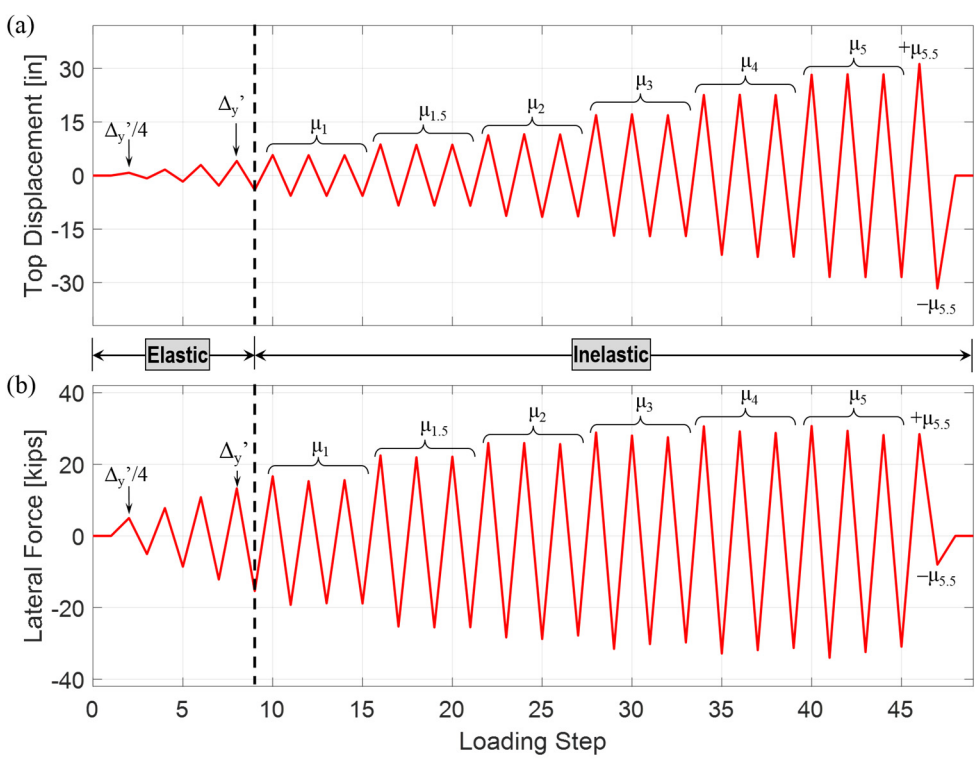

Figure 10-26 Test 2: (a) displacement and (b) loading histories

Specimen Response

Specimen #2 performed very well through the elastic portion of the test and during all three cycles of ductility level 5.0 (μ_5). It is believed that the onset of buckling occurred during the displacement cycles at ductility level 4.0 (μ_4) as minor loss of strength was observed in each cycle at that displacement level. A significant loss of strength, indicating failure, occurred during the first pull cycle at ductility level 5.5 ($\mu_{5.5}$). Figure 10-27 and Figure 10-28 present the lateral force vs. top displacement response and envelopes, respectively. It can be seen that, the system has a characteristic large energy dissipation capacity due to both damping sources, that is, the pile itself and the surrounding soil. In addition, it can be clearly seen from both figures that a significant loss of strength (~76.5%) occurred during the first pull cycle of ductility level 5.5 ($\mu_{5.5}$).

Figure 10-29 presents Specimen # 2 and the gaps in the soil at the last pull cycle at first yield; at this level of displacement the size of the gap was ~3 in. Notice that at this level of displacement the gap was not filled by the soil. This was observed up until the last cycles at ductility 1.0 (μ_1) when the soil started to slowly fall filling the gap. At this point of the test strain profiles on the sides of the pile were verified in order to further conduct the test at the aforementioned ductility levels. Figure 10-30 presents the strain profiles recorded during the first portion of the test. Notice that a tensile strain larger than the yield strain (ε_y = 1700 $\mu\varepsilon$) was recorded in the steel tube during the pull cycle when the predicted first yield displacement was imposed to the system. In Figure 10-30 the symbols N and S in the legend refer to the North and South sides, Δ_y' is the first yield displacement, and a depth equal to 0 ft. represents the soil surface. Before proceeding with the testing program, the specimen was taken to zero displacement, the point at which the gap on both sides was of similar magnitude (i.e., ~1.5 in).

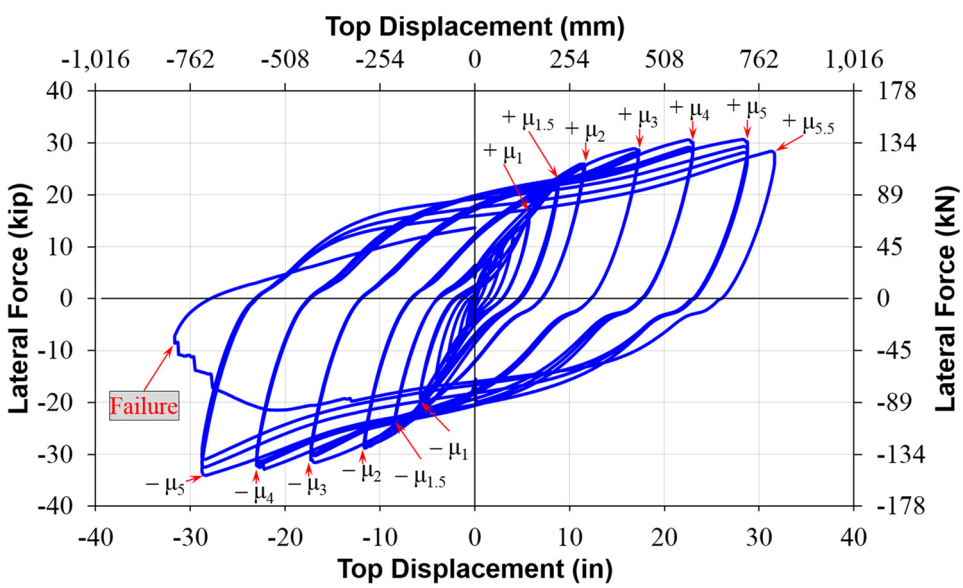

Figure 10-27 Test 2: lateral force vs. top displacement response

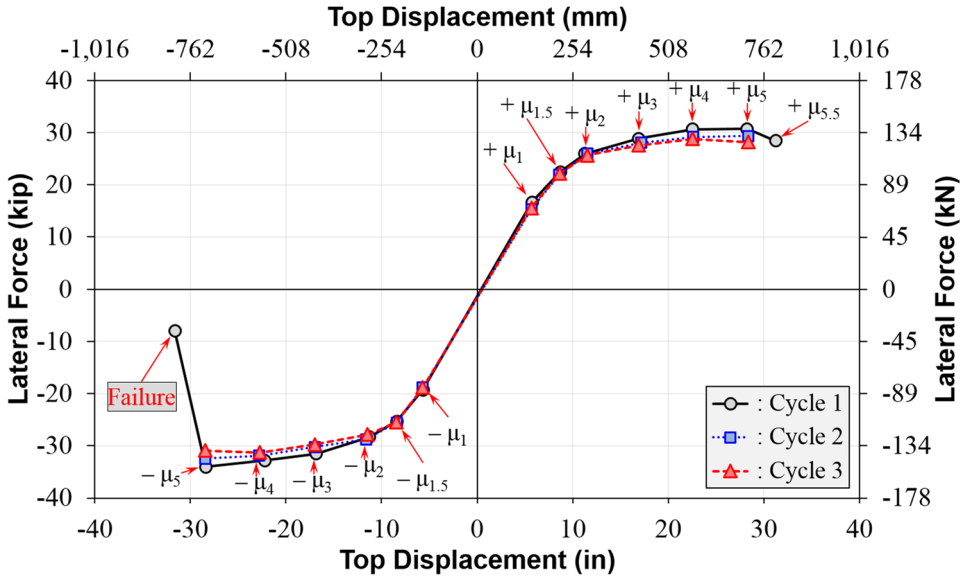

Figure 10-28 Test 2: lateral force vs. top displacement envelopes

Figure 10-29 Test specimen #2 at last pull cycle of elastic portion of the test: (a) deformed shape, (b) South side and (c) North side

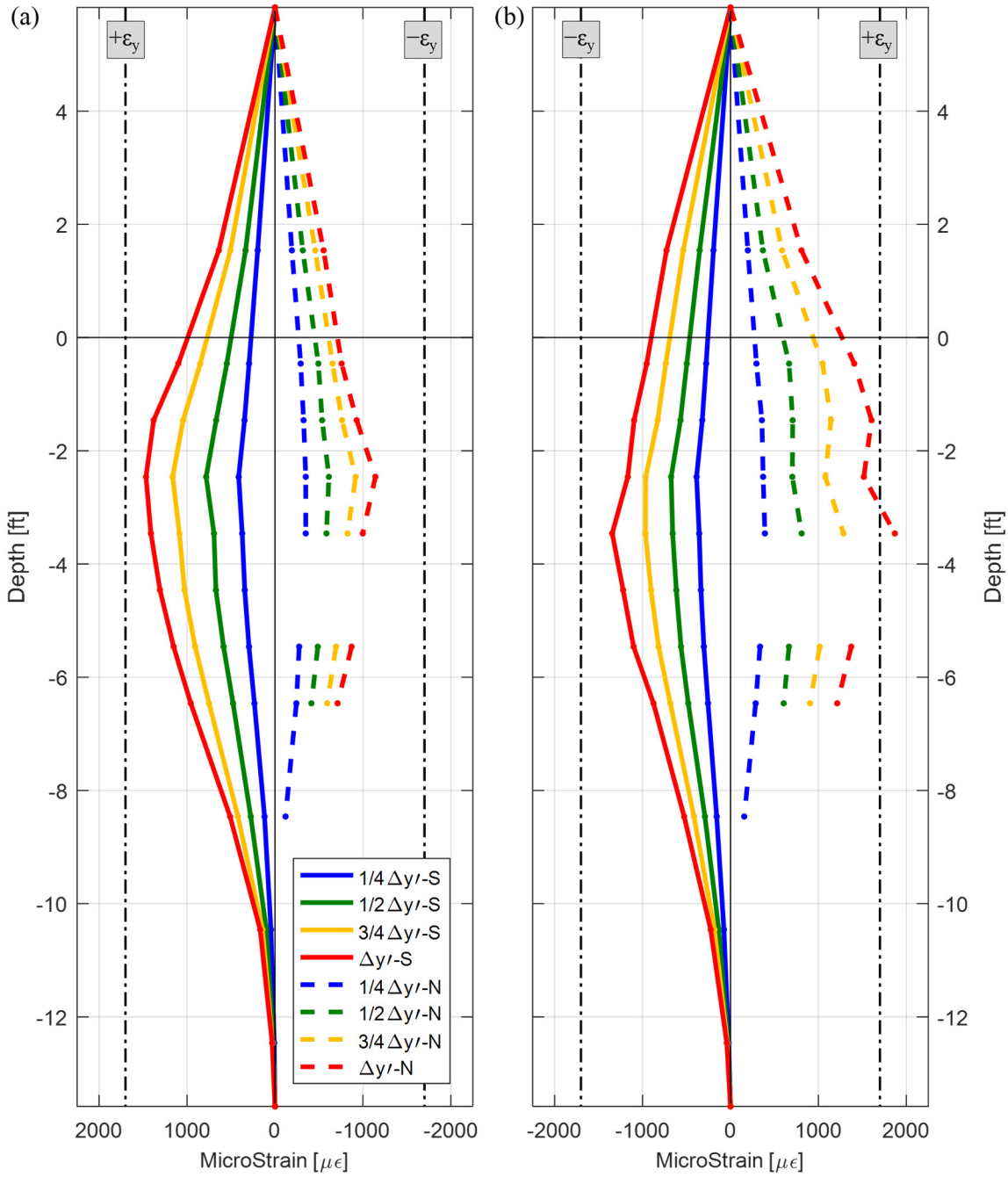

Figure 10-30 Test 2: strain profiles from elastic (a) push and (b) pull cycles

As the test continued, the gap on the sides of the pile increased in size as the displacement ductility level increased. Minor loss of strength was observed up until all ductility level 4.0 (μ_4) cycles. In addition, onset of twist of the pile occurred at that level of displacement. A significant twist was observed during all push cycles at ductility level 5.0 (μ_5), similar to that observed in the last push cycle at ductility level 5.5 (μ5.5), as shown in Figure 10-31.

The test was terminated (Figure 10-31) after the first pull cycle load at ductility 5.5 ($\mu_{5.5}$) when a significant drop in the force of the actuator was observed (i.e., ~76.5%). Sounds indicating steel fracture were heard at the same time the strength loss occurred, indicating probable bar or tube fracture. Finally, the specimen was taken to zero displacement in order to facilitate its extraction from the soil. Figure 10-32 presents the strain profiles for the first push and pull cycles at different displacement ductility levels. Notice that the largest tensile and compressive strains in the pipe were recorded at a depth between 1 ft. and 5ft. In Figure 10-32 the symbols N and S in the legend refer to the North and South sides, and μ is the displacement ductility level.

Figure 10-31 Test specimen #2 at maximum displacement: (a) deformed shape, (b) South side and (c) North side

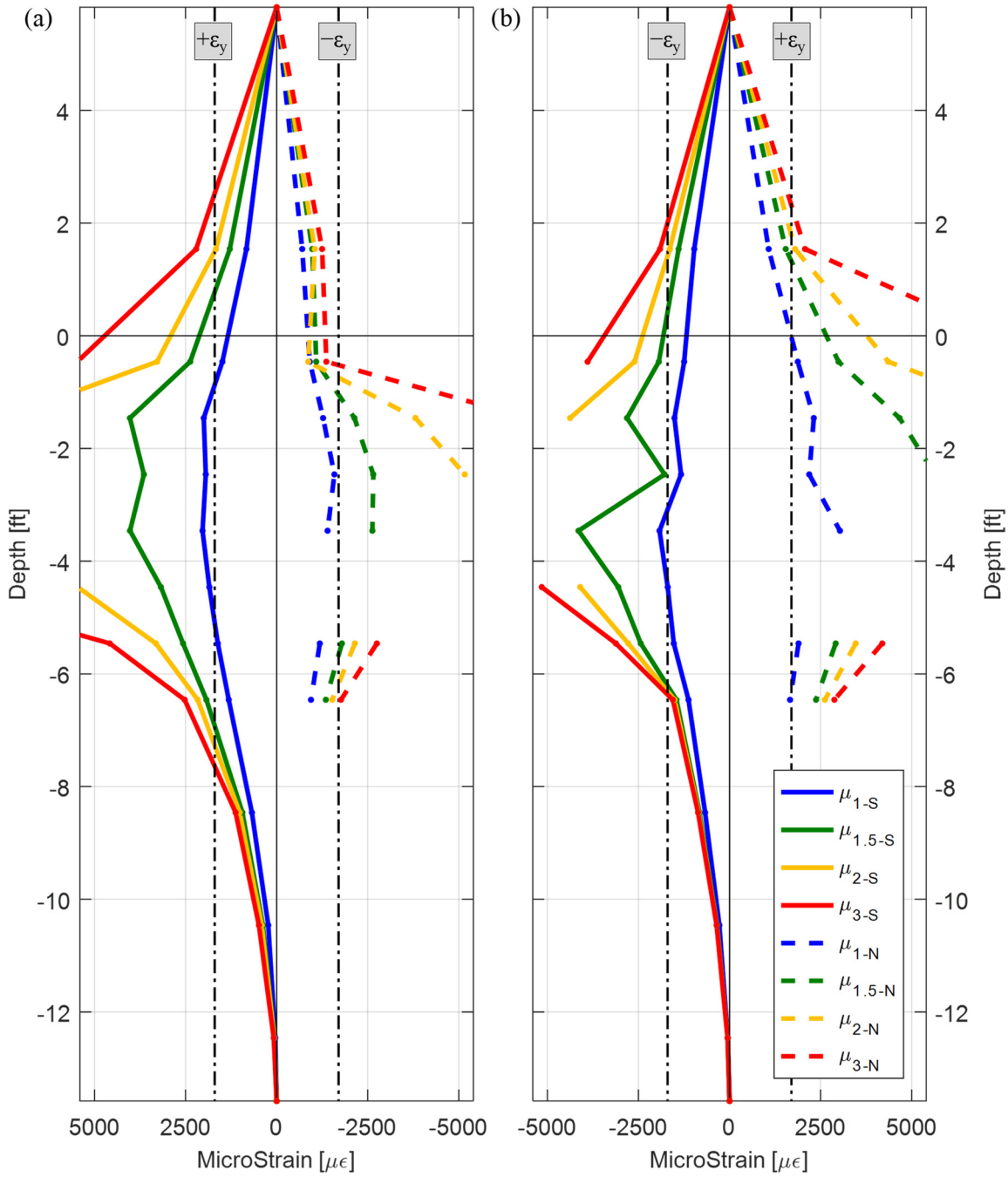

Figure 10-32 Test 2: strain profiles from inelastic (a) push and (b) pull cycles

Figure 10-33 shows the state of the soil surface after the test was completed. Notice that despite the presence of the half-moon RC plates in the surface, deformations in the soil followed an expected oval-shaped failure surface in which active and passive pressures developed around the pile. This surface extended ~18 in. on both sides of the direction of loading and ~15 in. on the perpendicular direction. The average settlement of the RC plates during the test was 3.13 in. This value was averaged based on the vertical displacement of 4 points on the RC plates. Figure 10-34 shows the average settlement of the half-moon RC plates during the test as a function of the imposed displacements in the top of the pile. Note that, as the displacement history is applied, the settlement increases, though its magnitude is larger at the beginning of the test. The total average settlement, including that due to the surcharge applied prior starting the test, was ~3.63 in.

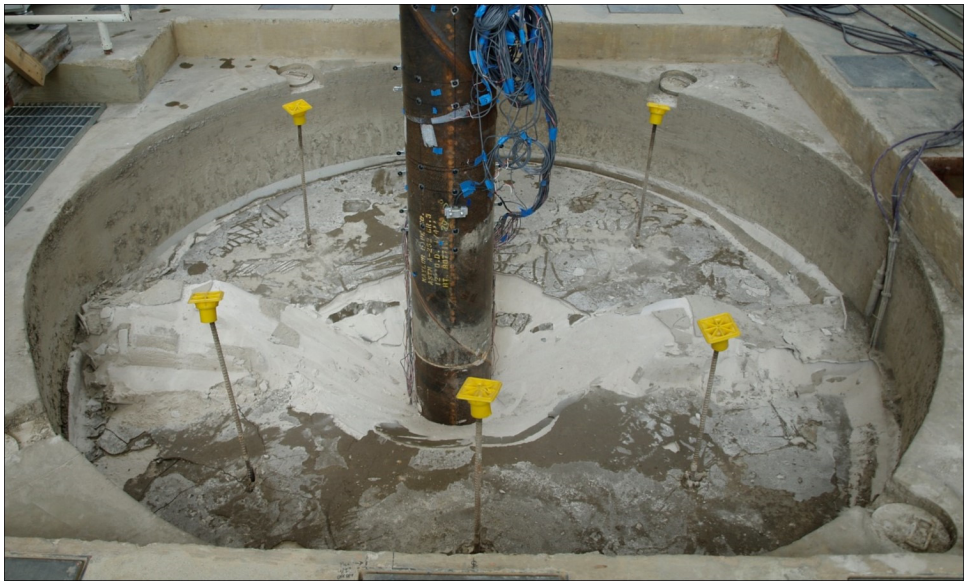

Figure 10-33 Test 2: soil surface after testing

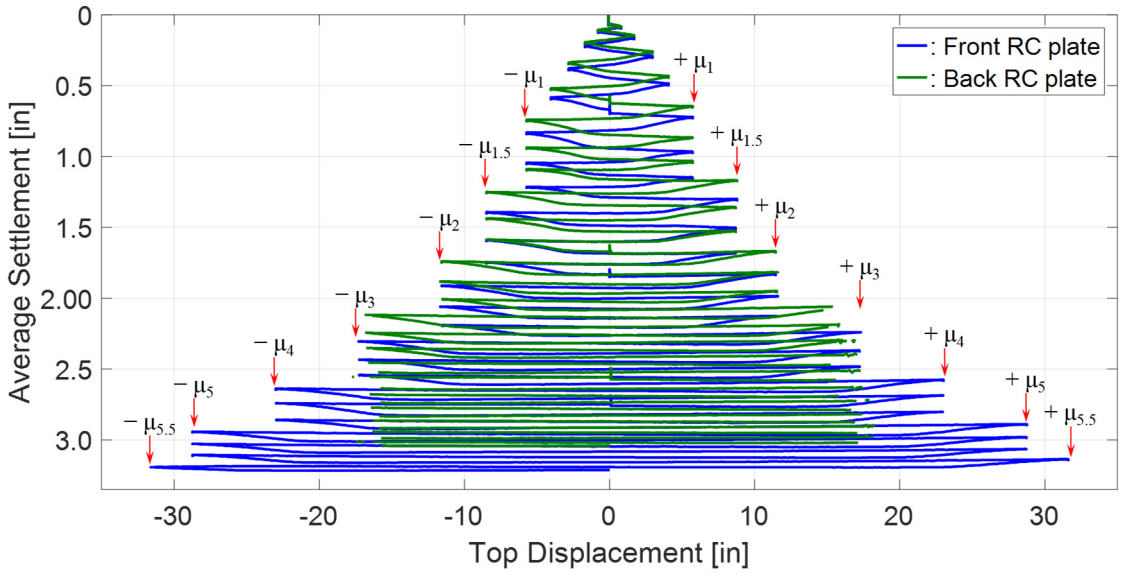

Figure 10-34 Test 2: half-moon RC plate settlement during testing

Figure 10-35 through Figure 10-37 present the damage observed after the pile was extracted from the soil. As thought during the test, tube fracture, tube local buckling, and bar buckling and fracture did occur. Note that tube local buckling developed on both sides of the specimen. The sections with the largest local buckling occurred at a depth of 1 ft. – 9 in. and 2 ft. – 5 ½ in. on both sides of the specimen. It can be seen from Figure 10-35 that three main local buckling zones developed on both South and North sides of the specimen. The plastic hinge developed at an average depth of 2 ft. – 6 ¼ in. with respect to the soil surface. Minor buckled regions were observed on both sides of the specimen, adjacent to the main buckled regions. Figure 10-36 presents measurements of the main buckled regions. Note that deformations due to buckling protruded ~ 5/8 in. on both sides of the specimen.

Pipe fracture (Figure 10-35) occurred on the North side of the specimen and it extended about half of the cross-section perimeter, resulting in a significant drop in strength due to lost tension capacity. Therefore, after rupture, tension capacity is provided by the longitudinal reinforcement, which has a smaller area in comparison to that provided by the steel tube, inducing high stresses and deformations, resulting in bar rupture (Figure 10-37).

In order to further investigate the significant strength loss and to verify that bar fracture occurred, a portion of the tube (i.e., 8 in. x 18 in.) was removed at the ruptured section on the North side, extreme fiber (Figure 10-37). Notice that the core concrete was crushed close to the ruptured area and in the main buckled regions; it was relatively easy to remove. However, digging further to the center of the section the concrete was not crushed and thus more difficult to remove. It can be seen from Figure 10-37 that a large crack developed in the concrete between the main buckled zones on the North side. In addition, several smaller cracks can be seen perpendicular to the longitudinal direction of the specimen. A total of three (3) bars ruptured and one (1) bar buckled. One of the bars that fractured was located on the extreme fiber of the North side, and the other two were adjacent to that extreme fiber bar.

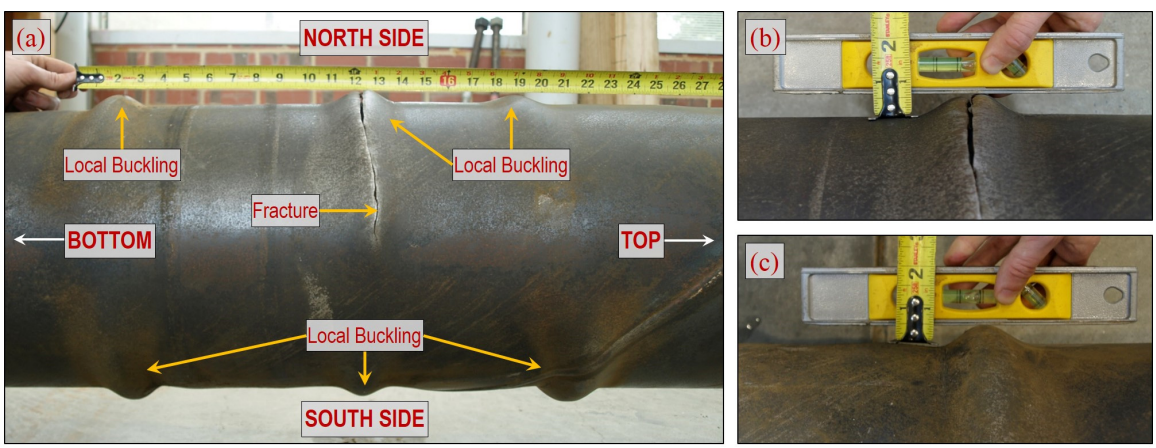

Figure 10-35 Test 2: (a) Final observed damage, (b) tube fracture, and (c) tube local buckling

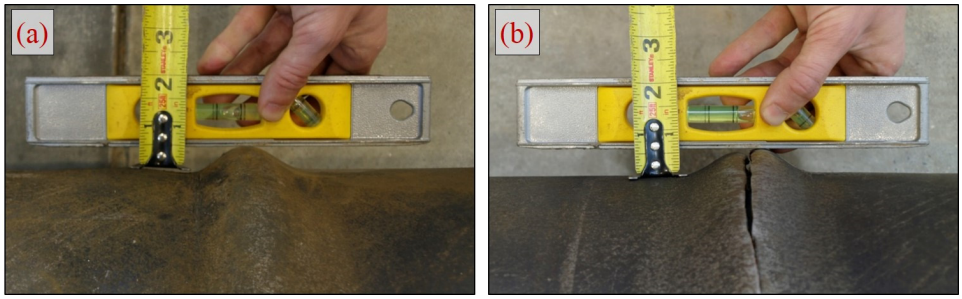

Figure 10-36 Test 2: primary buckled sections on (a) South side and (b) North side

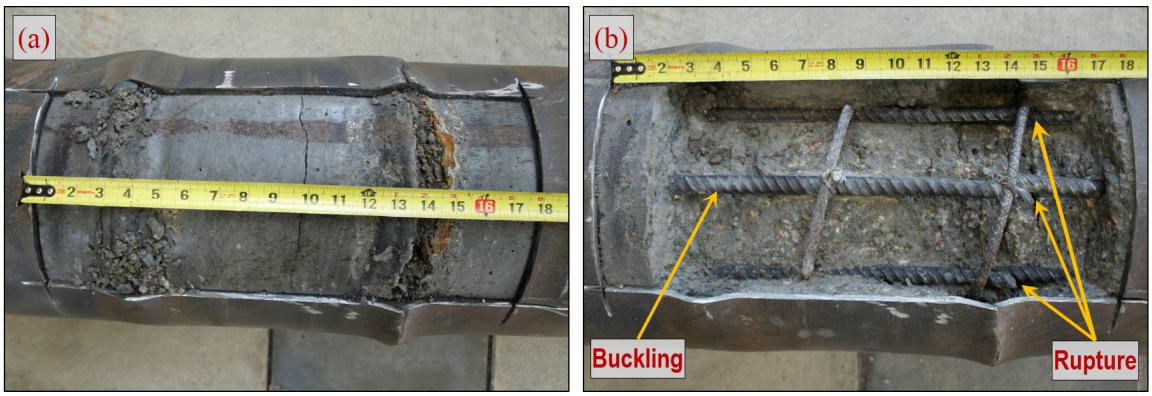

Figure 10-37 Test 2: observed damage in (a) concrete and (b) internal reinforcement on North side

Conclusions

Test specimen #2 showed a reliable response through all ductility 5.0 (μ_5) cycles. It is believed that the onset of local buckling occurred during the test at a ductility level 4.0 (μ_4), when subtle strength loss was observed. The test specimen completed all cycles of ductility 5.0 (μ_5) without significant loss of strength. Failure of the specimen occurred at ductility level 5.5 ($\mu_{5.5}$) when a significant drop in the strength was observed. Further investigations revealed that failure occurred due to a combination of tube local buckling, tube fracture, bar buckling, and bar fracture. It is believed that this particular specimen is capable of having a reliable displacement up to ductility 5.0 (μ_5). The main buckles as well as tube fracture did not occur over the spiral weld, so the tube spiral welds do not appear to negatively influence the behavior.

Test 3 Summary Report

June 4, 2015

Prepared for

Alaska Department of Transportation

Alaska University Transportation Center

Project Team

RA: Diego Aguirre

PIs: Mervyn Kowalsky, James Nau, Mo Gabr

Other Senior Personnel: Greg Lucier, Ben Smith

North Carolina State University

Executive Summary

Test 3 was conducted May 29th, 2015 at the North Carolina State University Constructed Facilities Laboratory. The tested pile-column specimen was a reinforced concrete filled steel tube with a diameter-to-thickness (D/t) ratio of 95. No surcharge was applied to the soil; thus, the soil stiffness was not modified. The test was successfully conducted to failure, which was caused by a combination of tube local buckling and fracture of the tube spiral weld, resulting in a large strength degradation (~36.35%) in the first cycle at ductility level 3.0 (μ_3).

Specimen and Test Description

Test 3 consisted of a 19-foot-5-inch long, reinforced concrete filled, 12-3/4-inch diameter spirally welded steel tube without skelp or splice welds. The pile specimen was embedded 13 ft. – 11 in. into clean sand in the soil-structure interaction facility at the NCSU-CFL. Lateral load was applied at the pinned connection at the top of the pile specimen by means of a 100-kip, 70-inch stroke hydraulic actuator. The nominal wall thickness of the tube was 0.134 in., providing a nominal diameter-to-thickness ratio (D/t) of 95. The test was conducted with a 5-foot-6-inch cantilever length, measured from the soil surface to the point at which the lateral load was applied. Figure 10-38 and Figure 10-39 present a schematic of the test setup (elevation) and the specimen #3 cross-section, respectively, while Figure

10-40 show the instrumentation used for testing. A photograph of the test setup is included in Figure 10-41.

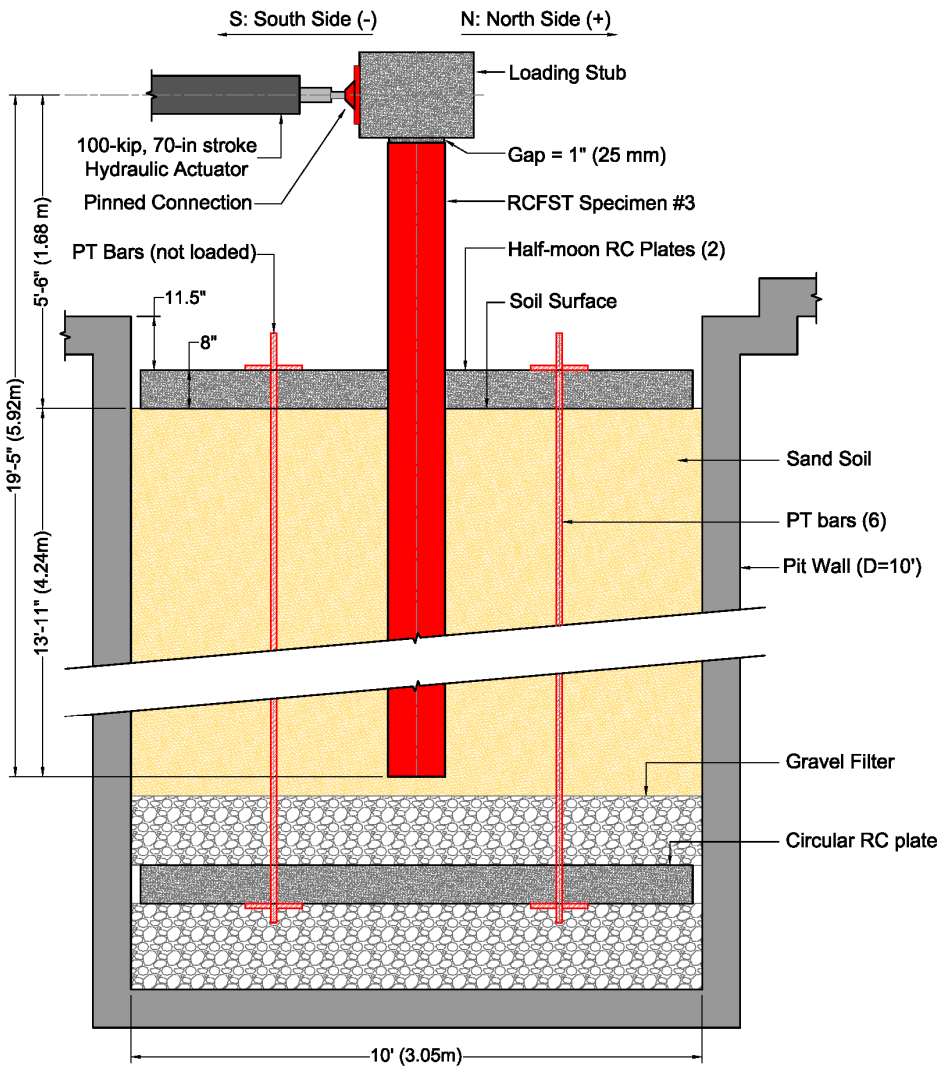

Figure 10-38 Test 3: test setup elevation schematic

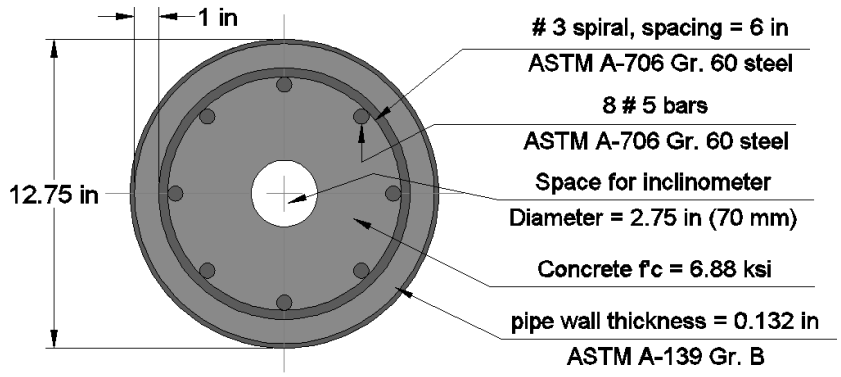

Figure 10-39 Test 3: RCFST specimen cross section

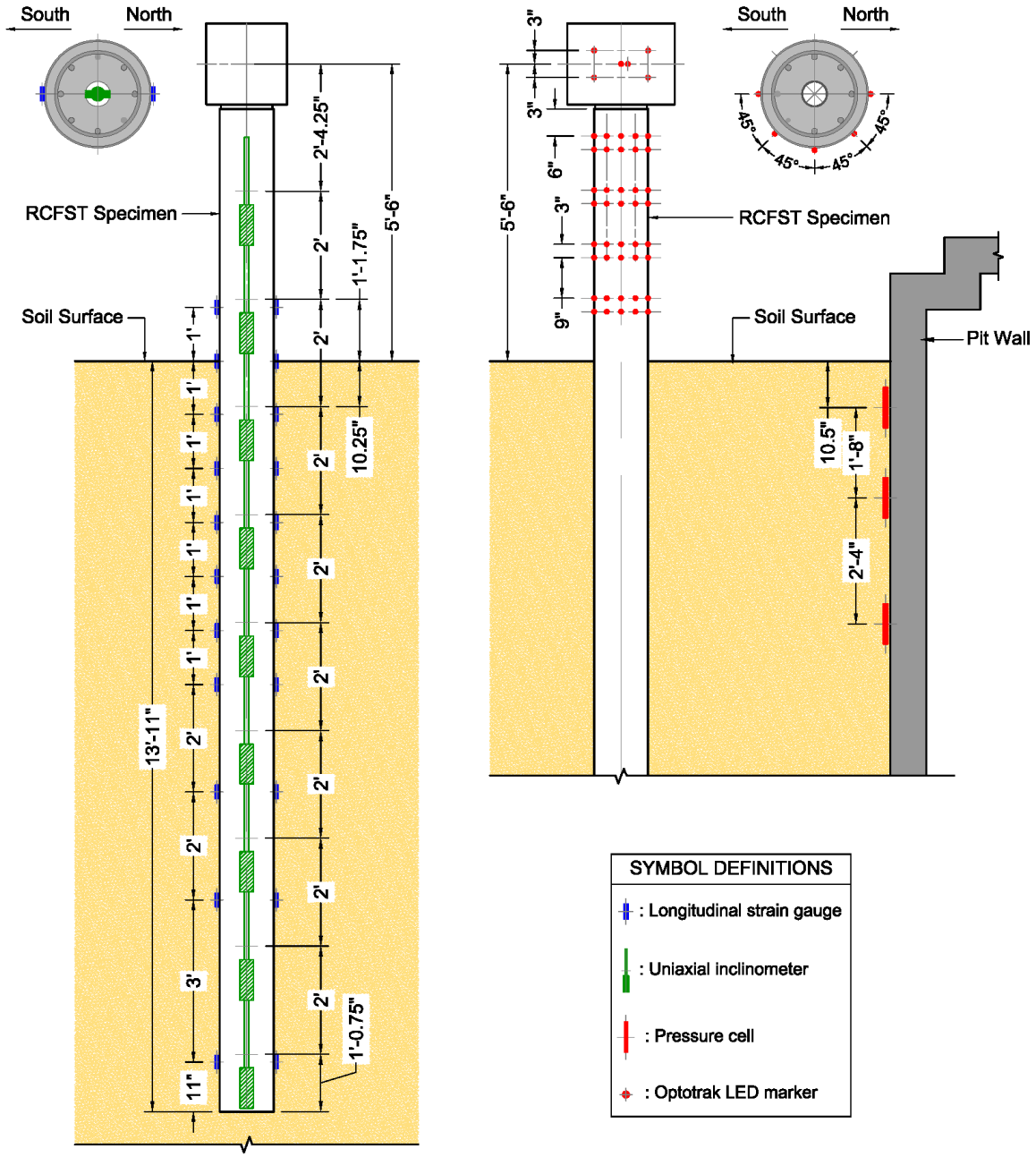

Figure 10-40 Test 3: instrumentation

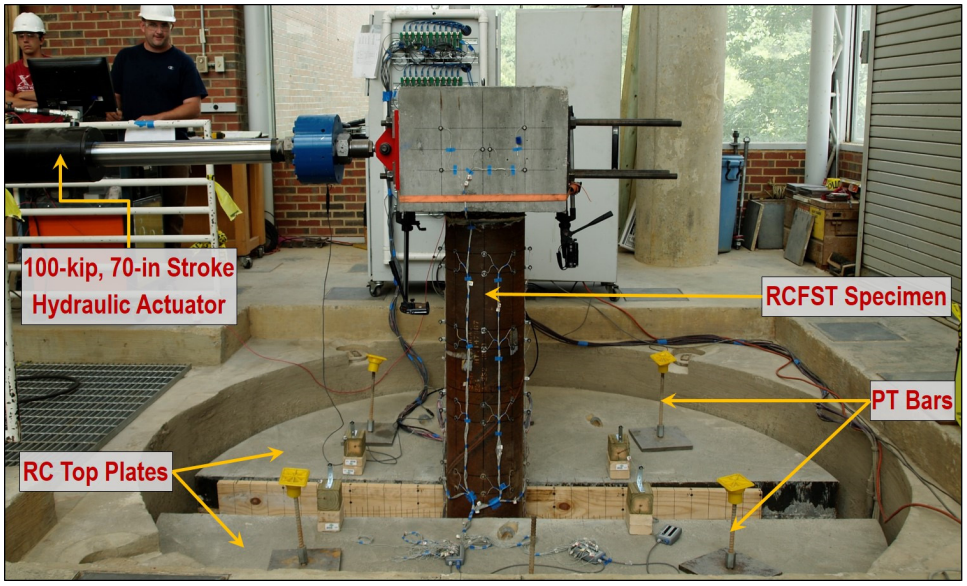

Figure 10-41 Test 3: pinned-head, RCFST pile-column test setup

Material properties were determined by in-house material tests. The yield and ultimate stresses of the ASTM A706 Grade 60 longitudinal reinforcement were 66.5 ksi and 90.3 ksi, respectively, based on tests conducted on six (6) bar specimens from the same heat of the longitudinal reinforcement. The yield and ultimate stresses of the spiral reinforcement were 72.1 ksi and 101.6 ksi, respectively, based on tests conducted on six (6) specimens from the same heat of the transverse reinforcement. An average concrete compressive strength of 6.88 ksi (standard deviation of ± 0.16 ksi) was determined from three (3) compression tests of 4”x8” concrete cylinders. Based on mill certifications, the yield and ultimate stresses of the steel tube were assumed as 52.5 ksi and 74.5 ksi, respectively.

Soil properties were also determined by in-house material tests. Based on a measured particle size distribution, the soil was classified as poorly-graded sand (SP). The unit weight, friction angle, and moisture content (γ = 90 pcf, ϕ = 35°, and w = 2.5%, respectively) were reasonably assumed based upon results of previous tests. Active surcharge was not applied, so only the self-weight of the half-moon RC plates was acting in the soil surface (i.e., ~100 psf).

The load history applied to the pile specimen consisted of standard three-cycle sets intended to evaluate both the elastic and inelastic response of the specimen. The first portion (i.e., pile elastic response up to first yield) of the test consisted of single reversed, displacement-controlled cycles, ramping up to the first yield displacement in ¼ increments. Given the non-linear response from the beginning of the test due to the characteristic soil behavior, target displacements in this portion of the test were determined based on the results of a monotonic pushover analysis performed using a detailed non-linear, fiber-based, finite element model developed using the OpenSees framework software. Soil-structure interaction was included by means of non-linear springs at 1-foot interval depths, with spring properties assigned based on p-y curves.

The first yield force (F_y) and nominal force (F_n), which is defined as the force at a concrete compressive strain of 0.004 or at a tube/bar tensile strain of 0.015 (whichever occurs first), were determined based upon tensile and compressive strains, monitored during the numerical simulation (i.e., pushover analysis), as 15.34 kips and 21.98 kips, respectively. Table 10-3 summarizes the target displacements for the first portion of the test. After the first portion of the test was completed, the measured average strain at the predicted first yield displacement ($\Delta'y$ = 3.84 in) was 1620 ($\mu\varepsilon$), which is below the steel tube yield strain (ε_y = 1810 $\mu\varepsilon$). Therefore, the average first yield displacement was modified by the observed yield-to-maximum observed strain ratio at the theoretical first yield displacement, as shown in Equation 10-5. This value (Δ'_y*) was then modified by the nominal-to-first yield force ratio in order to determine the displacement ductility level 1.0 (μ_1 = 6.15 in), as shown in Equation 10-6. The remainder of the test was completed using reversed three-cycle sets in displacement-controlled increments at different levels of displacement ductility until failure, as shown in Equation 10-7. The entire displacement and load histories can be seen in Figure 10-42. Positive loads and displacements correspond to rightward (North) motion of the pile in the test setup. The positive legs of all cycles were completed before the negative legs.

Table 10-3 Test 3: predictions for elastic portion

Performance Level	Displacement (in)	Force (in)
1/4 Δy'	0.74	4.63
1/2 Δy'	1.66	8.61
3/4 Δy'	2.73	12.25
1 Δy'	3.84	15.34

$$\Delta'_y * = 3.84\left(\frac{1810}{1620}\right) = 4.29\,in \qquad \text{Equation 10-5}$$

$$\Delta_y = \mu_1 = \Delta'_y \cdot \frac{F_n}{F_y} = 4.29\,in \cdot \frac{21.98\,kip}{15.34\,kip} = 6.15\,in \qquad \text{Equation 10-6}$$

$$\mu_i = i \cdot \mu_1 \rightarrow i = 1.0,\ 1.5,\ 2.0,\ 3.0,\ 4.0 \qquad \text{Equation 10-7}$$

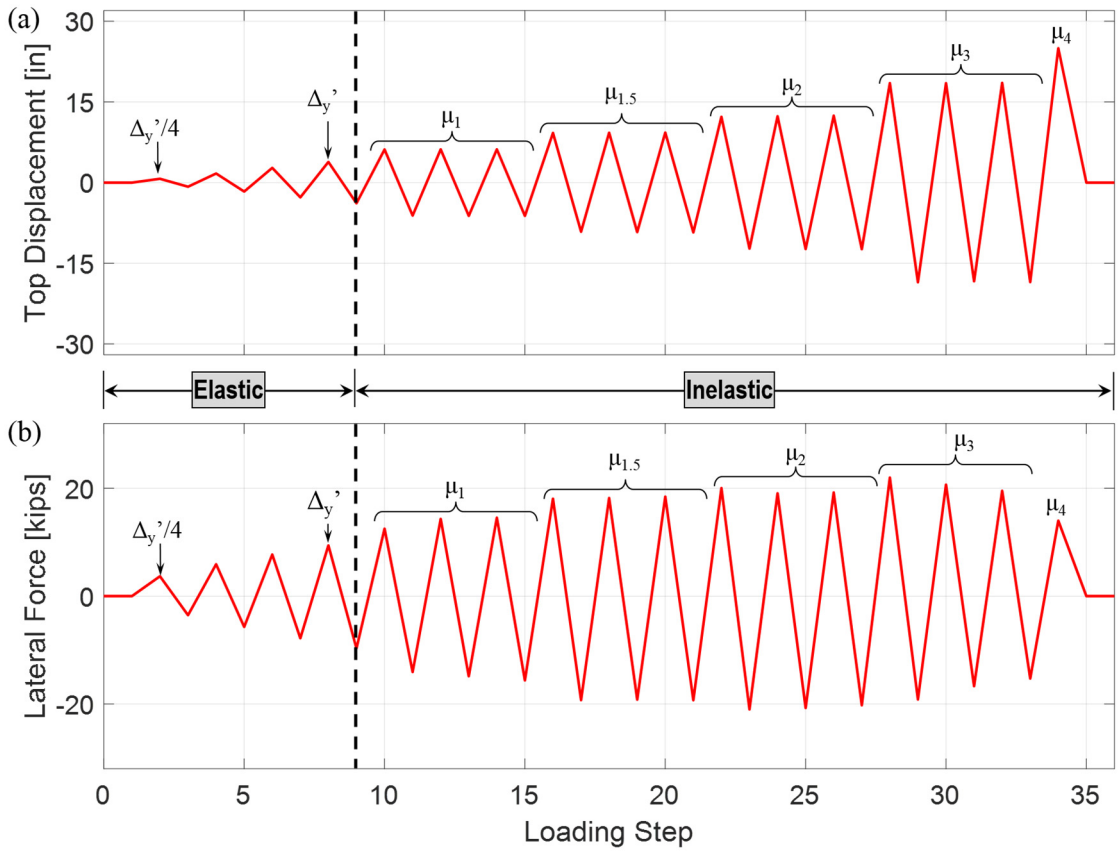

Figure 10-42 Test 3: (a) displacement and (b) loading histories

Specimen Response

Specimen #3 performed well through the elastic portion of the test and during all three cycles of ductility level 2.0 (μ_2). It is believed that onset of tube buckling occurred early during the displacement cycles at ductility level 1.5 ($\mu_{1.5}$) as one of the strain gauges located in the North side of the pile indicated large values during the pull cycles (South displacements) at that ductility level. An 8.9% strength loss, indicating onset of tube fracture, occurred during the first pull cycle at ductility level 3.0 (μ_3). Subsequently, a significant loss of strength (36.4 %) was recorded at the same time spiral weld fracture was observed, during the first push cycle at ductility level 4.0 (μ_4). Figure 10-43 and Figure 10-44 present the lateral force vs. top displacement response and envelopes, respectively. It can be clearly seen from these figures the strength loss indicating fracture in both sides of the specimen. Note from Figure 10-44 that for both the push and pull cycles at ductility level 1 (μ_1), the strength is higher for the second and third cycles in comparison to that of the first cycle. It is believed that this occurred because the soil did not develop its full strength but only until all cycles of that performance level were completed.

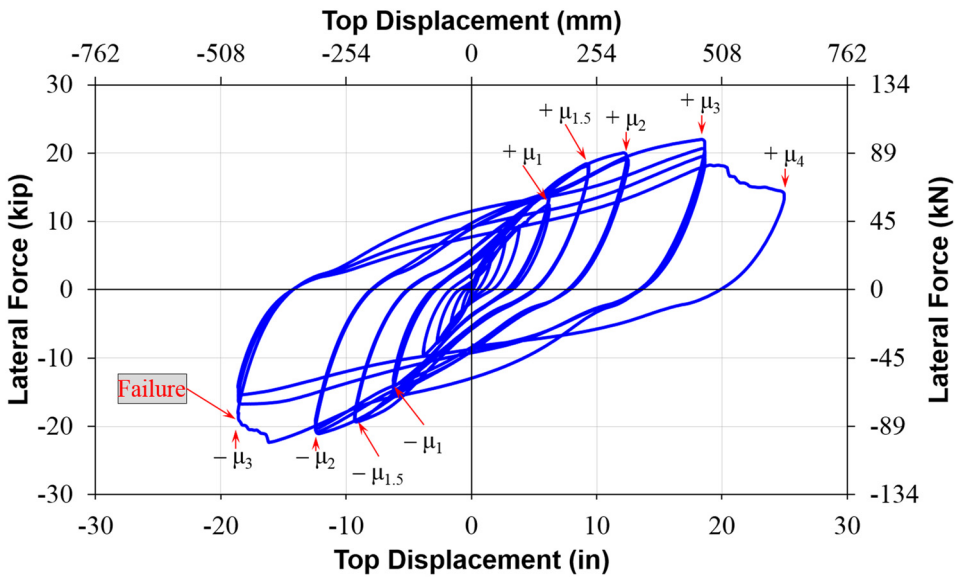

Figure 10-43 Test 3: lateral force vs. top displacement response

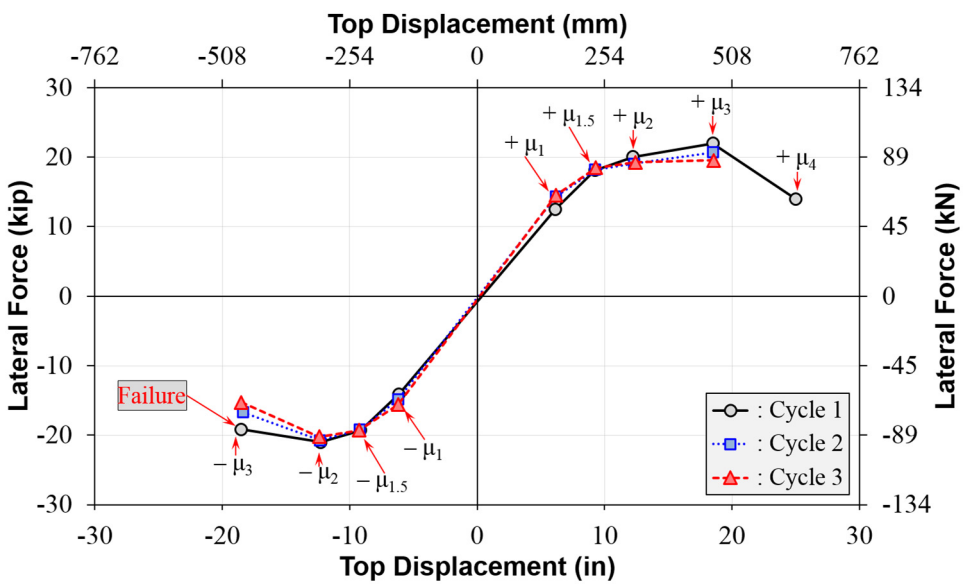

Figure 10-44 Test 3: lateral force vs. top displacement envelopes

Figure 10-45 presents the specimen and the soil-pile gaps at zero displacement after the elastic portion of the test was conducted; the size of the gap was ~1.5 in. on both sides of the specimen. As it was previously explained, at this point of the test strain profiles on the sides of the pile were verified in order to further conduct the test at the aforementioned ductility levels. Figure 10-46 presents the strain profiles recorded during the first portion of the test. Notice that tensile strains of 1430 (με) and 1620 (με) were recorded in the tube during the push and pull cycles, respectively, when the predicted first yield displacement was imposed to the system. In Figure 10-46 the symbols N and S in the legend refer to the North and South sides, Δ_y' is the first yield displacement, and a depth equal to 0 ft. represents the soil surface.

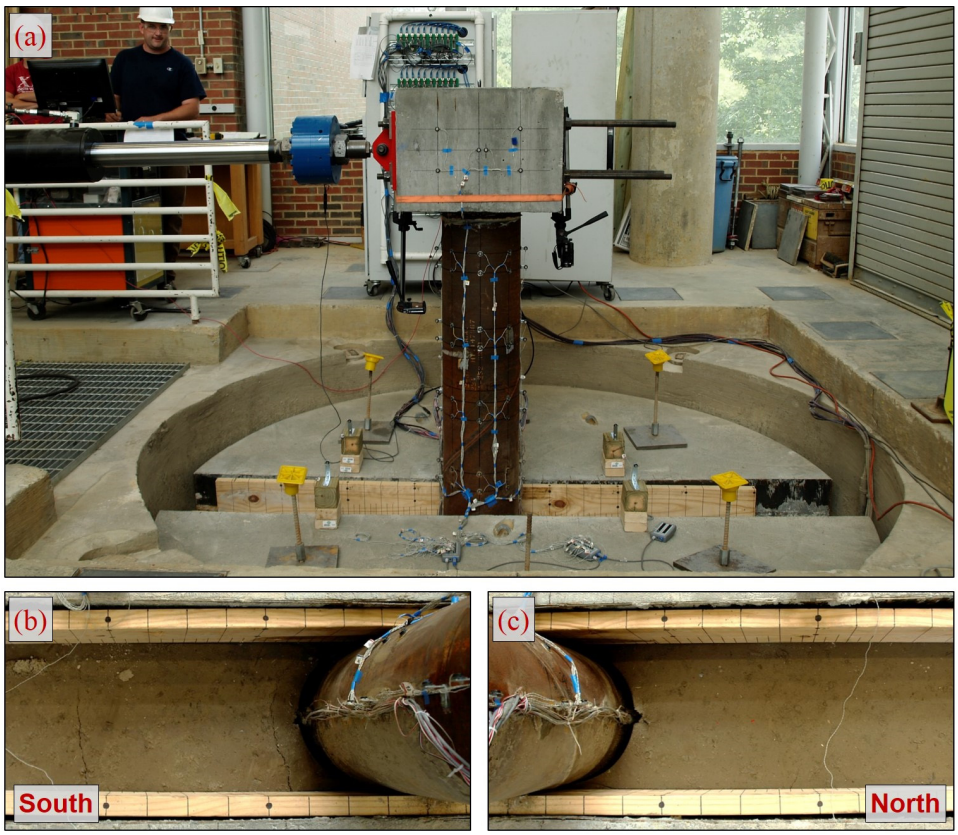

Figure 10-45 Test specimen #3 after elastic portion was completed: (a) deformed shape, (b) South side and (c) North side

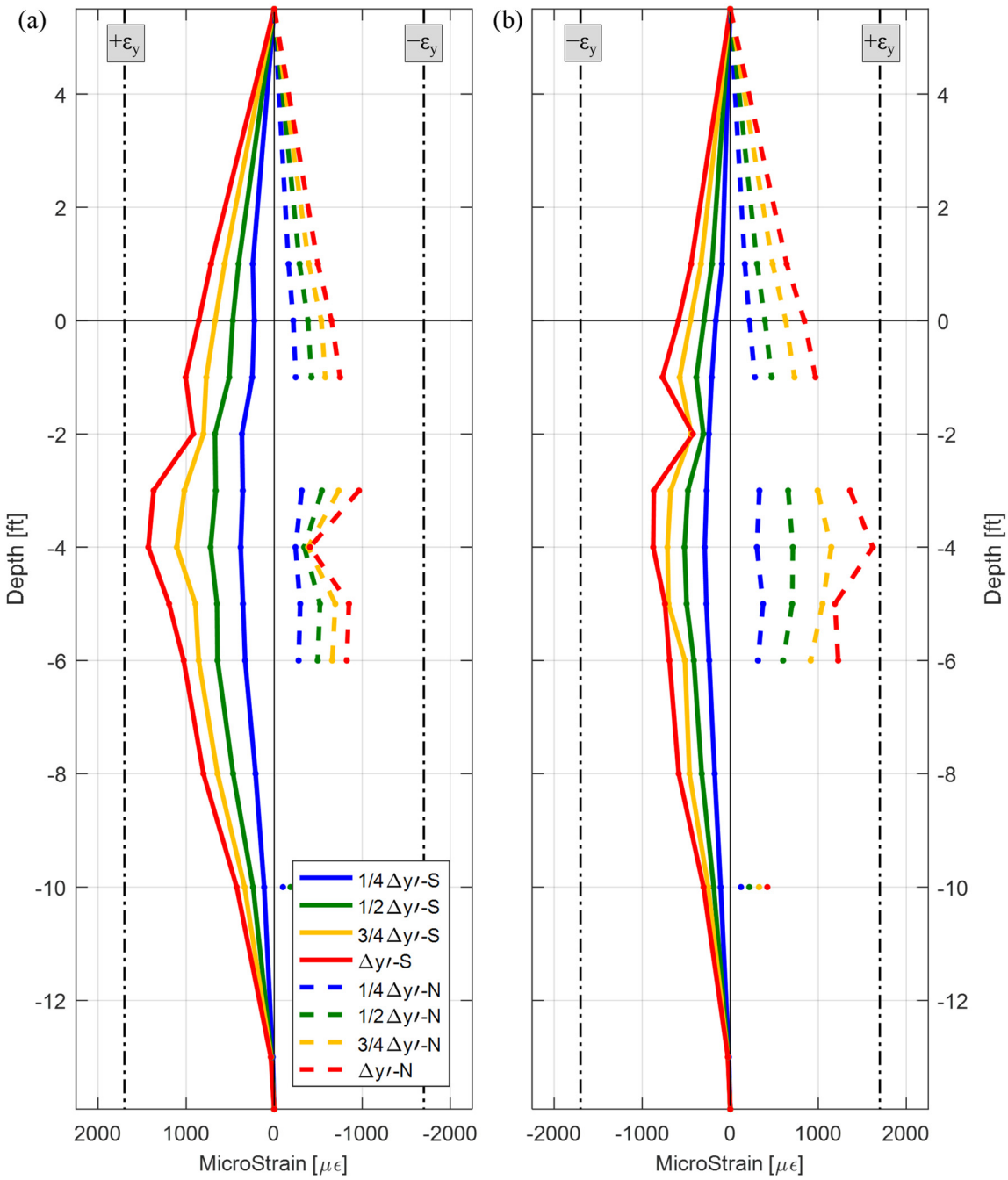

Figure 10-46 Test 3: strain profiles from elastic (a) push and (b) pull cycles

As the test continued, the gap on the sides of the pile increased in size as the displacement ductility level increased. Minor loss of strength was observed up until all ductility level 3.0 (μ_3) cycles. In addition, onset of twist of the pile occurred at that level of displacement. The test was terminated (Figure 10-47) after the first push cycle load at ductility 4.0 (μ_4) when a significant drop in the force in the actuator was observed (i.e., ~36.4%). In addition, spiral weld fracture was also observed at this level of displacement (Figure 10-48). Sounds indicating steel fracture were not heard as in previous tests. Finally, the specimen was taken to zero displacement in order to facilitate its extraction from the soil. Figure 10-49 presents the strain profiles for the first push and pull cycles at different displacement ductility levels. Notice that the largest tensile and compressive strains in the tube were recorded at a depth between 1 ft. and 6ft. In Figure 10-49, the symbols N and S in the legend refer to the North and South sides, and μ is the displacement ductility level.

Figure 10-50 shows the state of the soil surface after the test was completed. Notice that despite the presence of the half-moon RC plates in the surface, deformations in the soil followed an expected oval-shaped failure surface in which active and passive pressures developed around the pile. This surface extended ~25 in. on both sides of the direction of loading and ~16 in. on the perpendicular direction. The total average settlement of the RC plates was 1.8 in. This value was averaged based on the vertical displacement of 4 points on the RC plates. Figure 10-51 shows the average settlement of the half-moon RC plates during the test as a function of the imposed displacements in the top of the pile. Note that, as the displacement history is applied, the settlement increases, though its magnitude is larger at the beginning of the test.

Figure 10-52 through Figure 10-54 present the damage observed after the pile was extracted from the soil. As thought during the test, tube fracture and tube buckling did occur. It can be seen that tube local buckling developed on both sides of the specimen; however, more buckled zones were observed on the North side of the specimen. The sections with the largest tube local buckling occurred at a depth of 4 ft. – 1 3/8 in. and 2 ft. – 5 ½ in. on the South and North sides, respectively. It can be seen in Figure 10-52 that three local buckling zones developed on the North side, whereas only one developed on the South side. As such, the plastic hinge developed at an average depth of 2 ft. – 11 5/8 in. with respect to the soil surface. Figure 10-53 presents measurements of the main buckled regions. Note that the maximum deformations due to tube buckling protruded ~3/8 in. on both sides of the specimen.

Tube fracture (Figure 10-52) occurred on both North and South sides of the specimen along a segment of the spiral weld, and it extended to the East and West extreme fibers, resulting in the strength loss observed in both pull and push cycles due to loss of tension capacity. Note from Figure 10-49 that large tensile strains were recorded early during the test at ductility level 1.5 ($\mu_{1.5}$).

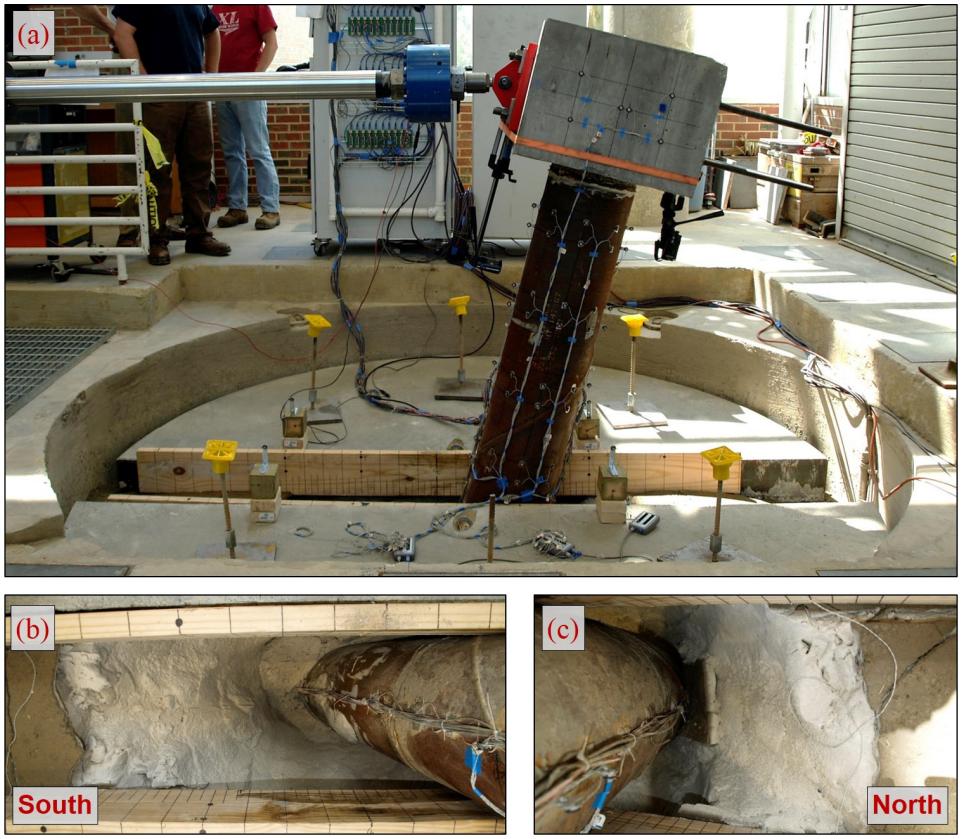

Figure 10-47 Test specimen #3 at maximum displacement: (a) deformed shape, (b) South side and (c) North side

Figure 10-48 Test 3: observed spiral weld fracture

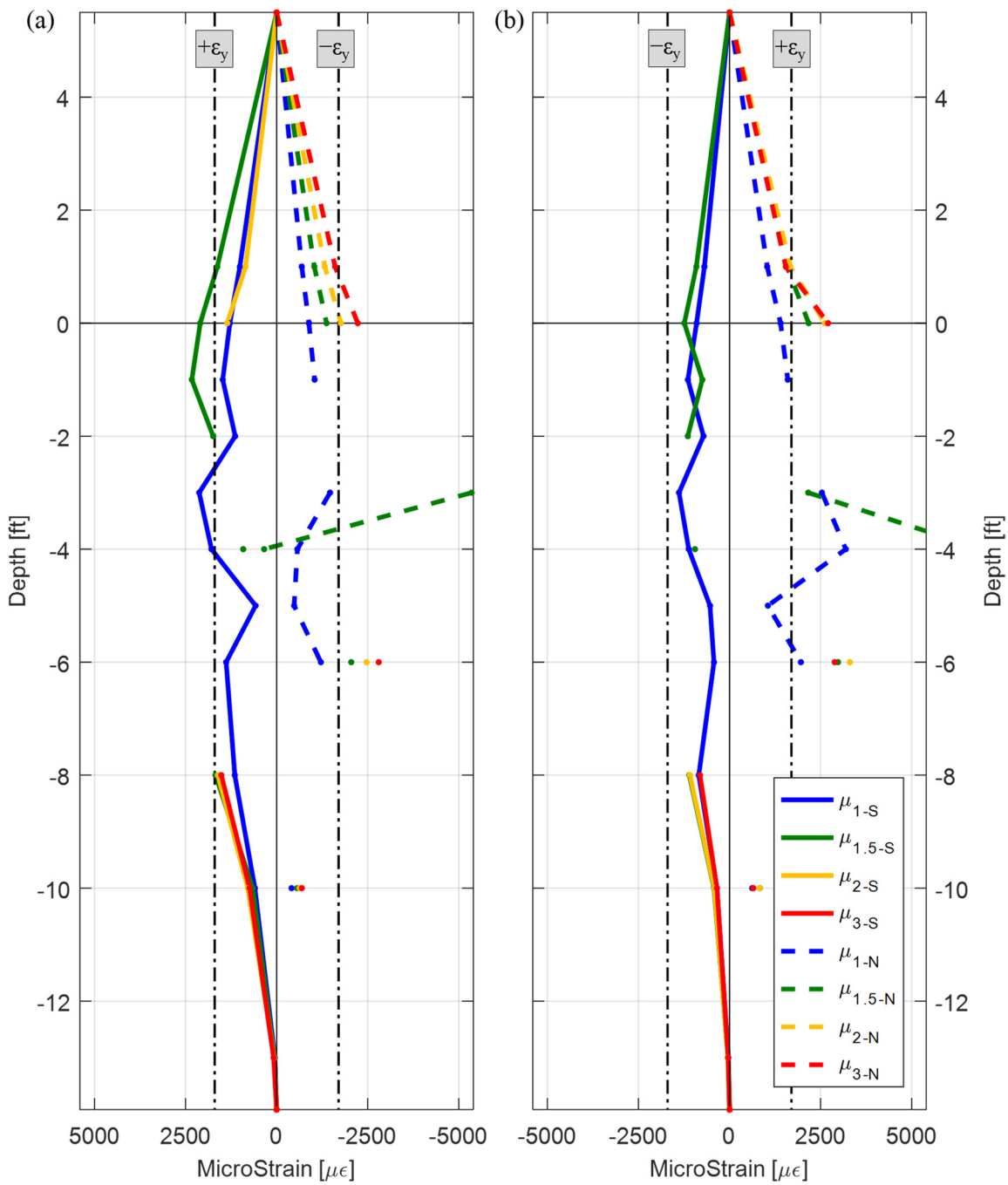

Figure 10-49 Test 3: strain profiles from inelastic (a) push and (b) pull cycles

Figure 10-50 Test 3: soil surface after testing

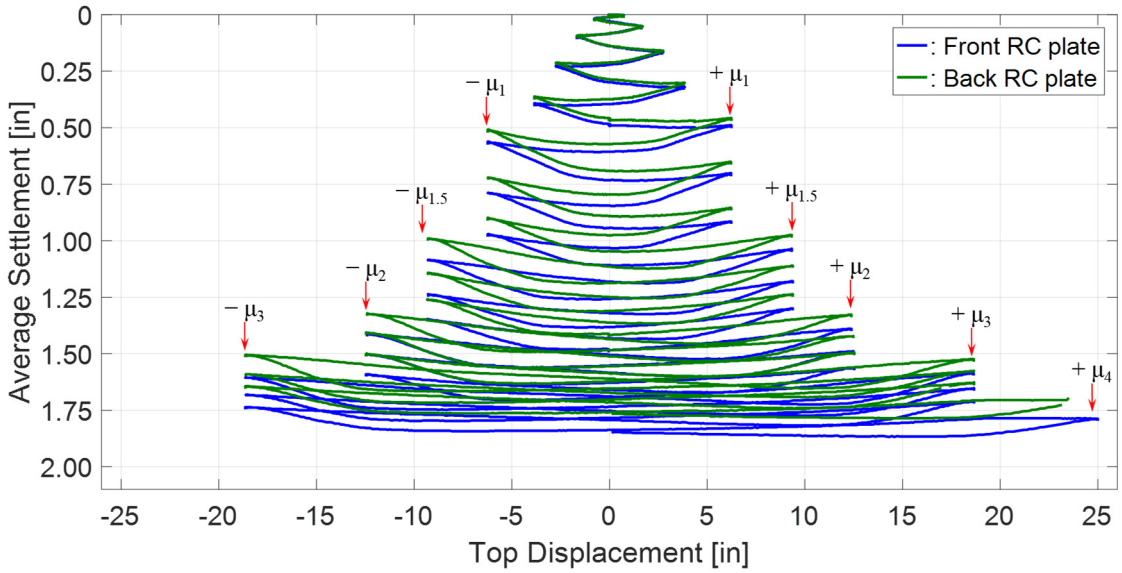

Figure 10-51 Test 3: half-moon RC plate settlement during testing

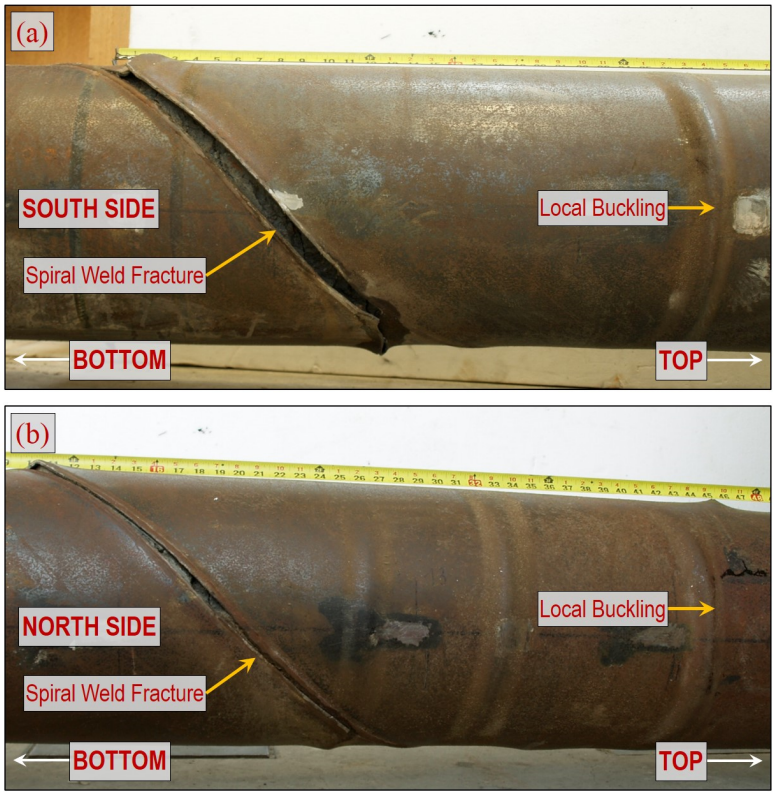

Figure 10-52 Test 3: (a) Final observed damage, (b) tube fracture, and (c) tube local buckling

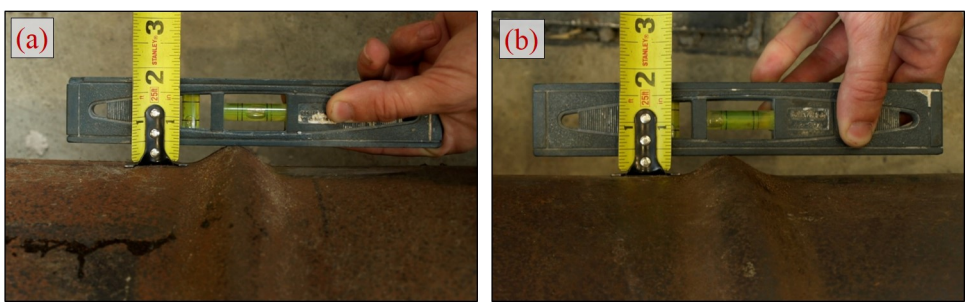

Figure 10-53 Test 3: primary buckled sections on (a) North side and (b) South side

In order to further investigate the significant strength loss and to verify whether bar fracture occurred, a portion of the tube (i.e., 9 in. x 18 in.) was removed at the ruptured section on the North side, extreme fiber (Figure 10-54). Note that several cracks developed in this area of the concrete, perpendicular to the longitudinal direction of the specimen; the largest crack (~1/8 in) was located at 3 ft. – 8 in. from the soil surface. Due to extensive cracking, the core concrete was crushed close to the ruptured area, following the shape of the spiral weld, indicating loss of confinement along the ruptured section. This portion of the core concrete was easy to remove; however, digging further to the center of the section the concrete was not crushed and thus more difficult to remove. Bar buckling and bar fracture were not observed.

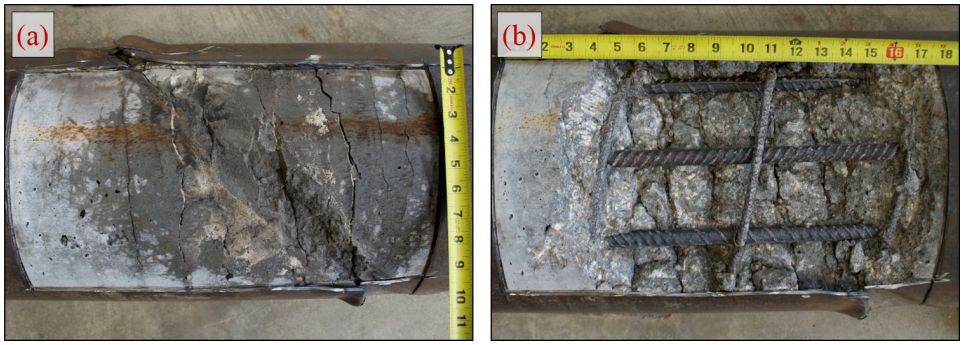

Figure 10-54 Test 3: observed damage in (a) concrete and (b) internal reinforcement on South side

Conclusions

Test specimen #3 showed a reliable response through all ductility 2.0 (μ_2) cycles. It is believed that the onset of local buckling occurred early during the test at ductility level 1.5 ($\mu_{1.5}$), when large tensile strains were recorded. The test specimen completed all cycles of ductility 3.0 (μ_3) without significant loss of strength, though indicating onset of tube spiral weld fracture. A significant drop in strength occurred at ductility level 4.0 (μ_4) when fracture of the spiral weld was observed. Further investigations revealed that failure occurred due to a combination of tube local buckling and tube spiral weld fracture. It is believed that this particular specimen is capable of having a reliable displacement up to ductility 2.0 (μ_2). Tube fracture occurred over the spiral weld, so the tube spiral welds appear to negatively influence the behavior limiting the deformation capacity of this particular specimen.

Test 4 Summary Report

June 25, 2015

Prepared for

Alaska Department of Transportation

Alaska University Transportation Center

Project Team

RA: Diego Aguirre

PIs: Mervyn Kowalsky, James Nau, Mo Gabr

Other Senior Personnel: Greg Lucier, Ben Smith

North Carolina State University

Executive Summary

Test 4 was conducted June 16th, 2015 at the North Carolina State University Constructed Facilities Laboratory. The tested pile-column specimen was a reinforced concrete filled steel tube with a diameter-to-thickness (D/t) ratio of 95. A surcharge of ~960 psf was applied to the soil prior to and during the test, so the soil stiffness was expected to change. The test was successfully conducted to failure, which was caused by a combination of tube local buckling and fracture of the tube spiral weld, resulting in a large strength degradation (~37.2%) in the second cycle at ductility level 2.0 (μ_2).

Specimen and Test Description

Test 4 consisted of a 19-foot-5-inch long, reinforced concrete filled, 12-3/4-inch diameter spirally welded steel tube without skelp or splice welds. The pile specimen was embedded 13 ft. – 11 in. into clean sand in the soil-structure interaction facility at the NCSU-CFL. Lateral load was applied at the pinned connection at the top of the pile specimen by means of a 100-kip, 70-inch stroke hydraulic actuator. The nominal wall thickness of the tube was 0.134 in., providing a nominal diameter-to-thickness ratio (D/t) of 95. The test was conducted with a 5-foot-6-inch cantilever length, measured from the soil surface to the point at which the lateral load was applied. Figure 10-55 and Figure 10-56 present a schematic of the test setup (elevation) and the specimen #4 cross-section, respectively, while Figure

10-57 shows the instrumentation used for testing. A photograph of the test setup is included in Figure 10-58.

Material properties were determined by in-house material tests. The yield and ultimate stresses of the steel tube were 45.4 ksi and 66.6 ksi, respectively, based on tests conducted on three (3) coupons cut from the end of the test pile specimen. The yield and ultimate stresses of the ASTM A706 Grade 60 longitudinal reinforcement were 66.5 ksi and 90.3 ksi, respectively, based on tests conducted on six (6) bar specimens from the same heat of the longitudinal reinforcement. The yield and ultimate stresses of the spiral reinforcement were 72.1 ksi and 101.6 ksi, respectively, based on tests conducted on six (6) specimens from the same heat of the transverse reinforcement. An average concrete compressive strength of 7.14 ksi (standard deviation of ± 0.15 ksi) was determined from three (3) compression tests of 4”x8” concrete cylinders.

Soil properties were also determined by in-house material tests. Based on a measured particle size distribution, the soil was classified as poorly-graded sand (SP). The unit weight and moisture content (γ = 90 pcf and w = 3.35 %, respectively) were measured on June 11th, 2015. An active surcharge was applied to the soil surface by means of 40-kip, 2-inch stroke hydraulic jacks reacting on the half-moon RC plates. An axial load of 10.1 kips was applied to each of the six (6) PT bars, resulting on a surcharge pressure q = 960 psf. Based on the soil properties and due to the applied active surcharge, an internal friction angle, ϕ = 35°, was reasonably assumed. In addition to the active pressure, the self-weight of the half-moon RC plates was acting on the soil surface as well (i.e., ~100 psf).

In an attempt to modify the soil properties prior to pile testing, five surcharge cycles were performed using the same surcharge level to be applied during the test, i.e. q = 960 psf. All surcharge cycles were applied one day prior to pile testing, that is, on June 15th, 2015. Cycles 1 through 4 were applied without sustaining the pressure, namely, they were load-unload cycles which took approximately 30 minutes each. The fifth surcharge cycle was then applied and the pressure was sustained all the way until pile testing was completed. The average settlement of the RC plates prior the pile testing was ~0.64 in. This value was averaged based on the vertical displacement of 4 points on the RC plates. Results of the surcharge cycles are presented in Figure 10-59.

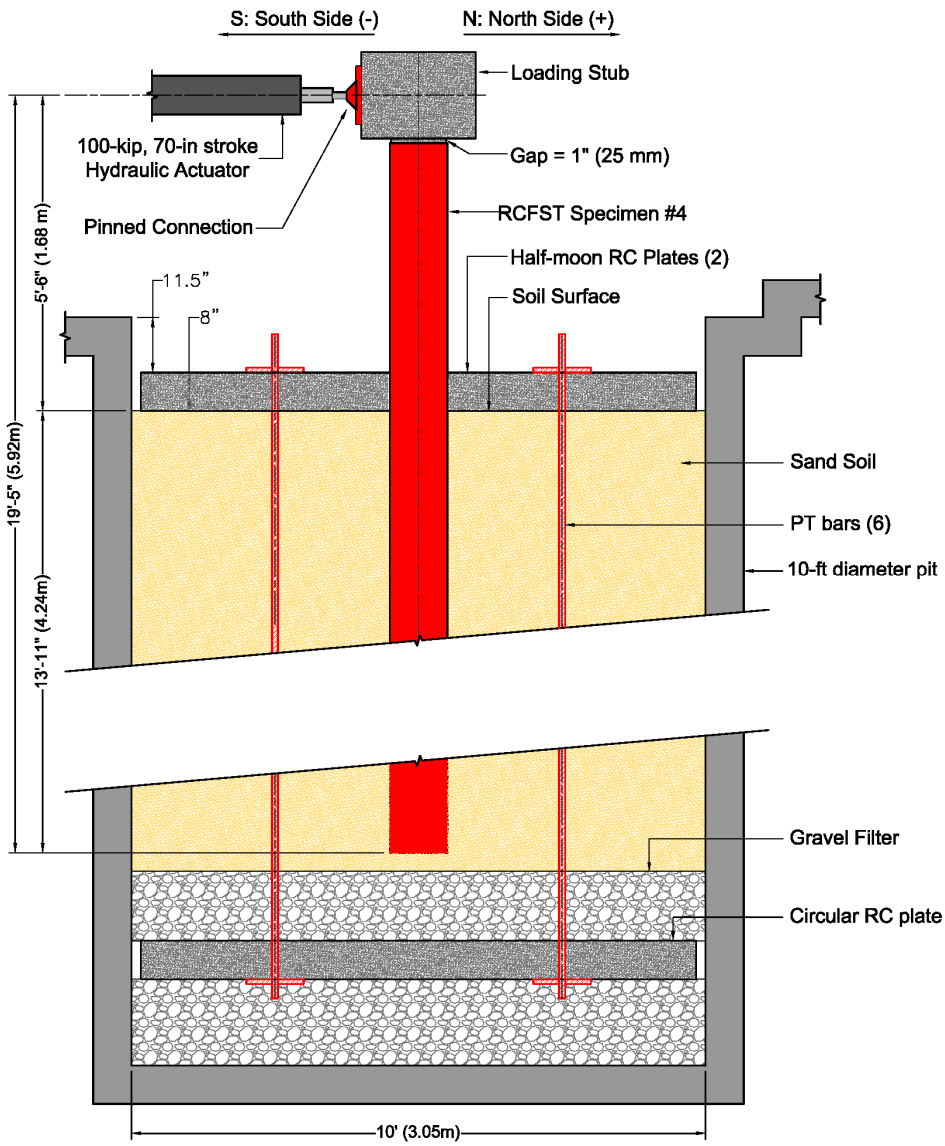

Figure 10-55 Test 4: test setup elevation schematic

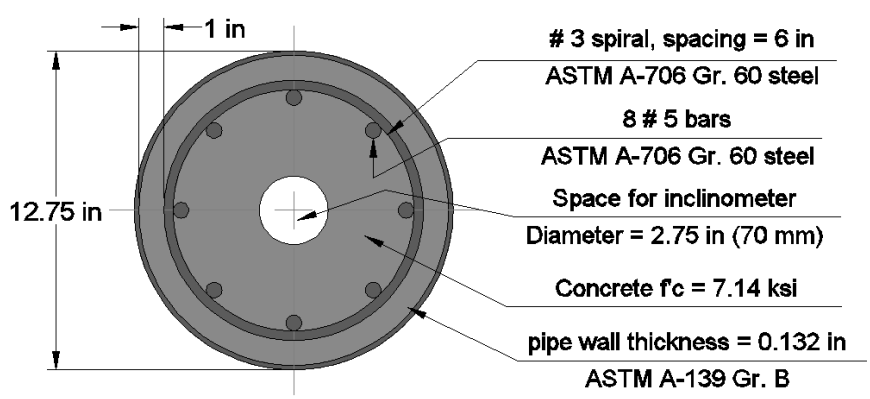

Figure 10-56 Test 4: RCFST specimen cross section

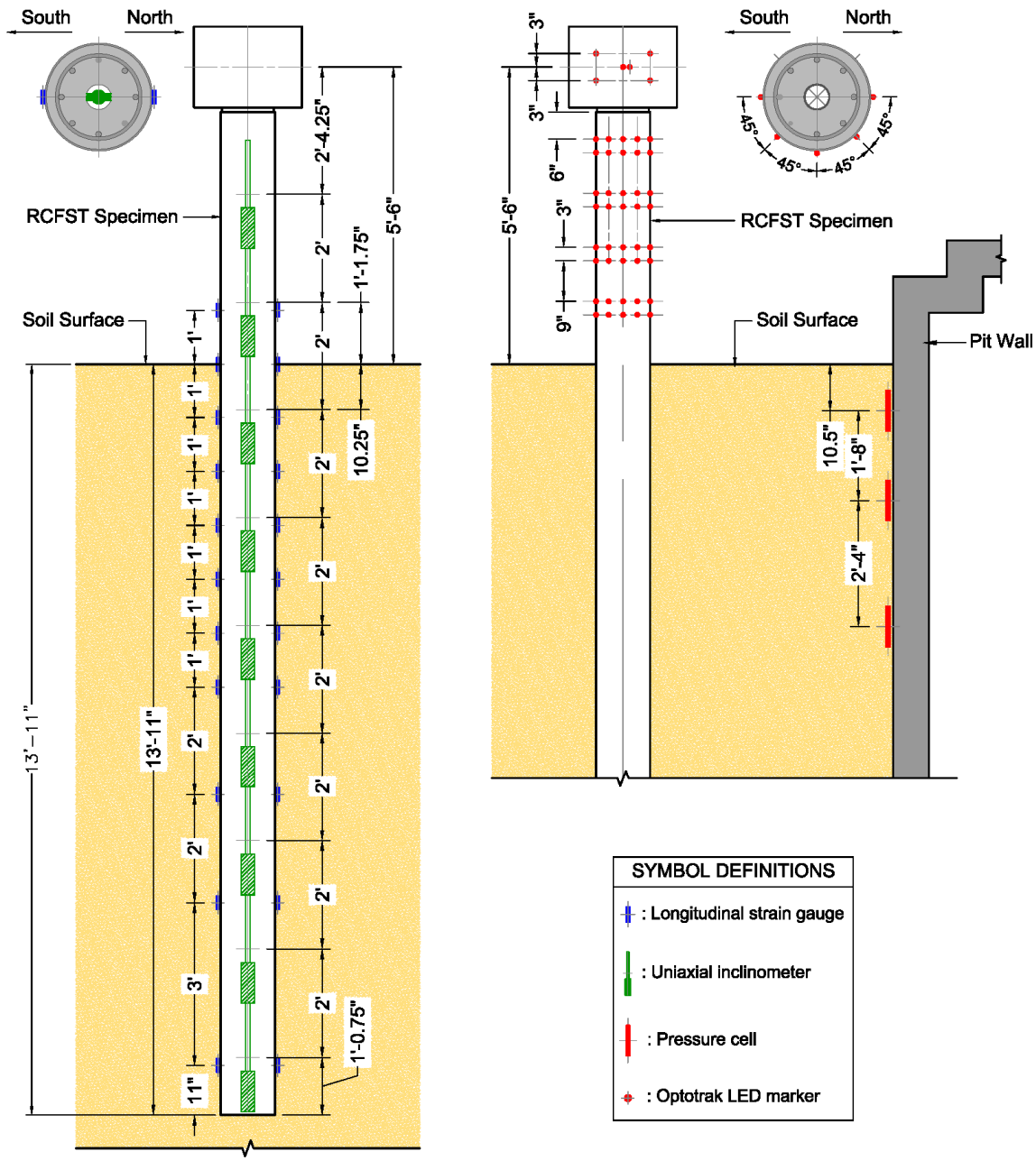

Figure 10-57 Test 4: instrumentation

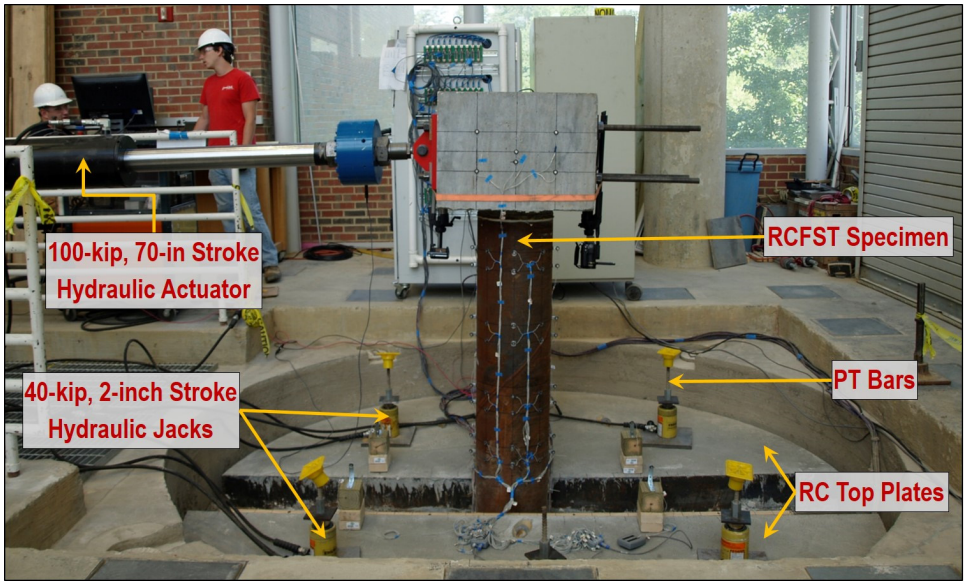

Figure 10-58 Test 4: pinned-head, RCFST pile-column test setup

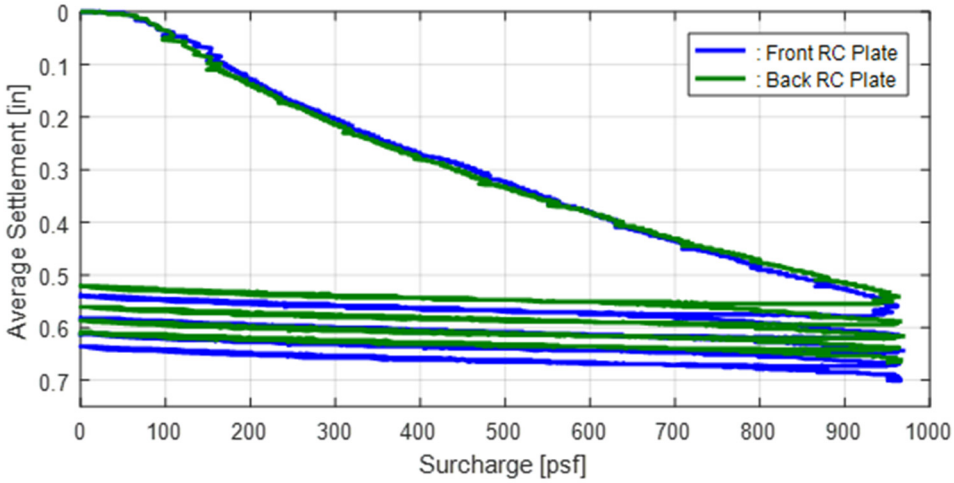

Figure 10-59 Test 4: half-moon RC plate settlement prior testing

The load history applied to the pile specimen consisted of standard three-cycle sets intended to evaluate both the elastic and inelastic response of the specimen. The first portion (i.e., pile elastic response up to first yield) of the test consisted of single reversed, displacement-controlled cycles, ramping up to the first yield displacement in ¼ increments. Given the non-linear response from the beginning of the test due to the characteristic soil behavior, target displacements in this portion of the test were determined based on the results of a monotonic pushover analysis performed using a detailed non-linear, fiber-based, finite element model developed using the OpenSees framework software. Soil-structure interaction was included by means of non-linear springs at 1-foot interval depths, with spring properties assigned based on p-y curves.

The first yield force (F_y) and nominal force (F_n), which is defined as the force at a concrete compressive strain of 0.004 or at a tube/bar tensile strain of 0.015 (whichever occurs first), were determined based upon tensile and compressive strains, monitored during the numerical simulation (i.e., pushover analysis), as 13.92 kips and 22.23 kips, respectively. Table 10-4 summarizes the target displacements for the first portion of the test.

After the first portion of the test was completed, the measured average strain at the predicted first yield displacement (Δ'_y = 3.47 in) was 1750 (με), which correlates well with the tube yield strain (ε_y = 1560 με). The measured average displacement at the first yield displacement (Δ'_y = 3.47 in) was modified by the nominal-to-first yield force ratio in order to determine the displacement ductility level 1.0 (μ_1 = 5.53 in), as shown in Equation 10-8. The remainder of the test was completed using reversed three-cycle sets in displacement-controlled increments at different levels of displacement ductility until failure, as shown in Equation 10-9. The entire displacement and load histories can be seen in Figure 10-60. Positive loads and displacements correspond to rightward (North) motion of the pile in the test setup. The positive legs of all cycles were completed before the negative legs.

Table 10-4 Test 4: predictions for elastic portion

Performance Level	Displacement (in)	Force (kips)
1/4 Δy'	0.78	3.84
1/2 Δy'	1.60	7.46
3/4 Δy'	2.49	10.83
1 Δy'	3.47	13.92

$$\Delta_y = \mu_1 = \Delta'_y \cdot \frac{F_n}{F_y} = 3.47\,in \cdot \frac{22.23\,kip}{13.92\,kip} = 5.53\,in \qquad \text{Equation 10-8}$$

$$\mu_i = i \cdot \mu_1 \rightarrow i = 1.0,\ 1.5,\ 2.0 \qquad \text{Equation 10-9}$$

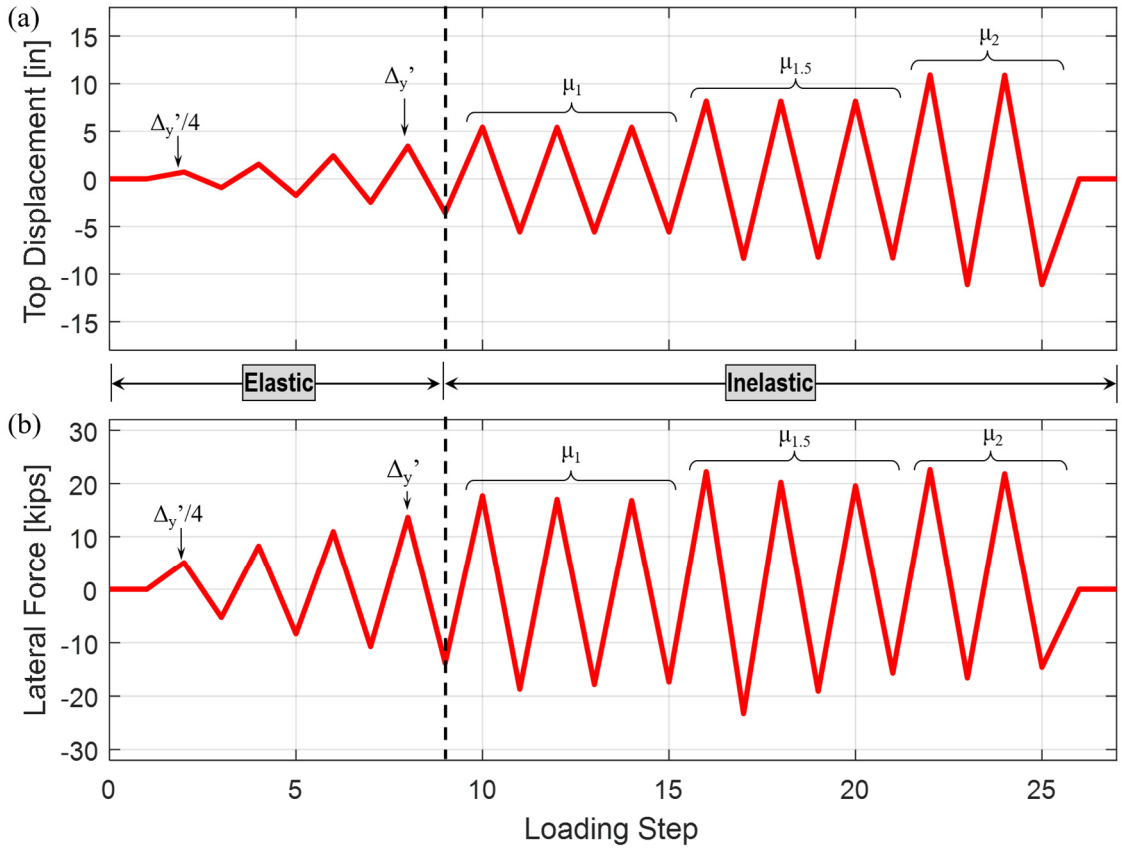

Figure 10-60 Test 4: (a) displacement and (b) loading histories

Specimen Response

Specimen #4 performed well through the elastic portion of the test and during all three cycles of ductility level 1.0 (μ_1). It is believed that onset of tube buckling and spiral weld fracture occurred early during the displacement cycles at ductility level 1.5 ($\mu_{1.5}$) as strength drops were recorded in both push and pull cycles at this level. An 18% strength loss, indicating onset of fracture, was recorded during the second pull cycle at ductility level 1.5 ($\mu_{1.5}$). A significant loss of strength (37.2 %), indicating failure, occurred during the second pull cycle at ductility level 2.0 (μ_2); at the same time spiral weld fracture was observed and the test was terminated. Figure 10-61 and Figure 10-62 present the lateral force vs. top displacement response and envelopes, respectively. It can be clearly seen the strength loss indicating fracture during a pull cycle of the specimen at ductility level 2.0 (μ_2).

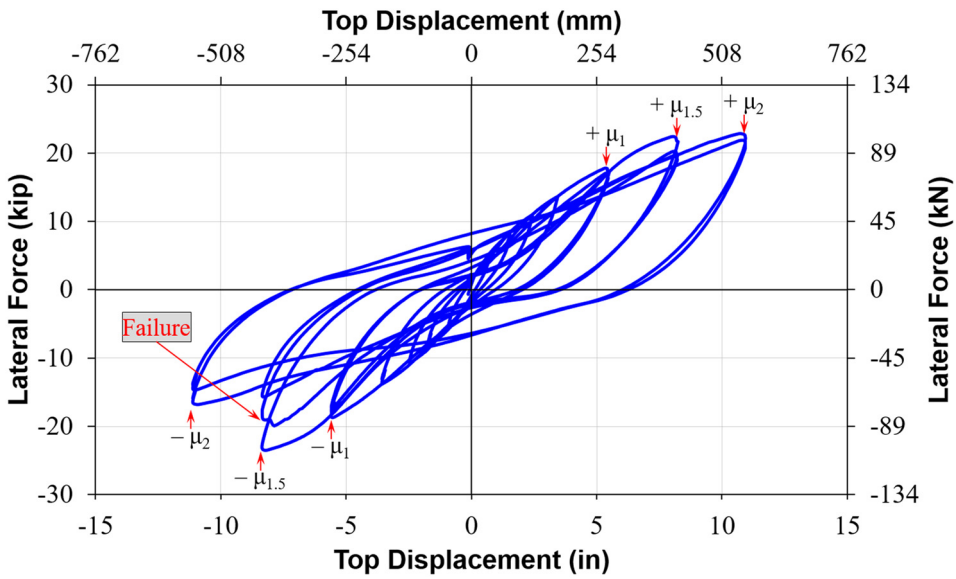

Figure 10-61 Test 4: lateral force vs. top displacement response

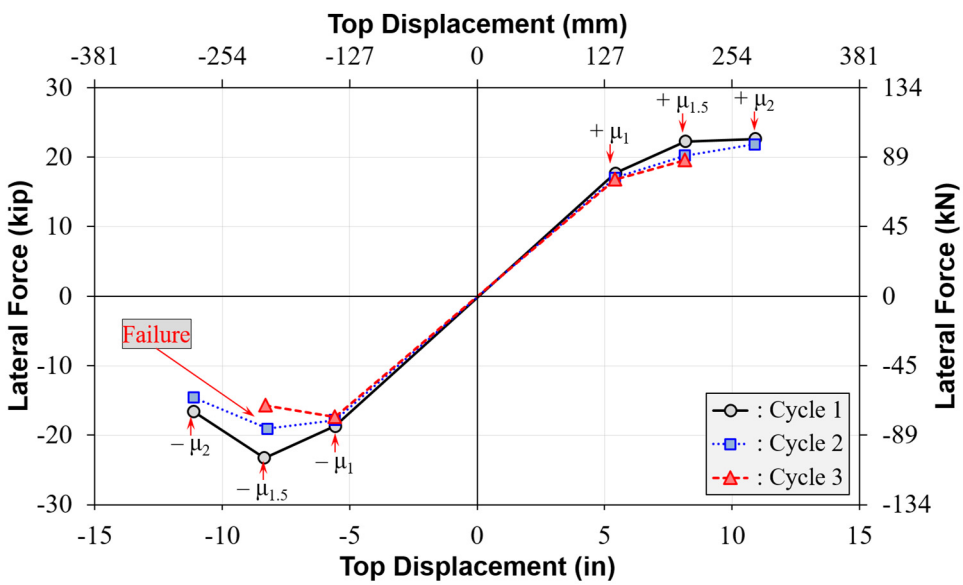

Figure 10-62 Test 4: lateral force vs. top displacement envelopes

Figure 10-63 presents the soil-pile gaps at zero displacement after the elastic portion of the test was conducted; the size of the gap was ~1.25 in. on both sides of the specimen. As it was previously explained, at this point of the test strain profiles on the sides of the specimen were verified in order to further conduct the test at the aforementioned ductility levels. Figure 10-64 presents the strain profiles recorded during the first portion of the test. Notice that tensile strains of 1690 (με) and 1800 (με) were recorded in the tube during the push and pull cycles, respectively, when the predicted first yield displacement was imposed to the system. In Figure 10-64 the symbols N and S in the legend refer to the North and South sides, Δ_y' is the first yield displacement, and a depth equal to 0 ft. represents the soil surface.

As the test continued, the gap on the sides of the pile increased in size as the displacement ductility level increased. Minor loss of strength was observed up until all ductility level 1.0 (μ_1) cycles. The test was terminated (Figure 10-65) after the second pull cycle load at ductility 2.0 (μ_2) when a significant drop in the force in the actuator was observed (i.e., ~37.2%). In addition, spiral weld fracture was also observed at this level of displacement (Figure 10-66). Sounds indicating reinforcing steel fracture were not heard as in previous tests. Finally, the specimen was taken to zero displacement in order to facilitate its extraction from the soil.

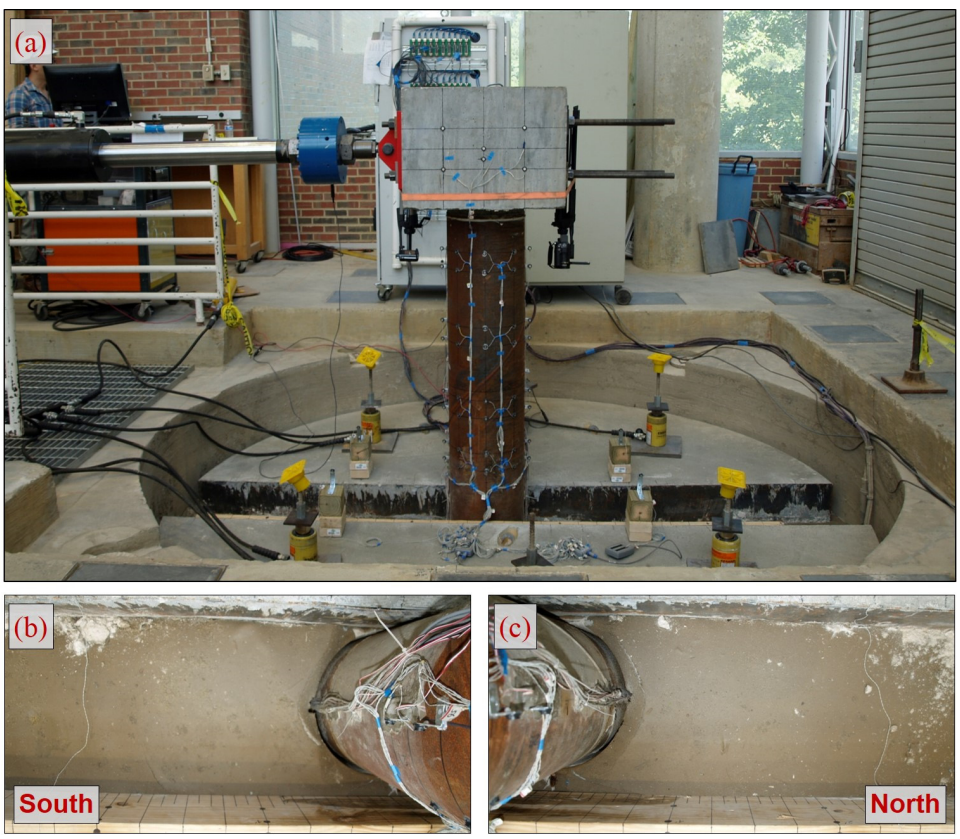

Figure 10-63 Test specimen #4 after the elastic portion was completed: (a) deformed shape, (b) South side and (c) North side

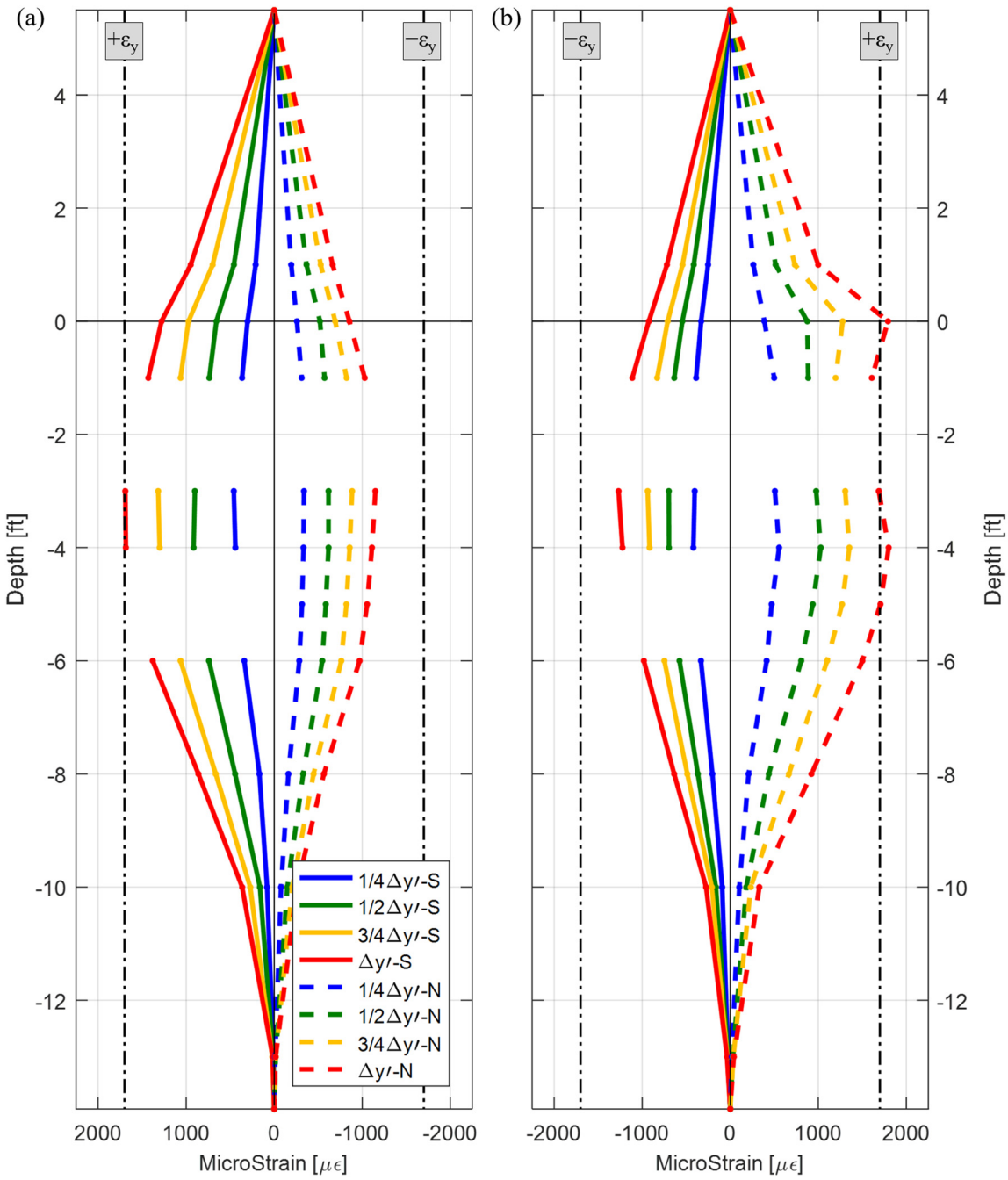

Figure 10-64 Test 4: strain profiles from elastic (a) push and (b) pull cycles

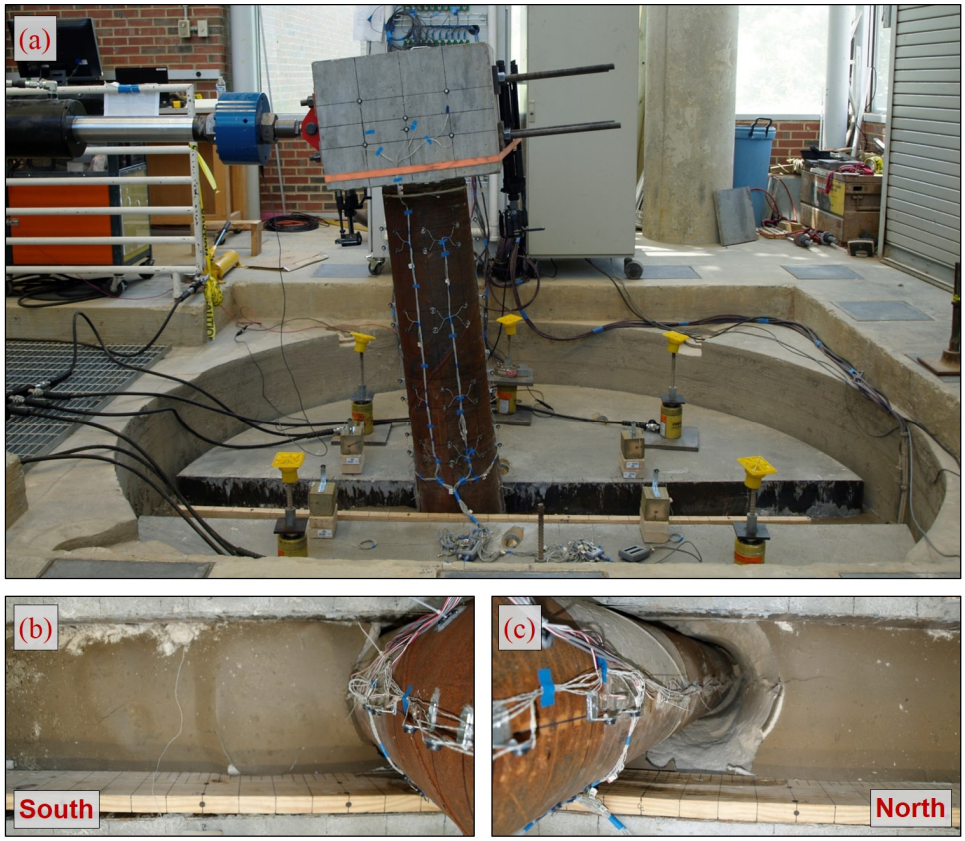

Figure 10-65 Test specimen #4 at maximum displacement: (a) deformed shape, (b) South side and (c) North side

Figure 10-66 Test 4: observed spiral weld fracture

Figure 10-67 presents the strain profiles for the first push and pull cycles at different displacement ductility levels. Notice that the largest tensile and compressive strains in the tube were recorded at a depth between 1 ft. and 6ft. In Figure 10-67 the symbols N and S in the legend refer to the North and South sides, and μ is the displacement ductility level.

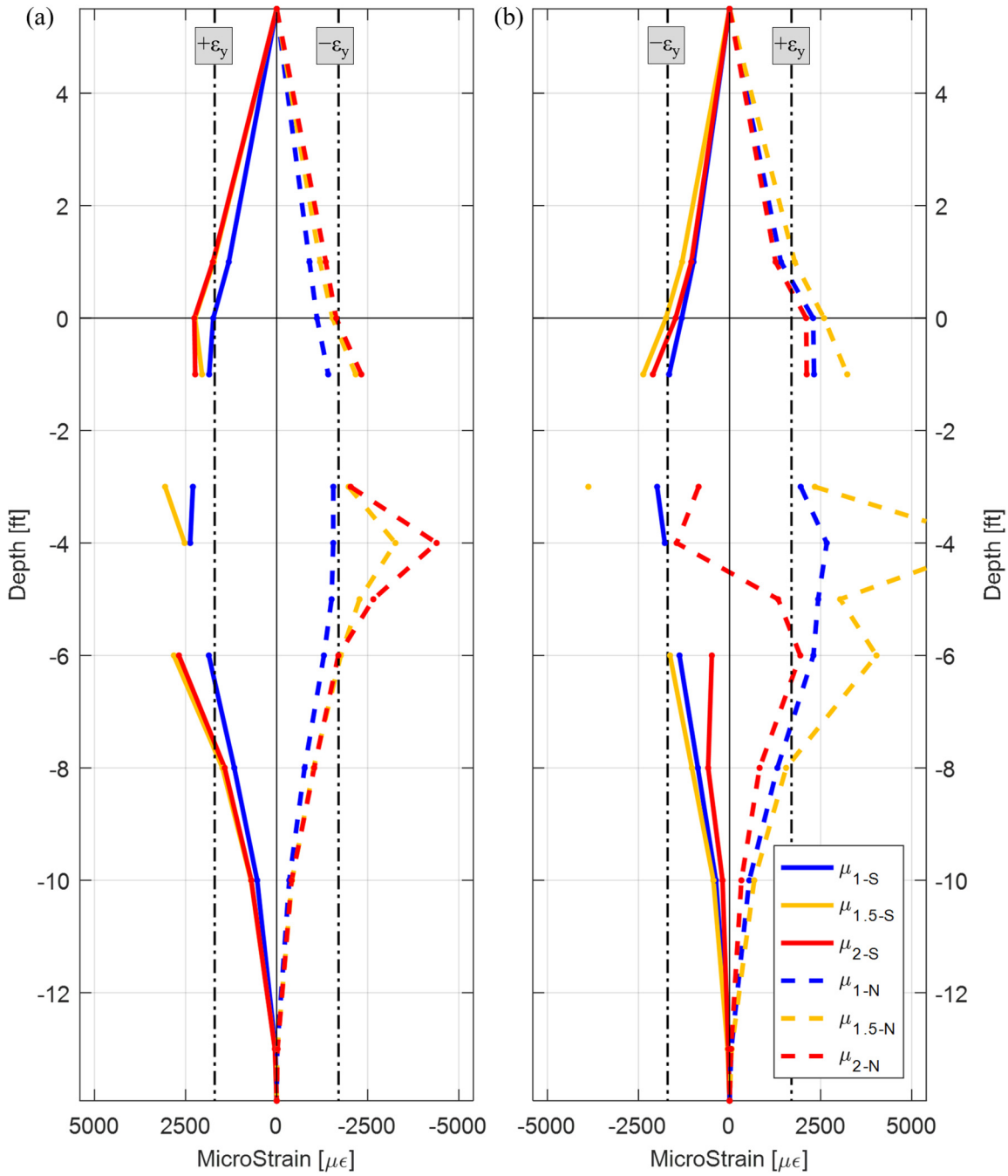

Figure 10-67 Test 4: strain profiles from inelastic (a) push and (b) pull cycles

Figure 10-68 shows the state of the soil surface after the test was completed. Notice that the size of the failure surface is not as large as in previous tests, though displacements reached during this particular test were not as high as in other tests as well. This surface extended ~4.25 in. on both sides of the direction of loading and ~4 in. on the perpendicular direction. The total average settlement of the RC plates was ~1.96 in. This value was averaged based on the vertical displacement of 4 points on the RC plates. Figure 10-69 shows the average settlement of the half-moon RC plates during the test as a function of the imposed displacements at the top of the pile. Note that, as the displacement history is applied, the settlement increases, though its magnitude is larger at the beginning of the test.

Figure 10-68 Test 4: soil surface after testing

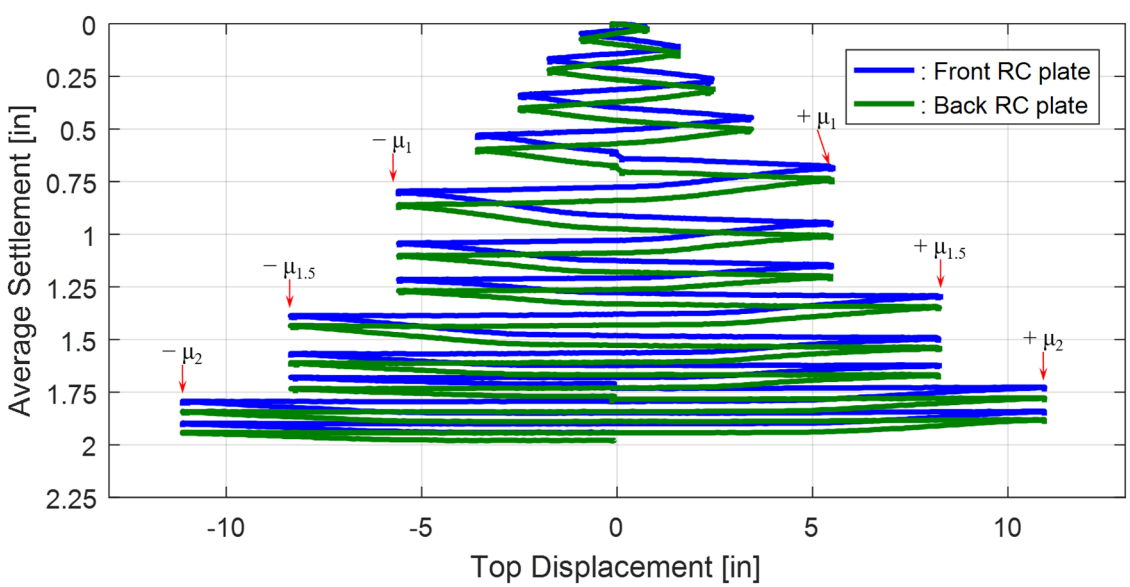

Figure 10-69 Test 4: half-moon RC plate settlement during testing

Figure 10-70 and Figure 10-71 present the damage observed after the pile was extracted from the soil. As thought during the test, tube fracture and buckling did occur. Pipe fracture occurred on the North side of the specimen along a segment of the spiral weld, and it extended to the East and West extreme fibers, resulting in the strength loss observed in the pull cycles due to loss of tension capacity. As previously shown in Figure 10-67, large tensile strains were recorded early during the test at ductility level 1.5 ($\mu_{1.5}$). The spiral weld that fractured was centered at an average depth of 3 ft. – 3 in. It can be seen from Figure 10-70 that tube local buckling developed only on the South side of the specimen, located at a depth of 3 ft. – 1 1/2 in. The deformation due to tube buckling protruded ~1/4 in.

In order to further investigate the significant strength loss and to verify whether bar fracture or buckling occurred, a portion of the tube (i.e., 10 in. x 20 in.) was removed at the ruptured section on the North side, extreme fiber (Figure 10-71). It can be noticed that several cracks developed in this area of the concrete, perpendicular to the longitudinal direction of the specimen; the largest crack (~1/8 in) was located at 3 ft. – 8 in. from the soil surface. Due to the extensive cracking, the core concrete was crushed close to the ruptured area, following the shape of the spiral weld, indicating loss of confinement along the ruptured section. This portion of the core concrete was easy to remove; however, digging further to the center of the section the concrete was not crushed and thus more difficult to remove. Neither bar buckling nor bar fracture were observed.

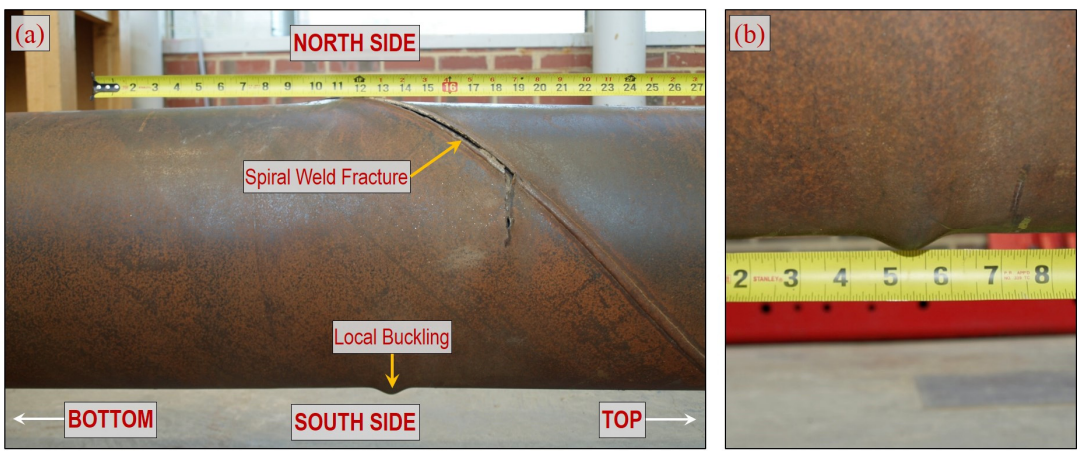

Figure 10-70 Test 4: (a) Final observed damage, (b) tube fracture, and (c) tube local buckling

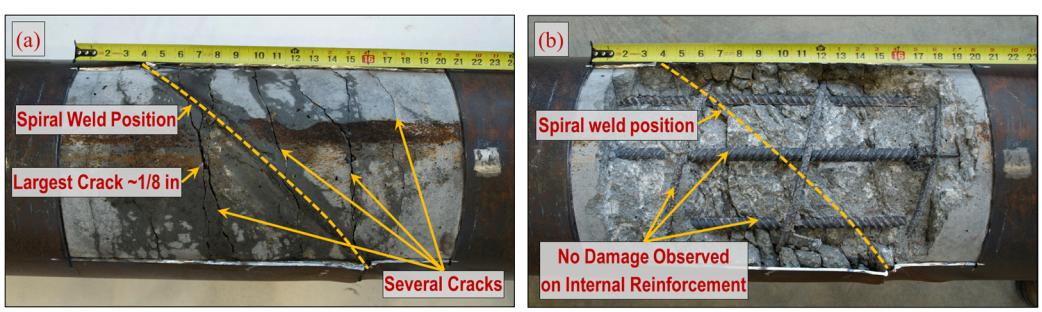

Figure 10-71 Test 4: observed damage in (a) concrete and (b) internal reinforcement on North side

Conclusions

Test specimen #4 showed a reliable response through all ductility 1.0 (μ_1) cycles. It is believed that onset of tube fracture and tube local buckling occurred early during the test at a ductility level of 1.5 ($\mu_{1.5}$), when large tensile strains were recorded along with strength losses. The test specimen completed all cycles of ductility 1.5 ($\mu_{1.5}$) with a moderate loss of strength, indicating onset of tube fracture. A significant drop in strength occurred at ductility level 2.0 (μ_2) when fracture of the tube spiral weld was observed. Further investigations revealed that failure occurred due to a combination of tube local buckling and fracture of the tube spiral weld. It is believed that this particular specimen is capable of having a reliable displacement up to ductility 1.0 (μ_1). Tube fracture occurred over the spiral weld, so the tube spiral welds appear to negatively influence the behavior limiting the deformation capacity of this particular specimen.

Upon further examination of the inside of the spirally welded tube, it was determined that the thin wall tubes which made up tests 3 and 4 were not welded along the inside surface, but rather only upon the outside surface (Figure 10-72), indicating a partial joint penetration (PJP) weld detail. Furthermore, tension tests done on coupons across the spiral weld after the tests were completed, indicated abrupt rupture at low strain levels (Figure 10-73). The tube manufacturer confirmed that the thin wall tubes sent to NC State that were used for tests 3 and 4 had a PJP weld detail. A new set of tubes with D/t = 95 were received. These replacement tubes were welded on both surfaces, indicating a complete joint penetration (CJP) weld detail. Figure 10-74 shows a coupon cut from the end of one of the replacement tubes, while Figure 10-75 shows results of the tension tests performed on coupons cut off the end of such replacement tubes. Using the aforementioned replacement tubes, test 3 and 4 were repeated as tests 5 and 6.

Figure 10-72 Steel tube coupon spiral weld on: (a) outside and (b) inside surfaces

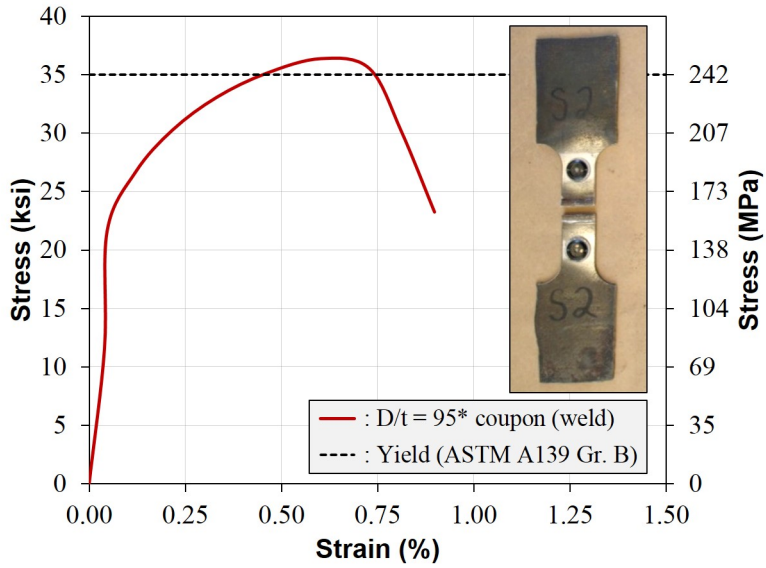

Figure 10-73 Tension test results of spiral weld coupon with D/t = 95*

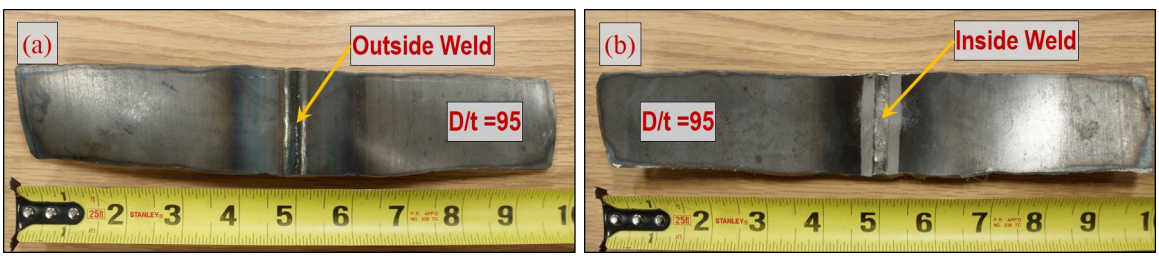

Figure 10-74 Steel tube coupon with D/t = 95: (a) outside, and (b) inside surface

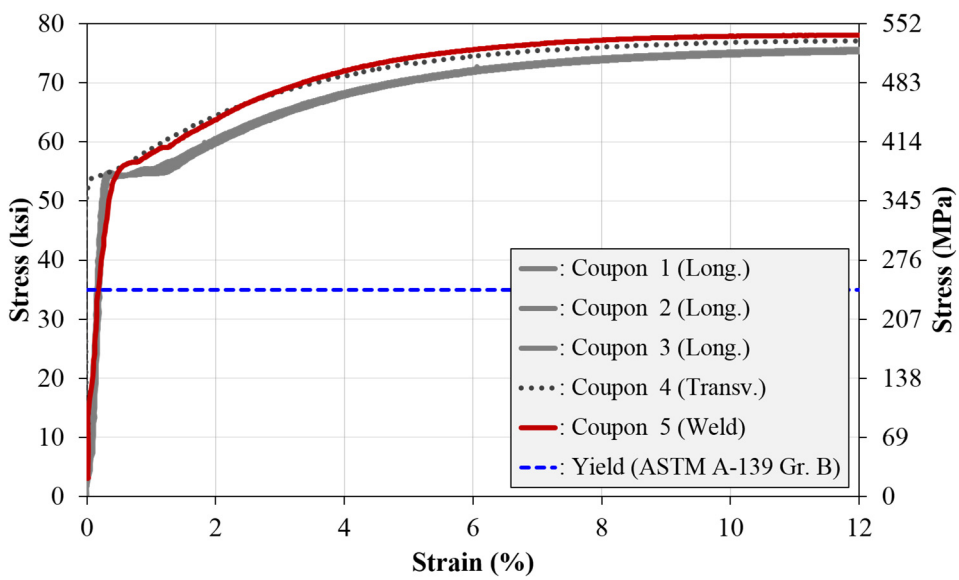

Figure 10-75 Tension test results of coupons with D/t = 95

Test 5 Summary Report

October 16, 2015

Prepared for

Alaska Department of Transportation

Alaska University Transportation Center

Project Team

RA: Diego Aguirre

PIs: Mervyn Kowalsky, James Nau, Mo Gabr

Other Senior Personnel: Greg Lucier, Ben Smith

North Carolina State University

Executive Summary

Test 5 was conducted September 28th, 2015 at the North Carolina State University Constructed Facilities Laboratory. The tested pile-column specimen was a reinforced concrete filled steel tube with a diameter-to-thickness (D/t) ratio of 95. No surcharge was applied to the soil, thus the soil stiffness was not modified. The test was successfully conducted to failure, which was caused by a combination of tube local buckling and tube fracture, resulting in a large strength degradation (~44.53%) in the third cycle at ductility level 4.0 (μ_4).

Specimen and Test Description

Test 5 consisted of a 19-foot-5-inch long, reinforced concrete filled, 12-3/4-inch diameter spirally welded steel tube without skelp or splice welds. The pile-column specimen was embedded 13 ft. – 9 in. into clean sand in the soil-structure interaction facility at the NCSU-CFL. Lateral load was applied at the pinned connection at the top of the pile specimen by means of a 100-kip, 70-inch stroke hydraulic actuator. The nominal wall thickness of the tube was 0.128 in., providing a nominal diameter-to-thickness ratio (D/t) of 95. The test was conducted with a 5-foot-8.25-inch cantilever length, measured from the soil surface to the point at which the lateral load was applied. Figure 10-76 and Figure 10-77 present a schematic of the test setup (elevation) and the specimen #5 cross-section, respectively, while

Figure 10-78 shows the instrumentation used for testing. A photograph of the test setup is included in Figure 10-79.

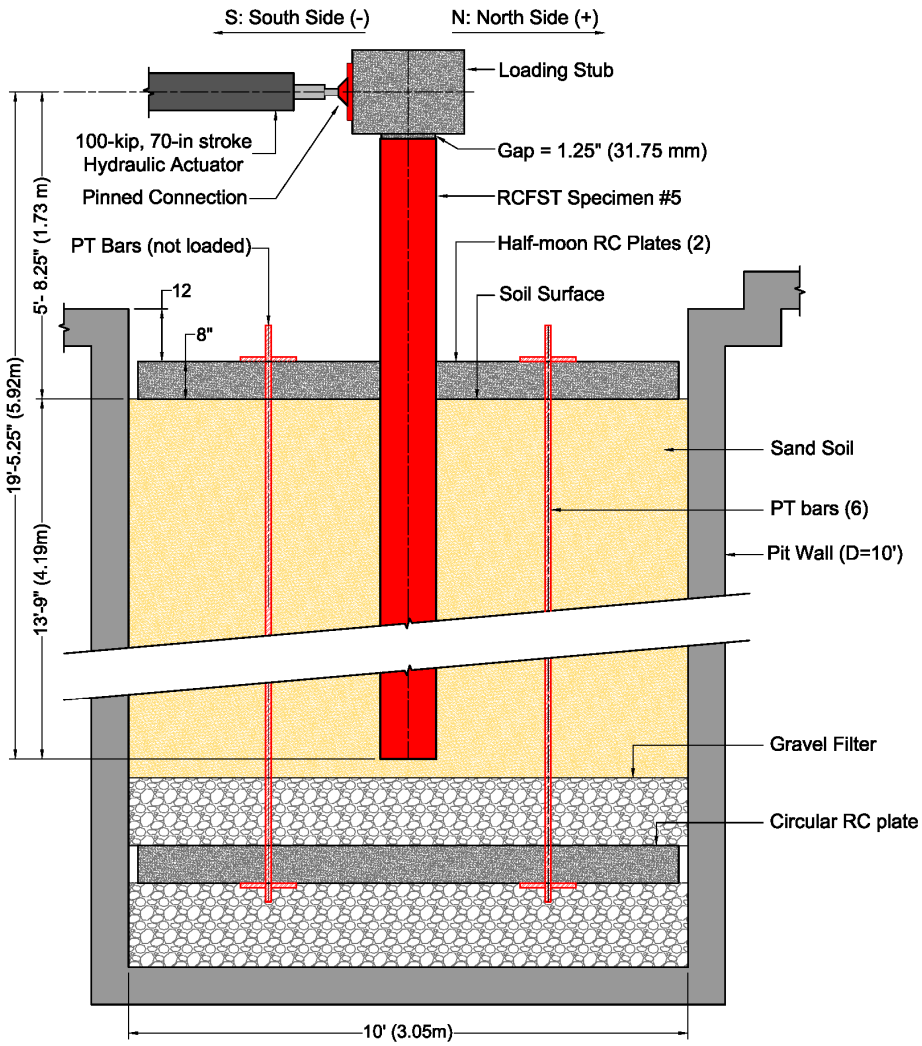

Figure 10-76 Test 5: test setup elevation schematic

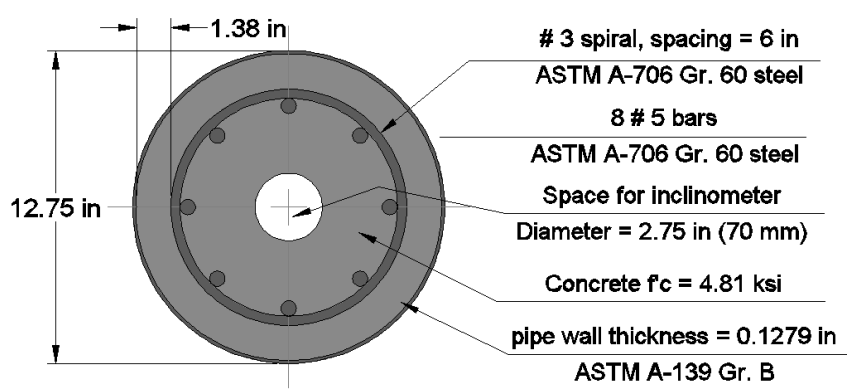

Figure 10-77 Test 5: RCFST specimen cross section

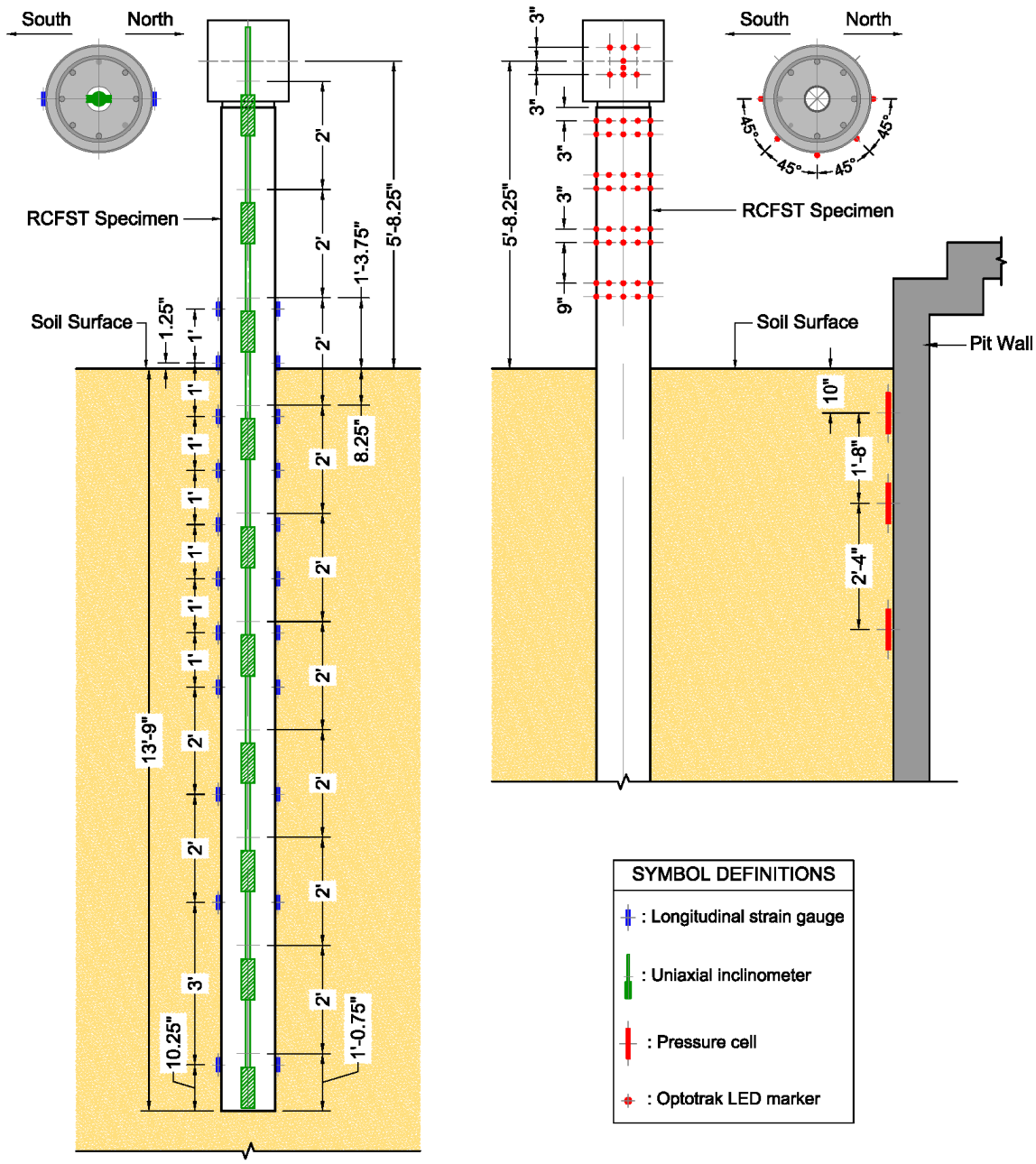

Figure 10-78 Test 5: instrumentation

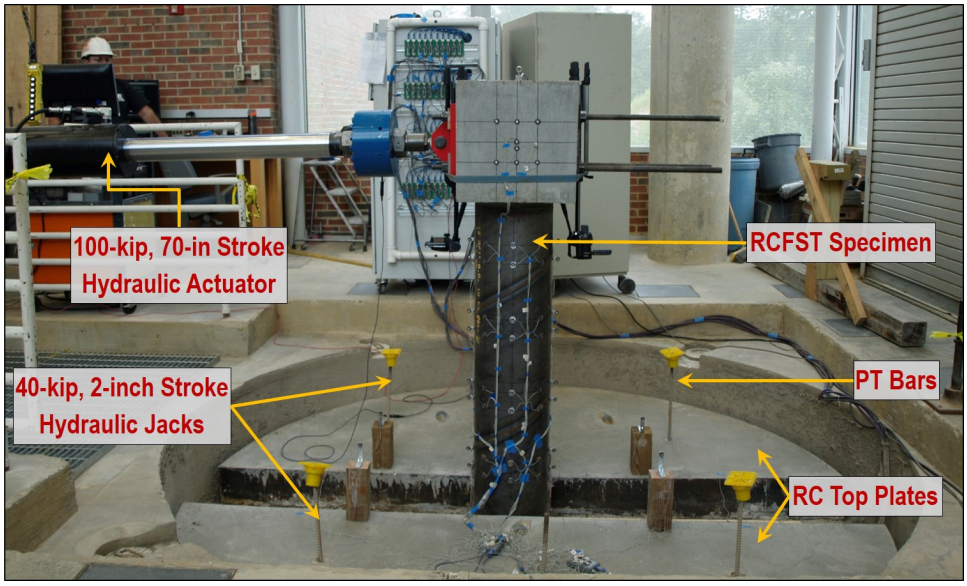

Figure 10-79 Test 5: pinned-head, RCFST pile-column test setup

Material properties were determined by in-house material tests. The yield and ultimate stresses of the steel tube were 54.3 ksi and 75.6 ksi, respectively, based on tests conducted on three (3) coupons cut from the end of the test pile specimen. The yield and ultimate stresses of the ASTM A706 Grade 60 longitudinal reinforcement were 70.7 ksi and 99.6 ksi, respectively, based on tests conducted on six (6) bar specimens from the same heat of the longitudinal reinforcement. The yield and ultimate stresses of the spiral reinforcement were 64.6 ksi and 95.3 ksi, respectively, based on tests conducted on six (6) bar specimens from the same heat of the transverse reinforcement. An average concrete compressive strength of 4.81 ksi (standard deviation of ± 0.32 ksi) was determined from three (3) compression tests of 4”x8” concrete cylinders.

Soil properties were also determined by in-house material tests. Based on a measured particle size distribution, the soil was classified as poorly-graded sand (SP). The unit weight, friction angle, and moisture content (γ = 90 pcf, ϕ = 35°, and w = 2.5%, respectively) were reasonably assumed based upon results of previous tests. Active surcharge was not applied, so only the self-weight of the half-moon RC plates was acting in the soil surface (i.e., ~100 psf).

The load history applied to the pile specimen consisted of standard three-cycle sets intended to evaluate both the elastic and inelastic response of the specimen. The first portion (i.e., pile elastic response up to first yield) of the test consisted of single reversed, displacement-controlled cycles, ramping up to the first yield displacement in ¼ increments. Given the non-linear response from the beginning of the test due to the characteristic soil behavior, target displacements in this portion of the test were determined based on the results of a monotonic pushover analysis performed using a detailed non-linear, fiber-based, finite element model developed using the OpenSees framework software. Soil-structure interaction was included by means of non-linear springs at 1-foot interval depths, with spring properties assigned based on p-y curves.

The first yield force (F_y) and nominal force (F_n), which is defined as the force at a concrete compressive strain of 0.004 or at a tube/bar tensile strain of 0.015 (whichever occurs first), were determined based upon tensile and compressive strains, monitored during the numerical simulation (i.e., pushover analysis), as 14.51 kips and 21.71 kips, respectively. Table 10-5 summarizes the target displacements for the first portion of the test. After the first portion of the test was completed, the measured average strain at the predicted first yield displacement ($\Delta'y$ = 3.77 in) was 1510 ($\mu\varepsilon$), which correlates well with the tube yield strain (εy = 1870 $\mu\varepsilon$). The measured average displacement at the first yield displacement ($\Delta'y$ = 3.77 in) was modified by the nominal-to-first yield force ratio in order to determine the displacement ductility level 1.0 (μ_1 = 5.64 in), as shown in Equation 10-10. The remainder of the test was completed using reversed three-cycle sets in displacement-controlled increments at different levels of displacement ductility until failure, as shown in Equation 10-11. The entire displacement and load histories can be seen in Figure 10-80. Positive loads and displacements correspond to rightward (North) motion of the pile in the test setup. The positive legs of all cycles were completed before the negative legs.

Table 10-5 Test 5: predictions for elastic portion

Performance Level	Displacement (in)	Force (in)
1/4 $\Delta y'$	0.77	4.29
1/2 $\Delta y'$	1.65	8.11
3/4 $\Delta y'$	2.66	11.52
1 $\Delta y'$	3.77	14.51

$$\Delta_y = \mu_1 = \Delta'_y \cdot \frac{F_n}{F_y} = 3.77\,in \cdot \frac{21.71\,kip}{14.51\,kip} = 5.64\ in \qquad \text{Equation 10-10}$$

$$\mu_i = i \cdot \mu_1 \rightarrow i = 1.0,\ 1.5,\ 2.0,\ 3.0,\ 4.0,\ 5.0 \qquad \text{Equation 10-11}$$

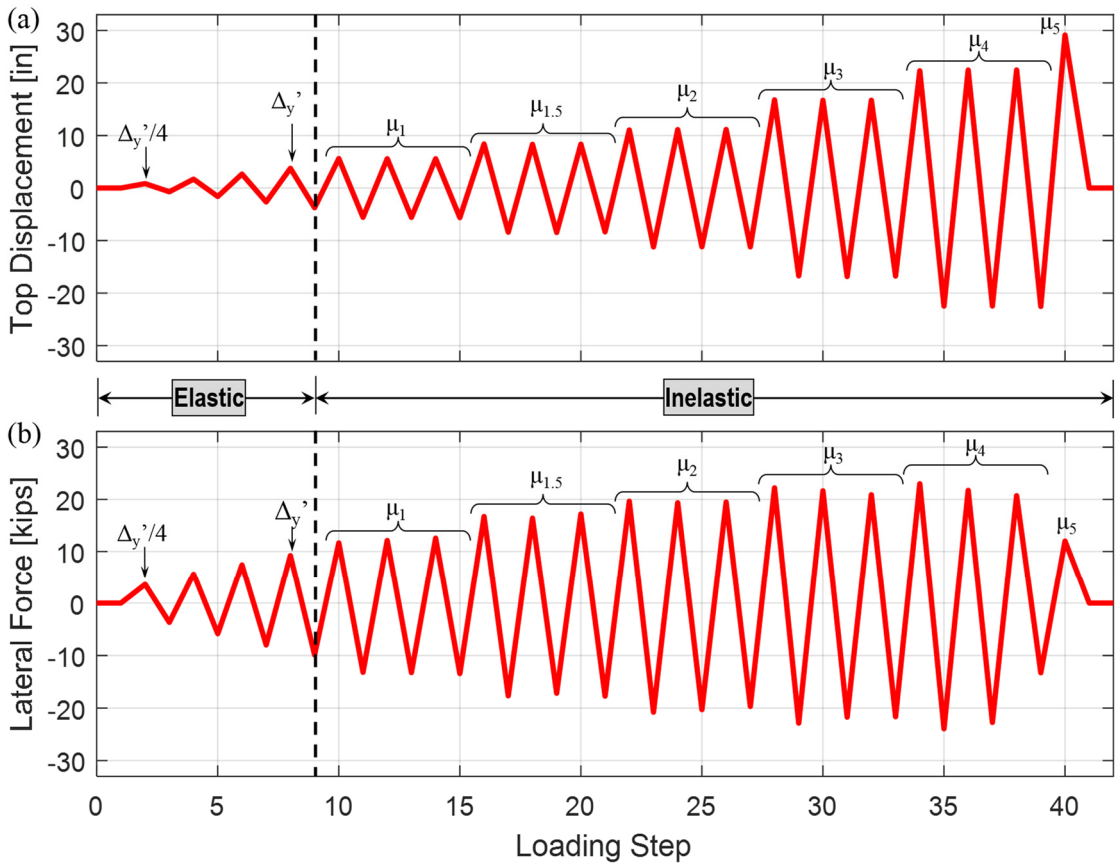

Figure 10-80 Test 5: (a) displacement and (b) loading histories

Specimen Response

Specimen #5 performed well through the elastic portion of the test and during all three cycles of ductility level 3.0 (μ_3). It is believed that the onset of tube buckling occurred early during the displacement cycles at ductility level 1.5 ($\mu_{1.5}$) as some of the strain gauges located on the both sides of the pile indicated large values during both push and pull cycles at the aforementioned ductility level. A significant loss of strength, indicating failure, occurred during the third pull cycle at ductility level 4.0 (μ_4). Figure 10-81 and Figure 10-82 present the lateral force vs. top displacement response and envelopes, respectively. It can be seen that the system has a characteristic large energy dissipation capacity due to both damping sources, that is, the pile itself and the surrounding soil. In addition, it can be clearly seen from both figures that a significant loss of strength (~44.5%) occurred during the third cycle of ductility level 4.0 (μ_4). Moreover, the specimen was subjected to an additional push cycle at ductility level 5.0 (μ_5) which also resulted in loss of strength (47.7%).

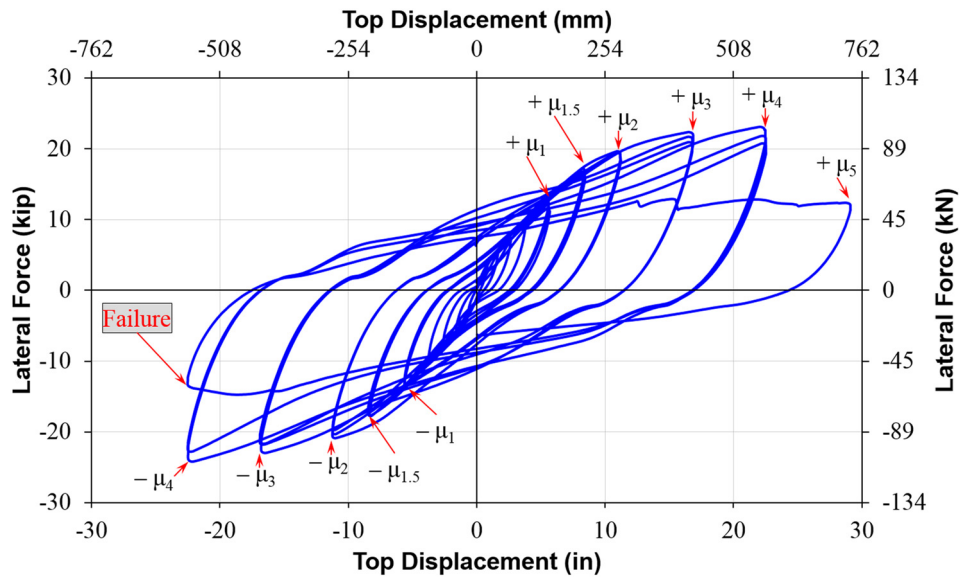

Figure 10-81 Test 5: lateral force vs. top displacement response

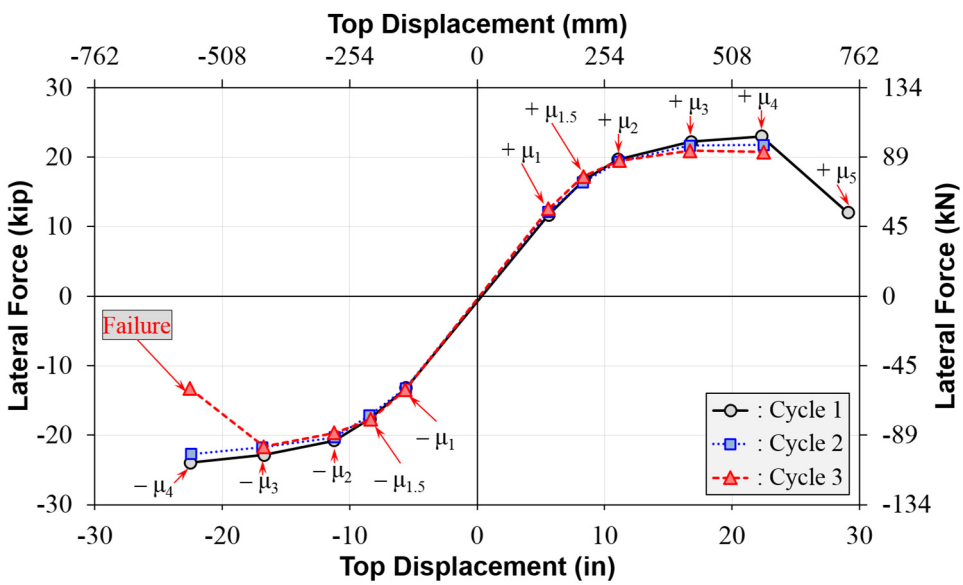

Figure 10-82 Test 5: lateral force vs. top displacement envelopes

Figure 10-83 presents the deformed shape and the soil-pile gaps at zero displacement after the elastic portion of the test was conducted; the size of the gap was ~1.5 in on both sides of the specimen. As it was previously explained, at this point of the test strain profiles on the sides of the pile were verified in order to further conduct the test at the aforementioned ductility levels. Figure 10-84 presents the strain profiles recorded during the first portion of the test. Note that tensile strains of 1460 (με) and 1510 (με) were recorded in the pipe during the push and pull cycles, respectively, when the predicted first yield displacement was imposed to the system. Based on the rotation data recorded with the inclinometer placed inside the pile along its length, specimen curvature, rotation, and displacement profiles are presented in Figure 10-85 and Figure 10-86 for the first push and pull cycles, respectively. Note that there are small rotations and displacements at the pile tip which indicates that there is a point of rotation (at ~10 ft.) rather than a point of fixity; inelastic action was developed in the pile nonetheless. The circles in the top portion of the displacement profiles in Figure 10-85 and Figure 10-86 represent the Optotrak LED markers; note that they are in agreement with the calculated displacement profiles. In Figure 10-84 through Figure 10-86 the symbols N and S in the legend refer to the North and South sides, Δ_y' is the first yield displacement, $Ø_y'$ stands for the first yield curvature , and a depth equal to 0 ft. represents the soil surface.

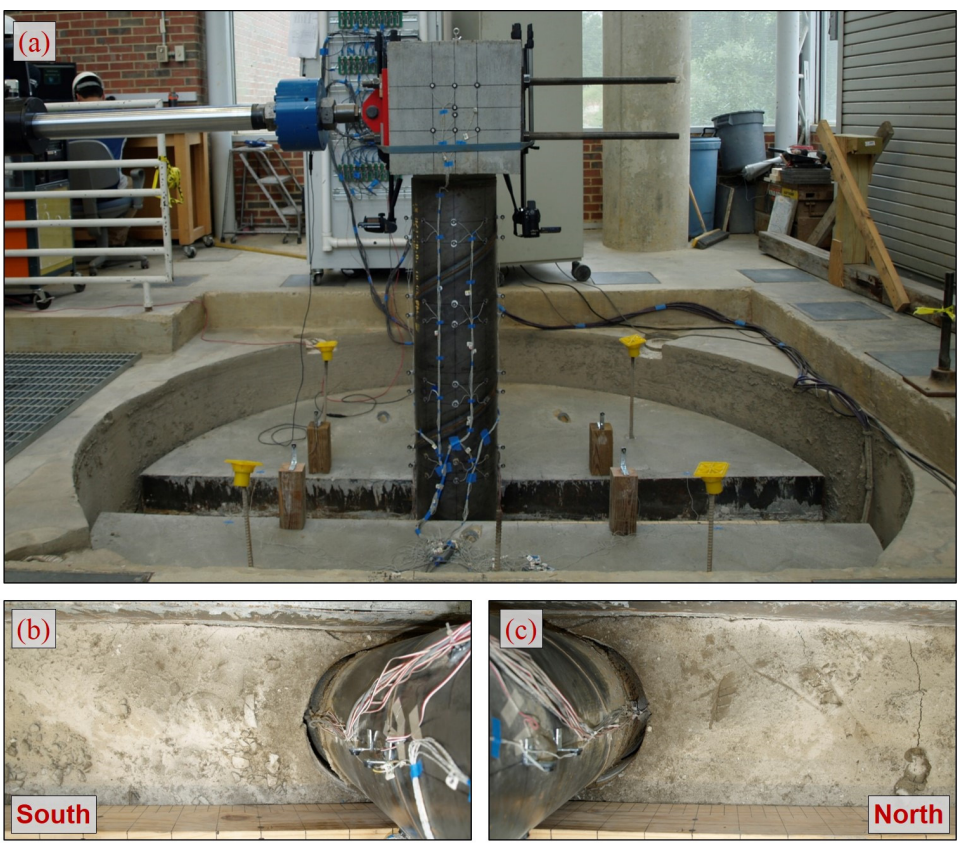

Figure 10-83 Test specimen #5 after the elastic portion was completed: (a) deformed shape, (b) South side and (c) North side

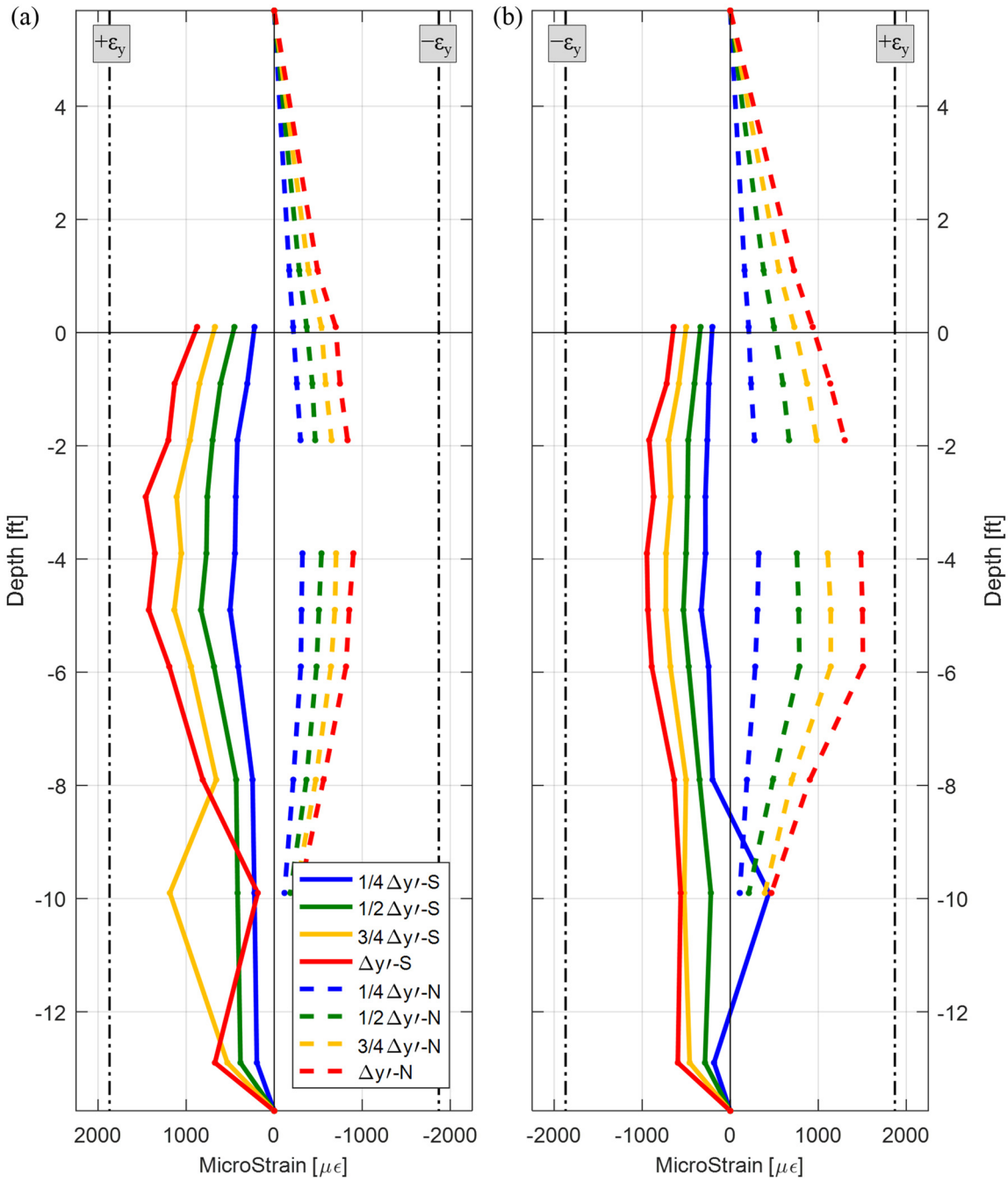

Figure 10-84 Test 5: strain profiles from elastic (a) push and (b) pull cycles

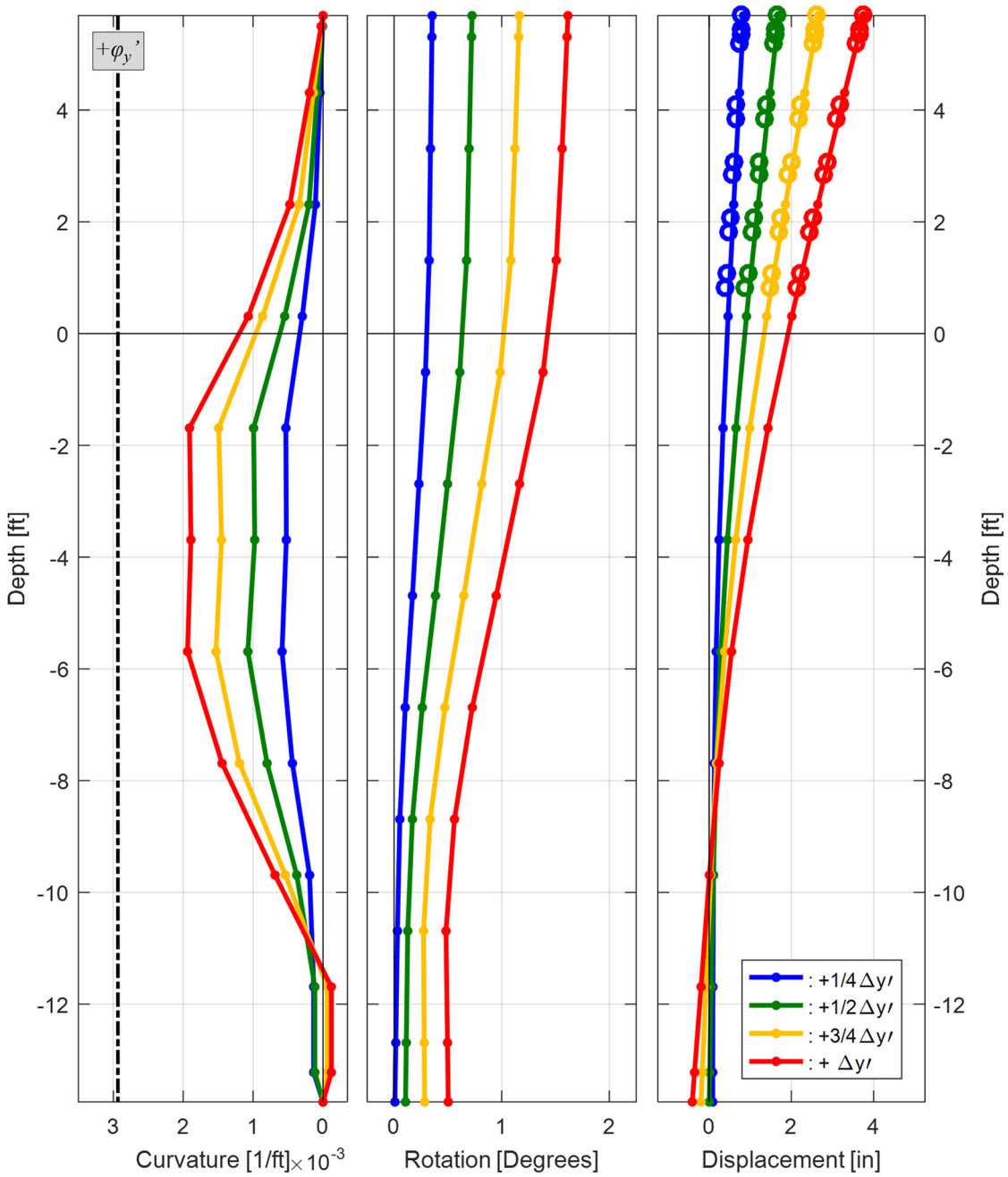

Figure 10-85 Test 5: curvature, rotation, and displacement profiles (elastic push cycles)

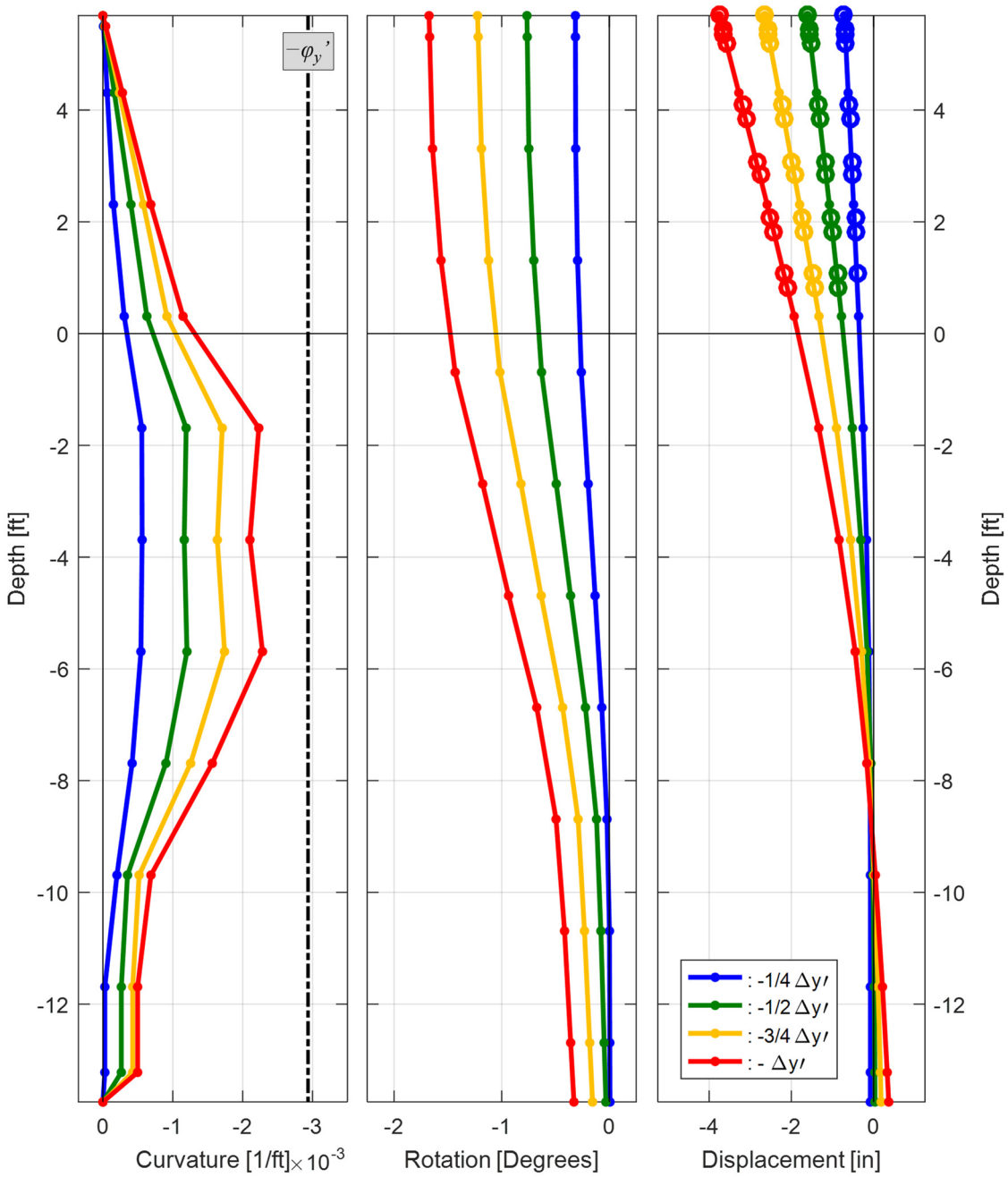

Figure 10-86 Test 5: curvature, rotation, and displacement profiles (elastic pull cycles)

As the test continued, the gap on the sides of the pile increased in size as the displacement ductility level increased. Minor loss of strength was observed up until all ductility level 3.0 (μ_3) cycles. The specimen failure (Figure 10-87) occurred at the third cycle load at ductility 4.0 (μ_4) when a significant drop in the force in the actuator was observed (i.e., ~44.5%). An additional push cycle load at ductility 5.0 (μ_5) was applied in order to evaluate bar rupture after failure. Sounds indicating steel fracture were heard at the same time when the strength loss occurred, indicating probable rebar or tube fracture. Moreover, a twist rotation of the pile occurred for all push cycles at ductility level 4.0 (μ_4). Finally, the test was terminated and the specimen was taken to zero displacement in order to facilitate its extraction from the soil.

Figure 10-88 presents the strain profiles for the first push and pull cycles at different displacement ductility levels. Notice that the largest tensile and compressive strains in the tube were recorded at a depth between 1 ft. and 5 ft. In Figure 10-88 the symbols N and S in the legend refer to the North and South sides, and μ is the displacement ductility level. Curvature, rotation, and displacement profiles are presented in Figure 10-89 and Figure 10-90 for the first push and pull cycles, respectively. Note that the point of rotation for the inelastic is located at a depth of ~3.5 ft., which correlates well with the position of the observed plastic hinge, determined after the test was completed.

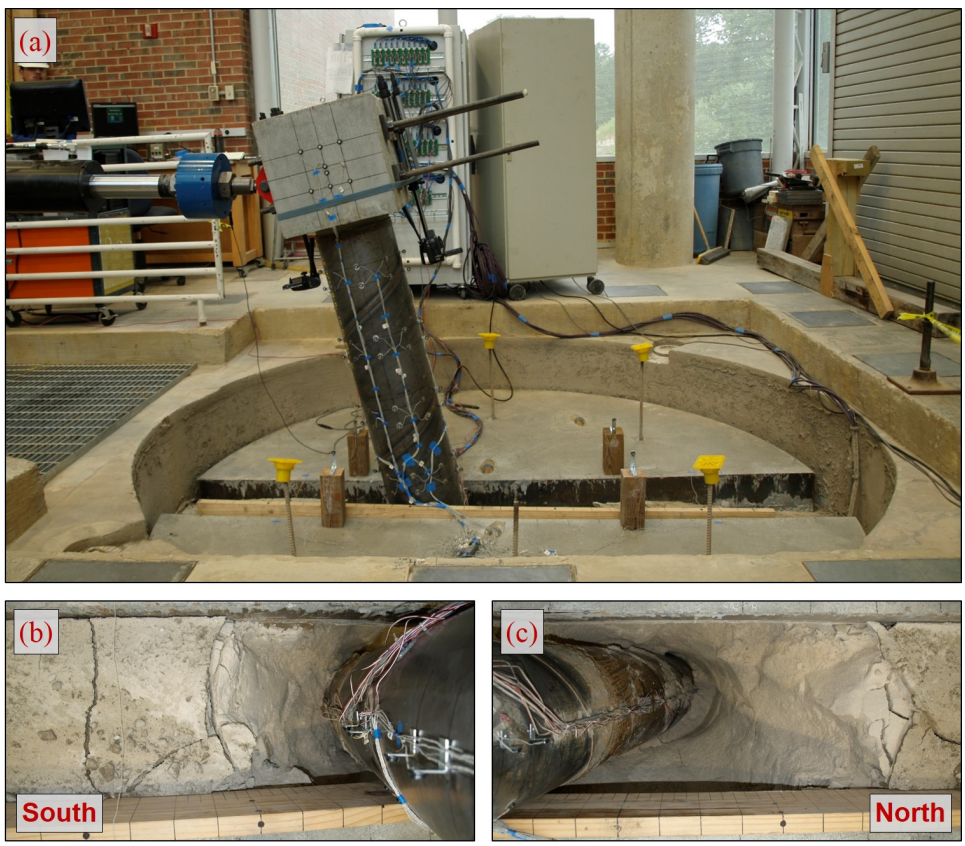

Figure 10-87 Test specimen #5 at maximum displacement: (a) deformed shape, (b) South side and (c) North side

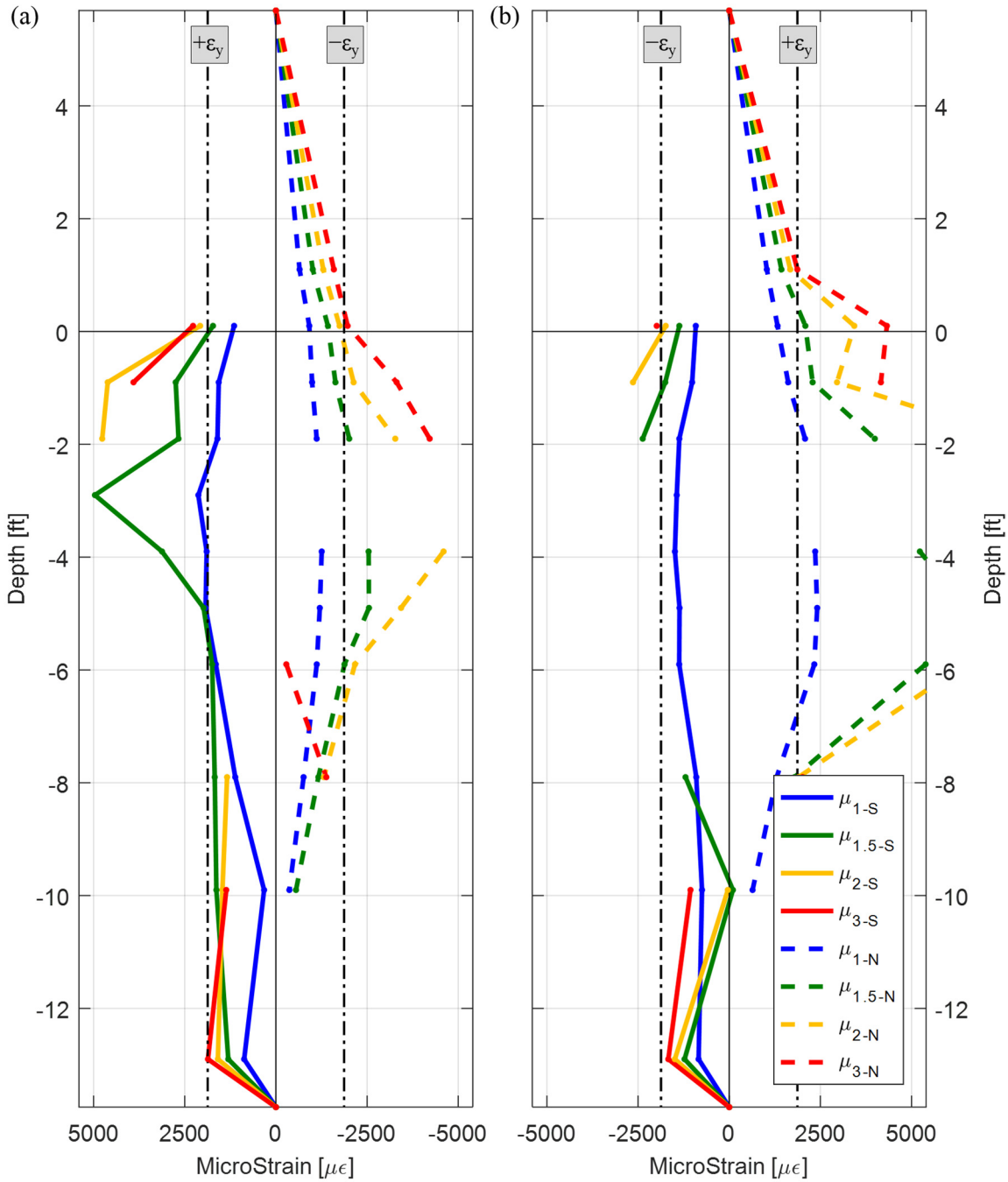

Figure 10-88 Test 5: strain profiles from inelastic (a) push and (b) pull cycles

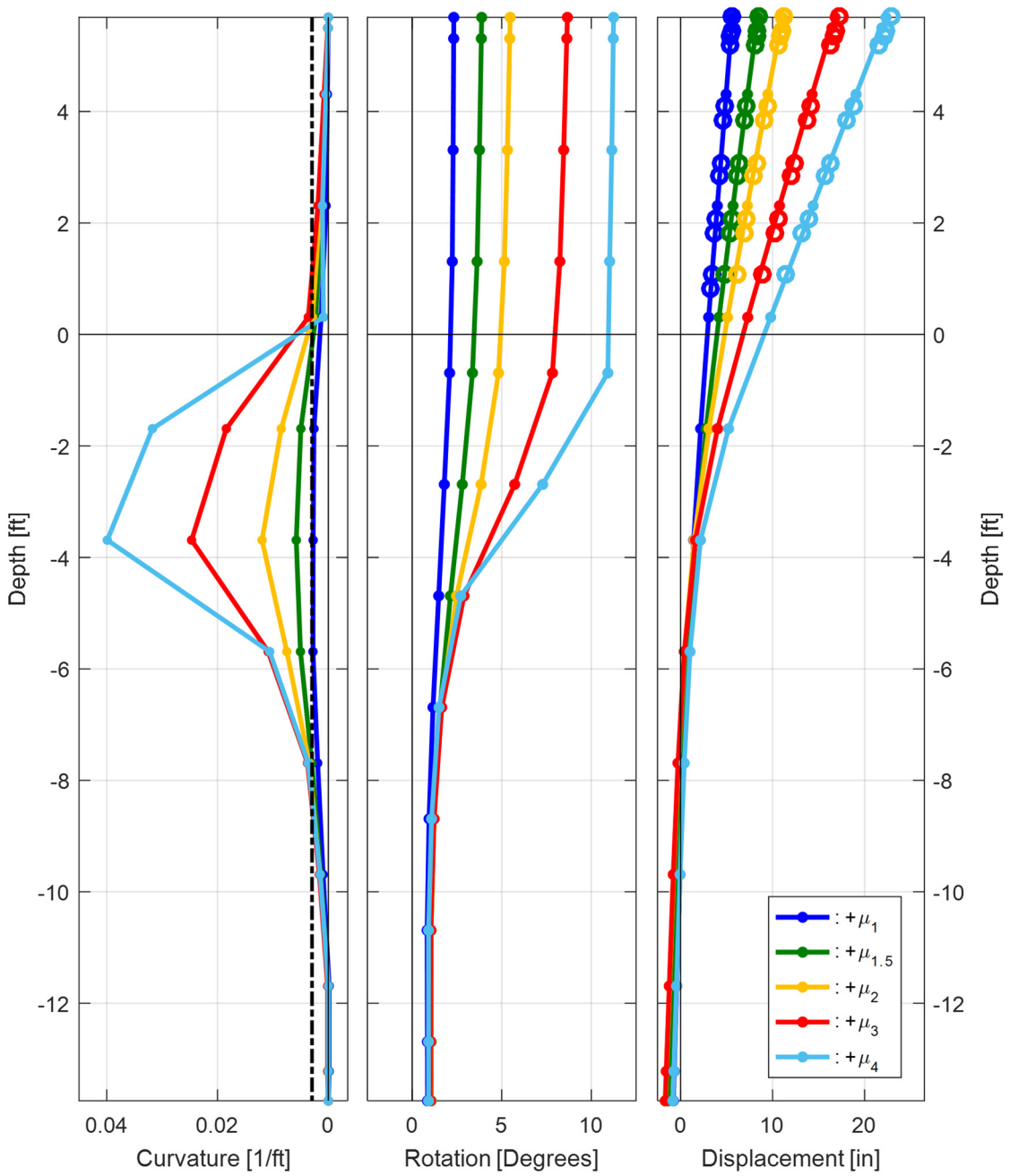

Figure 10-89 Test 5: curvature, rotation, and displacement profiles (inelastic push cycles)

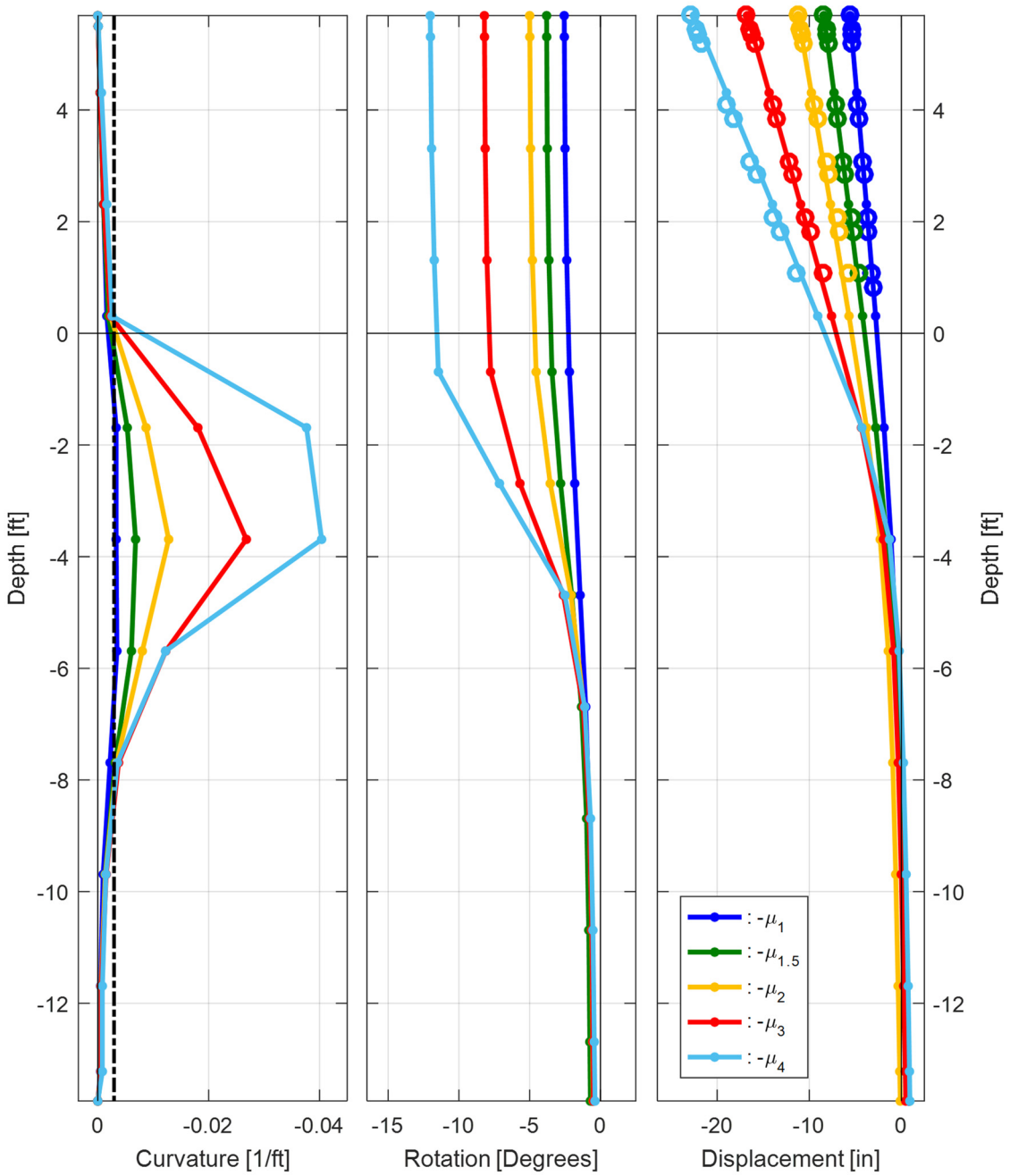

Figure 10-90 Test 5: curvature, rotation, and displacement profiles (inelastic pull cycles)

Figure 10-91 shows the state of the soil surface after the test was completed. Notice that despite the presence of the half-moon RC plates in the surface, deformations in the soil are large and followed an expected oval-shaped surface failure in which active and passive pressures developed around the pile. This surface extended ~19.5 in. on both sides of the direction of loading and ~16 in. on the perpendicular direction. The total average settlement of the RC plates was ~1.8 in. This value was averaged based on the vertical displacement of 4 points on the RC plates. Figure 10-92 shows the average settlement of the half-moon RC plates during the test as a function of the imposed displacements at the top of the pile. Note that, as the displacement history is applied, the settlement increases, though its magnitude is larger at the beginning of the test.

Figure 10-91 Test 5: soil surface after testing

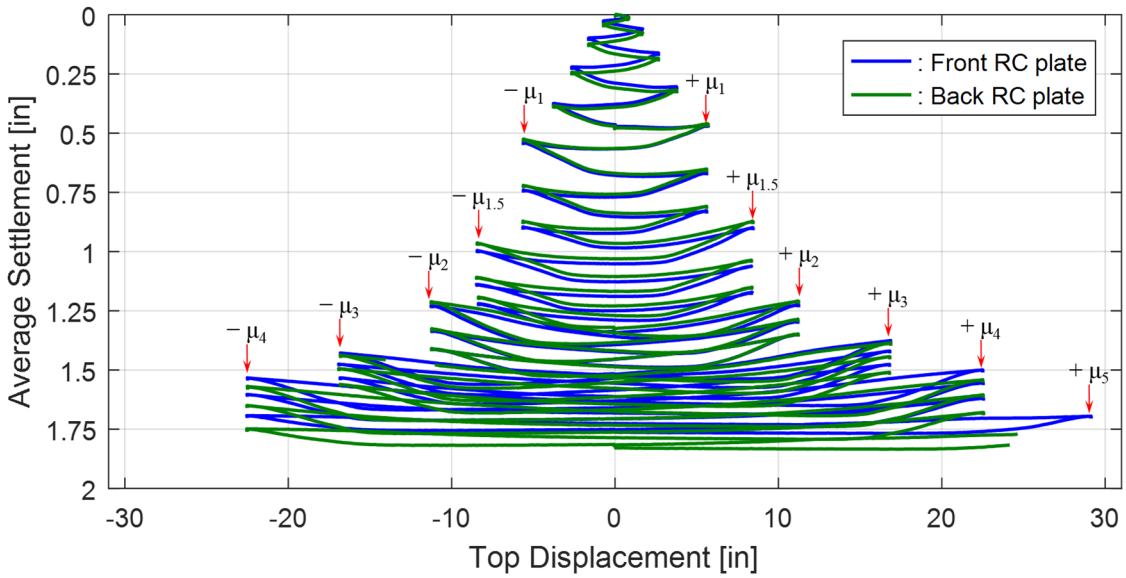

Figure 10-92 Test 5: half-moon RC plate settlement during testing

Figure 10-93 through Figure 10-97 present the damage observed after the pile was extracted from the soil. As thought during the test, tube fracture, tube buckling, and bar buckling did occur; bar fracture was not observed. It can be seen that tube local buckling developed on both sides of the specimen. The sections with the largest buckling occurred at a depth of 3 ft. – ¼ in. and 2 ft. – 10 in. on the North and South sides of the specimen, respectively, which means that the plastic hinge developed at an average depth of 2 ft. – 11-1/8 in. with respect to the soil surface.

Tube fracture (Figure 10-93) occurred on both sides of the specimen and it extended about half of the cross-section perimeter, resulting in a significant drop in strength due to lost tension capacity. As a consequence, after rupture, tension capacity is provided by the longitudinal reinforcement, which has a smaller area in comparison with that provided by the tube, inducing high stresses and deformations. Upon further investigations, bar buckling was observed on the South side of the specimen; it is believed that this occurred when tube fracture developed on the North side during the last pull cycle at ductility level 4.0 (μ_4). Note that tube fracture occurred in the section with the largest local buckling, in which deformations protruded ~7/8 in. and ~1/2 in. on the North and South sides of the pile, respectively. Several minor buckled regions were observed equally spaced (~6 in.) on both sides of the specimen, next to the main buckled regions. Figure 10-94 presents measurements of the secondary buckled regions. It can be seen that the deformations due to buckling protruded ~3/8 in. and ~1/4 in. on the North and South sides of the specimen, respectively.

In order to further investigate the significant strength loss and to verify whether bar fracture or buckling occurred, a portion of the tube (i.e., 10 in. x 12 in.) was removed at the ruptured section in the extreme fiber on both sides of the pile (Figure 10-95 and Figure 10-96). It can be seen that several cracks developed in this area of the concrete, perpendicular to the longitudinal direction of the specimen. Note also that the concrete cracking extended further to the center of the section. Note that concrete cracking only occurred close to the section of tube fracture; concrete cracks beyond the spiral are not observed. On the other hand, bar buckling was observed in three longitudinal bars on the South side of the specimen (Figure 10-97). It is believed that this occurred during the last pull cycle at ductility level 4.0 (μ_4) while tube fracture developed on the North side of the pile. Similarly to the concrete cracking, note that bar buckling occurred only in the section of the largest crack in the concrete, located beneath the ruptured section of the tube. Beyond the visible spiral (to the left in Figure 10-97) the longitudinal bars do not have deformations due to buckling.

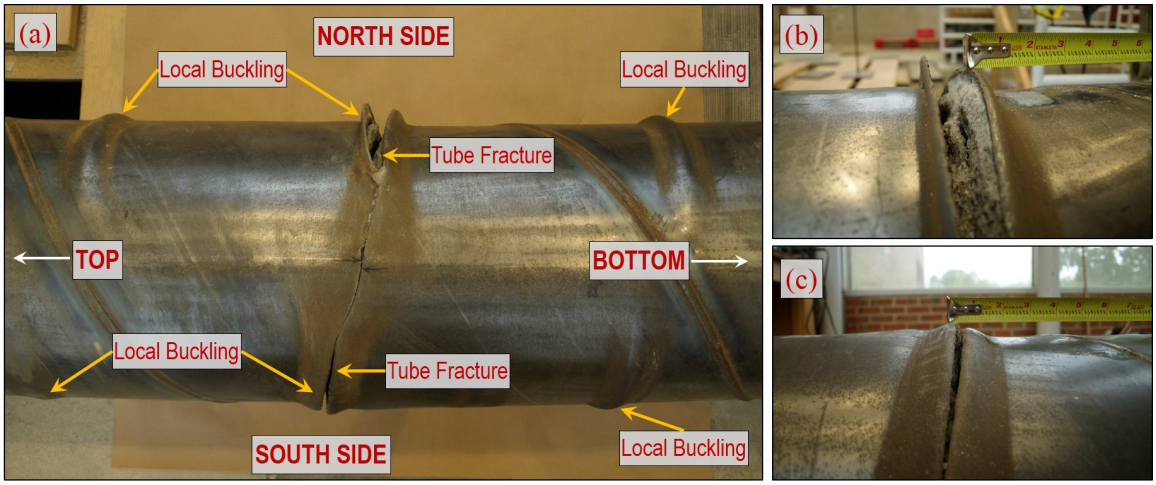

Figure 10-93 Test 5: (a) Final observed damage, (b) tube fracture, and (c) tube local buckling

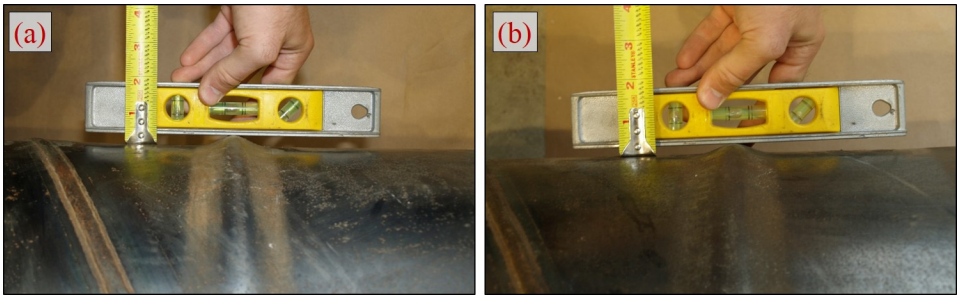

Figure 10-94 Test 5: secondary buckled sections on (a) North side and (b) South side

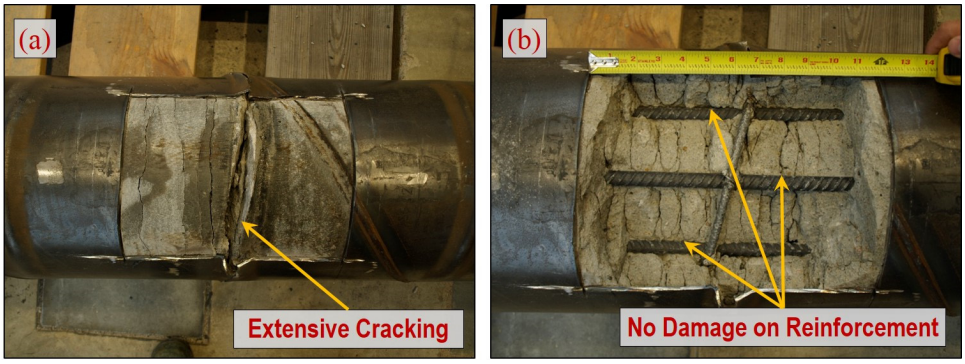

Figure 10-95 Test 5: observed damage in (a) concrete and (b) internal reinforcement on North side

Figure 10-96 Test 5: observed damage in (a) concrete and (b) internal reinforcement on South side

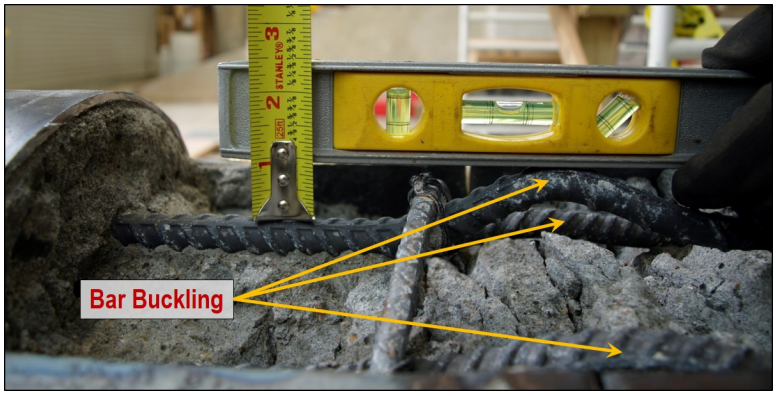

Figure 10-97 Test 5: observed bar buckling on South side

Conclusions

Test specimen #5 showed a reliable response through all ductility 3.0 (μ_3) cycles. It is believed that onset of tube local buckling occurred early during the test at a ductility level of 1.5 ($\mu_{1.5}$), when large tensile strains were recorded. The test specimen completed all cycles of ductility 3.0 (μ_3) with minor loss of strength. A significant drop in strength occurred at displacement ductility level 4.0 (μ_4) when tube fracture developed on the North side of the specimen during the third pull cycle at this level. Further investigations revealed that failure occurred due to a combination of tube local buckling, tube fracture, and bar buckling. It is believed that this particular specimen is capable of having a reliable displacement up to ductility 3.0 (μ_3). The main buckles as well as tube fracture did not occur over the spiral weld, so the spiral welds do not appear to negatively influence the behavior.

Test 6 Summary Report

November 4, 2015

Prepared for

Alaska Department of Transportation

Alaska University Transportation Center

Project Team

RA: Diego Aguirre

PIs: Mervyn Kowalsky, James Nau, Mo Gabr

Other Senior Personnel: Greg Lucier, Ben Smith

North Carolina State University

Executive Summary

Test 6 was conducted October 21st, 2015 at the North Carolina State University Constructed Facilities Laboratory. The tested pile-column specimen was a reinforced concrete filled steel tube with a diameter-to-thickness (D/t) ratio of 95. A surcharge of ~960 psf was applied to the soil prior to and during the test, thus the soil stiffness was expected to change. The test was successfully conducted to failure, which was caused by a combination of tube local buckling and tube fracture, resulting in a large strength degradation (~34.67%) in the third cycle at ductility level 4.0 (μ_4).

Specimen and Test Description

Test 6 consisted of a 19-foot-5.25-inch long, reinforced concrete filled, 12-3/4-inch diameter spirally welded steel tube without skelp or splice welds. The pile-column specimen was embedded 13 ft. – 6.75 in. into clean sand in the soil-structure interaction facility at the NCSU-CFL. Lateral load was applied at the pinned connection at the top of the pile specimen by means of a 100-kip, 70-inch stroke hydraulic actuator. The nominal wall thickness of the tube was 0.134 in., providing a nominal diameter-to-thickness ratio (D/t) of 95. The test was conducted with a 5-foot-10.5-inch cantilever length, measured from the soil surface to the point at which the lateral load was applied. Figure 10-98 and Figure 10-99 present a schematic of the test setup (elevation) and the specimen #6 cross-section,

respectively, while Figure 10-100 shows the instrumentation used for testing. A photograph of the test setup is included in Figure 10-101.

Material properties were determined by in-house material tests. The yield and ultimate stresses of the steel tube were 54.3 ksi and 75.6 ksi, respectively, based on tests conducted on three (3) coupons cut from the end of the test pile specimen. The yield and ultimate stresses of the ASTM A706 Grade 60 longitudinal reinforcement were 70.7 ksi and 99.6 ksi, respectively, based on tests conducted on six (6) bar specimens from the same heat of the longitudinal reinforcement. The yield and ultimate stresses of the spiral reinforcement were 64.6 ksi and 95.3 ksi, respectively, based on tests conducted on six (6) bar specimens from the same heat of the transverse reinforcement. An average concrete compressive strength of 6.58 ksi (standard deviation of ± 0.37 ksi) was determined from three (3) compression tests of 4”x8” concrete cylinders.

Soil properties were also determined by in-house material tests. Based on a measured particle size distribution, the soil was classified as poorly-graded sand (SP). The unit weight and friction angle (γ = 90 pcf, ϕ = 35°, respectively) were reasonably assumed based upon results of previous tests. The moisture content (w = 2.34%) was measured on October 16th, 2015. An active surcharge was applied to the soil surface during the test by means of 40-kip, 2-inch stroke hydraulic jacks reacting on the half-moon RC plates. An axial load of 10.1 kips was applied to each of the six (6) PT bars, resulting in a surcharge pressure of q = 960 psf. In addition to the active pressure, the self-weight of the half-moon RC plates was acting on the soil surface as well (i.e., ~100 psf).

In an attempt to modify the soil properties prior to pile testing, four surcharge cycles were performed. The first three cycles were conducted using 80% of surcharge level to be applied during the test, i.e. q = 768 psf. The remaining cycle was applied using the same surcharge level to be applied during the test, i.e. q = 960 psf. All surcharge cycles were applied one day prior to pile testing, that is, on October 20th, 2015. Cycles 1 through 3 were applied without sustaining the pressure, namely, they were load-unload cycles which took approximately 30 minutes each. The fourth surcharge cycle was then applied and the pressure was sustained all the way until the pile testing was completed. The average settlement of the RC plates prior the pile testing was ~0.83 in. This value was averaged based on the vertical displacement of 4 points on the RC plates. Results of the surcharge cycles are presented in Figure 10-102.

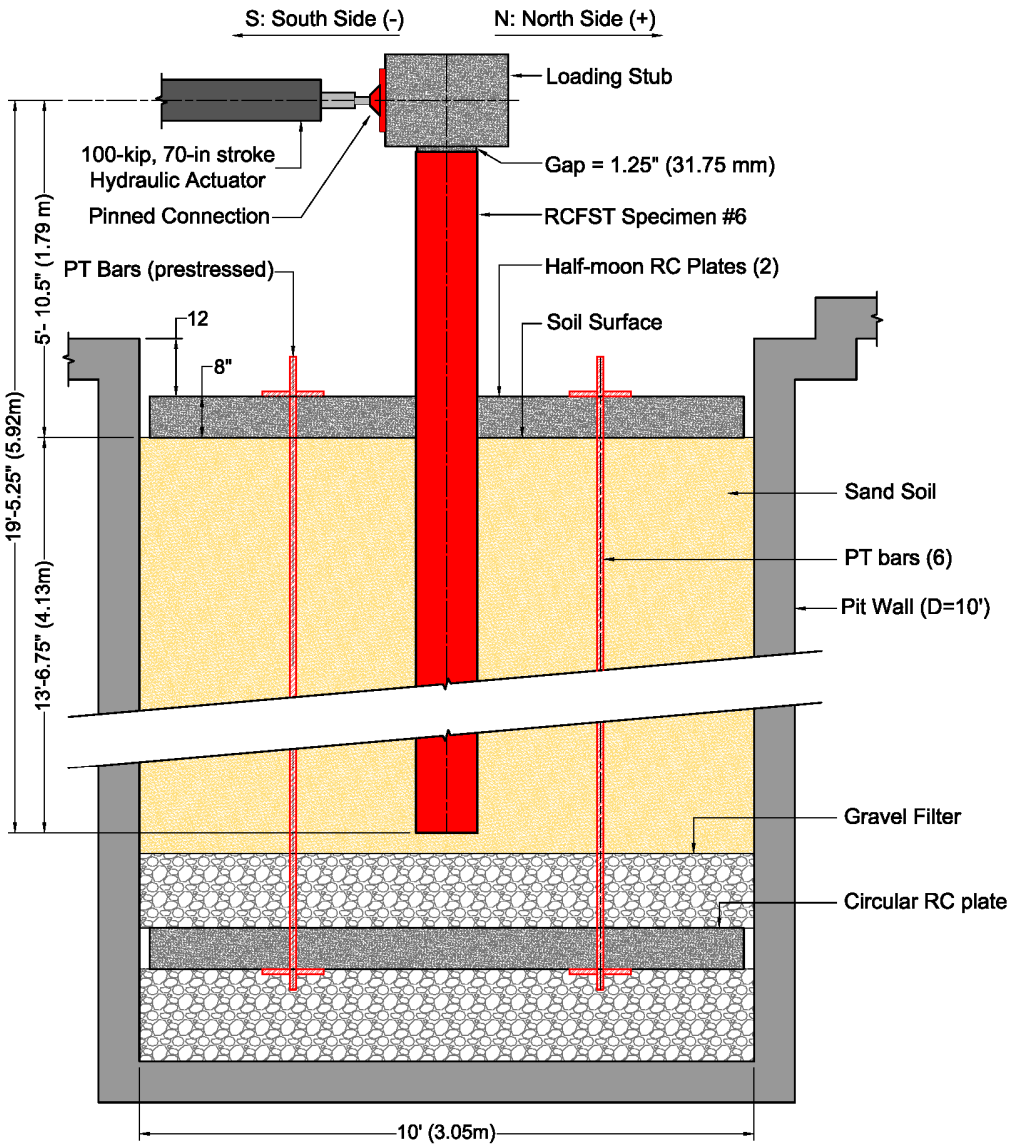

Figure 10-98 Test 6: test setup elevation schematic

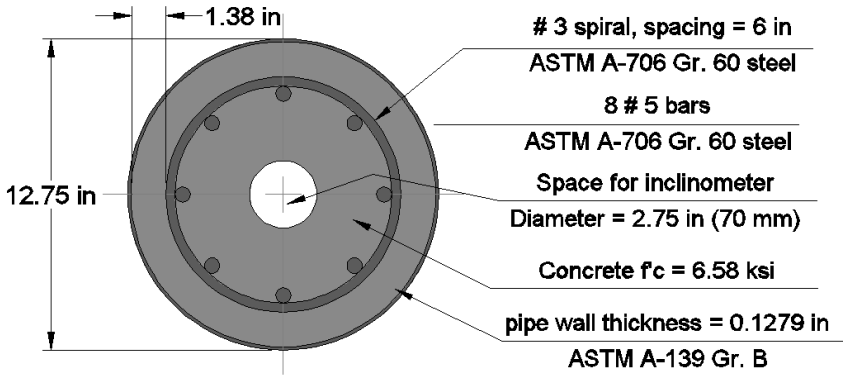

Figure 10-99 Test 6: RCFST specimen cross section

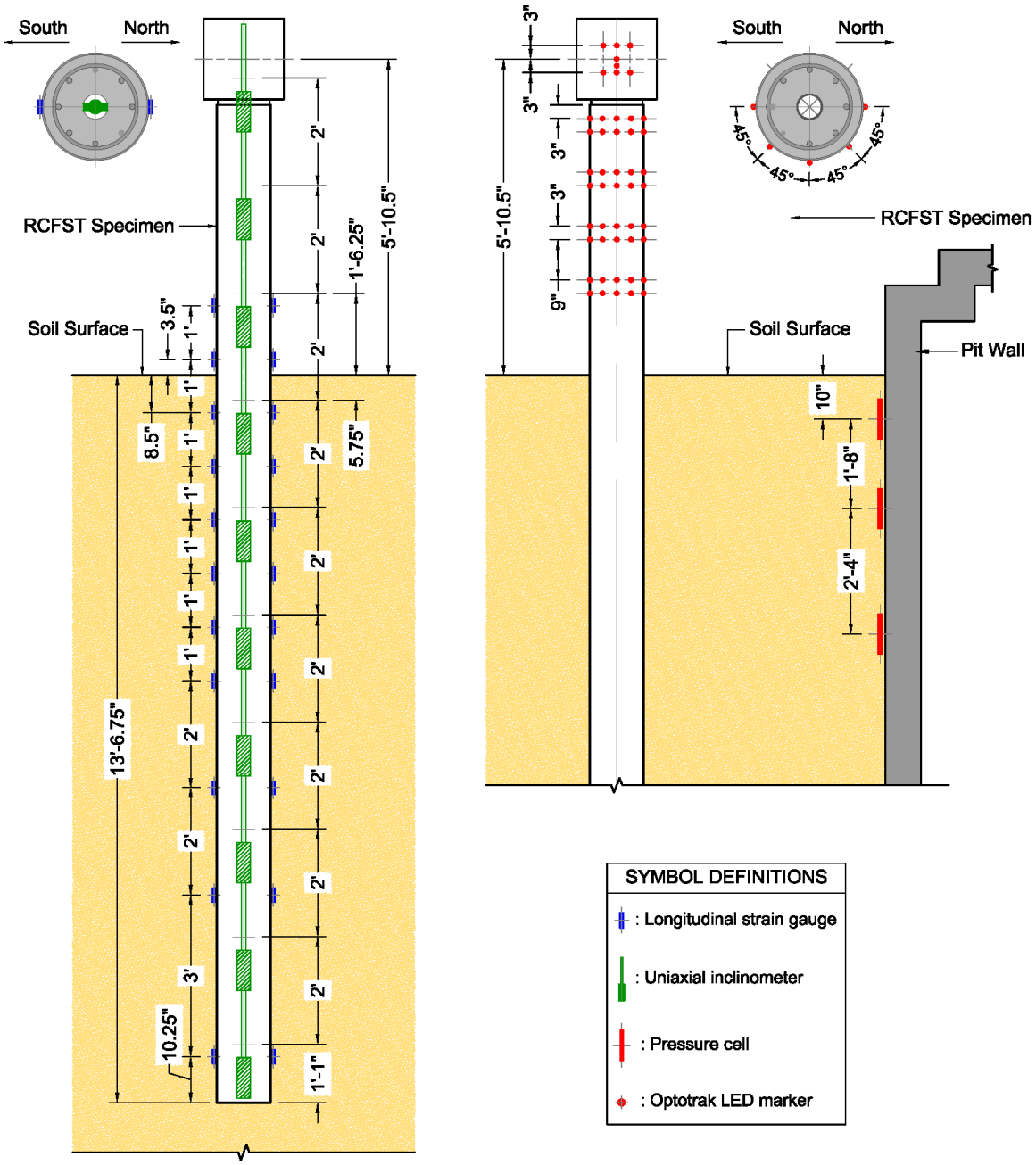

Figure 10-100 Test 6: instrumentation

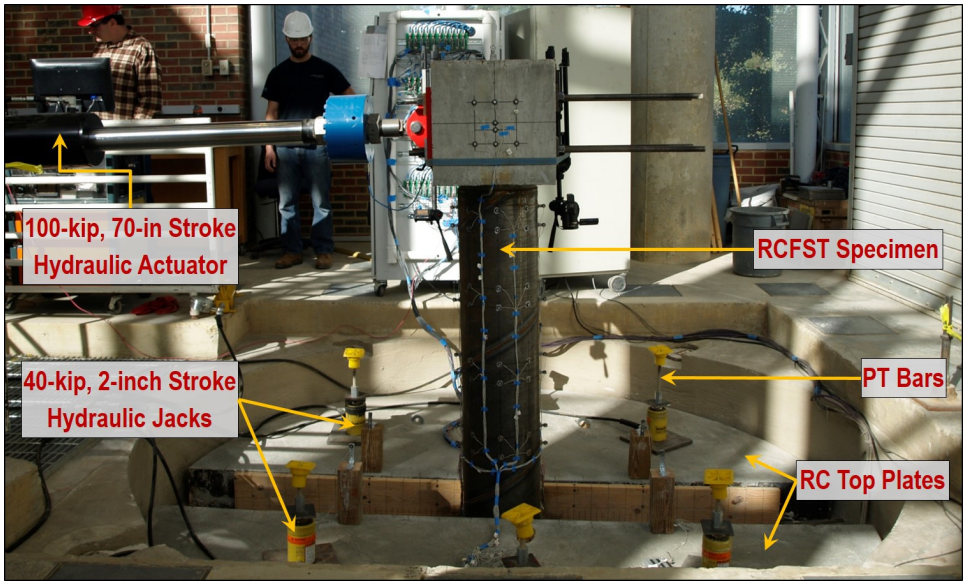

Figure 10-101 Test 6: pinned-head, RCFST pile-column test setup

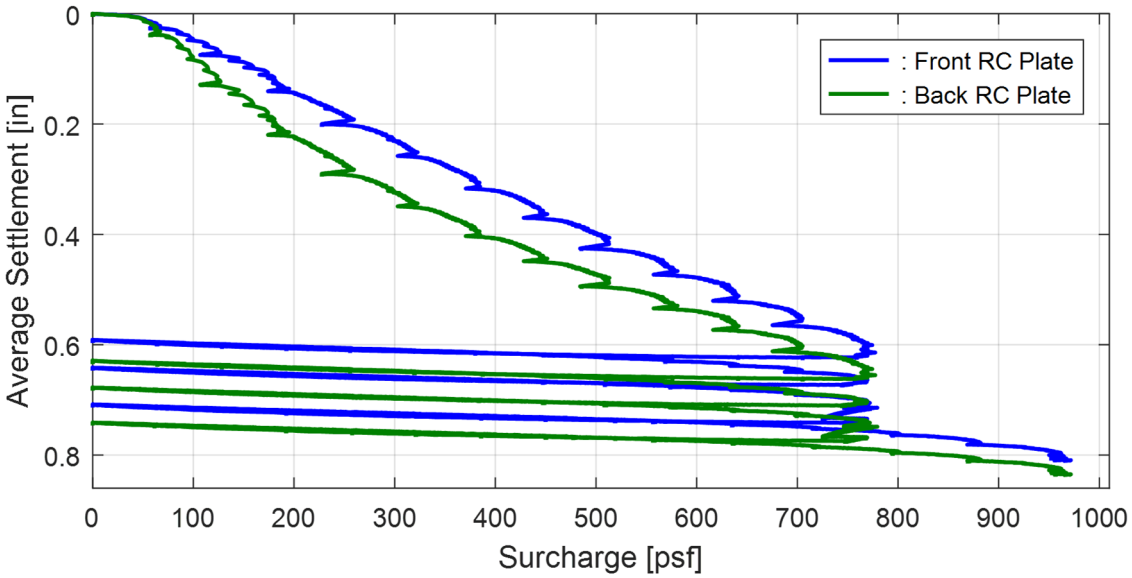

Figure 10-102 Test 6: half-moon RC plate settlement prior testing

The load history applied to the pile specimen consisted of standard three-cycle sets intended to evaluate both the elastic and inelastic response of the specimen. The first portion (i.e., pile elastic response up to first yield) of the test consisted of single reversed, displacement-controlled cycles, ramping up to the first yield displacement in ¼ increments. Given the non-linear response from the beginning of the test due to the characteristic soil behavior, target displacements in this portion of the test were determined based on the results of a monotonic pushover analysis performed using a detailed non-linear, fiber-based, finite element model developed using the OpenSees framework software. Soil-structure interaction was included by means of non-linear springs at 1-foot interval depths, with spring properties assigned based on p-y curves.

The first yield force (F_y) and nominal force (F_n), which is defined as the force at a concrete compressive strain of 0.004 or at a tube/bar tensile strain of 0.015 (whichever occurs first), were determined based upon tensile and compressive strains monitored during the numerical simulation (i.e., pushover analysis), as 14.52 kips and 21.72 kips, respectively. Table 10-6 summarizes the target displacements for the first portion of the test. After the first portion of the test was completed, the measured average strain at the predicted first yield displacement ($\Delta'y$ = 3.57 in) was 1830 ($\mu\varepsilon$), which correlates well with the tube yield strain (εy = 1870 $\mu\varepsilon$). The measured average displacement at the first yield displacement ($\Delta'y$ = 3.57 in) was modified by the nominal-to-first yield force ratio in order to determine the displacement ductility level 1.0 (μ_1 = 5.34 in), as shown in Equation 10-12. The remainder of the test was completed using reversed three-cycle sets in displacement-controlled increments at different levels of displacement ductility until failure, as shown in Equation 10-13. The entire displacement and load histories can be seen in Figure 10-103. Positive loads and displacements correspond to rightward (North) motion of the pile in the test setup. The positive legs of all cycles were completed before the negative legs.

Table 10-6 Test 6: predictions for elastic portion

Performance Level	Displacement (in)	Force (in)
1/4 Δy'	0.62	4.37
1/2 Δy'	1.47	8.14
3/4 Δy'	2.46	11.53
1 Δy'	3.57	14.53

$$\Delta_y = \mu_1 = \Delta'_y \cdot \frac{F_n}{F_y} = 3.57\,in \cdot \frac{21.72\,kip}{14.52\,kip} = 5.34\,in \qquad \text{Equation 10-12}$$

$$\mu_i = i \cdot \mu_1 \rightarrow i = 1.0,\ 1.5,\ 2.0,\ 3.0,\ 4.0 \qquad \text{Equation 10-13}$$

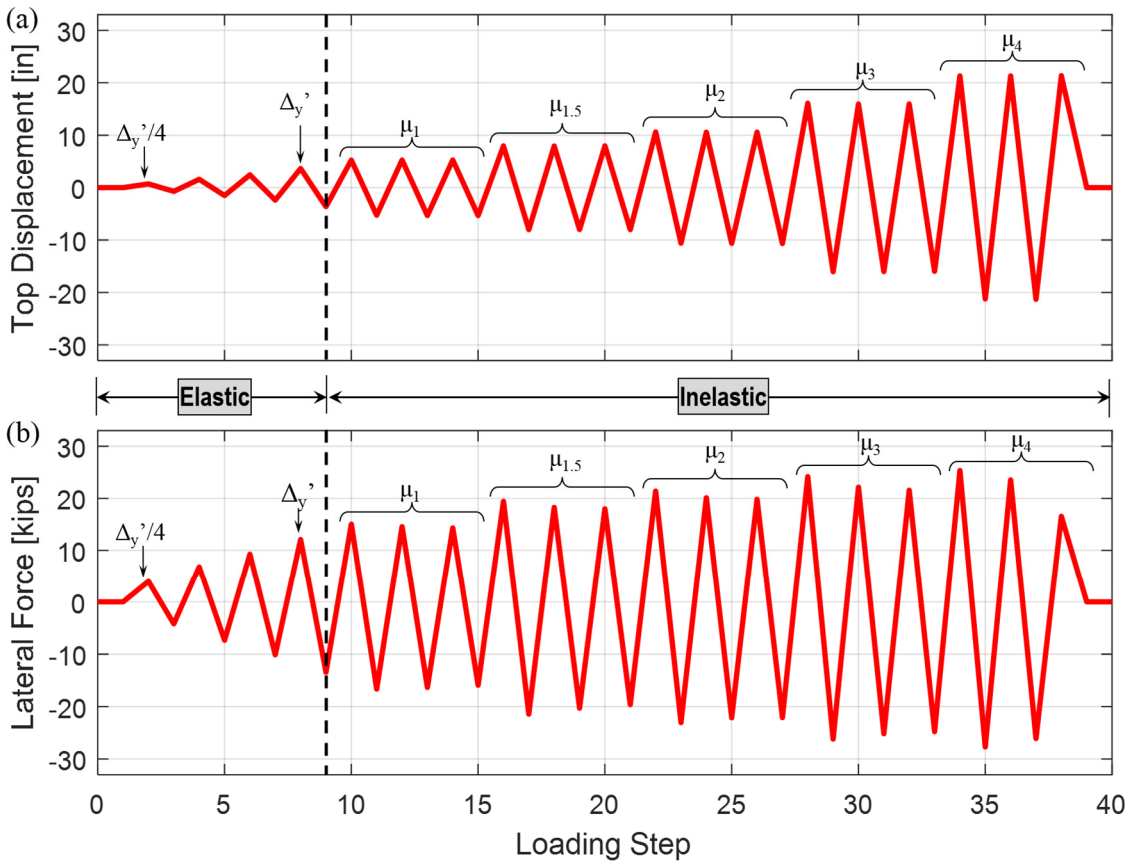

Figure 10-103 Test 6: (a) displacement and (b) loading histories

Specimen Response

Specimen #6 performed well through the elastic portion of the test and also during all three cycles of ductility level 3.0 (μ_3). It is believed that the onset of buckling occurred early during the displacement cycles at ductility level 1.5 ($\mu_{1.5}$) as some of the strain gauges located on both sides of the pile indicated large values during both push and pull cycles at the aforementioned ductility level. A significant loss of strength, indicating failure, occurred during the third push cycle at ductility level 4.0 (μ_4). Figure 10-104 and Figure 10-105 present the lateral force vs. top displacement response and envelopes, respectively. It can be seen that the system has a characteristic large energy dissipation capacity due to both damping sources, that is, the pile itself and the surrounding soil. In addition, it can be clearly seen from both figures that a significant loss of strength (~34.7%) occurred during the third push cycle of ductility level 4.0 (μ_4).

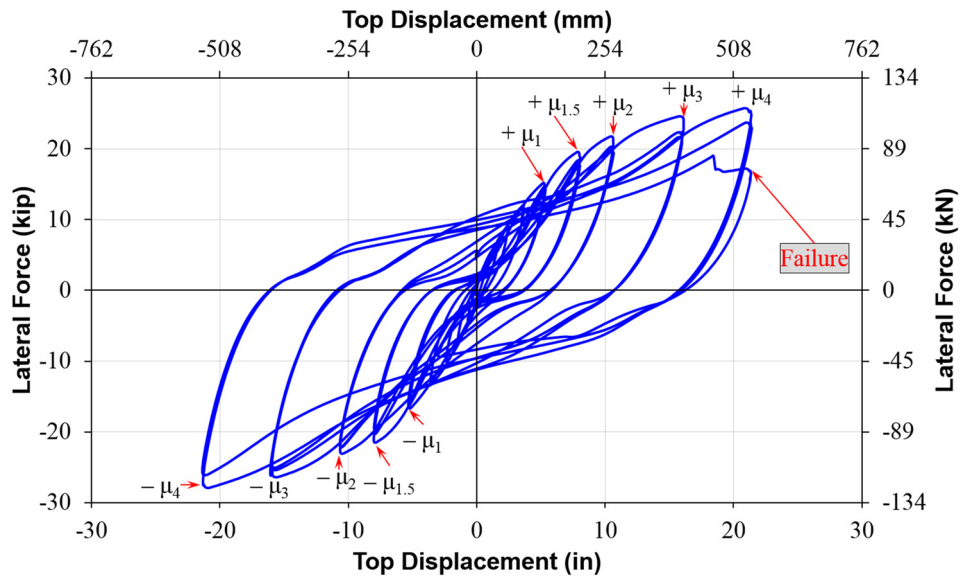

Figure 10-104 Test 6: lateral force vs. top displacement response

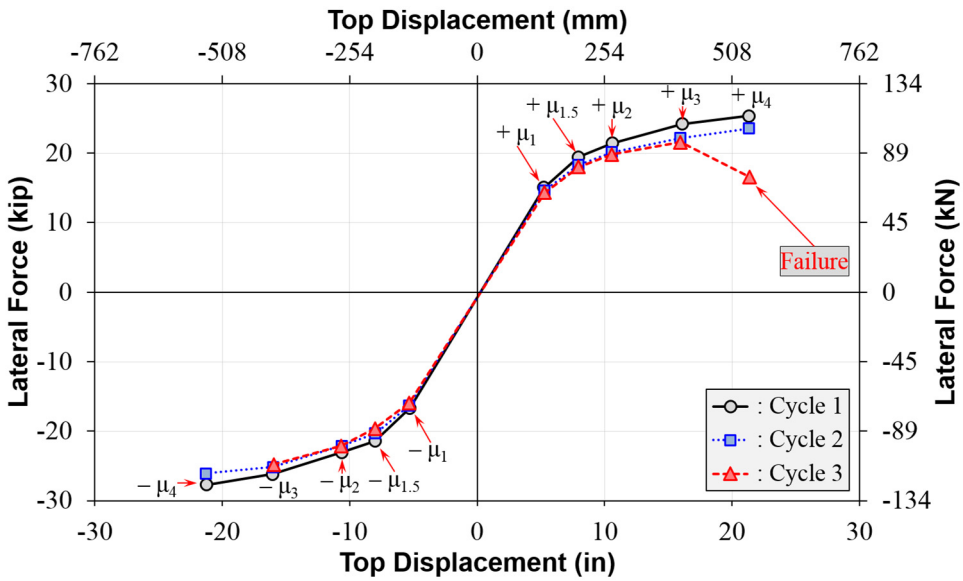

Figure 10-105 Test 6: lateral force vs. top displacement envelopes

Figure 10-106 presents the deformed shape and the soil-pile gaps at zero displacement after the elastic portion of the test was conducted; the size of the gap was ~1.25 in on both sides of the specimen. As it was previously explained, at this point of the test strain profiles on the sides of the pile were verified in order to further conduct the test at the aforementioned ductility levels. Figure 10-107 presents the strain profiles recorded during the first portion of the test. Note that tensile strains of 1740 (με) and 1920 (με) were recorded in the tube during the push and pull cycles, respectively, when the predicted first yield displacement was imposed to the system. Based on the rotation data recorded with the inclinometer placed inside the pile along its length, specimen curvature, rotation, and displacement profiles are presented in Figure 10-108 and Figure 10-109 for the first push and pull cycles, respectively. Note that there are small rotations and displacements at the pile tip which indicates that there is a point of rotation (at ~10 ft.) rather than a point of fixity; inelastic action was developed in the pile nonetheless. The circles in the top portion of the displacement profiles in Figure 10-108 and Figure 10-109 represent the Optotrak LED markers; note that they are in agreement with the calculated displacement profiles. In Figure 10-107 through Figure 10-109 the symbols N and S in the legend refer to the North and South sides, Δ_y' is the first yield displacement, $Ø_y'$ stands for the first yield curvature, and a depth equal to 0 ft. represents the soil surface.

Figure 10-106 Test specimen #6 after elastic portion was completed: (a) deformed shape, (b) South side and (c) North side

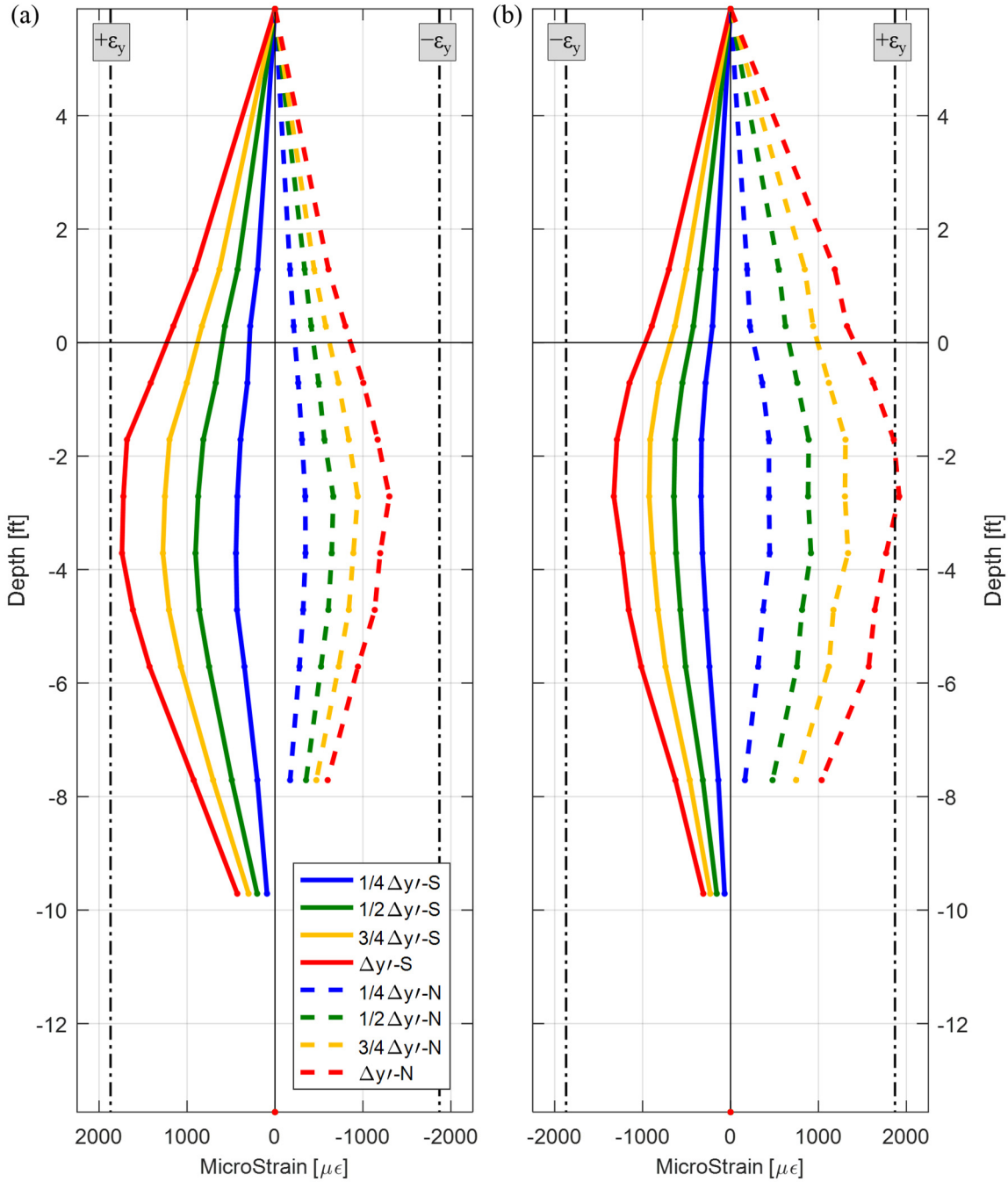

Figure 10-107 Test 6: strain profiles from elastic (a) push and (b) pull cycles

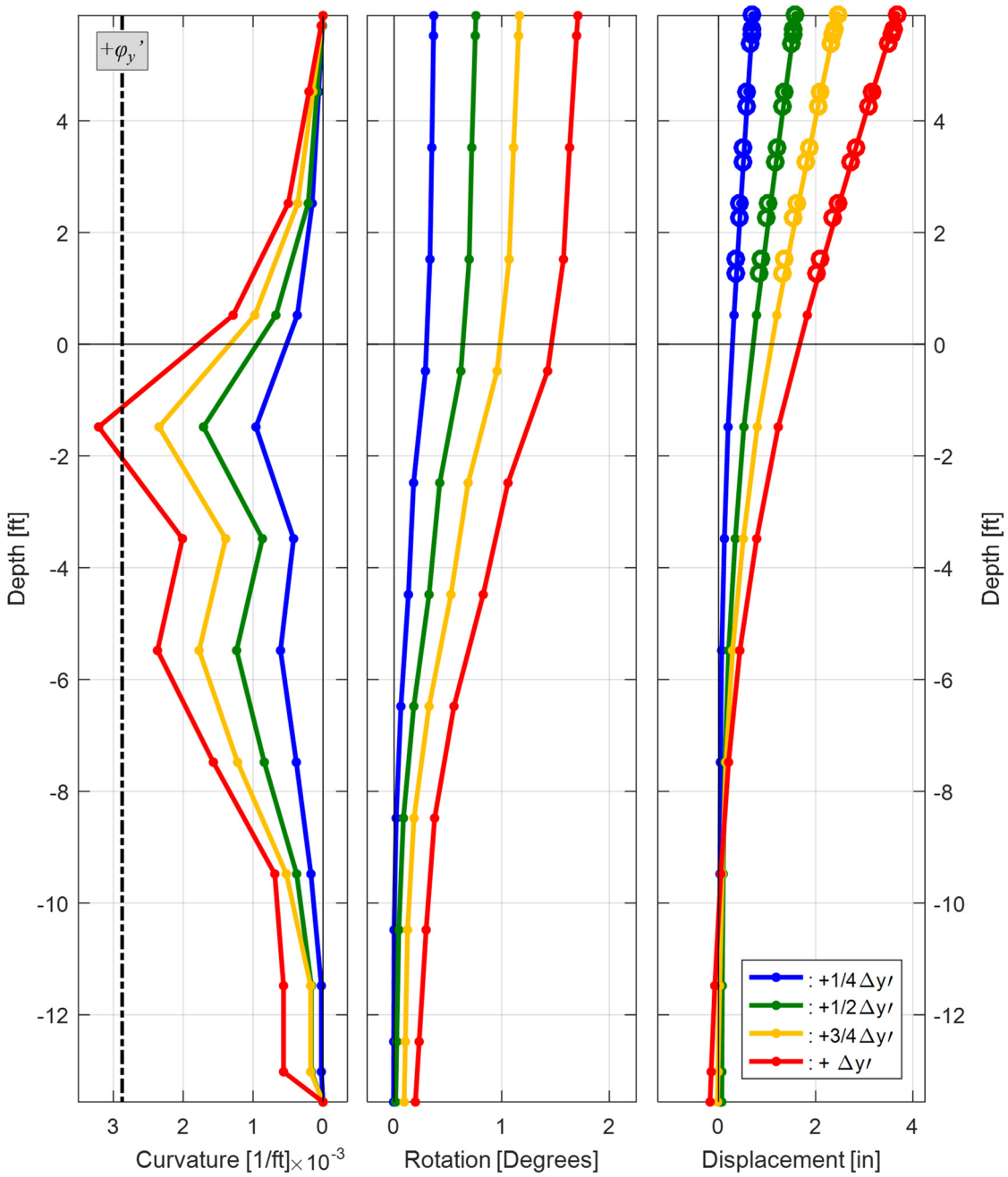

Figure 10-108 Test 6: curvature, rotation, and displacement profiles (elastic push cycles)

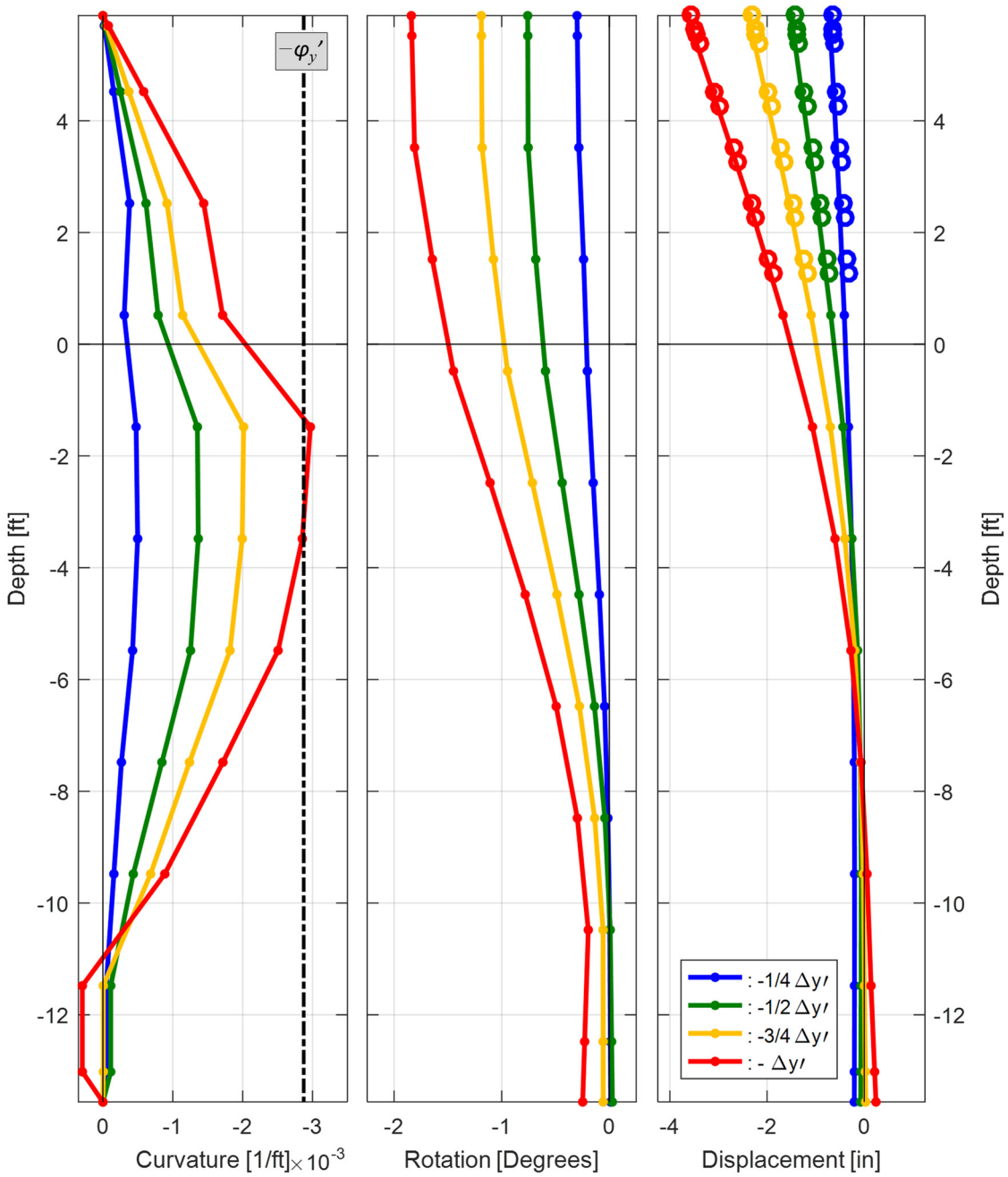

Figure 10-109 Test 6: curvature, rotation, and displacement profiles (elastic pull cycles)

As the test continued, the gap on the sides of the pile increased in size as the displacement ductility level increased. Minor loss of strength was observed up until all ductility level 3.0 (μ_3) cycles. The specimen failure (Figure 10-110) occurred at the third cycle load at ductility 4.0 (μ_4) when a significant drop in the force in the actuator was observed (i.e., ~34.7%). Sounds indicating steel fracture were heard at the same time when the strength loss occurred, indicating probable tube or bar fracture. Moreover, minor twist rotation of the pile occurred for all push cycles at ductility level 4.0 (μ_4). Finally, the test was terminated and the specimen was taken to zero displacement in order to facilitate its extraction from the soil.

Figure 10-111 presents the strain profiles for the first push and pull cycles at different displacement ductility levels. Notice that the largest tensile and compressive strains in the tube were recorded at a depth between 0 ft. and 4 ft. In Figure 10-111 the symbols N and S in the legend refer to the North and South sides, and μ is the displacement ductility level. Curvature, rotation, and displacement profiles are presented in Figure 10-112 and Figure 10-113 for the first push and pull cycles, respectively. Note that the maximum curvature occurred at a depth of ~2 ft. which correlates well with the position of the observed plastic hinge, determined after the test was completed.

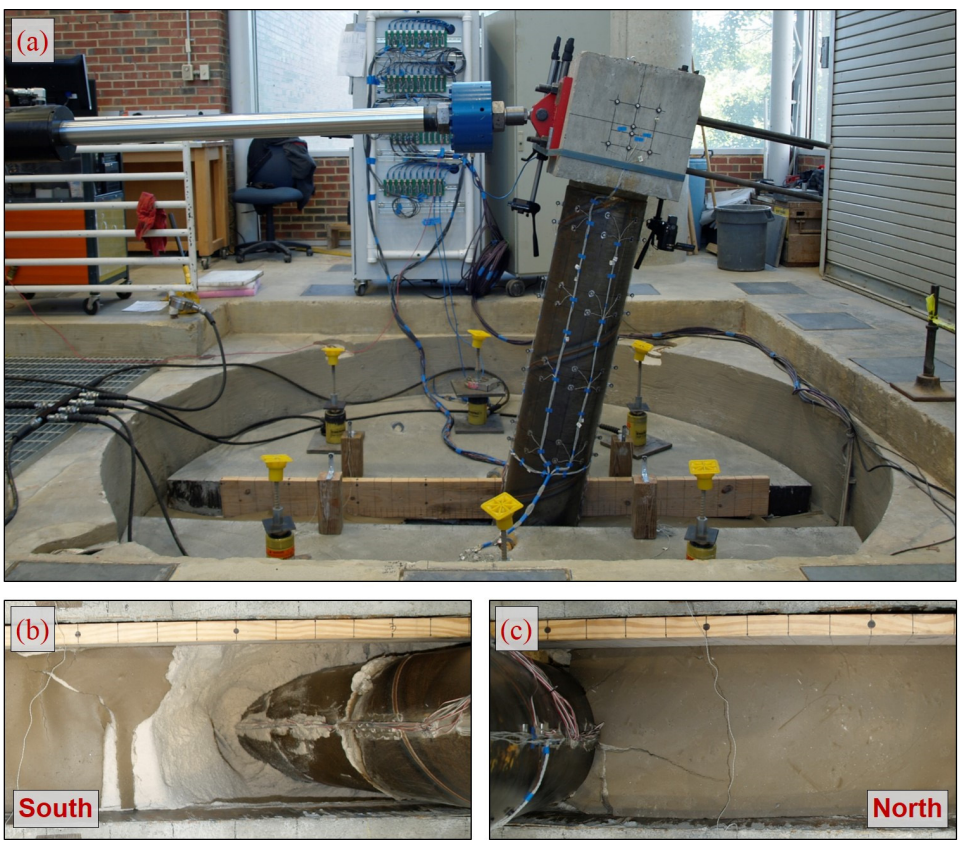

Figure 10-110 Test specimen #6 at maximum displacement: (a) deformed shape, (b) South side and (c) North side

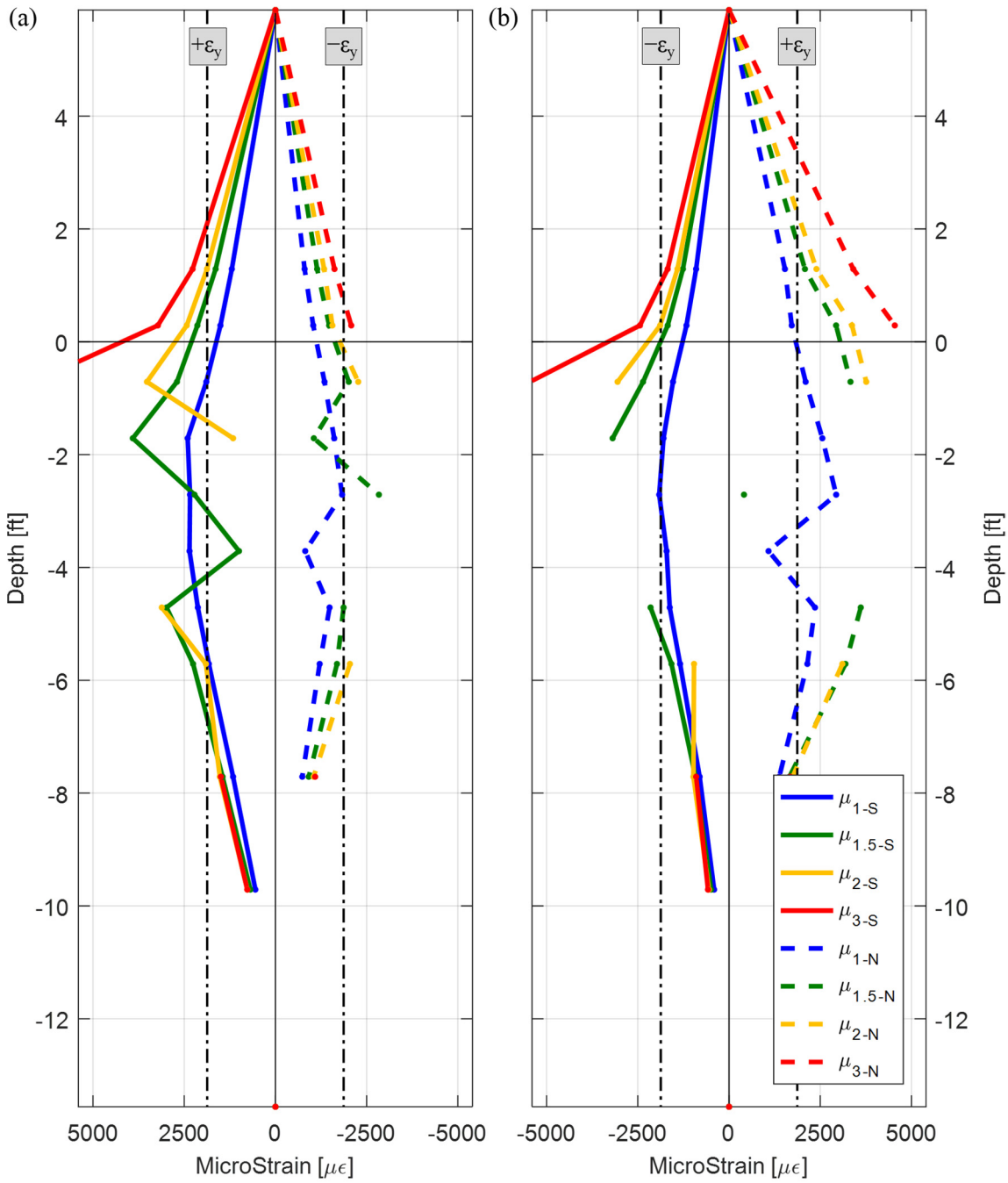

Figure 10-111 Test 6: strain profiles from inelastic (a) push and (b) pull cycles

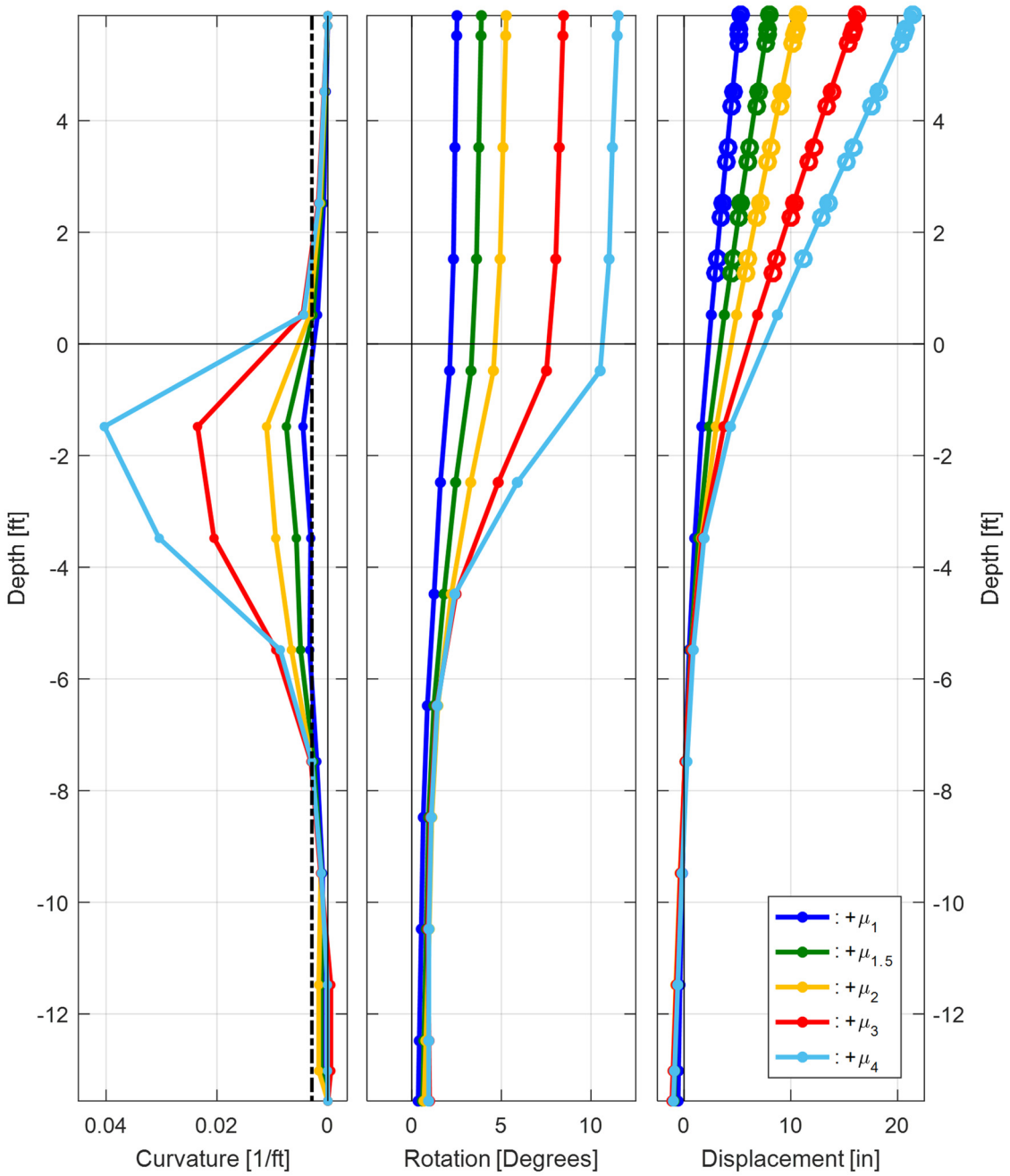

Figure 10-112 Test 6: curvature, rotation, and displacement profiles (inelastic push cycles)

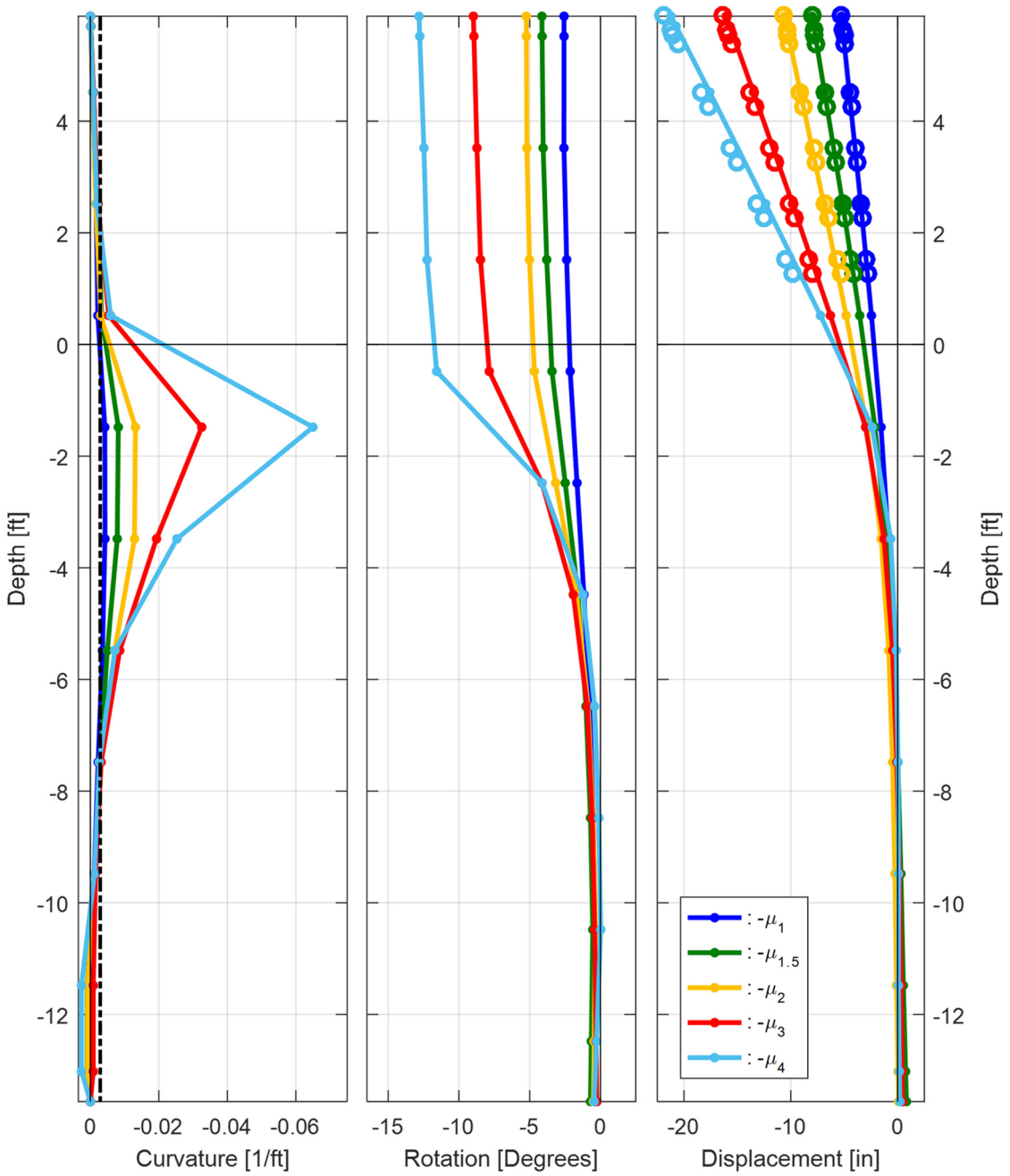

Figure 10-113 Test 6: curvature, rotation, and displacement profiles (inelastic pull cycles)

Figure 10-114 shows the state of the soil surface after the test was completed. Notice that despite the presence of the half-moon RC plates in the surface, deformations in the soil followed an expected oval-shaped failure surface in which active and passive pressures developed around the pile. This surface extended ~9.75 in. on both sides of the direction of loading and ~7.25 in. on the perpendicular direction. The total average settlement of the RC plates during the test was ~2.67 in. This value was averaged based on the vertical displacement of 4 points on the RC plates. Figure 10-115 shows the average settlement of the half-moon RC plates during the test as a function of the imposed displacements at the top of the pile. Note that, as the displacement history is applied, the settlement increases, though its magnitude is larger at the beginning of the test.

Figure 10-114 Test 6: soil surface after testing

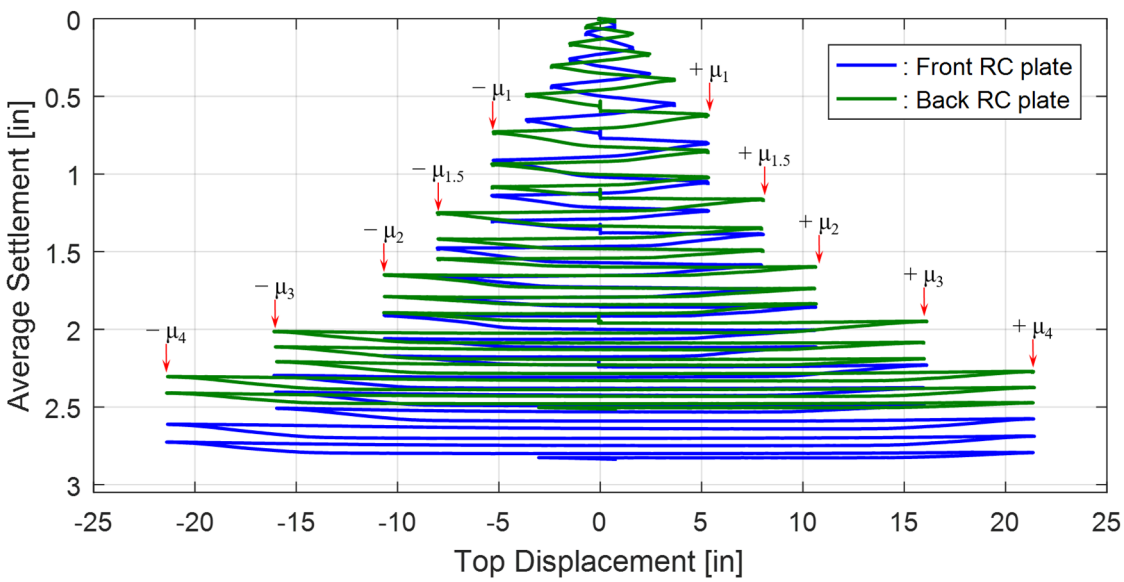

Figure 10-115 Test 6: half-moon RC plate settlement during testing

Figure 10-116 through Figure 10-119 present the damage observed after the pile was extracted from the soil. As thought during the test, tube fracture and tube buckling did occur; bar fracture and bar buckling were not observed. It can be seen that tube local buckling developed on both sides of the specimen. The sections with the largest buckling occurred at a depth of 2 ft. – 6 in. and 2 ft. – 8 in. on the South and North sides of the specimen, respectively, which implies that the plastic hinge developed at an average depth of 2 ft. – 7 in. with respect to the soil surface. Notice that on the South side of the specimen only one main buckled section developed. This correlates well with the fact that the sand was filling the gap with the pile only on the South side. It is believed that the critical section during the push cycles was the same throughout the test as the lever arm did not change, whereas the depth to maximum moment did change for the pull cycles as the sand was filling the gap with the pile. As a consequence, only one main buckled section developed on the South side in contrast with the two main buckled regions observed on the North Side. Ripples close to the section with tube buckling were observed on both sides of the specimen.

Tube fracture (Figure 10-116) occurred on the South side of the specimen and it extended about half of the cross-section perimeter, resulting in a significant drop in strength due to lost tension capacity. As a consequence, after rupture, tension capacity is provided by the longitudinal reinforcement, which has a smaller area in comparison with that provided by the tube, inducing high stresses and deformations. Upon further investigations, bar buckling as well as bar fracture were not observed neither on the South nor on the North sides of the specimen. Note that tube fracture occurred in the section with the largest tube buckling, in which deformations protruded ~1/2 in. on both South and North sides of the pile. A minor buckled region was observed at a depth of 1 ft. – 7.5 in. on the North side of the specimen, next to the main buckled region. Figure 10-117 presents measurements of the primary and secondary buckled regions on the North side of the pile. It can be seen that the deformations due to buckling protruded ~1/2 in. and ~7/16 in., respectively.

In order to further investigate the significant strength loss and to verify whether bar fracture or bar buckling occurred, a portion of the tube (i.e., 10 in. x 12 in.) was removed at the ruptured section in the extreme fiber on both sides of the pile (Figure 10-118 and Figure 10-119). It can be seen that several cracks developed in this area of the concrete, perpendicular to the longitudinal direction of the specimen. Cracks in the concrete extended further to the center of the section. Neither bar fracture nor bar buckling were observed on either side of the specimen.

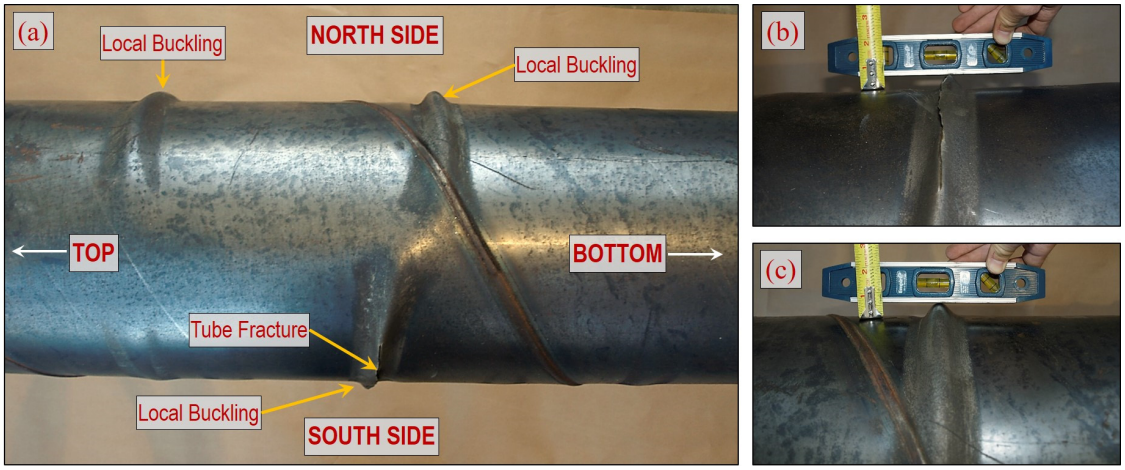

Figure 10-116 Test 6: (a) Final observed damage, (b) tube fracture, and (c) tube local buckling

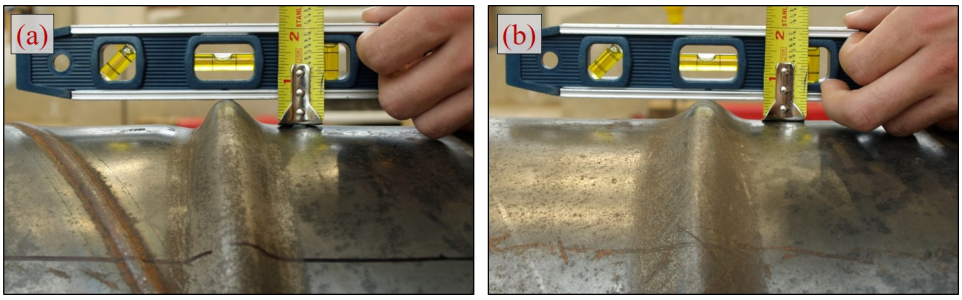

Figure 10-117 Test 6: (a) primary and (b) secondary buckled sections on North side

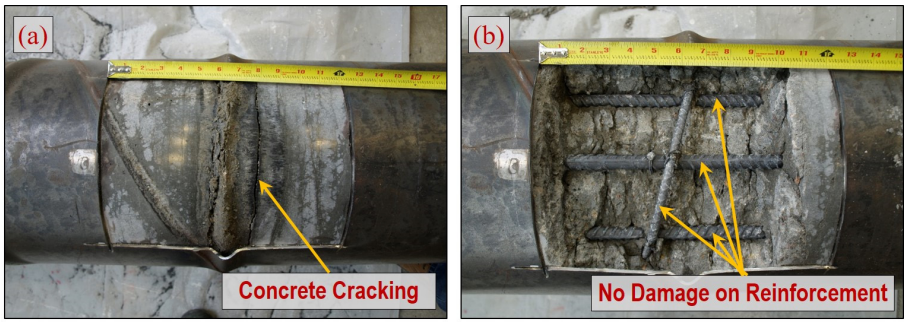

Figure 10-118 Test 6: observed damage in (a) concrete and (b) internal reinforcement on North side

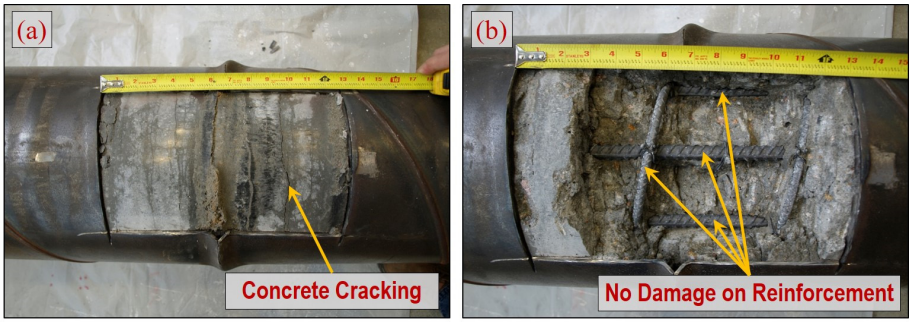

Figure 10-119 Test 6: observed damage in (a) concrete and (b) internal reinforcement on South side

Conclusions

Test specimen #6 showed a reliable response through all ductility 3.0 ($\mu 3$) cycles. It is believed that onset of tube local buckling occurred early during the test at ductility level 1.5 ($\mu_{1.5}$), when large tensile strains were recorded. The test specimen completed all cycles of ductility 3.0 (μ_3) with minor loss of strength. A significant drop in strength occurred at ductility level 4.0 (μ_4) when tube fracture developed on the South side of the specimen during the third push cycle at this level. Further investigations revealed that failure occurred due to a combination of tube local buckling and tube fracture. Neither bar fracture nor bar buckling were observed in the internal reinforcement. It is believed that this particular specimen is capable of having a reliable displacement up to ductility 3.0 (μ_3). The main buckles as well as tube fracture did not occur over the spiral weld, so the tube spiral welds do not appear to negatively influence the behavior.

Test 7 Summary Report

December 7, 2015

Prepared for

Alaska Department of Transportation

Alaska University Transportation Center

Project Team

RA: Diego Aguirre

PIs: Mervyn Kowalsky, James Nau, Mo Gabr

Other Senior Personnel: Greg Lucier, Ben Smith

North Carolina State University

Executive Summary

Test 7 was conducted November 11th, 2015 at the North Carolina State University Constructed Facilities Laboratory. The tested pile-column specimen was a reinforced concrete filled steel tube with a diameter-to-thickness (D/t) ratio of 68. No surcharge was applied to the soil, thus the soil stiffness was not modified. The test was successfully conducted to failure, which was caused by a combination of tube local buckling, tube fracture, and bar buckling, resulting in a large strength degradation (~25.36%) in the second cycle at ductility level 5.0 (μ_5).

Specimen and Test Description

Test 7 consisted of a 19-foot-5.25-inch long, reinforced concrete filled, 12-3/4-inch diameter spirally welded steel tube without skelp or splice welds. The pile-column specimen was embedded 13 ft. – 8 in. into clean sand in the soil-structure interaction facility at the NCSU-CFL. Lateral load was applied at the pinned connection at the top of the pile specimen by means of a 100-kip, 70-inch stroke hydraulic actuator. The nominal wall thickness of the tube was 0.187 in., providing a nominal diameter-to-thickness ratio (D/t) of 68. The test was conducted with a 5-foot-9.25-inch cantilever length, measured from the soil surface to the point at which the lateral load was applied. Figure 10-120 and Figure 10-121 present a schematic of the test setup (elevation) and the specimen #7 cross-section, respectively, while

Figure 10-122 shows the instrumentation used for testing. A photograph of the test setup is included in Figure 10-123.

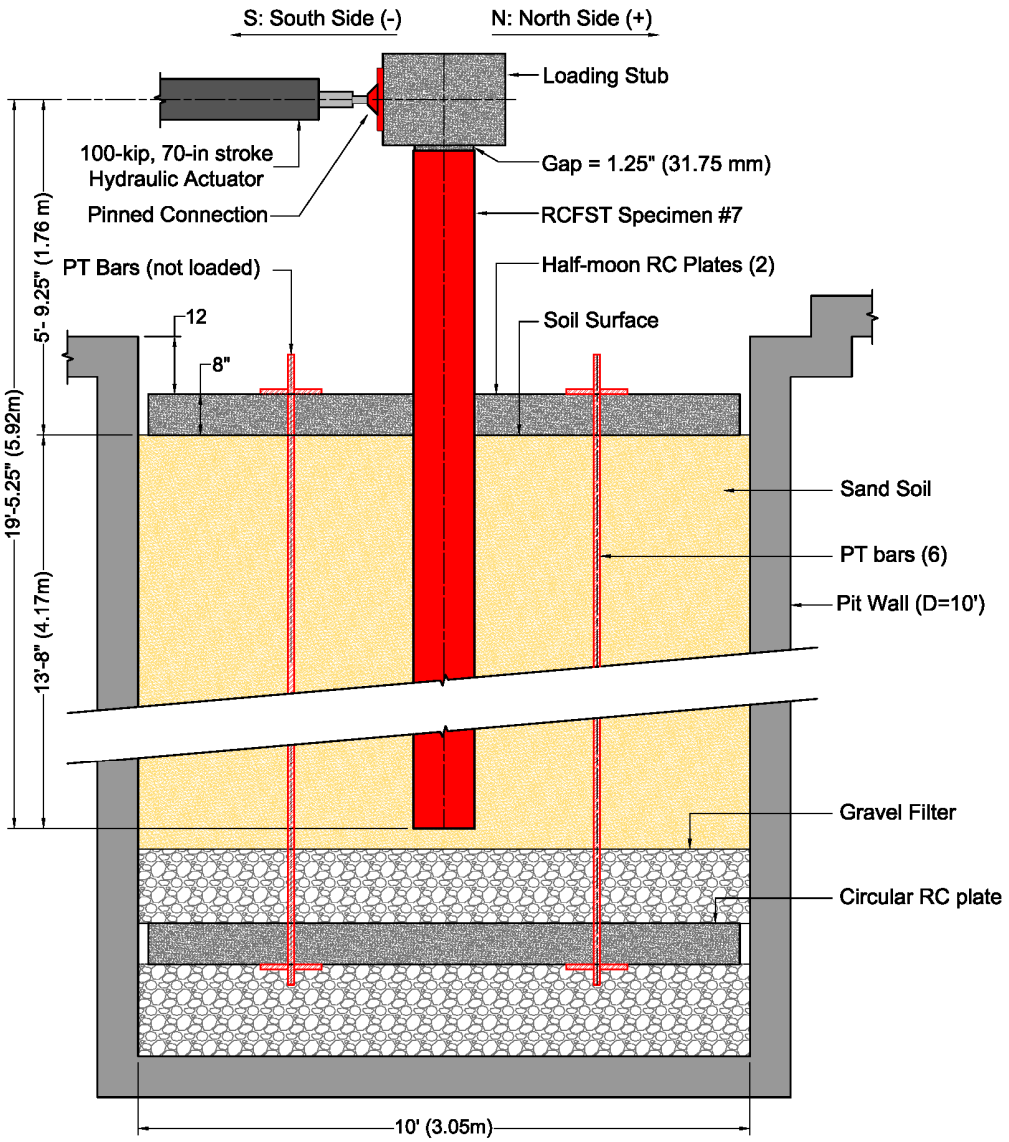

Figure 10-120 Test 7: test setup elevation schematic

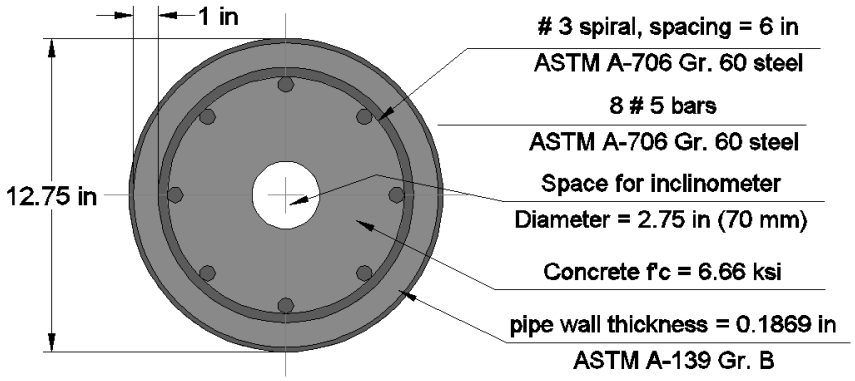

Figure 10-121 Test 7: RCFST specimen cross section

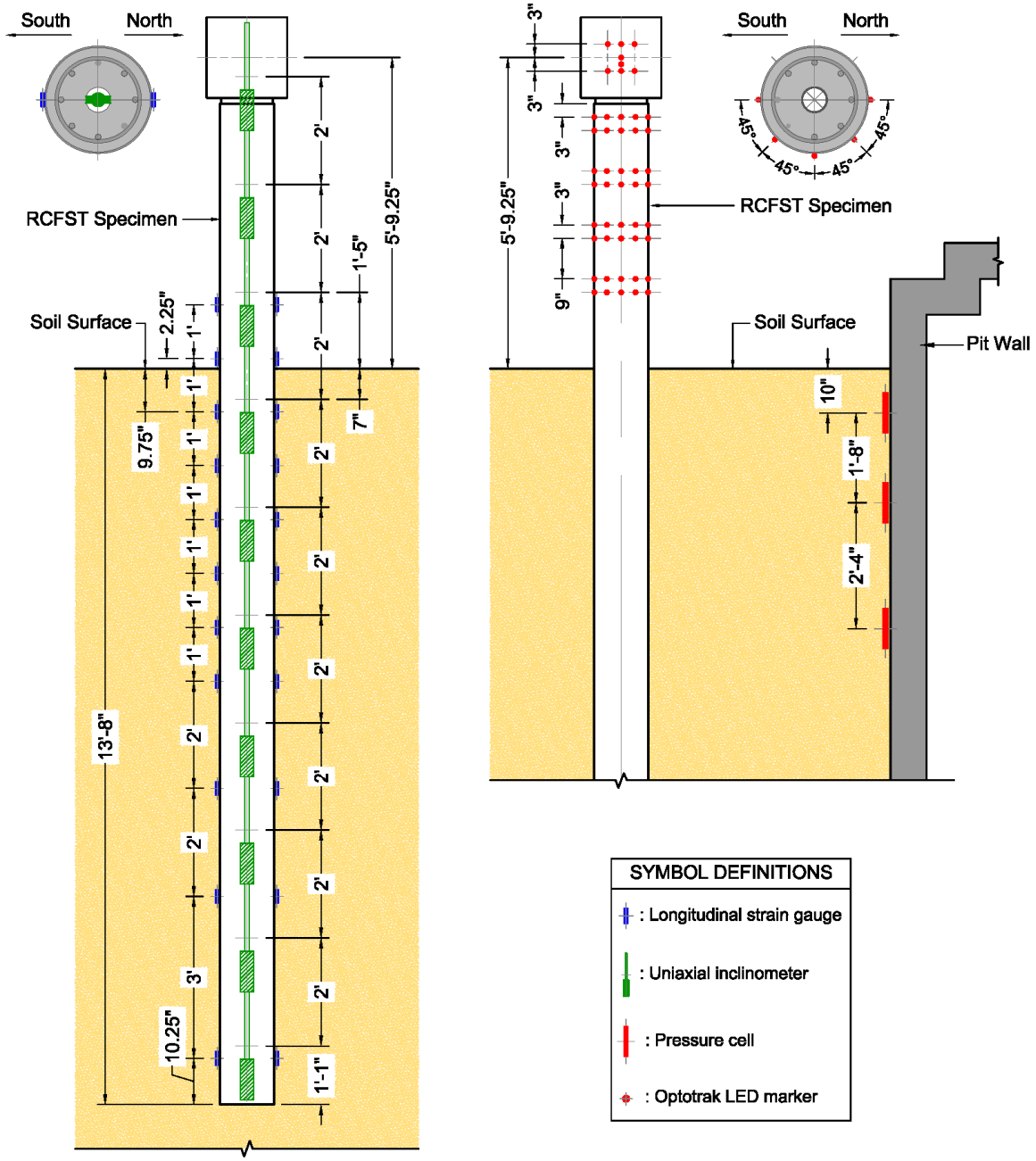

Figure 10-122 Test 7: instrumentation

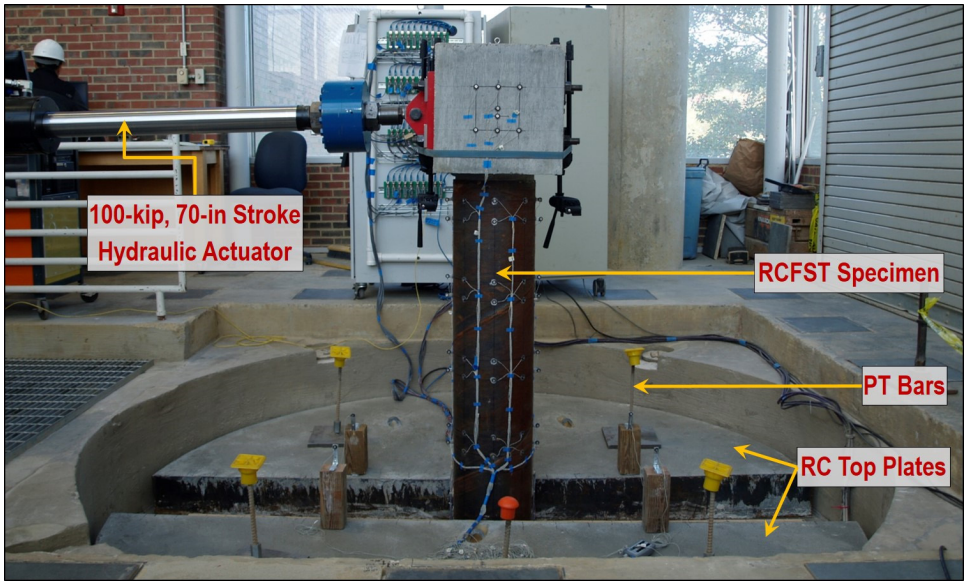

Figure 10-123 Test 7: pinned-head, RCFST pile-column test setup

Material properties were determined by in-house material tests. The yield and ultimate stresses of the steel tube were 55.6 ksi and 74.7 ksi, respectively, based on tests conducted on three (3) coupons cut from the end of the test pile specimen. The yield and ultimate stresses of the ASTM A706 Grade 60 longitudinal reinforcement were 70.7 ksi and 99.6 ksi, respectively, based on tests conducted on six (6) bar specimens from the same heat of the longitudinal reinforcement. The yield and ultimate stresses of the spiral reinforcement were 64.6 ksi and 95.3 ksi, respectively, based on tests conducted on six (6) bar specimens from the same heat of the transverse reinforcement. An average concrete compressive strength of 6.66 ksi (standard deviation of ± 0.26 ksi) was determined from three (3) compression tests of 4”x8” concrete cylinders.

Soil properties were also determined by in-house material tests. Based on a measured particle size distribution, the soil was classified as poorly-graded sand (SP). The unit weight, friction angle, and moisture content (γ = 90 pcf, ϕ = 35°, and w = 2.5%, respectively) were reasonably assumed based upon results of previous tests. Active surcharge was not applied, so only the self-weight of the half-moon RC plates was acting in the soil surface (i.e., ~100 psf).

The load history applied to the pile specimen consisted of standard three-cycle sets intended to evaluate both the elastic and inelastic response of the specimen. The first portion (i.e., pile elastic response up to first yield) of the test consisted of single reversed, displacement-controlled cycles, ramping up to the first yield displacement in ¼ increments. Given the non-linear response from the beginning of the test due to the characteristic soil behavior, target displacements in this portion of the test were determined based on the results of a monotonic pushover analysis performed using a detailed non-linear, fiber-based, finite element model developed using the OpenSees framework software. Soil-structure interaction was included by means of non-linear springs at 1-foot interval depths, with spring properties assigned based on p-y curves.

The first yield force (F_y) and nominal force (F_n), which is defined as the force at a concrete compressive strain of 0.004 or at a tube/bar tensile strain of 0.015 (whichever occurs first), were determined based upon tensile and compressive strains monitored during the numerical simulation (i.e., pushover analysis), as 18.87 kips and 26.37 kips, respectively. Table 10-7 summarizes the target displacements for the first portion of the test.

After the first portion of the test was completed, the measured average strain at the predicted first yield displacement (Δ'y = 4.30 in) was 1430 (με), based on limited strain data that is shown in subsequent sections. This average strain corresponds to 75% that of the tube yield strain (ε_y = 1920 με). However, it was decided to continue the test assuming the predicted first yield displacement was correct. The measured average displacement at the first yield displacement (Δ'y = 4.30 in) was modified by the nominal-to-first yield force ratio in order to determine the displacement ductility level 1.0 (μ1 = 6.02 in), as shown in Equation 10-14. The remainder of the test was completed using reversed three-cycle sets in displacement-controlled increments at different levels of displacement ductility until failure, as shown in Equation 10-15. The entire displacement and load histories can be seen in Figure 10-124. Positive loads and displacements correspond to rightward (North) motion of the pile in the test setup. The positive legs of all cycles were completed before the negative legs.

Table 10-7 Test 7: predictions for elastic portion

Performance Level	Displacement (in)	Force (kips)
1/4 Δy'	0.82	5.75
1/2 Δy'	1.81	10.64
3/4 Δy'	3.03	15.16
1 Δy'	4.30	18.87

$$\Delta_y = \mu_1 = \Delta'_y \cdot \frac{F_n}{F_y} = 4.30\,in \cdot \frac{26.37\,kip}{18.87\,kip} = 6.02\ in \qquad \text{Equation 10-14}$$

$$\mu_i = i \cdot \mu_1 \rightarrow i = 1.0,\ 1.5,\ 2.0,\ 3.0,\ 4.0,\ 5.0 \qquad \text{Equation 10-15}$$

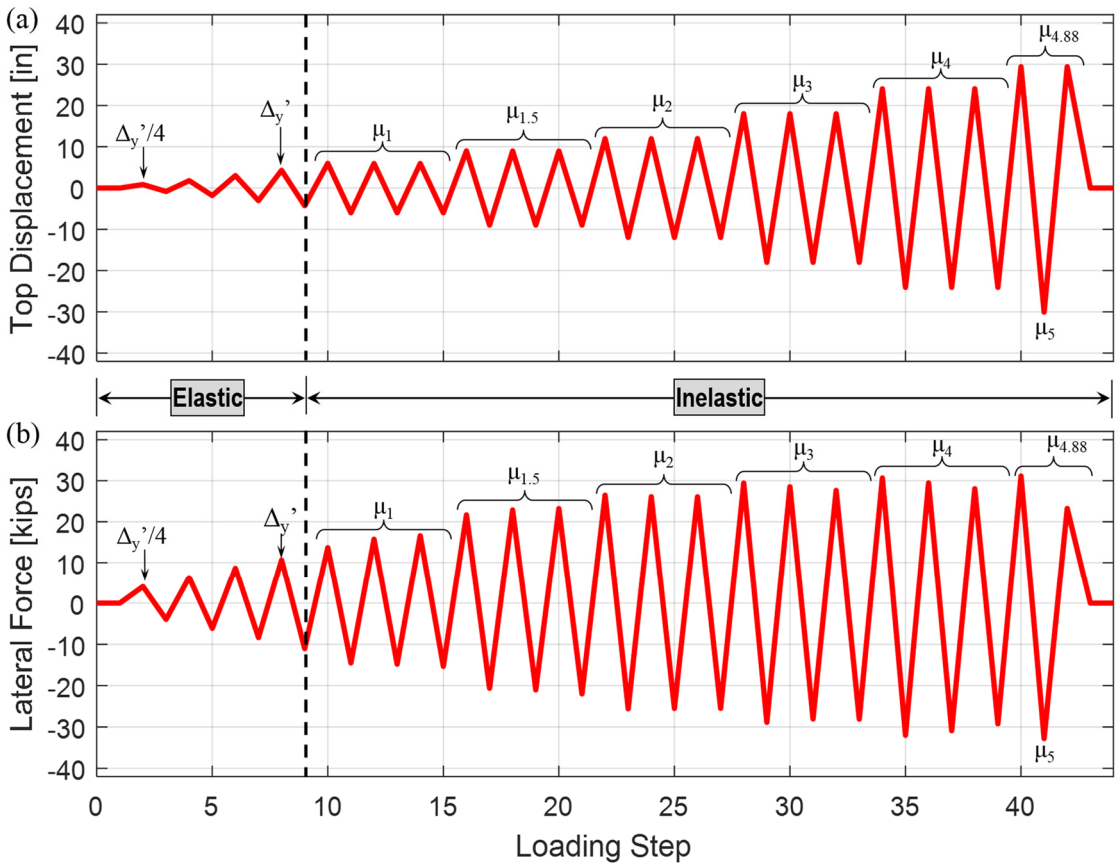

Figure 10-124 Test 7: (a) displacement and (b) loading histories

Specimen Response

Specimen #7 performed well through the elastic portion of the test and during all three cycles of ductility level 4.0 (μ_4). It is believed that the onset of tube buckling occurred during the displacement cycles at ductility level 2.0 (μ_2) as some of the strain gauges located on both sides of the pile indicated large values during the push and pull cycles at that ductility level. A significant loss of strength, indicating failure, occurred during the second push cycle at ductility level 5.0 (μ_5). As previously indicated in Figure 10-124 and subsequent figures, it is important to mention that the push cycles at ductility level 5.0 (μ_5) correspond in fact to ductility level 4.88 ($\mu_{4.88}$) due to an issue with the controller of the actuator, which allowed for a maximum displacement in the positive direction of 29.41 in. (i.e., $\mu_{4.88}$). However, considering the proximity to the target ductility and the fact that the pull cycles at this level were successfully conducted to the target displacement (μ_5), the push cycles in this report will also be referred to as ductility level 5.0 (μ_5), though parameter values shown in figures correspond to the actual displacements induced during the test.

Figure 10-125 and Figure 10-126 present the lateral force vs. top displacement response and envelopes, respectively. It can be seen from Figure 10-125 that the system has a characteristic large energy dissipation capacity due to both damping sources, that is, the pile itself and the surrounding soil. In addition, it can be clearly seen from both figures that a

significant loss of strength (~34%) occurred during the second cycle of ductility level 5.0 (μ_5).

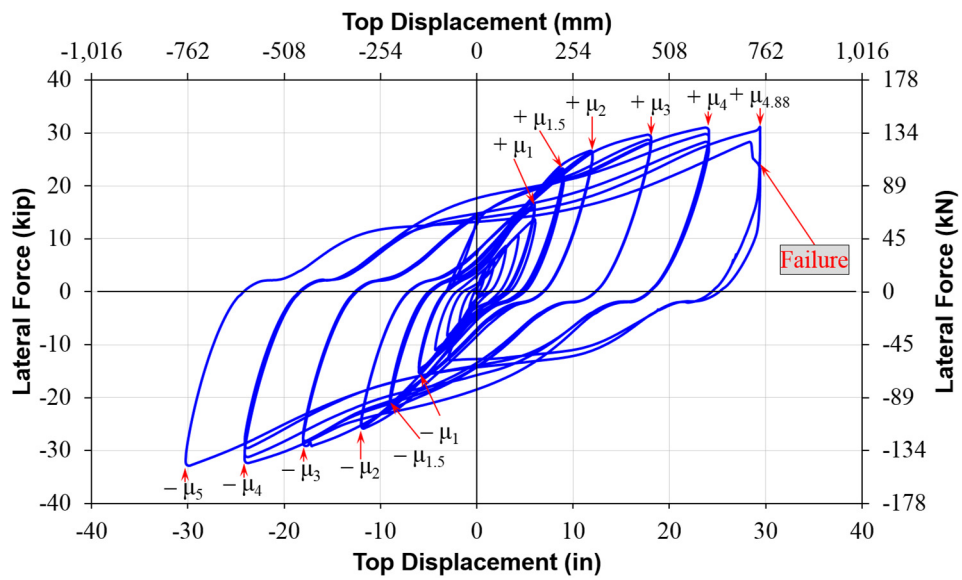

Figure 10-125 Test 7: lateral force vs. top displacement response

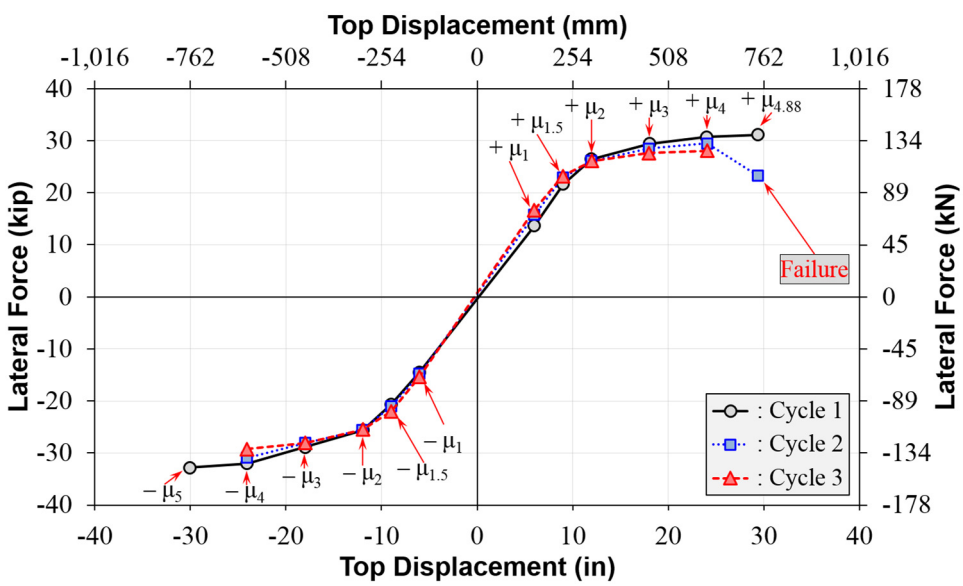

Figure 10-126 Test 7: lateral force vs. top displacement envelopes

Figure 10-127 presents the deformed shape and the soil-pile gaps at zero displacement after the elastic portion of the test was conducted; the size of the gap was ~1-5/8 in. on both sides of the specimen. As it was previously explained, at this point of the test strain profiles on the sides of the pile were verified in order to further conduct the test at the aforementioned ductility levels. Figure 10-128 presents the strain profiles recorded during the first portion of the test. Notice that tensile strains of 1090 ($\mu\varepsilon$) and 1430 ($\mu\varepsilon$) were recorded in the tube during the push and pull cycles, respectively, when the predicted first yield displacement was imposed to the system. Note that these values are rather low in comparison with the tube yield strain (ε_y = 1920 $\mu\varepsilon$). However, notice from Figure 10-128 that limited strain data was available from the strain gauges; it is believed that the strain gauges were damaged during the pile insertion process. This issue caused the need to also verify the curvature profiles before continuing with the inelastic portion of the test. After verifying some of the inclinometer data, it was concluded that curvature values where within ~25% of the first yield curvature value ($Ø'_y$ = 0.0030 1/ft) determined from a moment-curvature analysis using CUMBIA PIPE. Thus, it was decided to continue the test assuming the predicted first yield displacement was correct.

Based on the rotation data recorded with the inclinometer placed inside the pile along its length, specimen curvature, rotation, and displacement profiles are presented in Figure 10-129 and Figure 10-130 for the first push and pull cycles, respectively. Note that there are small rotations and displacements at the pile tip which indicate that there is a point of rotation (at ~10 ft.) rather than a point of fixity; inelastic action was developed in the pile nonetheless. The circles in the top portion of the displacement profiles in Figure 10-129 and Figure 10-130 represent the Optotrak LED markers; note that they are in agreement with the calculated displacement profiles. In Figure 10-128 through Figure 10-130, the symbols N and S in the legend refer to the North and South sides, Δ_y' is the first yield displacement, $Ø_y'$ is the first yield curvature, and a depth equal to 0 ft. represents the soil surface.

As the test continued, the gap on the sides of the pile increased in size as the displacement ductility level increased. Minor loss of strength was observed up until all ductility level 3.0 (μ_3) cycles. The specimen failure (Figure 10-131) occurred at the second cycle load at ductility 5.0 (μ_5) when a significant drop in the force in the actuator was observed (i.e., ~34%). Moreover, twist rotation of the pile occurred for all push cycles at ductility levels 4.0 (μ_4) and 5.0 (μ_5). Finally, the test was terminated and the specimen was taken to zero displacement in order to facilitate its extraction from the soil.

Figure 10-132 presents the strain profiles for the first push and pull cycles at different displacement ductility levels, respectively. Notice that the largest tensile and compressive strains in the pipe were recorded at a depth between 1 ft. and 6 ft. In Figure 10-132 the symbols N and S in the legend refer to the North and South sides, and μ is the displacement ductility level. Curvature, rotation, and displacement profiles are presented in Figure 10-133 and Figure 10-134 for the first push and pull cycles, respectively. Note that the maximum curvature developed at a depth within 3 ft. and 4 ft., which is in agreement with the strain gauge data.

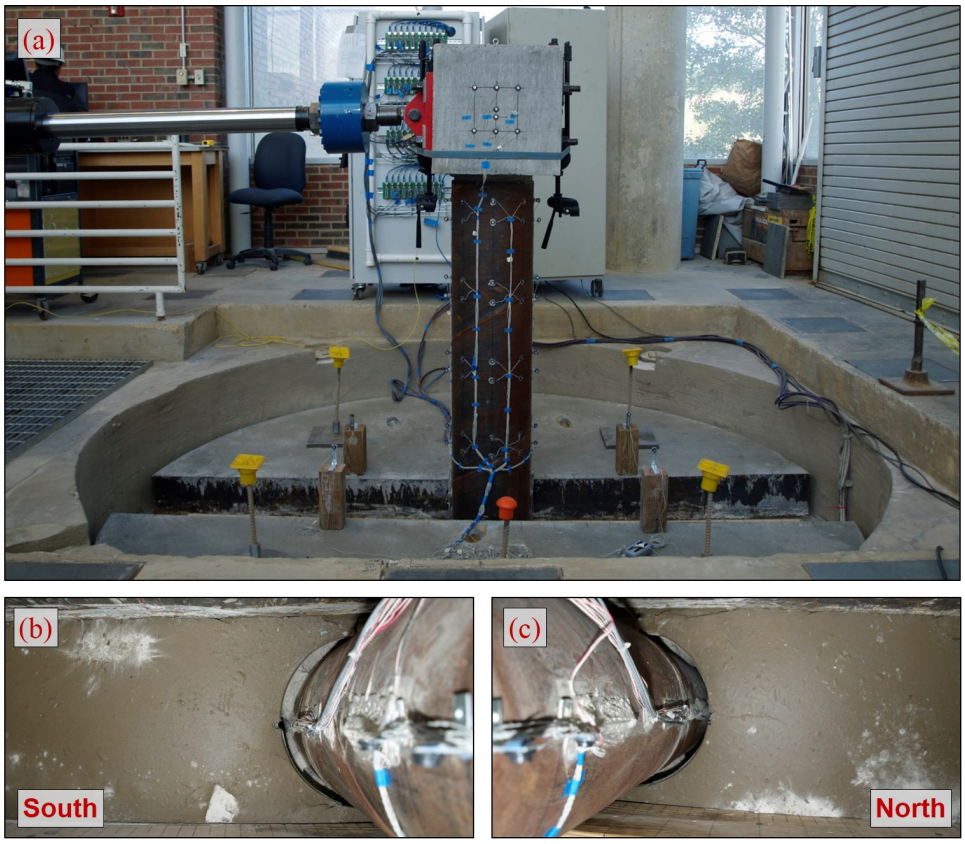

Figure 10-127 Test specimen #7 after elastic portion of the test was completed: (a) deformed shape, (b) South side and (c) North side

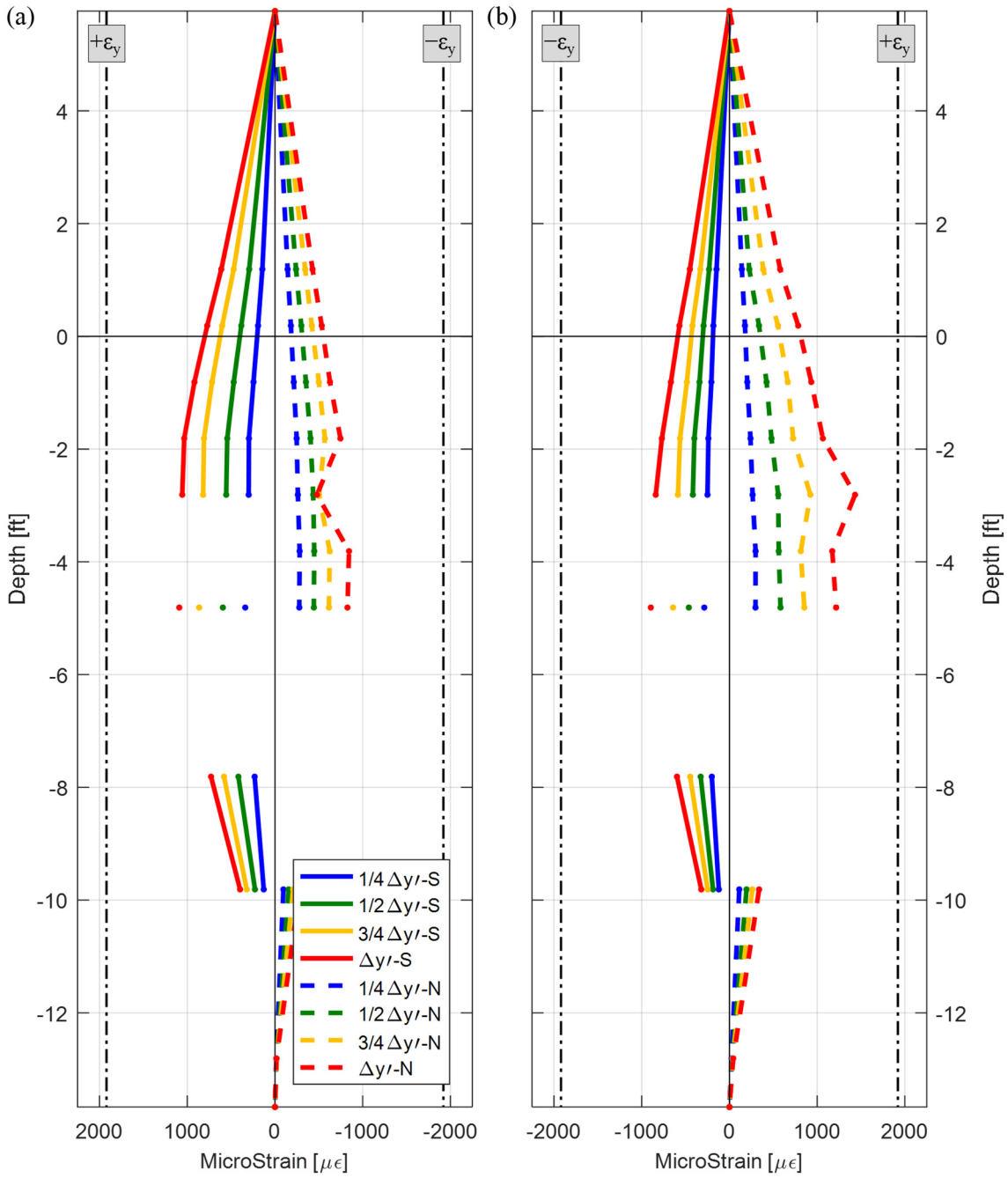

Figure 10-128 Test 7: strain profiles from elastic (a) push and (b) pull cycles

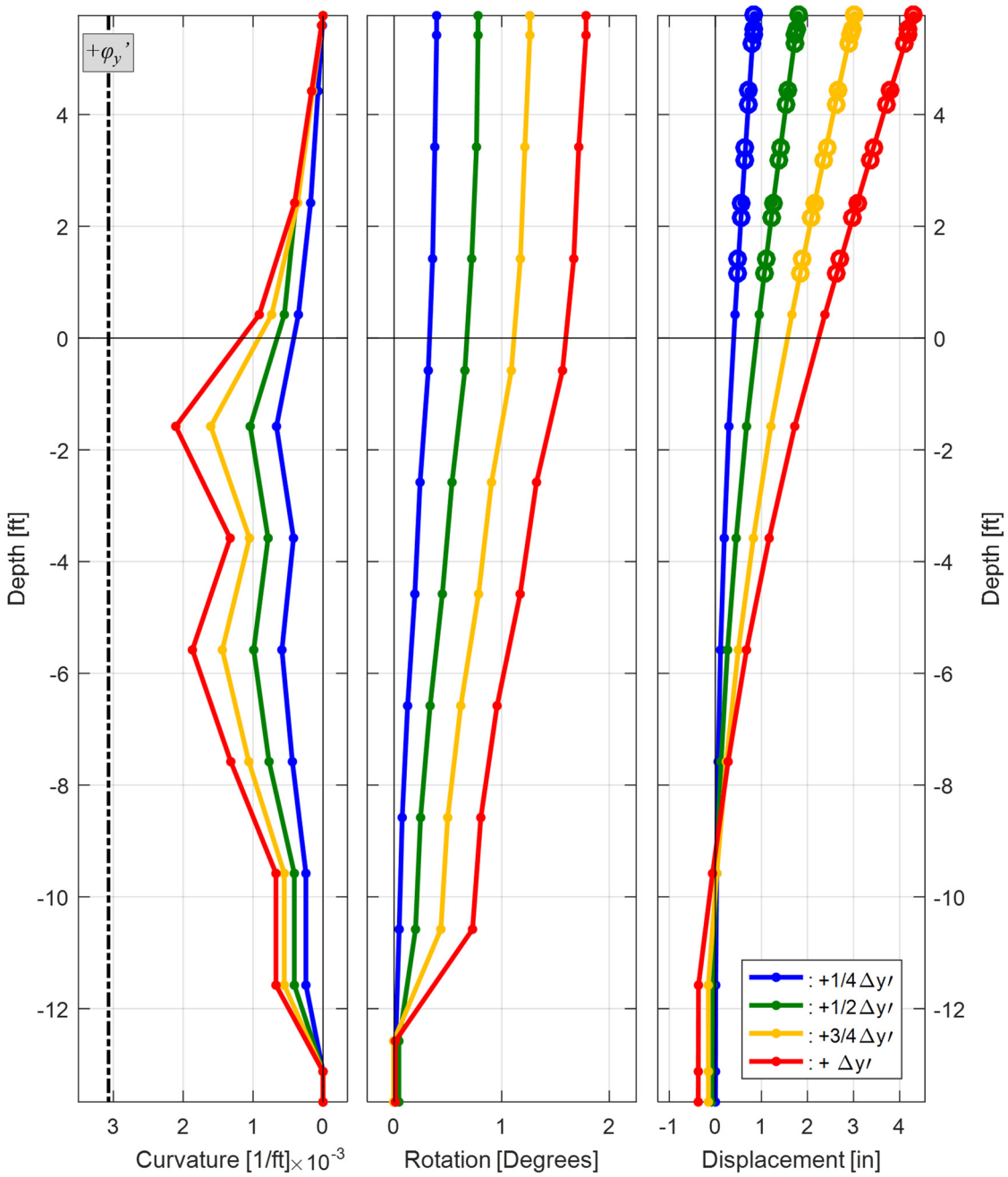

Figure 10-129 Test 7: curvature, rotation, and displacement profiles (elastic push cycles)

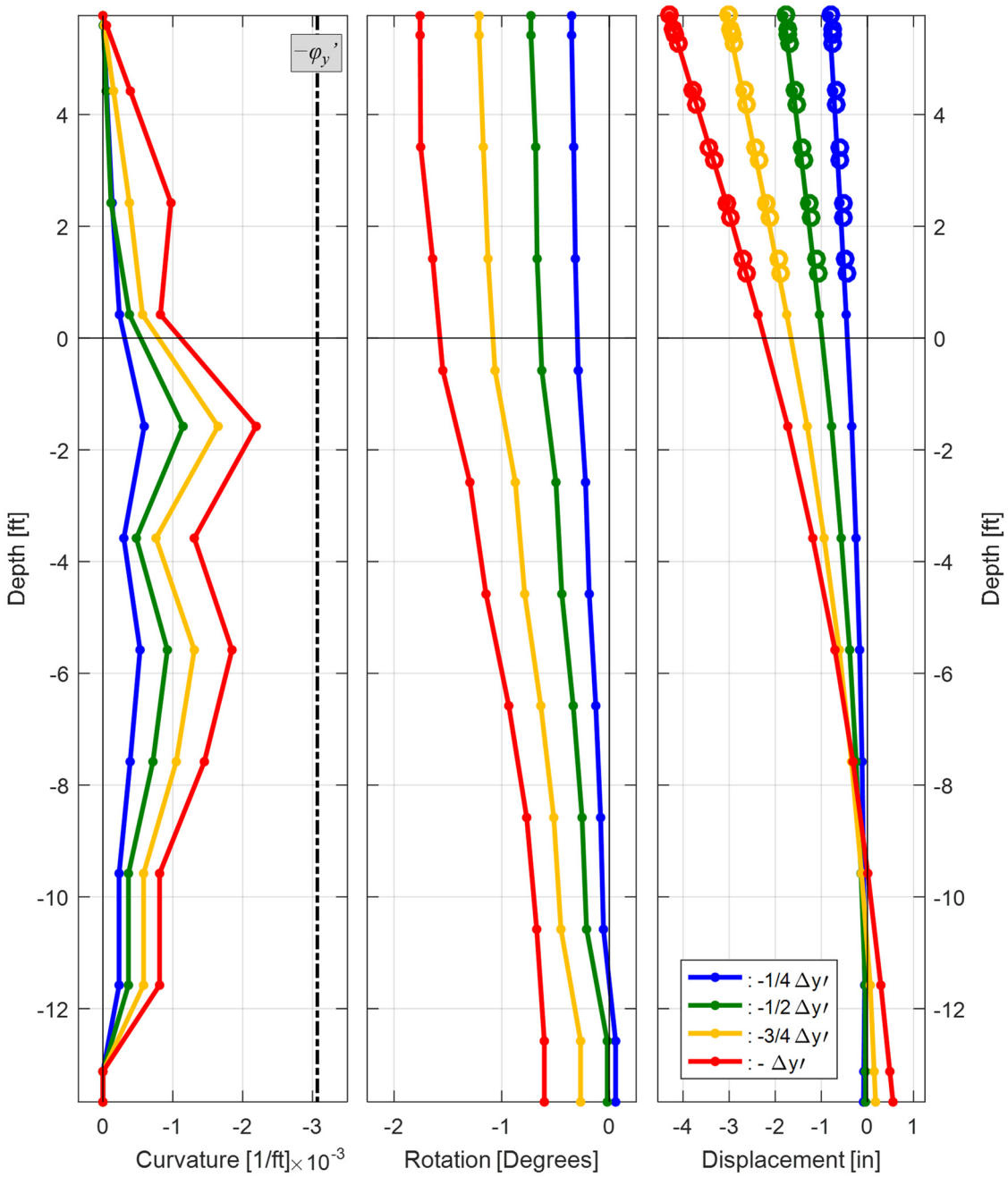

Figure 10-130 Test 7: curvature, rotation, and displacement profiles (elastic pull cycles)

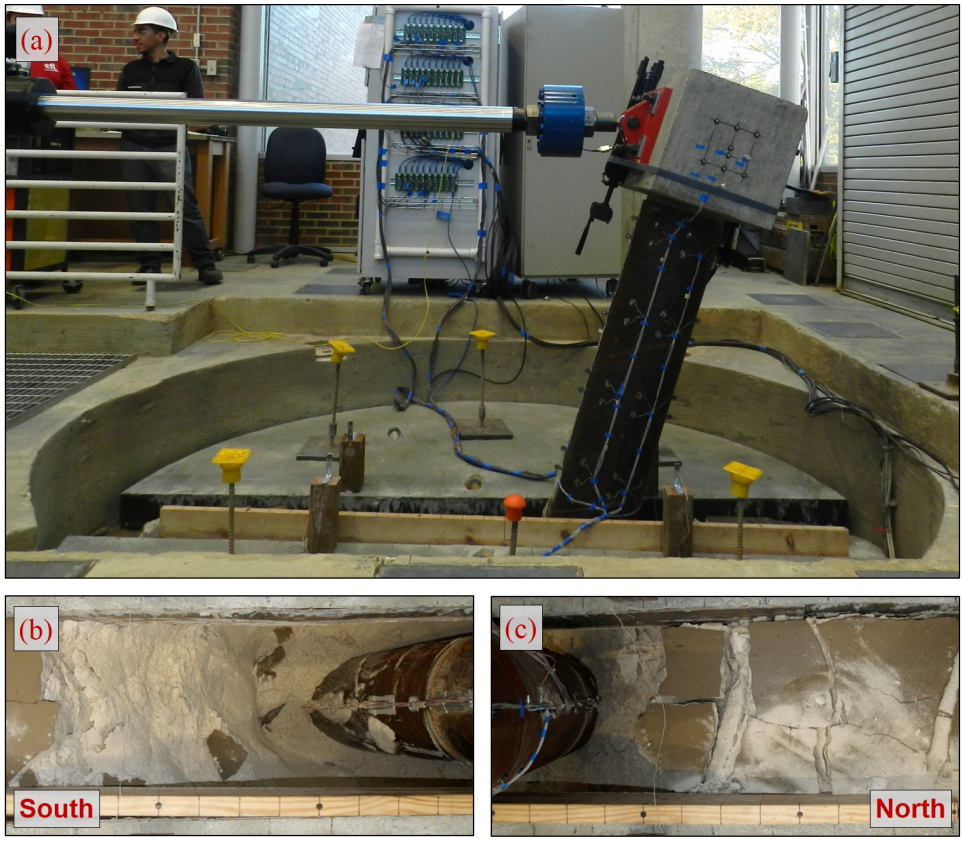

Figure 10-131 Test specimen #7 at maximum displacement: (a) deformed shape, (b) South side and (c) North side

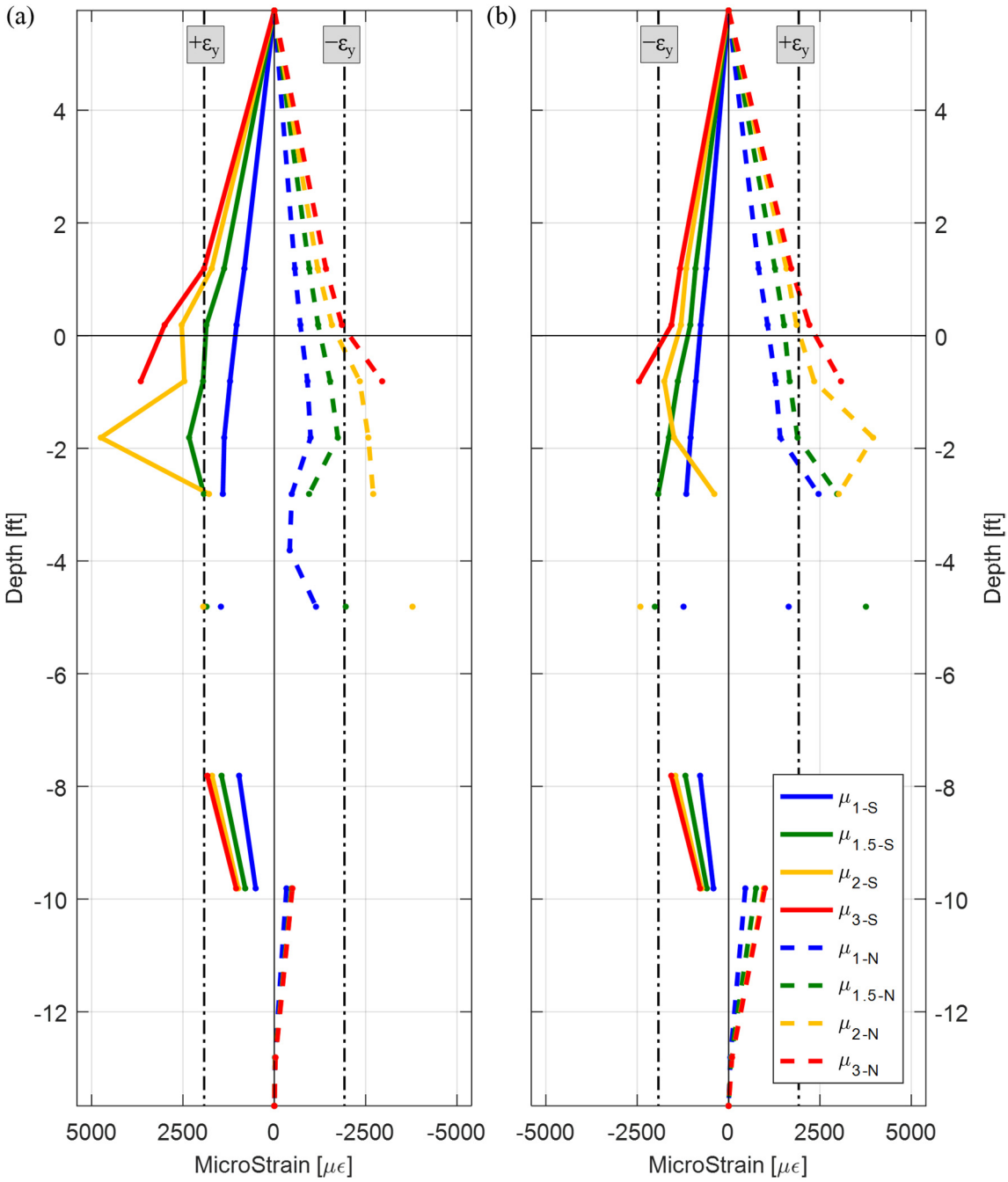

Figure 10-132 Test 7: strain profiles from inelastic (a) push and (b) pull cycles

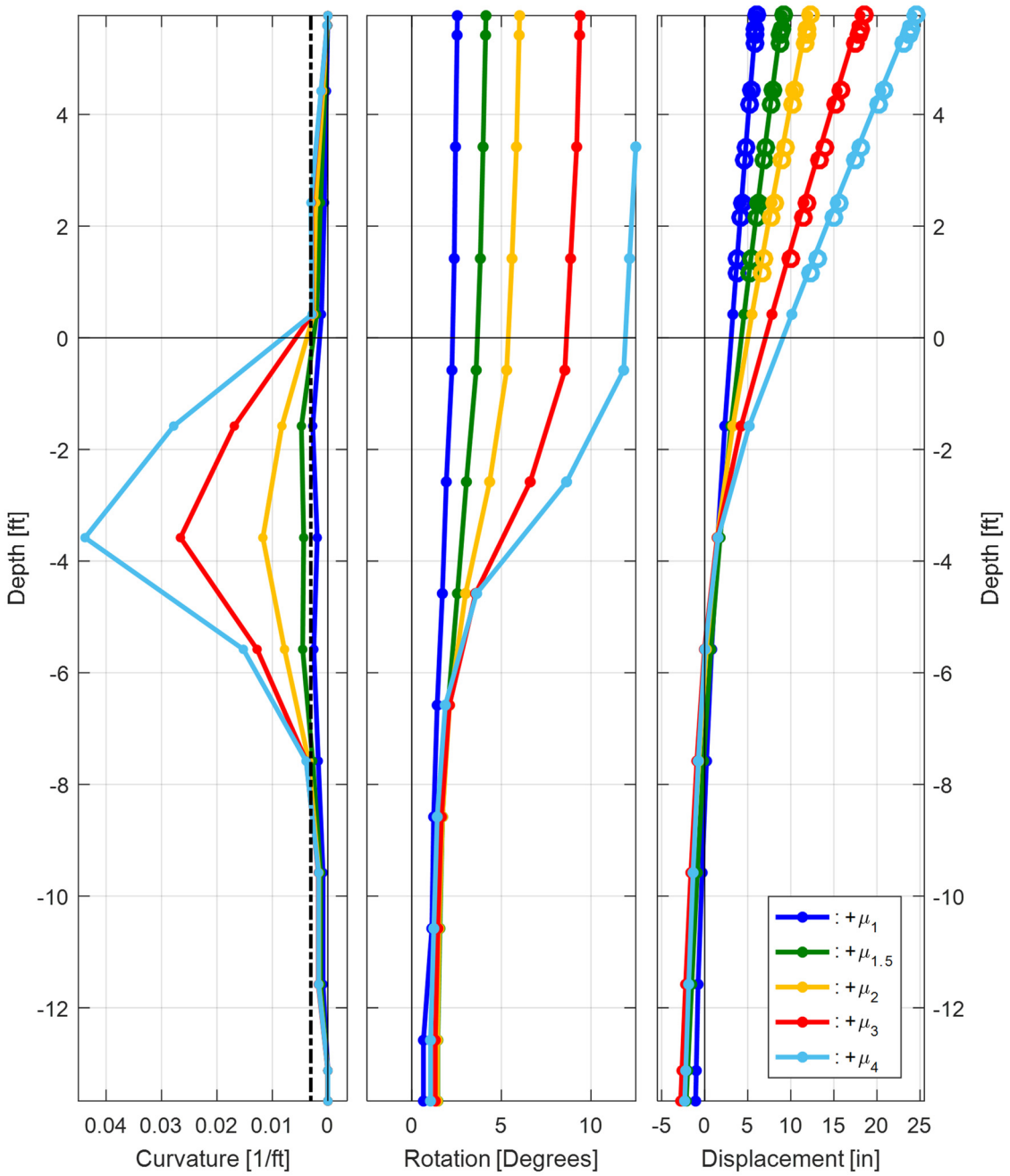

Figure 10-133 Test 7: curvature, rotation, and displacement profiles (inelastic push cycles)

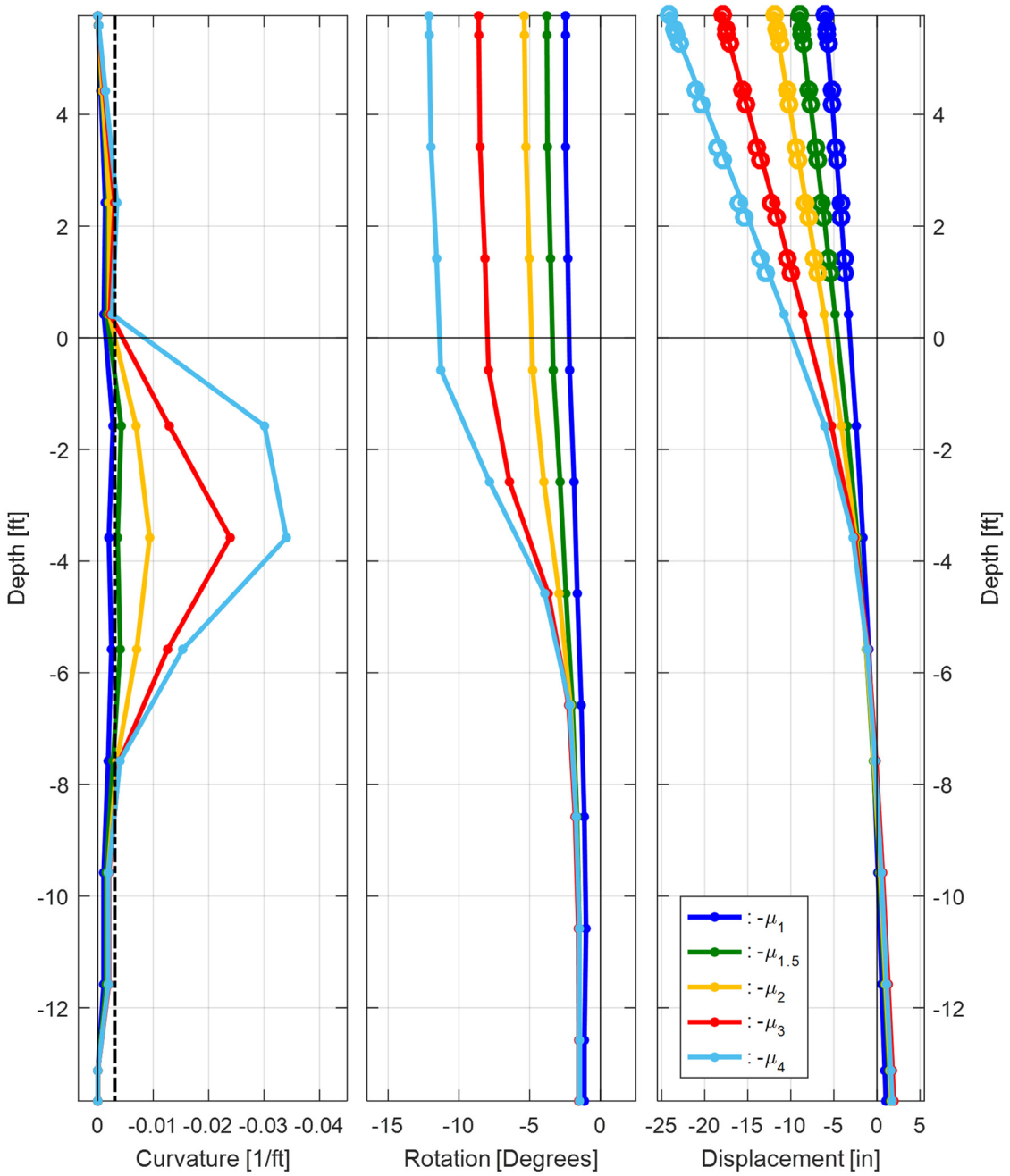

Figure 10-134 Test 7: curvature, rotation, and displacement profiles (inelastic pull cycles)

Figure 10-135 shows the state of the soil surface after the test was completed. Notice that despite the presence of the half-moon RC plates on the surface, deformations in the soil were large and followed an expected oval-shaped failure surface, in which active and passive pressures developed around the pile. This surface extended ~26.5 in. on both sides of the direction of loading and ~20 in. on the perpendicular direction. The total average settlement of the RC plates was ~2.47 in. This value was averaged based on the vertical displacement of 4 points on the RC plates. Figure 10-136 shows the average settlement of the half-moon RC plates during the test as a function of the imposed displacements in the top of the pile. Note that, as the displacement history is applied, the settlement increases, though its magnitude is larger at the beginning of the test.

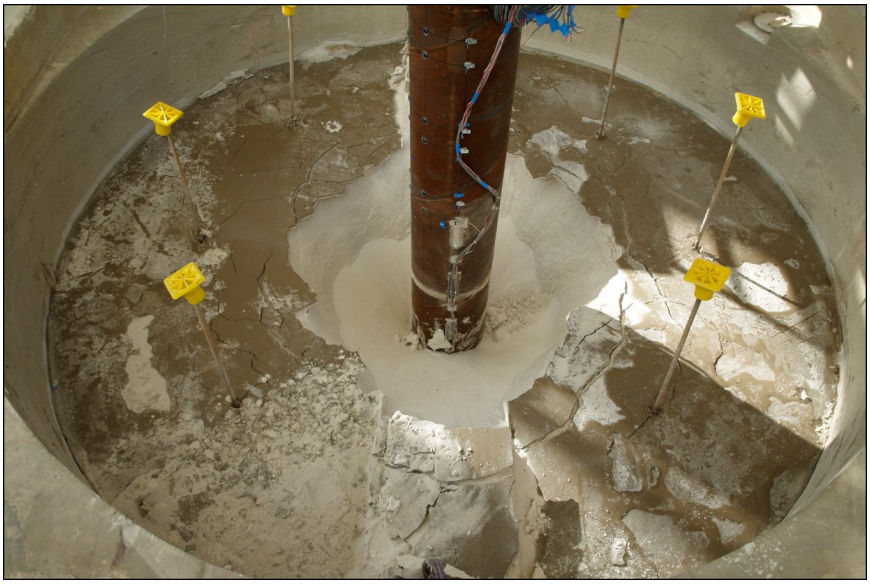

Figure 10-135 Test 7: soil surface after testing

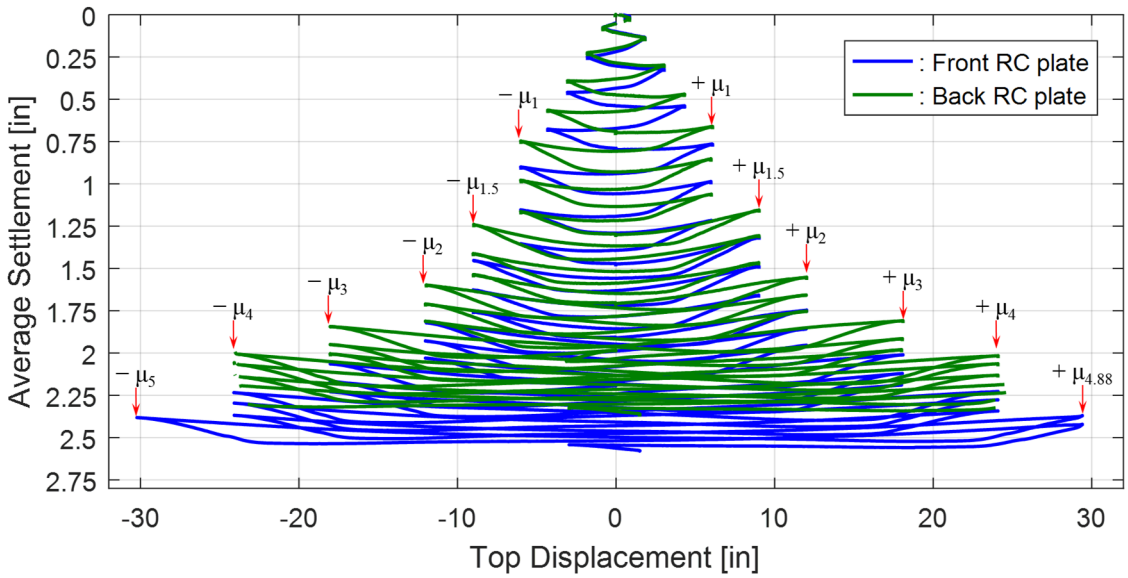

Figure 10-136 Test 7: half-moon RC plate settlement during testing

Figure 10-137 through Figure 10-141 present the damage observed after the pile was extracted from the soil. As thought during the test, tube fracture and tube buckling as well as bar buckling did occur; bar fracture was not observed. It can be seen that tube buckling developed on both sides of the specimen. The sections with the largest buckling occurred at a depth of 2 ft. – 8 ¼ in. on both North and South sides of the specimen. Secondary buckled regions were observed equally on both sides of the specimen, next to the main buckled regions at depths of 3 ft. – 8 ¼ in. and 3 ft. – 7 ½ in. on the North and South sides of the specimen. Figure 10-138 presents measurements of the secondary buckled regions. It can be seen that the deformations due to buckling protruded ~1/2 in. and ~3/8 in. on the North and South sides of the specimen, respectively. The plastic hinge developed at an average depth of 3 ft. – 3/16 in. with respect to the soil surface.

Tube fracture (Figure 10-137) occurred on the South side of the specimen and it extended about a quarter of the cross-section perimeter, resulting in a significant drop in strength due to lost tension capacity. As a consequence, after rupture, tension capacity is provided by the longitudinal reinforcement, which has a smaller area in comparison with that provided by the tube, inducing high stresses and deformations. Upon further investigations, bar buckling was observed only on the south side of the specimen. Note that tube fracture occurred in the section with the largest pipe buckling, in which deformations protruded ~5/8 in. on the South side of the pile.

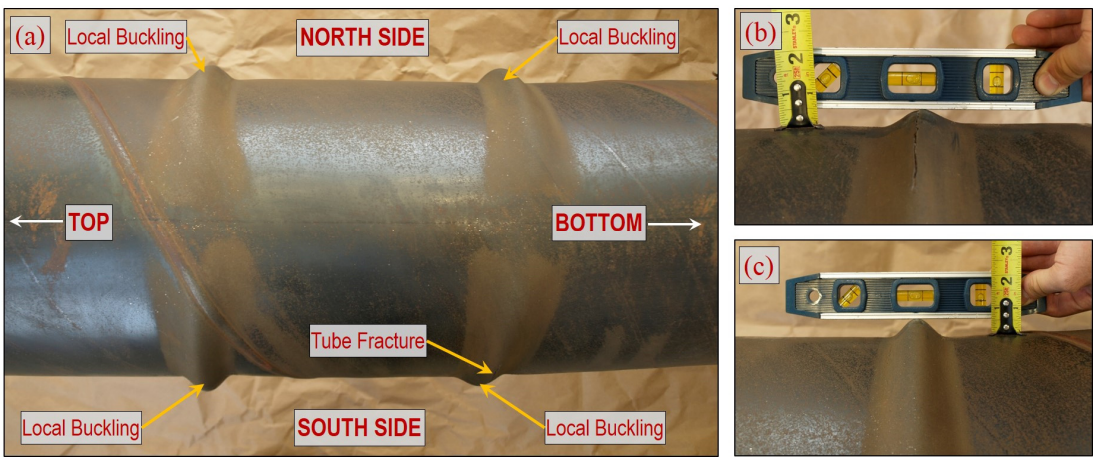

Figure 10-137 Test 7: (a) Final observed damage, (b) tube fracture, and (c) tube local buckling

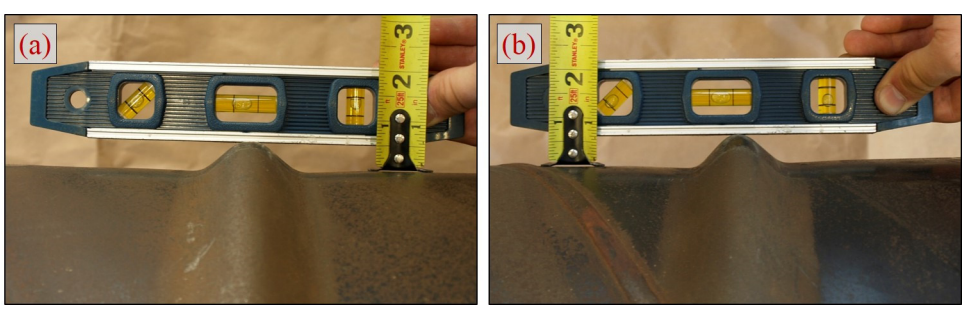

Figure 10-138 Test 7: secondary buckled sections on (a) North side and (b) South side

In order to further investigate the significant strength loss and to verify whether bar fracture or bar buckling occurred, a portion of the tube (i.e., 10 in. x 12 in.) was removed at the ruptured section in the extreme fiber on both sides of the pile (Figure 10-139 and Figure 10-140). It can be noticed that several cracks developed in this area of the concrete, perpendicular to the longitudinal direction of the specimen. Note also that the concrete cracking extended further to the center of the section. Note that concrete cracking only occurred close to the section of tube fracture and tube buckling; concrete cracks beyond this section were not observed. On the other hand, bar buckling was observed in three longitudinal bars on the South side of the specimen (Figure 10-141). It is believed that this occurred during the first pull cycle at ductility level 5.0 (μ_5), prior tube fracture in the subsequent push cycle at that ductility level. Note that bar buckling occurred only in the section of the largest crack in the concrete, located beneath the ruptured section of the tube.

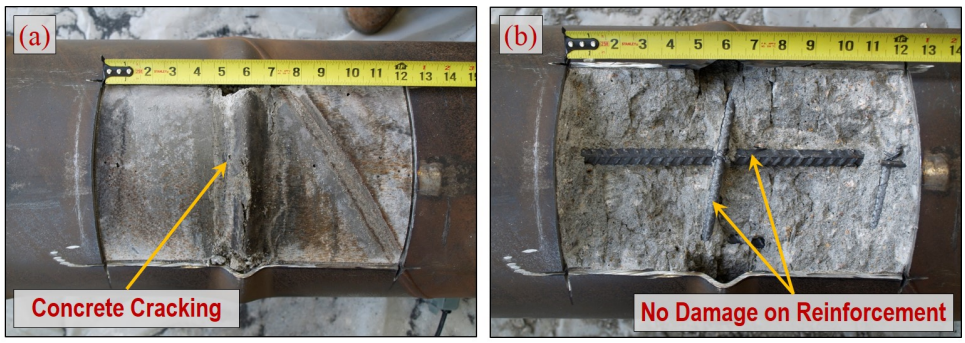

Figure 10-139 Test 7: observed damage in (a) concrete and (b) internal reinforcement on North side

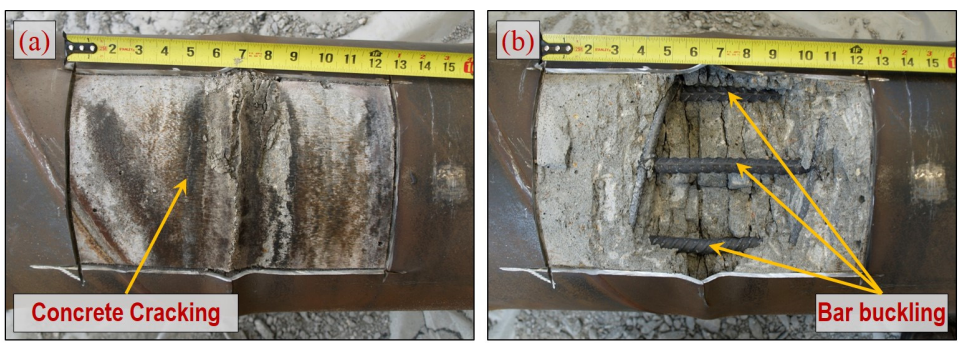

Figure 10-140 Test 7: observed damage in (a) concrete and (b) internal reinforcement on South side

Figure 10-141 Test 7: observed bar buckling on South side

Conclusions

Test specimen #7 showed a reliable response through all ductility 4.0 (μ_4) cycles. It is believed that onset of tube local buckling occurred during the test at ductility level 2.0 (μ_2), when large tensile strains were recorded. The test specimen completed all cycles of ductility 4.0 (μ_4) with minor loss of strength. A significant drop in strength occurred at ductility level 4.88 ($\mu_{4.88}$) when tube fracture developed on the South side of the specimen during the second push cycle at this level. Further investigations revealed that failure occurred due to a combination of tube local buckling, tube fracture, and bar buckling. Although the specimen was subjected to a maximum displacement ductility of 4.88 ($\mu_{4.88}$) in the pull cycles, it is believed that this particular specimen is capable of having a reliable displacement up to ductility 4.0 (μ_4). The main buckles as well as tube fracture did not occur over the spiral weld, so the tube spiral welds do not appear to negatively influence the behavior.

Test 8 Summary Report

January 20, 2016

Prepared for

Alaska Department of Transportation

Alaska University Transportation Center

Project Team

RA: Diego Aguirre

PIs: Mervyn Kowalsky, James Nau, Mo Gabr

Other Senior Personnel: Greg Lucier, Ben Smith

North Carolina State University

Executive Summary

Test 8 was conducted December 9th, 2015 at the North Carolina State University Constructed Facilities Laboratory. The tested pile-column specimen was a reinforced concrete filled steel tube with a diameter-to-thickness (D/t) ratio of 68. A surcharge of ~960 psf was applied to the soil prior to and during the test, thus the soil stiffness was expected to change. The test was successfully conducted to failure, which was caused by a combination of tube local buckling and tube fracture, resulting in a large strength degradation (~24.83%) in the third cycle at ductility level 4.0 (μ_4).

Specimen and Test Description

Test 8 consisted of a 19-foot-5.25-inch long, reinforced concrete filled, 12-3/4-inch diameter spirally welded steel tube without skelp or splice welds. The pile-column specimen was embedded 13 ft. – 8 in. into clean sand in the soil-structure interaction facility at the NCSU-CFL. Lateral load was applied at the pinned connection at the top of the pile specimen by means of a 100-kip, 70-inch stroke hydraulic actuator. The nominal wall thickness of the tube was 0.187 in., providing a nominal diameter-to-thickness ratio (D/t) of 68. The test was conducted with a 5-foot-9.25-inch cantilever length, measured from the soil surface to the point at which the lateral load was applied. Figure 10-142 and Figure 10-143 present a schematic of the test setup (elevation) and the specimen #8 cross-section, respectively, while

Figure 10-144 shows the instrumentation used for testing. A photograph of the test setup is included in Figure 10-145.

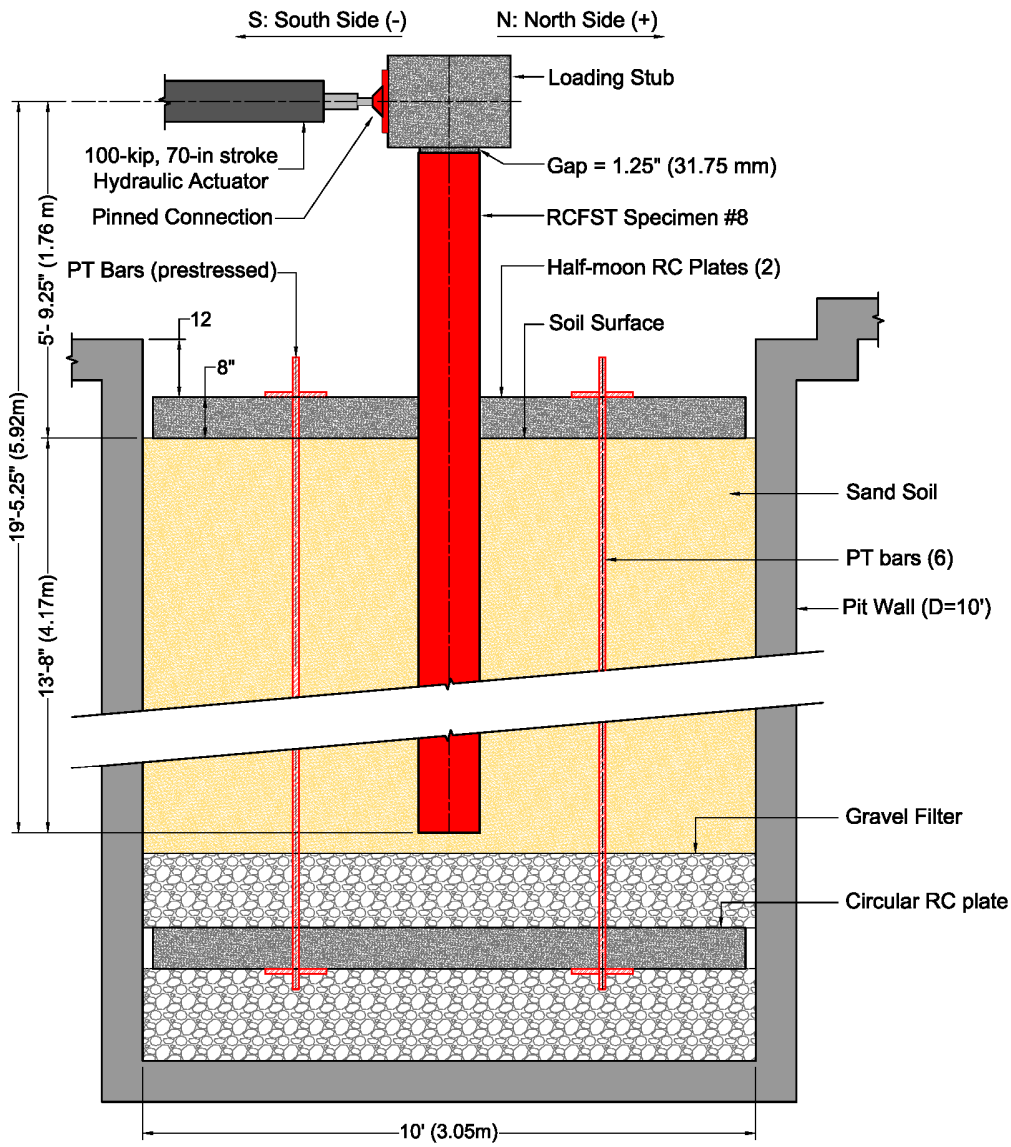

Figure 10-142 Test 8: test setup elevation schematic

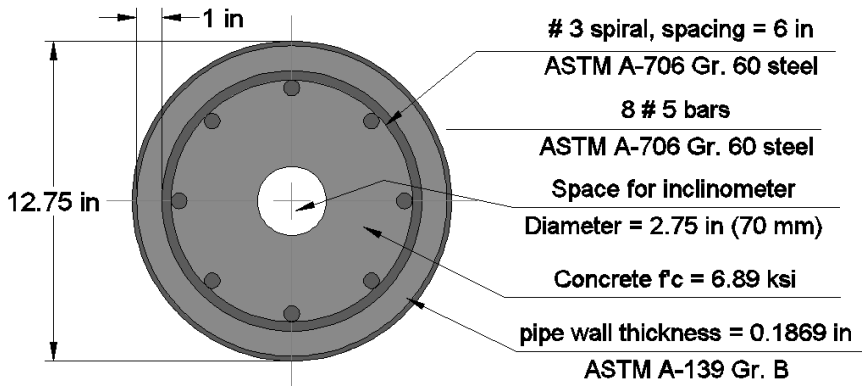

Figure 10-143 Test 8: RCFST specimen cross section

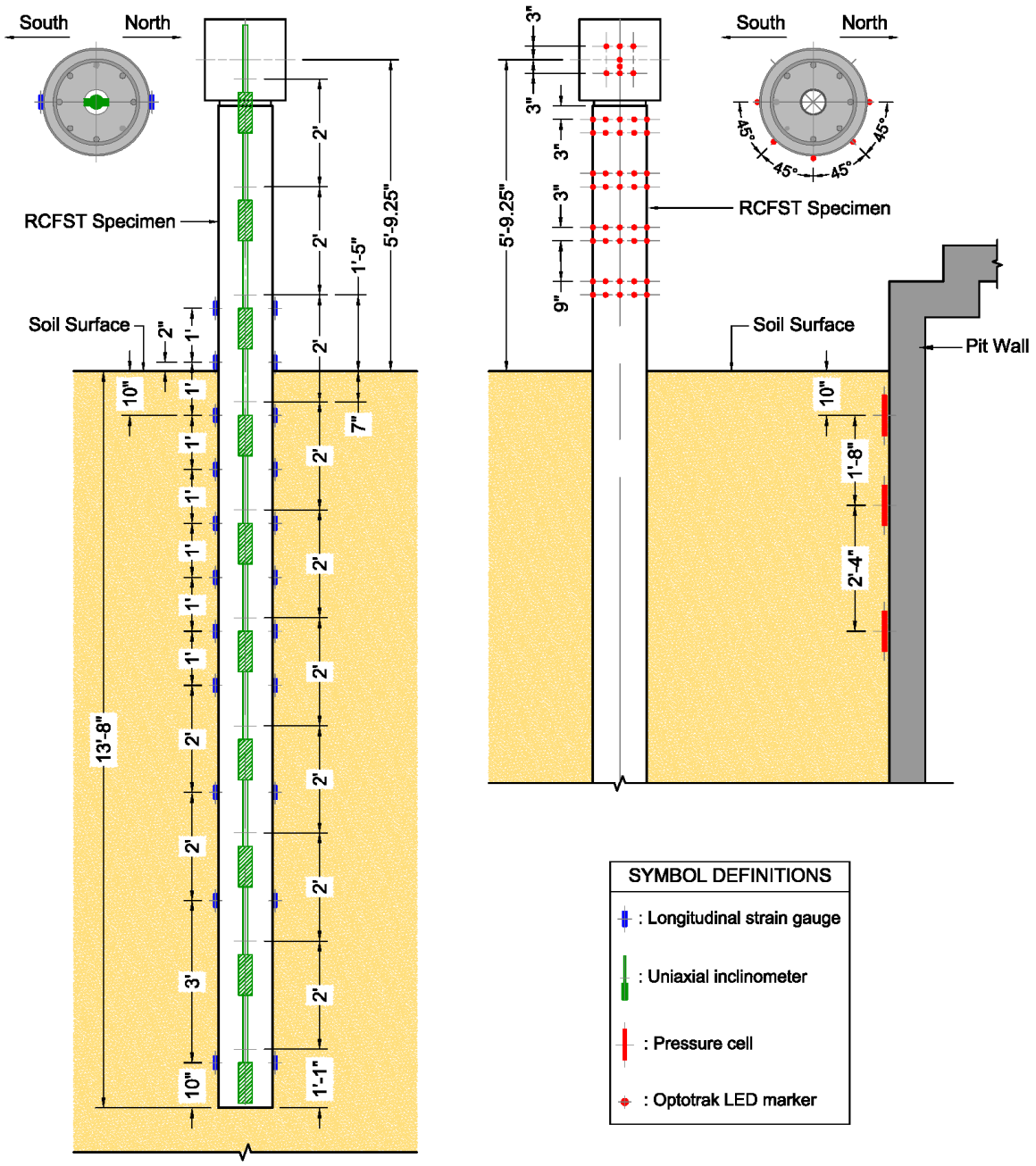

Figure 10-144 Test 8: instrumentation

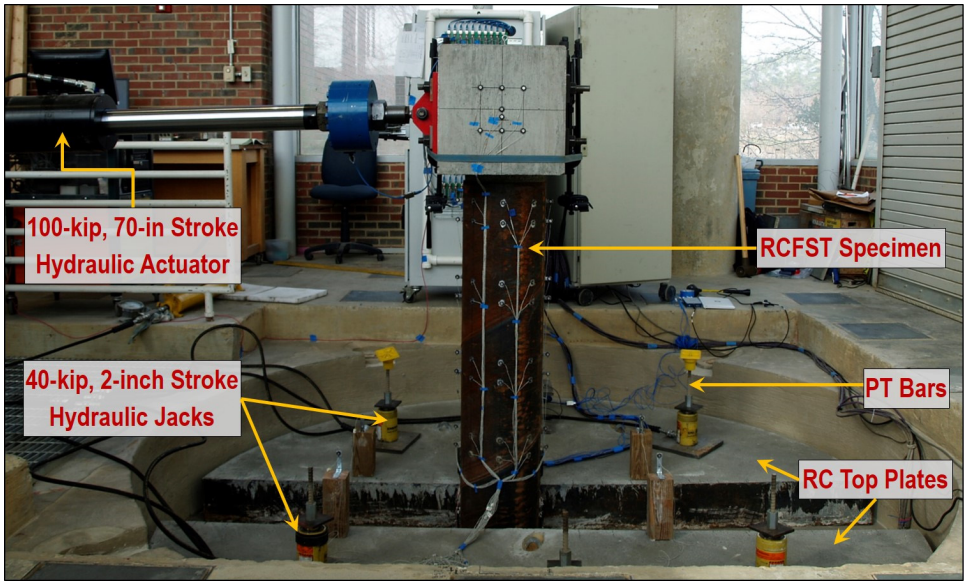

Figure 10-145 Test 8: pinned-head, RCFST pile-column test setup

Material properties were determined by in-house material tests. The yield and ultimate stresses of the steel tube were 55.6 ksi and 74.7 ksi, respectively, based on tests conducted on three (3) coupons cut from the end of the test pile specimen. The yield and ultimate stresses of the ASTM A706 Grade 60 longitudinal reinforcement were 70.7 ksi and 99.6 ksi, respectively, based on tests conducted on six (6) bar specimens from the same heat of the longitudinal reinforcement. The yield and ultimate stresses of the spiral reinforcement were 64.6 ksi and 95.3 ksi, respectively, based on tests conducted on six (6) bar specimens from the same heat of the transverse reinforcement. An average concrete compressive strength of 6.89 ksi (standard deviation of ± 0.32 ksi) was determined from three (3) compression tests of 4”x8” concrete cylinders.

Soil properties were also determined by in-house material tests. Based on a measured particle size distribution, the soil was classified as poorly-graded sand (SP). The unit weight, friction angle, and moisture content (γ = 90 pcf, ϕ = 35°, and w = 2.5%, respectively) were reasonably assumed based upon results of previous tests. An active surcharge was applied to the soil surface during the test by means of 40-kip, 2-inch stroke hydraulic jacks reacting on the half-moon RC plates. An axial load of 10.1 kips was applied to each of the six (6) PT bars, resulting in a surcharge pressure of 960 psf. In addition to the active pressure, the self-weight of the half-moon RC plates was acting on the soil surface as well (i.e., ~100 psf).

In an attempt to modify the soil properties prior to pile testing, five surcharge cycles were performed. The first four cycles were conducted using 80% of surcharge level to be applied during the test, i.e., q = 768 psf. The remaining cycle was applied using the same surcharge level to be applied during the test, i.e., q = 960 psf. All surcharge cycles were applied one day prior to pile testing, that is, on December 8th, 2015. Cycles 1 through 4 were applied without sustaining the pressure, namely, they were load-unload cycles which took approximately 30 minutes each. The fifth surcharge cycle was then applied and the pressure was sustained all the way until the pile testing was completed. The average settlement of the RC plates prior the pile testing was ~0.46 in. This value was averaged based on the vertical

displacement of 4 points on the RC plates. Results of the surcharge cycles are presented in Figure 10-146.

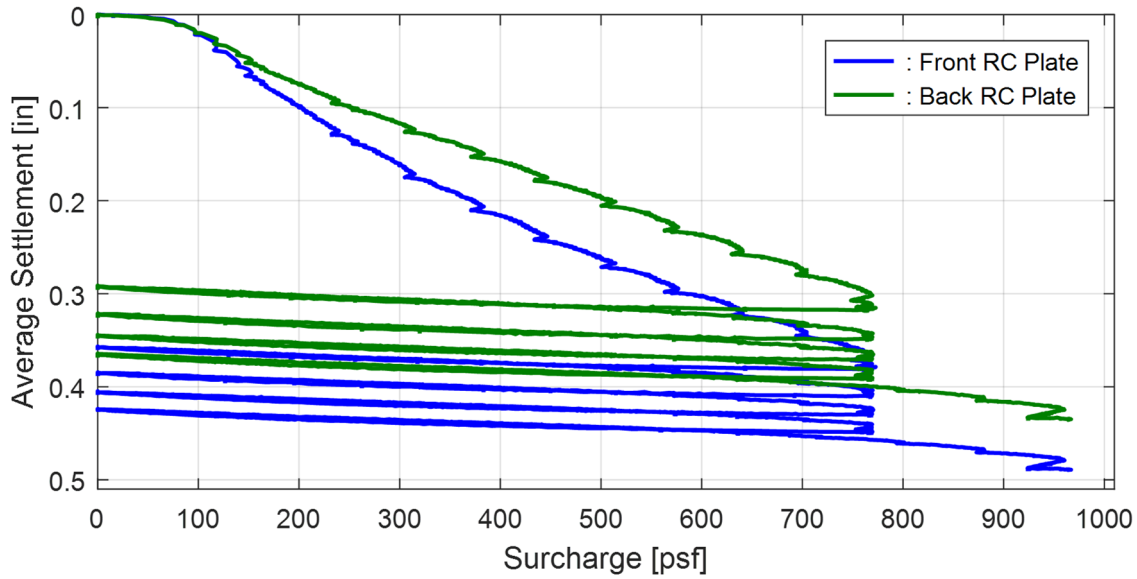

Figure 10-146 Test 8: half-moon RC plate settlement prior testing

The load history applied to the pile specimen consisted of standard three-cycle sets intended to evaluate both the elastic and inelastic response of the specimen. The first portion (i.e., pile elastic response up to first yield) of the test consisted of single reversed, displacement-controlled cycles, ramping up to the first yield displacement in ¼ increments. Given the non-linear response from the beginning of the test due to the characteristic soil behavior, target displacements in this portion of the test were determined based on the results of a monotonic pushover analysis performed using a detailed non-linear, fiber-based, finite element model developed using the OpenSees framework software. Soil-structure interaction was included by means of non-linear springs at 1-foot interval depths, with spring properties assigned based on p-y curves. The first yield force (F_y) and nominal force (F_n), which is defined as the force at a concrete compressive strain of 0.004 or at a tube/bar tensile strain of 0.015 (whichever occurs first), were determined based upon tensile and compressive strains monitored during the numerical simulation (i.e., pushover analysis), as 19.1 kips and 26.8 kips, respectively. Table 10-8 summarizes the target displacements for the first portion of the test.

After the first portion of the test was completed, the measured average strain at the predicted first yield displacement (Δ'_y = 4.10 in) was 1600 (με), which correlates well with the tube yield strain (ε_y = 1920 με). The measured average displacement at the first yield displacement (Δ'_y = 4.10 in) was modified by the nominal-to-first yield force ratio in order to determine the displacement ductility level 1.0 (μ_1 = 5.75 in), as shown in Equation 10-16. The remainder of the test was completed using reversed three-cycle sets in displacement-controlled increments at different levels of displacement ductility until failure, as shown in Equation 10-17. The entire displacement and load histories can be seen in Figure 10-147. Positive loads and displacements correspond to rightward (North) motion of the pile in the test setup. The positive legs of all cycles were completed before the negative legs.

Table 10-8 Test 8: predictions for elastic portion

Performance Level	Displacement (in)	Force (kips)
1/4 Δy'	0.69	5.87
1/2 Δy'	1.65	10.80
3/4 Δy'	2.84	15.36
1 Δy'	4.10	19.15

$$\Delta_y = \mu_1 = \Delta'_y \cdot \frac{F_n}{F_y} = 4.10\,in \cdot \frac{26.8\,kip}{19.1\,kip} = 5.75\ in \qquad \text{Equation 10-16}$$

$$\mu_i = i \cdot \mu_1 \rightarrow i = 1.0,\ 1.5,\ 2.0,\ 3.0,\ 4.0 \qquad \text{Equation 10-17}$$

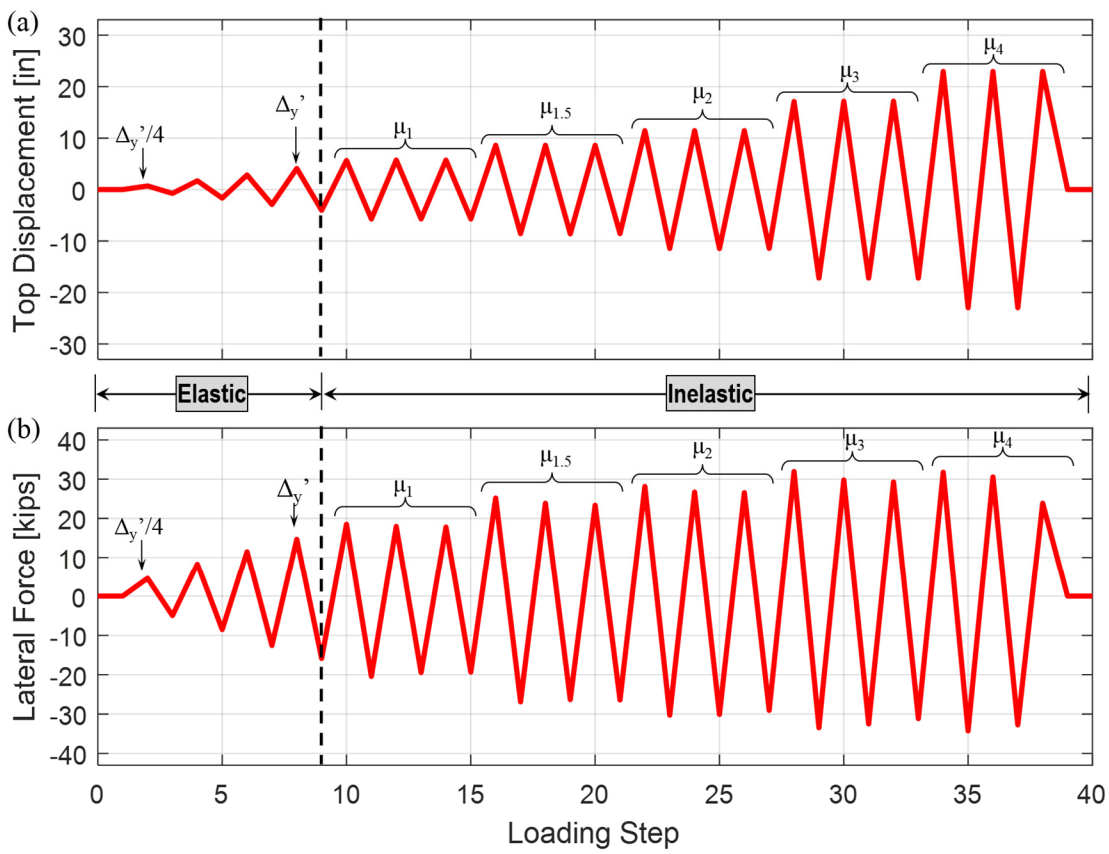

Figure 10-147 Test 8: (a) displacement and (b) loading histories

Specimen Response

Specimen #8 performed well through the elastic portion of the test and during all three cycles of ductility level 3.0 (μ_3). It is believed that the onset of tube buckling occurred early during the displacement cycles at ductility level 2 (μ_2) as some of the calculated curvatures indicated large values during both push and pull cycles at the aforementioned ductility level. A significant loss of strength, indicating failure, occurred during the third push cycle at ductility level 4.0 (μ_4). Figure 10-148 and Figure 10-149 present the lateral force vs. top displacement response and envelopes, respectively. It can be seen that the system has a characteristic large energy dissipation capacity due to both damping sources, that is, the pile itself and the surrounding soil. In addition, it can be clearly seen from both figures that a significant loss of strength (~25.3%) occurred during the third push cycle of ductility level 4.0 (μ_4).

Figure 10-150 presents the deformed shape and the soil-pile gaps at zero displacement after the elastic portion of the test was conducted; the size of the gap was ~1.5 in on both sides of the specimen. As it was previously explained, at this point of the test strain profiles on the sides of the pile were verified in order to further conduct the test at the aforementioned ductility levels. Figure 10-151 presents the strain profiles recorded during the first portion of the test. Notice that tensile strains of 1510 ($\mu\varepsilon$) and 1690 ($\mu\varepsilon$) were recorded in the tube during the push and pull cycles, respectively, when the predicted first yield displacement was imposed to the system. Based on the rotation data recorded with the inclinometer placed inside the pile along its length, specimen curvature, rotation, and displacement profiles are presented in Figure 10-152 and Figure 10-153 for the first push and pull cycles, respectively. Note that there are small rotations and displacements at the pile tip which indicates that there is a point of rotation (at ~10 ft.) rather than a point of fixity; inelastic action was developed in the pile nonetheless. The circles in the top portion of the displacement profiles in Figure 10-152 and Figure 10-153 represent the Optotrak LED markers; note that they are in agreement with the calculated displacement profiles. In Figure 10-151 through Figure 10-153 the symbols N and S in the legend refer to the North and South sides, Δ_y' is the first yield displacement, $Ø_y$' is the first yield displacement, and a depth equal to 0 ft. represents the soil surface.

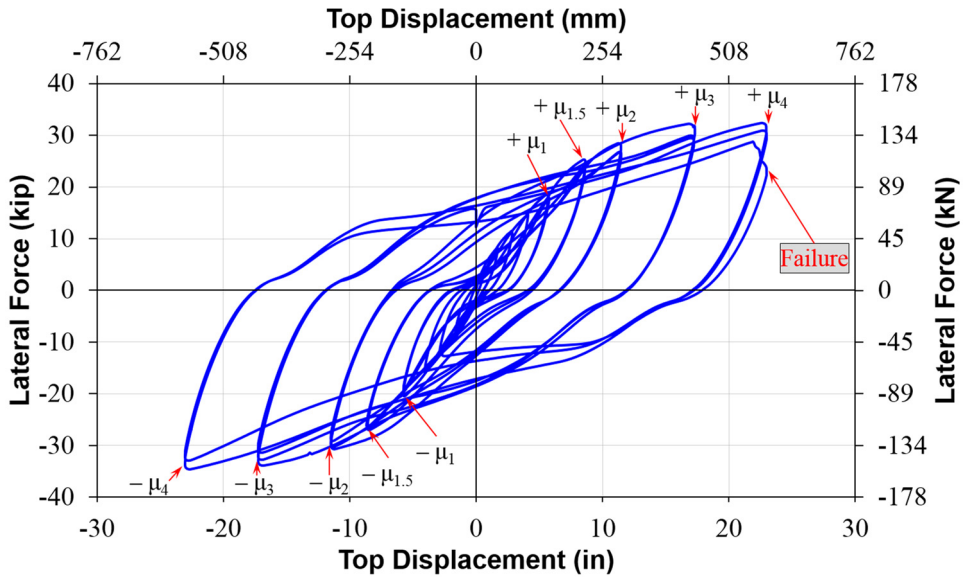

Figure 10-148 Test 8: lateral force vs. top displacement response

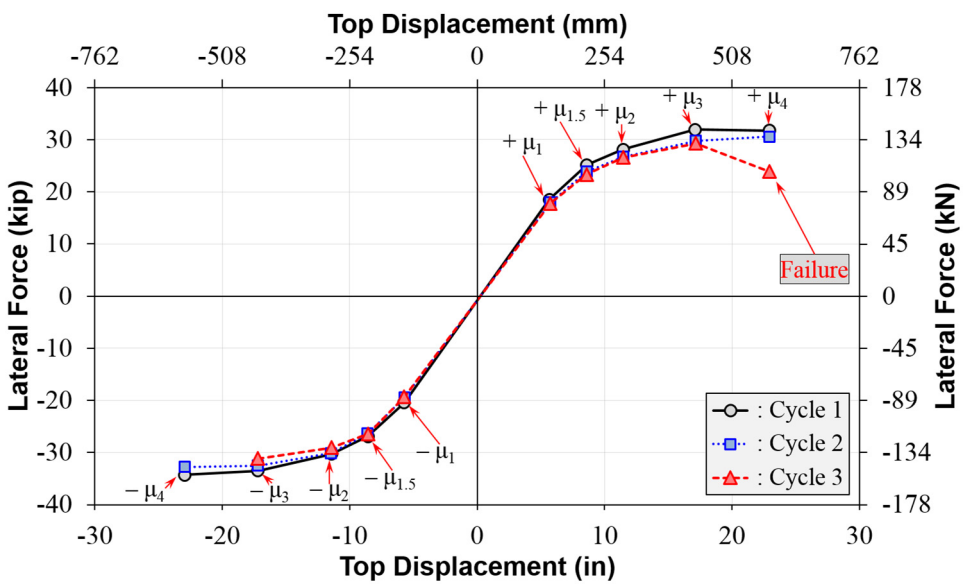

Figure 10-149 Test 8: lateral force vs. top displacement envelopes

Figure 10-150 Test specimen #8 after elastic portion of the test was completed: (a) deformed shape, (b) South side and (c) North side

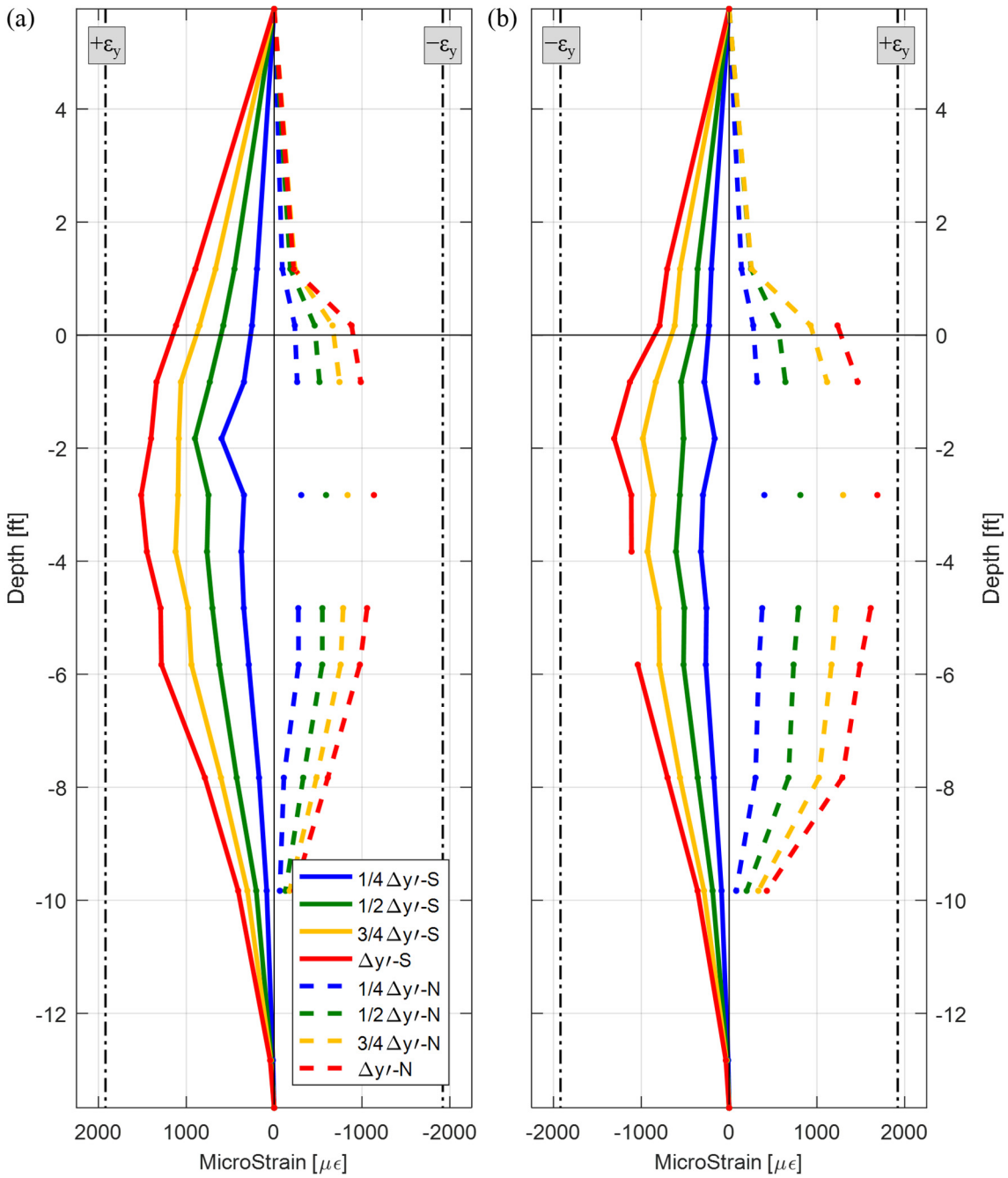

Figure 10-151 Test 8: strain profiles from elastic (a) push and (b) pull cycles

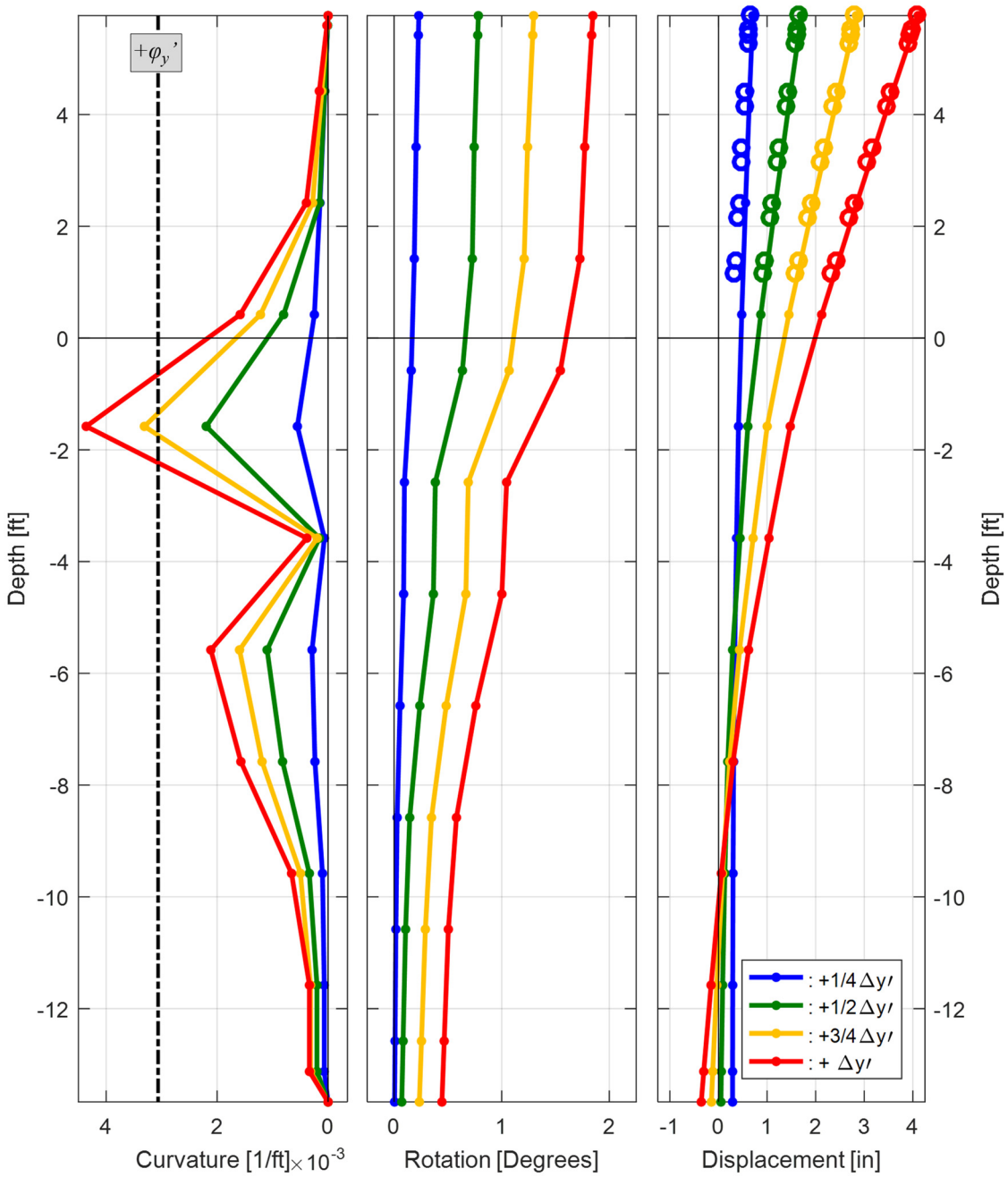

Figure 10-152 Test 8: curvature, rotation, and displacement profiles (elastic push cycles)

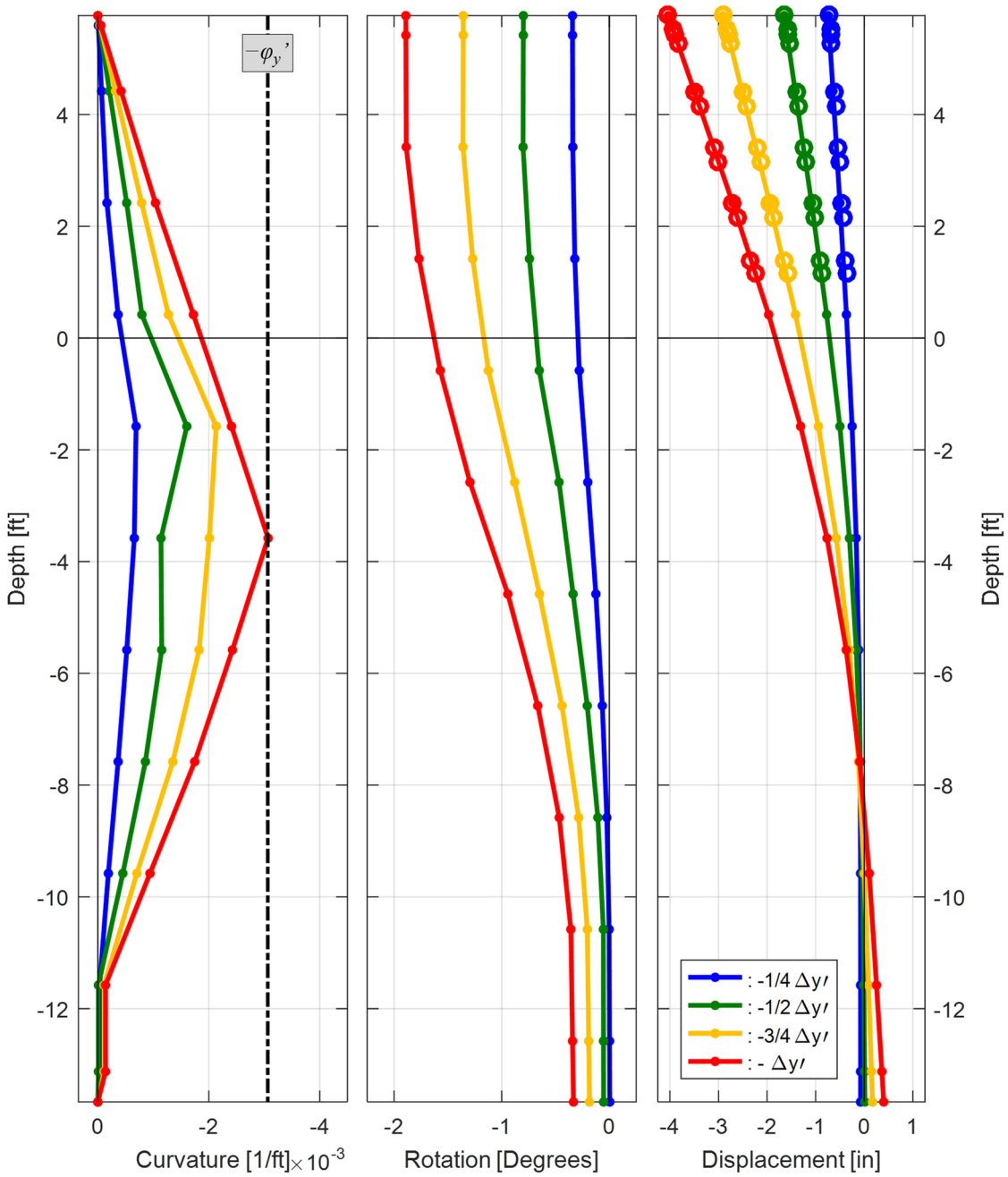

Figure 10-153 Test 8: curvature, rotation, and displacement profiles (elastic pull cycles)

As the test continued, the gap on the sides of the pile increased in size as the displacement ductility level increased. Minor loss of strength was observed up until all ductility level 3.0 (μ_3) cycles. The specimen failure (Figure 10-154) occurred at the third cycle load at ductility 4.0 (μ_4) when a significant drop in the force in the actuator was observed (i.e., ~25.3%). Sounds indicating steel fracture were heard at the same time when the strength loss occurred, indicating probable tube or bar fracture. Moreover, twist rotation of the pile occurred for all push cycles at ductility levels 3 (μ_3) and 4 (μ_4). Finally, the test was terminated and the specimen was taken to zero displacement in order to facilitate its extraction from the soil.

Figure 10-155 presents the strain profiles recorded during the inelastic portion of the test. Although the available data is limited, it can be seen that large tensile strains were recorded at a depth between 1 ft. and 5 ft., which correlates well with the observed damage. Curvature, rotation, and displacement profiles are presented in Figure 10-156 and Figure 10-157 for the first push and pull cycles, respectively. Note that the largest curvature occurred at a depth between ~1 ft. and ~4 ft., which correlates well with the position of the observed plastic hinge, determined after the test was completed.

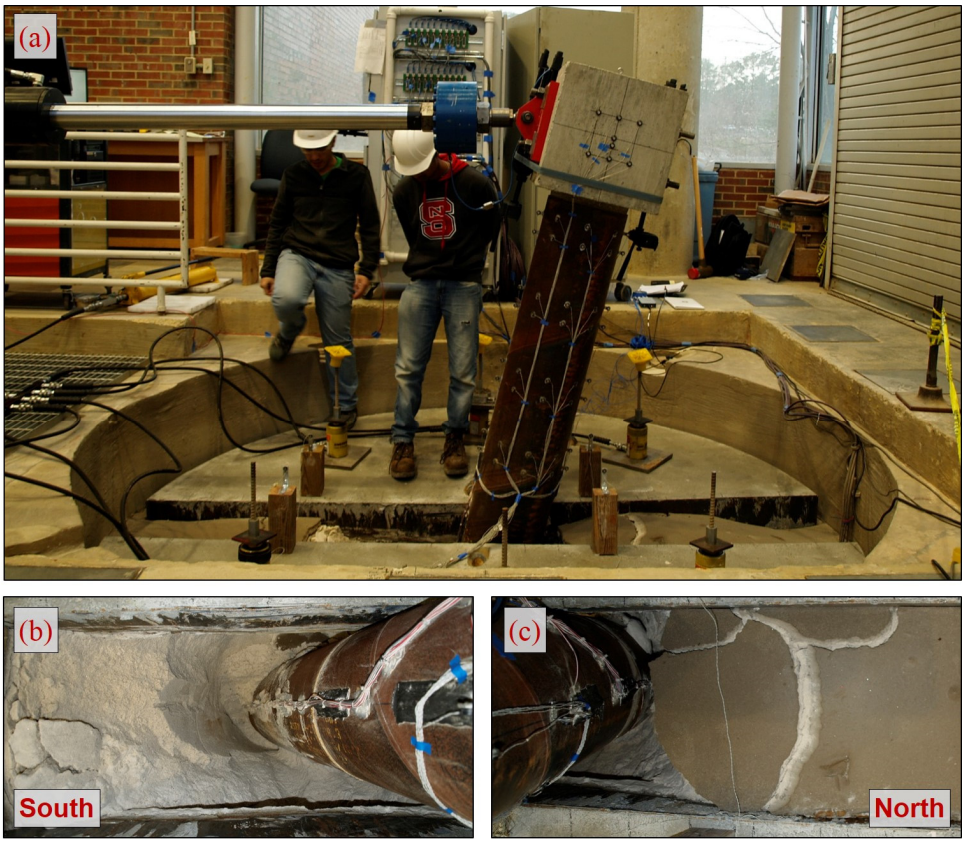

Figure 10-154 Test specimen #8 at maximum displacement: (a) deformed shape, (b) South side and (c) North side

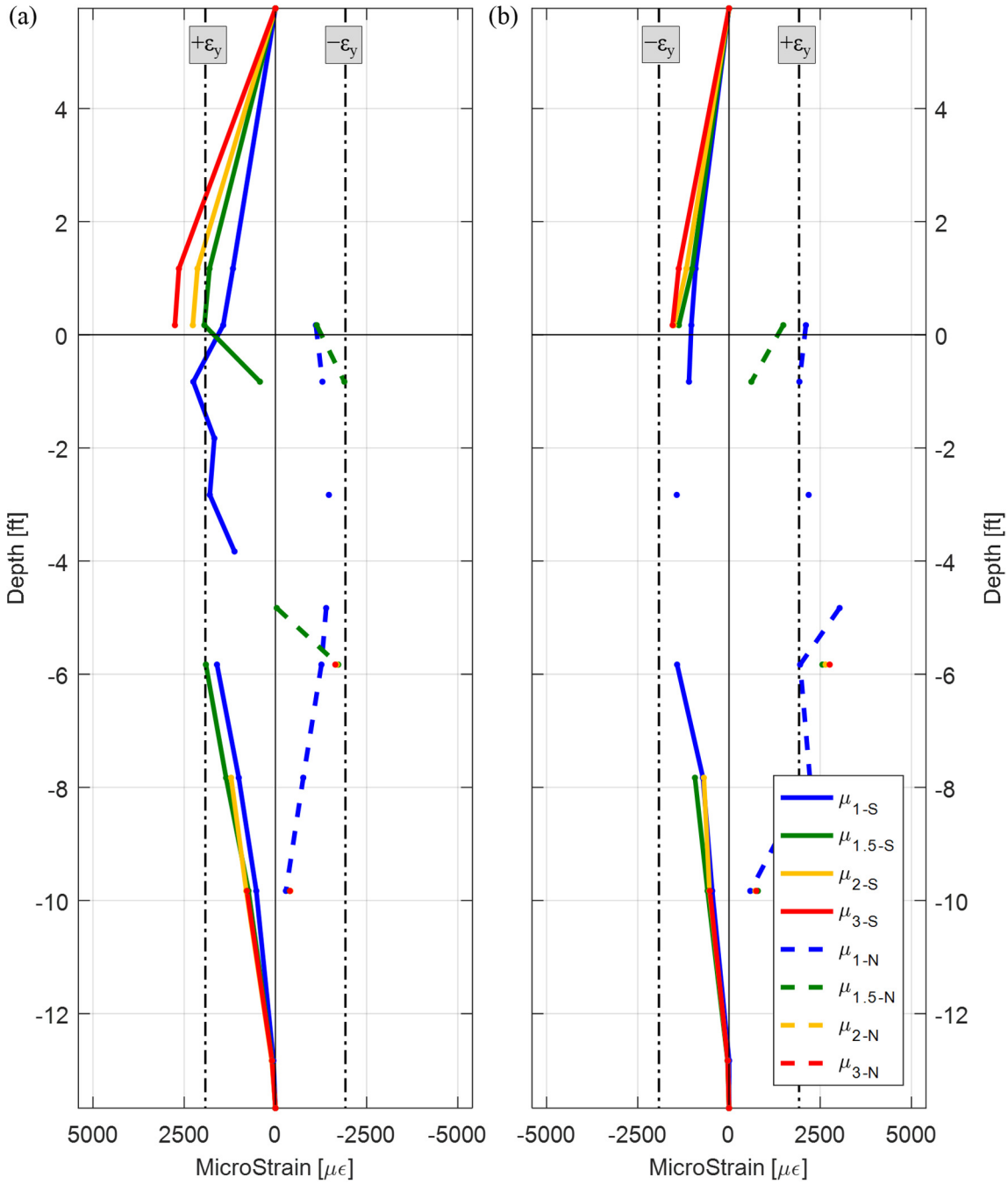

Figure 10-155 Test 8: strain profiles from inelastic (a) push and (b) pull cycles

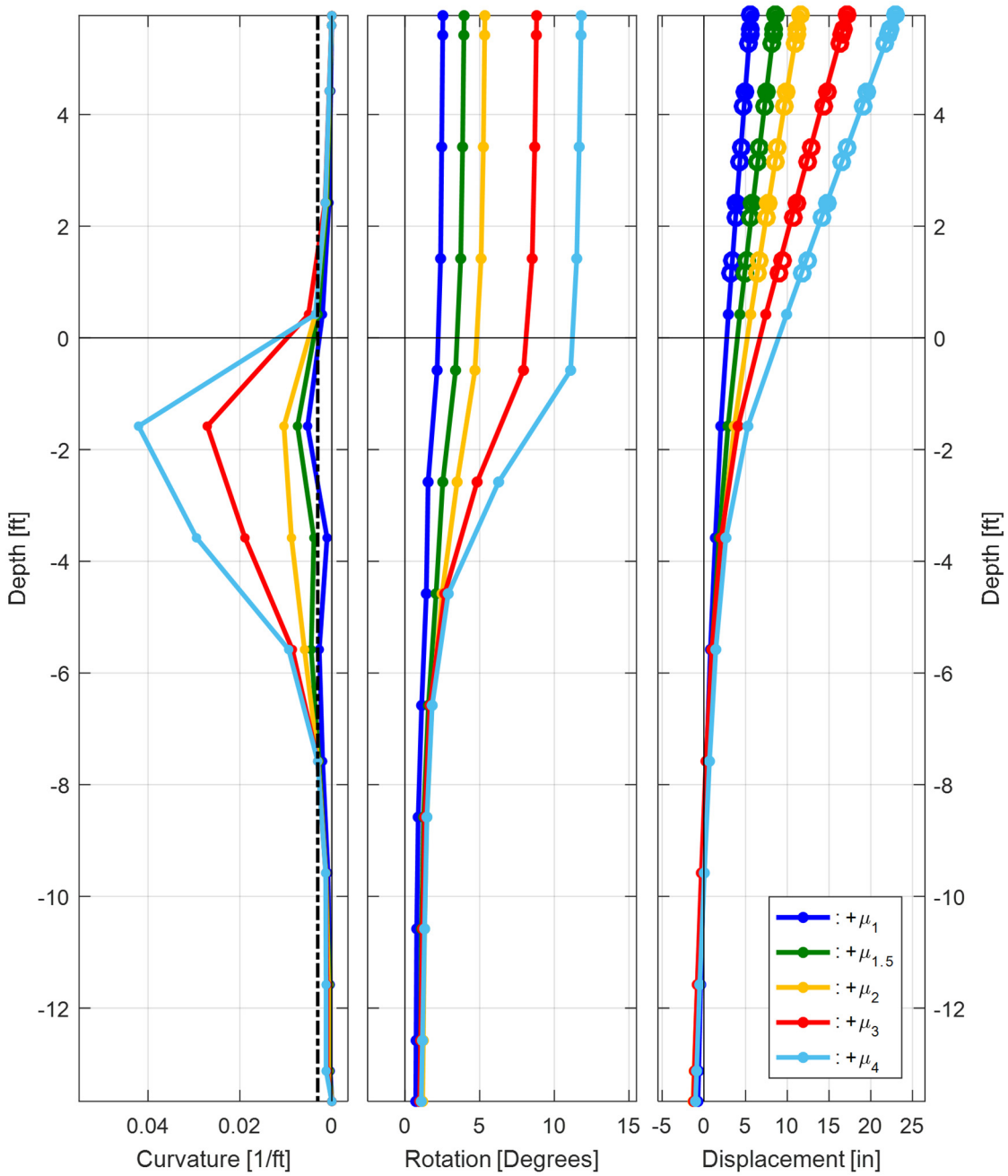

Figure 10-156 Test 8: curvature, rotation, and displacement profiles (inelastic push cycles)

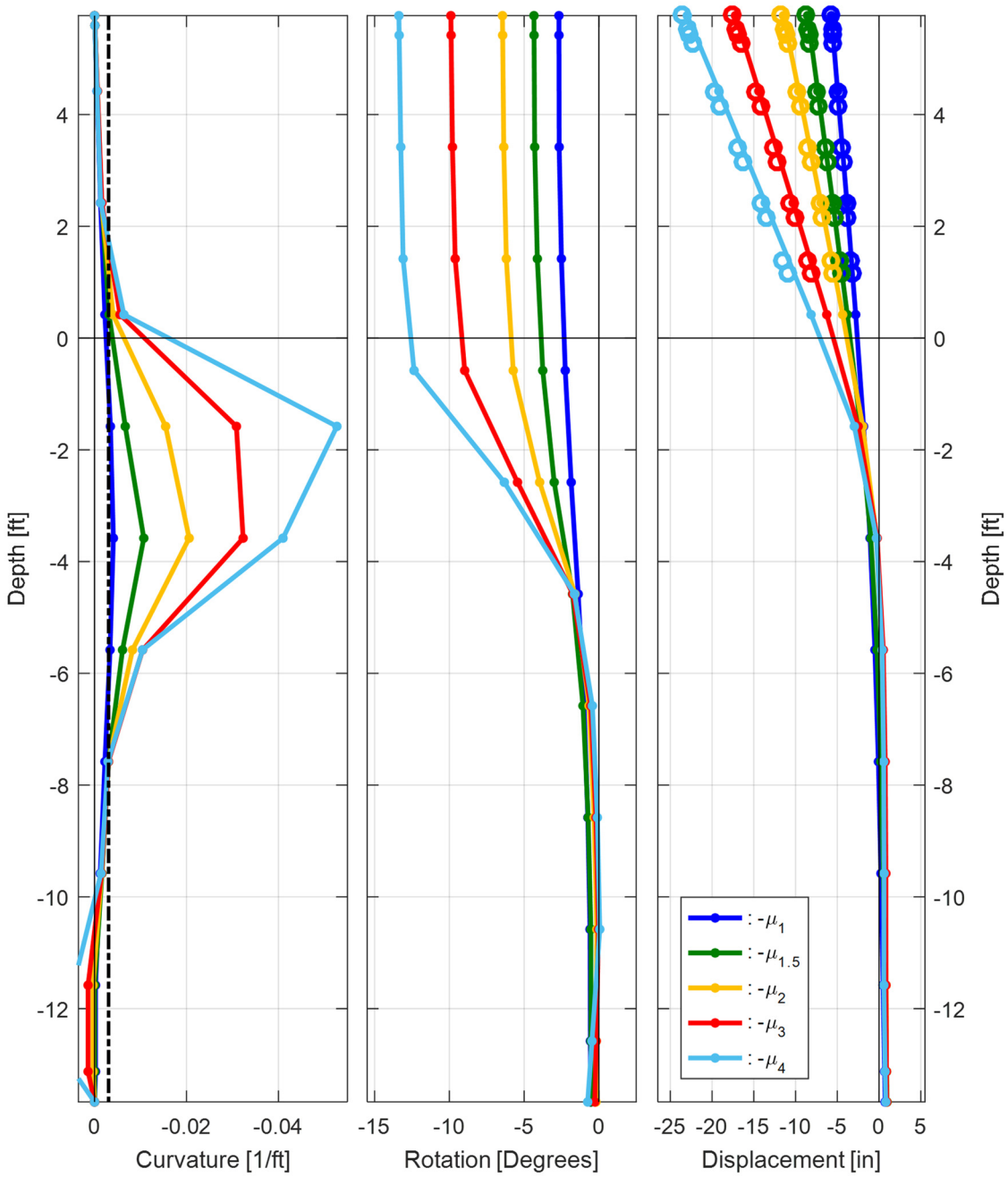

Figure 10-157 Test 8: curvature, rotation, and displacement profiles (inelastic pull cycles)

Figure 10-158 shows the state of the soil surface after the test was completed. Notice that despite the presence of the half-moon RC plates in the surface, deformations in the soil followed an expected oval-shaped failure surface in which active and passive pressures developed around the pile. This surface extended ~19 in. on both sides of the direction of loading and ~10.5 in. on the perpendicular direction. The total average settlement of the RC plates during the test was ~3.28 in. This value was averaged based on the vertical displacement of 4 points on the RC plates. Figure 10-159 shows the average settlement of the half-moon RC plates during the test as a function of the imposed displacements at the top of the pile. Note that, as the displacement history is applied, the settlement increases, though its magnitude is larger at the beginning of the test.

Figure 10-158 Test 8: soil surface after testing

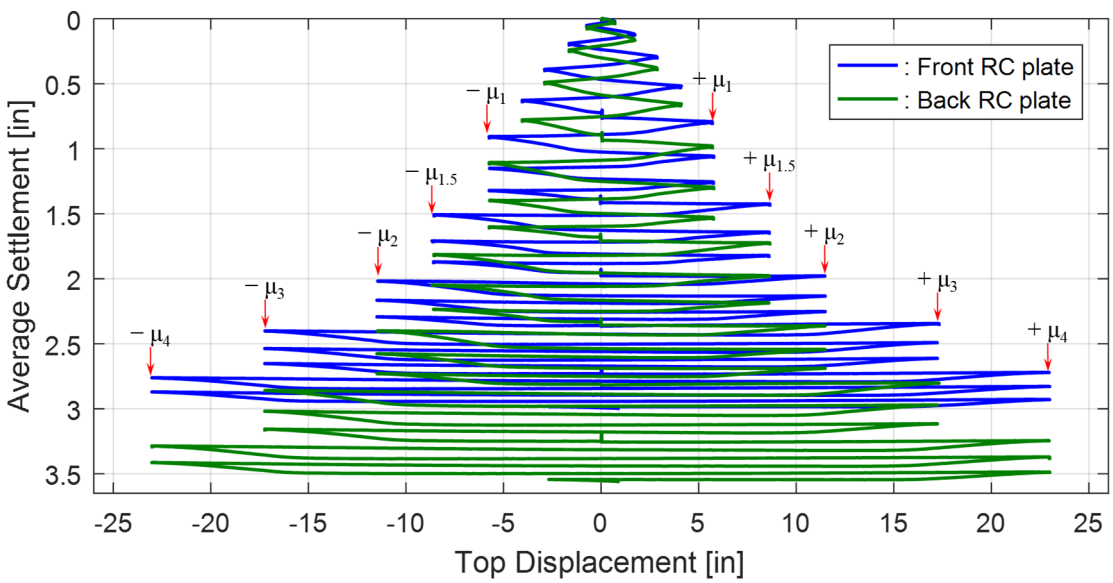

Figure 10-159 Test 8: half-moon RC plate settlement during testing

Figure 10-160 through Figure 10-162 present the damage observed after the pile was extracted from the soil. As thought during the test, tube fracture and tube buckling did occur; bar fracture and bar buckling were not observed. It can be seen that local buckling developed on both sides of the specimen. The sections with the largest buckling occurred at a depth of 2 ft. – 5.5 in. and 2 ft. – 7 in. on the South and North sides of the specimen, respectively, which implies that the plastic hinge developed at an average depth of 2 ft. – 6.25 in. with respect to the soil surface. Several ripples were observed mostly on the North side of the specimen, which correlates well with the fact that the sand was filling the gap with the pile faster on the South side than on the North side. Thus, it is believed that the critical section during the push cycles was about the same throughout the test as the lever arm did not change much, whereas the depth to maximum moment did change for the pull cycles as the sand was filling the gap with the pile faster. As a consequence, only one main buckled section and a small ripple developed on the South side in contrast with the main buckled region and several ripples observed on the North Side.

Tube fracture (Figure 10-160) occurred on the South side of the specimen. It can be seen from Figure 10-160(b) that two small fractures developed, one in the top and the other in the bottom part of the main buckled section on the South side of the specimen. Both fractured zones extended about a quarter of the cross section perimeter, resulting in a significant drop in strength due to lost tension capacity. As a consequence, after rupture, tension capacity is provided by the longitudinal reinforcement, which has a smaller area in comparison with that provided by the tube, inducing high stresses and deformations. Upon further investigations, bar buckling as well as bar fracture were not observed on the South side of the specimen. Note that tube fracture occurred in the section with the largest tube buckling, in which deformations protruded ~5/8 in. on both South and North sides of the pile. Figure 10-161 presents measurements of the primary buckled regions of the pile.

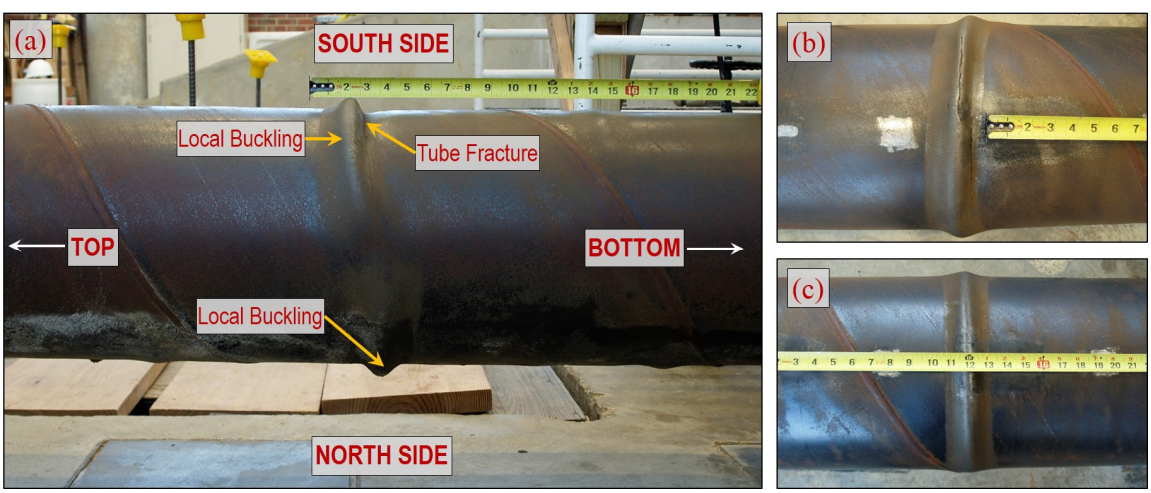

Figure 10-160 Test 8: (a) Final observed damage, (b) tube fracture, and (c) tube local buckling

In order to further investigate the significant strength loss and to verify whether bar fracture or bar buckling occurred, a portion of the tube (i.e., 10 in. x 12 in.) was removed at the ruptured section in the extreme fiber on the fractured side of the pile (Figure 10-162). It can be noticed that several cracks developed in this area of the concrete, perpendicular to the longitudinal direction of the specimen. Cracks in the concrete extended further to the center of the section. Neither bar fracture nor bar buckling were observed on the South side of the specimen.

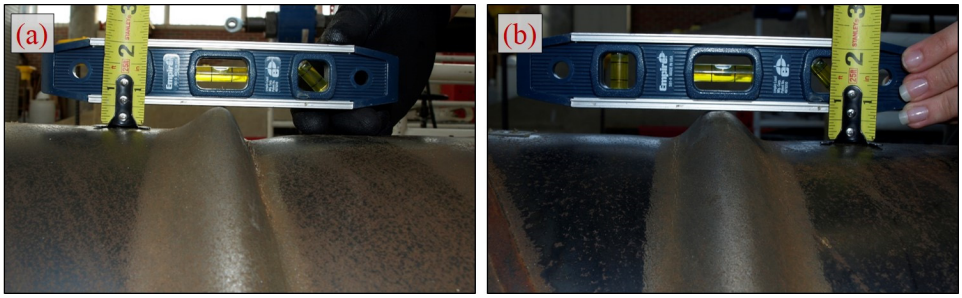

Figure 10-161 Test 8: primary buckled sections on (a) North side and (b) South side

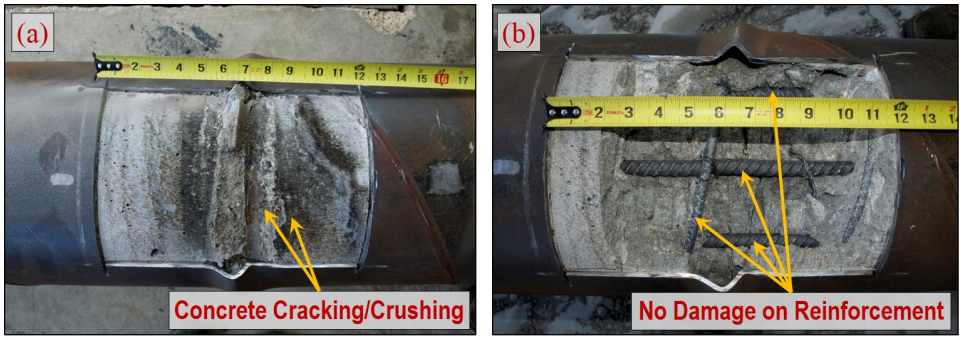

Figure 10-162 Test 8: observed damage in (a) concrete and (b) internal reinforcement on South side

Conclusions

Test specimen #8 showed a reliable response through all ductility 3.0 (μ_3) cycles. It is believed that onset of tube local buckling occurred early during the test at a ductility level of 2.0 (μ_2), when large curvatures were recorded. The test specimen completed all cycles of ductility 3.0 (μ_3) with minor loss of strength. A significant drop in strength occurred at ductility level 4.0 (μ_4) when tube fracture developed on the South side of the specimen during the third push cycle at this level. Further investigations revealed that failure occurred due to a combination of tube local buckling and tube fracture. Neither bar fracture nor bar buckling were observed in the internal reinforcement on the South side of the specimen. It is believed that this particular specimen is capable of having a reliable displacement up to ductility 3.0 (μ_3). The main buckles as well as tube fracture did not occur over the spiral weld, so the tube spiral welds do not appear to negatively influence the behavior.

Test 9 Summary Report

July 28, 2016

Prepared for

Alaska Department of Transportation

Alaska University Transportation Center

Project Team

RA: Diego Aguirre

PIs: Mervyn Kowalsky, James Nau, Mo Gabr

Other Senior Personnel: Greg Lucier, Ben Smith

North Carolina State University

Executive Summary

Test 9 was conducted July 13th, 2016 at the North Carolina State University Constructed Facilities Laboratory. The tested pile-column specimen was a reinforced concrete filled steel tube with a diameter-to-thickness (D/t) ratio of 48. Test 9 was conducted in two phases. First, the specimen was tested in its elastic range using a soil surcharge of ~1920 psf prior and during pile testing. Subsequently, the specimen was removed from the pit and the soil was regenerated to its pristine conditions by liquefying the pit. Then, for the second phase of the test, the specimen was inserted in the pit and was tested in both elastic and inelastic ranges using a soil surcharge of ~960 psf prior and during pile testing. Phase 1 revealed that by increasing the soil surcharge the effective soil stiffness does increase thereby increasing the lateral strength and tensile strains. For Phase 2, the test was successfully conducted to failure, which was caused by a combination of tube local buckling, tube fracture, and bar fracture, resulting in a large strength degradation (~80.33%) in the third push cycle at ductility level 5.0 (μ_5). This report is focused on results from Phase 2. A brief comparison with results from Phase 1 is presented at the end.

Specimen and Test Description

Test 9 consisted of a 19-foot-5.25-inch long, reinforced concrete filled, 12-inch diameter spirally welded steel tube without skelp or splice welds. The pile-column specimen was embedded 13 ft. – 8 in. into clean sand in the soil-structure interaction facility at the NCSU-CFL. Lateral load was applied at the pinned connection at the top of the pile specimen by means of a 100-kip, 70-inch stroke hydraulic actuator. The nominal wall thickness of the tube was 0.25 in., providing a nominal diameter-to-thickness ratio (D/t) of 48. The test was conducted with a 5foot-9.25-inch cantilever length, measured from the soil surface to the point at which the lateral load was applied. Figure 10-163 and Figure 10-164 present a schematic of the test setup (elevation) and the specimen #9 cross-section, respectively, while Figure 10-165 shows the instrumentation used for testing. A photograph of the test setup is included in Figure 10-166.

Material properties were determined by in-house material tests. The yield and ultimate stresses of the steel tube were 49.5 ksi and 71.3 ksi, respectively, based on tests conducted on three (3) coupons cut from the end of the test pile specimen. The yield and ultimate stresses of the ASTM A706 Grade 60 longitudinal reinforcement were 72.8 ksi and 97.1 ksi, respectively, based on tests conducted on six (6) bar specimens from the same heat of the longitudinal reinforcement. The yield and ultimate stresses of the spiral reinforcement were 64.9 ksi and 96.9 ksi, respectively, based on tests conducted on six (6) bar specimens from the same heat of the transverse reinforcement. An average concrete compressive strength of 7.24 ksi (standard deviation of ± 0.04 ksi) was determined from three (3) compression tests of 4”x8” concrete cylinders.

Soil properties were also determined by in-house material tests. Based on a measured particle size distribution, the soil was classified as poorly-graded sand (SP). The unit weight and friction angle (γ = 90 pcf and ϕ = 35°, respectively) were reasonably assumed based upon results performed on soil samples taken from the pit in previous tests.

In an attempt to modify the soil properties prior to pile testing, a surcharge was applied to the soil surface prior and during the test by means of 40-kip, 2-inch stroke hydraulic jacks reacting on the half-moon RC plates. An axial load of 10.1 kips was applied to each of the six (6) PT bars, resulting in a surcharge pressure of q = 960 psf. In addition to the active pressure, the self-weight of the half-moon RC plates was acting on the soil surface as well (i.e., ~100 psf). Five surcharge cycles were performed, all of which were applied one day prior to pile testing, that is, on July 12th, 2015. Cycles 1 through 4 were applied without sustaining the pressure, namely, they were load-unload cycles which took approximately 30 minutes each. The fifth surcharge cycle was then applied and the pressure was sustained all the way until pile testing was completed. The average settlement of the RC plates prior the pile testing was ~0.45 in. This value was averaged based on the vertical displacement of 4 points on the RC plates. Results of the surcharge cycles are presented in Figure 10-167.

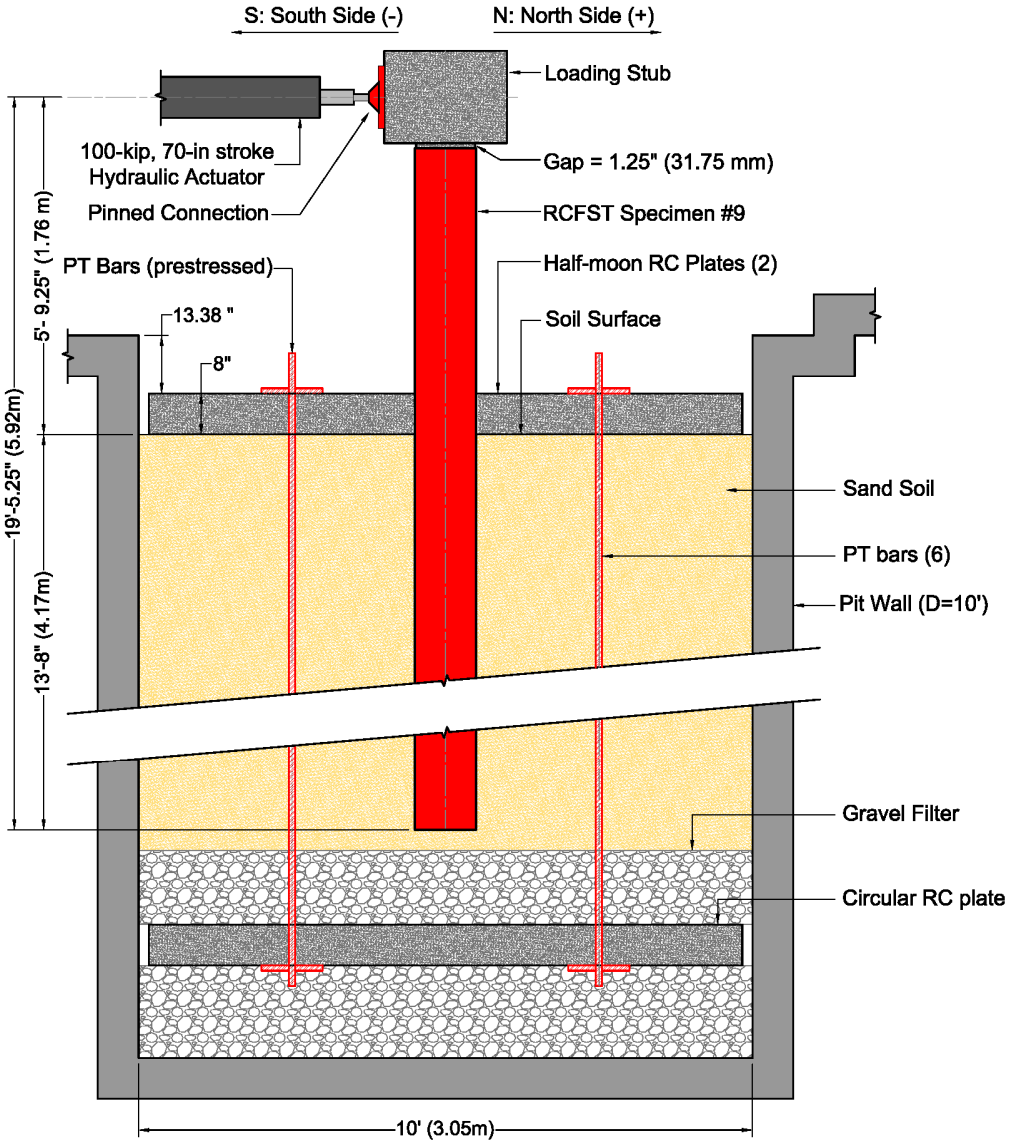

Figure 10-163 Test 9: test setup elevation schematic

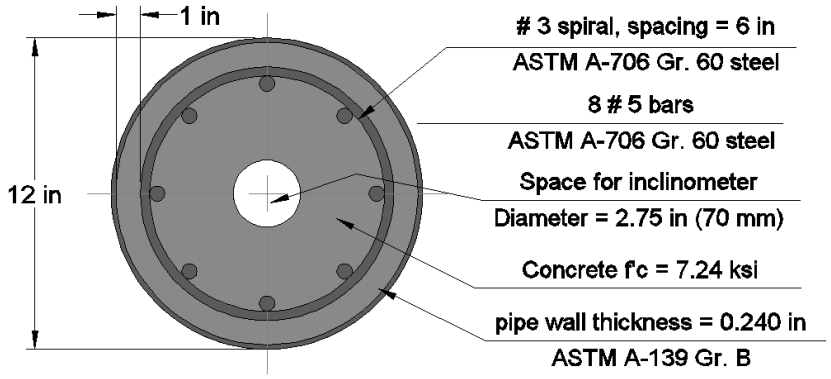

Figure 10-164 Test 9: RCFST specimen cross section

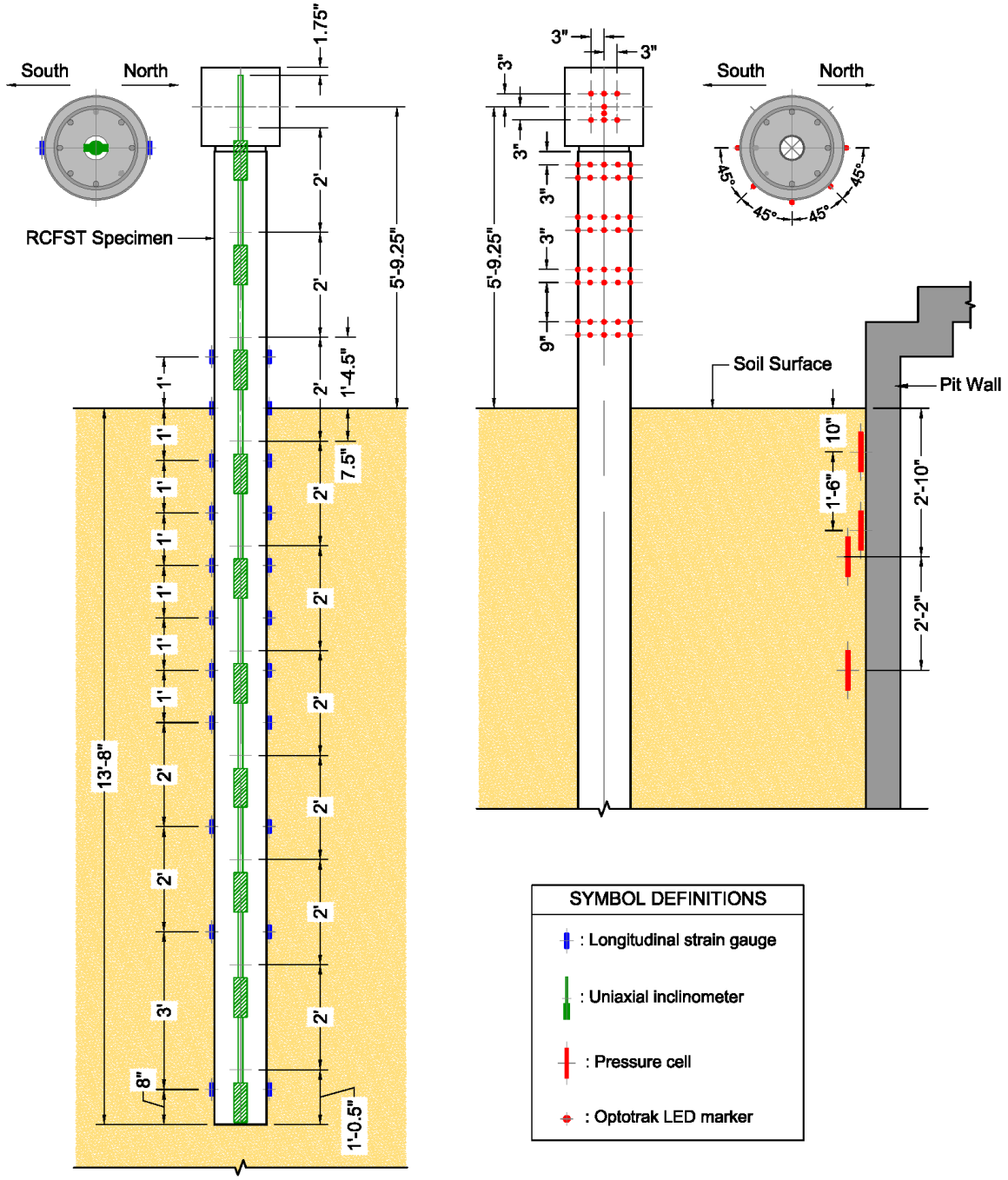

Figure 10-165 Test 9: instrumentation

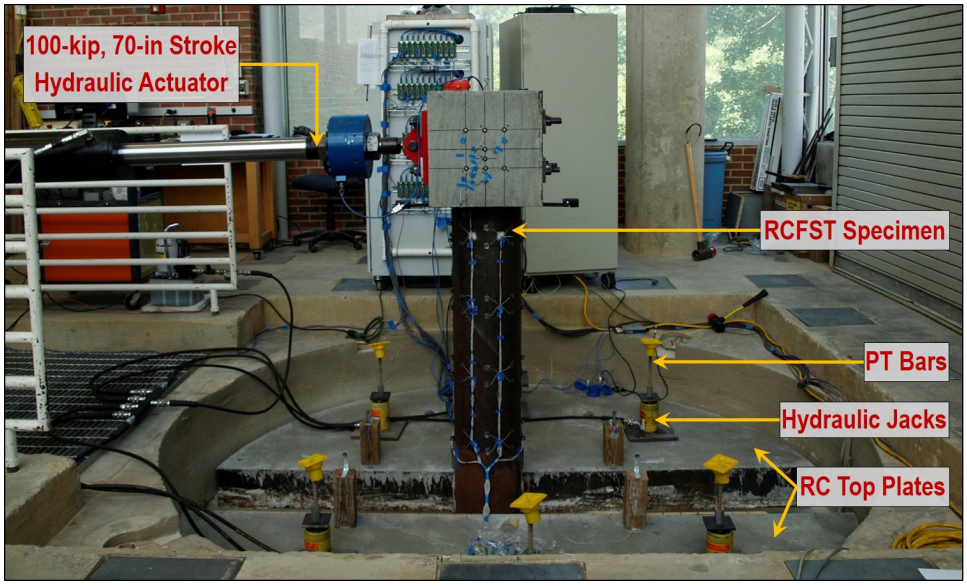

Figure 10-166 Test 9: pinned-head, RCFST pile-column test setup

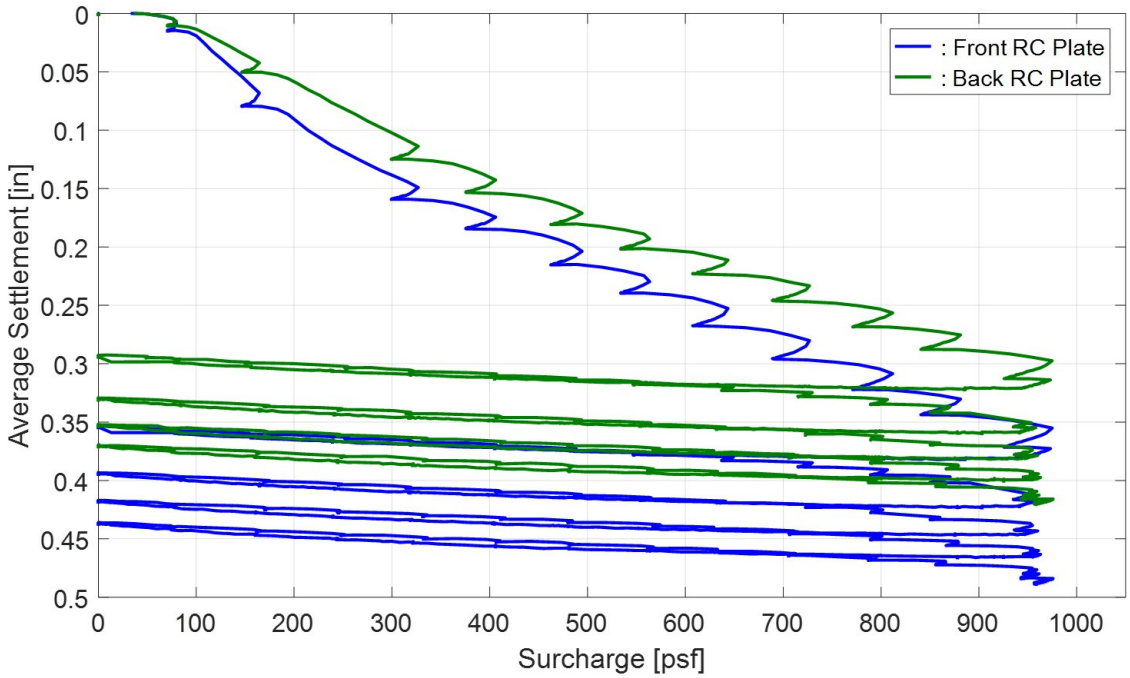

Figure 10-167 Test 9: half-moon RC plate settlement prior testing

The load history applied to the pile specimen consisted of standard three-cycle sets intended to evaluate both the elastic and inelastic response of the specimen. The first portion (i.e., pile elastic response up to first yield) of the test consisted of single reversed, displacement-controlled cycles, ramping up to the first yield displacement in ¼ increments. Given the non-linear response from the beginning of the test due to the characteristic soil behavior, target displacements in this portion of the test were determined based on the results of a monotonic pushover analysis performed using a detailed non-linear, fiber-based, finite element model developed using the OpenSees framework software. Soil-structure

interaction was included by means of non-linear springs at 1-foot interval depths, with spring properties assigned based on p-y curves.

The first yield force (F_y) and nominal force (F_n), which is defined as the force at a concrete compressive strain of 0.004 or at a tube/bar tensile strain of 0.015 (whichever occurs first), were determined based upon tensile and compressive strains monitored during the numerical simulation (i.e., pushover analysis), as 18.1 kips and 26.8 kips, respectively. Table 10-9 summarizes the target displacements for the first portion of the test.

After the first portion of the test was completed, the measured average strain at the predicted first yield displacement (Δ'_y) was 1560 (με), which correlates well with the tube yield strain (ε_y = 1700 με). The measured average displacement at the first yield displacement (Δ'_y = 3.98 in) was modified by the nominal-to-first yield force ratio in order to determine the displacement ductility level 1.0 (μ_1 = 5.89 in), as shown in Equation 10-18. The remainder of the test was completed using reversed three-cycle sets in displacement-controlled increments at different levels of displacement ductility until failure, as shown in Equation 10-19. The entire displacement and load histories can be seen in Figure 10-168. Positive loads and displacements correspond to rightward (North) motion of the pile in the test setup. The positive legs of all cycles were completed before the negative legs.

Table 10-9 Test 9: predictions for elastic portion

Performance Level	Displacement (in)	Force (kips)
1/4 Δy'	0.81	5.41
1/2 Δy'	1.78	10.14
3/4 Δy'	2.88	14.51
1 Δy'	3.98	18.14

$$\Delta_y = \mu_1 = \Delta'_y \cdot \frac{F_n}{F_y} = 3.98\,in \cdot \frac{26.8\,kip}{18.1\,kip} = 5.89\ in \qquad \text{Equation 10-18}$$

$$\mu_i = i \cdot \mu_1 \rightarrow i = 1.0,\ 1.5,\ 2.0,\ 3.0,\ 4.0,\ 5.0 \qquad \text{Equation 10-19}$$

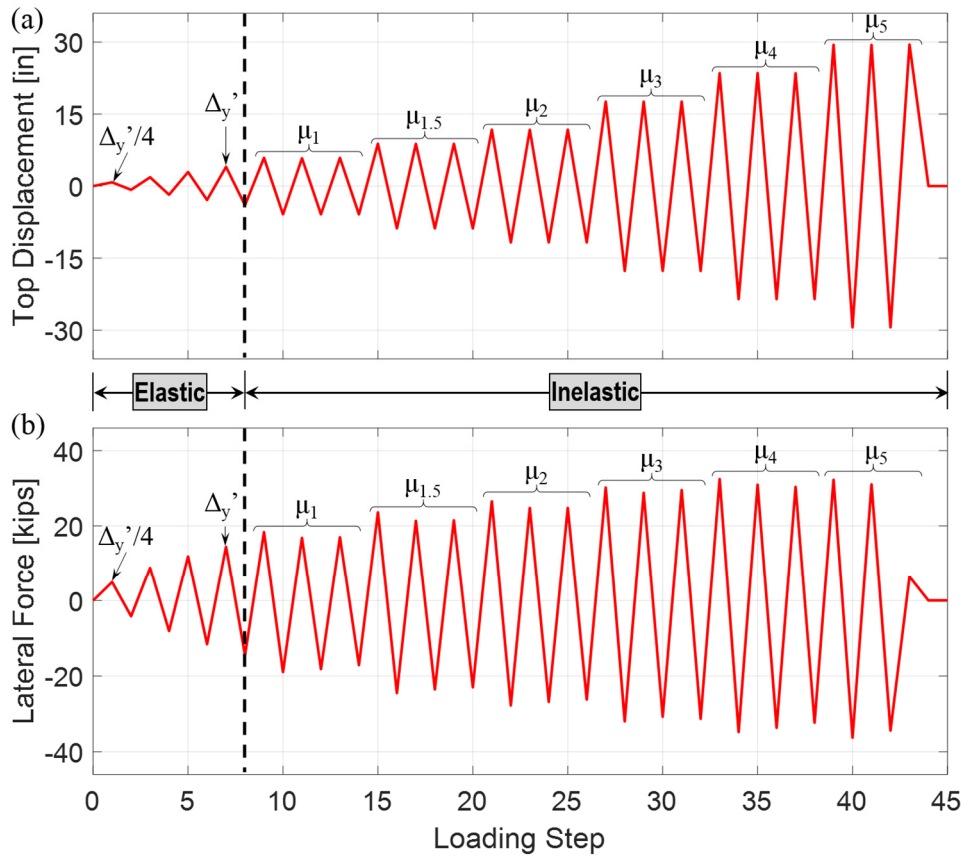

Figure 10-168 Test 9: (a) displacement and (b) loading histories

Specimen Response

Specimen #9 performed well through the elastic portion of the test and also during all three cycles of ductility level 4.0 (μ_4). It is believed that the onset of tube buckling occurred early during the displacement cycles at that ductility level as minor loss of strength was observed at the second and third cycles at that displacement level. A significant loss of strength, indicating failure, occurred during the third push cycle at ductility level 5.0 (μ_5). Figure 10-169 and Figure 10-170 present the lateral force vs. top displacement response and envelopes, respectively. It can be seen that the system has a characteristic large energy dissipation capacity due to both damping sources, that is, the pile itself and the surrounding soil. In addition, it can be clearly seen from both figures that a significant loss of strength (~80%) occurred during the third push cycle of ductility level 5.0 (μ_5).

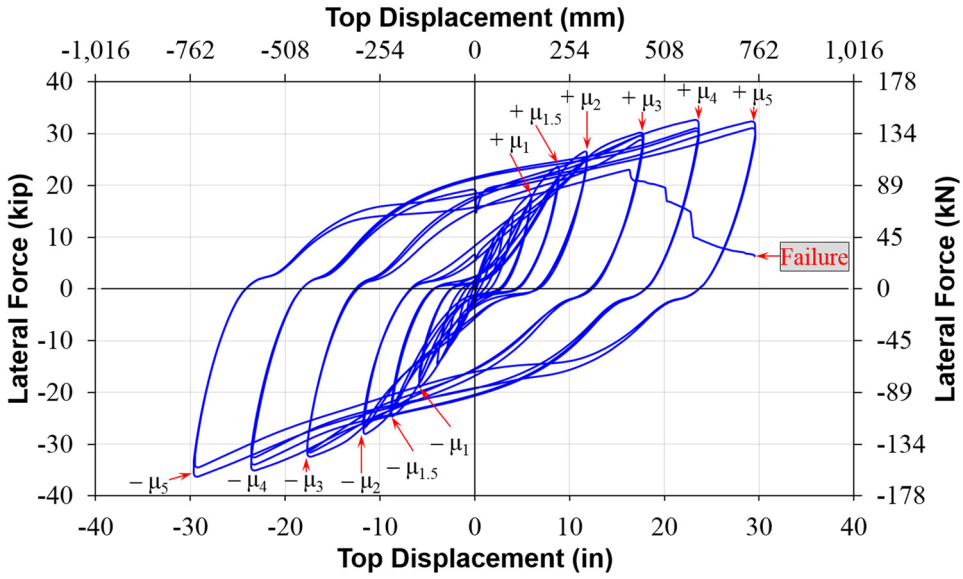

Figure 10-169 Test 9: lateral force vs. top displacement response

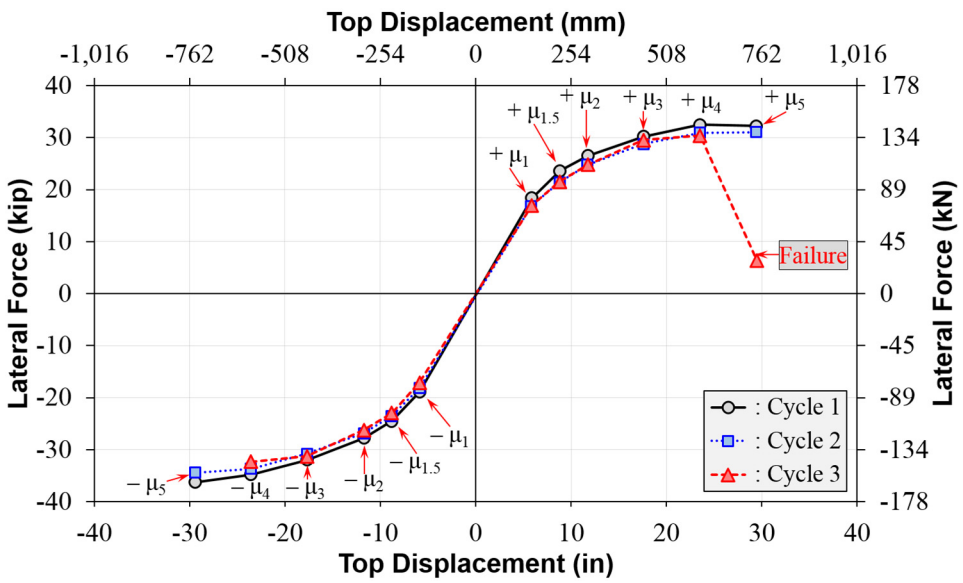

Figure 10-170 Test 9: lateral force vs. top displacement envelopes

Figure 10-171 presents the deformed shape and the soil-pile gaps at zero displacement after the elastic portion of the test was conducted; the size of the gap was ~1.50 in. on both sides of the specimen. As it was previously explained, at this point of the test strain profiles on the sides of the pile were verified in order to further conduct the test at the aforementioned ductility levels. Figure 10-172 presents the strain profiles recorded during the elastic portion of the test. Notice that tensile strains of 1530 (με) and 1580 (με) were recorded in the tube during the push and pull cycles, respectively, when the predicted first yield displacement was imposed to the system. Based on the rotation data recorded with the inclinometer placed inside the pile along its length, specimen curvature, rotation, and displacement profiles are presented in Figure 10-173 and Figure 10-174 for the elastic push and pull cycles, respectively. Note that there are small rotations and displacements at the pile tip which indicates that there is a point of rotation (at ~9 ft.) rather than a point of fixity; inelastic action was developed in the pile nonetheless. The circles in the top portion of the displacement profiles in Figure 10-173 and Figure 10-174 represent the Optotrak LED markers; note that they are in agreement with the calculated displacement profiles. In Figure 10-172 through Figure 10-174 the symbols N and S in the legend refer to the North and South sides, Δ_y' is the first yield displacement, $Ø_y'$ is the first yield curvature, and a depth equal to 0 ft. represents the soil surface.

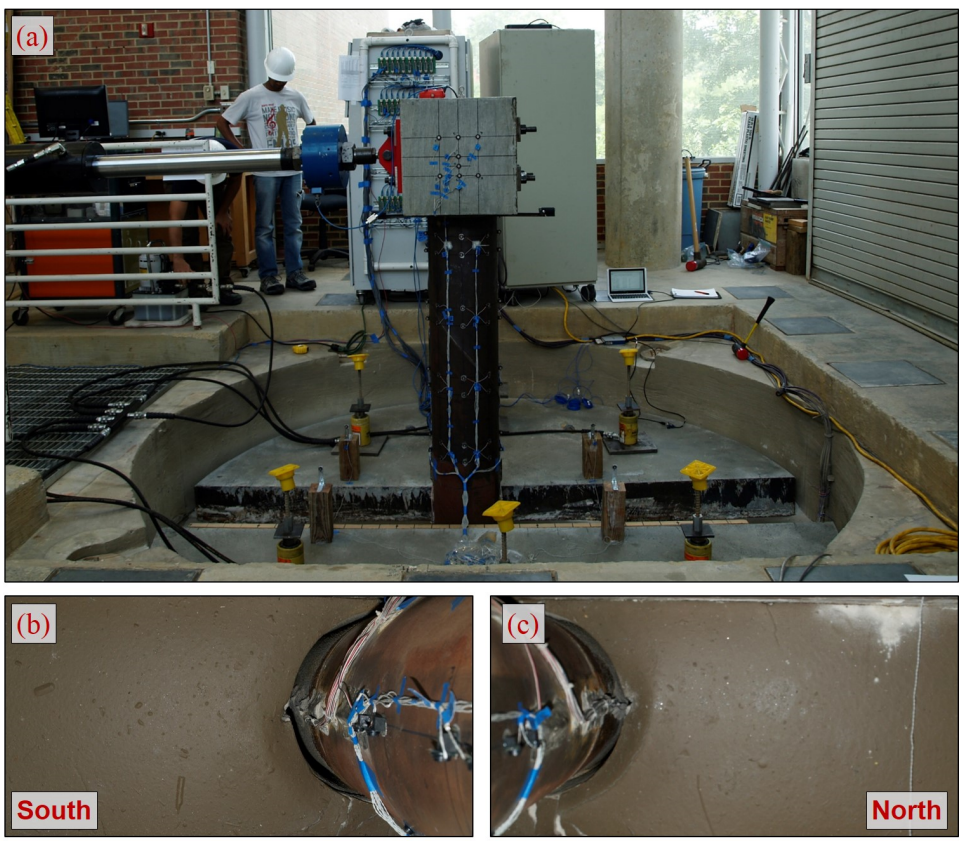

Figure 10-171 Test specimen #9 after elastic portion of the test was completed: (a) deformed shape, (b) South side and (c) North side

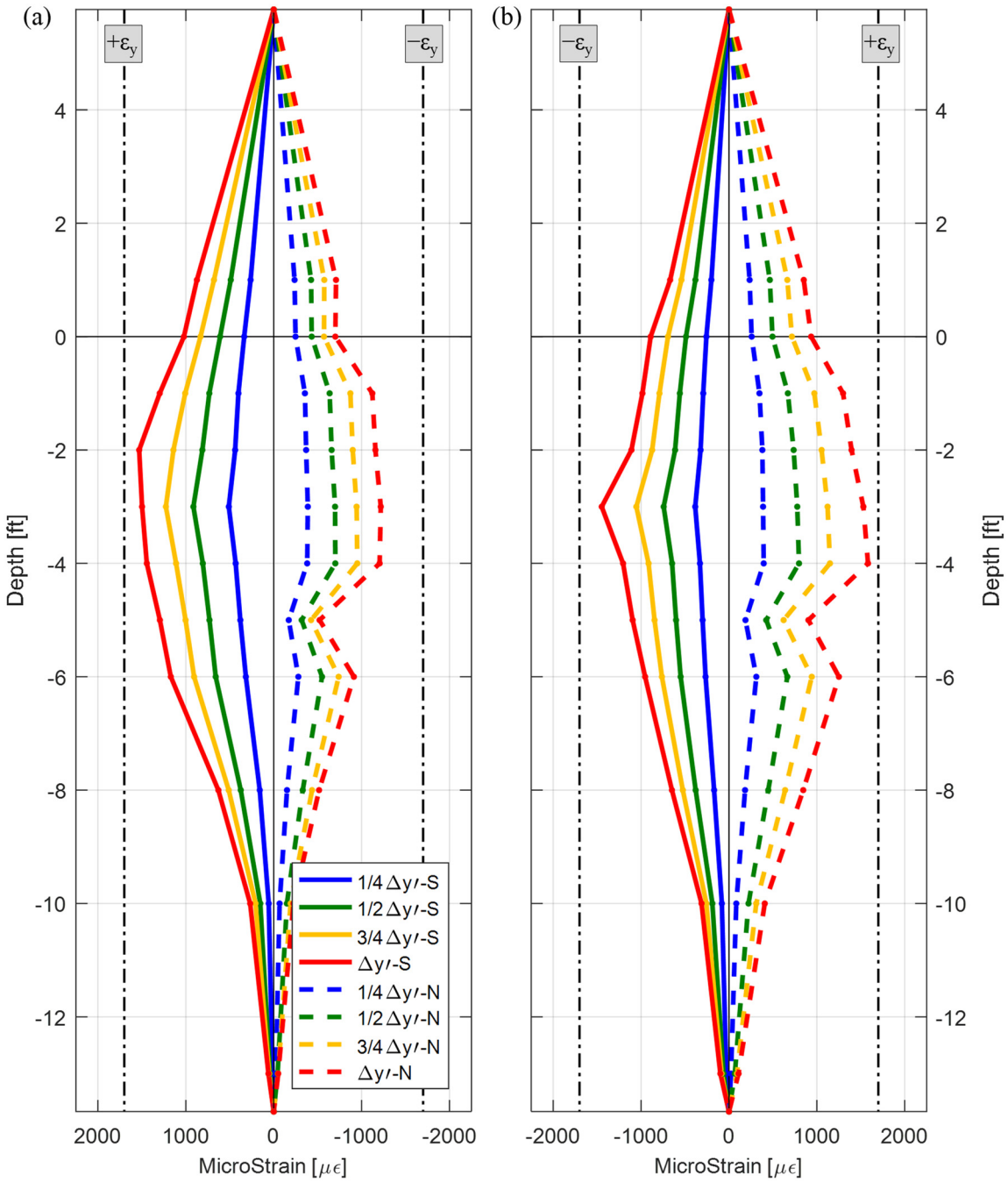

Figure 10-172 Test 9: strain profiles from elastic (a) push and (b) pull cycles

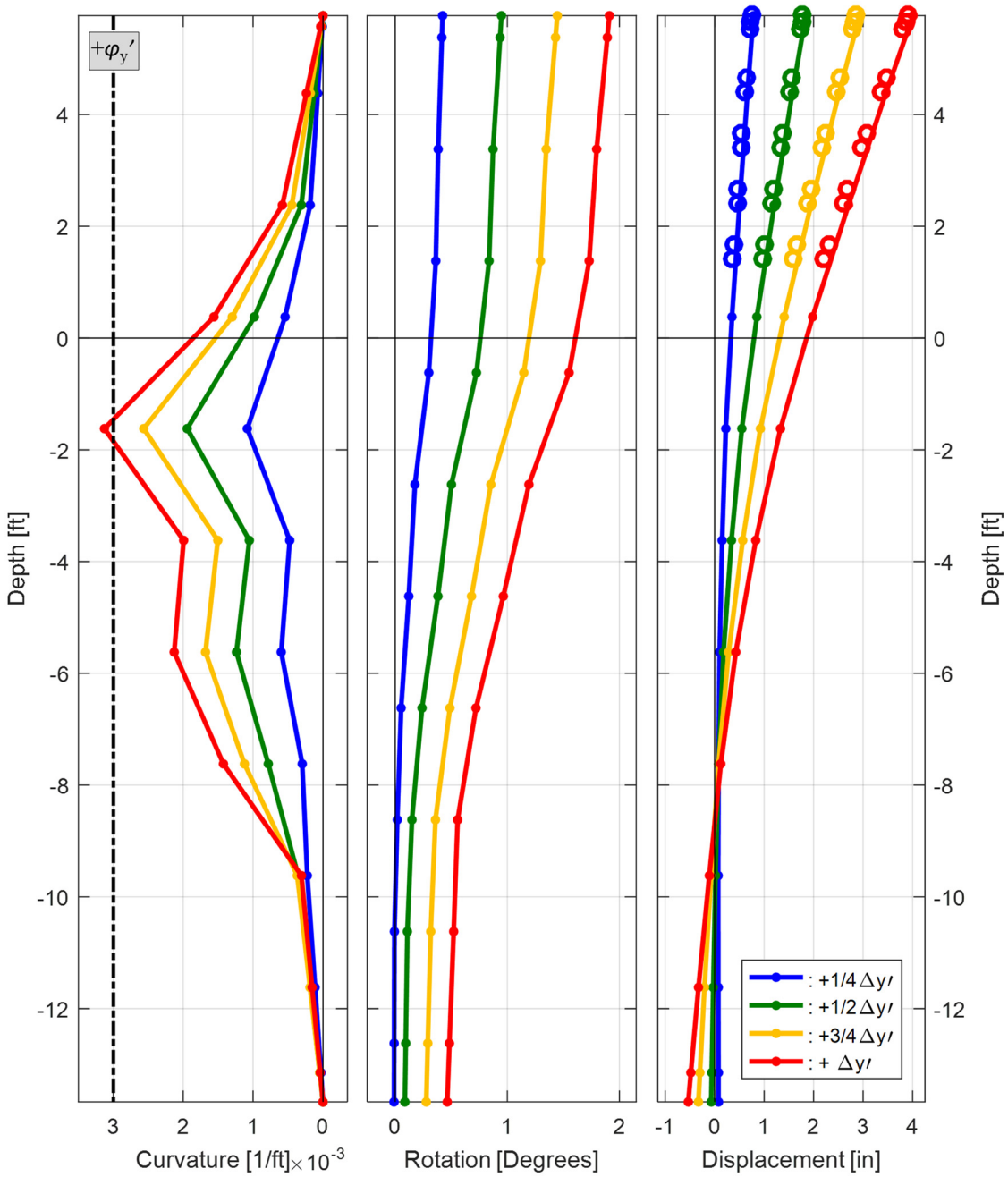

Figure 10-173 Test 9: curvature, rotation, and displacement profiles (elastic push cycles)

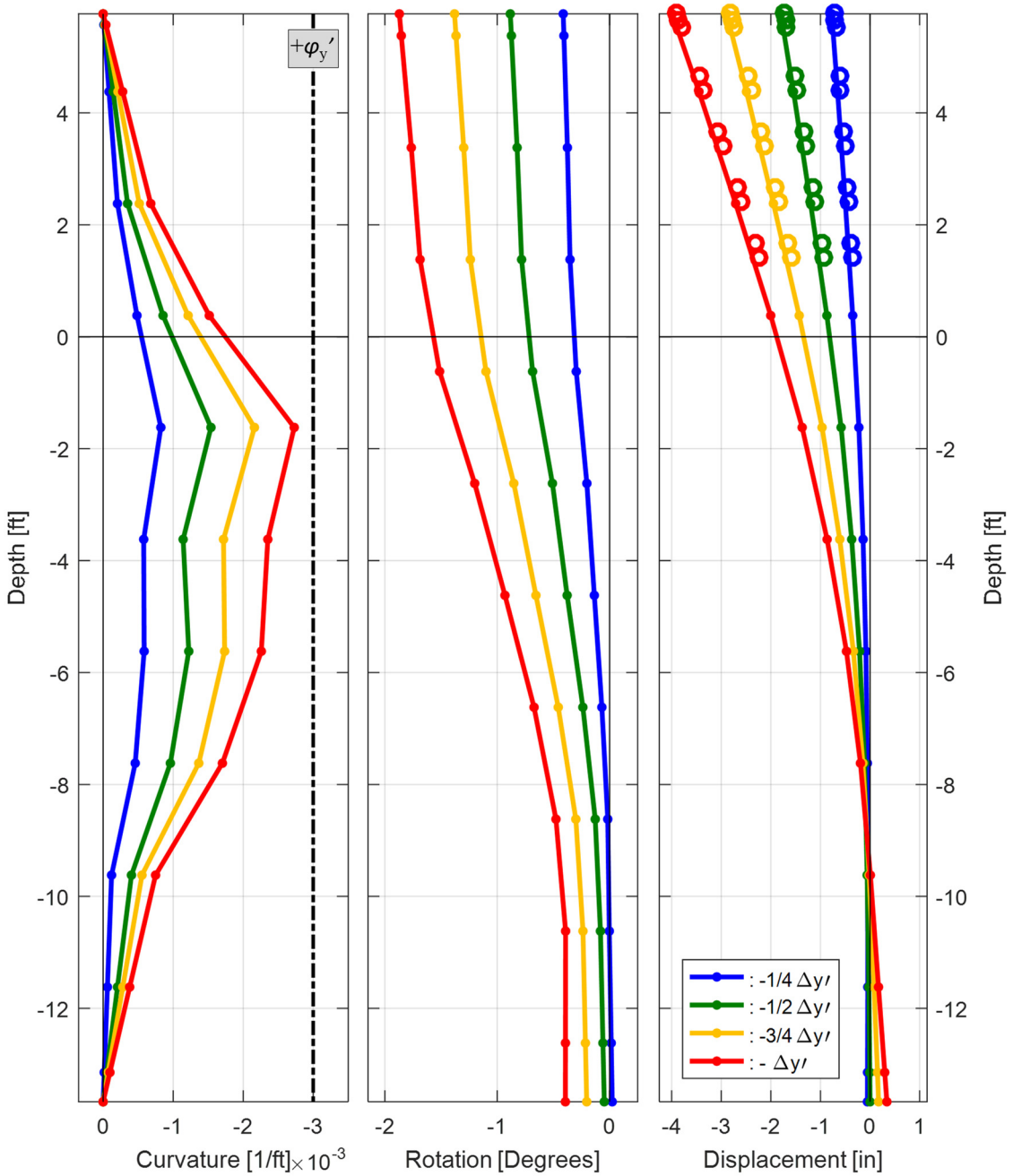

Figure 10-174 Test 9: curvature, rotation, and displacement profiles (elastic pull cycles)

As the test continued, the gap on the sides of the pile increased in size as the displacement ductility level increased. Minor loss of strength was observed up until all ductility level 4.0 (μ_4) cycles. The specimen failure (Figure 10-175) occurred at the third cycle load at ductility 5.0 (μ_5) when a significant drop in the force of the actuator was observed (i.e., ~80%). Sounds indicating steel fracture were heard at the same time when the strength loss occurred, indicating probable tube or bar fracture. Moreover, twist rotation of the pile observed during all push cycles at ductility levels 4 (μ_4) and 5 (μ_5). Finally, the test was terminated and the specimen was taken to zero displacement in order to facilitate its extraction from the soil.

Figure 10-176 presents strain profiles for the first push and pull cycles at different displacement ductility levels; the symbols N and S in the legend refer to the North and South sides, μ is the displacement ductility, and a depth equal to 0 ft. represents the soil surface. Note that the largest tensile and compressive strains were recorded at a depth between 1 ft. and 5 ft., which correlates well with the curvature, rotation, and displacement profiles presented in Figure 10-177 and Figure 10-178 for the inelastic push and pull cycles of the test, respectively. Note that the largest changes in rotation (i.e., curvature) occurred at a depth between 0. 5 ft. and 4.5 ft., which correlates well with the observed damage zone.

Figure 10-175 Test specimen #9 at maximum displacement: (a) deformed shape, (b) South side and (c) North side

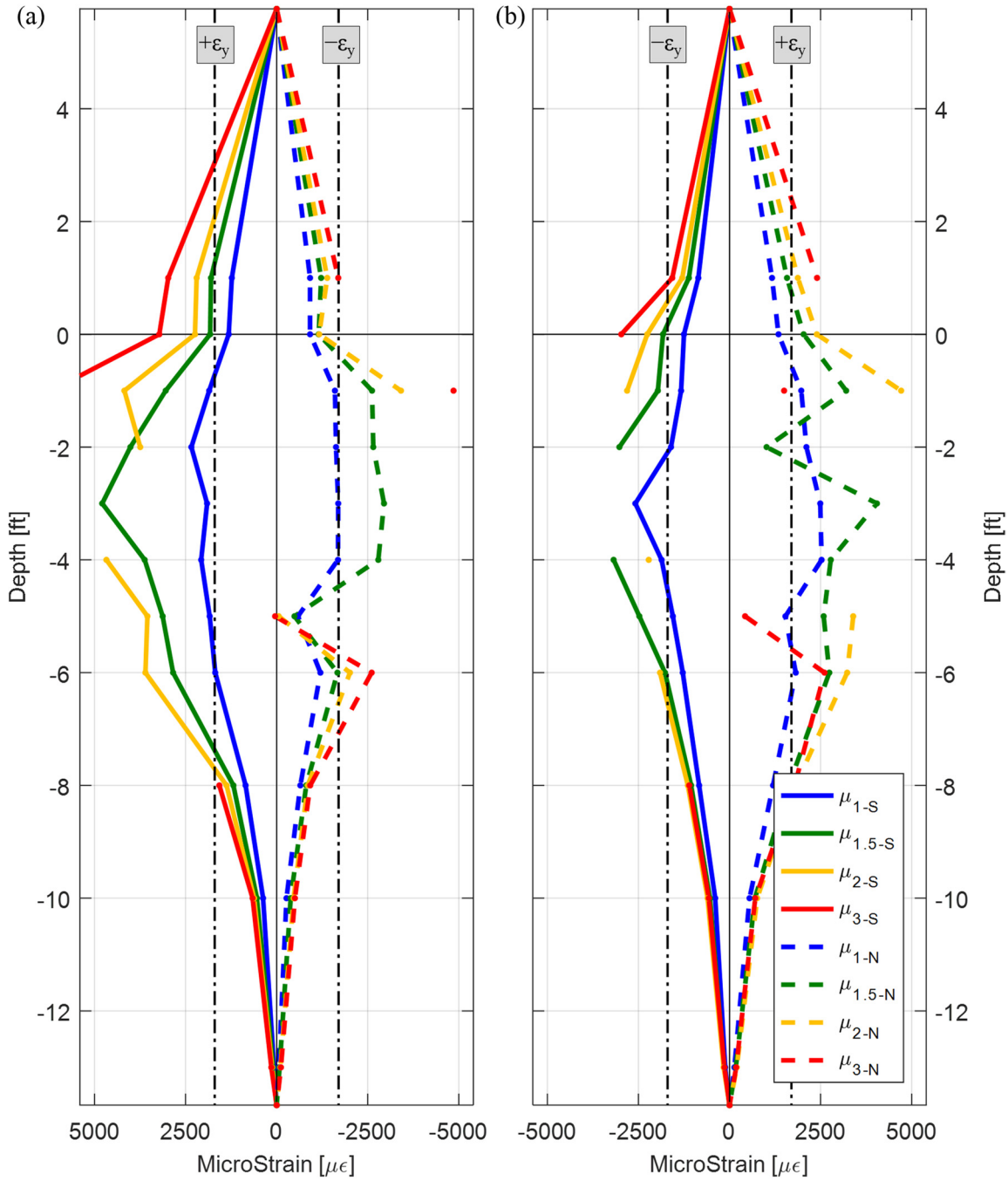

Figure 10-176 Test 9: strain profiles from inelastic (a) push and (b) pull cycles

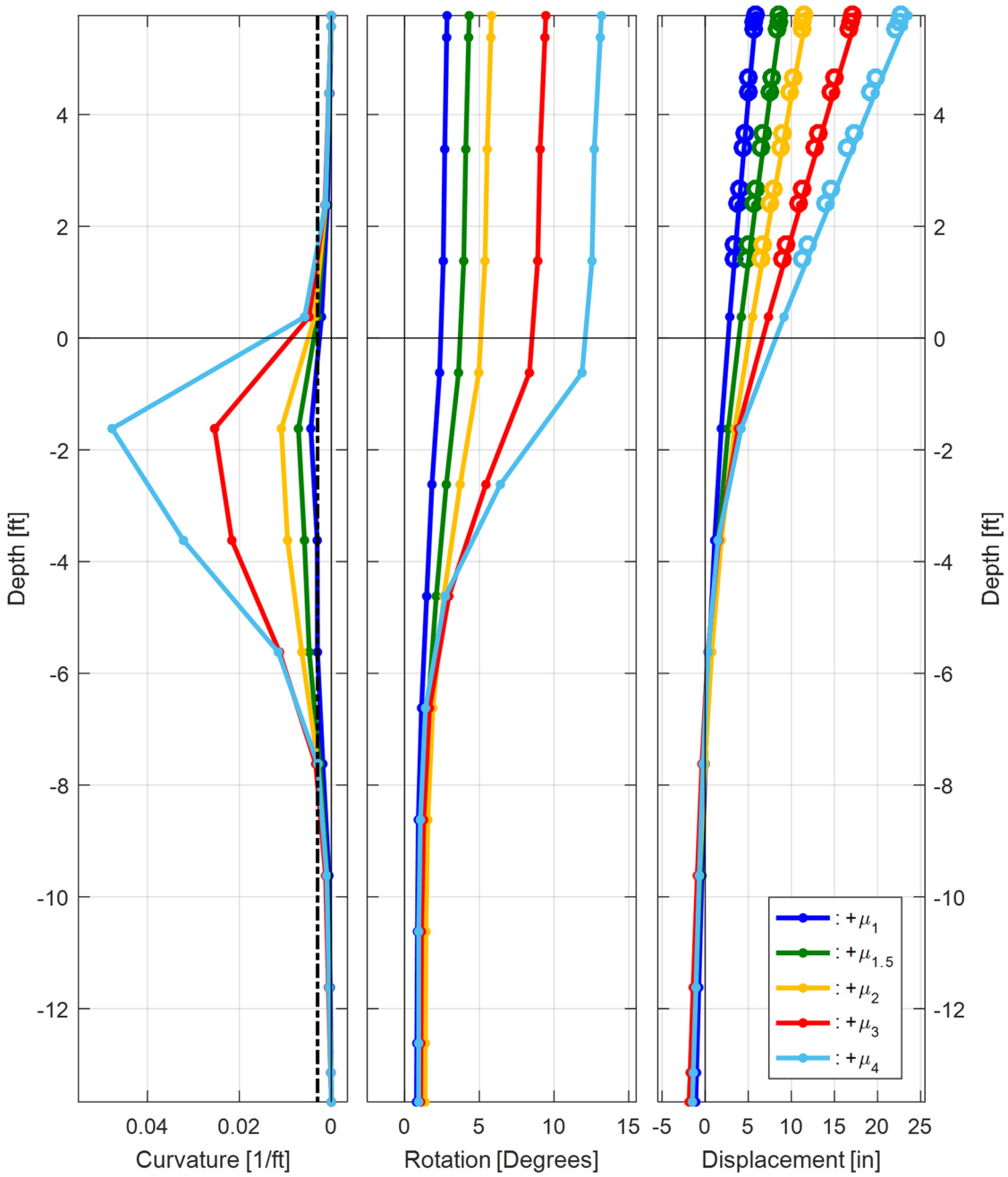

Figure 10-177 Test 9: curvature, rotation, and displacement profiles (inelastic push cycles)

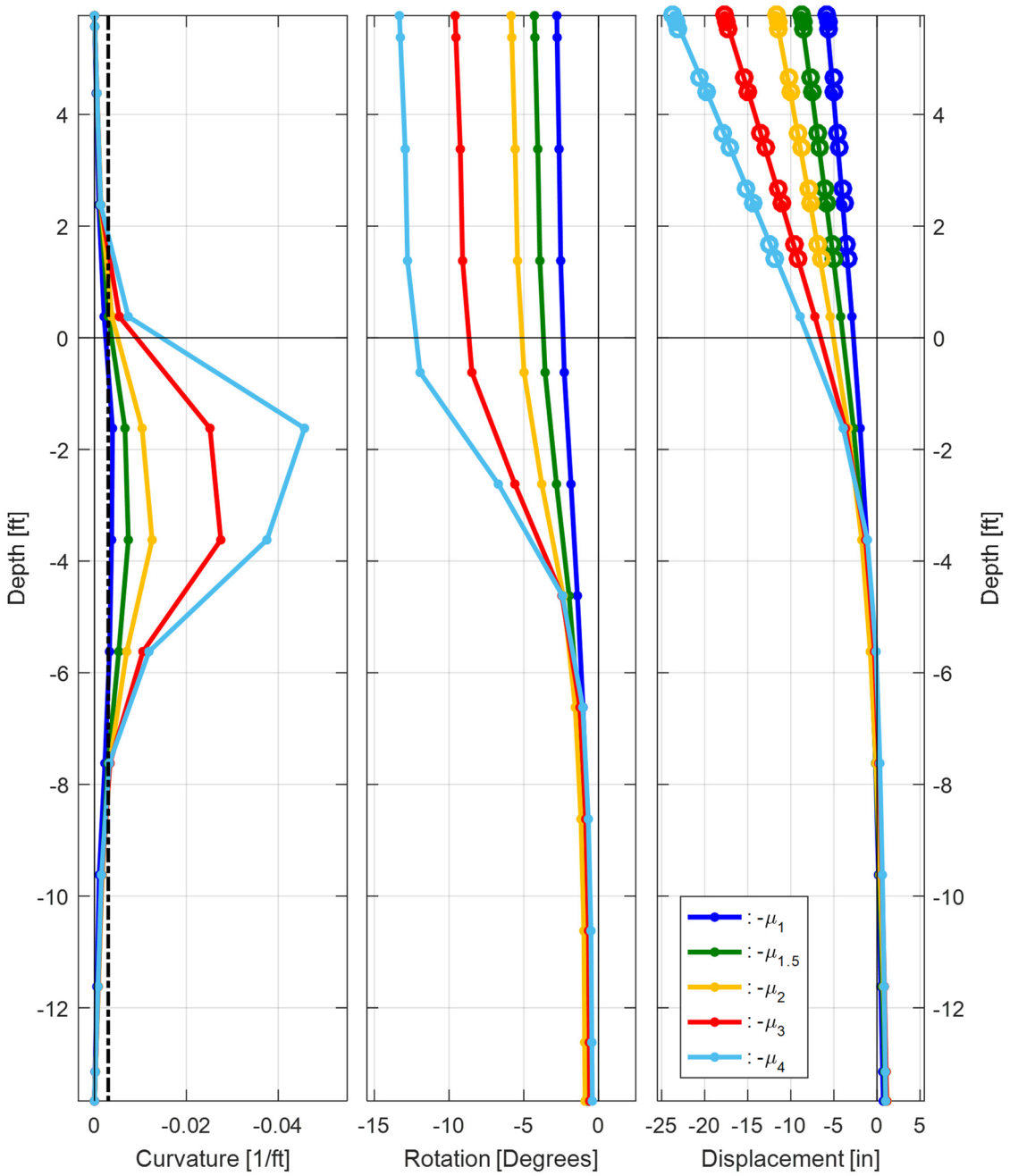

Figure 10-178 Test 9: curvature, rotation, and displacement profiles (inelastic pull cycles)

Figure 10-179 shows the state of the soil surface after the test was completed. Notice that despite the presence of the half-moon RC plates in the surface, deformations in the soil followed an expected oval-shaped failure surface in which active and passive pressures developed around the pile. This surface extended ~22 in. on both sides of the direction of loading and ~10.5 in. on the perpendicular direction. The total average settlement of the RC plates during the test was ~3.45 in. This value was averaged based on the vertical displacement of 4 points on the RC plates. Figure 10-180 shows the average settlement of the half-moon RC plates during the test as a function of the imposed displacements in the top of the pile. Note that, as the displacement history is applied, the settlement increases, though its magnitude is larger at the beginning of the test.

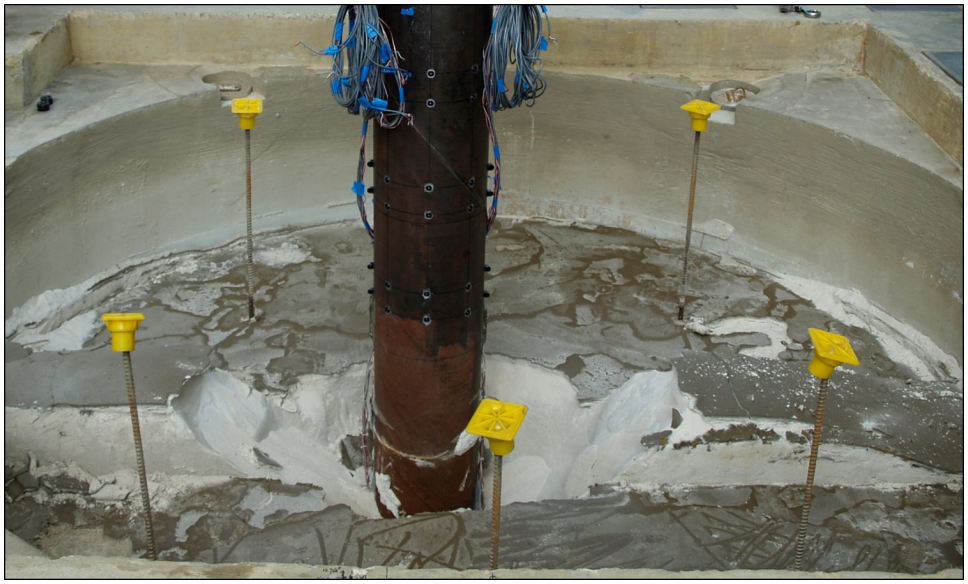

Figure 10-179 Test 9: soil surface after testing

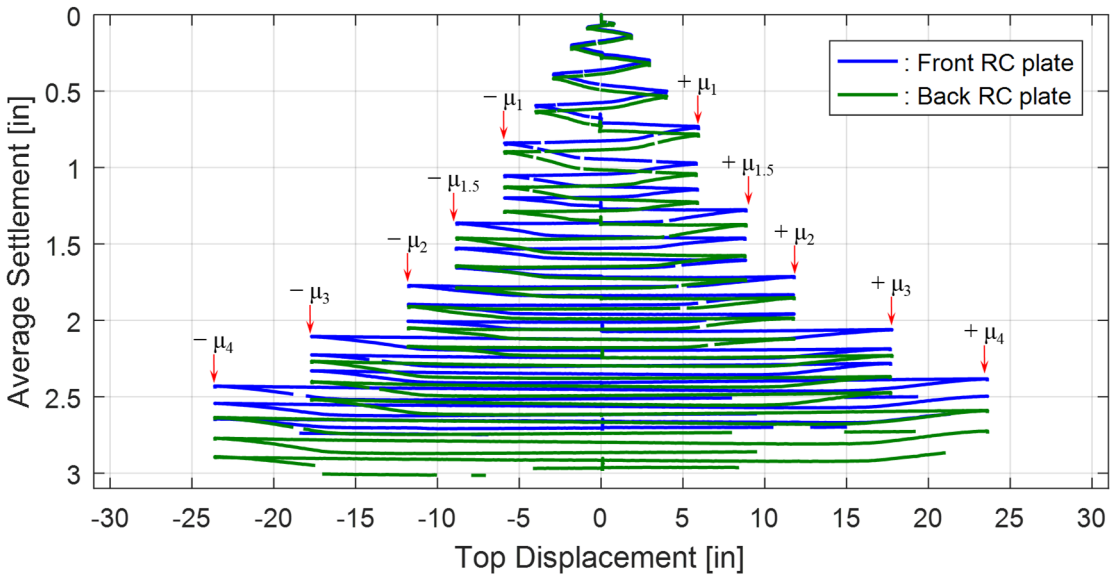

Figure 10-180 Test 9: half-moon RC plate settlement during testing

Figure 10-181 through Figure 10-184 present the damage observed after the pile was extracted from the soil. As thought during the test, tube fracture and tube buckling did occur as did bar fracture; bar buckling was not observed. It can be seen that local buckling developed on both sides of the specimen. The sections with the largest buckling occurred at a depth of 2 ft. – 2 in. and 2 ft. – 4 in. on the South and North sides of the specimen, respectively, which implies that the plastic hinge developed at an average depth of 2 ft. – 3 in. with respect to the soil surface. Several ripples were observed on both South and North sides of the specimen.

Tube fracture (Figure 10-181) occurred on the South side of the specimen and it extended about half of the cross-section perimeter, resulting in a significant drop in strength due to lost tension capacity; also note from Figure 10-181 (b) that onset fracture on the North side of the specimen is evident. As a consequence, after rupture, tension capacity is provided by the longitudinal reinforcement, which has a smaller area in comparison with that provided by the tube, inducing high stresses and deformations. Upon further investigations, bar fracture was observed on the South side of the specimen; however, bar buckling was not observed neither on the South nor the North side of the specimen. Note that tube fracture occurred on the section with the largest local buckling, in which deformations protruded ~5/8 in. on both South and North sides of the pile. Figure 10-182 presents measurements of the primary buckled regions of the pile.

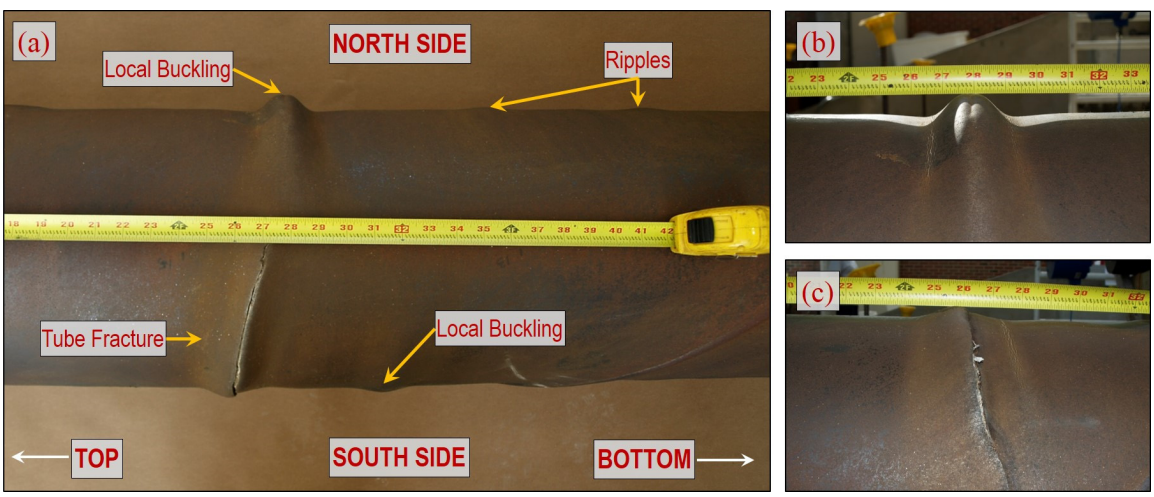

Figure 10-181 Test 9: (a) Final observed damage, (b) tube local buckling, and (c) tube fracture

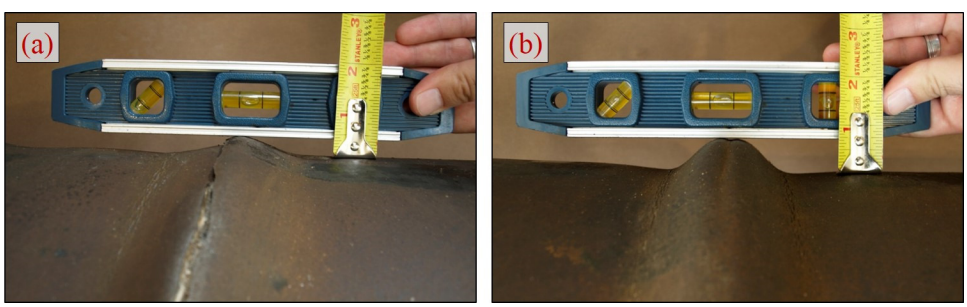

Figure 10-182 Test 9: primary buckled sections on (a) North side and (b) South side

In order to further investigate the significant strength loss, and to verify whether bar fracture or bar buckling occurred, a portion of the tube (i.e., 10 in. x 20 in.) was removed on both North and South sides of the specimen, in the extreme fibers at ruptured and buckled sections, as shown in Figure 10-183 and Figure 10-184, respectively. It can be noticed significant cracking and crushing of the concrete in the critical section of the plastic hinge, perpendicular to the direction of the specimen. Cracks in the concrete extended further to the center of the section. Bar buckling was not observed on either side. Note that on the North side of the specimen, which corresponds to the compression zone at tube fracture on the South side, the position of the spiral prevented buckling to occur, as shown in Figure 10-183(b). As suspected during the test, bar fracture did occurred on the South side of the specimen, a total of three (3) bar fractured, one of them located in the extreme fiber and the other two adjacent to that one.

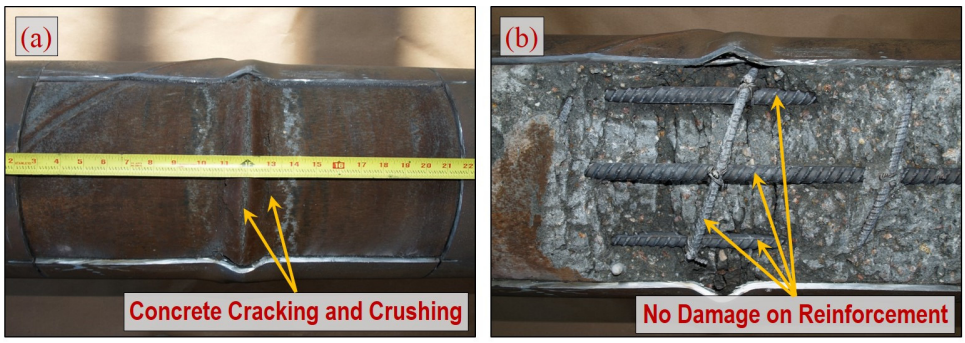

Figure 10-183 Test 9: observed damage in (a) concrete and (b) internal reinforcement on North side

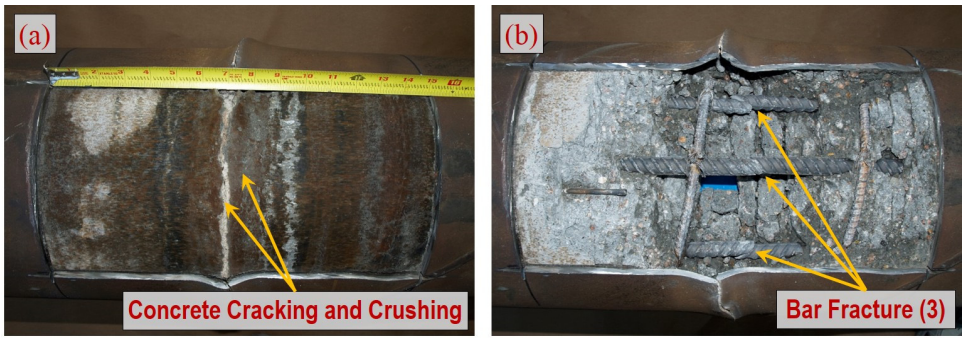

Figure 10-184 Test 9: observed damage in (a) concrete and (b) internal reinforcement on South side

Response Comparison

For comparison purposes, the performance of specimen #9 is compared using results from two surcharge levels, namely, 960 psf and 1920 psf. Figure 10-185 through Figure 10-187 present the effects of surcharge level on the elastic response of pile specimen #9. As previously mentioned, Test 9 was conducted in two phases. Phase one aimed to study the elastic behavior of specimen #9 using a higher level of surcharge (i.e., q = 1920 psf). Phase 2, on the other hand, aimed to study the elastic and inelastic behavior of specimen #9 using the same level of surcharge utilized in previous tests (i.e., q = 960 psf). It is worth noting that between Phase 1 and Phase 2, the soil properties were regenerated by removing the specimen from the pit and liquefying the soil. Target displacements for the elastic loading

history of Phase 1 and Phase 2 were the same and were presented in Table 10-9, with the exception that the first yield displacement (Δ_y') was not imposed to the system during Phase 1, so as to prevent yielding of the tube.

Note from Figure 10-185 that the lateral strength developed by specimen #9 in the stiffer soil profile (q = 1920 psf) was higher than that using a surcharge of 960 psf; this figure indicates the difference of the lateral force between both soil conditions recorded at ¼ and ½ of the first yield displacement (Δ_y'). In the last displacement cycle (¾ Δy') of specimen #9 with q = 1920 psf, the actuator was stopped at 2.25 in. of displacement as strains in the order of 1300 με were observed from the strain gauge data. Note from Figure 10-186 that while the displacement of specimen #9 with q = 1920 psf was ~3/4 in. smaller, the tensile strains developed in the tube are higher than when the surcharge was only 960 psf. This can also be seen from Figure 10-187 where curvature values are slightly larger for q = 1920 psf, though the displacement profiles are different.

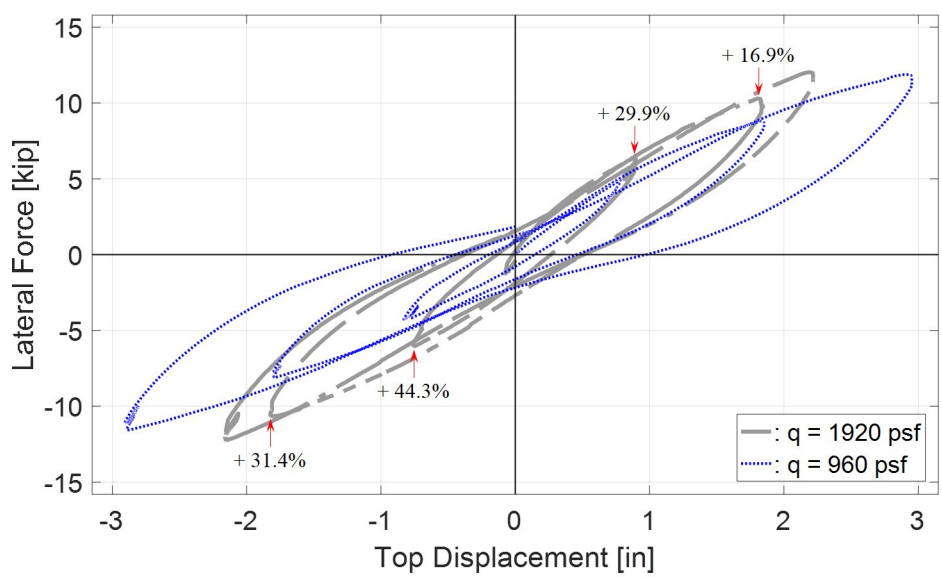

Figure 10-185 Test 9: effect of surcharge level on elastic force vs. displacement response

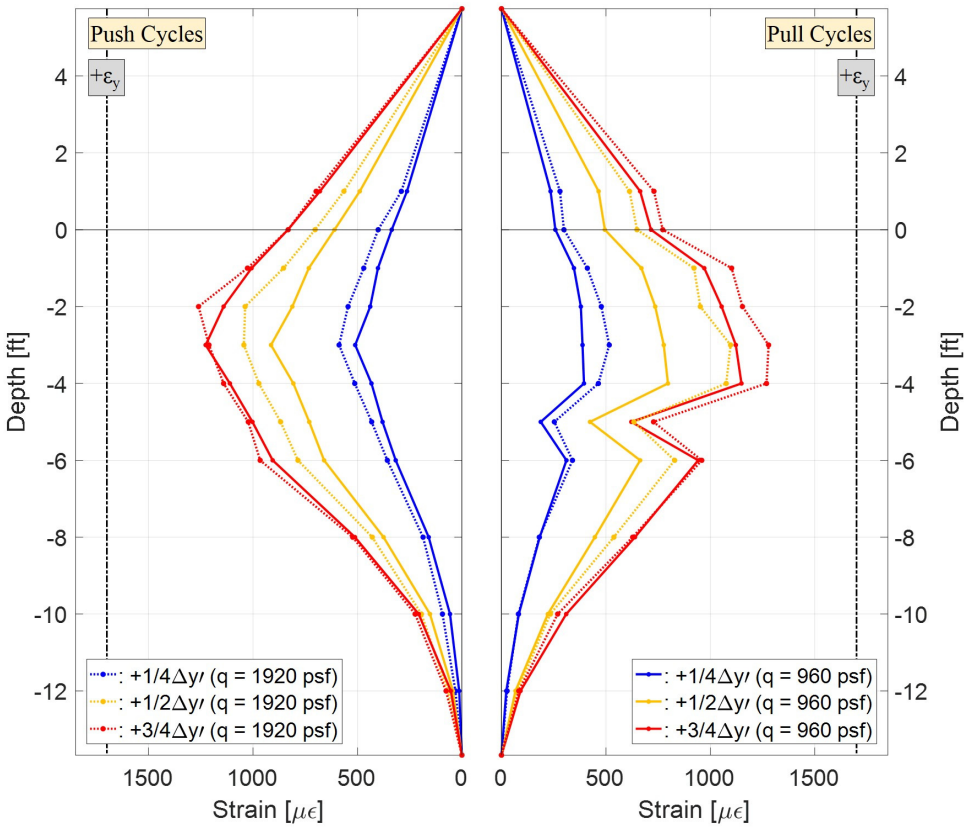

Figure 10-186 Test 9: effect of surcharge level on elastic tensile strains

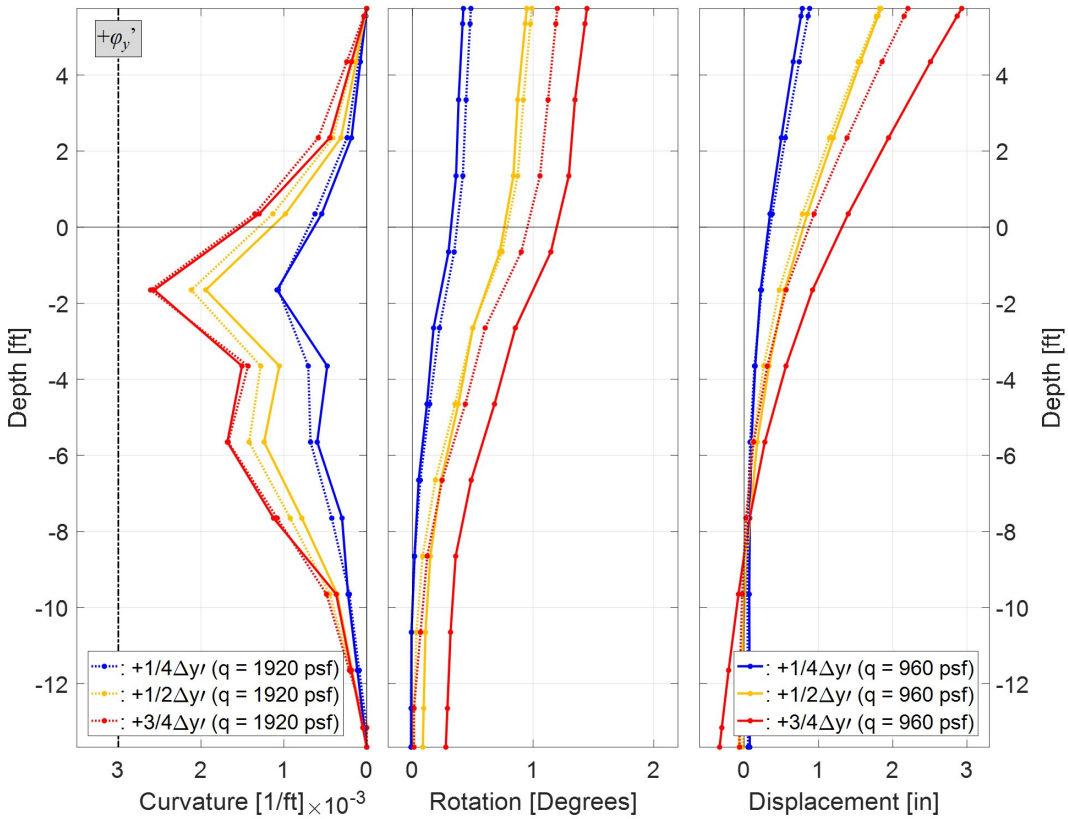

Figure 10-187 Test 9: effect of surcharge level on elastic curvature, rotation, and displacement

Conclusions

Test specimen #9 showed a reliable response through all ductility 4.0 (μ_4) cycles. It is believed that onset of local buckling occurred at that ductility level as subtle strength loss was observed. The test specimen completed all cycles of ductility 4.0 (μ_4) with minor loss of strength. Failure of the specimen occurred at ductility level 5.0 (μ_5) when a significant drop in the strength was observed as the third push cycle was imposed at the pile specimen head. Further investigations revealed that failure occurred due to a combination of tube local buckling, tube fracture, and bar fracture. It is believed that this particular specimen is capable of having a reliable displacement capacity up to ductility 4.0 (μ_4). The main buckles as well as the tube fracture did not occur over the spiral weld, so the tube spiral welds do not appear to negatively influence the behavior.

As evidenced from the results with different surcharge levels, while the overall force vs. displacement response is rather similar, the impact of the soil stiffness is significant in terms of the local deformations (i.e., rotation, curvature, strain). In addition, the depth to the location of such maximum deformations also change as a function of the effective stiffness of the soil profile, which could result in an increase in the shear demand of the pile specimen.

Test 10 Summary Report

August 23, 2016

Prepared for

Alaska Department of Transportation

Alaska University Transportation Center

Project Team

RA: Diego Aguirre

PIs: Mervyn Kowalsky, James Nau, Mo Gabr

Other Senior Personnel: Greg Lucier, Ben Smith

North Carolina State University

Executive Summary

Test 10 was conducted August 5th, 2016 at the North Carolina State University Constructed Facilities Laboratory. The tested pile-column specimen was a reinforced concrete filled steel tube with a diameter-to-thickness (D/t) ratio of 48. No surcharge was applied to the soil, thus the soil stiffness was not modified. The above-ground height (column length) was increased by 2 ft. when compared to previous tests using the same D/t ratio. The test was successfully conducted to failure, which was caused by a combination of tube local buckling, tube fracture, and bar fracture, resulting in a large strength degradation (~73%) in an additional push cycle at ductility level 5.0 (μ_5), after three cycle sets at that level were completed. Due to setup constrains, displacements in the pull direction only reached a maximum displacement ductility level 3.0 (μ_3) for all pull cycles of displacement ductility levels 4.0 (μ_4) and 5.0 (μ_5).

Specimen and Test Description

Test 10 consisted of a 21-foot-5.25-inch long, reinforced concrete filled, 12-inch diameter spirally welded steel tube without skelp or splice welds. The pile specimen was embedded 13 ft. – 8 in. into clean sand in the soil-structure interaction facility at the NCSU-CFL. Lateral load was applied at the pinned connection at the top of the pile specimen by means of a 100-kip, 70-inch stroke hydraulic actuator. The nominal wall thickness of the tube was

0.25 in., providing a nominal diameter-to-thickness ratio (D/t) of 48. The test was conducted with a 7-foot-9.25-inch cantilever length, measured from the soil surface to the point at which the lateral load was applied. Figure 10-188 and Figure 10-189 present a schematic of the test setup (elevation) and the specimen #10 cross-section, respectively, while Figure 10-190 shows the instrumentation used for testing. A photograph of the test setup is included in Figure 10-191.

Material properties were determined by in-house material tests. The yield and ultimate stresses of the steel tube were 49.5 ksi and 71.3 ksi, respectively, based on tests conducted on three (3) coupons cut from the end of the test pile specimen. The yield and ultimate stresses of the ASTM A706 Grade 60 longitudinal reinforcement were 72.8 ksi and 97.1 ksi, respectively, based on tests conducted on six (6) bar specimens from the same heat of the longitudinal reinforcement. The yield and ultimate stresses of the spiral reinforcement were 64.9 ksi and 96.9 ksi, respectively, based on tests conducted on six (6) bar specimens from the same heat of the transverse reinforcement. An average concrete compressive strength of 8.40 ksi (standard deviation of ± 0.14 ksi) was determined from three (3) compression tests of 4”x8” concrete cylinders.

Soil properties were also determined by in-house material tests. Based on a measured particle size distribution, the soil was classified as poorly-graded sand (SP). The unit weight and friction angle (γ = 90 pcf and ϕ = 35°, respectively) were reasonably assumed based upon results from previous tests.

The load history applied to the pile specimen consisted of standard single-cycle and three-cycle sets intended to evaluate both the elastic and inelastic response of the specimen. The first portion (i.e., pile elastic response up to first yield) of the test consisted of single reversed, displacement-controlled cycles, ramping up to the first yield displacement in ¼ increments. Given the non-linear response from the beginning of the test due to the characteristic soil behavior, target displacements in this portion of the test were determined based on the results of a monotonic pushover analysis performed using a detailed non-linear, fiber-based, finite element model developed using the OpenSees framework software. Soil-structure interaction was included by means of non-linear springs at 1-foot interval depths, with spring properties assigned based on p-y curves.

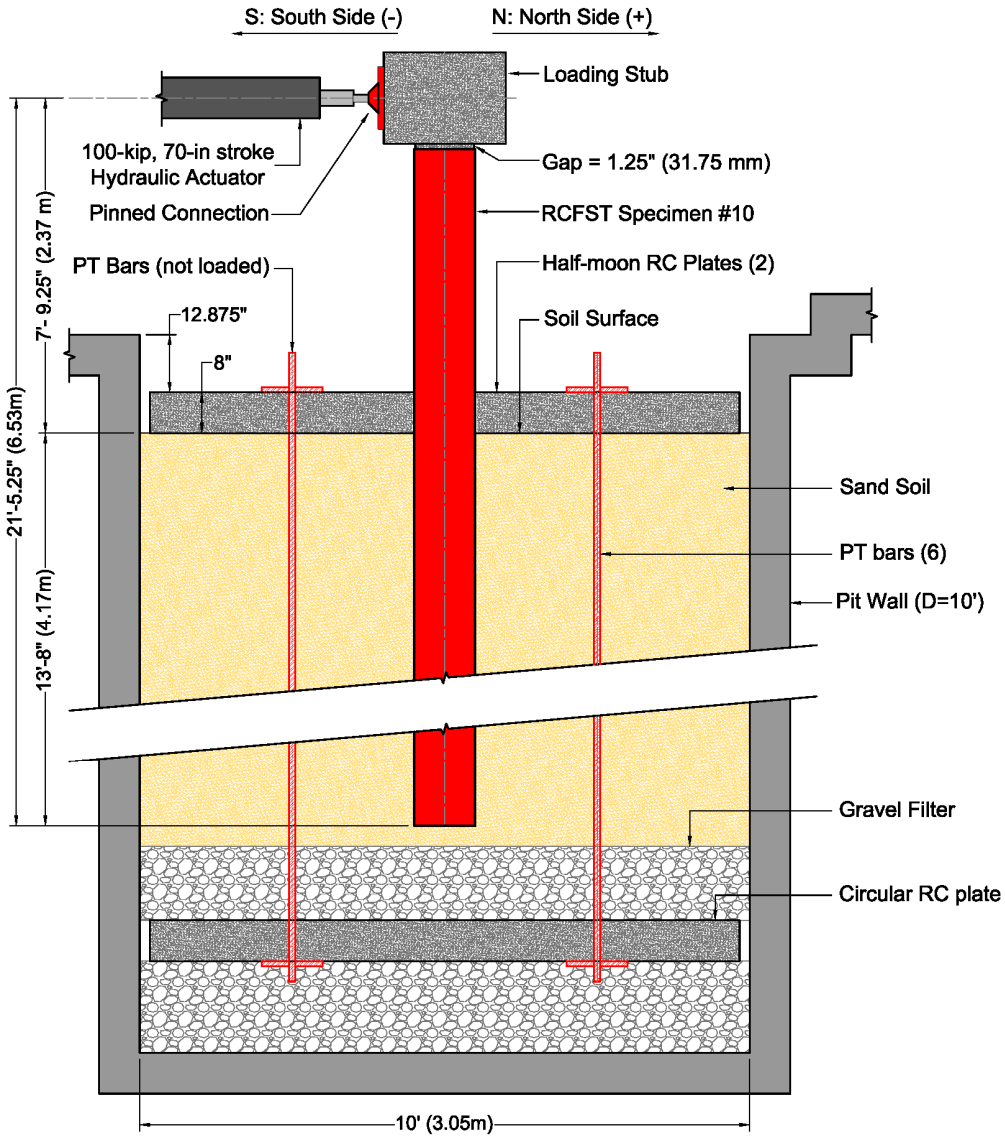

Figure 10-188 Test 10: test setup elevation schematic

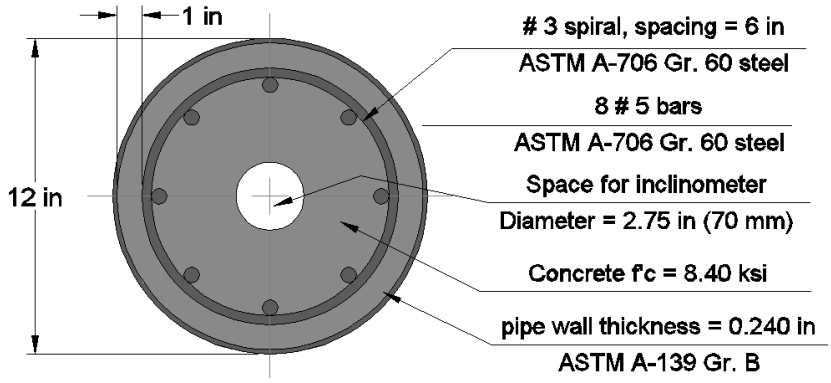

Figure 10-189 Test 10: RCFST specimen cross section

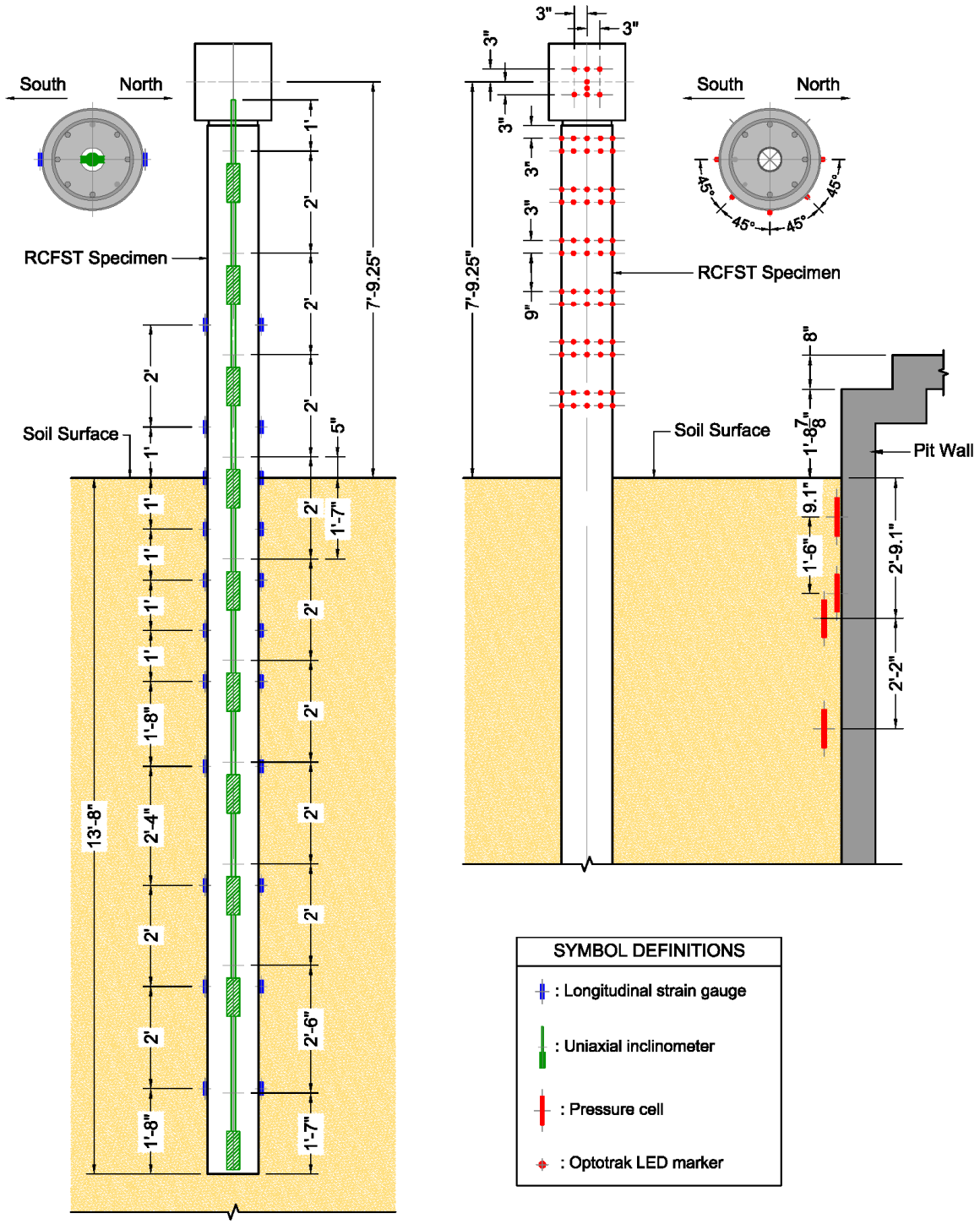

Figure 10-190 Test 10: instrumentation

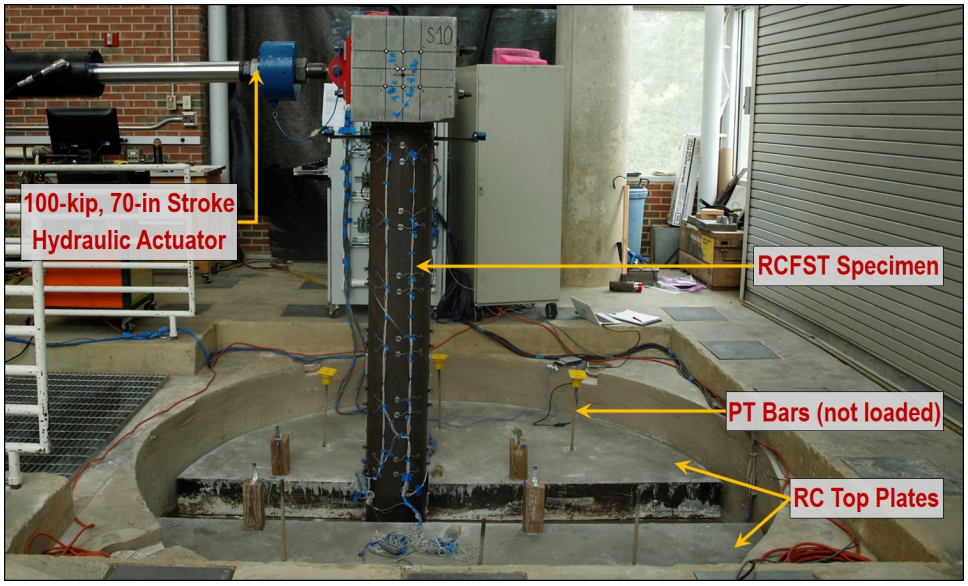

Figure 10-191 Test 10: pinned-head, RCFST pile-column test setup

The first yield force (F_y) and nominal force (F_n), which is defined as the force at a concrete compressive strain of 0.004 or at a tube/bar tensile strain of 0.015 (whichever occurs first), were determined based upon tensile and compressive strains monitored during the numerical simulation (i.e., pushover analysis), as 12.6 kips and 19.2 kips, respectively. Table 10-10 summarizes the target displacements for the first portion of the test.

After the first portion of the test was completed, the measured average strain at the predicted first yield displacement (Δ'_y) was 1295 ($\mu\varepsilon$), which correlates well with the tube yield strain (ε_y = 1700 $\mu\varepsilon$). The measured average displacement at the first yield displacement (Δ'_y = 5.09 in) was modified by the nominal-to-first yield force ratio in order to determine the displacement ductility level 1.0 (μ_1 = 7.80 in), as shown in Equation 10-20. The remainder of the test was completed using reversed three-cycle sets in displacement-controlled increments at different levels of displacement ductility until failure, as shown in Equation 10-21. However, as previously mentioned, for the pull cycles at displacement ductility levels 4 (μ_4) and 5 (μ_5), a maximum displacement corresponding to that of ductility 3 (μ_3) was imposed at the pile head due to setup constrains, namely, 23.4 in. The entire displacement and load histories can be seen in Figure 10-192. Positive loads and displacements correspond to rightward (North) motion of the pile in the test setup. The positive legs of all cycles were completed before the negative legs.

Table 10-10 Test 10: predictions for elastic portion

Performance Level	Displacement (in)	Force (kips)
1/4 Δy'	1.17	3.55
1/2 Δy'	2.44	6.83
3/4 Δy'	3.81	9.98
1 Δy'	5.09	12.57

$$\Delta_y = \mu_1 = \Delta'_y \cdot \frac{F_n}{F_y} = 5.09\,in \cdot \frac{19.2\,kip}{12.6\,kip} = 7.80\,in \qquad \text{Equation 10-20}$$

$$\mu_i = i \cdot \mu_1 \rightarrow i = 1.0,\ 1.5,\ 2.0,\ 3.0,\ 4.0,\ 5.0 \qquad \text{Equation 10-21}$$

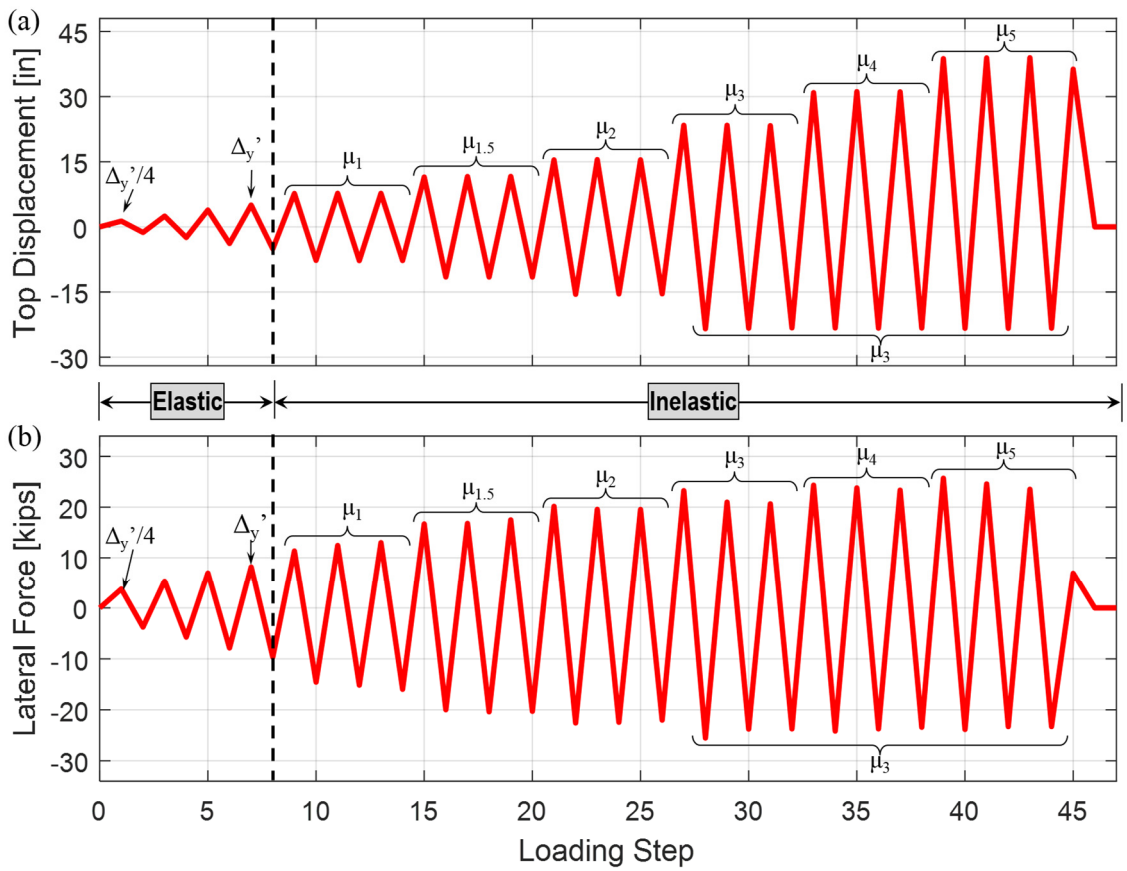

Figure 10-192 Test 10: (a) displacement and (b) loading histories

Specimen Response

Specimen #10 performed well through the elastic portion of the test and during all three cycles of ductility level 4.0 (μ_4). It is believed that the onset of tube buckling occurred early during the displacement cycles at ductility level 3.0 (μ_3) as minor loss of strength was observed at the second and third cycles at that displacement level. A significant loss of strength, indicating failure, occurred during an additional push cycle at ductility level 5.0 (μ_5), after all three-cycle sets at that level were applied. Figure 10-193 and Figure 10-194 present the lateral force vs. top displacement response and envelopes, respectively. It can be seen that the system has a characteristic large energy dissipation capacity due to both damping sources, that is, the pile itself and the surrounding soil. In addition, it can be clearly seen from both figures that a significant loss of strength (~73%) occurred during the fourth push cycle of ductility level 5.0 (μ_5).

Figure 10-195 presents the deformed shape and the soil-pile gaps at zero displacement after the elastic portion of the test was conducted; the size of the gap was ~1.50 in. on both sides of the specimen. As it was previously explained, at this point of the test strain profiles on the sides of the pile were verified in order to further conduct the test at the aforementioned ductility levels. Figure 10-196 presents the strain profiles recorded during the elastic portion of the test. Notice that tensile strains of 1200 (με) and 1390 (με) were recorded in the pipe during the push and pull cycles, respectively, when the predicted first yield displacement was imposed to the system. Based on the rotation data recorded with the inclinometer placed inside the pile along its length, specimen curvature, rotation, and displacement profiles are presented in Figure 10-197 and Figure 10-198 for the elastic push and pull cycles, respectively. Note that there are small rotations and displacements at the pile tip which indicates that there is a point of rotation (at ~9 ft.) rather than a point of fixity; inelastic action was developed in the pile nonetheless. The circles in the top portion of the displacement profiles in Figure 10-197 and Figure 10-198 represent the Optotrak LED markers; note that they are in agreement with the calculated displacement profiles. In Figure 10-196 through Figure 10-198 the symbols N and S in the legend refer to the North and South sides, Δ_y' is the first yield displacement, $Ø_y'$ is the first yield curvature, and a depth equal to 0 ft. represents the soil surface.

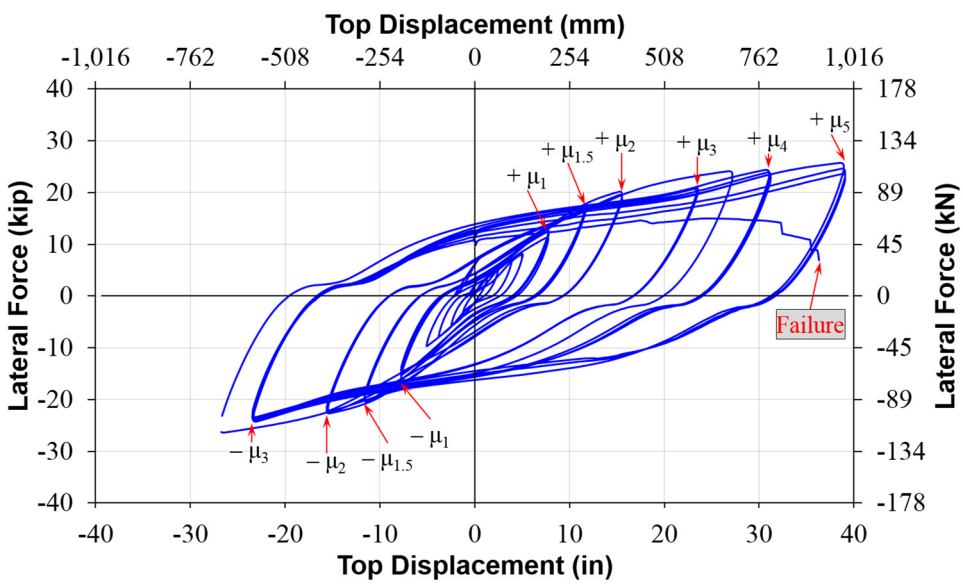

Figure 10-193 Test 10: lateral force vs. top displacement response

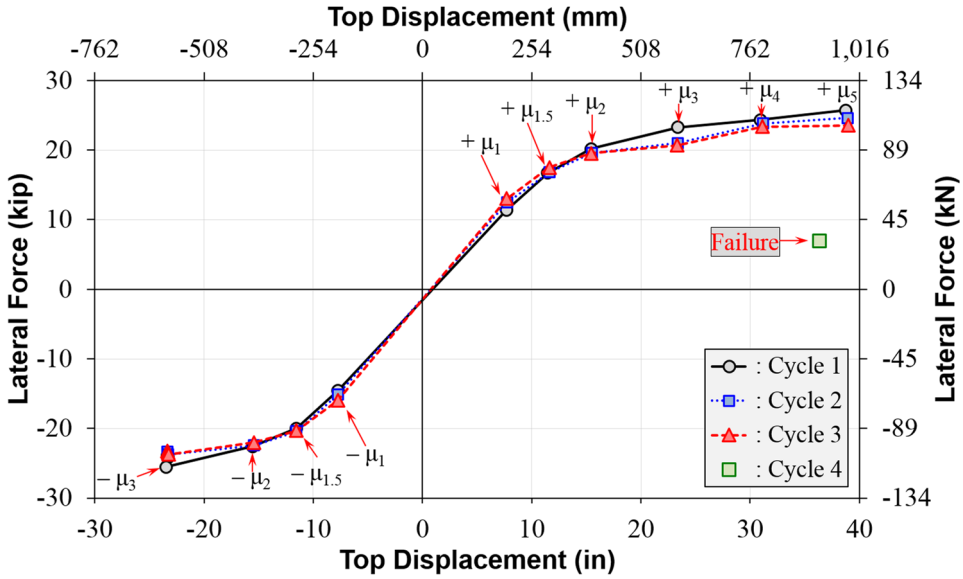

Figure 10-194 Test 10: lateral force vs. top displacement envelopes

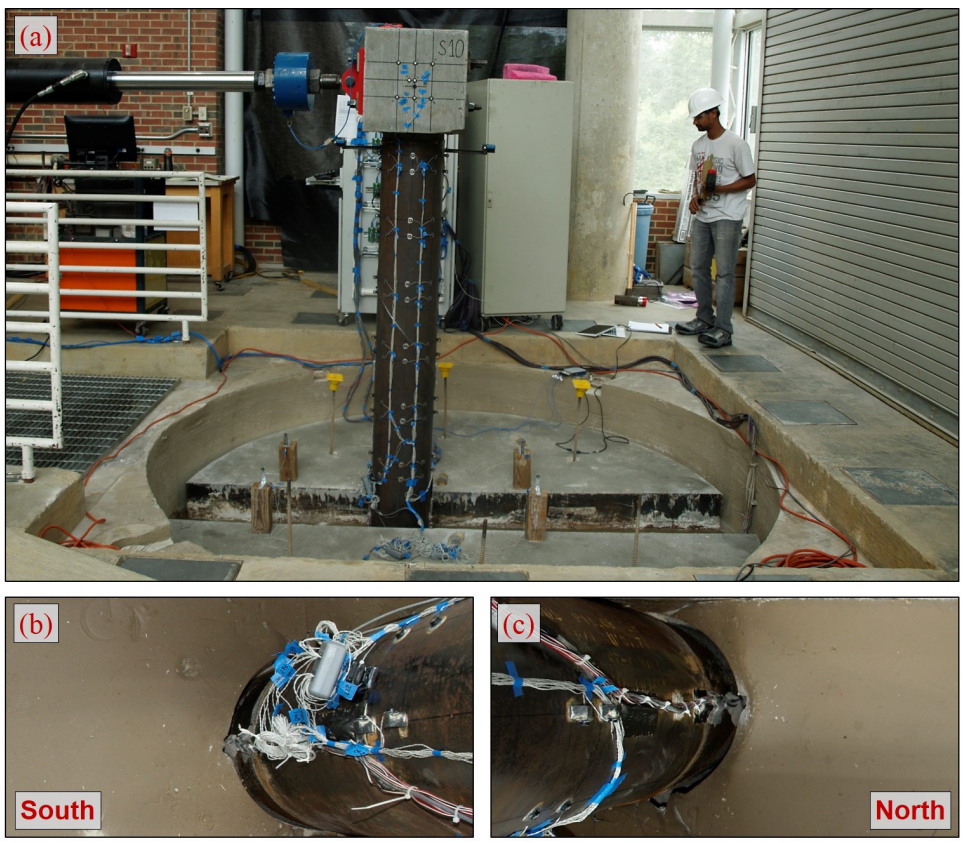

Figure 10-195 Test specimen #10 after elastic portion of the test was completed: (a) deformed shape, (b) South side and (c) North side

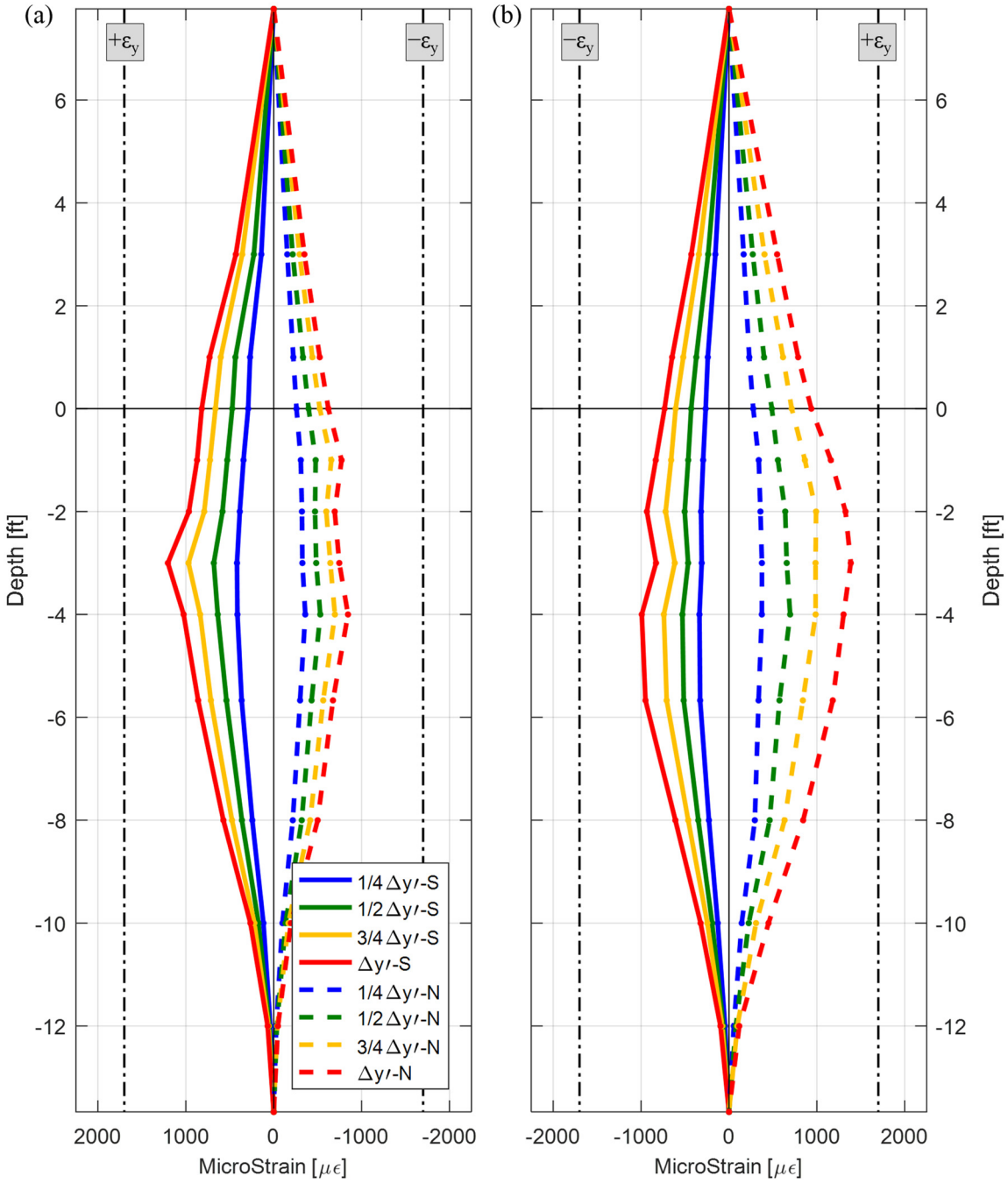

Figure 10-196 Test 10: strain profiles from elastic (a) push and (b) pull cycles

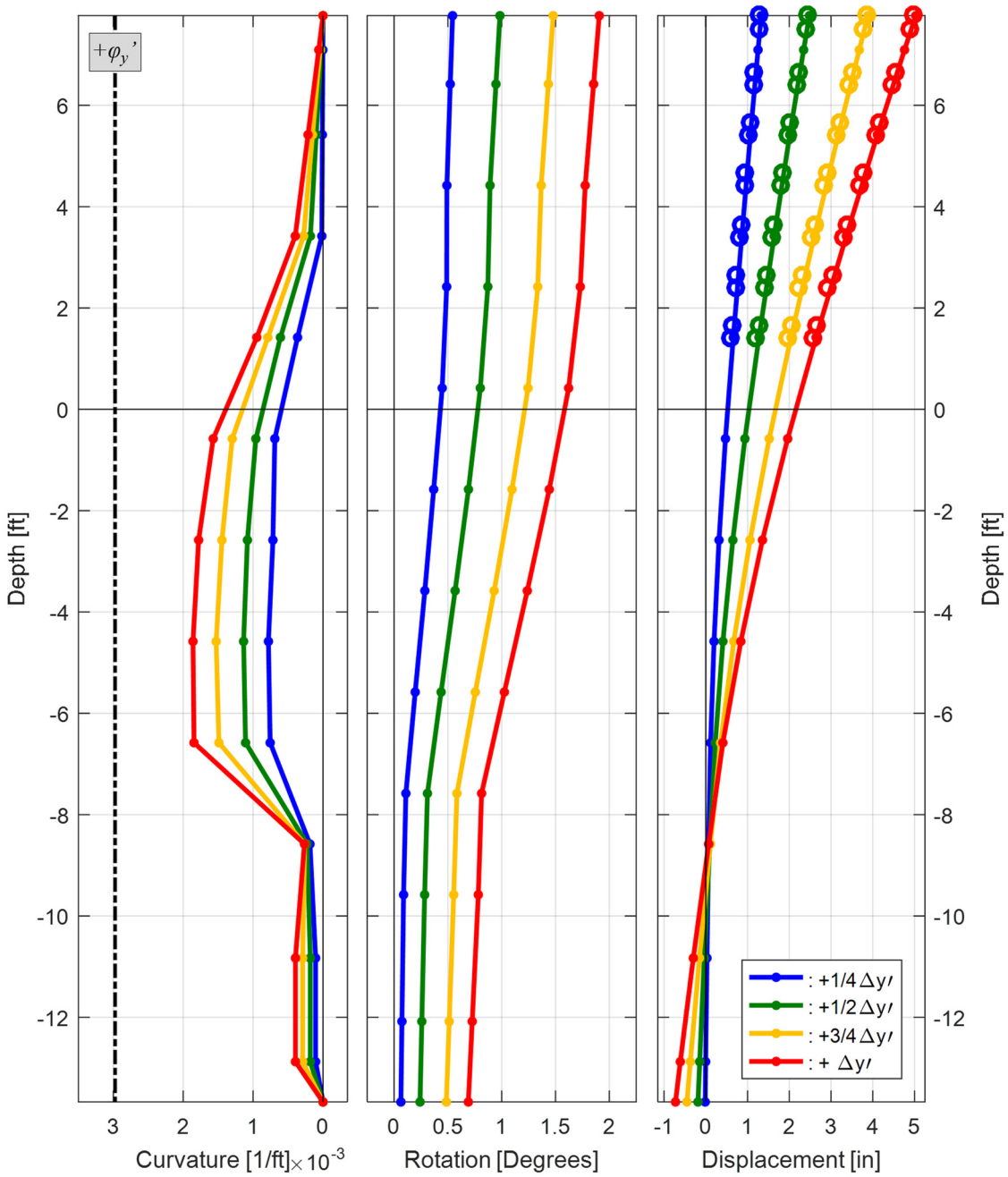

Figure 10-197 Test 10: curvature, rotation, and displacement profiles (elastic push cycles)

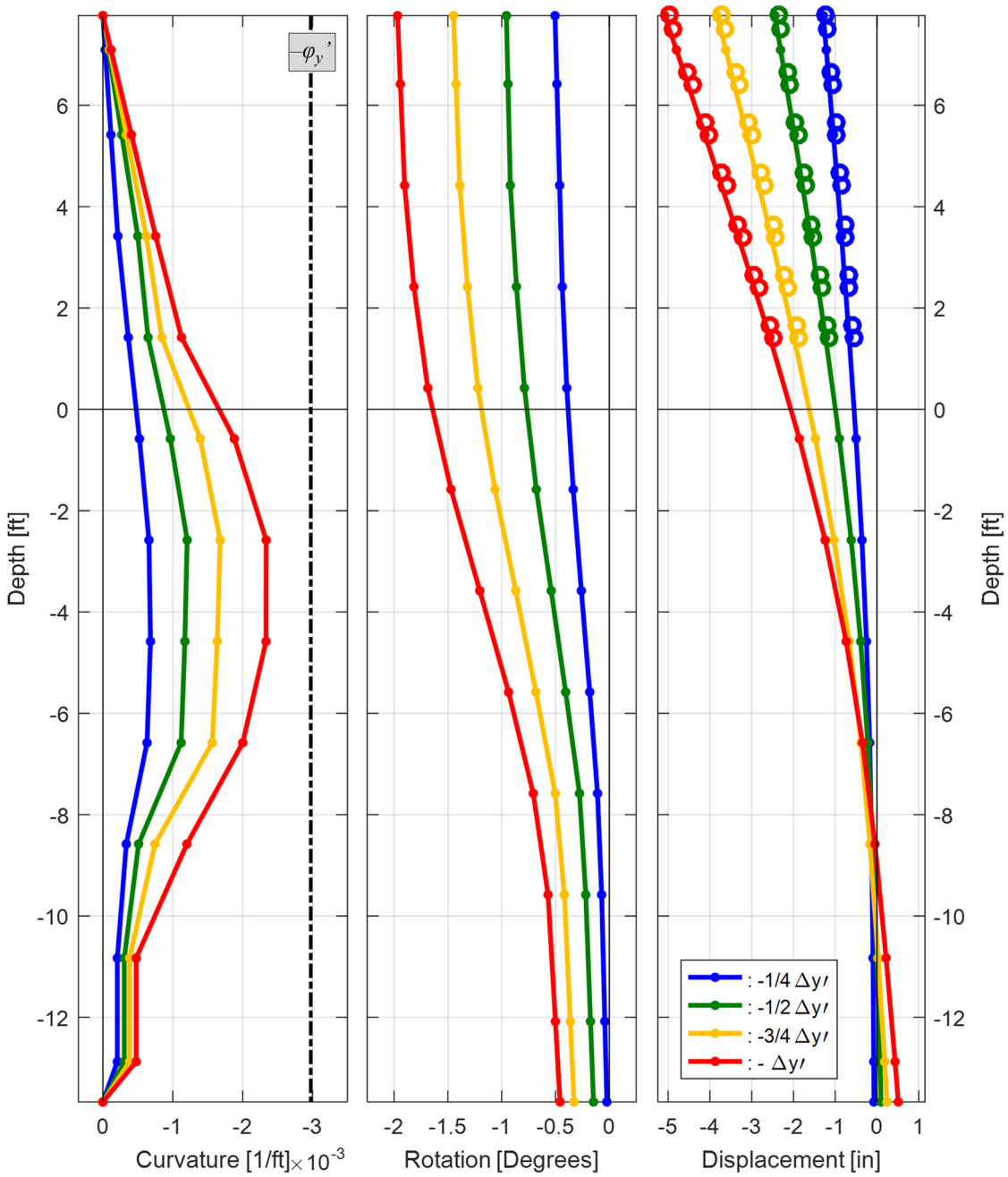

Figure 10-198 Test 10: curvature, rotation, and displacement profiles (elastic pull cycles)

As the test continued, the gap on the sides of the pile increased in size as the displacement ductility level increased. Minor loss of strength was observed up until all ductility level 4.0 (μ_4) cycles. The specimen failure (Figure 10-199) occurred at the fourth cycle load at ductility 5.0 (μ_5) when a significant drop in the force of the actuator was observed (i.e., ~73%). Sounds indicating steel fracture were heard at the same time when the strength loss occurred, indicating probable tube or bar fracture. Moreover, twist rotation of the pile was observed during all push cycles at ductility levels 4 (μ_4) and 5 (μ_5). Finally, the test was terminated and the specimen was taken to zero displacement in order to facilitate its extraction from the soil.

Figure 10-200 presents strain profiles for the first push and pull cycles at different displacement ductility levels; the symbols N and S in the legend refer to the North and South sides, μ is the displacement ductility, and a depth equal to 0 ft. represents the soil surface. Note from Figure 10-200 that the largest tensile and compressive strains were recorded at a depth between 1 ft. and 5 ft., which correlates well with the curvature, rotation, and displacement profiles presented in Figure 10-201 and Figure 10-202 for the inelastic push and pull cycles of the test, respectively. Note that the largest changes in rotation (i.e., curvature) occurred at a depth between 0.5 ft. and 4.5 ft., which correlates well with the observed damage zone.

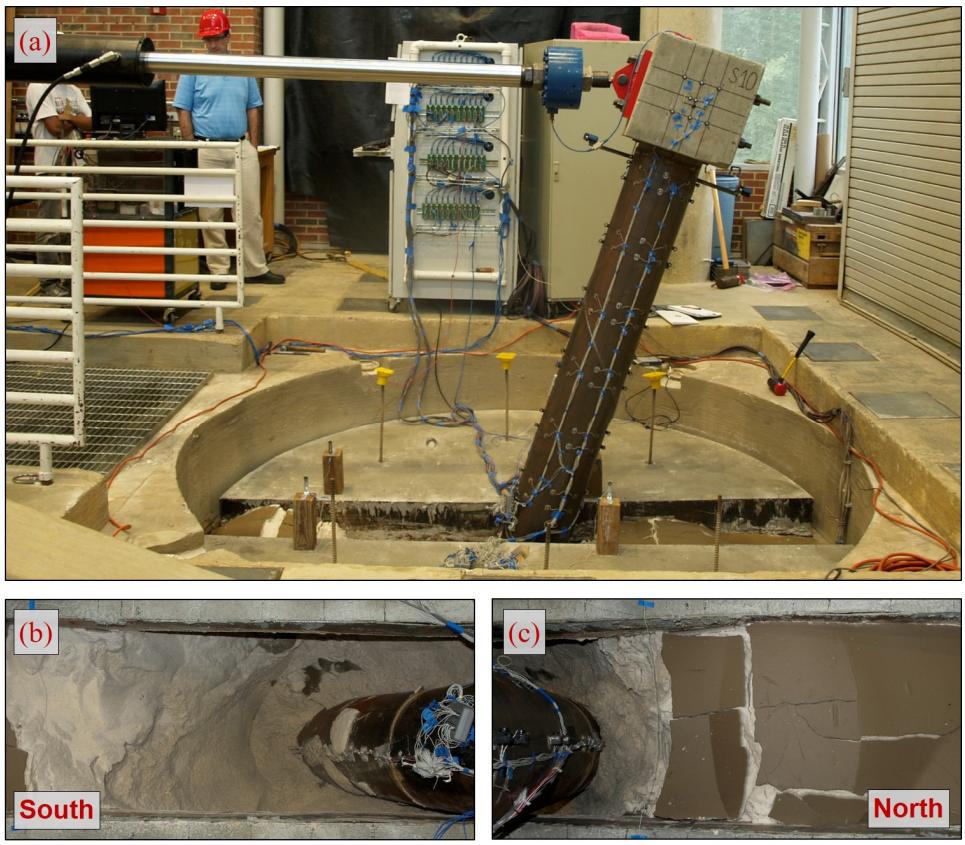

Figure 10-199 Test specimen #10 at maximum displacement: (a) deformed shape, (b) South side and (c) North side

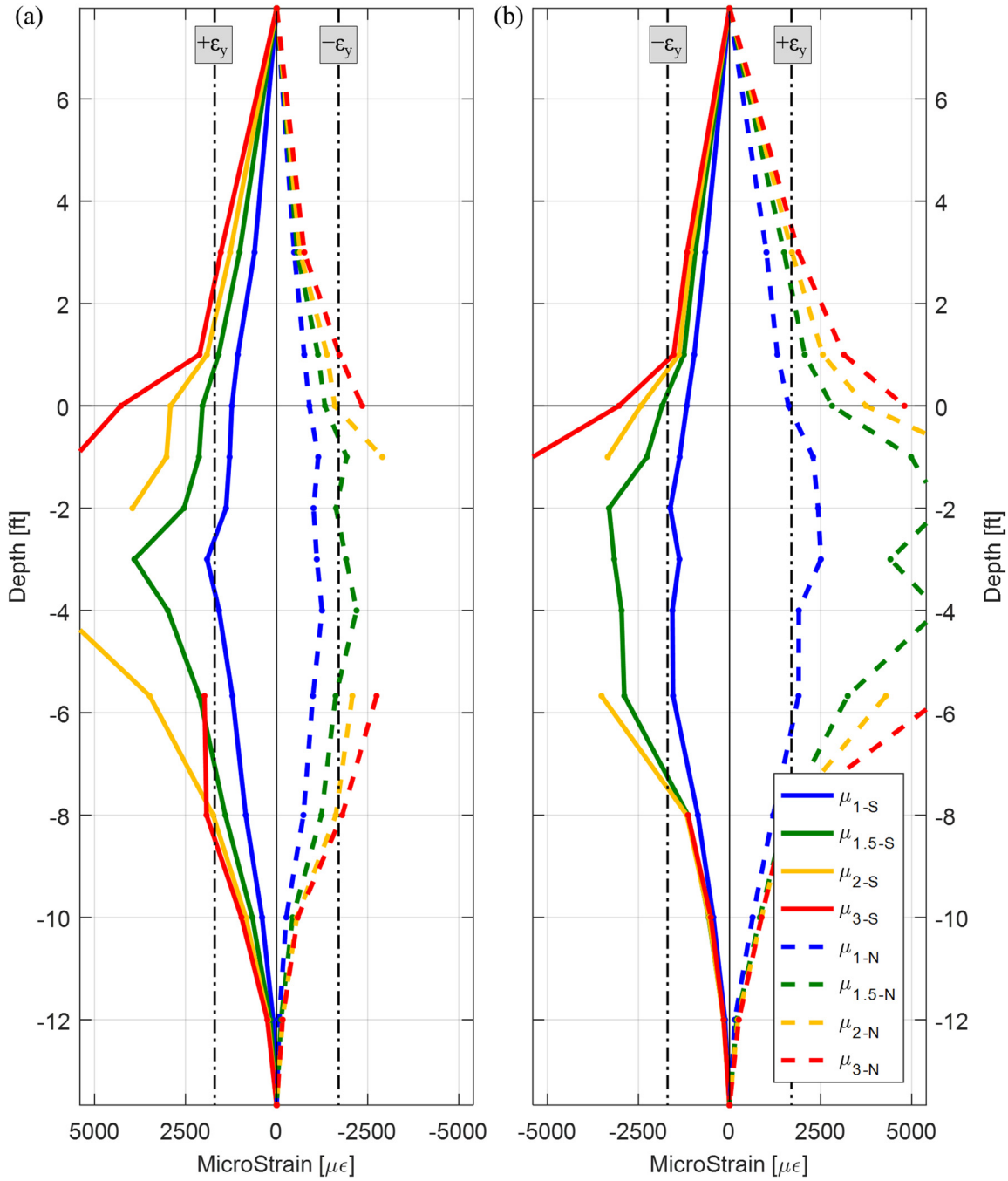

Figure 10-200 Test 10: strain profiles from inelastic (a) push and (b) pull cycles

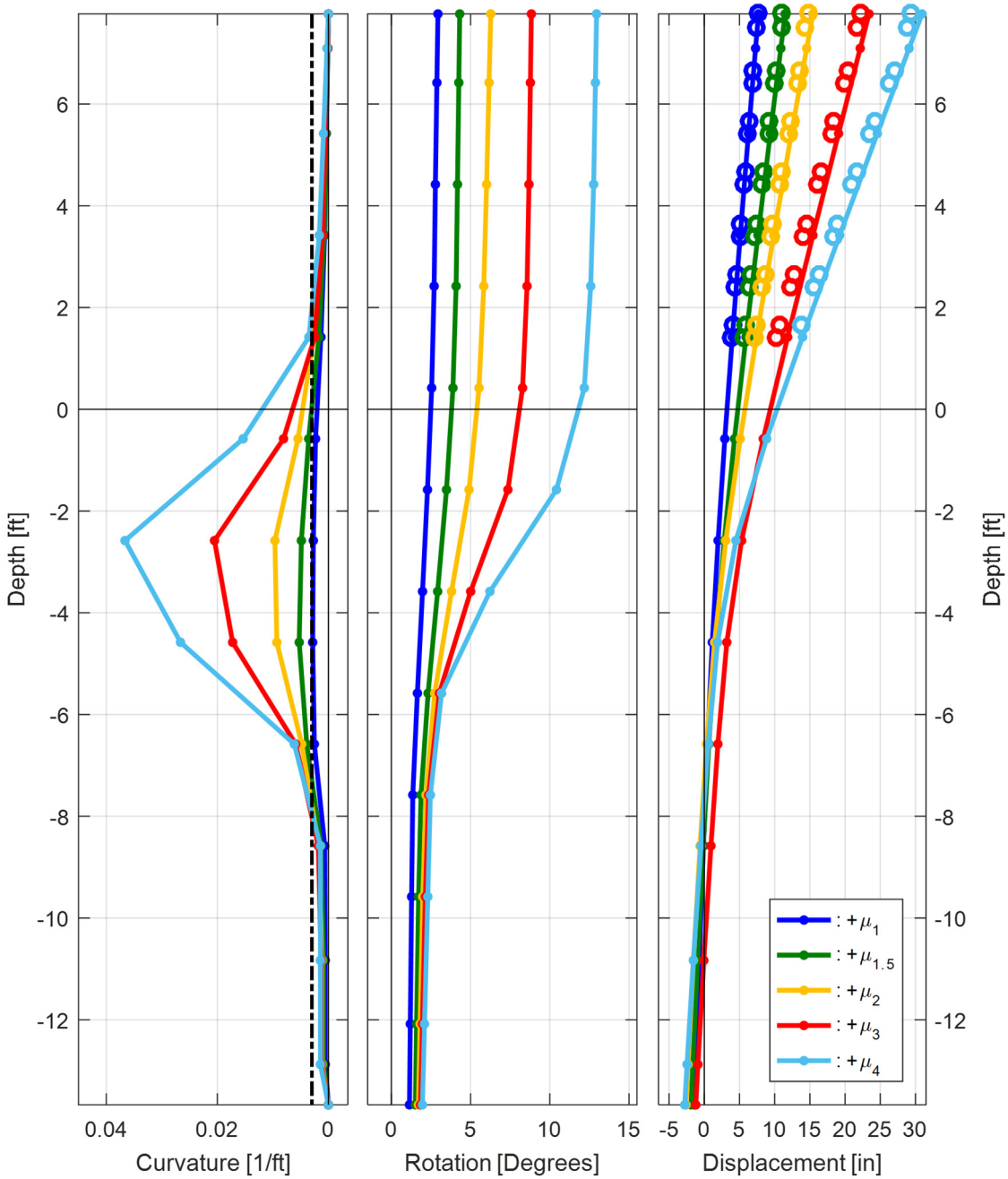

Figure 10-201 Test 10: curvature, rotation, and displacement profiles (inelastic push cycles)

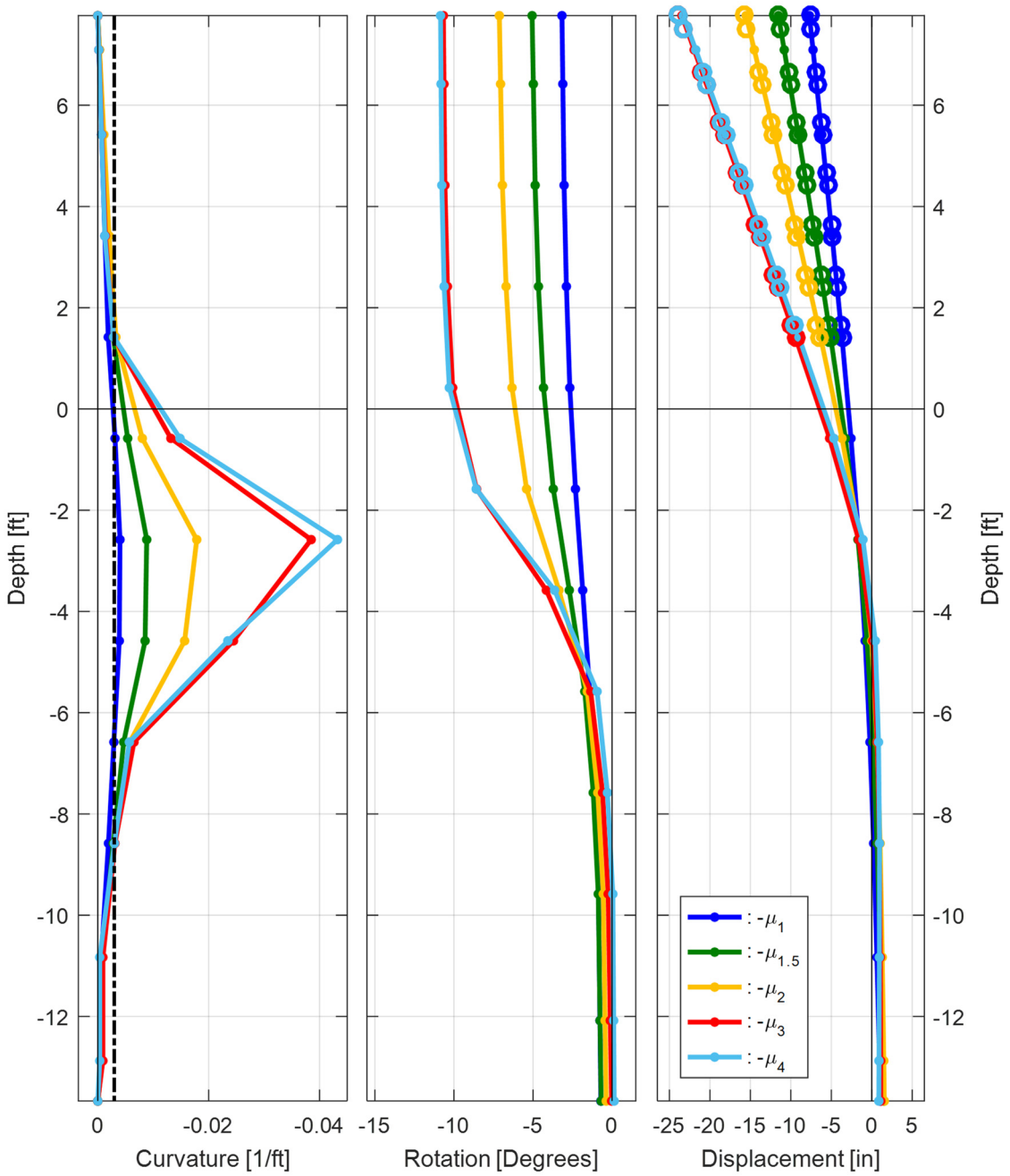

Figure 10-202 Test 10: curvature, rotation, and displacement profiles (inelastic pull cycles)

Figure 10-203 shows the state of the soil surface after the test was completed. Notice that despite the presence of the half-moon RC plates in the surface, deformations in the soil followed an expected oval-shaped failure surface in which active and passive pressures developed around the pile. This surface extended ~24 in. on both sides of the direction of loading and ~19 in. on the perpendicular direction. The total average settlement of the RC plates during the test was ~2.28 in. This value was averaged based on the vertical displacement of 4 points on the RC plates. Figure 10-204 shows the average settlement of the half-moon RC plates during the test as a function of the imposed displacements in the top of the pile. Note that, as the displacement history is applied, the settlement increases, though its magnitude is larger at the beginning of the test.

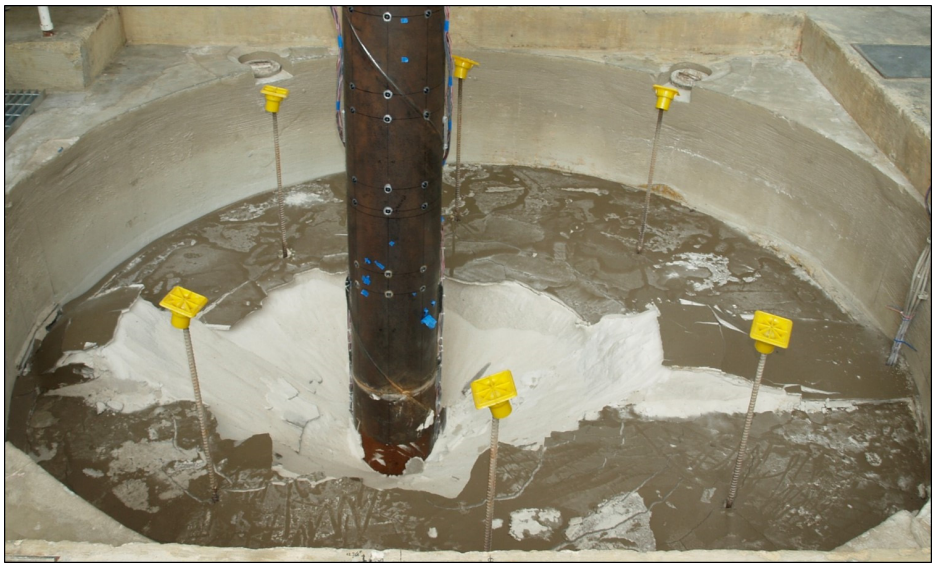

Figure 10-203 Test 10: soil surface after testing

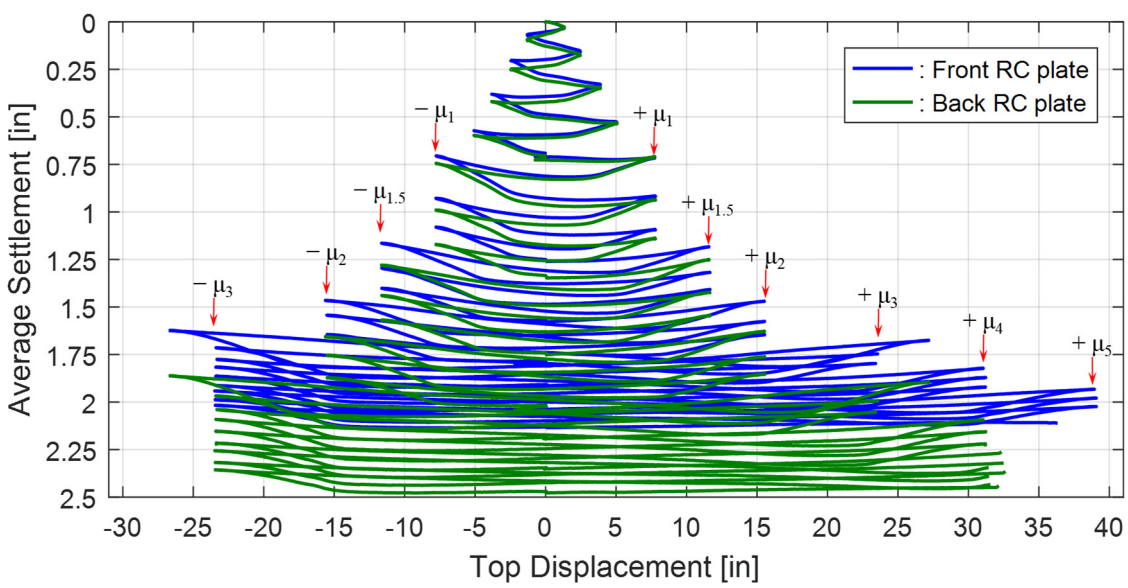

Figure 10-204 Test 10: half-moon RC plate settlement during testing

Figure 10-205 through Figure 10-208 present the damage observed after the pile was extracted from the soil. As thought during the test, tube fracture and tube buckling did occur as did bar fracture; bar buckling was not observed. It can be seen that local buckling developed on both sides of the specimen. The sections with the largest buckling occurred at a depth of 3ft. – ½ in. on the South side and 2 ft. – 9.5 in. and 3 ft. – 4 in. on the North side of the specimen, which implies that the plastic hinge developed at an average depth of 3 ft. – 0.67 in. with respect to the soil surface. Several ripples were observed on both South and North sides of the specimen above the plastic hinge region and close to the soil surface.

Tube fracture (Figure 10-205) occurred on the South side of the specimen and it extended about half of the cross-section perimeter, resulting in a significant drop in strength due to lost tension capacity. As a consequence, after rupture, tension capacity is provided by the longitudinal reinforcement, which has a smaller area in comparison with that provided by the tube, inducing high stresses and deformations. Upon further investigations, bar fracture was observed on the South side of the specimen; however; bar buckling was not observed neither on the South nor the North sides. Note that tube fracture occurred on the section with the largest tube buckling, in which deformations protruded ~5/8 in. on the South side and ~1/2 in. on the North side of the pile; notice that 2 minor buckle sections developed on the North side. Figure 10-206 presents measurements of the primary buckled regions of the pile.

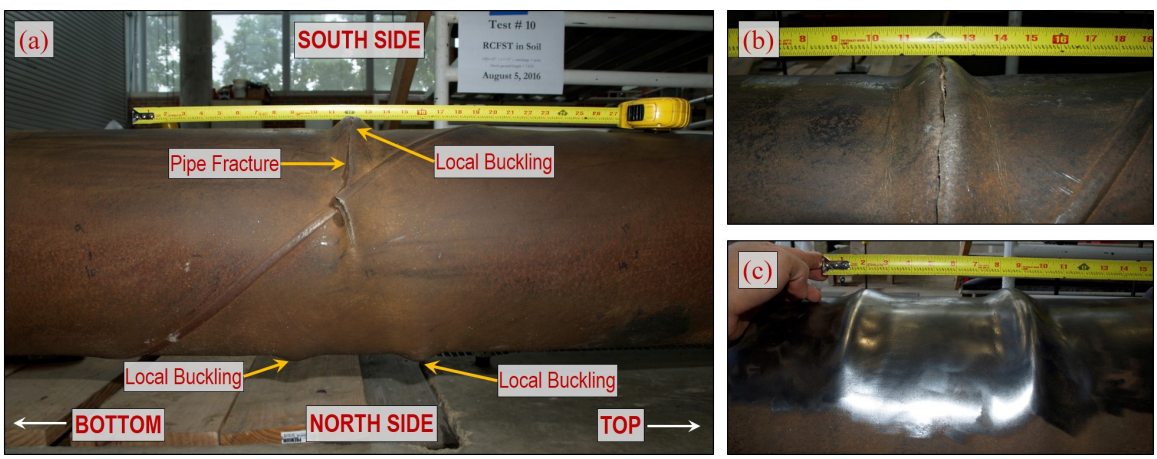

Figure 10-205 Test 10: (a) Final observed damage, (b) tube fracture, and (c) tube local buckling

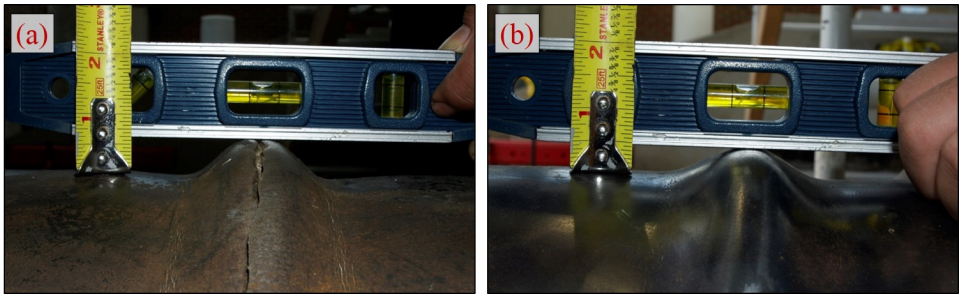

Figure 10-206 Test 10: primary buckled sections on (a) North side and (b) South side

In order to further investigate the significant strength loss, and to verify whether bar fracture or bar buckling occurred, a portion of the tube (i.e., 10 in. x 12 in.) was removed on both North and South sides of the specimen, in the extreme fibers at the ruptured and buckled sections, as shown in Figure 10-207 and Figure 10-208, respectively. It can be noticed significant cracking and crushing of the concrete in the critical section of the plastic hinge, perpendicular to the direction of the specimen. Cracks in the concrete extended further to the center of the section. No bar buckling was observed on either side. Note that on the North side of the specimen, which corresponds to the compression zone at tube fracture on the South side, the position of the spiral prevented occurrence of bar buckling at the two main buckled sections, as shown in Figure 10-207(b). As suspected during the test, bar fracture did occur on the South side of the specimen, a total of three (3) bars rupture, one of them located in the extreme fiber and the other two adjacent to that one.

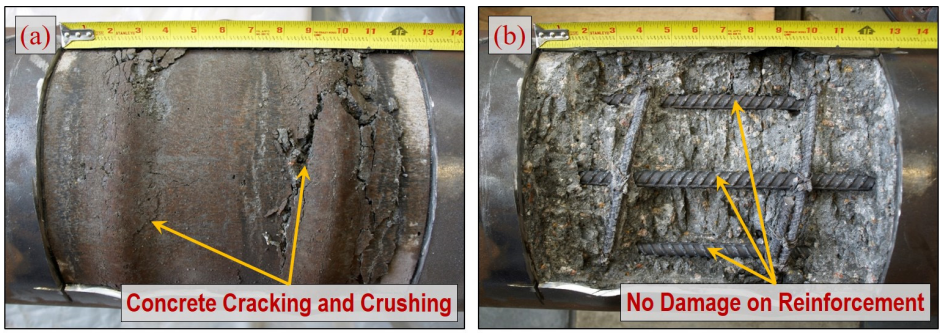

Figure 10-207 Test 10: observed damage in (a) concrete and (b) internal reinforcement on North side

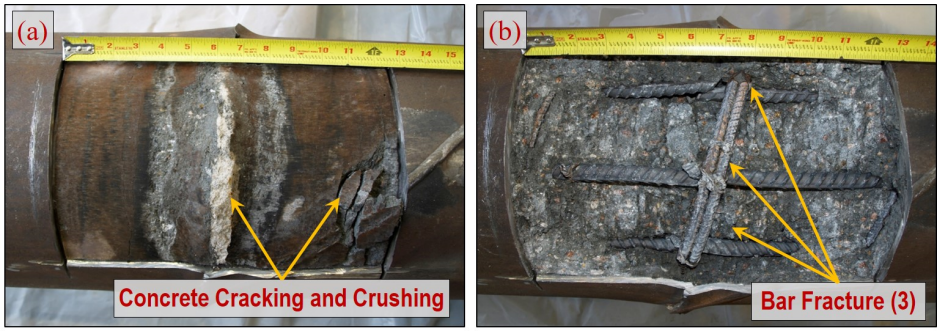

Figure 10-208 Test 10: observed damage in (a) concrete and (b) internal reinforcement on South side

Conclusions

Test specimen #10 showed a reliable response through all ductility 4.0 (μ_4) cycles. It is believed that onset of tube local buckling occurred at ductility level 3.0 (μ_3) as subtle strength loss was observed. The test specimen completed all cycles of ductility 4.0 (μ_4) without significant loss of strength. After all ductility 5.0 (μ_5) cycles were completed, an additional push cycle at the same ductility level was induced at the specimen head. Failure of the specimen occurred during that additional push cycle when a significant drop in the strength was observed. Further investigations revealed that failure occurred due to a combination of tube local buckling, tube fracture, and bar fracture. Although in the pull direction the specimen was subjected only to a displacement ductility level 3.0 (μ_3), it is believed that this particular specimen is capable of having a reliable displacement capacity up to ductility 5.0 (μ_5). The main buckles as well as tube fracture did not occur over the spiral weld, so the tube spiral welds do not appear to negatively influence the behavior.

Test 11 Summary Report

October 13, 2016

Prepared for

Alaska Department of Transportation

Alaska University Transportation Center

Project Team

RA: Diego Aguirre

PIs: Mervyn Kowalsky, James Nau, Mo Gabr

Other Senior Personnel: Greg Lucier, Ben Smith

North Carolina State University

Executive Summary

Test 11 was conducted August 19th, 2016 at the North Carolina State University Constructed Facilities Laboratory. The tested pile-column specimen was a reinforced concrete filled steel tube with a diameter-to-thickness (D/t) ratio of 95. No surcharge was applied to the soil, thus the soil stiffness was not modified. The above-ground height (column length) was increased by 2 ft. when compared to previous tests using the same D/t ratio. The test was successfully conducted to failure, which was caused by a combination of tube local buckling, tube fracture, and bar buckling, resulting in a large strength degradation (~42.9%) in the third pull cycle at ductility level 4.0 (μ_4). Due to issues related to one of the data acquisition systems, part of the data from the experiment was lost. As such, unlike in previous test observations, where the lateral force vs. top displacement response is presented, the envelopes are presented since part of the lost information included the lateral force induced by the actuator. These envelopes were plotted using manually recorded data at different performance levels.

Specimen and Test Description

Test 11 consisted of a 21-foot-5.25-inch long, reinforced concrete filled, 12-3/4-inch diameter spirally welded steel tube without skelp or splice welds. The pile-column specimen was embedded 13 ft. – 9 in. into clean sand in the soil-structure interaction facility at the

NCSU-CFL. Lateral load was applied at the pinned connection at the top of the pile specimen by means of a 100-kip, 70-inch stroke hydraulic actuator. The nominal wall thickness of the tube was 0.134 in., providing a nominal diameter-to-thickness ratio (D/t) of 95. The test was conducted with a 7-foot-8.25-inch cantilever length, measured from the soil surface to the point at which the lateral load was applied. Figure 10-209 and Figure 10-210 present a schematic of the test setup (elevation) and the specimen #11 cross-section, respectively, while Figure 10-211 shows the instrumentation used for testing. A photograph of the test setup is included in Figure 10-212.

As previously mentioned, there was a problem with the data acquisition system during the test. This issue resulted in loss of a portion of the experimental data, which included force, displacement, strain, and soil pressure data. As a consequence, this report was generated using manually recorded data (at the peaks of each displacement ductility level) in combination with data from slope indicator sensors, as well as with LED position data from the Optotrak system. It is believed that the loss of data was related to the use of a triggering mechanism that was implemented to synchronize the data from the data acquisition system with the data from the Optotrak system. Such mechanism consisted of sending an electrical signal from the Optotrak system to the data acquisition system. It is believed that this mechanism affected the data file, not allowing the data to be extracted after the test was completed. The mitigation plan for future tests is to avoid the use of triggering mechanisms to synchronize data systems.

Material properties were determined by in-house material tests. The yield and ultimate stresses of the steel tube were 54.3 ksi and 75.6 ksi, respectively, based on tests conducted on three (3) coupons cut from the end of the test pile specimen. The yield and ultimate stresses of the ASTM A706 Grade 60 longitudinal reinforcement were 72.8 ksi and 97.1 ksi, respectively, based on tests conducted on six (6) bar specimens from the same heat of the longitudinal reinforcement. The yield and ultimate stresses of the spiral reinforcement were 64.9 ksi and 96.9 ksi, respectively, based on tests conducted on six (6) bar specimens from the same heat of the transverse reinforcement. An average concrete compressive strength of 8.85 ksi (standard deviation of ± 0.17 ksi) was determined from three (3) compression tests of 4”x8” concrete cylinders.

Soil properties were also determined by in-house material tests. Based on a measured particle size distribution, the soil was classified as poorly-graded sand (SP). The unit weight and friction angle (γ = 90 pcf and ϕ = 35°, respectively) were reasonably assumed based upon results from previous tests.

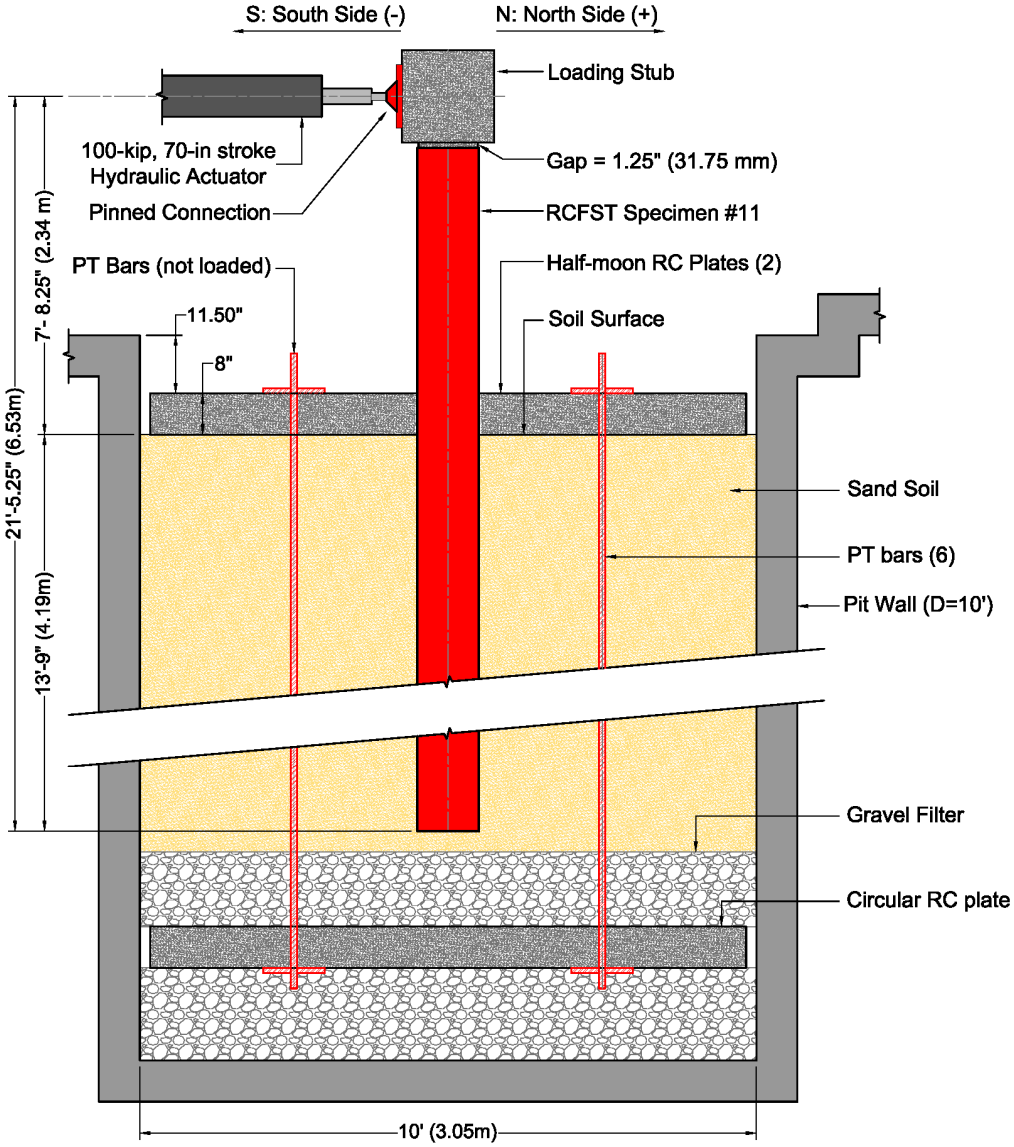

Figure 10-209 Test 11: test setup elevation schematic

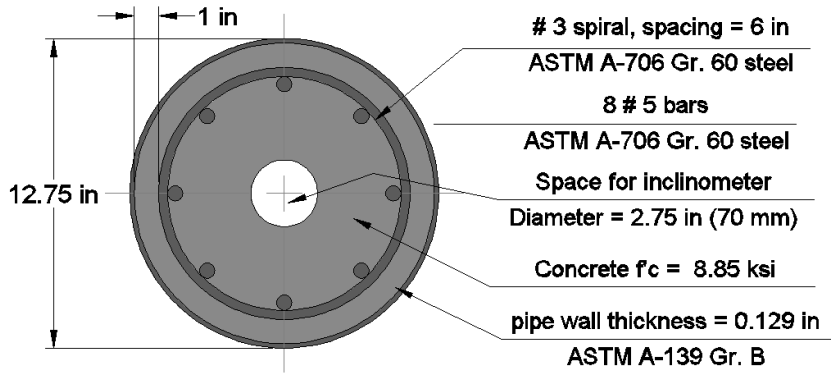

Figure 10-210 Test 11: RCFST specimen cross section

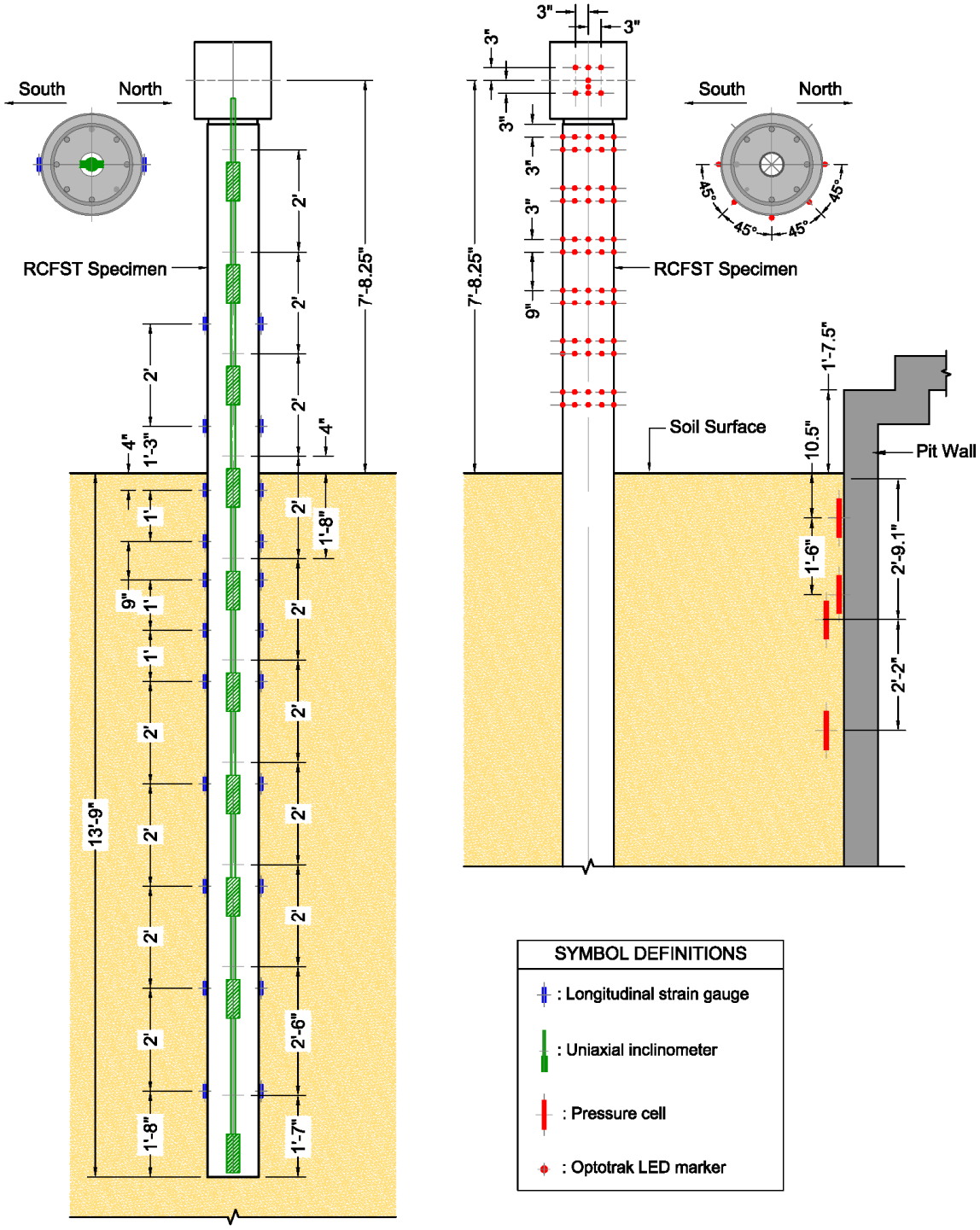

Figure 10-211 Test 11: instrumentation

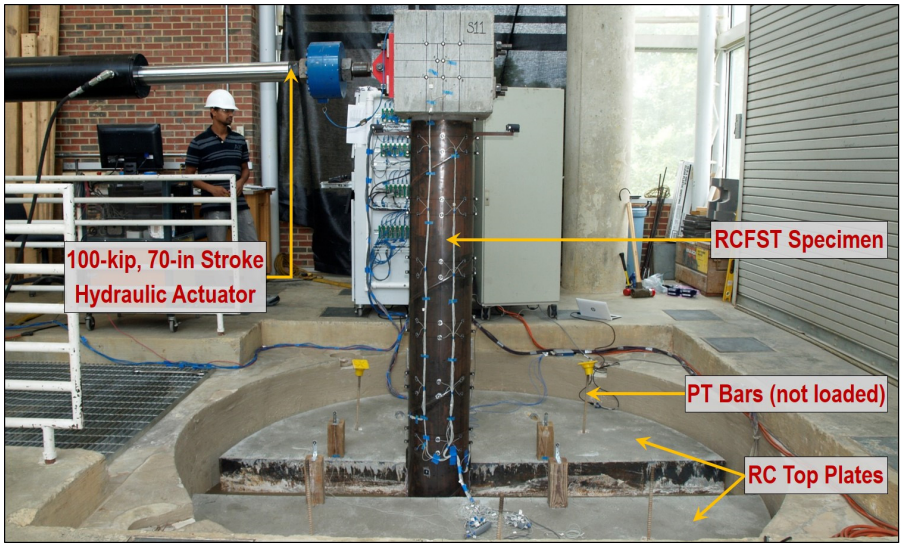

Figure 10-212 Test 11: pinned-head, RCFST pile-column test setup

The load history applied to the pile specimen consisted of standard single and three-cycle sets intended to evaluate both the elastic and inelastic response of the specimen. The first portion (i.e., pile elastic response up to first yield) of the test consisted of single reversed, displacement-controlled cycles, ramping up to the first yield displacement in ¼ increments. Given the non-linear response from the beginning of the test due to the characteristic soil behavior, target displacements in this portion of the test were determined based on the results of a monotonic pushover analysis performed using a detailed non-linear, fiber-based, finite element model developed using the OpenSees framework software. Soil-structure interaction was included by means of non-linear springs at 1-foot interval depths, with spring properties assigned based on p-y curves.

The first yield force (F_y) and nominal force (F_n), which is defined as the force at a concrete compressive strain of 0.004 or at a tube/bar tensile strain of 0.015 (whichever occurs first), were determined based upon tensile and compressive strains monitored during the numerical simulation (i.e., pushover analysis), as 10.40 kips and 16.97 kips, respectively. Table 10-11 summarizes the target displacements for the first portion of the test.

After the first portion of the test was completed, the measured average strain at the predicted first yield displacement (Δ'_y) was 1530 (με), which correlates well with the tube yield strain (ε_y = 1870 με). The average displacement at the first yield displacement (Δ'_y = 4.48 in) was modified by the nominal-to-first yield force ratio in order to determine the displacement ductility level 1.0 (μ_1 = 7.32 in), as shown in Equation 10-22. The remainder of the test was completed using reversed three-cycle sets in displacement-controlled increments at different levels of displacement ductility until failure, as shown in Equation 10-23. The entire displacement and load histories can be seen in Figure 10-213. Positive loads and displacements correspond to rightward (North) motion of the pile in the test setup. The positive legs of all cycles were completed before the negative legs.

Table 10-11 Test 11: predictions for elastic portion

Performance Level	Displacement (in)	Force (kips)
1/4 Δy'	1.04	2.90
1/2 Δy'	2.15	5.60
3/4 Δy'	3.34	8.21
1 Δy'	4.48	10.40

$$\Delta_y = \mu_1 = \Delta'_y \cdot \frac{F_n}{F_y} = 4.48 in \cdot \frac{16.97\, kip}{10.40\, kip} = 7.32\ in \qquad \text{Equation 10-22}$$

$$\mu_i = i \cdot \mu_1 \rightarrow i = 1.0,\ 1.5,\ 2.0,\ 3.0,\ 4.0 \qquad \text{Equation 10-23}$$

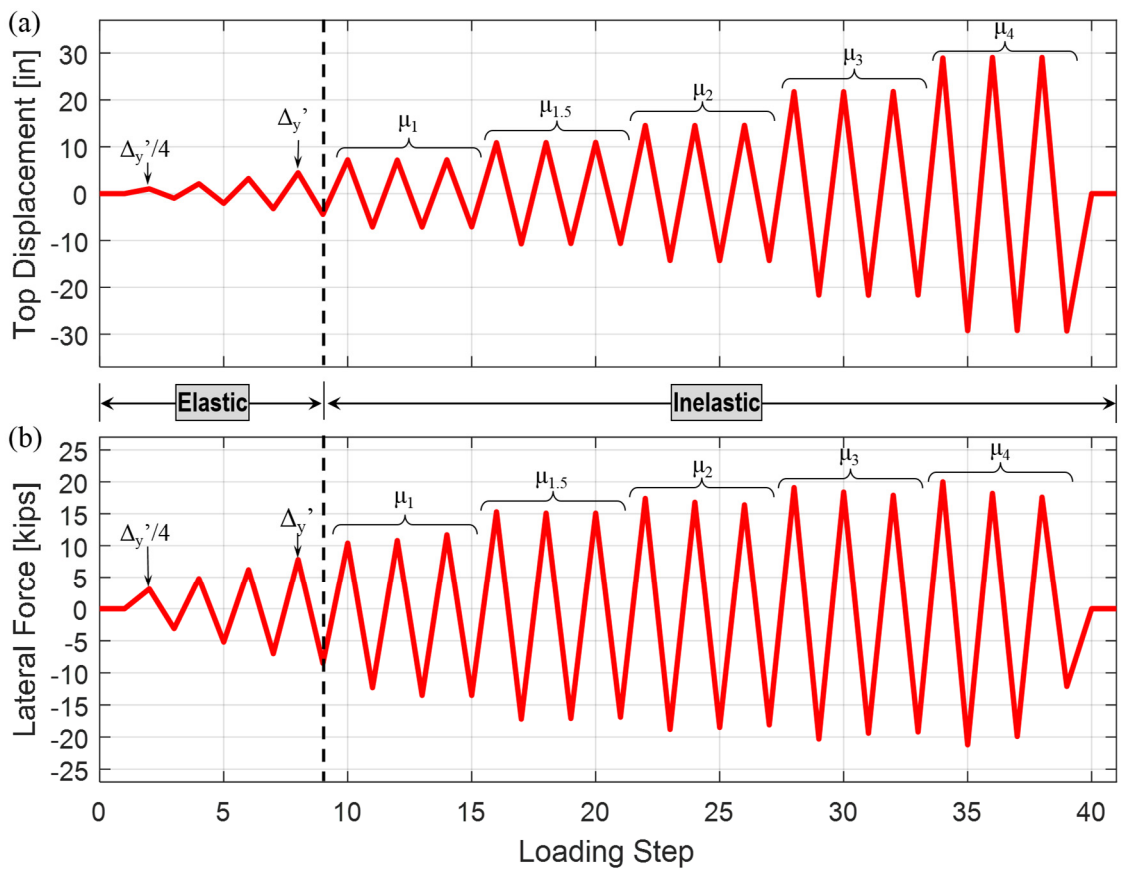

Figure 10-213 Test 11: (a) displacement and (b) loading histories

Specimen Response

Specimen #11 performed well through the elastic portion of the test and during all three cycles of ductility level 3.0 (μ_3). It is believed that the onset of tube buckling occurred early during the displacement cycles at ductility level 2.0 (μ_2) as minor loss of strength was observed at the second and third cycles at that displacement level. A significant loss of strength, indicating failure, occurred during the third pull cycle at ductility level 4.0 (μ_4). Figure 10-214 presents the lateral force vs. top displacement envelopes. It can be seen that a significant loss of strength (~43%) occurred during the third pull cycle at ductility level 4.0 (μ_4).

Figure 10-215 presents the deformed shape and the soil-pile gaps at zero displacement after the elastic portion of the test was conducted; the size of the gap was ~1.25 in. on both sides of the specimen. As it was previously explained, at this point of the test strain profiles on the sides of the pile were verified in order to further conduct the test at the aforementioned ductility levels. Tensile strains of 1570 ($\mu\varepsilon$) and 1480 ($\mu\varepsilon$) were observed in the tube during the push and pull cycles, respectively, when the predicted first yield displacement was imposed to the system. Based on the rotation data recorded with the inclinometer placed inside the pile along its length, specimen curvature, rotation, and displacement profiles are presented in Figure 10-216 and Figure 10-217 for the elastic push and pull cycles, respectively. Note that there are small rotations and displacements at the pile tip which indicates that there is a point of rotation (at ~9 ft.) rather than a point of fixity; inelastic action was developed in the pile nonetheless. In Figure 10-216 and Figure 10-217, the symbol $Ø_y$' represents the first yield curvature, and a depth equal to 0 ft. represents the soil surface. The circles plotted above the soil surface correspond to the position of Optotrak LEDs; note that they are in agreement with the displacement profiles calculated using data from the inclinometers.

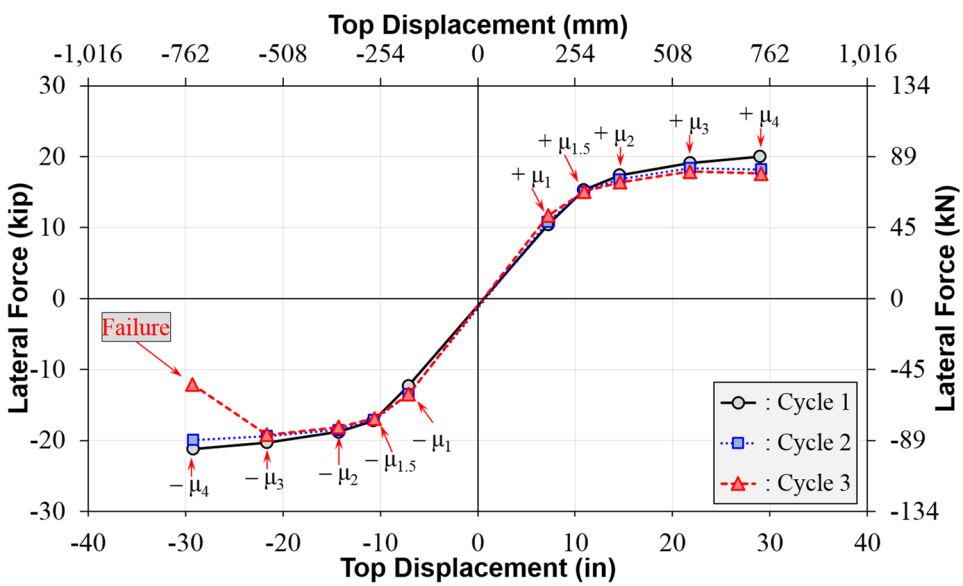

Figure 10-214 Test 11: lateral force vs. top displacement envelopes

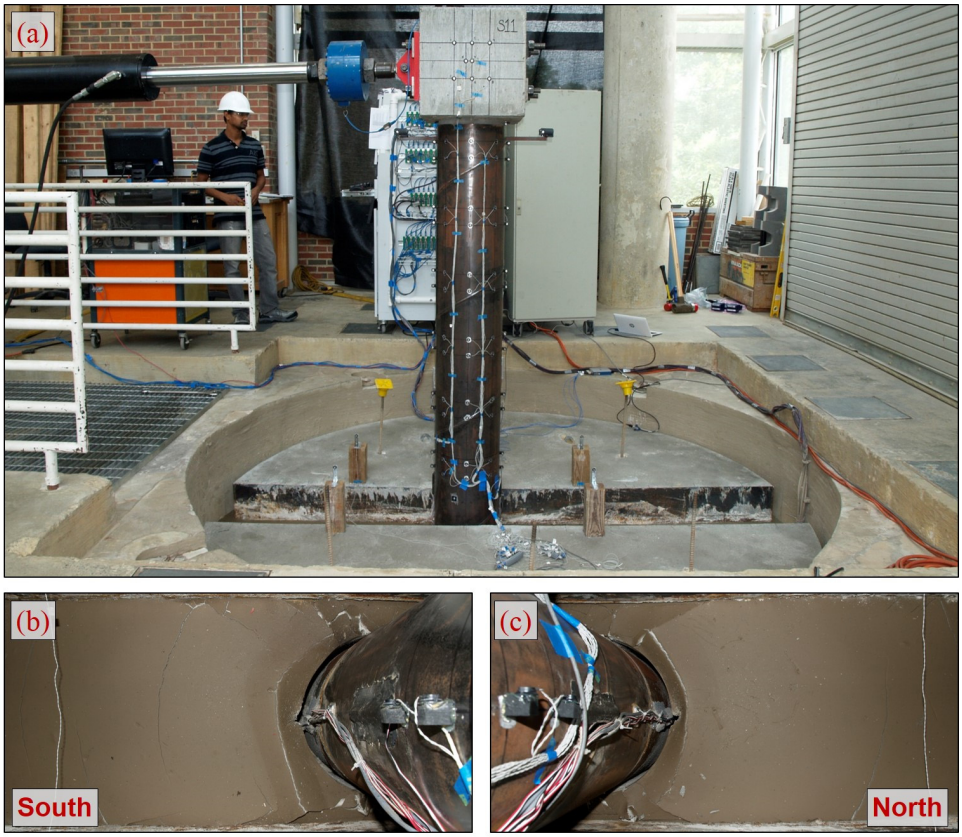

Figure 10-215 Test specimen #11 after elastic portion of the test was completed: (a) deformed shape, (b) South side and (c) North side

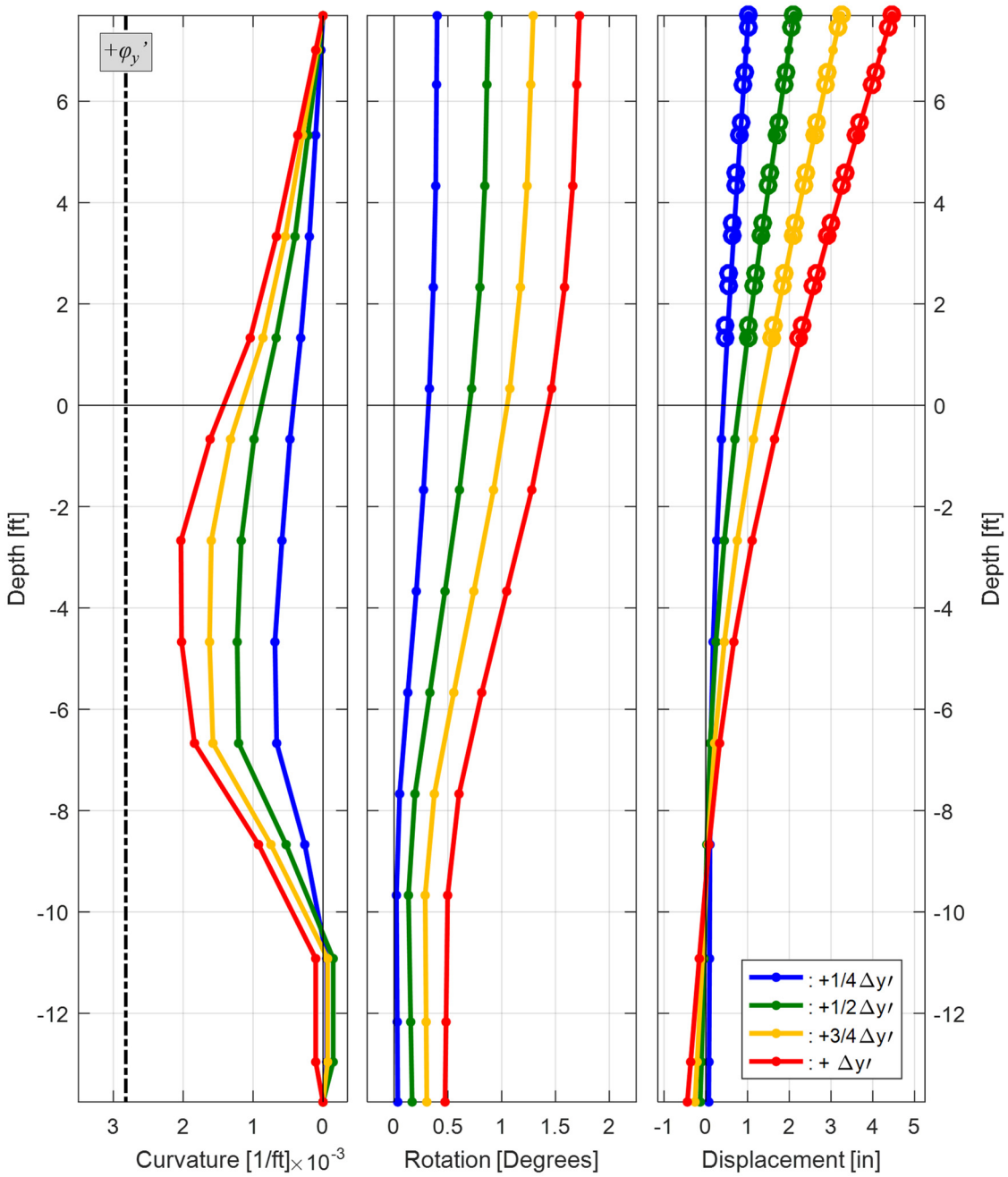

Figure 10-216 Test 11: curvature, rotation, and displacement profiles (elastic push cycles)

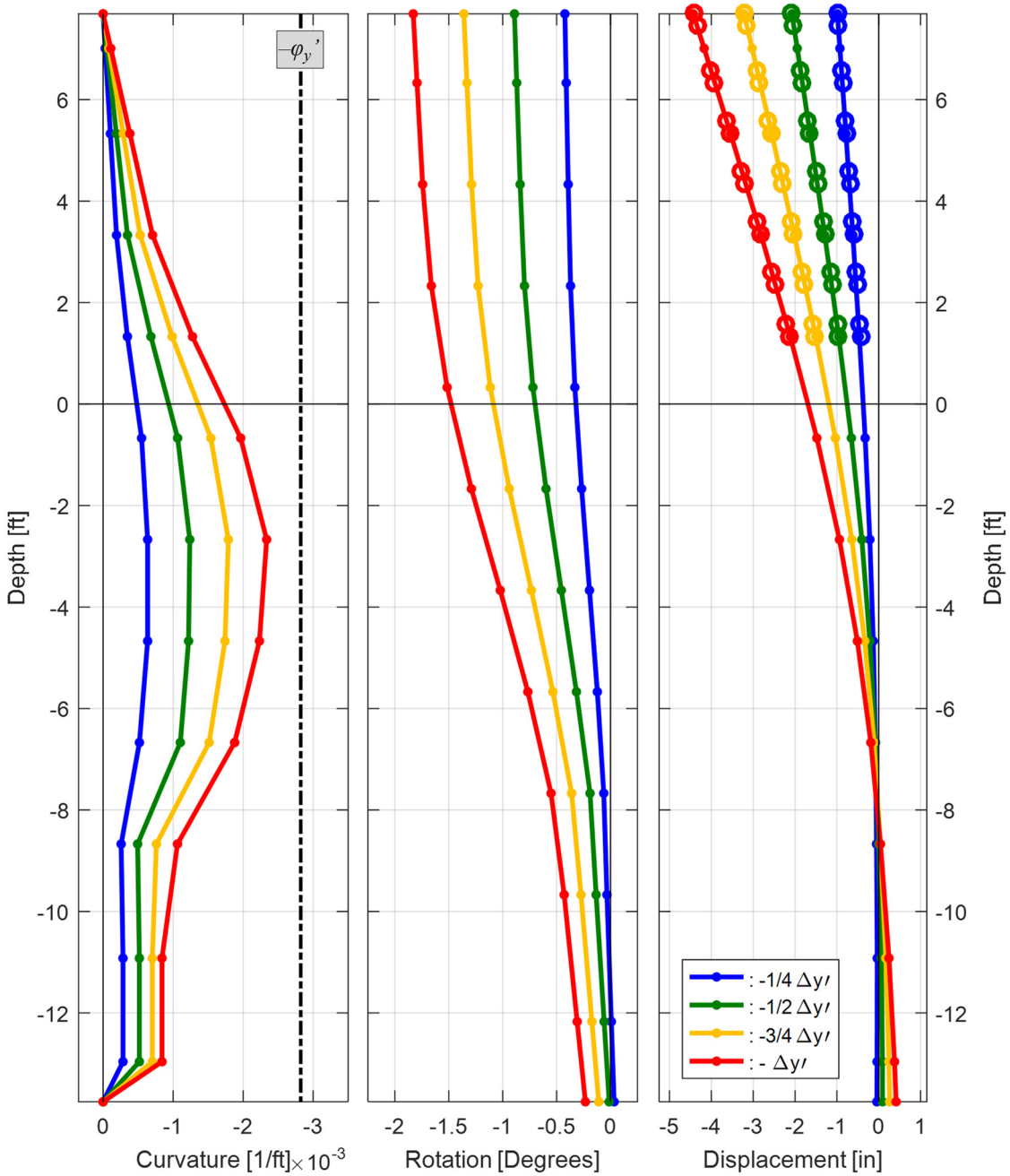

Figure 10-217 Test 11: curvature, rotation, and displacement profiles (elastic pull cycles)

As the test continued, the gap on the sides of the pile increased in size as the displacement ductility level increased. Minor loss of strength was observed up until all ductility level 3.0 (μ_3) cycles. The specimen failure (Figure 10-218) occurred at the third cycle load at ductility 4.0 (μ_4) when a significant drop in the force of the actuator was observed (i.e., ~43%). Sounds indicating steel fracture were heard at the same time when the strength loss occurred, indicating probable tube/bar fracture. Moreover, twist rotation of the pile occurred for all push cycles at ductility level 4 (μ_4). Finally, the test was terminated and the specimen was taken to zero displacement in order to facilitate its extraction from the soil.

Figure 10-219 and Figure 10-220 present the curvature, rotation, and displacement profiles for the inelastic push and pull cycles of the test, respectively. Note that the largest changes in rotation (i.e., curvature) occurred at a depth between 0.5 ft. and 5.0 ft., which correlates well with the observed damage zone.

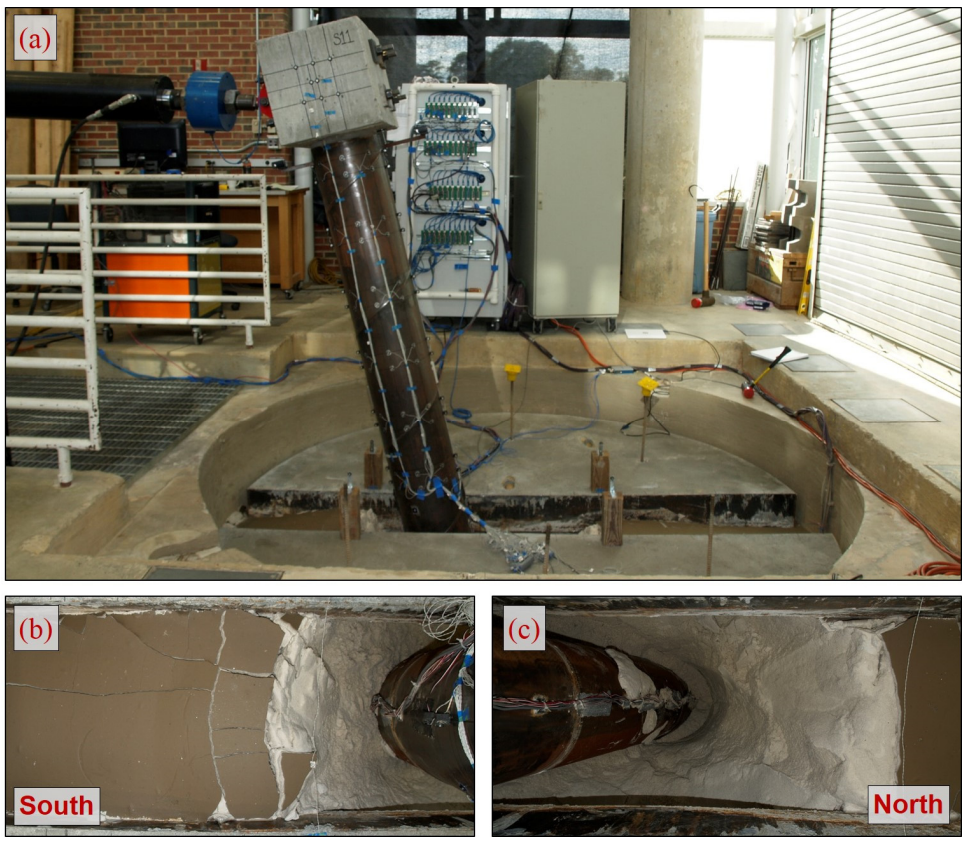

Figure 10-218 Test specimen #11 at maximum displacement: (a) deformed shape, (b) South side and (c) North side

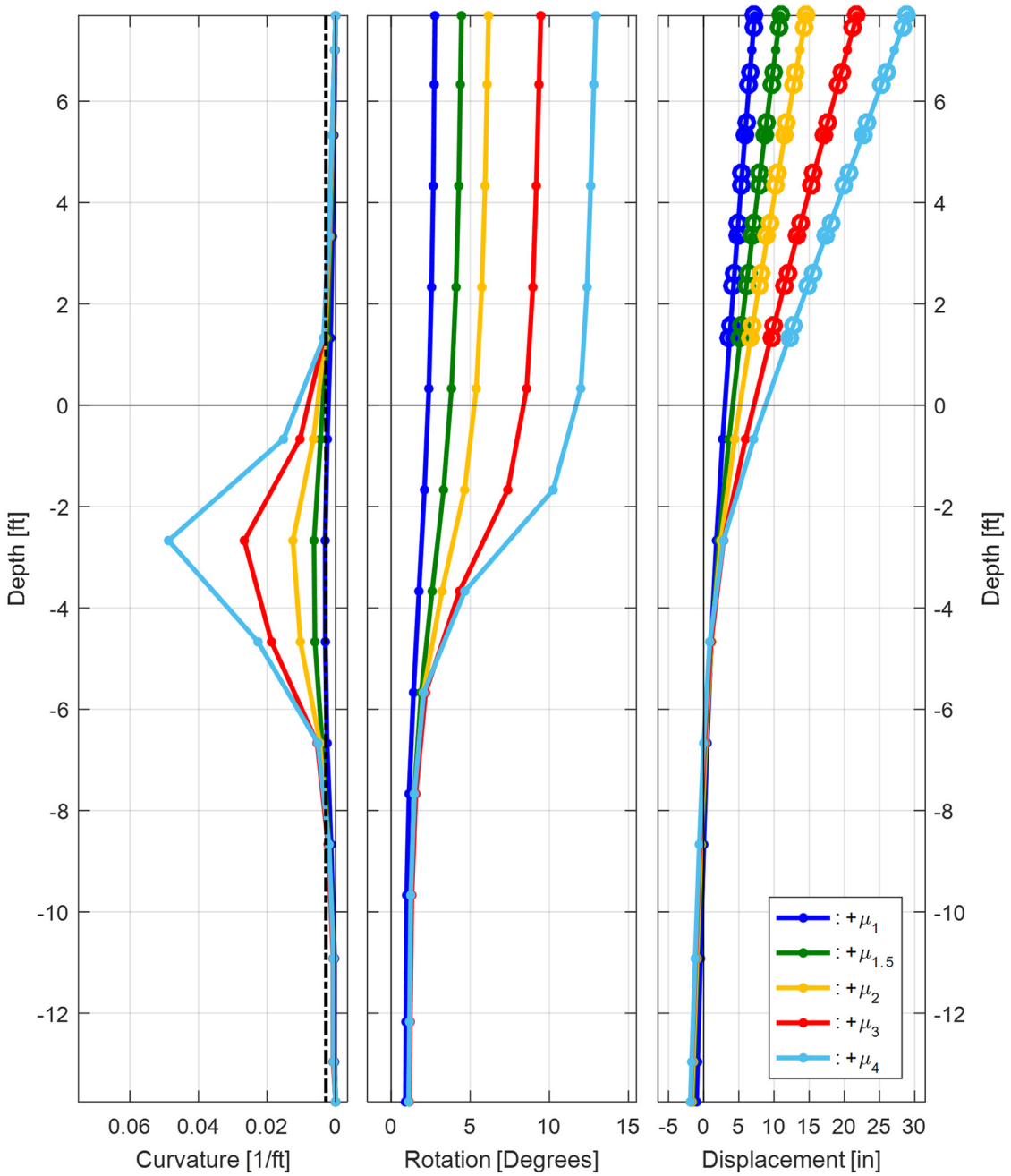

Figure 10-219 Test 11: curvature, rotation, and displacement profiles (inelastic push cycles)

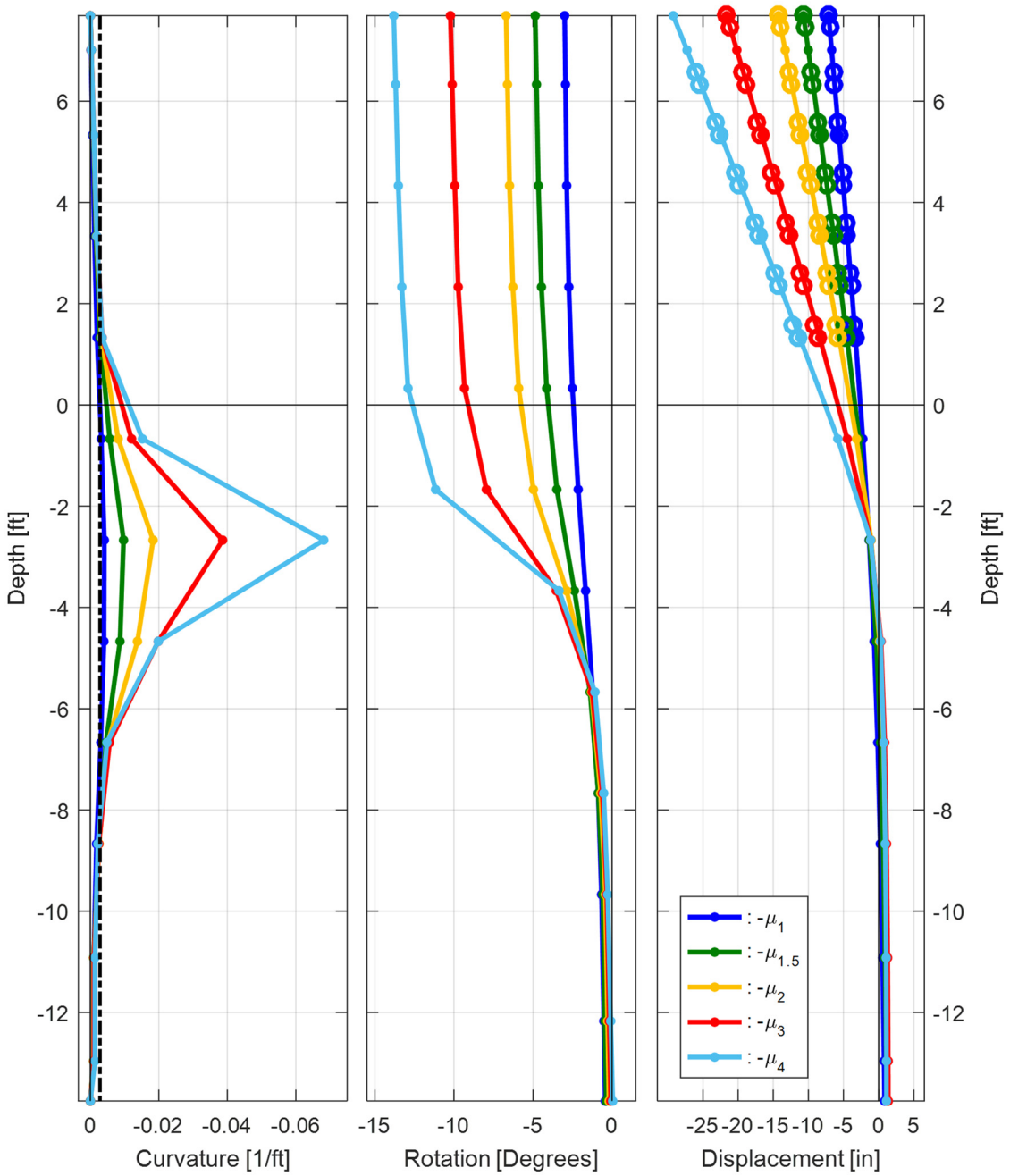

Figure 10-220 Test 11: curvature, rotation, and displacement profiles (inelastic pull cycles)

Figure 10-221 shows the state of the soil surface after the test was completed. Notice that despite the presence of the half-moon RC plates in the surface, deformations in the soil followed an expected oval-shaped failure surface in which active and passive pressures developed around the pile. This surface extended ~22.5 in. on both sides of the direction of loading and ~16.5 in. on the perpendicular direction. The total average settlement of the RC plates during the test was ~2.21 in. This value was averaged based on the vertical displacement of 4 points on the RC plates. Figure 10-222 shows the average settlement of the half-moon RC plates during the test as a function of the imposed displacements at the top of the pile. Note that, as the displacement history is applied, the settlement increases, though its magnitude is larger at the beginning of the test.

Figure 10-221 Test 11: soil surface after testing

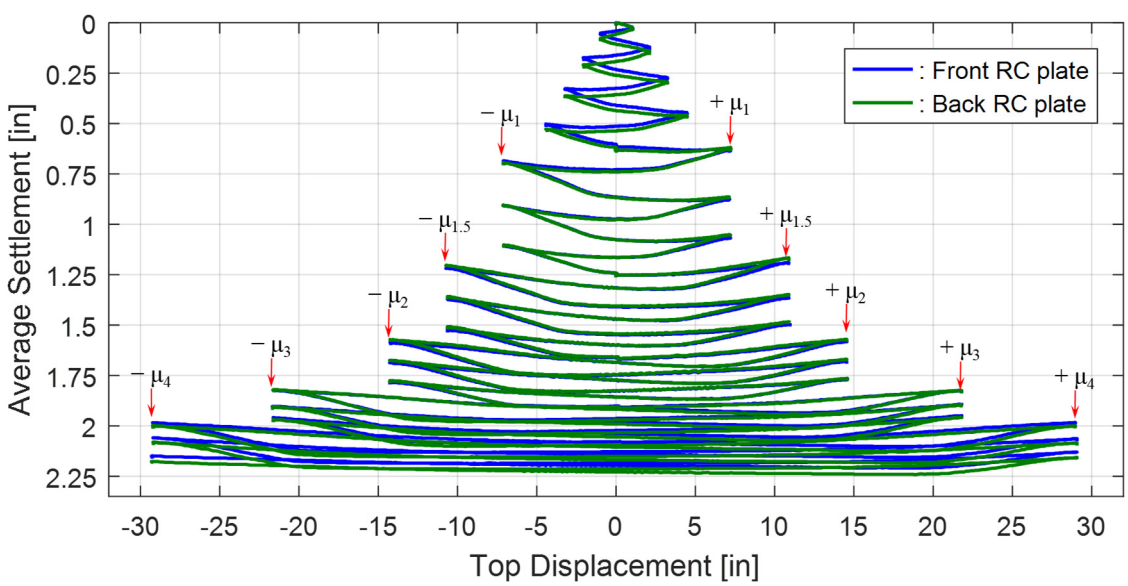

Figure 10-222 Test 11: half-moon RC plate settlement during testing

Figure 10-223 through Figure 10-226 present the damage observed after the pile was extracted from the soil. As thought during the test, tube fracture and tube buckling did occur as did bar buckling; bar fracture was not observed. It can be seen that two main buckled sections developed on both sides of the specimen. The sections with the largest buckling occurred at a depth of 2ft. – 5.5 in. and 3ft. – 6 in. on the South side and 2 ft. – 2.0 in. and 3 ft. – 3 in. on the North side of the specimen, which implies that the plastic hinge developed at an average depth of 2 ft. – 10.12 in. with respect to the soil surface. Several ripples were observed on both South and North sides of the specimen above the plastic hinge region and close to the soil surface.

Tube fracture (Figure 10-223) occurred on the North side of the specimen and it extended about half of the cross-section perimeter, resulting in a significant drop in strength due to lost tension capacity. As a consequence, after rupture, tension capacity is provided by the longitudinal reinforcement, which has a smaller area in comparison with that provided by the tube, inducing high stresses and deformations. Upon further investigations, bar fracture was not observed neither on the South nor on the North sides of the specimen; however, bar buckling was observed on the North side. Deformations due to tube buckling protruded ~½ in. on both North and South sides of the pile. Figure 10-224 presents measurements of the buckled regions.

In order to further investigate the significant strength loss, and to verify whether bar fracture or bar buckling occurred, a portion of the tube (i.e., 10 in. x 12 in.) was removed on both North and South sides of the specimen, in the extreme fibers at the ruptured and buckled sections, as shown in Figure 10-225 and Figure 10-226, respectively. It can be noticed severe cracking and crushing of the concrete in the critical section of the plastic hinge, perpendicular to the direction of the specimen. Cracks in the concrete extended further to the center of the section. Bar fracture was not observed on either side. Note that in the North side of the specimen, the position of the spiral did not prevent occurrence of bar buckling at the main buckled section, as shown in Figure 10-225(b).

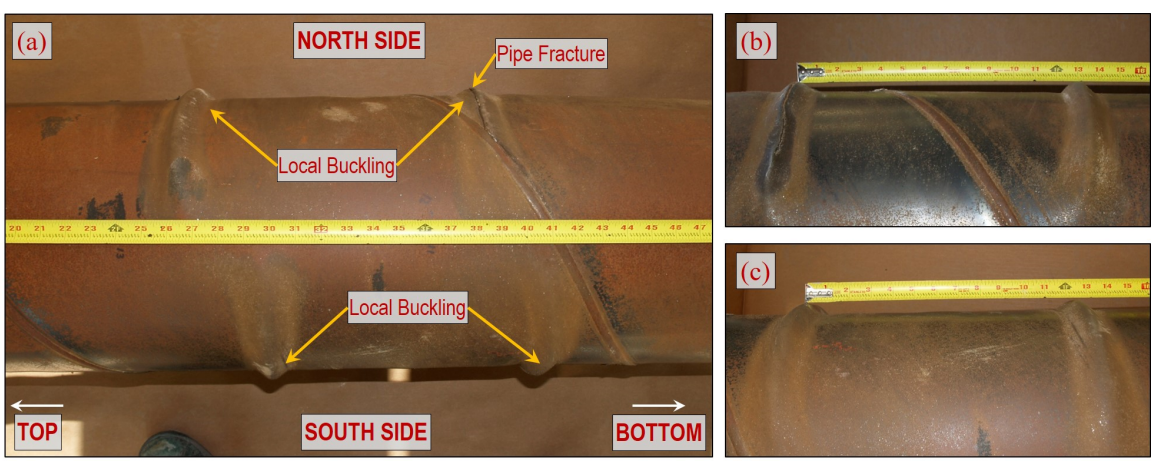

Figure 10-223 Test 11: (a) Final observed damage, (b) tube fracture, and (c) tube local buckling

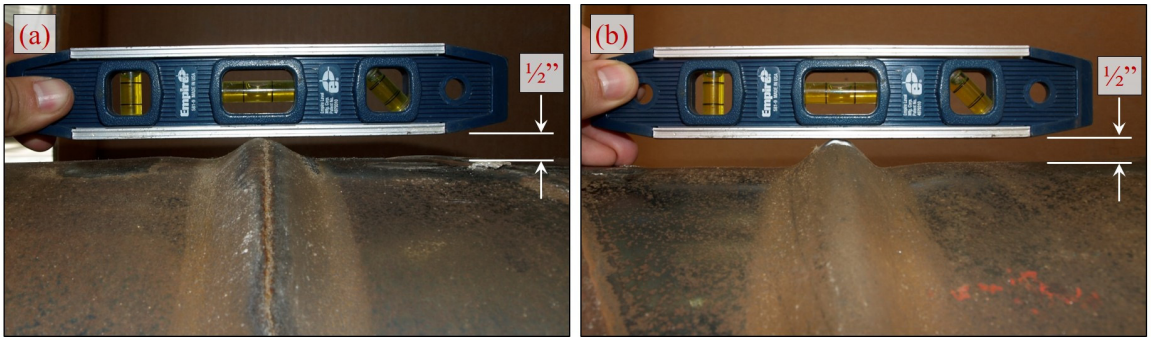

Figure 10-224 Test 11: primary buckled sections on (a) North side and (b) South side

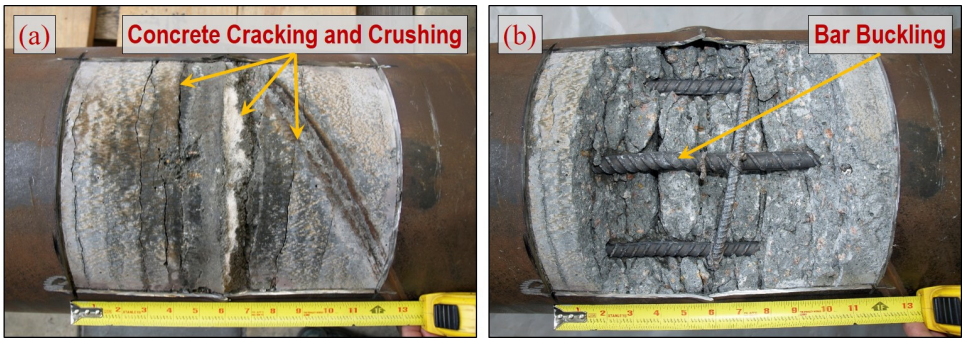

Figure 10-225 Test 11: observed damage in (a) concrete and (b) internal reinforcement on North side

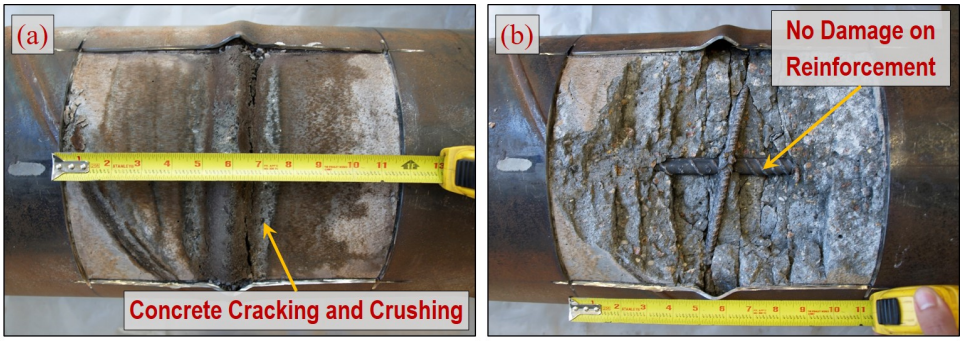

Figure 10-226 Test 11: observed damage in (a) concrete and (b) internal reinforcement on South side

Conclusions

Test specimen #11 showed a reliable response through all ductility 3.0 (μ_3) cycles. It is believed that onset of tube local buckling occurred at ductility level 2.0 (μ_2) as subtle strength loss was observed. The test specimen completed all cycles of ductility 3.0 (μ_3) without significant loss of strength. Failure of the specimen occurred during the third pull cycle at ductility level 4.0 (μ_4) when a significant drop in the strength was observed. Further investigations revealed that failure occurred due to a combination of tube local buckling, tube fracture, and bar buckling. It is believed that this particular specimen is capable of having a reliable displacement capacity up to ductility 3.0 (μ_3). The main buckles as well as tube fracture did not occur over the spiral weld, so the pipe spiral welds do not appear to negatively influence the behavior.

Test 12 Summary Report

October 26, 2016

Prepared for

Alaska Department of Transportation

Alaska University Transportation Center

Project Team

RA: Diego Aguirre

PIs: Mervyn Kowalsky, James Nau, Mo Gabr

Other Senior Personnel: Greg Lucier, Ben Smith

North Carolina State University

Executive Summary

Test 12 was conducted September 22nd, 2016 at the North Carolina State University Constructed Facilities Laboratory. The tested pile-column specimen was a reinforced concrete filled steel tube with a diameter-to-thickness (D/t) ratio of 68. No surcharge was applied to the soil, thus the soil stiffness was not modified. The above-ground height (column length) was increased by 2 ft. when compared to previous tests using the same D/t ratio. The test was successfully conducted to failure, which was caused by a combination of tube local buckling, tube fracture, bar buckling, and bar fracture, resulting in a large strength degradation (~57.9%) in the second pull cycle at ductility level 4.0 (μ_4). Due to setup constrains, displacements in the push direction only reached a maximum displacement ductility level 3.5 ($\mu_{3.5}$) for all push cycles corresponding to displacement ductility level 4.0 (μ_4).

Specimen and Test Description

Test 12 consisted of a 21-foot-5.25-inch long, reinforced concrete filled, 12-3/4-inch diameter spirally welded steel tube without skelp or splice welds. The pile-column specimen was embedded 13 ft. – 9 in. into clean sand in the soil-structure interaction facility at the NCSU-CFL. Lateral load was applied at the pinned connection at the top of the pile specimen by means of a 100-kip, 70-inch stroke hydraulic actuator. The nominal wall

thickness of the tube was 0.187 in., providing a nominal diameter-to-thickness ratio (D/t) of 68. The test was conducted with a 7-foot-8.25-inch cantilever length, measured from the soil surface to the point at which the lateral load was applied. Figure 10-227 and Figure 10-228 present a schematic of the test setup (elevation) and the specimen #12 cross-section, respectively, while Figure 10-229 shows the instrumentation used for testing. A photograph of the test setup is included in Figure 10-230.

Material properties were determined by in-house material tests. The yield and ultimate stresses of the steel tube were 55.6 ksi and 74.7 ksi, respectively, based on tests conducted on three (3) coupons cut from the end of the test pile specimen. The yield and ultimate stresses of the ASTM A706 Grade 60 longitudinal reinforcement were 72.8 ksi and 97.1 ksi, respectively, based on tests conducted on six (6) bar specimens from the same heat of the longitudinal reinforcement. The yield and ultimate stresses of the spiral reinforcement were 64.9 ksi and 96.9 ksi, respectively, based on tests conducted on six (6) bar specimens from the same heat of the transverse reinforcement. An average concrete compressive strength of 9.33 ksi (standard deviation of ± 0.28 ksi) was determined from three (3) compression tests of 4”x8” concrete cylinders.

Soil properties were also determined by in-house material tests. Based on a measured particle size distribution, the soil was classified as poorly-graded sand (SP). The unit weight and friction angle (γ = 90 pcf and ϕ = 35°, respectively) were reasonably assumed based upon results from previous tests.

The load history applied to the pile specimen consisted of standard single and three-cycle sets intended to evaluate both the elastic and inelastic response of the specimen. The first portion (i.e., pile elastic response up to first yield) of the test consisted of single reversed, displacement-controlled cycles, ramping up to the first yield displacement in ¼ increments. Given the non-linear response from the beginning of the test due to the characteristic soil behavior, target displacements in this portion of the test were determined based on the results of a monotonic pushover analysis performed using a detailed non-linear, fiber-based, finite element model developed using the OpenSees framework software. Soil-structure interaction was included by means of non-linear springs at 1-foot interval depths, with spring properties assigned based on p-y curves.

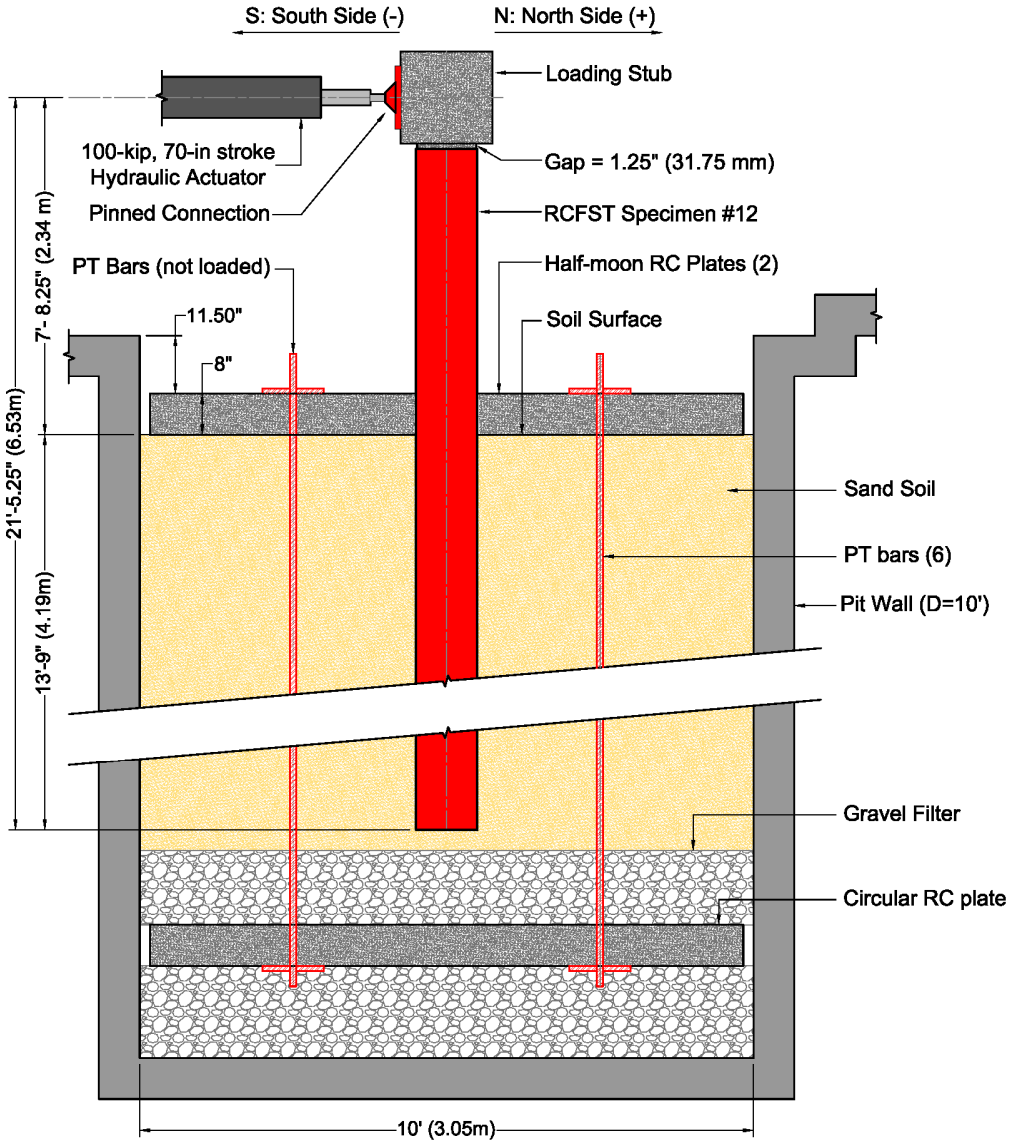

Figure 10-227 Test 12: test setup elevation schematic

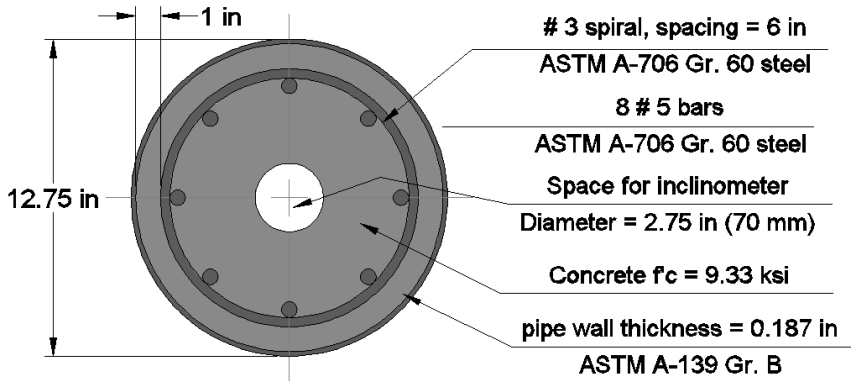

Figure 10-228 Test 12: RCFST specimen cross section

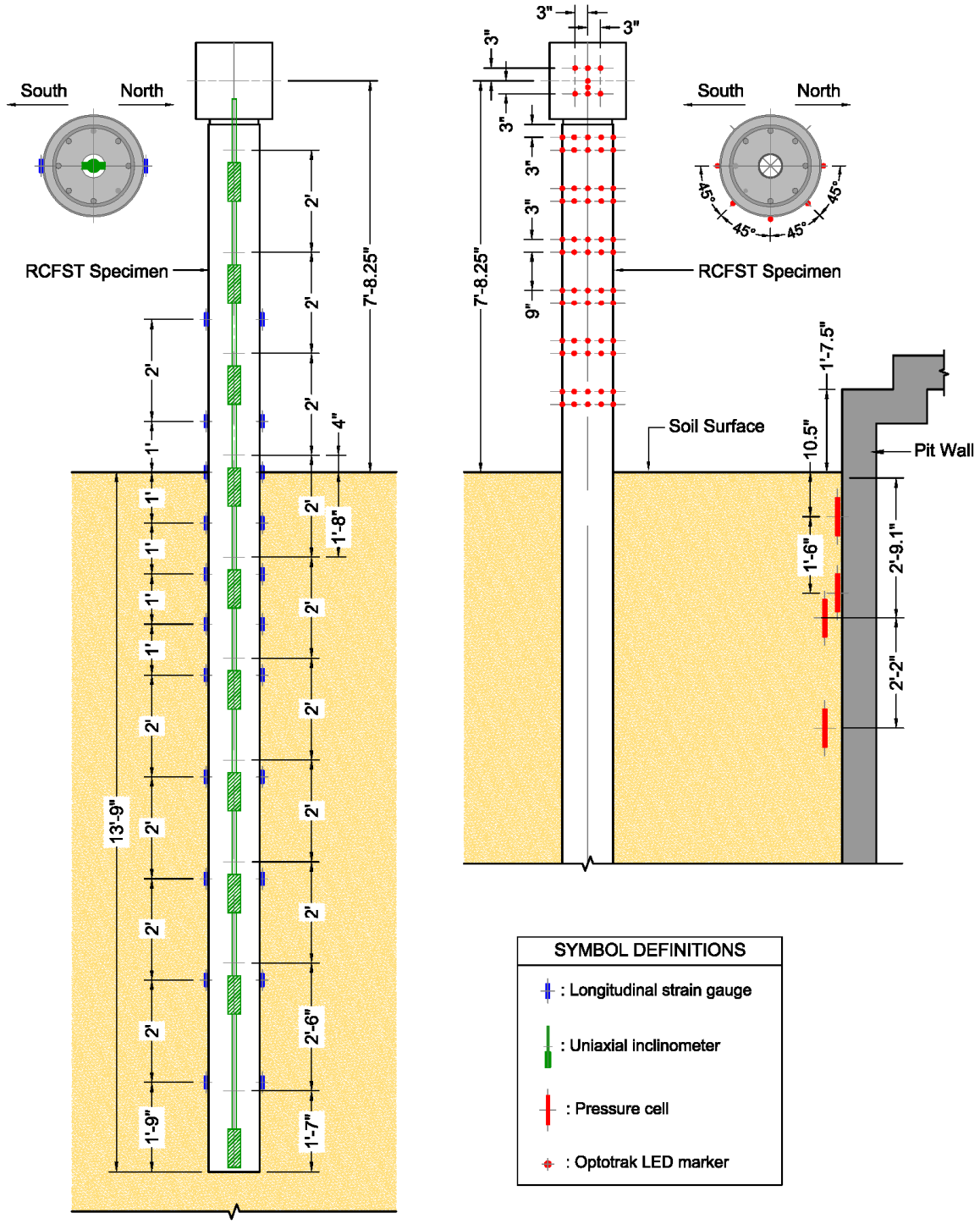

Figure 10-229 Test 12: instrumentation

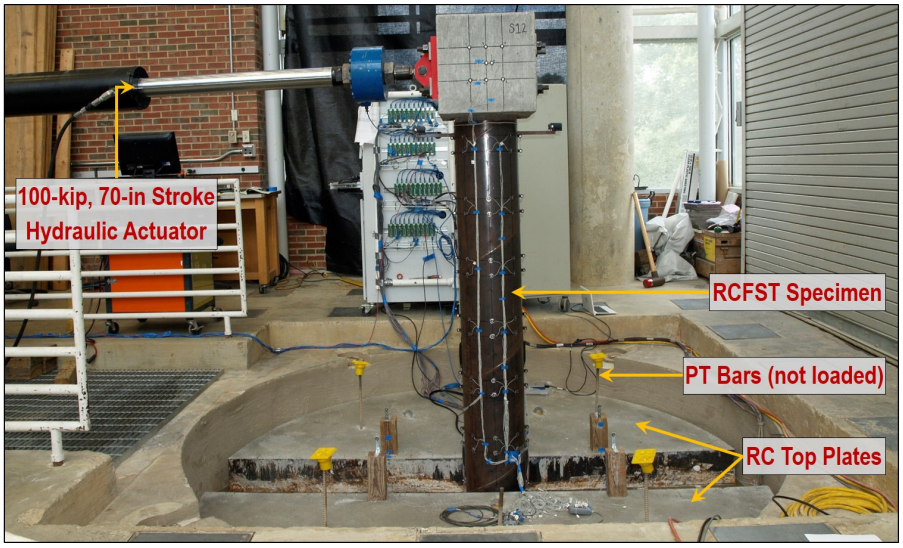

Figure 10-230 Test 12: pinned-head, RCFST pile-column test setup

The first yield force (F_y) and nominal force (F_n), which is defined as the force at a concrete compressive strain of 0.004 or at a tube/bar tensile strain of 0.015 (whichever occurs first), were determined based upon tensile and compressive strains monitored during the numerical simulation (i.e., pushover analysis), as 13.41 kips and 20.65 kips, respectively. Table 10-12 summarizes the target displacements for the first portion of the test.

After the first portion of the test was completed, the measured average strain at the predicted first yield displacement (Δ'_y) was 1320 (με); the tube yield strain was ε_y = 1920 με. The average displacement at the first yield displacement (Δ'_y = 5.26 in) was modified by the nominal-to-first yield force ratio in order to determine the displacement ductility level 1.0 (μ_1 = 8.10 in), as shown in Equation 10-24. The remainder of the test was completed using reversed three-cycle sets in displacement-controlled increments at different levels of displacement ductility until failure, as shown in Equation 10-25. The entire displacement and load histories can be seen in Figure 10-231. Positive loads and displacements correspond to rightward (North) motion of the pile in the test setup. The positive legs of all cycles were completed before the negative legs.

Table 10-12 Test 12: predictions for elastic portion

Performance Level	Displacement (in)	Force (kips)
1/4 Δy'	1.21	3.81
1/2 Δy'	2.52	7.34
3/4 Δy'	3.93	10.69
1 Δy'	5.26	13.41

$$\Delta_y = \mu_1 = \Delta'_y \cdot \frac{F_n}{F_y} = 5.26\,in \cdot \frac{20.6\,kip}{13.4\,kip} = 8.10\ in \qquad \text{Equation 10-24}$$

$$\mu_i = i \cdot \mu_1 \rightarrow i = 1.0,\ 1.5,\ 2.0,\ 3.0,\ 4.0 \qquad \text{Equation 10-25}$$

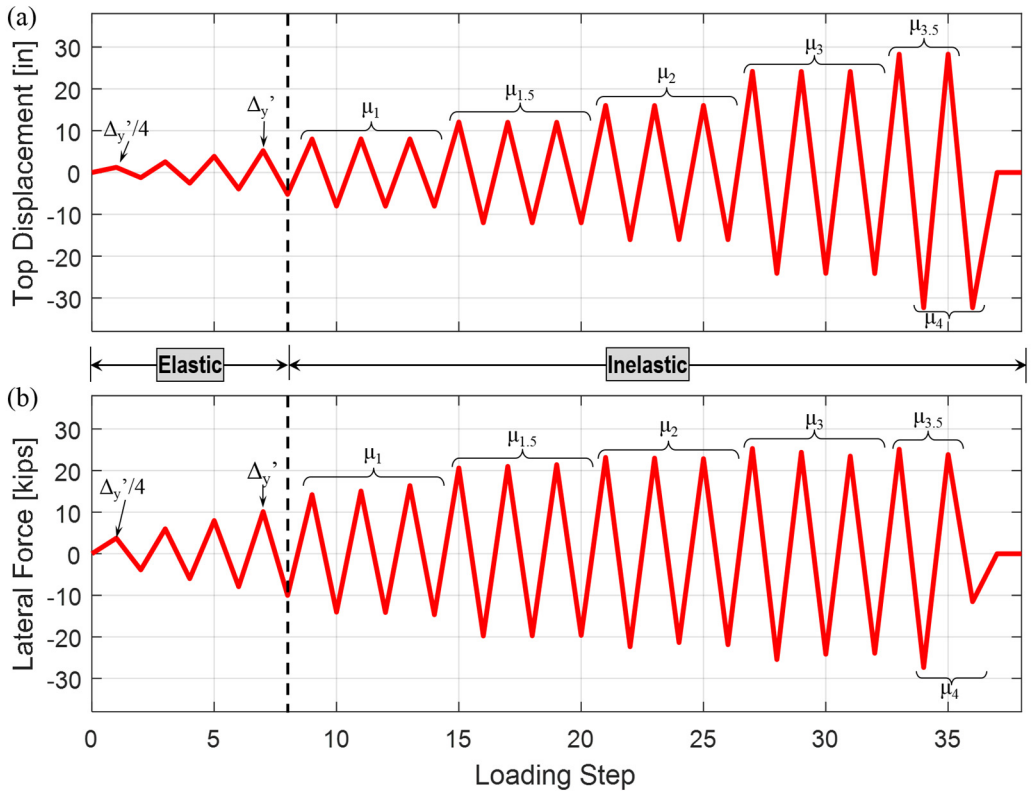

Figure 10-231 Test 12: (a) displacement and (b) loading histories

Specimen Response

Specimen #12 performed well through the elastic portion of the test and during all three cycles of ductility level 3.0 (μ_3). It is believed that the onset of tube local buckling occurred early during the displacement cycles at ductility level 2.0 (μ_2) as large tensile strains in combination with minor loss of strength were observed at the second and third cycles at that displacement level. A significant loss of strength, indicating failure, occurred during the second pull cycle at ductility level 4.0 (μ_4). Figure 10-232 and Figure 10-233 present the lateral force vs. top displacement response and envelopes, respectively. It can be seen that the system has a characteristic large energy dissipation capacity due to both damping sources, that is, the pile itself and the surrounding soil. In addition, it can be clearly seen from both figures that a significant loss of strength (~58%) occurred during the second pull cycle of ductility level 4.0 (μ4). Also, note from both Figure 10-232 and Figure 10-233 that, due to setup constrains, displacements in the push direction only reached a maximum displacement of 28.4 in. ($\mu_{3.5}$) for all push cycles corresponding to displacement ductility 4.0 (μ_4).

Figure 10-234 presents the deformed shape and the soil-pile gaps at zero displacement after the elastic portion of the test was conducted; the size of the gap was ~1.50 in. on both sides of the specimen. As it was previously explained, at this point of the test strain profiles on the sides of the pile were verified in order to further conduct the test at the aforementioned ductility levels. Figure 10-235 presents the strain profiles recorded during the elastic portion of the test. Notice that tensile strains of 1350 ($\mu\varepsilon$) and 1280 ($\mu\varepsilon$) were recorded in the tube

during the push and pull cycles, respectively, when the predicted first yield displacement was imposed to the system. Based on the rotation data recorded with the inclinometer, placed inside the pile along its length, specimen curvature, rotation, and displacement profiles are presented in Figure 10-236 and Figure 10-237 for the elastic push and pull cycles, respectively. Note that there are small rotations and displacements at the pile tip which indicates that there is a point of rotation (at ~9 ft.) rather than a point of fixity; inelastic action was developed in the pile nonetheless. In Figure 10-235 through Figure 10-237 the symbols N and S in the legends refer to the North and South sides, Δ_y' is the first yield displacement, $Ø_y'$ is the first yield displacement, and a depth equal to 0 ft. represents the soil surface. In the displacement profiles presented in Figure 10-236 and Figure 10-237, the circles plotted above the soil surface correspond to the position of Optotrak LEDs, note that they are in agreement with the profiles calculated using data from the inclinometers.

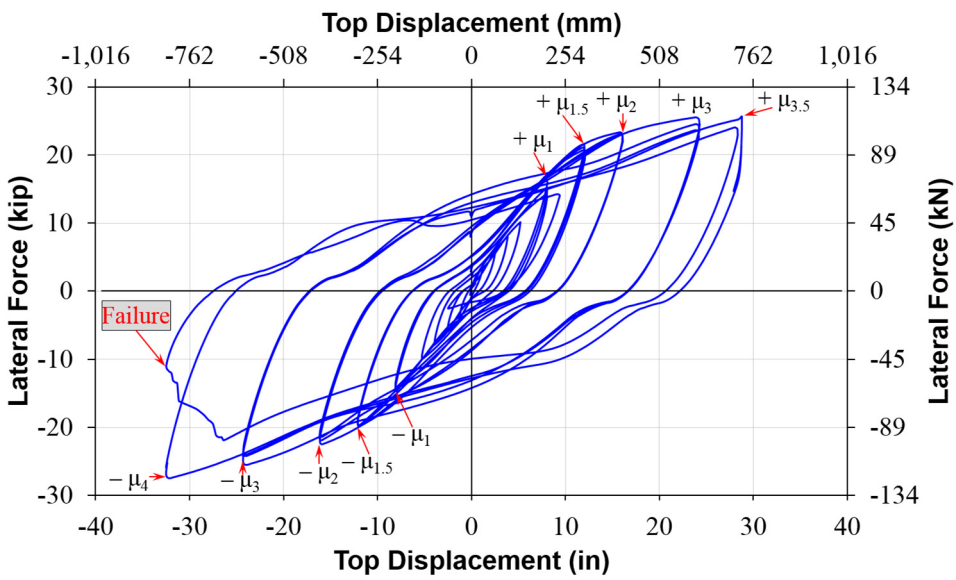

Figure 10-232 Test 12: lateral force vs. top displacement response

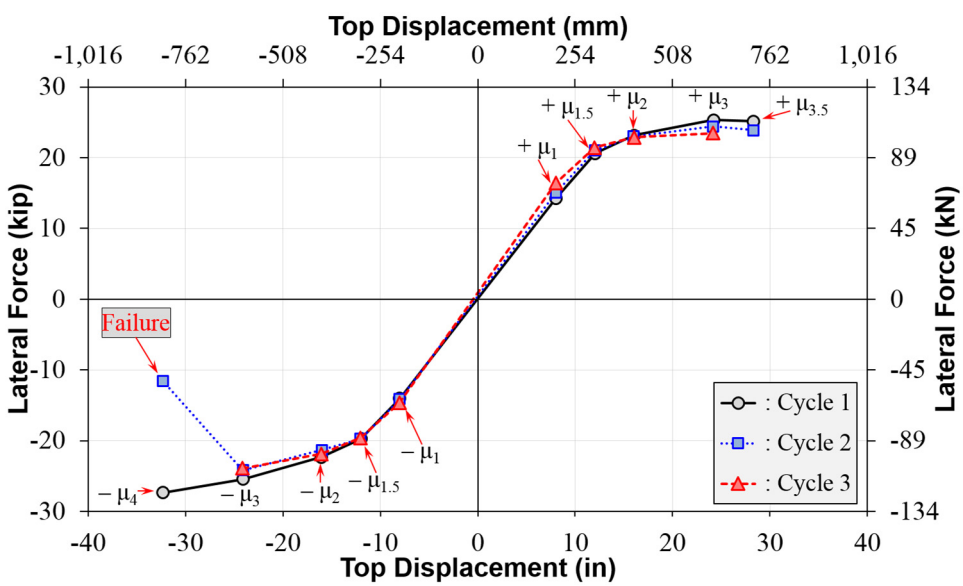

Figure 10-233 Test 12: lateral force vs. top displacement envelopes

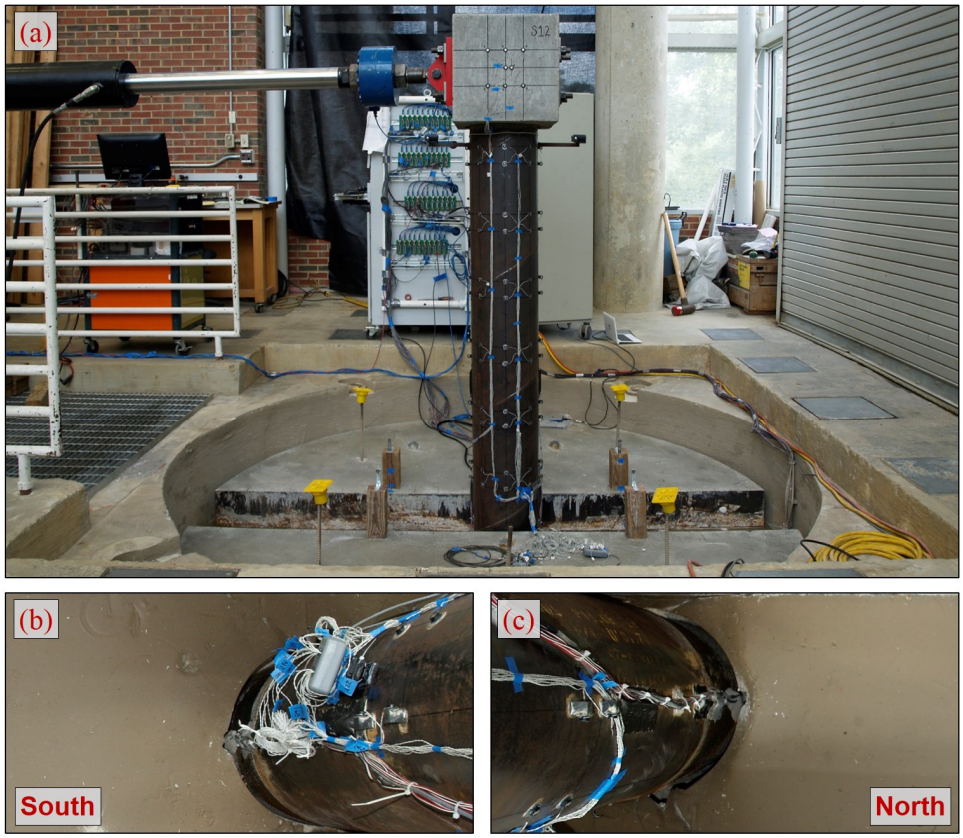

Figure 10-234 Test specimen #12 after elastic portion of the test was completed: (a) deformed shape, (b) South side and (c) North side

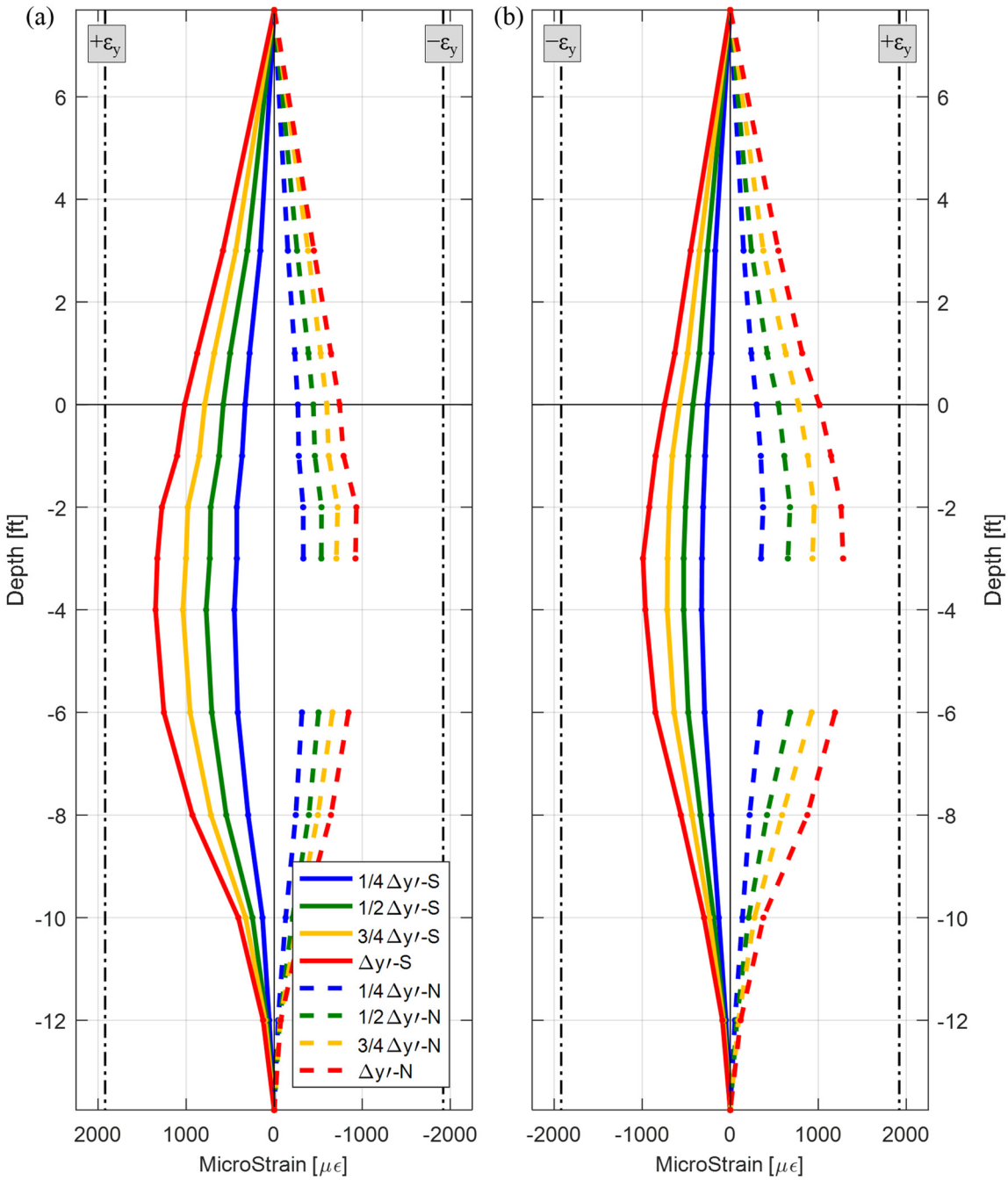

Figure 10-235 Test 12: strain profiles from elastic (a) push and (b) pull cycles

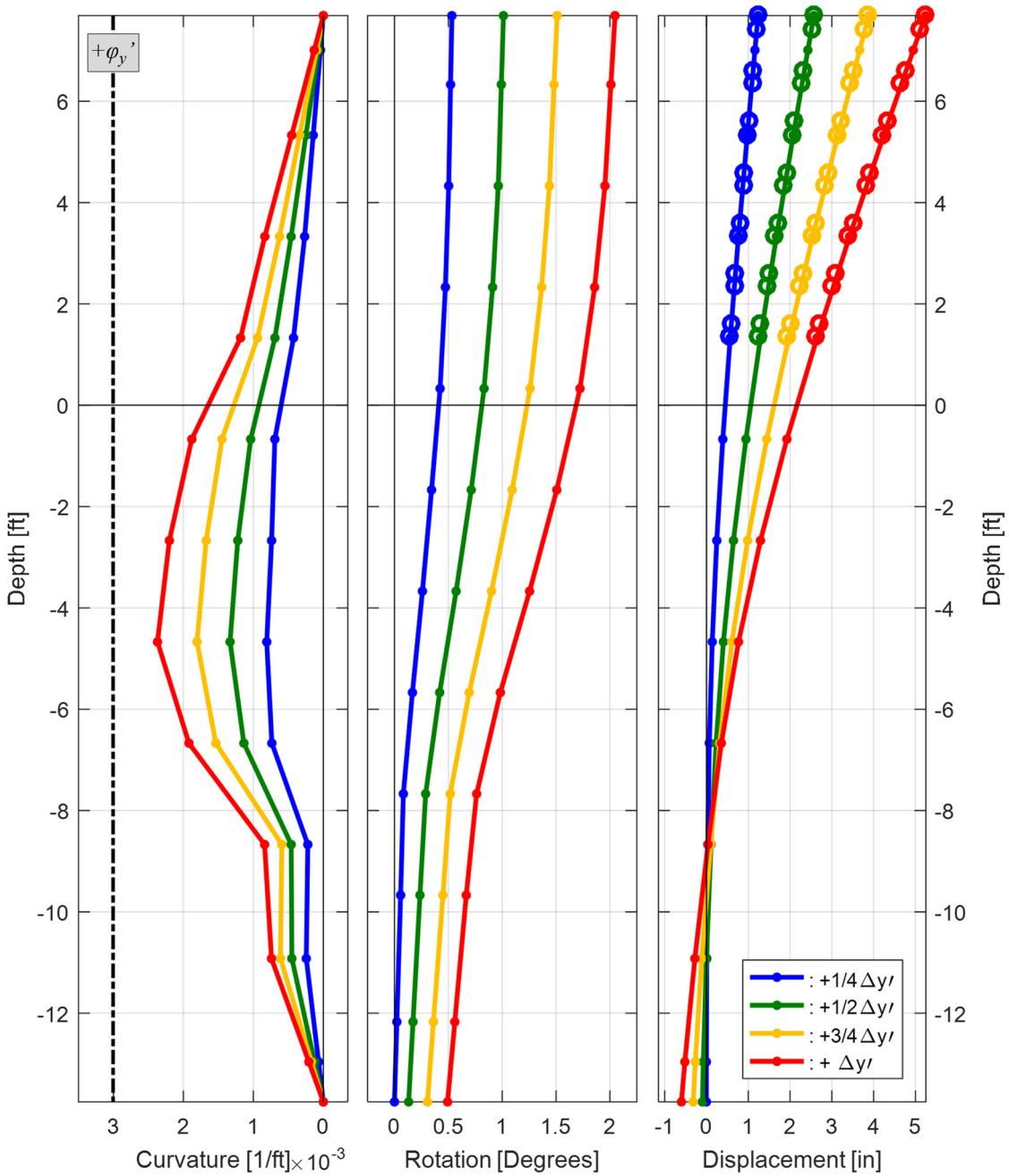

Figure 10-236 Test 12: curvature, rotation, and displacement profiles (elastic push cycles)

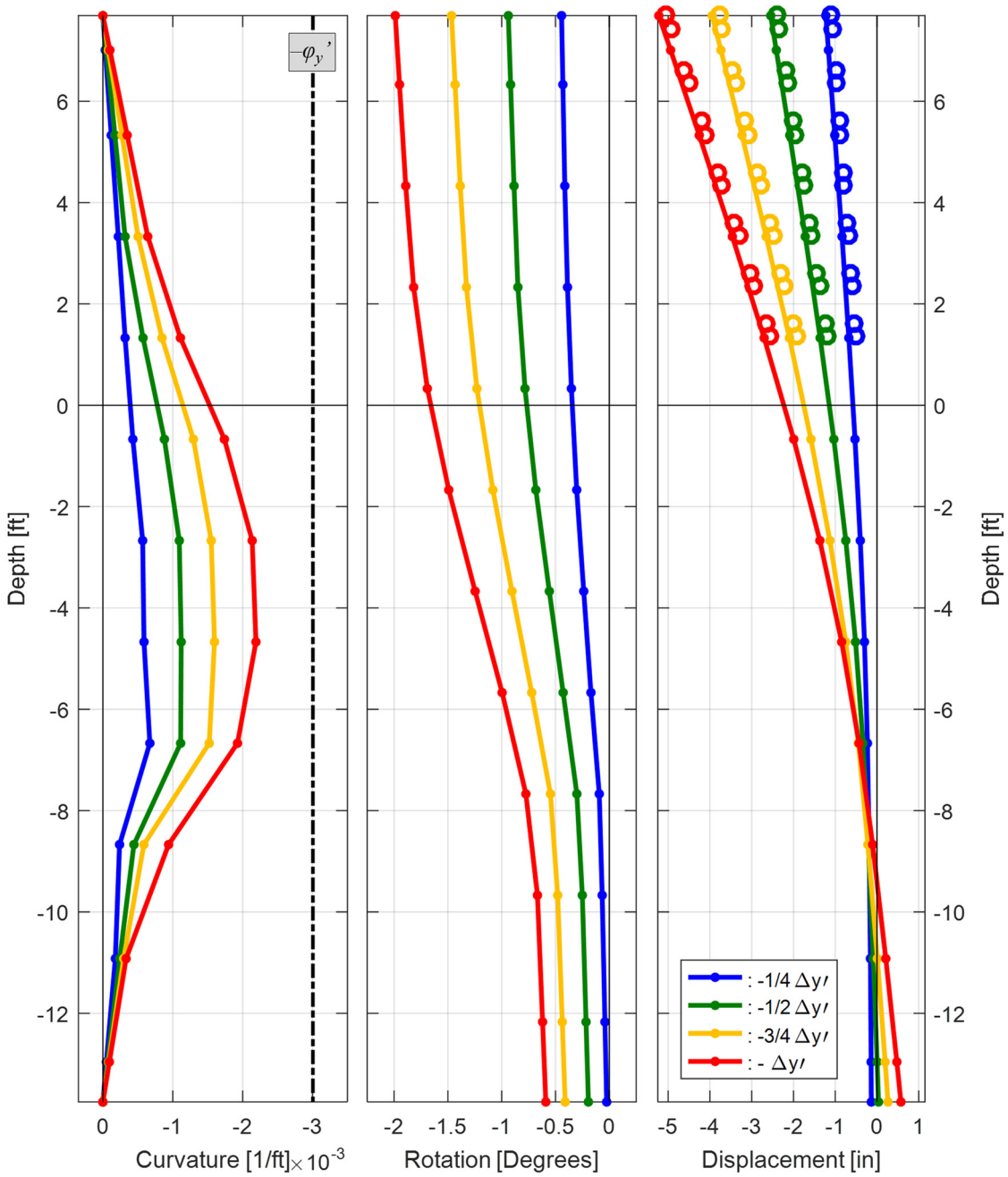

Figure 10-237 Test 12: curvature, rotation, and displacement profiles (elastic pull cycles)

As the test continued, the gap on the sides of the pile increased in size as the displacement ductility level increased. Minor loss of strength was observed up until all ductility level 3.0 (μ_3) cycles. The specimen failure (Figure 10-238) occurred at the second pull cycle load at ductility 4.0 (μ_4) when a significant drop in the force of the actuator was observed (i.e., ~58%). Sounds indicating steel fracture were heard at the same time when the strength loss occurred, indicating probable tube/bar fracture. Moreover, twist rotation of the pile occurred for all push cycles at ductility level 4 (μ_4). Finally, the test was terminated and the specimen was taken to zero displacement in order to facilitate its extraction from the soil.

Figure 10-239 presents strain profiles for the first push and pull cycles at different displacement ductility levels; the symbols N and S in the legends refer to the North and South sides, μ is the displacement ductility, and a depth equal to 0 ft. represents the soil surface. Note that the largest tensile and compressive strains were recorded at a depth between 0 ft. and 5 ft., which correlates well with the curvature, rotation, and displacement profiles presented in Figure 10-240 and Figure 10-241 for the inelastic push and pull cycles of the test, respectively. Note that the largest changes in rotation (i.e., curvature) occurred at a depth between 2.0 ft. and 4.0 ft., which correlates well with the observed damage zone. It is believed that the displacement and rotation profiles corresponding to the first push cycles at ductility level 4 (μ_4) are not accurate but rather they indicate that something occurred to the inclinometer sensor at that level of displacement, probably induced by the observed twist rotation.

Figure 10-238 Test specimen #12 at maximum displacement: (a) deformed shape, (b) South side and (c) North side

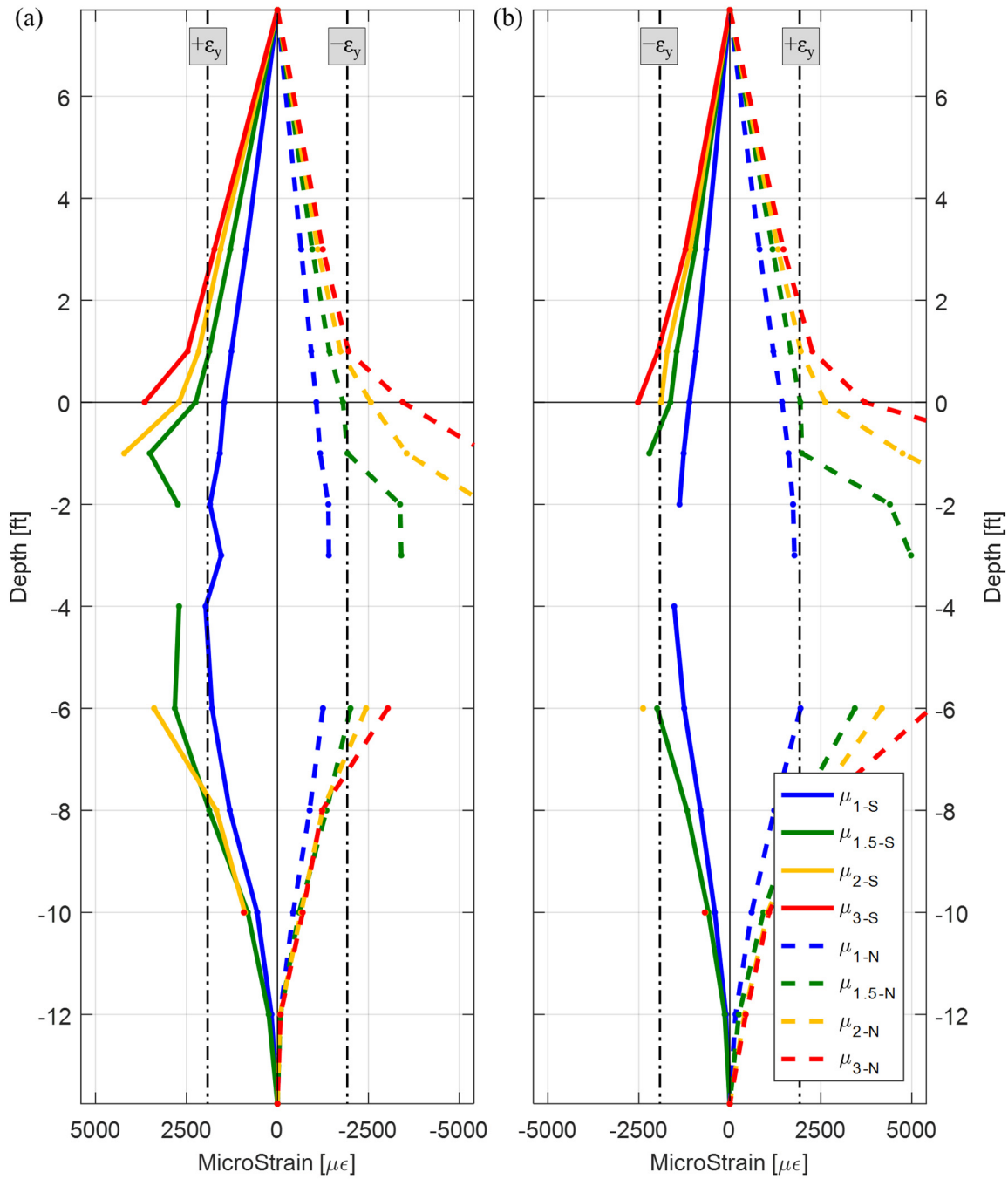

Figure 10-239 Test 12: strain profiles from inelastic (a) push and (b) pull cycles

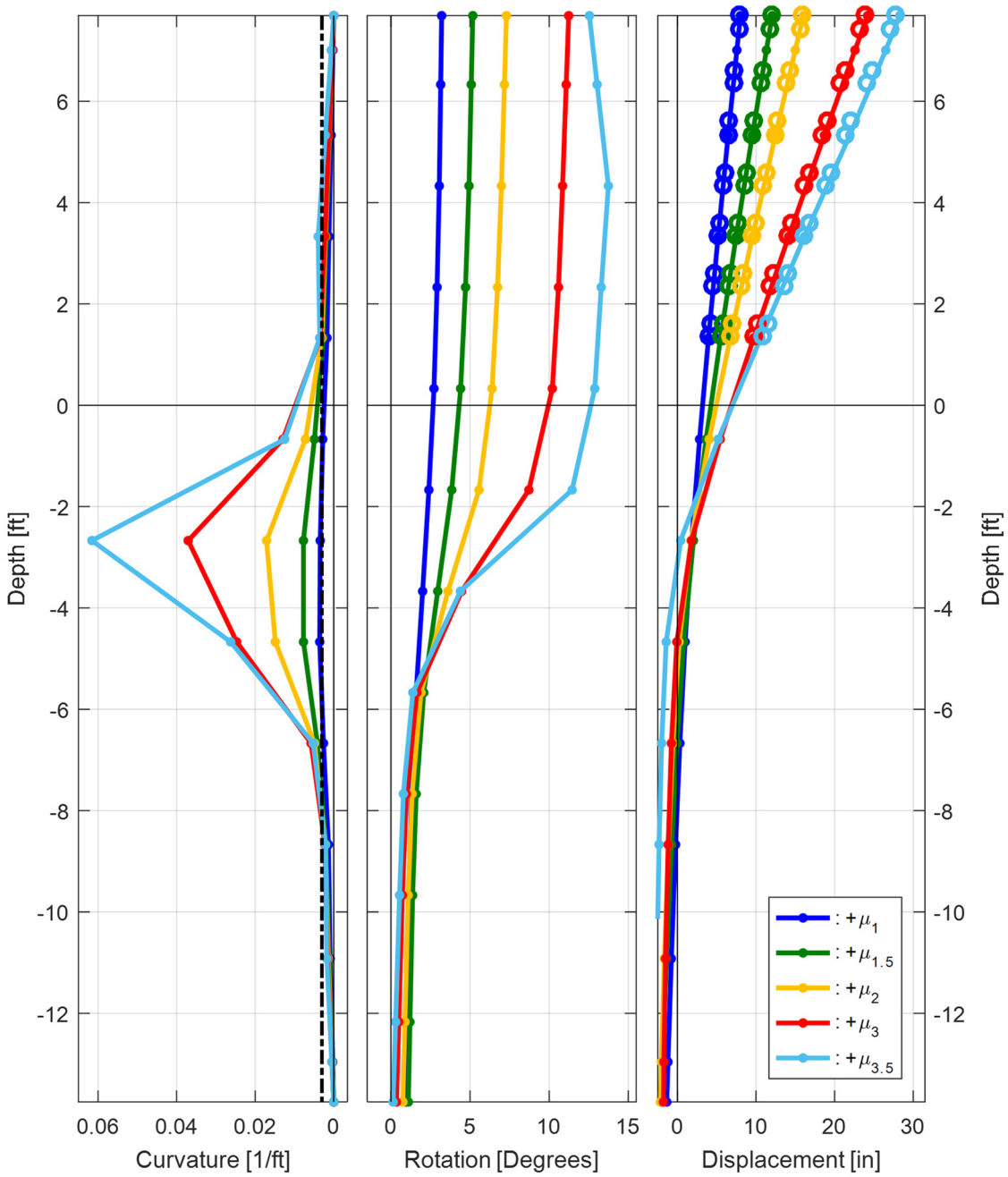

Figure 10-240 Test 12: curvature, rotation, and displacement profiles (inelastic push cycles)

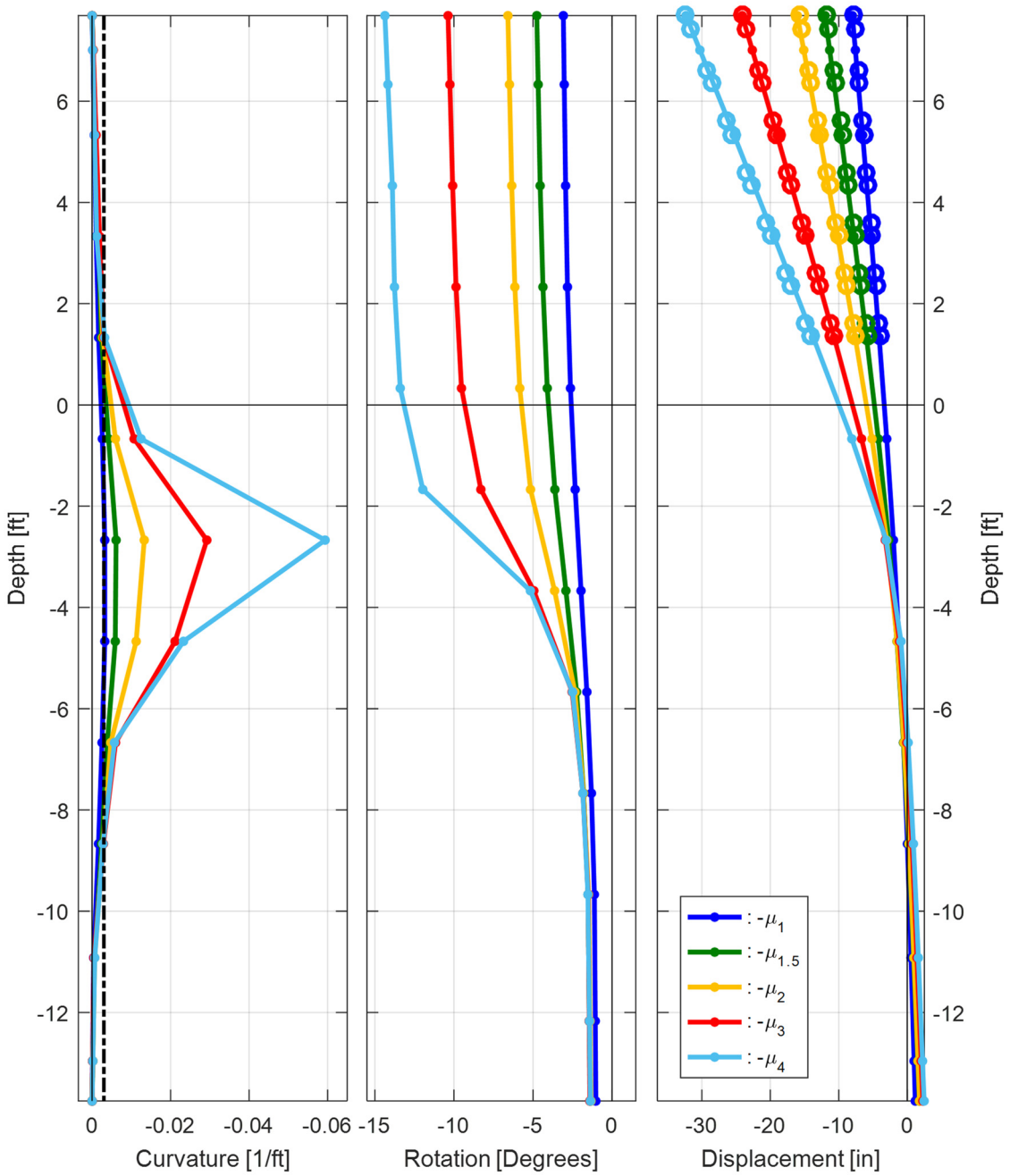

Figure 10-241 Test 12: curvature, rotation, and displacement profiles (inelastic pull cycles)

Figure 10-242 shows the state of the soil surface after the test was completed. Notice that despite the presence of the half-moon RC plates in the surface, deformations in the soil followed an expected oval-shaped failure surface in which active and passive pressures developed around the pile. This surface extended ~27 in. on both sides of the direction of loading and ~23 in. on the perpendicular direction. The total average settlement of the RC plates during the test was ~2.18 in. This value was averaged based on the vertical displacement of 4 points on the RC plates. Figure 10-243 shows the average settlement of the half-moon RC plates during the test as a function of the imposed displacements in the top of the pile. Note that, as the displacement history is applied, the settlement increases, though its magnitude is larger at the beginning of the test.

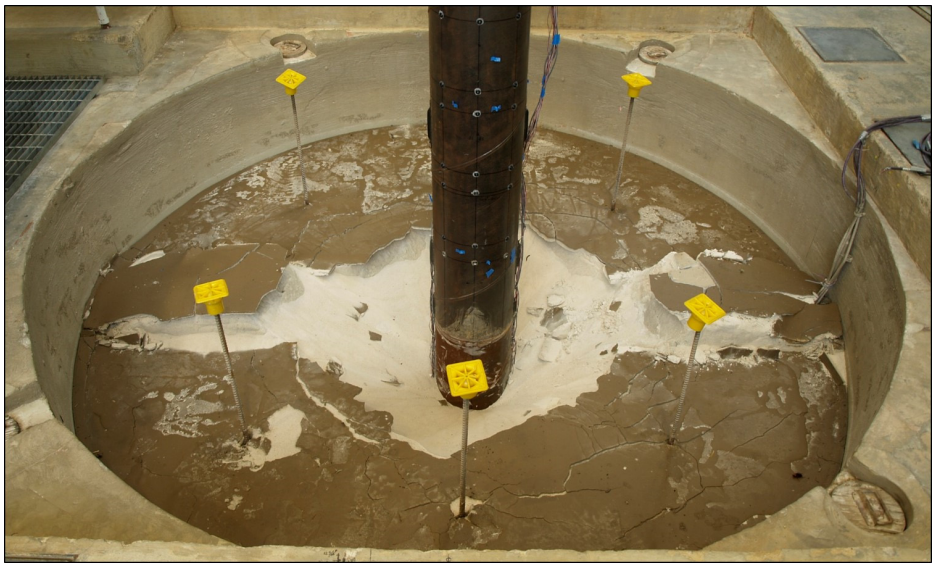

Figure 10-242 Test 12: soil surface after testing

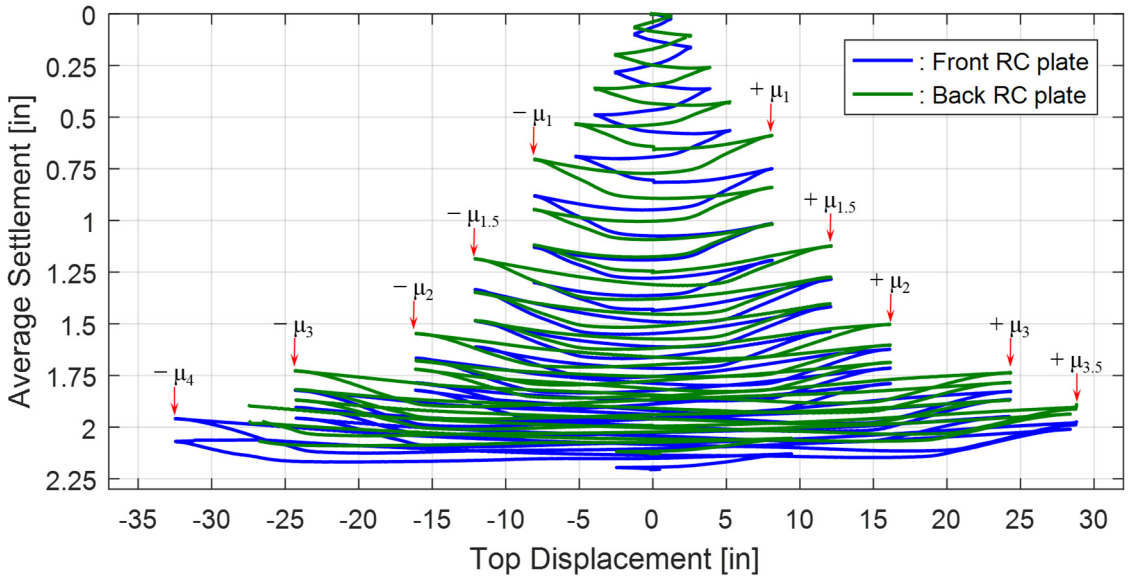

Figure 10-243 Test 12: half-moon RC plate settlement during testing

Figure 10-244 through Figure 10-247 present the damage observed after the pile was extracted from the soil. As thought during the test, tube fracture and tube buckling did occur as did bar fracture and bar buckling. It can be seen that local buckling developed on both sides of the specimen. The sections with the largest buckling occurred at a depth of 2ft. – 11.25 in. on the South side and 2 ft. – 11.5 in. on the North side of the specimen, which implies that the plastic hinge developed at an average depth of 2 ft. – 11.37 in. with respect to the soil surface. Several ripples were observed on both South and North sides of the specimen above and below the plastic hinge region.

Tube fracture (Figure 10-244) occurred on the North side of the specimen and it extended about half of the cross-section perimeter, resulting in a significant drop in strength due to lost tension capacity. As a consequence, after rupture, tension capacity is provided by the longitudinal reinforcement, which has a smaller area in comparison with that provided by the tube, inducing high stresses and deformations. Upon further investigations, bar fracture and bar buckling were observed only on the North side of the specimen. Note that tube fracture occurred in the section with the largest local buckling, in which deformations protruded ~3/4 in. on the North side and ~1/2 on the South side of the pile; note that two minor buckled sections developed on both North and South sides of the specimen. Figure 10-245 presents measurements of the primary buckled regions of the pile.

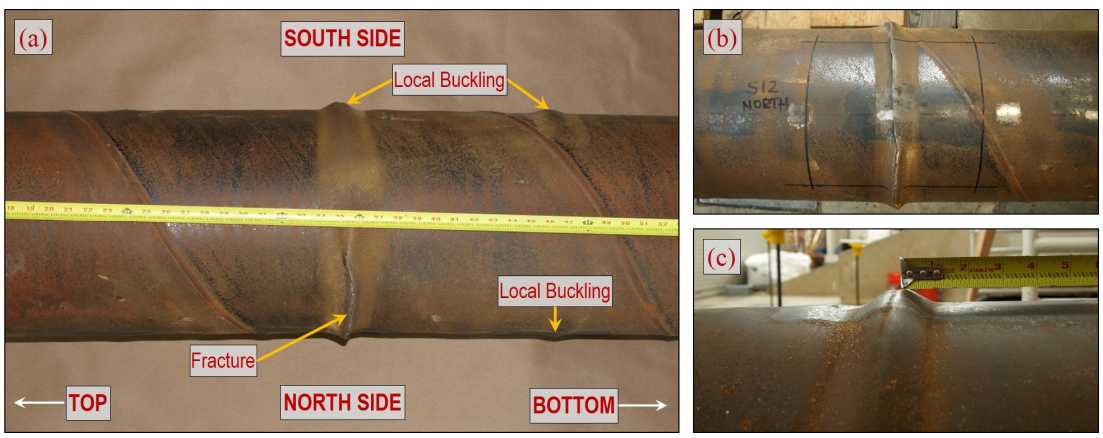

Figure 10-244 Test 12: (a) Final observed damage, (b) tube fracture, and (c) tube local buckling

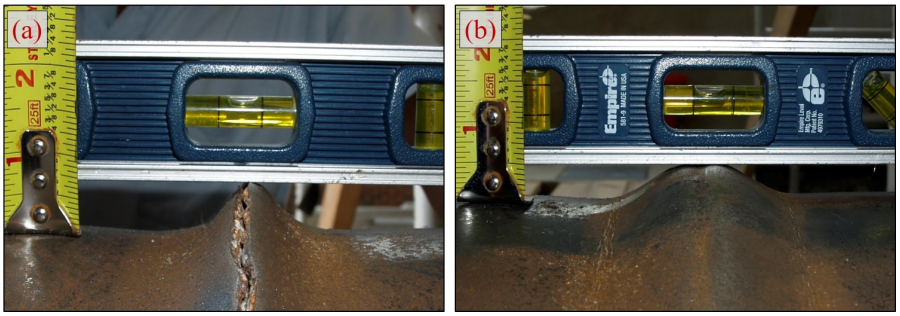

Figure 10-245 Test 12: primary buckled sections on (a) North side and (b) South side

In order to further investigate the significant strength loss, and to verify whether bar fracture or bar buckling occurred, a portion of the tube (i.e., 10 in. x 12 in.) was removed on both North and South sides of the specimen, in the extreme fibers at the ruptured and buckled sections, as shown in Figure 10-246 and Figure 10-247, respectively. It can be noticed significant cracking and crushing of the concrete in the critical section of the plastic hinge, perpendicular to the longitudinal direction of the specimen. Cracks in the concrete extended further to the center of the section. Bar buckling was observed on the North side of the specimen, which corresponds to the compression zone during the push cycles. A total of two (2) bars buckled, each adjacent to the bar located in the extreme fiber of the section. On the South side, on the other hand, the position of the spiral prevented occurrence of bar buckling, as shown in Figure 10-247(b). As suspected during the test, bar fracture did occur on the North side of the specimen, only one (1) bar fractured and it was located in the extreme fiber, as shown in Figure 10-246(b).

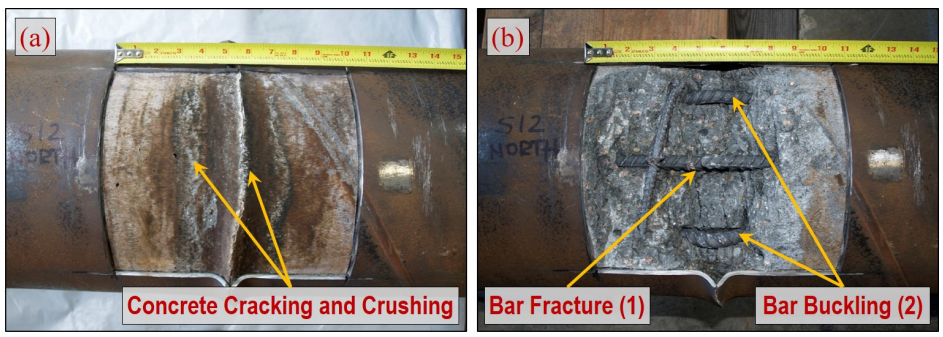

Figure 10-246 Test 12: observed damage in (a) concrete and (b) internal reinforcement on North side

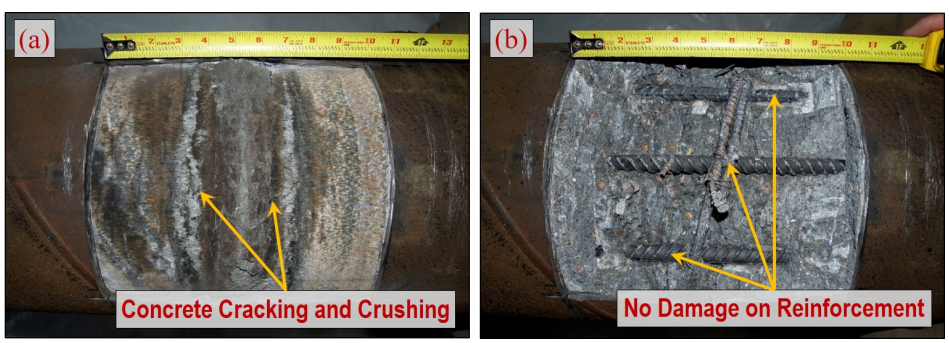

Figure 10-247 Test 12: observed damage in (a) concrete and (b) internal reinforcement on South side

Conclusions

Test specimen #12 showed a reliable response through all ductility 3.0 (μ_3) cycles. It is believed that onset of tube local buckling occurred at ductility level 2.0 (μ_2) as large tensile strains and subtle strength loss were observed. The test specimen completed all cycles of ductility 3.0 (μ_3) without significant loss of strength. Failure of the specimen occurred during the second pull cycle at ductility level 4.0 (μ_4) when a significant drop in the strength was observed. Further investigations revealed that failure occurred due to a combination of tube local buckling, tube fracture, bar buckling, and bar fracture. Although in the push direction the pile was subjected only to a displacement ductility level 3.5 ($\mu_{3.5}$), it is believed that this particular specimen is capable of having a reliable displacement capacity up to ductility 3.0 (μ_3). The main buckles as well as tube fracture did not occur over the spiral weld, so the tube spiral welds do not appear to negatively influence the behavior.

APPENDIX B: Force, displacement, and tensile strain data

The top displacement, lateral force, maximum curvature, depth-to-maximum curvature, and the corresponding tensile and compressive strains for each test at the end of each load cycle are tabulated in this appendix. It is worth noting that results for some of the tests include only the lateral force and top displacement as in some of the test data was not recorded or was lost due to problems related to instrumentation or to the data acquisition system.

Table 10-13 Test 1: peak cycle data (D/t = 48; La = 5.42D; No surcharge)

Cycle		Displ. (in)	Force (kips)	Max Curvature (1/ft)	Depth to Max. Curv. (ft)	Tensile Strain (%)	Comp. Strain (%)
1/4 Δy'	Push	0.83	4.00	0.00056	-3.94	0.03	-0.02
	Pull	-0.70	-4.36	-0.00051	-3.94	0.03	-0.02
1/2 Δy'	Push	1.86	6.45	0.00123	-3.94	0.07	-0.05
	Pull	-1.69	-7.20	-0.00130	-3.94	0.08	-0.05
3/4 Δy'	Push	3.07	8.72	0.00167	-3.94	0.10	-0.07
	Pull	-3.04	-10.14	-0.00206	-3.94	0.12	-0.08
Δy'	Push	4.46	10.83	0.00209	-1.94	0.12	-0.09
	Pull	-4.29	-12.92	-0.00305	-3.94	0.18	-0.13
Ductility 1	Push 1	6.11	15.31	0.00304	-1.94	0.18	-0.12
	Pull 1	-6.03	-18.69	-0.00520	-3.94	0.31	-0.20
	Push 2	6.01	15.63	0.00312	-1.94	0.18	-0.13
	Pull 2	-6.10	-19.03	-0.00551	-3.94	0.33	-0.21
	Push 3	6.00	16.37	0.00326	-1.94	0.19	-0.13
	Pull 3	-6.14	-19.43	-0.00582	-3.94	0.35	-0.22
Ductility 1.5	Push 1	9.04	21.15	0.00562	-3.94	0.34	-0.22
	Pull 1	-9.17	-24.86	-0.01171	-3.94	0.76	-0.40
	Push 2	9.11	21.74	0.00588	-3.94	0.36	-0.22
	Pull 2	-9.17	-24.64	-0.01237	-3.94	0.80	-0.42
	Push 3	9.08	22.40	0.00645	-3.94	0.40	-0.24
	Pull 3	-9.16	-24.41	-0.01274	-3.94	0.83	-0.43
Ductility 2	Push 1	11.90	25.44	0.01277	-3.94	0.83	-0.43
	Pull 1	-12.14	-27.73	-0.02032	-3.94	1.37	-0.64
	Push 2	12.20	25.12	0.01354	-3.94	0.89	-0.46
	Pull 2	-12.10	-27.96	-0.02162	-3.94	1.46	-0.68
	Push 3	12.18	25.47	0.01435	-3.94	0.94	-0.48
	Pull 3	-12.12	-27.11	-0.02207	-3.94	1.50	-0.69
Ductility 3	Push 1	18.25	29.21	0.02898	-3.94	1.99	-0.88
	Pull 1	-18.56	-34.42	-0.03475	-3.94	2.39	-1.05
	Push 2	18.21	28.02	0.02999	-3.94	2.06	-0.91
	Pull 2	-18.61	-33.50	-0.03626	-3.94	2.50	-1.09
	Push 3	18.23	28.36	0.03054	-3.94	2.10	-0.93
	Pull 3	-18.58	-33.42	-0.03736	-3.94	2.58	-1.12

Table 10-13 continued

Cycle		Displ. (in)	Force (kips)	Max Curvature (1/ft)	Depth to Max. Curv. (ft)	Tensile Strain (%)	Comp. Strain (%)
Ductility 4	Push 1	23.97	31.97	0.03855	-3.94	2.66	-1.16
	Pull 1	-25.07	-35.58	-0.05208	-3.94	3.62	-1.54
	Push 2	24.04	30.56	0.04099	-1.94	2.83	-1.23
	Pull 2	-24.83	-34.04	-0.05313	-3.94	3.69	-1.57
	Push 3	24.62	29.59	0.04305	-1.94	2.98	-1.28
	Pull 3	-24.62	-32.55	-0.05582	-3.94	3.88	-1.65
Ductility 5	Push 1	30.80	31.12	0.07139	-1.94	4.98	-2.08
	Pull 1	-31.30	-36.39	-0.07991	-1.94	5.59	-2.33
	Push 2	30.97	29.73	0.08999	-1.94	6.29	-2.62
	Pull 2	-31.15	-34.58	-0.08848	-1.94	6.18	-2.57
	Push 3	31.12	7.78	0.13870	-1.94	9.66	-4.07
	Pull 3	0.04	-13.32	-0.02840	-3.94	1.94	-0.87

Table 10-14 Test 2: peak cycle data (D/t = 48; La = 5.83D; Surcharge = 960 psf)

Cycle		Displ. (in)	Force (kips)
1/4 Δy'	Push	0.77	4.98
	Pull	-0.80	-5.05
1/2 Δy'	Push	1.67	7.78
	Pull	-1.69	-8.57
3/4 Δy'	Push	2.97	10.82
	Pull	-2.81	-12.14
Δy'	Push	4.08	13.27
	Pull	-4.04	-15.38
Ductility 1	Push 1	5.74	16.66
	Pull 1	-5.66	-19.25
	Push 2	5.70	15.31
	Pull 2	-5.69	-18.81
	Push 3	5.70	15.60
	Pull 3	-5.69	-18.86
Ductility 1.5	Push 1	8.71	22.49
	Pull 1	-8.40	-25.30
	Push 2	8.61	21.96
	Pull 2	-8.41	-25.53
	Push 3	8.65	22.14
	Pull 3	-8.46	-25.50
Ductility 2	Push 1	11.28	25.96
	Pull 1	-11.30	-28.32
	Push 2	11.57	25.95
	Pull 2	-11.58	-28.77
	Push 3	11.51	25.66
	Pull 3	-11.45	-27.81
Ductility 3	Push 1	16.93	28.89
	Pull 1	-16.87	-31.53
	Push 2	17.16	28.05
	Pull 2	-17.00	-30.21
	Push 3	16.91	27.56
	Pull 3	-16.96	-29.73

Table 10-14 continued

Cycle		Displ. (in)	Force (kips)
Ductility 4	Push 1	22.57	30.62
	Pull 1	-22.20	-32.83
	Push 2	22.63	29.20
	Pull 2	-22.79	-31.89
	Push 3	22.55	28.78
	Pull 3	-22.74	-31.29
Ductility 5	Push 1	28.25	30.72
	Pull 1	-28.41	-34.01
	Push 2	28.37	29.36
	Pull 2	-28.45	-32.42
	Push 3	28.35	28.20
	Pull 3	-28.44	-30.92
Ductility 5.5	Push 1	31.26	28.44
	Pull 1	-31.62	-7.99

Table 10-15 Test 3: peak cycle data (D/t = 95*; La = 5.18D; No surcharge)

Cycle		Displ. (in)	Force (kips)
1/4 Δy'	Push	0.71	3.69
	Pull	-0.76	-3.52
1/2 Δy'	Push	1.69	5.92
	Pull	-1.66	-5.70
3/4 Δy'	Push	2.74	7.72
	Pull	-2.74	-7.80
Δy'	Push	3.84	9.40
	Pull	-3.84	-9.69
Ductility 1	Push 1	6.16	12.51
	Pull 1	-6.13	-14.07
	Push 2	6.18	14.33
	Pull 2	-6.19	-14.85
	Push 3	6.19	14.55
	Pull 3	-6.19	-15.62
Ductility 1.5	Push 1	9.24	18.07
	Pull 1	-9.14	-19.28
	Push 2	9.28	18.20
	Pull 2	-9.20	-19.19
	Push 3	9.31	18.45
	Pull 3	-9.26	-19.30
Ductility 2	Push 1	12.24	20.04
	Pull 1	-12.27	-21.00
	Push 2	12.34	19.07
	Pull 2	-12.35	-20.73
	Push 3	12.45	19.22
	Pull 3	-12.38	-20.23
Ductility 3	Push 1	18.50	21.99
	Pull 1	-18.53	-19.17
	Push 2	18.49	20.68
	Pull 2	-18.35	-16.70
	Push 3	18.55	19.53
	Pull 3	-18.50	-15.28
Ductility 4	Push 1	24.99	13.99

Table 10-16 Test 4: peak cycle data (D/t = 95*; La = 5.18D; Surcharge = 960 psf)

Cycle		Displ. (in)	Force (kips)
1/4 Δy'	Push	0.72	5.06
	Pull	-0.92	-5.29
1/2 Δy'	Push	1.54	8.22
	Pull	-1.74	-8.35
3/4 Δy'	Push	2.43	10.95
	Pull	-2.47	-10.72
Δy'	Push	3.44	13.64
	Pull	-3.57	-13.83
Ductility 1	Push 1	5.43	17.69
	Pull 1	-5.57	-18.69
	Push 2	5.42	17.02
	Pull 2	-5.58	-17.82
	Push 3	5.42	16.81
	Pull 3	-5.58	-17.35
Ductility 1.5	Push 1	8.17	22.22
	Pull 1	-8.35	-23.27
	Push 2	8.16	20.23
	Pull 2	-8.22	-19.07
	Push 3	8.16	19.57
	Pull 3	-8.31	-15.70
Ductility 2	Push 1	10.92	22.62
	Pull 1	-11.11	-16.60
	Push 2	10.89	21.83
	Pull 2	-11.11	-14.61

Table 10-17 Test 5: peak cycle data (D/t = 95; La = 5.36D; No surcharge)

Cycle		Displ. (in)	Force (kips)	Max. Curvature (1/ft)	Depth to Max. Curv. (ft)	Tensile Strain (%)	Comp. Strain (%)
1/4 Δy'	Push	0.84	3.58	0.00057	-5.69	0.04	-0.02
	Pull	-0.71	-3.69	-0.00061	-3.69	0.04	-0.02
1/2 Δy'	Push	1.69	5.62	0.00106	-5.69	0.07	-0.04
	Pull	-1.61	-5.85	-0.00121	-5.69	0.08	-0.05
3/4 Δy'	Push	2.66	7.42	0.00152	-5.69	0.10	-0.06
	Pull	-2.65	-7.98	-0.00172	-5.69	0.11	-0.07
Δy'	Push	3.76	9.21	0.00193	-5.69	0.13	-0.08
	Pull	-3.76	-9.88	-0.00224	-5.69	0.15	-0.09
Ductility 1	Push 1	5.62	11.66	0.00278	-5.69	0.18	-0.11
	Pull 1	-5.58	-13.19	-0.00343	-5.69	0.22	-0.14
	Push 2	5.59	12.13	0.00307	-3.69	0.20	-0.13
	Pull 2	-5.60	-13.25	-0.00361	-5.69	0.23	-0.15
	Push 3	5.59	12.57	0.00332	-3.69	0.21	-0.14
	Pull 3	-5.63	-13.43	-0.00374	-3.69	0.24	-0.15
Ductility 1.5	Push 1	8.39	16.72	0.00578	-3.69	0.39	-0.22
	Pull 1	-8.41	-17.67	-0.00702	-3.69	0.48	-0.26
	Push 2	8.32	16.40	0.00617	-3.69	0.42	-0.24
	Pull 2	-8.46	-17.17	-0.00746	-3.69	0.51	-0.28
	Push 3	8.35	17.20	0.00681	-3.69	0.46	-0.26
	Pull 3	-8.34	-17.73	-0.00816	-3.69	0.56	-0.30
Ductility 2	Push 1	11.06	19.65	0.01200	-3.69	0.85	-0.42
	Pull 1	-11.21	-20.78	-0.01520	-3.69	1.10	-0.51
	Push 2	11.12	19.35	0.01257	-3.69	0.90	-0.43
	Pull 2	-11.18	-20.30	-0.01569	-3.69	1.14	-0.52
	Push 3	11.15	19.50	0.01318	-3.69	0.94	-0.45
	Pull 3	-11.20	-19.69	-0.01587	-3.69	1.15	-0.53
Ductility 3	Push 1	16.79	22.21	0.02476	-3.69	1.84	-0.78
	Pull 1	-16.72	-22.87	-0.02811	-3.69	2.09	-0.88
	Push 2	16.70	21.64	0.02712	-3.69	2.02	-0.85
	Pull 2	-16.84	-21.73	-0.02949	-3.69	2.20	-0.92
	Push 3	16.71	20.88	0.02886	-3.69	2.15	-0.90
	Pull 3	-16.75	-21.64	-0.03000	-3.69	2.24	-0.93

Table 10-17 continued

Cycle		Displ. (in)	Force (kips)	Max. Curvature (1/ft)	Depth to Max. Curv. (ft)	Tensile Strain (%)	Comp. Strain (%)
Ductility 4	Push 1	22.32	23.00	0.04088	-3.69	3.07	-1.25
	Pull 1	-22.47	-23.94	-0.04066	-3.69	3.05	-1.25
	Push 2	22.47	21.73	0.04302	-3.69	3.23	-1.31
	Pull 2	-22.46	-22.73	-0.04171	-3.69	3.13	-1.28
	Push 3	22.48	20.71	0.04431	-3.69	3.33	-1.35
	Pull 3	-22.54	-13.28	-0.05348	-1.69	4.03	-1.63
Ductility 5	Push 1	29.13	12.01	0.06328	-3.69	4.77	-1.92

Table 10-18 Test 6: peak cycle data (D/t = 95; La = 5.53D; Surcharge = 960 psf)

Cycle		Displ. (in)	Force (kips)	Max. Curvature (1/ft)	Depth to Max. Curv. (ft)	Tensile Strain (%)	Comp. Strain (%)
1/4 Δy'	Push	0.71	3.94	0.00096	-1.48	0.06	-0.04
	Pull	-0.72	-4.21	-0.00050	-3.48	0.03	-0.02
1/2 Δy'	Push	1.59	6.81	0.00171	-1.48	0.11	-0.07
	Pull	-1.51	-7.34	-0.00136	-3.48	0.09	-0.05
3/4 Δy'	Push	2.44	9.26	0.00235	-1.48	0.16	-0.09
	Pull	-2.38	-10.12	-0.00201	-1.48	0.13	-0.08
Δy'	Push	3.65	12.10	0.00321	-1.48	0.21	-0.13
	Pull	-3.64	-13.44	-0.00297	-1.48	0.20	-0.12
Ductility 1	Push 1	5.25	15.04	0.00448	-1.48	0.30	-0.17
	Pull 1	-5.26	-16.65	-0.00425	-3.48	0.29	-0.16
	Push 2	5.28	14.58	0.00435	-1.48	0.29	-0.17
	Pull 2	-5.34	-16.33	-0.00428	-3.48	0.29	-0.16
	Push 3	5.29	14.33	0.00433	-1.48	0.29	-0.17
	Pull 3	-5.33	-15.92	-0.00420	-3.48	0.28	-0.16
Ductility 1.5	Push 1	7.96	19.43	0.00748	-1.48	0.53	-0.26
	Pull 1	-8.02	-21.43	-0.00812	-1.48	0.58	-0.28
	Push 2	7.94	18.26	0.00682	-1.48	0.48	-0.24
	Pull 2	-7.99	-20.29	-0.00778	-1.48	0.55	-0.27
	Push 3	7.97	17.99	0.00674	-1.48	0.47	-0.24
	Pull 3	-8.01	-19.62	-0.00769	-3.48	0.54	-0.27
Ductility 2	Push 1	10.62	21.39	0.01106	-1.48	0.80	-0.37
	Pull 1	-10.59	-23.04	-0.01503	-1.48	1.12	-0.47
	Push 2	10.57	20.11	0.01070	-1.48	0.78	-0.36
	Pull 2	-10.63	-22.13	-0.01466	-1.48	1.09	-0.46
	Push 3	10.59	19.82	0.01159	-3.48	0.84	-0.38
	Pull 3	-10.66	-22.09	-0.01530	-1.48	1.14	-0.48
Ductility 3	Push 1	16.10	24.17	0.02351	-1.48	1.79	-0.70
	Pull 1	-16.05	-26.19	-0.03299	-1.48	2.53	-0.96
	Push 2	15.95	22.14	0.02421	-1.48	1.84	-0.71
	Pull 2	-16.01	-25.18	-0.03874	-1.48	2.98	-1.12
	Push 3	15.97	21.56	0.02500	-1.48	1.91	-0.74
	Pull 3	-15.96	-24.77	-0.04302	-1.48	3.31	-1.24

Table 10-18 continued

Cycle		Displ. (in)	Force (kips)	Max. Curvature (1/ft)	Depth to Max. Curv. (ft)	Tensile Strain (%)	Comp. Strain (%)
Ductility 4	Push 1	21.31	25.34	0.04032	-1.48	3.10	-1.16
	Pull 1	-21.23	-27.69	-0.06522	-1.48	5.01	-1.88
	Push 2	21.31	23.54	0.04301	-1.48	3.31	-1.24
	Pull 2	-21.30	-26.08	-0.06904	-1.48	5.31	-1.99
	Push 3	21.36	16.56	0.04671	-1.48	3.60	-1.34

Table 10-19 Test 7: peak cycle data (D/t = 68; La = 5.43D; No surcharge)

Cycle		Displ. (in)	Force (kips)	Max. Curvature (1/ft)	Depth to Max. Curv. (ft)	Tensile Strain (%)	Comp. Strain (%)
1/4 Δy'	Push	0.85	4.03	0.00067	-1.58	0.04	-0.03
	Pull	-0.83	-3.96	-0.00059	-1.58	0.04	-0.02
1/2 Δy'	Push	1.80	6.27	0.00104	-1.58	0.07	-0.04
	Pull	-1.81	-6.14	-0.00115	-1.58	0.07	-0.05
3/4 Δy'	Push	3.02	8.63	0.00161	-1.58	0.10	-0.07
	Pull	-3.06	-8.36	-0.00165	-1.58	0.11	-0.07
Δy'	Push	4.30	10.64	0.00211	-1.58	0.13	-0.09
	Pull	-4.30	-11.03	-0.00219	-1.58	0.14	-0.09
Ductility 1	Push 1	6.00	13.67	0.00272	-1.58	0.17	-0.11
	Pull 1	-6.01	-14.49	-0.00274	-1.58	0.17	-0.11
	Push 2	5.97	15.75	0.00314	-1.58	0.20	-0.13
	Pull 2	-6.01	-14.79	-0.00290	-1.58	0.18	-0.12
	Push 3	5.96	16.59	0.00330	-1.58	0.21	-0.14
	Pull 3	-6.01	-15.32	-0.00298	-1.58	0.19	-0.12
Ductility 1.5	Push 1	9.00	21.67	0.00477	-1.58	0.31	-0.19
	Pull 1	-8.98	-20.61	-0.00423	-1.58	0.28	-0.17
	Push 2	8.97	22.87	0.00524	-1.58	0.35	-0.21
	Pull 2	-8.98	-21.02	-0.00437	-1.58	0.28	-0.18
	Push 3	8.96	23.20	0.00583	-3.58	0.39	-0.22
	Pull 3	-8.98	-21.98	-0.00471	-1.58	0.31	-0.19
Ductility 2	Push 1	11.97	26.47	0.01172	-3.58	0.83	-0.40
	Pull 1	-11.97	-25.58	-0.00936	-3.58	0.65	-0.33
	Push 2	11.96	26.10	0.01306	-3.58	0.94	-0.44
	Pull 2	-11.98	-25.52	-0.01002	-3.58	0.70	-0.35
	Push 3	11.98	26.09	0.01384	-3.58	1.00	-0.46
	Pull 3	-11.97	-25.49	-0.01050	-3.58	0.74	-0.37
Ductility 3	Push 1	18.02	29.44	0.02659	-3.58	1.99	-0.82
	Pull 1	-18.01	-28.87	-0.02389	-3.58	1.78	-0.74
	Push 2	18.00	28.52	0.02815	-3.58	2.11	-0.86
	Pull 2	-18.00	-28.05	-0.02410	-3.58	1.80	-0.75
	Push 3	18.00	27.64	0.02936	-3.58	2.20	-0.89
	Pull 3	-18.01	-28.10	-0.02471	-3.58	1.84	-0.76

Table 10-19 continued

Cycle		Displ. (in)	Force (kips)	Max. Curvature (1/ft)	Depth to Max. Curv. (ft)	Tensile Strain (%)	Comp. Strain (%)
Ductility 4	Push 1	24.05	30.68	0.04380	-3.58	3.32	-1.30
	Pull 1	-24.08	-32.01	-0.03402	-3.58	2.56	-1.03
	Push 2	24.05	29.47	0.04694	-3.58	3.57	-1.38
	Pull 2	-24.07	-30.89	-0.03640	-3.58	2.75	-1.09
	Push 3	24.05	28.05	0.05055	-3.58	3.85	-1.49
	Pull 3	-24.07	-29.22	-0.03912	-3.58	2.96	-1.17
Ductility 5	Push 1	29.39	31.14	0.06846	-3.58	5.23	-1.99
	Pull 1	-30.07	-32.79	-0.05431	-3.58	4.14	-1.59
	Push 2	29.41	23.24	0.08115	-3.58	6.21	-2.35

Table 10-20 Test 8: peak cycle data (D/t = 68; La = 5.43D; Surcharge = 960 psf)

Cycle		Displ. (in)	Force (kips)	Max. Curvature (1/ft)	Depth to Max. Curv. (ft)	Tensile Strain (%)	Comp. Strain (%)
1/4 Δy'	Push	0.71	4.55	0.00055	-1.58	0.04	-0.02
	Pull	-0.74	-4.98	-0.00069	-1.58	0.04	-0.03
1/2 Δy'	Push	1.71	8.29	0.00220	-1.58	0.14	-0.09
	Pull	-1.65	-8.53	-0.00160	-1.58	0.10	-0.07
3/4 Δy'	Push	2.84	11.47	0.00331	-1.58	0.21	-0.14
	Pull	-2.90	-12.57	-0.00213	-1.58	0.14	-0.09
Δy'	Push	4.11	14.67	0.00436	-1.58	0.28	-0.18
	Pull	-4.03	-15.87	-0.00307	-3.58	0.20	-0.13
Ductility 1	Push 1	5.67	18.51	0.00528	-1.58	0.35	-0.21
	Pull 1	-5.72	-20.42	-0.00410	-3.58	0.27	-0.17
	Push 2	5.75	17.97	0.00500	-1.58	0.33	-0.20
	Pull 2	-5.71	-19.45	-0.00400	-3.58	0.26	-0.16
	Push 3	5.74	17.80	0.00495	-1.58	0.33	-0.20
	Pull 3	-5.71	-19.32	-0.00412	-3.58	0.27	-0.17
Ductility 1.5	Push 1	8.61	25.19	0.00748	-1.58	0.51	-0.28
	Pull 1	-8.56	-26.89	-0.01071	-3.58	0.76	-0.37
	Push 2	8.60	23.86	0.00680	-1.58	0.46	-0.25
	Pull 2	-8.60	-26.32	-0.01179	-3.58	0.84	-0.40
	Push 3	8.59	23.35	0.00652	-1.58	0.44	-0.25
	Pull 3	-8.55	-26.41	-0.01252	-3.58	0.90	-0.42
Ductility 2	Push 1	11.45	28.14	0.01043	-1.58	0.74	-0.36
	Pull 1	-11.44	-30.28	-0.02057	-3.58	1.53	-0.64
	Push 2	11.45	26.71	0.01032	-1.58	0.73	-0.36
	Pull 2	-11.45	-30.09	-0.02171	-3.58	1.61	-0.68
	Push 3	11.46	26.57	0.01113	-1.58	0.79	-0.38
	Pull 3	-11.43	-29.06	-0.02195	-3.58	1.63	-0.68
Ductility 3	Push 1	17.11	31.94	0.02711	-1.58	2.03	-0.83
	Pull 1	-17.19	-33.47	-0.03231	-3.58	2.44	-0.97
	Push 2	17.17	29.79	0.02726	-1.58	2.04	-0.83
	Pull 2	-17.19	-32.51	-0.03234	-3.58	2.44	-0.97
	Push 3	17.18	29.28	0.02834	-1.58	2.13	-0.86
	Pull 3	-17.20	-31.14	-0.03460	-1.58	2.62	-1.03

Table 10-20 continued

Cycle		Displ. (in)	Force (kips)	Max. Curvature (1/ft)	Depth to Max. Curv. (ft)	Tensile Strain (%)	Comp. Strain (%)
Ductility 4	Push 1	22.95	31.76	0.04206	-1.58	3.20	-1.24
	Pull 1	-22.96	-34.26	-0.05270	-1.58	4.02	-1.54
	Push 2	22.96	30.56	0.04797	-1.58	3.65	-1.41
	Pull 2	-22.96	-32.73	-0.05677	-1.58	4.34	-1.65
	Push 3	22.95	23.87	0.05110	-1.58	3.90	-1.49

Table 10-21 Test 9: peak cycle data (D/t = 48; La = 5.77D; Surcharge = 960 psf)

Cycle		Displ. (in)	Force (kips)	Max. Curvature (1/ft)	Depth to Max. Curv. (ft)	Tensile Strain (%)	Comp. Strain (%)
1/4 Δy'	Push	0.78	4.91	0.00108	-1.62	0.06	-0.04
	Pull	-0.77	-4.17	-0.00082	-1.62	0.05	-0.03
1/2 Δy'	Push	1.84	8.80	0.00194	-1.62	0.11	-0.08
	Pull	-1.80	-8.09	-0.00154	-1.62	0.09	-0.06
3/4 Δy'	Push	2.93	11.87	0.00257	-1.62	0.15	-0.10
	Pull	-2.89	-11.56	-0.00216	-1.62	0.13	-0.09
Δy'	Push	4.01	14.44	0.00313	-1.62	0.18	-0.13
	Pull	-3.99	-14.48	-0.00273	-1.62	0.16	-0.11
Ductility 1	Push 1	5.88	18.36	0.00446	-1.62	0.27	-0.17
	Pull 1	-5.88	-18.94	-0.00393	-1.62	0.23	-0.16
	Push 2	5.80	16.83	0.00410	-1.62	0.24	-0.16
	Pull 2	-5.88	-18.17	-0.00388	-1.62	0.23	-0.15
	Push 3	5.88	16.99	0.00412	-1.62	0.25	-0.16
	Pull 3	-5.89	-17.11	-0.00371	-1.62	0.22	-0.15
Ductility 1.5	Push 1	8.82	23.61	0.00717	-1.62	0.45	-0.26
	Pull 1	-8.80	-24.50	-0.00737	-3.62	0.46	-0.27
	Push 2	8.79	21.37	0.00642	-1.62	0.40	-0.24
	Pull 2	-8.82	-23.53	-0.00705	-3.62	0.44	-0.26
	Push 3	8.81	21.53	0.00649	-1.62	0.40	-0.24
	Pull 3	-8.82	-22.96	-0.00688	-3.62	0.43	-0.25
Ductility 2	Push 1	11.76	26.53	0.01088	-1.62	0.70	-0.37
	Pull 1	-11.74	-27.78	-0.01255	-3.62	0.82	-0.42
	Push 2	11.74	24.80	0.01249	-3.62	0.82	-0.42
	Pull 2	-11.74	-26.84	-0.01243	-3.62	0.81	-0.42
	Push 3	11.75	24.80	0.01211	-3.62	0.79	-0.41
	Pull 3	-11.74	-26.21	-0.01327	-3.62	0.87	-0.44
Ductility 3	Push 1	17.61	30.21	0.02539	-1.62	1.74	-0.77
	Pull 1	-17.68	-31.97	-0.02749	-3.62	1.89	-0.83
	Push 2	17.60	28.81	0.02624	-1.62	1.80	-0.79
	Pull 2	-17.68	-30.76	-0.02835	-3.62	1.95	-0.85
	Push 3	17.60	29.55	0.03030	-1.62	2.09	-0.91
	Pull 3	-17.68	-31.31	-0.02949	-1.62	2.04	-0.88

Table 10-21 continued

Cycle		Displ. (in)	Force (kips)	Max. Curvature (1/ft)	Depth to Max. Curv. (ft)	Tensile Strain (%)	Comp. Strain (%)
Ductility 4	Push 1	23.54	32.46	0.04769	-1.62	3.33	-1.39
	Pull 1	-23.56	-34.80	-0.04569	-1.62	3.19	-1.33
	Push 2	23.54	30.95	0.04953	-1.62	3.46	-1.44
	Pull 2	-23.57	-33.67	-0.04837	-1.62	3.38	-1.41
	Push 3	23.53	30.38	0.05239	-1.62	3.67	-1.52
	Pull 3	-23.56	-32.33	-0.05051	-1.62	3.53	-1.47
Ductility 5	Push 1	29.44	32.26	0.07012	-1.62	4.94	-2.00
	Pull 1	-29.43	-36.29	-0.07714	-1.62	5.44	-2.20
	Push 2	29.42	31.05	0.07833	-1.62	5.52	-2.23
	Pull 2	-29.43	-34.40	-0.08583	-1.62	6.06	-2.44
	Push 3	29.50	6.34	0.14594	-1.62	10.31	-4.14

Table 10-22 Test 10: peak cycle data (D/t = 48; La = 7.77D; No surcharge)

Cycle		Displ. (in)	Force (kips)	Max. Curvature (1/ft)	Depth to Max. Curv. (ft)	Tensile Strain (%)	Comp. Strain (%)
1/4 Δy'	Push	1.33	3.75	0.00078	-4.58	0.05	-0.03
	Pull	-1.29	-3.77	-0.00068	-4.58	0.04	-0.03
1/2 Δy'	Push	2.48	5.37	0.00114	-4.58	0.07	-0.05
	Pull	-2.44	-5.74	-0.00121	-2.58	0.07	-0.05
3/4 Δy'	Push	3.88	6.99	0.00153	-4.58	0.09	-0.06
	Pull	-3.83	-7.86	-0.00168	-2.58	0.10	-0.07
Δy'	Push	5.03	8.19	0.00186	-4.58	0.11	-0.07
	Pull	-5.08	-9.67	-0.00234	-2.58	0.14	-0.09
Ductility 1	Push 1	7.70	11.36	0.00284	-4.58	0.17	-0.11
	Pull 1	-7.71	-14.56	-0.00401	-2.58	0.24	-0.16
	Push 2	7.74	12.45	0.00306	-4.58	0.18	-0.12
	Pull 2	-7.77	-15.16	-0.00417	-2.58	0.25	-0.16
	Push 3	7.72	13.01	0.00312	-4.58	0.18	-0.12
	Pull 3	-7.75	-15.97	-0.00479	-2.58	0.29	-0.18
Ductility 1.5	Push 1	11.48	16.70	0.00526	-4.58	0.32	-0.20
	Pull 1	-11.54	-19.98	-0.00883	-2.58	0.57	-0.31
	Push 2	11.60	16.81	0.00534	-4.58	0.33	-0.20
	Pull 2	-11.54	-20.39	-0.00896	-2.58	0.58	-0.31
	Push 3	11.63	17.50	0.00554	-4.58	0.34	-0.21
	Pull 3	-11.55	-20.29	-0.01061	-2.58	0.69	-0.36
Ductility 2	Push 1	15.43	20.17	0.00964	-2.58	0.62	-0.33
	Pull 1	-15.53	-22.58	-0.01786	-2.58	1.21	-0.55
	Push 2	15.49	19.57	0.00972	-2.58	0.63	-0.33
	Pull 2	-15.43	-22.44	-0.01917	-2.58	1.31	-0.59
	Push 3	15.44	19.54	0.01048	-2.58	0.68	-0.35
	Pull 3	-15.41	-22.02	-0.01952	-2.58	1.34	-0.60
Ductility 3	Push 1	23.40	23.26	0.02052	-2.58	1.41	-0.62
	Pull 1	-23.46	-25.53	-0.03850	-2.58	2.71	-1.10
	Push 2	23.40	20.99	0.02347	-2.58	1.62	-0.70
	Pull 2	-23.33	-23.78	-0.04105	-2.58	2.89	-1.17
	Push 3	23.31	20.66	0.02304	-2.58	1.59	-0.69
	Pull 3	-23.26	-23.74	-0.04191	-2.58	2.95	-1.19

Table 10-22 continued

Cycle		Displ. (in)	Force (kips)	Max. Curvature (1/ft)	Depth to Max. Curv. (ft)	Tensile Strain (%)	Comp. Strain (%)
Ductility 4	Push 1	30.93	24.34	0.03663	-2.58	2.57	-1.05
	Pull 1	-23.29	-24.17	-0.04324	-2.58	3.05	-1.23
	Push 2	31.15	23.80	0.03746	-2.58	2.63	-1.08
	Pull 2	-23.32	-23.74	-0.04527	-2.58	3.20	-1.29
	Push 3	31.11	23.35	0.03830	-2.58	2.69	-1.10
	Pull 3	-23.30	-23.42	-0.04747	-2.58	3.36	-1.34
Ductility 5	Push 1	38.75	25.71	0.05748	-2.58	4.08	-1.61
	Pull 1	-23.36	-23.85	-0.05242	-2.58	3.71	-1.48
	Push 2	38.92	24.58	0.06281	-2.58	4.46	-1.76
	Pull 2	-23.36	-23.29	-0.05470	-2.58	3.88	-1.54
	Push 3	38.97	23.53	0.06948	-2.58	4.94	-1.94
	Pull 3	-23.34	-23.28	-0.05880	-2.58	4.17	-1.65
	Push 4	36.33	6.95	0.09671	-2.58	6.89	-2.69

Table 10-23 Test 11: peak cycle data (D/t = 95; La = 7.24D; No surcharge)

Cycle		Displ. (in)	Force (kips)	Max. Curvature (1/ft)	Depth to Max. Curv. (ft)	Tensile Strain (%)	Comp. Strain (%)
1/4 Δy'	Push	1.02	3.10	0.00069	-4.67	0.05	-0.03
	Pull	-0.99	-3.10	-0.00064	-4.67	0.04	-0.02
1/2 Δy'	Push	2.11	4.80	0.00123	-4.67	0.08	-0.05
	Pull	-2.07	-5.20	-0.00124	-2.67	0.08	-0.05
3/4 Δy'	Push	3.23	6.20	0.00162	-4.67	0.11	-0.06
	Pull	-3.22	-7.00	-0.00179	-2.67	0.12	-0.07
Δy'	Push	4.46	7.80	0.00203	-2.67	0.14	-0.08
	Pull	-4.43	-8.50	-0.00234	-2.67	0.16	-0.09
Ductility 1	Push 1	7.23	10.40	0.00304	-2.67	0.20	-0.12
	Pull 1	-7.12	-12.30	-0.00407	-2.67	0.28	-0.15
	Push 2	7.16	10.80	0.00330	-4.67	0.22	-0.13
	Pull 2	-7.13	-13.50	-0.00458	-2.67	0.31	-0.17
	Push 3	7.22	11.70	0.00361	-2.67	0.24	-0.14
	Pull 3	-7.09	-13.50	-0.00480	-2.67	0.33	-0.18
Ductility 1.5	Push 1	10.87	15.30	0.00631	-2.67	0.45	-0.22
	Pull 1	-10.71	-17.20	-0.00969	-2.67	0.71	-0.31
	Push 2	10.90	15.10	0.00648	-2.67	0.46	-0.22
	Pull 2	-10.64	-17.10	-0.01042	-2.67	0.77	-0.33
	Push 3	10.94	15.10	0.00687	-2.67	0.49	-0.23
	Pull 3	-10.63	-16.90	-0.01069	-2.67	0.79	-0.34
Ductility 2	Push 1	14.55	17.40	0.01245	-2.67	0.93	-0.38
	Pull 1	-14.26	-18.80	-0.01831	-2.67	1.42	-0.52
	Push 2	14.54	16.80	0.01425	-2.67	1.08	-0.42
	Pull 2	-14.28	-18.50	-0.01939	-2.67	1.50	-0.54
	Push 3	14.58	16.40	0.01474	-2.67	1.12	-0.43
	Pull 3	-14.27	-18.10	-0.01976	-2.67	1.53	-0.55
Ductility 3	Push 1	21.76	19.10	0.02662	-2.67	2.09	-0.72
	Pull 1	-21.64	-20.30	-0.03862	-2.67	3.06	-1.02
	Push 2	21.75	18.40	0.03037	-2.67	2.39	-0.81
	Pull 2	-21.68	-19.40	-0.04204	-2.67	3.33	-1.11
	Push 3	21.80	17.90	0.03297	-2.67	2.60	-0.87
	Pull 3	-21.63	-19.20	-0.04517	-2.67	3.58	-1.19

Table 10-23 continued

Cycle		Displ. (in)	Force (kips)	Max. Curvature (1/ft)	Depth to Max. Curv. (ft)	Tensile Strain (%)	Comp. Strain (%)
Ductility 4	Push 1	28.94	20.00	0.04873	-2.67	3.86	-1.28
	Pull 1	-29.24	-21.20	-0.06813	-2.67	5.40	-1.79
	Push 2	29.07	18.20	0.05216	-2.67	4.14	-1.36
	Pull 2	-29.21	-19.90	-0.07216	-2.67	5.71	-1.90
	Push 3	29.07	17.60	0.05472	-2.67	4.34	-1.43
	Pull 3	-29.31	-12.10	-0.09098	-2.67	7.18	-2.42

Table 10-24 Test 12: peak cycle data (D/t = 68; La = 7.24D; No surcharge)

Cycle		Displ. (in)	Force (kips)	Max. Curvature (1/ft)	Depth to Max. Curv. (ft)	Tensile Strain (%)	Comp. Strain (%)
1/4 Δy'	Push	1.24	3.75	0.00081	-4.67	0.05	-0.03
	Pull	-1.23	-3.88	-0.00067	-6.67	0.04	-0.03
1/2 Δy'	Push	2.57	6.00	0.00133	-4.67	0.09	-0.05
	Pull	-2.55	-5.99	-0.00112	-4.67	0.07	-0.05
3/4 Δy'	Push	3.88	7.98	0.00181	-4.67	0.12	-0.07
	Pull	-3.95	-7.92	-0.00160	-4.67	0.10	-0.06
Δy'	Push	5.24	10.12	0.00237	-4.67	0.15	-0.10
	Pull	-5.23	-10.01	-0.00219	-4.67	0.14	-0.09
Ductility 1	Push 1	8.02	14.21	0.00357	-4.67	0.23	-0.14
	Pull 1	-8.02	-14.03	-0.00323	-4.67	0.21	-0.13
	Push 2	8.03	15.07	0.00395	-4.67	0.26	-0.16
	Pull 2	-8.03	-14.11	-0.00322	-4.67	0.21	-0.13
	Push 3	8.02	16.38	0.00442	-4.67	0.29	-0.17
	Pull 3	-8.04	-14.66	-0.00335	-2.67	0.22	-0.13
Ductility 1.5	Push 1	12.06	20.62	0.00772	-2.67	0.54	-0.27
	Pull 1	-12.01	-19.76	-0.00611	-2.67	0.42	-0.22
	Push 2	12.01	21.00	0.00894	-2.67	0.64	-0.31
	Pull 2	-12.02	-19.72	-0.00637	-2.67	0.44	-0.23
	Push 3	12.01	21.42	0.01006	-2.67	0.72	-0.34
	Pull 3	-12.02	-19.62	-0.00656	-2.67	0.45	-0.24
Ductility 2	Push 1	16.03	23.16	0.01710	-2.67	1.28	-0.52
	Pull 1	-16.05	-22.34	-0.01327	-2.67	0.98	-0.42
	Push 2	16.01	23.00	0.01907	-2.67	1.44	-0.57
	Pull 2	-16.03	-21.35	-0.01298	-2.67	0.95	-0.42
	Push 3	16.03	22.85	0.02038	-2.67	1.55	-0.60
	Pull 3	-16.04	-21.86	-0.01431	-2.67	1.06	-0.45
Ductility 3	Push 1	24.19	25.31	0.03705	-2.67	2.87	-1.03
	Pull 1	-24.11	-25.44	-0.02923	-2.67	2.25	-0.83
	Push 2	24.15	24.40	0.03918	-2.67	3.04	-1.09
	Pull 2	-24.10	-24.16	-0.03081	-2.67	2.38	-0.87
	Push 3	24.15	23.48	0.04194	-2.67	3.26	-1.16
	Pull 3	-24.14	-23.92	-0.03459	-2.67	2.68	-0.97

Table 10-24 continued

Cycle		Displ. (in)	Force (kips)	Max. Curvature (1/ft)	Depth to Max. Curv. (ft)	Tensile Strain (%)	Comp. Strain (%)
Ductility 4	Push 1	28.29	25.13	0.06157	-2.67	4.81	-1.68
	Pull 1	-32.33	-27.35	-0.05936	-2.67	4.64	-1.62
	Push 2	28.30	23.85	0.06537	-2.67	5.11	-1.79
	Pull 2	-32.32	-11.53	-0.08162	-2.67	6.38	-2.23

APPENDIX C: Steel tube mill certs

12" O.D. 1/4"

11/1/2013

CERTIFIED REPORT OF CHEMICAL ANALYSIS AND MECHANICAL TESTS

ACCREDITED
TESTING CERT # 2914.01

This report will not be reproduced in whole or in part without the prior written approval from ArcelorMittal USA LLC.

SOLD TO	VENDOR
NAYLOR PIPE 1230 E 92ND STREET CHICAGO IL	ArcelorMittal Riverdale LLC. 13500 South Perry Avenue Riverdale, IL 60827

SHIP TO	ORDER INFORMATION
NAYLOR PIPE C/O NATIONAL PROCESSING C/O NATIONAL PROCESSING CO PLANT #2 4506 W CLINE AVE EAST CHICAGO IN	PO#: 55881 Invoice # 0500134855 SO#: 677455 Carrier: Sowka Express Shipped: 10/30/2013

DIMENSIONAL INFORMATION

Heat	Coil	Thickness (in)	Width (in)	Weight (tons)	Reduction Ratio
B07718	925563	0.238	59.750	28.8	89.01% (9:1)
B07718	925564	0.238	59.750	29.1	89.01% (9:1)

PRODUCT INFORMATION

Grade	Part Number	Comments
SAE 1022 MOD4	HB2385975-20	Conv to ASTM A252 Grade 3 w/ 50ksi min yield

This material was melted and manufactured in the USA. All products are strand cast and free of mercury or radioactive elements. Elongation based on 2" gage length.

MECHANICAL / PHYSICAL TEST RESULTS *

Heat	Coil	Yield (ksi)	Tensile (ksi)	El (%)	Dir	N-Value	N-Range	Hardness	Ft-lbs	°F	Size	Dir
B07718	925563	57.8KSI	75.0 KSI	31.0 %	T							
B07718		58.7KSI	75.1 KSI	28.0 %	T							

Note: Steel tubes with D/t = 48 → Specimens 1, 2, 9, 10

* Material tested in accordance with ISO 17025 by an accredited lab.

CHEMICAL TEST RESULTS (%wt)

Heat	C	Mn	P	S	Si	Cu	Ni	Cr	Mo	Cb	V	Al
B07718	.19	.73	.007	.002	.04	.02	.01	.02	.00	.001	.003	.039

N	Sn	B	Ti	Ca	Sb
.0067	.002	.0000	.0020	.0015	.0010

Chemical analysis was performed by ArcelorMittal Riverdale, Inc. in accordance with the Current revision of ASTM E415 and E1019.

We hereby certify the above is correct as contained in the records of the corporation. All tests peformed to the current standard to date unless otherwise noted. Uncertainties of measurements estimated and are available upon request. These results relate only to the items tested. Test results marked with an asterisk (*) were reported by an external accredited lab and with double asterisk(**) were reported by an internal labratory.

K.M. Clifford

Kevin M Clifford
Division Manager - Quality

Figure 10-248 Mill certifications for steel tubes with D/t = 48

12 3/4" OD 3/16"

GALLATIN STEEL

Gallatin Steel Company
4831 U.S. Highway 42 West
Ghent, KY, 41045-9704
Phone: 1(800)581-3853 Fax: (859)567-3165

METALLURGICAL TEST REPORT

InvoiceTo: Millennium Metal Corp
P.O. Box 649
Deerfield, IL 60015

Ship To: Millennium Metal Corp
Pick Up

Customer No: 5835
Mill Order No: 179139-5

Customer P.O. No: 3507
Customer Reference No: NA

Date: 01/10/14
Load No: 569521

This product was melted and manufactured in the USA to meet the requirements of:

Excess,
Excess HR Sheet Steel Bands

Ordered Size: Nom 0.185 (In.) X 43.02 (In.) X Coil

Coil Number(s): 1197871

CHEMICAL ANALYSIS (Weight %)

Heat No	C	Mn	P	S	Si	Cu	Ni	Cr	Mo	Al	Ca	Nb	V	B	Ti	N	Sn
A70028	0.20	0.70	0.011	0.004	0.03	0.11	0.05	0.05	0.02	0.032	0.0014	0.004	0.001	0.0001	0.002	0.0090	0.006

Note: Steel tubes with D/t = 68 → Specimens 7, 8, 12

Hot rolled coils manufactured through Gallatin Steel do not contain welds or weld repairs at the time of shipment (fca mill). Mercury was not added during production of this material. The material was produced using a fully killed fine grain practice.

Above tests performed in accordance to ASTM standards E8 (yield strength determined using 0.2% offset method and elongation determined using after fracture method) or JIS Z2241, E18, E415, and E1019 and are correct as contained in the records of the company.

The elongation original gage length is 2 inches for ASTM test method and 1.97 inches for JIS test method.
Above test results were performed in accordance to EN 10204 3.1

This report shall not be reproduced, except in full, without written approval of the undersigned laboratory managers.
* This mechanical property has been tested at a subcontractor's laboratory.

Stephen S. Sipple
Chemical Laboratory
Mechanical Laboratory

Page 1 of 1

The information contained in this report may be confidential information intended only for the use of the individual or entity named above.
If the reader of this message is not the intended recipient, you are hereby notified that any dissemination, distribution, or copying of this communication is strictly prohibited. If you have received this communication in error, please notify us immediately by telephone and destroy the original message. Thank You.

Figure 10-249 Mill certifications for steel tubes with D/t = 68

12 3/4" #10GA

11/1/2013

CERTIFIED REPORT OF CHEMICAL ANALYSIS AND MECHANICAL TESTS

ACCREDITED
TESTING CERT # 2914.01

This report will not be reproduced in whole or in part without the prior written approval from ArcelorMittal USA LLC.

SOLD TO	VENDOR
NAYLOR PIPE COMPANY	ArcelorMittal Riverdale LLC. 13500 South Perry Avenue Riverdale, IL 60827

SHIP TO	ORDER INFORMATION
NAYLOR PIPE	PO#: 55880 Invoice # SO#: 677454 Carrier: Shipped: 10/31/2013

DIMENSIONAL INFORMATION

Heat	Coil	Thickness (in)	Width (in)	Weight (tons)	Reduction Ratio
B07801	926294	0.238	57.037	25.6	89% (9:1)

Note: Steel tubes with D/t = 95 * → Specimens 3,4

PRODUCT INFORMATION

Grade	Part Number	Comments
SAE 1022 MOD4	HB2385675-04	Conv to ASTM A252 Grade 3 w/ 50ksi min yield

This material was melted and manufactured in the USA. All products are strand cast and free of mercury or radioactive elements. Elongation based on 2" gage length.

MECHANICAL / PHYSICAL TEST RESULTS *

Heat	Coil	Yield (ksi)	Tensile (ksi)	El (%)	Dir	N-Value	N-Range	Hardness	Ft-lbs	°F	Size	Dir
B07801	926294	57.6KSI	77.0 KSI	27.0 %	T							
B07801		58.8KSI	77.1 KSI	26.0 %	T							
B07801	926297	64.0KSI	81.8 KSI	23.0 %	L							
B07801		63.7KSI	81.6 KSI	24.0 %	L							

* Material tested in accordance with ISO 17025 by an accredited lab.

CHEMICAL TEST RESULTS (%wt)

Heat	C	Mn	P	S	Si	Cu	Ni	Cr	Mo	Cb	V	Al
B07801	.19	.79	.010	.002	.03	.02	.01	.02	.00	.002	.005	.043

N	Sn	B	Ti	Ca	Sb
.0091	.002	.0000	.0020	.0013	.0010

Chemical analysis was performed by ArcelorMittal Riverdale, Inc. in accordance with the Current revision of ASTM E415 and E1019.

We hereby certify the above is correct as contained in the records of the corporation. All tests peformed to the current standard to date unless otherwise noted. Uncertainties of measurements estimated and are available upon request. These results relate only to the items tested. Test results marked with an asterisk (*) were reported by an external accredited lab and with double asterisk(**) were reported by an internal labratory.

K.M. Clifford

Kevin M Clifford
Division Manager - Quality

Figure 10-250 Mill certifications for steel tubes with D/t = 95*

12/9/2014

ACCREDITED

TESTING CERT # 2914.01

CERTIFIED REPORT OF CHEMICAL ANALYSIS AND MECHANICAL TESTS

ArcelorMittal

This report will not be reproduced in whole or in part without the prior written approval from ArcelorMittal USA LLC.

SOLD TO	VENDOR
NAYLOR PIPE COMPANY	ArcelorMittal Riverdale LLC. 13500 South Perry Avenue Riverdale, IL 60827
SHIP TO	**ORDER INFORMATION**
NAYLOR PIPE	PO#: 56098 Invoice # SO#: 755625 Carrier: Date Of Issuance/Shipped: 12/5/2014

DIMENSIONAL INFORMATION

Heat	Coil	Thickness (in)	Width (in)	Weight (tons)	Reduction Ratio
A42826	964855	0.128	57.155	26.3	94.09% (17:1)
A42826	964856	0.128	57.162	25.2	94.09% (17:1)
A42826	964857	0.128	57.189	25.2	94.09% (17:1)

HEAT NUMBER IS BEING USED AS CERTIFICATE NUMBER. COUNTRY OF ORIGIN/EXPORT COUNTRY IS USA. FOR QUESTIONS CONCERNING IMPORTATION OF THIS MATERIAL PLEASE CONTACT: JOSE CISNEROS; 1 SOUTH DEARBORN ST. , CHICAGO, IL, 60603; TEL +11 (312) 899.3796 EML Jose.Cisneros@arcelormittal.com

PRODUCT INFORMATION

Grade	Part Number	Product Description	Comments
SAE 1022 MOD4	HB1285675-09	Hot Band Prime	A-252 Grade 3 with 50,000 min yield

This material was melted and manufactured in the USA. All products are strand cast and free of mercury or radioactive elements. Elongation based on 2" gage length.

MECHANICAL / PHYSICAL TEST RESULTS *

Heat	Coil	Yield (ksi)	Tensile (ksi)	El (%)	Dir	N-Value	N-Range	Hardness	Ft-lbs	°F	Size	Dir
A42826	964855	60.9KSI	79.2 KSI	28.0 %	L							

Note: Steel tubes with D/t=95 → Specimens 5, 6, 11

* Material tested in accordance with ISO 17025 by an accredited lab.

CHEMICAL TEST RESULTS (%wt)

Heat	C	Mn	P	S	Si	Cu	Ni	Cr	Mo	Cb	V	Al
A42826	.20	.76	.008	.003	.05	.03	.02	.03	.00	.001	.006	.031

N	Sn	B	Ti	Ca	Sb
.0038	.003	.0001	.0030	.0019	.0010

Chemical analysis was performed by ArcelorMittal Riverdale, Inc. in accordance with the Current revision of ASTM E415 and E1019.

We hereby certify the above is correct as contained in the records of the corporation. All tests peformed to the current standard to date unless otherwise noted. Uncertainties of measurements estimated and are available upon request. These results relate only to the items tested. Test results marked with an asterisk (*) were reported by an external accredited lab and with double asterisk(**) were reported by an internal labratory.

R. N. Fritz

Ryan N Fritz
Manager - Quality
13500 South Perry Ave., Riverdale IL 60827
T+708 392 1077 | Ryan.Fritz@ArcelorMittal.com

Figure 10-251 Mill certifications for steel tubes with D/t = 95

12 3/4" 3/16"

KIEH

METALLURGICAL SERVICES
(708) 544-8811 544-8820 FAX

We accept no responsibility nor liability for results derived from misinformation, nor samples not representative of the corresponding material, nor a limited sampling plan nor insufficient testing. The information provided is for the private use of our client and may not be published without our expressed consent.

Laboratory:
837 MANNHEIM RD.
BELLWOOD, IL 60104

Date received 06-Mar-2014
05-Mar-2014
Report 114 10042 a of e pages
Account 1302
P.O. 3490

Naylor Pipe Company
1230 E. 92nd St.
Chicago, IL 60619-7997

Attn : James Martin

our 35th year est. 1979

Test report /

Sample identity	Y.S. lbs/in^2	T.S. lbs/in^2	%E 2"
E48599 3/16x20&22" Gallatin A70028	52,500	74,500	31.0

Minimum requirements of an ASTM:

A139 grB	35,000	60,000	24.00
A252 gr2	35,000	60,000	20.00
A252 gr3	45,000	66,000	16.00

This samples reported properties conform to the requirements of an ASTM:
A139 grB / A252 gr2 / A252 gr3 material.

Mechanical:ASTM E8/A370 Y.S.0.2%offset []trans. *broke out of g.l. !1"g.l.

Figure 10-252 Mill certifications for steel tubes labeled as ASTM A-139 Gr. B Steel

APPENDIX C: Internal reinforcement mill certs

Page 1 of 1

GERDAU

CHARLOTTE STEEL MILL
6601 LAKEVIEW ROAD
CHARLOTTE NC 28269 USA

Chemical and Physical Test Report

MADE IN UNITED STATES

CUSTOMER: NORTH CAROLINA STATE UNIV.

PROJECT: A706 RESEARCH

SHAPE + SIZE	GRADE	SPECIFICATION	SALES ORDER	CUST P.O. NUMBER
X16MM REBAR (# 5)	420 (60)A706	ASTM A706-08A & ASTM A706-08 &ASTM A706-09B		

HEAT I.D.	C	Mn	P	S	Si	Cu	Ni	Cr	Mo	V	Sn	C Eqv
C015969	.27	1.12	.016	.041	.21	.38	.10	.14	.020	.031	.013	.48

Mechanical Test: Yield 68642 PSI, 473.27 MPA Tensile: 91510 PSI, 630.94 MPA %El: 17.6/8in, 17.6/200MM Bend: OK Def HT: .052, 1.32MM Def Gap: .125, 3.18MM Def SP: .375, 9.53MM %l/h 3.7L Red R 81

Customer Requirements CASTING: STRAND CAST

Mechanical Test: Yield 68358 PSI, 471.31 MPA Tensile: 91103 PSI, 628.13 MPA %El: 20.0/8in, 20.0/200MM Bend: OK Def HT: .049, 1.24MM Def Gap: .125, 3.18MM Def SP: .387, 9.83MM %l/h 4.2L Red R 81

Customer Requirements CASTING: STRAND CAST

Note: Longitudinal #5 bars phase 1 → Specimens 1,2,3,4

This material, including the billets, was melted and manufactured in the United States of America

Bhaskar Yalamanchili
Quality Director
Gerdau

THE ABOVE FIGURES ARE CERTIFIED CHEMICAL AND PHYSICAL TEST RECORDS AS CONTAINED IN THE PERMANENT RECORDS OF COMPANY.

Metallurgical Services Manager
CHARLOTTE STEEL MILL

Seller warrants that all material furnished shall comply with specifications subject to standard published manufacturing variations. NO OTHER WARRANTIES, EXPRESSED OR IMPLIED, ARE MADE BY THE SELLER, AND SPECIFICALLY EXCLUDED ARE WARRANTIES OF MERCHANTABILITY AND FITNESS FOR A PARTICULAR PURPOSE.
In no event shall seller be liable for indirect, consequential or punitive damages arising out of or related to the materials furnished by seller.
Any claim for damages for materials that do not conform to specifications must be made from buyer to seller immediately after delivery of same in order to allow the seller the opportunity to inspect the material in question.

Figure 10-253 Mill certifications for #5 (longitudinal) bars (Tests 1, 2, 3, 4)

EVRAZ ROCKY MOUNTAIN STEEL
A DIVISION OF EVRAZ INC. NA

P.O. Box 316
Pueblo, CO 81002 USA

MATERIAL TEST REPORT

Date Printed: 23–MAY–14

Date Shipped: 23–MAY–14 **Product:** DEF #3 (3/8") **Specification:** ASTM A–706/A–615

FWIP: 52815363 **Customer:** STEEL SPECIALTIES OF MISSISSIPPI INC **Cust. PO:** TODD 5–21

CHEMICAL ANALYSIS

(Heat chemistry entered 03/17/14)

Heat Number	C	Mn	P	S	Si	Cu	Ni	Cr	Mo	Al	V	B	Cb	Sn	N	Ti
112038 C	.26	1.23	.013	.019	.25	.03	.09	.11	.023	.002	.043			.012	.0119	

MECHANICAL PROPERTIES

Heat Number	Sample No.		Yield (Psi)	Ultimate (Psi)	Elongation (%)	Reduction (%)	Bend	Wt/ft
112038	01	0.2% offset	73552	106970	14.1		ok	0.380
112038	02		70527	106860	15.0		ok	0.379
		0.0035 EUL						

Note: Spirals phase 1 → specimens 1,2,3,4

All melting and manufacturing processes of the material subject to this test certificate occurred in the United States of America.
ERMS also certifies this material to be free from Mercury contamination.

This material has been produced and tested in accordance with the requirements of the applicable specifications. We hereby certify that the above test results represent those contained in the records of the Company.

Mark F Espamer

Quality Assurance Department

Figure 10-254 Mill certifications for #3 spirals utilized for tests specimens 1, 2, 3, 4

GERDAU

US-ML-CHARLOTTE
6601 LAKEVIEW ROAD
CHARLOTTE, NC 28269
USA

CERTIFIED MATERIAL TEST REPORT

Page 1/1

CUSTOMER SHIP TO	CUSTOMER BILL	GRADE	SHAPE / SIZE
GERDAU AMERISTEEL US INC 301 BLACK SATCHEL DRIVE CHARLOTTE,NC 28216 USA		A706-60	Rebar / #5 (16MM)

LENGTH	WEIGHT	HEAT / BATCH
60'00"	0	**54144510**/02

SALES ORDER	CUSTOMER MATERIAL Nº	SPECIFICATION / DATE or REVISION
		ASTM A706/A706M-14

CUSTOMER PURCHASE ORDER NUMBER	BILL OF LADING	DATE

CHEMICAL COMPOSITION

C %	Mn %	P %	S %	Si %	Cu %	Ni %	Cr %	Mo %	Sn %	V %	Nb %	CEqvA706 %
0.29	1.23	0.017	0.031	0.20	0.42	0.15	0.11	0.030	0.014	0.030	0.002	0.52

MECHANICAL PROPERTIES

YS PSI	YS MPa	UTS PSI	UTS MPa	G/L Inch	Elong. %
73410	506	100248	691	8.000	17.60

MECHANICAL PROPERTIES

BendTest
OK

GEOMETRIC CHARACTERISTICS

%Light %	Def Hgt Inch	Def Gap Inch	DefSpace Inch
5.80	0.049	0.133	0.394

COMMENTS / NOTES

Note: Long. #5 bars phase 2 → Specimens 5,6,7,8

The above figures are certified chemical and physical test records as contained in the permanent records of company. We certify that these data are correct and in compliance with specified requirements. This material, including the billets, was melted and manufactured in the USA. CMTR complies with EN 10204 3.1.

BHASKAR YALAMANCHILI
QUALITY DIRECTOR

JORDAN FOSTER
QUALITY ASSURANCE MGR.

Figure 10-255 Mill certifications for #5 (longitudinal) bars utilized in test specimens 5, 6, 7, and 8

EVRAZ ROCKY MOUNTAIN STEEL
A DIVISION OF EVRAZ INC. NA

2100 S. Freeway
Pueblo, CO 81004 USA

MATERIAL TEST REPORT

Date Printed: 22–JUN–15

Date Shipped: 22–JUN–15 | Product: BAR #3 (3/8") | Specification: ASTM A–706 / A–615

FWIP: 52815366 | Customer: STEEL SPECIALTIES OF MISSISSIPPI INC | Cust. PO: todd 06182015

CHEMICAL ANALYSIS (In Weight %, uncertainty of measurement 0.005%) (Heat cast 05/21/15)

Heat Number	C	Mn	P	S	Si	Cu	Ni	Cr	Mo	Al	V	B	Cb	Sn	N	Ti
579906	0.28	1.22	0.009	0.020	0.24	0.18	0.07	0.08	0.019	0.002	0.037	0.0004	0.000	0.010	0.0084	0.001

Carbon Equivalent = 0.495

Note: Spirals phase 2 → Specimens 5, 6, 7, 8

MECHANICAL PROPERTIES (Tensiles test date 05/27/15)

Heat Number	Sample No.		Yield (Psi)	Ultimate (Psi)	Elongation (%)	Reduction (%)	Bend	Wt/ft
579906	01		66572	99360	15.9		ok	0.373
		(MPa)	459.0	685.1				
579906	02		65887	100690	16.1		ok	0.374
		(MPa)	454.3	694.2				

All melting and manufacturing processes of the material subject to this test certificate occurred in the United States of America.
ERMS also certifies this material to be free from Mercury contamination.

This material has been produced, tested and conforms to the requirements of the applicable specifications. We hereby certify that the above test results represent those contained in the records of the Company.

Valoree V. Varick

Valoree Varick
General Supervisor of Quality

Figure 10-256 Mill certifications for #3 spirals utilized for tests specimens 5, 6, 7, and 8

GERDAU

US-ML-CHARLOTTE
6601 LAKEVIEW ROAD
CHARLOTTE, NC 28269
USA

MADE IN UNITED STATES

Page 1/1

CUSTOMER SHIP TO	CUSTOMER BILL TO	GRADE	SHAPE / SIZE
NORTH CAROLINA STATE UNIV DEPT 2414 CAMPUS SHORE DR RALEIGH,NC 27695 USA	NORTH CAROLINA STATE UNIV RALEIGH,NC 27695-0001 USA	A706-60	REBAR ROUND / #5 (16MM)
		LENGTH	FABRICATION PLANT US-FB-RALEIGH 2126 GARNER ROAD RALEIGH, NC 27610 USA
SALES ORDER 3508228/000030		SPECIFICATION / DATE or REVISION ASTM A706/A706M-14	

CUSTOMER PURCHASE ORDER NUMBER	BILL OF LADING	DATE
04233182	2840-0000005074	03/28/2016

HEAT/BATCH	C %	Mn %	P %	S %	Si %	Cu %	Ni %	Cr %	Mo %	Sn %	V %	Nb %	CEqvA70 %	YS PSI	YS MPa	UTS PSI	UTS MPa	G/L Inches	Elong. %	BendTes	%Light %	Def Hgt Inches	Def Gap Inches	DefSpac Inches
5414130902	0.29000	1.18	0.01	0.029	0.200	0.40	0.09	0.12	0.02	0.011	0.036	0.002	0.51	73237	505	96029	662	8.000	17.8	OK.	4.10	0.051	0.109	0.394

COMMENTS / NOTES

Note: longitudinal #5 bars phase 3 → Specimens 9, 10, 11, 12

The above figures are certified chemical and physical test records as contained in the permanent records of company. We certify that these data are correct and in compliance with specified requirements. This material, including the billets, was melted and manufactured in the USA. CMTR complies with EN 10204 3.1.

Bhaskar — BHASKAR YALAMANCHILI, QUALITY DIRECTOR

Jordan Foster — JORDAN FOSTER, QUALITY ASSURANCE MGR.

Figure 10-257 Mill certifications for #5 (longitudinal) bars utilized in test specimens 9, 10, 11, and 12

NUCOR
NUCOR STEEL CONNECTICUT, INC.

Mill Certification
3/15/2016

MTR #: W1-179011
35 Toelles Road
WALLINGFORD, CT 06492
(203) 265-0615
Fax: (203) 284-8125

Sold To: STEEL SPECIALTIES
PO BOX 54128
PEARL, MS 39288-4128
(601) 939-2690

Ship To: (REB) STEEL SPECIALTIES
111 MIDCO RD
PEARL, MS 39288-4128
(601) 939-2690

Customer P.O.	Verball.Todd.3.14.16	Sales Order	233198.1
Product Group	Rebar	Part Number	95010276CT38000
Grade	ASTM A615-15a / A706-15 & AASHTO M 31-15 Gr 60	Lot #	WL1690000519
Size	#3 Rebar (Coil)	Heat #	AU15106039
Product	#3 Coiled Rebar - 28'6 ASTM A615/A706 GR60	B.L. Number	W1-476854
Description	A615/A706 GR60 (CT1)	Load Number	W1-179011
Customer Spec		Customer Part #	

I hereby certify that the material described herein has been manufactured in accordance with the specifications and standards listed above and that it satisfies those requirements.

Melt Date: 10/12/2015

C	Mn	P	S	Si	Cu	Ni	Cr	Mo	V	Cb	Sn
0.28%	1.16%	0.022%	0.042%	0.26%	0.41%	0.12%	0.21%	0.028%	0.0310%	0.001%	0.022%
CEA706 0.51%											

CEA706: A706 CARBON EQUIVALENT

Roll Date: 1/24/2016

Yield 1: 70,100psi
Bend OK

Tensile 1: 103,400psi
Tensile/Yield: 1.47

Elongation: 16.3% in 8"(% in 203.3mm)

Specification Comments:

1. Except where noted, all manufacturing processes including melting were performed in the USA.
2. No mercury, mercury compounds or mercury containing devices came into contact with this product.
3. Weld repair was not performed on this material.
4. Hexavalent Chromium, Radium or Alpha Source materials in in any form were not used in the production or testing of this material

Note: #3 spirals phase 3 → specimens 9, 10, 11, 12

Charlie Hyatt
Division Metallurgist

NBMG-10 January 1, 2012

Page 1 of 1

Figure 10-258 Mill certifications for #3 spirals utilized for tests specimens 9, 10, 11, and 12